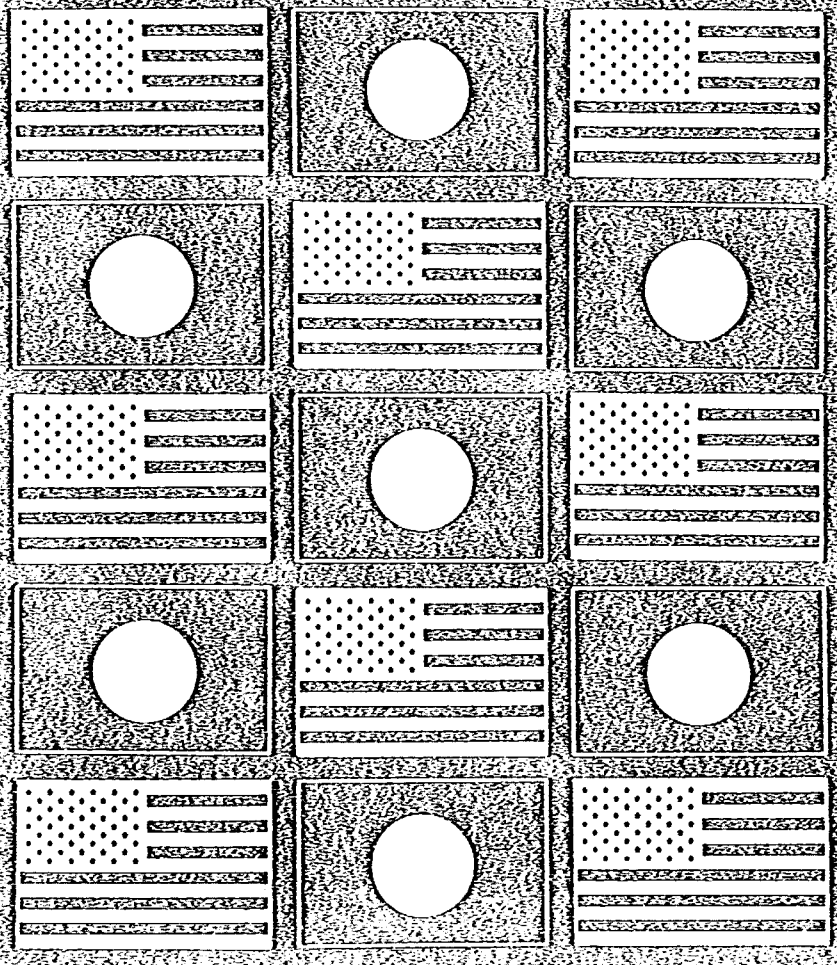
ISSN 0386-5878
Technical Memorandum
of PWRI No. 3230

PROCEEDINGS OF THE NINTH U.S. - JAPAN BRIDGE ENGINEERING WORKSHOP



MAY 10 - 11, 1993

PUBLIC WORKS RESEARCH INSTITUTE

TSUKUBA SCIENCE CITY, JAPAN

Copyright ©1994 by P.W.R.I.

All rights reserved. No part of this book may be reproduced by any means, nor translated into a machine language without the written permission of the Director General of P.W.R.I.

この報告書は，土木研究所長の承認を得て刊行したものである。したがって，本報告書の全部又は一部の転載，複製は，土木研究所長の文書による承認を得ずしてこれを行ってはならない。

Technical Memorandum
of PWRI No. 3230

PROCEEDINGS OF THE NINTH U.S.-JAPAN BRIDGE ENGINEERING WORKSHOP

MAY 10 AND 11, 1993
PUBLIC WORKS RESEARCH INSTITUTE
TSUKUBA SCIENCE CITY, JAPAN

Synopsis:

These proceedings document the results of the 9th U.S.–Japan Bridge Engineering Workshop which was held at the Public Works Research Institute, Tsukuba Science City, Japan, on May 10 and 11, 1993 under the auspices of the Panel on Wind and Seismic Effects, UJNR. The Workshop was organized by the Task Committee J "Wind and Earthquake Engineering for Transportation Systems" (U.S. side chairman: J.D. Cooper, FHWA, Japan side chairman: M. Fujiwara) of the Panel.

Key word: Bridge, Design Method, Seismic Design, Wind Resistant Design, Maintenance Technology

FORWARD

These proceedings document the results of the 9th U.S.–Japan Bridge Engineering Workshop which was held at the Public Works Research Institute, Tsukuba Science City, Japan, on May 10 and 11, 1993 under the auspices of the Panel on Wind and Seismic Effects, UJNR. The Workshop was organized by the Task Committee J "Wind and Earthquake Engineering for Transportation Systems" (U.S. side chairman: J.D. Cooper, FHWA, Japan side chairman: M. Fujiwara) of the Panel. The Workshop was coordinated by Mr. K. Nishikawa, Head of Bridge Division of the Public Works Research Institute.

The purposes of the Workshop are:

(1) To stimulate collaborative research work in the important area of bridge engineering for better design construction, performance, rehabilitation, and strengthening of bridge structures in both countries.
(2) To facilitate the exchange of technical information and ideas and to promote the broadening of viewpoints for those involved.
(3) To ensure a first-hand exchange of information resulting form the unique problems each country is faced with; for example, the development and implementation of bridge management systems and limit state or load and resistant factor design methods.

A broad range of special technical topics were presented at the Workshop. These included the following items.

1) Dynamic control and seismic isolation of bridge structures
2) System identification techniques for wind and seismic engineering
3) Nondestructive evaluation techniques
4) Experimental and analytical studies on the effects of dynamic soil characteristics
5) Retrofitting and strengthening methodologies for bridge structures
6) Development of design criteria based on limit-state concepts
7) Jointless bridge design
8) Use and performance of new and enhanced structural materials
9) Development of standard test procedures for base isolation devices

In total 31 papers were presented in the Workshop; 17 papers from Japan side and 14 papers from the U.S. side.

The following proceedings include (1) all technical papers that were presented during the Workshop in their order of presentation, (2) the resolutions that were unanimously ap-

proved by the participants during the closing session of the Workshop, (3) Workshop program and list of participants, and (4) photos of the Workshop and Study Tour.

In concluding the forward, I wish to express our profound gratitude and sincere appreciation to all participants in the Workshop for supporting the Workshop by active presentations and discussion. In particular, I would like to thank Prof. Bruce M. Douglas and Prof. Emmanuel A. Maragakis for organizing the U.S. members. And I would like to thank Mr. James D. Cooper his encouragement for holding the Workshop.

January 1994

Minoru Fujiwara
Structure and Bridge Department
Public Works Research Institute

TABLE OF CONTENTS

Papers

(2) Session 2 Superstructure (1) 1

1) Structural Behavior of Prestressed Concrete Beams Using FRP Tendons 3
(K. Nishikawa, M. Kanda* and K. Uchida)

2) Management Decisions for Bridge Deck Rehabilitation/Replacement 11
(G. Runco* and P. Brinckerhoff)

3) Damage and Its Reinforcement of Post-tensioned Prestressed Concrete Bridge Slab 27
(I. Sugie*, Y. Yamaguchi, K. Kobayashi and K. Kuzume)

(3) Session 3 Superstructure (2) 35

4) Strengthening of Steel-Stringer Bridges by Post-Tensioning 37
(F.W. Klaiber*, K.F. Dunker, T.J. Wipf and F.S. Fanous)

5) Application of Buried Joint in Cold and Snowy Region 51
(T. Shirono*, H. Nishi, O. Nakano and K. Kumagai)

(4) Session 4 Wind Resistant Design (1) 67

6) An Experimental Study on Aerodynamic Sound Generated From Handrails of Flat Plate Cascades 69
(K. Kimura, Y. Fujino* and S. Hiejima)

7) Simulation Techniques for Bridge Aerodynamic Investigations at the Turner-Fairbank Highway Research Center 79
(O.U. Onyemelukwe and H.R. Bosch to be presented by J.D. Cooper)

8) Analytical Study on Flutter of Suspension Bridge 95
(H. Sato and R. Toriumi*)

(5) Session 5 Wind Resistant Design (2) 107

9) Aerodynamic Stability of Central Nagoya Port Bridge 109
(K. Nomura*, Y. Suzuki, K. Kuroda and Y. Igase)

10) Aerodynamic Stability of Nakajima Bridge (Provisional Name) 123
(M. Kamei*, M. Kawakami, K. Ikushima, H. Tanaka and M. Hosomi)

11) Aerodynamic Stability of Trans-Tokyo-Bay Highway Bridge 137
(Y. Shioi, Y. Yoshida and K. Saga*)

(6) Session 6 Seismic Design (1) 147

12) An Experimental Study of Horizontal Displacement Behavior Using Large-Size Model Pier 149
(K. Kosa, Y. Hashimoto and K. Kobayashi)

13) Comparison of the Seismic Design of Highway Bridges in California and in Japan 161
(M. Sultan* and K. Kawashima)

14) Analysis of Ground Motion Characteristics 177
(H. Ohtsuka, K. Tokida, K. Tamura, M. Kaneko* and H. Fukada)

(7) Session 7 Seismic Design (2) **193**

15) Seismic Base Isolation of Curved Highway Bridges 195
(K.H. Chen and D.A. Foutch*)

16) Evaluation of Modal Damping Ratio of Bridges Based on Strain Energy Proportional Method 211
(K. Kawashima*, H. Nagashima and H. Iwasaki)

17) Developments in Seismic Prioritization of Bridges in California 227
(A.D. Gilbert*)

(8) Session 8 Seismic Design (3) **241**

18) Structural Modeling Implications from Snap-Back Tests on a Slab-on-Girder Bridge 243
(S.S. Chen*, J.B. Mander, D.S. MacEwan and D.K. Kim)

19) Seismic Response of Reinforced Concrete Bridge Piers subjected to Eccentric Loading 257
(K. Kawashima, S. Unjoh* and H. Mukai)

20) Evaluation of the Seismic Response of Bridges with Hinge Restrainers 273
(E. Maragakis*, M. Saiidi, S. Feng, S. Abdel-Ghaffar and D. O'Connor)

21) Dynamic Strength and Ductility Characteristics of Steel Bridge Piers 289
(K. Kawashima, H. Sugita* and T. Nakajima)

(9) Session 9 Seismic Design (4) **309**

22) SR5 Lake Washington Ship Canal Bridge Seismic Vulnerability Assessment 311
(J.H. Clark*)

23) Research on Adoption of Vane-Dampers for the Tsurumi Fairway Bridge 325
(N. Ito* and M. Okada)

24) Seismic Performance and Retrofit of the Golden Gate Bridge 339
(C. Seim*, S. Rodriguez and T. Ingham)

25) Lateral-Load Response Models of a Reinforced Concrete Bridge 353
(M. Eberhard)

(10) Session 10 Substructure (1) **369**

26) Retrofit of Bridge Footings for Improved Seismic Performance 371
(Y. Xiao*, M.J.N. Priestley, F. Seible and N. Hamada)

27) Earthquake Resistant Capacity of RC Pier Retrofitted with Carbon Fibre 385
(N. Ogata, Y. Maeda, A. Murayama, H. Andoh*, Y. Kobatake and S. Ohno)

28) Retrofit Solutions for Inadequate Anchorage of Column Bars into Pier Caps 401
(D.H. Sanders, B.M. Douglas* and K. Cornell)

(11) Session 11 Substructure (2) **415**

29) Vertical Bearing Capacity of Shallow Foundations 417
(M. Okahara, M. Nakano, Y. Kimura*, K. Chimi and A. Inoue)

30) Evaluation and Upgrading of Multi-Column Bridges 431
(J.P. Moehle*, C.R. Thewalt and S.A. Mahin)

31) Designing the Substructure of the Main Tower of Hakucho Ohashi Bridge 449
(K. Kumagai, M. Takahashi, S. Nishimoto and Y. Saito*)

Resolution **465**

Appendices **469**

Workshop Program 471

List of Participants 479

Photos of Study Tour 489

(2) Session 2

Superstructure (1)

1) Structural Behavior of Prestressed Concrete Beams Using FRP Tendons
(K. Nishikawa, M. Kanda* and K. Uchida)

2) Management Decisions for Bridge Deck Rehabilitation/Replacement
(G. Runco* and P. Brinckerhoff)

3) Damage and Its Reinforcement of Post-tensioned Prestressed Concrete Bridge Slab
(I. Sugie*, Y. Yamaguchi, K. Kobayashi and K. Kuzume)

Structural Behavior of Prestressed Concrete Beams Using FRP Tendons

Kazuhiro Nishikawa
Head, Bridge Division
Public Works Research Institute, Ministry of Construction

Masayuki Kanda
Researcher, Bridge Division
Public Works Research Institute, Ministry of Construction

Kenichi Uchida
Bridge Division
Public Works Research Institute, Ministry of Construction

SUMMARY

The data necessary for the design of bridges could be obtained from the tests of the bending and shearing, and the bending fatigue for the prestressed concrete beams using various FRP tendons. It is possible to calculate flexural capacity according to the plane holding's law. When shear capacity is calculated based on the Japan specifications for highway bridge, it is within the limits of safe side well. The properties of bending fatigue assumed serviceability limit state was good. Further,the bending fatigue produced bending cracks,it had good flexural capacity.

1.INTRODUCTION

FRP materials are receiving attention as reinforcement materials in concrete members,because of their high strength,light weight,non-magnetic and resistance to corrosion. Its application has been studied at various fields. Among the rest, the method using FRP prestressing tendon is supposed to be superior on the material properties of FRP and the cost. The object of this study is to develop a new technique for the tendons of prestressed concrete bridges,as a part of Comprehensive Research and Development Project "Development of New Base Materials and New Materials Utilization Techniques in Construction Project", Ministry of Construction since 1989.

This paper describes the dynamic properties of the prestressed concrete beams using various FRP tendons, and intends to propose design technique.

2.SPECIFICATIONS OF FRP TENDONS

The specifications of the FRP tendons used for this study are shown in table 1. There are five types in the FRP tendons applied for prestressed concrete as tendons: two types using carbon fibers, two types using aramid fibers and one type using glass fibers. For the experiment, we used four types except glass fibers.

Table 1 Charactristics of FRP tendons

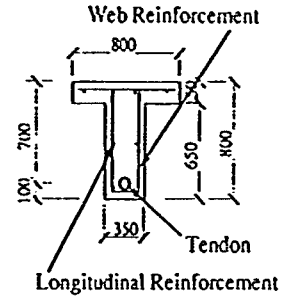
Tendon	Shape	Nominal Diameter (mm)	Nominal Tensile Strength (MPa)	Average Tensile Strength (MPa)	Young's Modulus (MPa)	Elongation (%)
C1	Strand	12.5	1885	2188	137000	1.6
C2	Rod	8.0	1550	2109	148000	1.2
A1	Braid	12.0	1263	1295	60800	2.2
A2	Rod	6.0	1777	1942	53000	3.3
G	Rod	8.0	1480	1687	44100	2.6

3.STATIC BENDING TEST

Stress-strain relations of FRP tendons are different from that of steel, and they have linearity up to break. Therefore, it has been considered to show flexural properties different from that of prestressed concrete members using prestressing steel. In order to clarify the flexural properties and the calculating method of the flexural capacity of the prestressed concrete beams using FRP tendons, the static bending tests of the prestressed concrete beams made by pretensioning and post tensioning systems were performed.

3.1 Outline of Experiment

The section and loading method of the pretensioning beams are shown in Fig.1. The section of the beams was rectangular: 250mm deep and 350mm wide. In order to adjust failure mode, the quantities of FRP tendons and effective depth of beams were changed. The loading method was the symmetric four-point loading of 3000mm span. The parameters and results of the experiment are shown in table 2. As for the parameters, there are five levels by the types of tendons, two levels of 40% (0.4Pu) and 60% (0.6Pu) of the nominal tensile strength as the magnitude of effective prestressing



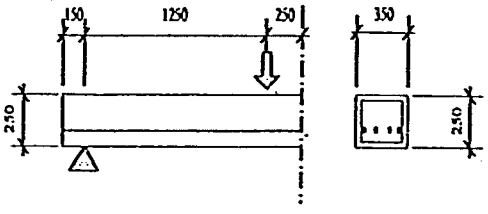


Fig.1 Pretensioning beam specimens

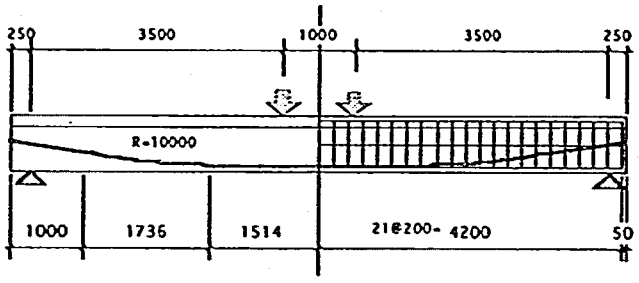


Fig.2 Posttensioning beam specimens

Table 2 Summary of pretensioning beams data in static bending test

Specimen tendon-prestress-failure-stage	Speciment details				Bending crack load			Bending ultimate load		
	fc (MPa)	Ap (mm^2)	Prestressing force (kN)	Effectiv depth (mm)	Calculated (kN)	Measured (kN)	Calculated / Measured	Calculated (kN)	Measured (kN)	Calculated / Measured
C1-06-T-1	48.9	228	256	167	37.4	39.2	1.05	117	124	1.06
C1-04-T-1	58.7	228	171	167	54.2	31.4	0.58	115	124	1.08
C1-06-T-2	48.9	228	256	167	53.1	56.9	1.07	110	120	1.10
C1-06-C-1	42.6	456	512	167	81.1	80.4	0.99	167	175	1.04
C2-06-T-1	53.4	264	247	167	42.2	33.4	0.79	129	145	1.13
C2-04-T-1	54.8	264	165	167	54.0	58.9	1.09	129	146	1.13
C2-06-T-2	42.4	264	247	167	53.1	54.9	1.04	114	134	1.17
C2-06-C-1	54.5	264	247	75	16.3	17.7	1.08	39	51	1.30
A1-06-T-1	46.5	180	135	167	27.0	25.5	0.95	48	74	1.53
A1-04-T-1	47.7	180	90	167	36.6	31.4	0.86	46	71	1.54
A1-06-T-2	49.5	270	204	167	47.9	45.3	0.95	65	104	1.59
A1-06-C-1	45.1	540	407	167	70.1	62.8	0.90	142	153	1.08
A2-06-T-1	38.8	113	120	200	37.2	41.2	1.11	63	78	1.24
A2-04-T-1	63.6	113	80	200	43.2	47.1	1.09	63	76	1.21
A2-06-T-2	42.4	170	181	183	57.0	56.9	1.00	83	104	1.26
A2-06-C-1	53.5	340	360	167	65.8	84.4	1.28	133	175	1.32
PC-06-Y-1	52.3	279	287	167	54.2	54.0	1.00	129	124	0.96
PC-06-Y-2	50.3	279	287	167	56.7	62.8	1.11	127	122	0.96

force, two levels of a tendon break mode(T) and concrete compressive failure mode(C), and two levels of one stage and two stages arrangement of tendons.

The section and loading method of the post tensioning beams are shown in Fig.2. The section was a T-beam:with an effective depth of 700mm,compressive flange width of 800mm. Each FRP tendon was multi-cables. FEP pipes are used for the sheathes. The loading method was a symmetric four-point loading of 8000mm span. The parameters and results of the experiment are shown in table 3. The experimental parameters have five levels as the types of tendons.

3.2 Results of Experiment

The calculated values in the table 3 were calculated by the following way. The flexural crack load is the load which brings the stress of the lower edge concrete up to the tensile strength (cylinder crack-split tensile strength). The flexural capacity is a smaller load either which brings the stress of the tendons at the most tensile side up to its average tensile strength or which brings the strain of the upper edge concrete up to 0.0035.

Pretensioning beam specimens

The calculated value of the flexural crack load of every specimen almost agrees with the measured value. Therefore, it is understandable that the concrete compressive stress due to prestressing in each specimen is almost introduced. The calculated value of the flexural capacity is within a safety side, though it indicates the amount of scatter. The scatter is due to the indistinctness of the tensile strength of FRP tendons in the members of the pretensioning beams. It is considered that the result of tensile test, as it is, is not equivalent to the tensile strength of the FRP tendons in the members. And the specimens lost capacity with the compressive failure of concrete including the members using prestressing steel also vary widely. As for the influence of the arrangement number of stages on flexural capacity, the two stages specimens are a little larger than that of one stage specimens. In the case of multiple stages, the calculating method of this paper is within the safety side. Therefore, the method using the effective depth of beam is supposed to be dangerous because FRP tendons have no plastic range. As for the influence of effective tensile force on flexural capacity, the ratios of the calculated value to the measured one at the specimens of 0.4 and 0.6 Pu are almost equal. This conforms well to the ordinary calculating method. And, the properties of deformation of all the FRP tendons at the flexural ultimate load, compared with the beams using the PC steel, showed the deformation properties to make the prediction of failure possible.

Post tensioning beam specimens

The ratios of the measured value to the calculated one of the flexural crack load are almost constant except A2 specimen. Consequently, it is understandable that the theory of prestressed concrete is applicable to the beams of post tensioning system also. The ultimate loads vary widely: the ratios of measured value to calculated one are 0.89 to 1.48. This is due to the difficulty of the evaluation way for tensile strength of whole cable in the case of multi cables. This time, the nominal tensile strength of the multi cables used in the introduction of prestressing is set up with the product

Table 3 Summary of posttensioning beams data in static bending test

Tendon	Spacement ditails				Bending crack load			Bending ultimate load		
	f'c (MPa)	Ap (cm^2)	Prestr-essing force (kN)	Reduc-tion factor	Calc. (kN)	Meas. (kN)	Meas. / Calc.	Calc. (kN)	Meas. (kN)	Meas. / Calc.
C1	53.7	4.56	410	0.80	181	162	0.90	372	366	0.98
C2	43.0	7.02	466	0.72	182	162	0.89	556	497	0.89
A1	48.0	10.86	342	0.84	154	137	0.89	238	352	1.48
A2	49.3	3.96	420	1.00	184	132	0.72	289	330	1.14
PC	54.7	8.04	449	1.00	186	162	0.87	368	394	1.07

of nominal tensile strength per each one and reduction factor. While,as to the calculation of the flexural capacity,the tepsile strength of the FRP multi cables is the average tensile strength of one cable. Therefore, the evaluation of the true tensile strength of multi cables in the members is necessary.

3.2 Design Technique

The flexural capacity of the prestressed concrete beams using FRP tendons can be evaluated with the strict application of the plane holding's law. However, the evaluation way of the material characteristics of each FRP tendon differs from each other. Therefore, its standardization is required.

4. BENDING FATIGUE TEST

According to the Japan specifications for highway bridge, the flexural crack of prestressed concrete bridges is unacceptable to design. Consequently, in order to clarify the bending fatigue properties of the beams using FRP tendons,we carried out the bending fatigue tests of the pretensioning beams assumed the high load state produced flexural cracks by unexpected load, and of the post tensioning beams assumed serviceability limit state.

4.1 Outline of Experiment

The section and loading method of the pretensioning beams loaded under the state produced flexural cracks are shown in Fig.3. The standard effective depth of beam was 350mm, and the beam width was 200mm. Effective prestressing force was 60% of the nominal tensile strength of tendons. The loading method was a symmetric four-point loading of 3000mm span. The parameters of the experiment and ultimate loads after the fatigue test are shown in table 4. The lower limit flexural moment is 75% of the decompression moment at each specimen. The upper limit moment, so as to receive equal fatigue damage, is set up as follow. First, on the basis of the specimen using prestressing steel as tendon,the moment that the amplitude stress of prestressing steel becomes 98.1MPa is set up as standard moment. Next,the moment subtracted the decompression moment of the specimen using prestressing steel from the standard moment is distributed proportionately with the magnitude of the nominal tensile strength of the tendons arranged in each specimen. The moment added the distributed moment to the decompression moment of each specimen is regarded as the upper limit moment for each. The tests were repeated up to 2 millions times with the

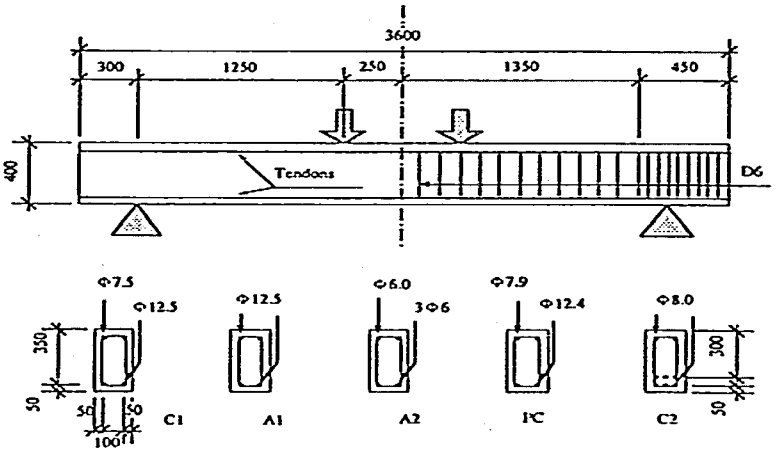


Fig.3 Pretensioning beamspecimens

Table 4 Summary of pretensioning beams data in bending fatigue test

Tendon	Speciment details				Loading condition				Ultimate load after fatigue	
	fc (MPa)	Ap (cm^2)	d (cm)	Mu-cal (kN m)	Mlower / Mu-cal	Mupper / Mu-cal	Δ σ p (MPa)	Δ σ c (MPa)	Mu-mea (kN m)	Mu-mea / Mu-cal
C1	47.09	1.50	35.0	108	0.21	0.51	78.97	16.97	120	1.12
C2	50.23	2.20	32.5	134	0.20	0.49	110.36	19.82	136	1.02
A1	65.43	2.72	35.0	117	0.25	0.58	54.74	21.39	141	1.20
A2	48.36	1.69	35.0	108	0.23	0.55	50.33	20.40	129	1.20
PC	52.68	1.86	35.0	100	0.26	0.62	98.10	17.56	119	1.19

loading speed of 2Hz. The do-not-rupture specimen was forced to be failed with applying static load after the fatigue test.

The specifications of the post tensioning beams assumed serviceability limit state were same as that of the static bending test. Moreover,FRP materials were used as web reinforcement of the specimens of C1,A1 and A2. The experimental parameters and results are shown in table 5. The upper and lower limit flexural moment are set up so that the lower edge stress of the concrete of the beams will come to same value. That is, the lower limit moment is set up at the compression of 2MPa, and the upper limit moment is set up at the tension of 0.3MPa(The tensile stress block of concrete corresponds to the yielding load of the lower edge tension reinforcing bars.). Therefore, the amplitude load (58.2kN) of all specimens and amplitude displacement (0.96mm) are equal. The tests were repeated up to 2 millions times with the loading speed of 5Hz. The specimens were forced to be failed with applying static load after the fatigue test.

4.2 Results of Experiment

Pretensioning beam specimens

All the specimens did not rupture even with the loading of 2 million times. They were forced to be failed with applying static load after the fatigue test. The typical relationship between load and displacement is shown in Fig.4. From the figure,it is understandable that a fatigue loading does not worsen the deformation performance of the specimens. The relationship between the increasing ratio of the maximum displacement to the 10th data and the number of repetitions is shown in Fig.5. The maximum displacement has a tendency to increase in the whole specimens. The increasing ratios of the deformation after two million times are distributed widely: 1.3 to 1.8. Even from the comparison of the static ultimate loads after the fatigue loading with the calculated value,a tendency to worsen with the fatigue loading is

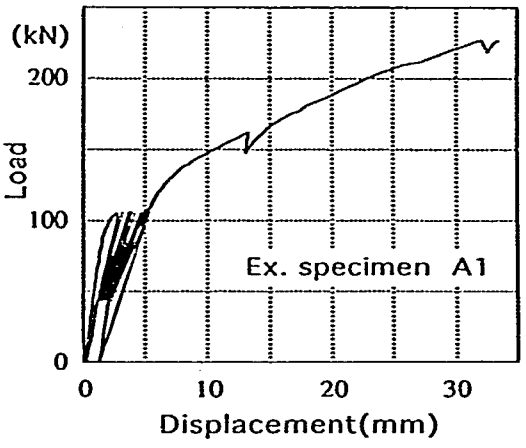


Fig.4 Example of load -displacement curve

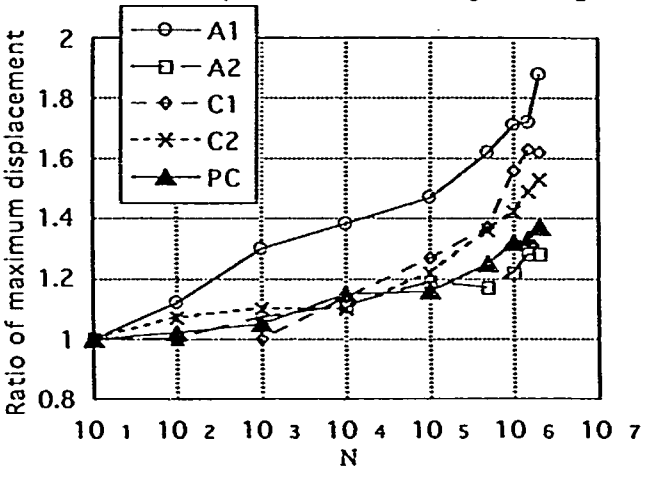


Fig.5 Relationship between times and increase of maximum displacement

Table 5 Summary of posttensioning beams data in bending fatigue test

Tendon	Cyclic load		Bending crack load			Bending ultimate load		
	Maximum load	Minimum load	No fatigue	Fatigue	Fatigue / No fatigue	No fatigue	Fatigue	Fatigue / No fatigue
C1	27.6	85.7	161.9	157.0	0.97	365.9	372.8	1.02
C2	43.4	101.5	161.9	157.0	0.97	497.4	468.9	0.94
A1	8.4	66.6	137:3	137.3	1.00	352.2	335.5	0.95
A2	30.3	88.6	132.4	157.0	1.19	329.6	308.0	0.93
PC	38.7	96.9	161.9	206.0	1.27	394.4	365.9	0.93

not recognized.

Post tensioning beam specimens

The relationship between the increasing ratio of the amplitude displacement to 100th data and the number of repetition is shown in Fig.6. From the figure,it is recognized that there is not very much change of the amplitude displacement, and that the fatigue damage of the prestressed concrete beams without crack does not occur irrespective of tendons. From table 5,the flexural crack load and maximum load are almost same degree. Considering that the strength of concrete and effective prestressing force so on are a little different between a static loading specimen and a fatigue specimen,it may be said that the flexural properties and capacities after 2 million times repetition is not affected very much with the fatigue damage.

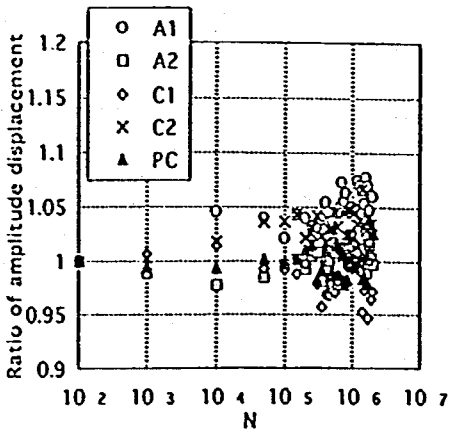


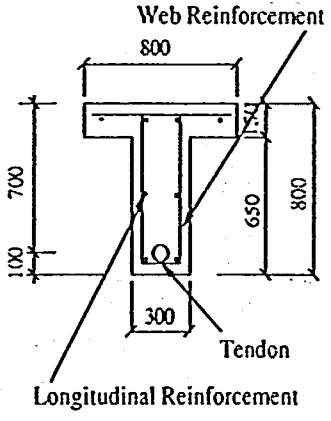
Fig.6 Relationship between fatigue times and ratio of amplitude displacement

4.3 Design Technique

The prestressed concrete beams using FRP tendons for the bending fatigue assumed serviceability limit state have an excellent durability. And,for the bending fatigue by the upper limit moment of the degree of cracking moment also, there was no deadly damage. Therefore,it is considered in the present circumstances that the prestressed concrete beams using FRP tendons should not produce flexural cracks.

5. SHEARING TEST

In the pretensioning beams experiment,in order to clarify the shear capacity of linear member using FRP tendons without web reinforcement and component of effective tensile force of tendons to parallel to the shear force. Furthermore, we performed the static loading test of the post tensioning beams of the shear failure mode designed according to the Japan specifications for highway bridge. As a result,the shearing properties were studied, and the design technique was confirmed.



5.1 Outline of Experiment

The section and loading method of the pretensioning beam specimens are shown in Fig.7. The beams had rectangular section: the effective depth of 350mm and the web thickness of 150mm.It was loaded with the symmetrical four point loading system of 2400mm span and 2.57 shear-span ratio(a/d). The experimental parameters and result are shown in table 6. The experimental parameters are the types of tendon and prestressing force. The effective prestressing force of a lower

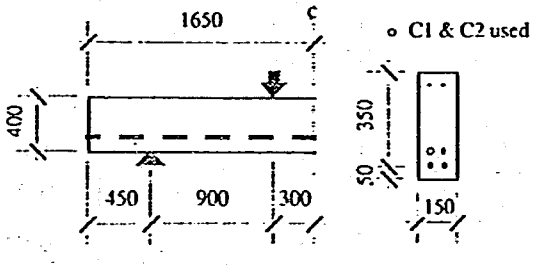


Fig.7 Pretension beam specimens

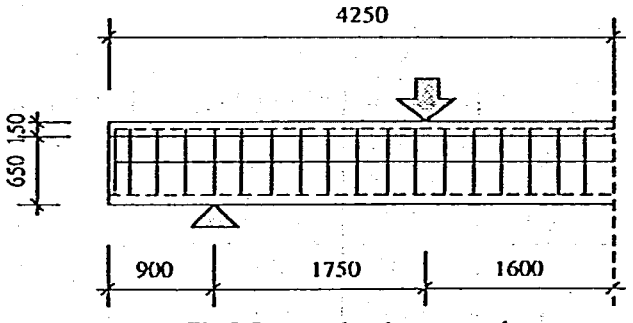


Fig.8 Posttension beam specimens

edge side tendons is set at 0%, 30% and 60% of the guarantee tensile strength of each tendon. The stress due to prestressing is zero at the upper edge, and the lower edge is shown in table 6.

The section and the loading method of the post tensioning beam specimens are shown in Fig.8. The specimens were T-beam:effective depth of 700mm, web thickness of 300mm and upper flange width of 800mm. It was loaded with the symmetry four points of 6700mm-span and 2.5-shearing span ratio. The experimental parameter and result are shown in table 6.The experimental parameter is the types of tendon. The shear capacity(*1) was calculated with the Eq.(1) according to the Japan specifications for highway bridge,and the shear capacity (*2) was calculated with the formula based on the past study [1]. The flexural capacity was calculated with the method described in Chapter 3.

Table 6 Summary of data in shearing test

	Beam	fc MPa	σ pl MPa	Af cm2	Pmea kN	Pc*1 kN	Mea Cal	Pc*2 kN	Mea Cal	Pbcal kN	Mea Cal
Pretension	C1-00	63.2	0.00	1.52	100	67	1.50	93	1.08	184	0.54
	C1-03	59.1	3.43	1.52	168	78	2.16	152	1.10	189	0.89
	C1-06	62.6	6.86	1.52	246	88	2.81	215	1.15	194	1.27
	C2-00	49.3	0.00	1.76	108	67	1.61	90	1.20	195	0.55
	C2-03	52.5	3.43	1.76	213	77	2.76	153	1.39	199	1.07
	C2-06	53.6	6.86	1.76	224	87	2.57	214	1.04	202	1.11
	A1-00	56.5	0.00	1.81	112	67	1.67	95	1.17	174	0.64
	A1-03	55.3	3.28	1.81	156	76	2.05	153	1.02	174	0.90
	A1-06	52.5	6.57	1.81	210	85	2.45	209	1.00	173	1.21
	A2-00	51.5	0.00	1.70	114	67	1.70	90	1.26	180	0.63
	A2-03	53.9	4.14	1.70	187	79	2.38	165	1.13	209	0.89
	A2-06	48.2	8.28	1.70	247	88	2.81	235	1.05	230	1.07
	PC-00	51.7	0.00	1.40	137	67	2.05	85	1.62	178	0.77
	PC-03	52.0	3.28	1.40	196	78	2.52	143	1.37	179	1.10
	PC-06	51.7	6.57	1.40	195	88	2.21	201	0.97	179	1.09
Post tension	C1-PS	42.9	5.17	4.56	804	609	1.32	1022	0.79	739	1.09
	C2-PS	42.9	5.90	7.02	980	601	1.63	1132	0.87	962	1.02
	A1-PS	42.9	4.28	5.43	638	602	1.06	957	0.67	541	1.18
	A2-PS	42.9	5.27	3.96	605	628	0.96	1018	0.59	588	1.03
	PC-PS	42.9	5.65	8.04	858	610	1.41	1124	0.76	800	1.07

$$Pu^{*1} = 2\left\{\tau_c\left(1+\frac{M_0}{M_d}\right)b\cdot d + \frac{A_w\cdot f_{wyd}}{1.15 s_s}\right\} \quad (1)$$

$$Pu^{*2} = 2\left\{0.20 f_c'^{1/3}\left(\frac{100 As}{bd}\right)^{1/3}\left(\frac{100}{d}\right)^{1/4}\left(0.75+\frac{1.4}{a/d}\right)b\cdot d + \frac{A_w\cdot f_{wyd}}{1.15 s_s} + 2\frac{M_0}{a}\right\} \quad (2)$$

5.2 Results of Experiment

Pretensioning beam specimens

The comparison of measured ultimate load of pretensioning beams to its calculated value are shown in Fig.9. It is understandable that the measured ultimate loads are increased according to the increase of prestressing force. The calculated shear capacity (*1) increases only a little comparing with the increase of prestressing force. Therefore, it doesn't appraise the increased shear capacity of linear member according to the increase of prestressing force adequately. On the other hand the calculated shear capacity (*2) can appraise the measured ultimate loads efficiently. The ultimate loads of high prestressing group approach to the calculated flexural capacity, and the failure mode also is transferred to the mixed mode of bending and shearing.

The comparison of ultimate loads by the type of tendons are shown in Fig.9. X-axis is a converted sectional area (Ap·Ep/Es): the product of the sectional area of the lower edge side tendons and the rate of Young's modulus based on prestressing steel. Y-axis is ultimate load. The solid marks in the figure show the failure caused by the break of the tendons. The effective prestressing force of each specimen illustrates the amount of scatter a little, but the qualitative trend of ultimate load seems to be judged. In this experiment, no remarkable effect from the converted sectional area was observed on the level of each prestressing force. However it is considered that

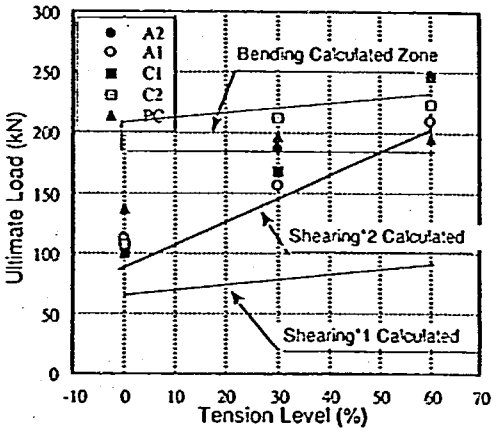


Fig.9 Relationship of Ultimate Load to prestressing

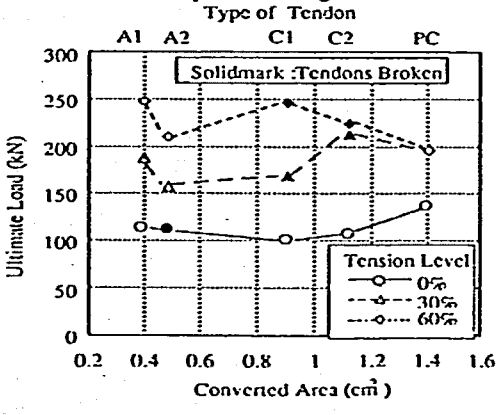


Fig.10 Sensitivity of Ultimate Load to Converted Area

the failure mode is influenced by the elongation-ability of tendon or its own shearing deformation. In the level of C1 and C2, where tension is introduced and the tendon with low residual elongation-ability are used,capacity is lost by the tensile break of the tendon at the part of the shearing crack or the flexural tensile failure. But in the level of PC, A1 and A2, where the tendon with high elongation-ability and capability to follow shearing deformation are used, the capacity is lost by the compressive failure at the upper edge of the concrete beams. Furthermore, in the case of C1 and C2 where tension is not introduced, it was caused by diagonal tensile failure. The factors which affect the mode of shearing failure are mostly elongation-ability, shearing deformability ability,bond ability and so on of tendons, and qualitative analysis remained untouched.

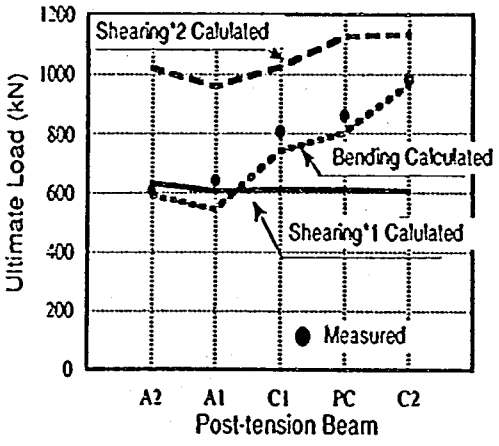


Fig.11 Comparison measured ultimate load with calculated capacity

Post tensioning beam specimens

As for the failure properties of the post tensioning beams, no shearing crack was observed except for C1 specimens. As for the beams using FRP tendons,capacity was lost by bending tensile failure. And, as for the beam using prestressing steel, it was lost by bending compressive failure. Fig.11 shows the comparison of the measured ultimate load of the post tensioning beams with the calculated value. From the figure, the ultimate load almost agrees to the calculated flexural capacity. Consequently, it is understandable that all the beams lost capacity by bending. While, the calculated shear capacity (*1) is within the safety side well.

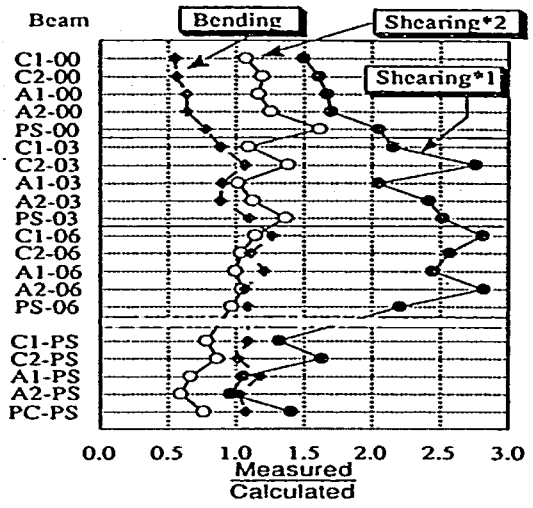


Fig.12 Ratio of measured ultimate load by calculated capacity

5.3 Design Technique

Fig.12 shows the ratio of the measured ultimate load to the calculated one. When the ratio of the calculated flexural capacity to the measured one exceeds 1.0,flexural failure occurs, and the calculation method has a high reliability. While, the calculated shear capacity (*1) is within the safety side at all the specimens. Furthermore, when the ratio of the calculated shear capacity(*2) to the experimental one exceeds 1.0, it is a shearing mode failure. When both it and the calculated flexural capacity exceed 1.0, it becomes failure mode mixed bending and shearing. If the ratio of the calculated value(*2) to the experimental value is less than 1.0, the specimens will be destroyed with bending. In this experiment, the failure mode depends on the type of tendons,but the evaluation of shear capacity is considered to be covered by the Eq.(2).

6. CONCLUSION

Basic experiments have been carried out for the construction of prestressed concrete highway bridges using FRP tendons. Prestressed concrete highway bridges using FRP tendons designed based on the Japan specifications for highway bridge has been assured to have sufficient safety. So, in order to extend their application,we will make the guide to apply FRP tendons for highway bridges.

REFERENCES

1. Seiichi Tottori et al.:Shearing Ultimate Load of RC and PC beams using FRP rods with axis and web reinforcements,Proceeding of symposium about Application Continuous Fiber Reinforcement Materials to Concrete Structures ,JSCE,Apr.1992,pp199-204

MANAGEMENT DECISIONS FOR BRIDGE DECK REHABILITATION/REPLACEMENT

Gary A. Runco, P.E.
Parsons, Brinckerhoff
formerly Wilbur Smith Assoc.

EXECUTIVE SUMMARY

Presented herein are excerpts from the final draft of a Pennsylvania Department of Transportation research project. Only limited data is presented in this paper and readers are encouraged to obtain a complete report for a better understanding of the project.

The initial phase of work included a review of the current policy and research effort behind the policy to determine positive and negative aspects of current statewide practice. Data from outside sources including neighboring states, vendors, etc. was compiled and assessed for inclusion in a new and improved policy. Of major importance was the input from PennDOT District Bridge Engineers. The second phase of work required coordination with the Department to determine the areas of research concentration which could result in the most positive impact for the Department. The focus was on the cost effective aspect with economic analysis and level of service high on the priority list.

The result is a two-part product: A research report which outlines known parameters and details specific parameters and Appendix A which provides the proposed Department Policy for bridge deck rehabilitation/replacement. The policy was developed in the same format as Design Manual Part 4 on structures and would be included in Chapter 5 on Rehabilitation Strategies.

The recommended policy provides guidelines for the decision process to program a bridge deck for either rehabilitation or replacement. It also provides guidelines which facilitate the rehabilitate or replace decision. For the first time the proposed policy provides a link between bridge inspection data, specifically condition rating, geometric and safety requirements, and the decision process. The policy also addresses level of service concepts for high, medium or low volume ADTT routes.

Through the use of a table, flow chart and spread sheet, the logic process is better defined and will be more uniformly applied statewide. Parameters such as Maintenance and Protection of Traffic, roadway user costs and other economic factors are included in the decision process. Finally, the Department's preferred methods of rehabilitation/replacement are more accurately established for the design engineer.

3.0 CONCLUSIONS

1. A great need exists for additional monies to repair and/or replace bridge decks in Pennsylvania. Currently the solution is to wait for the bridge deck to deteriorate beyond salvage and hope that other items of rehabilitation are required so that funding can be obtained for all work.

An estimate of the magnitude of the problem was prepared by BART and is included in Appendix C.

2. Additional funds are required to support increased bridge inspection efforts. This would include funds for manpower and equipment. The State's bridge inspection needs are overburdened resulting in predominantly visual only inspections of bridge decks. Follow-up inspection/testing is usually only provided for programming. Little testing is done to track the progress of deterioration. New Jersey DOT utilizes bridge deck inspection crews who issue independent deck reports.

TABLE 1
BRIDGE DECK EVALUATION
TESTING METHODS
Used By Various State Agencies

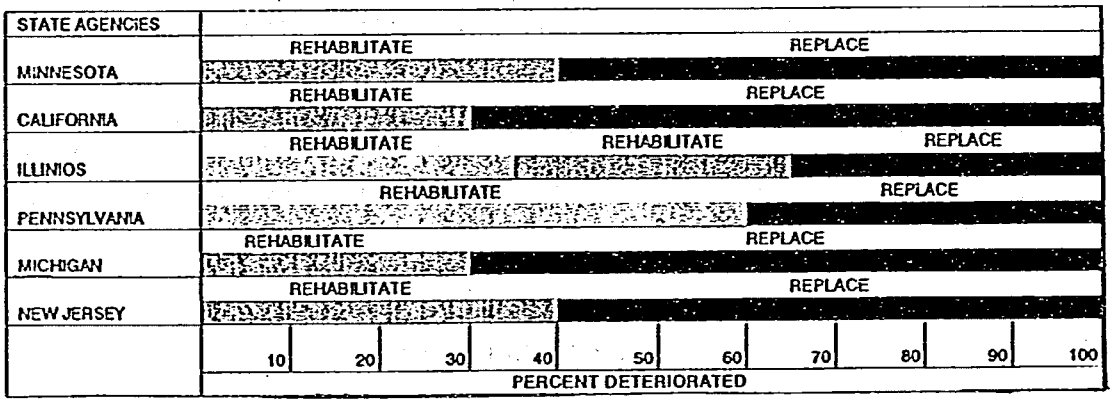
TEST METHODS

	VISUAL INSPECTION	SOUNDING	CHLORIDE CONTENT	ANALYSIS (PETROGRAPHICS)	FREEZE/THAW HALF-CELL POTENTIAL	DEPTH OF COVER	THERMO-GRAPHY	RADAR
Description	Field Study Photos Notes	A. Chain Drag B. Hamer C. Delama-tec	Test on cores taken from	Microscopic exam of core sample	Hook Volt-meter anode to rebar	Pacho-meter	Measure tempera-ture differential	Eletro-magnetic energy wave form
Results	Verifi-cation of conditions/ severity of the obvious	% area of Delaminations	LBS CL/CY	Ability to resist freeze/thaw damage	Level of corrosion activity	Amount of cover over top rat	Finds Delami-nations	Finds punky conc. (moist)
PennDOT	X	X	X	X (Not Routinely)	X	X		
Michigan	X	X	X					
Cal Trans	X	X (A,B)	X (4)					
Maryland	X	X	X	X	X	X	X	X
N.J.DOT	X	X	X		X	X		
Illinois	X	X (C Preferred)	X (2)		X	X (2)	X (2)	X (2)
N.Y.DOT	X	X						
Minn. (3)	X	X (A) (Not Delam.)	X (Not Routinely)		NO		X (Not Worth Cost)	X (Not Worth Cost)

(1) Information was extraplorated from various written state policies or obtained via telephone conversation.
(2) Test not required.
(3) Not in written policy by telephone conversation with Gary Ruoco. All tests after programming, pre-construction.
(4) Only where salt is used extensively/marine environment.

TABLE 3

THRESHOLD VALUES (CUTOFF POINTS) FOR REHABILITATION / REPLACEMENT



KEY

(1) LIGHT DECK DETERIORATION
(2) MODERATE DECK DETERIORATION
(3) EXTENSIVE DECK DETERIORATION

REHABILITATION

EACH STATE SURVEYED INITIALLY REMOVES THE DETERIORATED OR CONTAMINATED AREAS OF CONCRETE FOLLOWED BY THE USE OF THE FOLLOWING METHODS OF PROTECTION.

MINNESOTA : 2" LOW SLUMP DENSE CONCRETE
1 1/2" LMC OVERLAY.
CALIFORNIA : METHACRYLATE TREATMENT FOR EXTENSIVE CRACKS RAPID SET CONCRETE.
ILLINOIS : VARIOUS OPTIONS
PENNSYLVANIA : VARIOUS OPTIONS
MICHIGAN : 1/2" LMC OVERLAY
NEW JERSEY : MEMBRANE & B.C. OVERLAY
CATHODIC PROTECTION
LMC OVERLAY

3. Given additional funding, a better inspection program may be developed allowing for better prioritization across the State. Smaller states such as Maryland have a team of individuals responsible for prioritization of all decks statewide.

4. The 1979 version of the FHWA Coding Manual for Bridge Deck Condition Assessment included an expanded description of items with corresponding ratings. These include % spalls, % delaminations, chloride content and electrical potential. The FHWA has since deleted this table from the coding manual. PennDOT's BMS manual still includes the table which is the primary source for rating of bridge decks. The result is that current coding does not provide a broad enough spectrum for comparative ratings of bridge decks. A rating of 7 is acceptable and a rating of 2 implies structural inadequacy. Ratings of 6, 5, 4, 3, are all that remain to categorize various stages of deterioration. In effect, a four (4) number scale does not allow for accurate prioritization.

5. Rehabilitation schemes such as cathodic protection and latex modified concrete have moved forward slowly and without universal acceptance in Pennsylvania. Cathodic protection has only been utilized in two Districts and the state has not yet set standards for the use of Cathodic protection or truly endorsed one form of Cathodic protection.

Latex-modified concrete overlays while successful in nine Districts have been failures in two others. Again, the state has not endorsed a solid policy extoling the benefits of such a system.

6. Additional research is needed on high tech inspection procedures including infra-red thermograph, ground penetrating radar, etc. Current research indicates that ground penetrating radar by itself may be imperfect and that infra-red thermograph by itself may also be imperfect, however, in combination these two techniques may work very well. [g]

7. National and/or PennDOT research is needed on concrete sealants. All sealants are not equal. Concrete sealants are available which far exceed boiled linseed oil as an impermeable sealant. PennDOT should move to specify better products and establish a program for maintenance to reseal bridge decks on a regular basis.

8. Until PennDOT is committed to more and better maintenance, the problem (bridge deck deterioration of older decks) will continue to grow and at an accelerated pace.

9. Better data is needed on specific cost items for an economic analysis to be meaningful.

10. New design and construction practices may greatly change the economics of various strategies. These include hydrodermolition as used for Type 2 and Type 3 repairs and Isotropic bridge deck design which reduces greatly, the quantity of steel reinforcing.

11. The effort to tie bridge inspection to programming is good. The results will be of decreased value until the bridge inspection rating guidelines are revised.

12. Newer decks with epoxy coated reinforcement appear to be performing well statewide.

13. Other factors such as safety parapets, seismic retrofit, structural steel repair, bearing replacement may dictate a decision to replace a bridge deck more than the condition of the deck itself.

14. Maintenance and Protection of Traffic Costs and Roadway User costs are usually so large that they determine the outcome of the bridge deck action decision. In other words, these costs are large enough to favor the alternative which has the longest life span and requires the least M & P of T cost or least user inconvenience.

15. The District Bridge Engineers each have very strong opinions about the preferred way of handling bridge deck problems in their Districts. All would prefer a policy which is flexible.

4.0 RECOMMENDATIONS

Recommendations follow the order of the research activities. Recommendations from the research are not the same as the recommended policy and a distinction must be made. Therefore, the recommendations may include recommendations for future research, broad policy changes or specific action.

The recommended policy, on the other hand, provided in Appendix A is a recommendation for current action subject to the constraints defined for the research. This recommended policy more accurately reflects the productive results of the research assignment whereas the general recommendations may define shortcomings of the entire approach.

Test Methods

1. It is recommended that PennDOT, through additional research, in-house trial, contact with other agencies, etc. continue to monitor and evaluate new test methods. These include infrared thermography, radar and others that may evolve. This new technology may in time totally replace any other test methods or be a mandatory test method. This type of testing has the potential to result in a system-wide method for better defining and ranking a bridge deck's condition.

2. Depth of cover data obtained during construction inspection activities should be made available to bridge inspection and should be used in the evaluation process.

3. FHWA research has clearly established that active corrosion begins when chloride content reaches the 1.4-1.5 LBS./C.Y. range. What does not exist is an indicator of when deterioration begins. Active corrosion, internal to the deck may continue for a long period of time before visible deterioration is observed. Only when visible deterioration is observed and rideability is affected does corrective repair and/or maintenance begin. PennDOT should pursue with the FHWA these courses of action or issues. These include:

a. A formula or indicator to predict when the active corrosion will result in deterioration.

b. A method(s) to arrest the corrosive affects of chlorides once chlorides have exceeded the 1.4-1.5 LBS/C.Y. values.

c. A policy to determine acceptable levels of chloride concentration which can remain in place in a rehabilitated deck. Conversely, when is a deck so contaminated that it should be programmed for replacement.

4. PennDOT should provide increased inspection/documentation of bridge decks if the Department desires to have a well coordinated Bridge Deck Strategy. Sufficient data does not exist and prioritization based on condition ratings is too broad.

Rehabilitation Strategies

5. Statewide better coordination is required between bridge maintenance and bridge design. A better effort is needed to control the procurement and placement of various patching materials and sealants. Note certain patching materials may not be compatible with rehabilitation strategies. Bridge maintenance activities are not consistent from County to County within a District.

6. PennDOT needs to move forward in a stronger role with support of Cathodic protection and Latex Modified Concrete overlays.

7. PennDOT should continue to evaluate newer materials such as micro-silica and calcium nitrite.

Replacement Strategies

8. PennDOT should continue the evaluation of and trial of Isotropic decks.

9. Again micro-silica and calcium nitrite decks should be evaluated.

Preventive Maintenance

10. It is recommended that the Department begin an effort to pursue a course of preventative maintenance. At least one state (Oklahoma in particular) has moved ahead to have an on-going bridge deck sealing program. The hope is that a long term benefit will be realized from the program. The program should include scheduled maintenance activities which are consistent from County to County.

Construction Practices Strategies

11. Hydrodermolition has promise as a demolition tool, however, it does require a good specification and should be used at the discretion of PennDOT not of the contractor as reported to the researcher. Other states have adopted hydrodermolition as the only acceptable demolition method.

Other Parameters

12. Funding source is a reality. As such it should be reflected in PennDOT's policy. Even if it is not shown in the written policy it must be recognized that the actual decision making will reflect funding source.

13. Suppliers/Contractors should be evaluated by PennDOT to determine their ability to produce, supply, and construct various alternatives. Examples include latex overlays, cathodic protection, microsilica concrete, light weight aggregate and others. Conditions may be very different in District 1-0 than in District 6-0.

14. Roadway users cost should be considered. PennDOT should update the Roadway Users Manual and the corresponding computer program for use in other applications.

15. While biennial inspection data is used to establish condition ratings, much additional information is needed to establish bridge deck behavior. Assessing bridge decks per the biennial inspection data is similar to a doctor observing that a patient has an open wound. It does not address the cause of the wound. Bridge engineers need data on construction such as time of placement, temperature at time of placement, reinforcement bar depth of cover,

aggregate source, batch plant supplier, mix design, admixtures, traffic conditions during placement, etc. If all of this data were tracked and available to bridge engineers it may be possible to learn the course of problems and correspondingly respond to develop better procedures for construction.

16. Any policy should always include the extraneous items such as bearings, seismic retrofit, superstructure rehabilitation, etc., since they affect the decision process in a big way.

Economic Analysis

17. It should be clear that any analysis is only as good as the input data. Numerous variables such as traffic data, interest rate, cost of a strategy, maintenance free lives, etc., are based on averages and poorly documented historical data. The effort to develop a "Cost/Effective" approach to bridge deck rehabilitation/replacement is complex and the use of numerous approximations result in approximate answers. In other words, this effort is not very accurate. It is recommended that the policy be only a tool for use by educated bridge engineers who use this tool and their best judgement in the decision making process.

18. A recommended policy which incorporates this research is provided in Appendix A.

19. It is recommended that future research in this area be handled in two separate parts covering technical issues and policy issues. Consultants/researchers are more adept at addressing the technical aspects of a research assignment. Conversely, the Department would be better at development of a policy resulting from the research findings. This is particularly true when the policy reflects subjectively.

Recommended Policy for Cost Effective Rehabilitation/Replacement

5.4 BRIDGE DECKS

Each bridge and correspondingly each bridge deck is somewhat unique. This section provides a generalized policy for maintenance, programming and the decision to rehabilitate or replace a bridge deck. It is intended to provide a logical decision tree for routine conditions. Exceptions to the policy will exist. The general policy will, however, provide a methodology for documenting and selecting the preferred course of action and will provide uniformity statewide.

5.4.1. Concrete Decks Without Any Overlays

5.4.1.1 Deck Condition Ratings and other Decision Factors

5.4.1.1.1 Deck Condition Ratings

This policy is related in part to deck condition ratings, Item E17 from the Bridge Management System (BMS). BMS guidelines for rating a bridge deck includes assessment of visible spalls, chloride content and measured electrical potential. Use deck condition ratings as a starting point.

Collect the following information prior to determining the type of rehabilitation or course of action needed for a bridge deck.

a. Visible Spalls - extent of spalls expressed as a percentage of total deck area.

It is recommended but not required that the following additional information be obtained for use in decision making:

b. Delaminations expressed as a percentage of deck area. Use infrared thermography, chain dragging or other approved methods.

c. Chloride content in top 1" and at 2-1/2" depth.

d. Half-cell electrical potential (if required by the department).

5.4.1.1.1 Deck Condition Ratings

Collect the following additional information (as-needed) prior to determining the type of rehabilitation or course of action needed for bridge deck.

a. Air content (entrained). Expressed as a percentage by volume.

b. Concrete Strength - use concrete coring and testing, and Windsor probe results, if permitted.

c. Average concrete cover over the top reinforcing steel.

d. Age of the deck.

e. Level of Service - identify the bridge as a link in the priority commercial Network, Agri Access Network, Industrial Commercial Access Network, Coal routes or other exceptions (effect on local economy).

f. Average Daily Truck Traffic (ADTT)

Low Volume:	ADTT	<	100
Medium Volume:	ADTT		100 - 500
High Volume:	ADTT	>	500

g. Identify black steel versus coated steel reinforcement. Coating may be either epoxy or galvanized. (see listing in C 5.4.1).

h. Establish if the bridge deck is functionally obsolete, Item E25 from BMS (see Table 5.4.1.1.2, Page A-6).

i. Evaluate the need to replace parapets.

j. Estimate quantities of Type 2 and Type 3 repairs.

k. Evaluate seismic needs.

l. Evaluate bearing needs.

m. Evaluate approaches.

p. Evaluate expansion joints.

q. Evaluate other applicable items.

Use Items a, b, c and d (if required) to determine condition ratings. Use Table 5.4.1.3 to determine the appropriate course of action. Should Table 5.4.1.3 (Page A-8) not yield a definite result (i.e., the result is in the 'grey area'). Use the flow chart, Figure 5.4.1 and economic analysis as required (5.4.10).

5.4.2 Concrete Decks With Bituminous Overlays Without a Membrane

Replace these decks when the condition rating is 2 or less. Until such time, continue the maintenance function of patching and paving.

5.4.3 Concrete Decks With Bituminous Overlays and Membrane Waterproofing

Patch deteriorated concrete and replace affected membrane until the repaired area is 50% or more of the deck area. Follow Table 5.4.1.3 (Page A-8) thereafter.

5.4.4 Concrete Decks With Latex Modified Mortar or Concrete Overlay

Use Table 5.4.1.3 (Page A-8). If a new overlay is required, remove the existing overlay and deteriorated deck areas. Anticipate hydrodemolition for estimating repair quantities. This may result in increased quantities of Type 2 and Type 3 repair.

5.4.5 Concrete Decks With Epoxy or Galvanized Reinforcement Bars with Spalls

Provide Type 2 and Type 3 repairs. Complete the rehabilitation using a latex modified concrete overlay. Bituminous overlays are not recommended.

5.4.6 Open Steel Grid Deck

Program these decks, when loafing permits, for replacement with concrete filled grid deck or fill the existing deck with concrete. (see Section 5.4.7 for addition discussion).

Use a mechanical connection to fasten these decks to the supporting stringer and/or floorbeams in lieu of welded connections. This should minimize long term maintenance costs.

Specify shims to eliminate residual construction load stresses induced by placement of a load over the grid.

Anti-skid studs should be installed as-needed.

Do not specify this type of deck for new construction or deck replacement. Investigate light-weight concrete and filled grids as alternatives to the open grid deck.

5.4.7 Concrete Filled Steel Grid Deck

Remove deteriorated concrete, anticipate hydrodemolition when estimating quantities. If the concrete deterioration is typically greater than one-fourth the depth use normal weight concrete for the rehabilitation.

If the deterioration is typically the top quarter or less of the grid depth, overlay the deck. For short term repairs (i.e., < 5 years) use bituminous concrete. For intermediate repairs (i.e., 12+ years) use latex modified concrete. For long term repairs (i.e., 15-20 years) use an approved polymer resin. Follow appropriate procedures for Type 3 Repairs as required with any overlay.

This deck type may be used for deck replacement in special situations only.

5.4.8 Timber Decks

Locally replace deteriorated members as required to maintain rideability with treated lumber. When deck deterioration exceeds 25%, replace the entire deck.

5.4.9 Other Deck Types

Rehabilitation of other deck types will be evaluated on an individual basis. A rehabilitation strategy will be developed based on the characteristics, performance and condition of such decks. In some instances, special studies may be required.

5.4.10 Economic Analysis

The economic analysis has been simplified by the development of a spread sheet using the Lotus computer program. Copies of the worksheet file to be run within lotus are available through the Central office. A licensing agreement requires that the user own a copy of the Lotus program. A detailed discussion of the program is provided in Research Report 89-08. In general the economic evaluation considers the present-worth cost of an alternative. Suggested values for various inputs are provided. Each of these values can be changed by the designer, but must be documented in a report. Factors considered by the program include:

- Initial cost of a selected strategy
- Deck preparation costs (Type 2 and 3 Repairs, etc.)
- Annual Maintenance Costs
- Maintenance and Protection of Traffic Costs
- Roadway User Costs
- Associated Costs - joints, drains, etc.

An interest rate is included to reflect the cost of capital expenditures. Inflation is neglected in that the relative costs between strategies would be changed equally.

The economic analysis developed does not consider funding sources and provides comparison of total cost only.

Projects which may include more than one bridge deck should be evaluated using the total square footage of all decks combined as one. The purpose of this is to obtain true costs with Maintenance and Protection of Traffic and Roadway User Costs spread over the multiple deck project rather than unfairly lumped against a single deck.

Table 5.4.10 (Page ___) provides default input values for the various parameters in the economic analysis.

5.4.10.1 Bridge Deck Rehabilitation Worksheet Users Manual

- Initial Deck Strategy Cost - The calculated lump sum cost for an alternative. Derived by using $/S.F. for either LMC, cathodic, etc. (i.e., first cost of any alternative).
- Initial Maintenance and Protection of Traffic Cost - A lump sum value selected by the designer to reflect anticipated contractor cost.
- Roadway Users Cost - A calculated value derived by manual calculations or using the Departments LCC1 program. This cost item is documented in the Roadway Management Manual, Publication No. 242, Section 2.4 User Delay Costs.
- Planning Horizon - The term in years over which alternatives are to be compared.
- Interest Rate - This should be based on the Prime Lending Rate (documented by news service or banking information).
- Bridge Area - Bridge Deck area in square feet.
- Replacement Cost - Future replacement cost, as needed, if different from Initial Deck Strategy Cost.
- ANN - Annual Cost of Maintenance includes material, labor and Maintenance and Protection of Traffic for Department maintenance crew.
- INCR - Increase in annual maintenance cost (set at 4%).
- MOD - Initial Deck Modifications - include expansion joints, scuppers, etc.
- MPT - Maintenance and Protection of Traffic - set at a default of $5,000.00 (revise accordingly).
- PREP - Type 2 and Type 3 Repairs - set at a default of $5,000.00 (revise accordingly).
- REH - Rehabilitation of various strategies at N years in the future. This may be different than initial cost if expansion joints, scuppers, etc., have already been modified.
- USERS - Roadway user costs, see previous discussion.

Time Periods

P - Anticipated life of an alternative.
t - Anticipated life before rehabilitation is required.
n - Number of rehabilitation over the planning horizon.

TABLE 5.4.1.1.1

DECK CONDITION RATING

ITEM E17 OF THE 'BRIDGE MANAGEMENT SYSTEM'

January 1990 (Revised June 1991)

DECK	E17
Deck Condition Rating	

DESCRIPTION: This is a 1 digit field that indicates the condition of the bridge deck.

PROCEDURE: Enter the code which describes the overall condition of the bridge deck.

Concrete decks should be inspected for cracking, scaling, spalling, leaching, chloride contamination, potholing, delamination, and full or partial depth failures. Steel grid decks should be inspected for broken welds, broken grids, section loss, and growth of filled grids from corrosion. Timber decks should be inspected for splitting, crushing, fastener failure, and deterioration from rot.

The specialized table on the following page may be used as a guide for evaluating concrete deck conditions using different condition indicators.

NOTE:
The condition of the wearing surface/protective system, joints, expansion devices, curbs, sidewalks, parapets, fascias, bridge rail, and scuppers shall not be considered in the overall deck evaluation. However, their condition should be noted on the inspection form.

Decks integral with the superstructure will be rated as a deck only and not how they may influence the superstructure rating (for example, rigid frame, slab, deckgirder or T-beam, voided slab, box girder, etc.). Similarly, the superstructure of an integral deck-type bridge will not influence the deck rating.

Code 'N' for bridges under fill.

CODING: Refer to CONDITION RATING FOR CONCRETE BRIDGE DECK EVALUATION on the next panel.

CONDITION RATING FOR CONCRETE BRIDGE DECK EVALUATION

Note: This specialized table can be used as a guide for evaluating deck conditions using different condition indicators.

Category Classification	Rating	Condition Indicators: Deck Area (Visible Scale)	Deck Area (Determination)	Electrical Potential	Deck Area	Chloride Content (#/CY)	Deck Area
Category #3 Light Deterioration	9	none	none	0	entire	0	none
	8	none	none	> .35	none	> 1	none
	7	none	< 2%	< .35	45%	> 2	none
Category #2 Moderate Deterioration	6	<2% spalls or sum of all deteriorated and/or contaminated deck concrete (> or = 2#/C.Y.Cl) <20%					
	5	<5% spalls or sum of all deteriorated and/or contaminated deck concrete 20% to 40%					
Category #1 Extensive Deterioration	4	>5% spalls or sum of all deteriorated and/or contaminated deck concrete 40% to 60%					
	3	>5% spalls or sum of all deteriorated and/or contaminated deck concrete >60%					
Structurally Inadequate Deck	2	Deck structural capacity grossly inadequate					
	1	Deck has failed completely - Repairable by replacement only					
	0	Holes in deck - danger of other sections of deck failing					

NOTE	CONDITION RATING FOR CONCRETE BRIDGE DECK EVALUATION
	Use As A Guide For Evaluating Deck Conditions
(1)	
(2)	

NOTES:

(1) No evident cracking

(2) Hairline cracking observed

TABLE 5.4.1.1.2

DECK GEOMETRY APPRAISAL

ITEM E25 OF THE 'BRIDGE MANAGEMENT SYSTEM'

January 1990 (Revised June 1991)

E25	DK GM
Deck Geometry Appraisal	

DESCRIPTION: This is a 1 digit field that indicates the appraisal of bridge deck geometry.

PROCEDURE: The overall rating for deck geometry will include two evaluations; Item A31, the curb-to-curb or face-to-face of rail bridge width using Table 2A, 2B, 2C, or 2D and Item B22, the minimum vertical clearance over the bridge roadway using Table 2E. The lower of the codes obtained from these tables shall be used. When an individual table lists several deck geometry rating codes for the same roadway width under a specific ADT, use the lower code.

The curb-to-curb or face-to-face of rail dimension shall be taken from Item A31, Bridge Roadway Width, Curb-to-curb, Item B22, Minimum Vertical Clearance Over Bridge Roadway, shall be used to evaluate the vertical clearance.

CODING: Refer to Tables 2A, 2B, 2C, 2D, and 2E (on the following panels).

EXAMPLE: Table 2A lists deck geometry rating codes of 6,7, and 8 for a 44-foot roadway width and an ADT of >5000. Use the code of 6. Use the lower code for values between those listed in the tables.

TABLES 2A AND 2B

Rating by Comparison of ADT - Item B27, and Bridge Roadway Width, Curb-to-curb — Item A31

TABLE NOTES:

1. Use the lower rating code for values between those listed in the table.
2. Dimensions are in feet.
3. For 3 or more undivided lanes of 2-way traffic, use Table 2C, Other Multilane Divided Facilities.
4. Do not use Table 2B for code 9 and for codes 8 through 4 inclusive when the ADT >100. Single lane bridges less than 16 feet wide carrying 2-way traffic are always appraised at 3 or below if they carry more than an ADT of 100.

TABLE 2A & 2B
Rating by Comparison of ADT — Item B27
Bridge Roadway Width, Curb-to-curb — Item A31

Deck Geometry Rating Code (E25)	TABLE 2A: Bridge Roadway Width 2 lanes; 2-Way Traffic — ADT (Both Directions)						TABLE 2B: Bridge Roadway Width 1 lane; 2-Way Traffic — ADT (Both Directions)	
	0-100	101-400	401-1000	1001-2000	2001-5000	>5000	0-100	>100
9	>32	>36	>40	>44	>44	>48	—	—
8	32	36	40	44	44	44 *	15'-11"	—
7	28	32	36	40	44	44 *	15	—
6	24	26	30	34	40	44	14	—
5	20	24	26	28	34	38	13	—
4	18	20	22	24	28	32 (28)	12	—
3	16	18	20	22	26	30 (28)	11	15'-11"
2	Any width less than required for a rating code of 3 and structure is open.							
0	Bridge Closed.							

* Use value in parentheses for bridges longer than 200 feet.

TABLES 2C AND 2D

Rating by Comparison of No. of Lanes - Item B11, and Bridge Roadway Width, Curb-to-curb — Item A31

TABLE NOTES:

1. Use the lower rating code for values between those listed in the table.
2. Dimensions are in feet.
3. Use Table 2C, other Multilane Divided Facilities, for 3 or more undivided lanes of 2-way traffic.

* Use value in parentheses for bridges longer than 200 feet.

N = Number of lanes of traffic.

TABLE 2C & 2D
Rating by Comparison of Number of Lanes — Item B11
and Bridge Roadway Width, Curb-to-curb — Item A31

Deck Geometry Rating Code (E25)	TABLE 2C: Bridge Roadway Width 2 or More Lanes Each Direction — Interstate & Other Divided Freeways		Other Multilane Divided Facilities		TABLE 2D: Bridge Roadway Width 1-Way Traffic — Ramps Only	
	2 Lanes	3 or more Lanes	2 Lanes	3 or More Lanes	1 Lane	2 or More Lanes
9	>42	>12N+24	>42	>12N+16	>28	>12N+12
8	42	12N+24	42	12N+16	28	12N+12
7	40	12N+20	38	12N+15	24	12N+10
6	38	12N+16	36	12N+12	22	12N+8
5	36	12N+14	33	11N+10	20	12N+6
4	34(28)*	11N+12 (11N+7)*	30	11N+6	18	12N+4
3	33(28)	11N+11 (11N+6)*	27	11N+5	16	12N+2
2	Any width less than required for a rating code of 3 and structure is open.					
0	Bridge Closed.					

TABLE 2E

Rating by Comparison of Minimum Vertical Clearance- Item B22, and Functional Classification — Item B16

TABLE NOTES:

1. Use the lower rating code for values between those listed in the table.

* Use for routes in highly developed urban areas only when there is an alternative Interstate, freeway, or expressway facility with a minimum of 15'-0" clearance.

TABLE 2E
Rating by Comparison of Minimum Vertical Clearance- Item B22,
and Functional Classification — Item B16

Deck Geometry Rating Code (E25)	Minimum Vertical Clearance — Functional Class: Interstate & Other Freeways — All Routes - Except as noted for Urban Areas	Interstate & Other Freeways — Unacceptable Routes - Urban Areas*	Other Principal & Minor Arterials	Major & Minor Collectors & Locals
9	>17'-0"	>16'-6"	>16'-6"	>16'-6"
8	17'-0"	16'-6"	16'-6"	16'-6"
7	16'-9"	15'-6"	15'-6"	15'-6"
6	16'-6"	14'-6"	14'-6"	14'-6"
5	15'-9"	14'-3"	14'-3"	14'-3"
4	15'-0"	14'-0"	14'-0"	14'-0"
3	Vertical clearance less than value in rating code of 4 and requiring corrective action.			
2	Vertical clearance less than value in rating code of 4 and requiring replacement.			
0	Bridge Closed.			

TABLE 5.4.1.3
BRIDGE DECK REHABILITATION GUIDE (1)

DECK COND(2)	9-7						8 (6)						5						4-3						<=2					
% AIR(3)	<3%			=>3%			<3%			=>3%			<3%			=>3%			<3%			=>3%			<3%			=>3%		
DECK AGE(4)	POST 1976	1971-1976	PRE 1971	POST 1976	1971-1976	PRE 1971	POST 1976	1971-1976	PRE 1971	POST 1976	1971-1976	PRE 1971	POST 1976	1971-1976	PRE 1971	POST 1976	1971-1976	PRE 1971	POST 1976	1971-1976	PRE 1971	POST 1976	1971-1976	PRE 1971	POST 1976	1971-1976	PRE 1971	POST 1976	1971-1976	PRE 1971
REHAB/ REPLACE STRATEGIES(5)																														
(LO)	●	●	●	●	●	●	●	●	●	●	●	●	●	●	●	●	●	●												
(BP)																									•	•	•	•	•	•
(BO)																														
(RO)								L	L																					
(RMO)								M	M		L	L																		
(R)							●			●																				
(RL)								H	H		M,H	M,H										M,H	M,H	M,H						
(RC)												H											M,H	M,H						
(RCMO)																							M,H	M,H						
(RCL)																							M,H	M,H						
(RPL)																			H						●	●	●	●	●	●

KEY

\- Where options appear in more than one row, an economic evaluation is required and/or additional test data to support a decision.

● Denotes action for all occurences (level of service) of a given condition rating.

• With concurrence of the District Bridge Engineer.

L On low volume (ADTT) routes.
M On medium volume (ADTT) routes.
H On high volume (ADTT) routes (PCN + Exceptions).

Shaded area is "gray area" where other factors must be considered. Follow procedures in Figure 5.4.1.

NOTES TO TABLE 5.4.1.3

(1) The Bridge Deck Rehabilitation Guide as such, is for generalized usage. Exceptions will exist. These may include: monolithic deck systems, arches, concrete tee-beams, etc.

(2) Refers to deck condition rating established using BMS item E17.

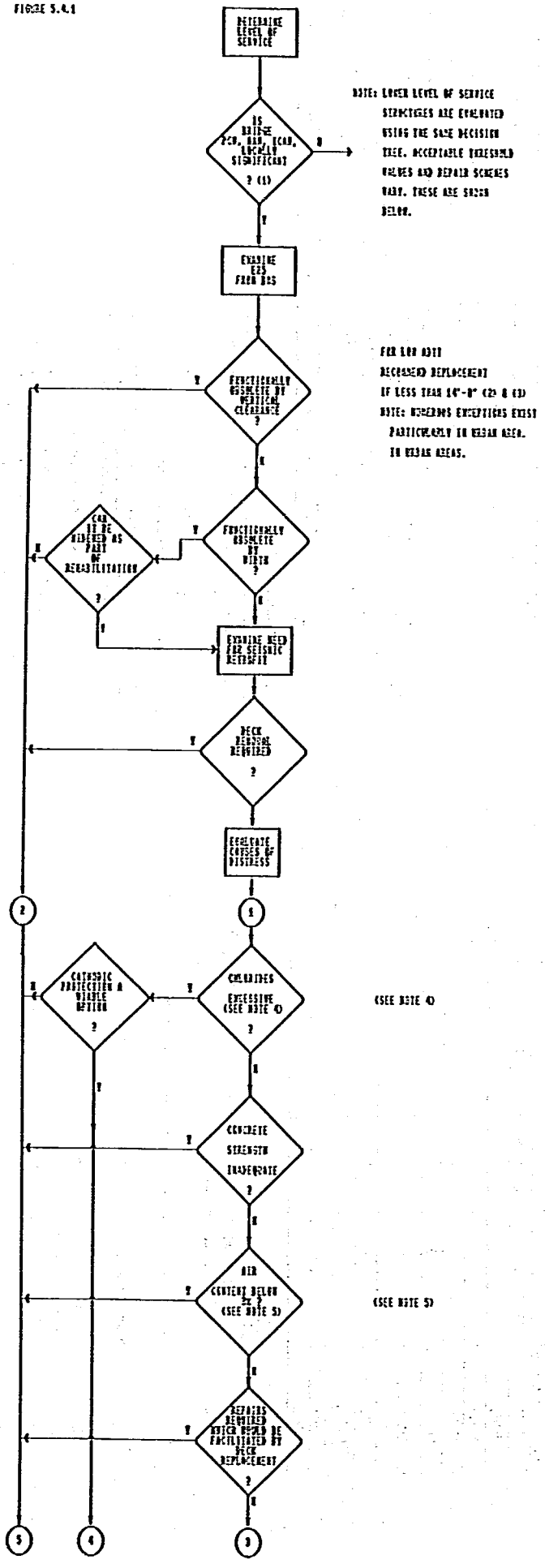
(3) Refers to measured entrained air content.

(4) Dates were established based on coated steel versus uncoated steel Pre-1971 black steel was used in PA, 1971-1976 both epoxy coated and galvanized, Post 1976 epoxy coated steel was utilized (refer Table C5.4.1).

(5) Rehabilitation, maintenenance and replacement options are listed per the following code:
LO = Linseed oil or other surface treatment (silane, etc.) at prescribed maintenance intervals (maintenenance activity).
BP = Bituminous patching only (maintenance activity).
BO = Bituminous overlay only (maintenance activity).
RO = Repair Types II and III plus bituminous overlay.
RMO = Repair Types II and III membrane waterproofing plus bituminous overlay (maintenance activity).
R = Repairs Types II and III
RL = Repairs Types II and III plus latex concrete overlay.
RC = Repairs Types II and III plus cathodic protection.
RCMO = RC plus membrane waterproofing and bituminous overlay.
RCL = RC plus latex modified concrete.
RPL = Replace the deck.

(6) Intuitively the Benefit/Cost ratio on lower volume roads will not support high cost rehabilitation options.

FIGURE 5.4.1



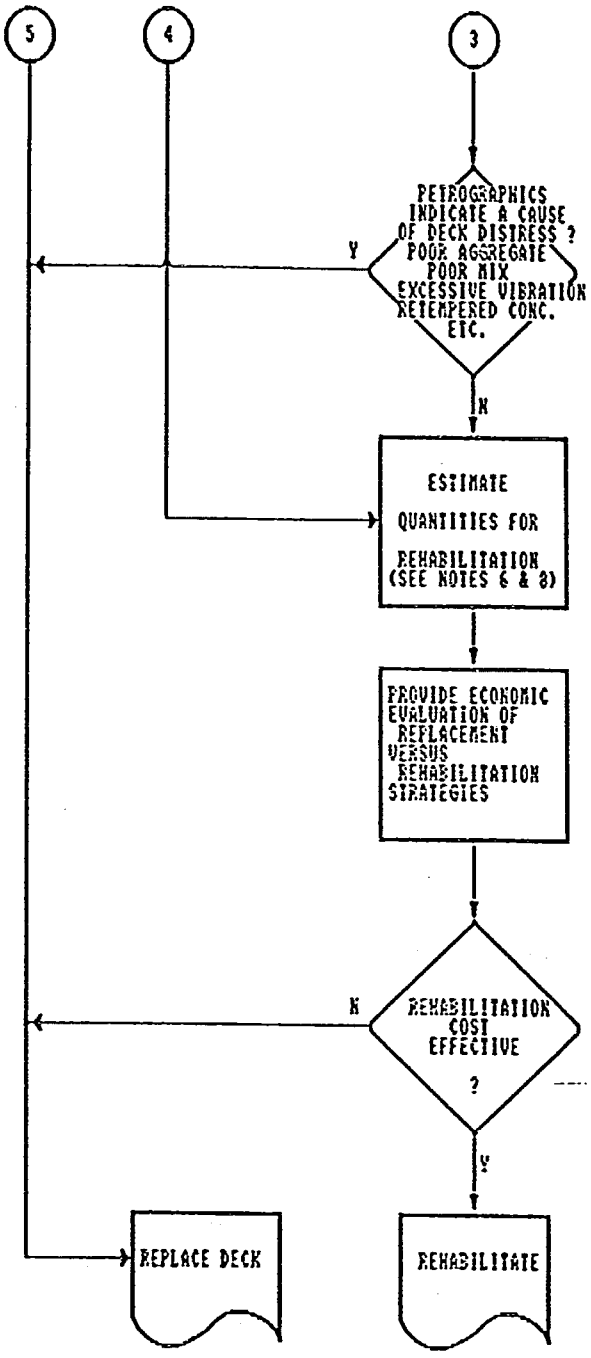
NOTE: LOWER LEVEL OF SERVICE STRATEGIES ARE EVALUATED USING THE SAME DECISION TREE. ACCEPTABLE THRESHOLD VALUES AND REPAIR SCHEMES VARY. THESE ARE SHOWN BELOW.

FOR LOW ADT
DECREASED REPLACEMENT
IF LESS THAN 14'-0" (2) & (3)
NOTE: NUMEROUS EXCEPTIONS EXIST PARTICULARLY IN URBAN AREA. IN URBAN AREAS.

(SEE NOTE 4)

(SEE NOTE 5)

FIGURE 5.4.1 CONT'



GENERAL NOTES FOR FIGURE 5.4.1:

(1) BRIDGES WHICH HAVE A SIGNIFICANT IMPACT ON THE LOACAL ECONOMY SHOULD BE INCLUDED IN THIS GROUP.

(2) REFERENCE AHLSKOG, O'CONNOR "LEVEL OF SERVICE APPROACH TO ESTIMATING NATIONAL BRIDGE NEEDS", IBC-89-71.

(3) CONDITION RATING OF 3 PER BMS.

(4) RESEARCH STUDIES HAVE FOUND CHLORIDE CONTAMINATION ACCELERATES CORROSION WHEN CHLORIDE LEVELS ARE BETWEEN 1.0 AND 1.4 LBS/C.Y.. FHWA HAS NOT MANDATED THRESHOLD VALUES FOR ACCEPTABLE LEVELS OF CHLORIDE CONCENTRATION. CONTAMINATION IS OFTEN DEEMED AS SIGNIFICANT AT THE 1.5 TO 2 LB./C.Y. LEVEL, HOWEVER, BRIDGE DECKS HAVE CONTINUED TO PERFORM WELL WITH 6-9 LBS./C.Y. HIGHER LEVELS OF CHLORIDE CONTAMINATION WILL BE ACCEPTABLE ON LOWER LEVEL ROUTES WHEN PROGRAMMING REHABILITATION/REPLACEMENT STRATEGIES. EACH BRIDGE WILL BE EVALUATED INDEPENDENTLY.

(5) AIR CONTENT WILL BE A FACTOR WHEN DETERMINING THE SALVAGE VALUE OF A BRIDGE DECK. ON FCN ROUTES LOW AIR LESS THAN 3% WILL BE JUSTIFICATION FOR REPLACEMENT. ON LOWER LEVEL SYSTEMS LOW AIR CONTENT WILL BE ACCEPTABLE FOR CERTAIN STRUCTURES, CONCRETE TEE-BEAMS, MONOLITHIC STRUCTURES, ARCHES, ETC. ON LOWER LEVEL ROUTES, LOW AIR CONTENT MAY BE ACCEPTABLE FOR OTHER CASES.

(6) ESTIMATED QUANTITIES FOR REHABILITATION SHOULD REFLECT THE ANTICIPATED QUANTITIES IN THE YEAR OF CONSTRUCTION. RECOMMENDED REHABILITATION SCHEMES FOR HIGH AND MEDIUM ADTT ROUTES INCLUDE CATHODIC AND LATEX MODIFIED CONCRETE.

(7) ESTIMATED QUANTITIES FOR REHABILITATION SHOULD REFLECT THE ANTICIPATED QUANTITIES IN THE YEAR OF CONSTRUCTION. RECOMMENDED REHABILITATION SCHEMES FOR LOW VALUE ADTT ROUTES INCLUDE BITUMINOUS OVERLAYS WITH MEMBRANE AND LATEX MODIFIED CONCRETE.

(8) BITUMINOUS OVERLAYS WITHOUT MEMBRANES ARE VIABLE OPTIONS ON ALL ROUTES WHEN THE BRIDGE DECK HAS BEEN PROGRAMMED FOR REPLACEMENT AND THE OVERLAY IS USED TO PROVIDE A SMOOTH RIDING SURFACE UNTIL REPLACEMENT CAN BE ACCOMPLISHED.

Damage and Its Reinforcement of Post-tensioned Prestressed Concrete Bridge Slab

Isao Sugie and Yoshihiro Yamaguchi
Chief Engineer of Hanshin Expressway Public Corporation
Japan

Kazuo Kobayashi
Professor of Osaka Institute of Technology
Japan

Kazuhiro Kuzume
President of Kokusai Structural Engineering Corp.
Japan

SUMMARY

The object of this study is to examine the causes for damages such as free-lime exudation and water leakage or depression of filler concrete at the joints in the slab of prestressed precast concrete T-girders bridge, and then to confirm the effect of reinforcing by means of steel plate bonding against them.

In the series of tests, strength of concrete filled into a joint between precast concrete elements, amount of introduced prestress and then existence of penetrated water through concrete surface were chosen as the main test variables and their influences on structural damages were studied by carrying out fatigue loading tests on beam models.

1. INTORODUCTION

In September 1989, an accident occurred on the Hanshin Expressway. A part of the paving covering an area of 45 cm in length and 54 cm in width collapsed at the joint of the bridge slab. The bridge slab was constructed by filling cast-in-situ concrete into an aperture between flanges of two adjacent post-tensioned prestressed concrete T-girders and by connecting them monolithicly with transverse prestressing. This type of slab joint is referred to as the "joint" hereafter. The accident was detected initially as a dislocation at the joint, and some concrete pieces of approximately 10 cm in thickness were found under the concerned expressway. The pieces were made both of prestressing steel (12-ϕ 5) and sheath for transverse prestressing, and were severely corroded and broken. The cast-in-situ concrete filler in the joint was completely separated from the flange of the T-girder, and therefore the structural soundness of bridge slab was considered to have been lost significantly.

The deteriorated bridge slab was reinforced immediately, in a manner so that the lower face of the joint was bonded with steel plate and then was supported against the web of main girders through a pair of rib and diagonal struts.

There are two methods of reinforcing the damaged joint: 1) to introduce prestress by using external tendons, and 2) to increase flexural rigidity of the main girder by bonding it with steel plate. Considering the simplicity of work, the time spent for work and the

necessity of traffic regulations on the main line of the expressway, the rib-strut method was adopted in combination with the steel plate bonding technique in this case. On the other hand, a more simple and practical reinforcing method has been investigated to mitigate the time spent for work and some problems of spoiling the appearance.

In this study, the causes of the above mentioned damage, as well as the effectiveness of reinforcement by means of steel plate bonding, were examined by carrying out a series of fatigue tests on the beam model specimens.

2. STATE OF DAMAGE OF BRIDGE SLAB WITH JOINT

In 1965, the joint of a bridge slab composed of flanges of prestressed concrete T-girders was dealt with in such manner that concrete was filled into an aperture without steel bars located between two adjacent upper flanges and then an appropriate amount of prestress was introduced to make a full monolithic connection. In this case, as shown in Fig. 1(b), the joint had two perpendicular surfaces without shear keys for transmitting shear force.

After 1980, however, the joint was provided with steel bars and their surfaces were tapered as shown in Fig. 1(a).

A total of 73 spans of post-tensioned prestressed concrete girders were constructed on the Loop Line of Hanshin Expressway, 22 of which have the joint of old type described above. There are a total of 404 panels, each being surrounded by two main girders and transverse diaphragms.

The results of the inspection done according to "Inspection Standard of Road Structures", severe types of damage, such as scaling, spalling or cave, are scarcely recognized, although some cracks occurred in nearly half of all panels. On the contrary, water leakage and free-lime exudation can be found on 348 panels, which corresponds to 86% of all panels. The significantly damaged panels have a high possibility of concrete falling at the joint as mentioned above, and therefore reinforcing shoud be done without delay.

3. OUTLINE OF FATIGUE TESTS

Test Program

Firstly, in order to identify the causes of damage induced at the joint, the strength of concrete filled into a joint between precast concrete elements, the amount of introduced prestress and the existence of penetrated water through the concrete surface were chosen as the main test variables, and their influences on structural behavior were studied by conducting fatigue tests on beam models.

The following parameters were prepared for each test variable.

i) strength of filler concrete : two kinds of design strength fck=300kgf/cm^2 and 180kgf/cm^2, in which the former was equal to normal design value.

ii) amont of introduced prestress : three levels of σ p=40kgf/cm^2, 20kgf/cm^2 and 10kgf/cm^2, in which the first corresponded to normal design value.

iii) existence of penetrated water : two kinds of wet and dry conditions with and without penetrated water, respectively.

Next, the effect of waterproof coating against penetration of water through the concrete surface and then the strengthening effect by means of steel plate bonding for deteriorated beams were examined by the beam model tests.

As shown in Fig. 2 the dimensions of the test beams are 500mm in width, 200mm in height and 2300mm in length.

A total of 17 beams were programmed in combination with the test variables and their parameters, as listed in Table 2.

Fabrication of Test Beams

A prestressing bar of ϕ 23mm with eccentricity ep= 15 mm through a metal sheath was tensioned 10 days after filling concrete into the 500mm wide joint part between precast concrete elements of design compressive strength 400kgf / cm^2 . Immediately after stressing the bar, the prestressing duct was grouted with an expanded cement paste in a water/ cement ratio of 40%.

Some beams were strengthened by steel plate of 4.5 mm in thickness bonded on the tension face by means epoxy adhesive and by supplementary anchor bolts extending through the beam at appropriate intervals. The steel plate bonding was done according to the specification for strengthening concrete slabs of bridges of the Hanshin Expressway Public Corporation.

Fatigue Tests

Each beam was simply supported over a span of 2000mm and was repeatedly loaded up to 2×10^6 cycles at maximum under symmetrical two -point loads, in which the loading rate was set to be 5.5 Hz using a hydraulic servo-jack system.

In the fatigue tests, the minimum load was one ton for all beams and the maximum load was varied considering the objective of each test as listed in Table 1. The load value of three tons in Table 1 indicates the design load of the normal beam being fck=300kgf/cm^2 and σ p=40kgf/cm^2 ,and being set at the decompression state.

The deflections and concrete strains were measured at the center- and quarter-points of the span by using electrical tranducers and electrical resistance strain gauges, respectively. The widths of crack opening were also measured by using π -shaped gauges at the joint surfaces. And then, the strain of prestressing bar was measured at the center-point of the beam span.

4. RESULTS AND DISCUSSION

The results of tests are listed in Table 2. The beams which survived 2×10^6 cycles of fatigue loading were again tested at higher levels of repeated loads or loaded up to failure under static loading.

Some typical midspan deflection-repeated cycles relations are shown in Fig. 3. And, in Fig. 4, the crack pattern and failure mode inside the joint part of the beams which failed due to fatigue are illustrated. Cracks scarcely occurred in the precast concrete elements.

It is found from the results of beams H2-3, H2-7 and H4-1 that the joint can sufficiently endure 2×10^6 cycles repetition at a load level of approximately 2.3 times the design load, even under wet conditions, in the case where both the amount of introduced prestress and the strength of filler concrete satisfy each design requirement (σ p=40kgf/cm^2 , fck= 300kgf/cm^2). In such beams, as shown in Fig. 3, an increase in deflection with repeated cycles as well as its absolute value is significantly small.

The results of beams H2-1, H2-4, H2-5 and H2-8 indicated that the fatigue failure did not occur up to 2×10^6 cycles repetition of the design load, even when either of amount of prestress or strength of filler concrete was reduced to 50% of each normal design value. And then,

even if both of them are down to 50% of the normal value as done for beam H2-6, similar behavior was recognized as the normal beam H4-1 when subjected to 2×10^6 cycles of the design load.

As far as these tests are concerned, the failure due to fatigue is not likely to occur at the design load, until the strength of filler concrete and the prestressing force fall to about 50% and 25%, respectively, of each prescribed design value. The fatigue strength of the joint, in particular, was found to be significantly affected by an existing amount of prestress.

Comparing, a dry beam with a wet one, for instance, beams H2-1/H2-5, H2-4/H2-8, and H3-7/H3-7, the fatigue life of the former was confirmed to be 1/100 ~ 1/10 of the latter.

As shown in Fig. 4, the joint part of tested beams without steel plate reinforcement failed finally in concrete crushing due to flexure after the predominant flexural crack at the joint surfaces grew vertically up to the mid-height of the beam section and thereafter extended almost horizontally, whereas a kind of punching shear failure was observed in an existing bridge slab.

Even in beam H4-2 ($\sigma p = 10 kgf/cm^2$, $fck = 180 kgf/cm^2$), satisfactory fatigue strength could be attained at 2.3 times the design load by bonding steel plate on the tensile surface of the section. Therefore, the steel plate bonding technique was confirmed to be very effective for improving the fatigue strength of the joint.

Beam H3-3 failed finally by breaking of the steel plate near the center-point of the span at about 10^6 cycles under loading equal to 65% of its static ultimate flexural strength, of which repeated load corresponded to 4.3 times the design load without plate bonding.

5. CONCLUSION

The results of the series of tests are summarized as follows.

1) The steel plate bonding technique was considered to be very effective for reinforcing the joint of a bridge slab. And, the joint was found not to become a weak point in the concrete slab of bridge when strengthened with steel plate

2) When both the amount of prestress and the strength of concrete for filling the joint satisfy the design requirement, the joint was confirmed to have sufficient fatigue strength even under a loading level of about 2.3 times the design load, which corresponded to the decompression state of the prestressed section.

3) Even if the amount of introduced prestress and the strength of filler concrete are reduced down to 50% of each normal design value, the joint was found to possess sufficient fatigue strength at the design load.

4) The amount of existing prestress was recognized to have a particularly important effect upon the fatigue strength of the joint.

5) When beam concrete was kept in a dry condition by applying an appropriate waterproof coating, the fatigue life of the joint could be extended up to 10~100 times that under a wet condition.

In addition to the beam model tests as done in this study,the effectiveness of reinforcement due to steel plate bonding shoud also be examined on the basis of fatigue loading tests using the slab models simulating the actual bridge decks.

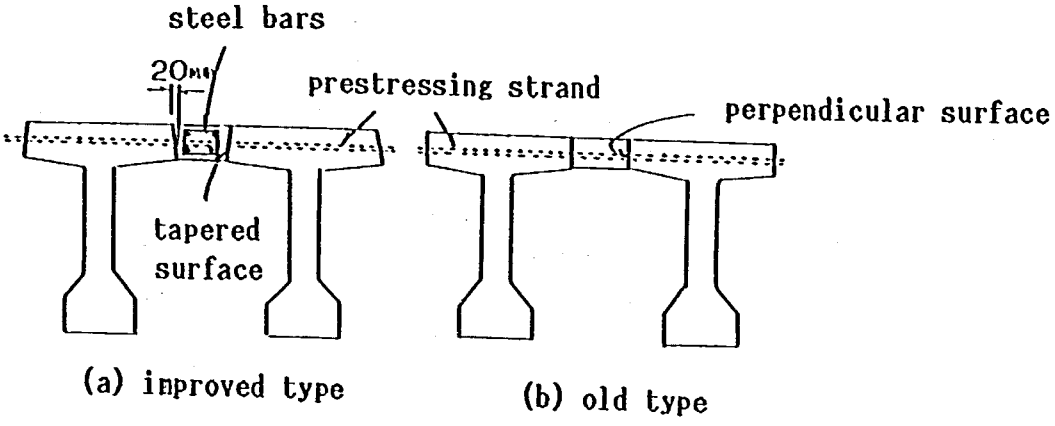


Fig. 1 Types of joint structure prestressing bar

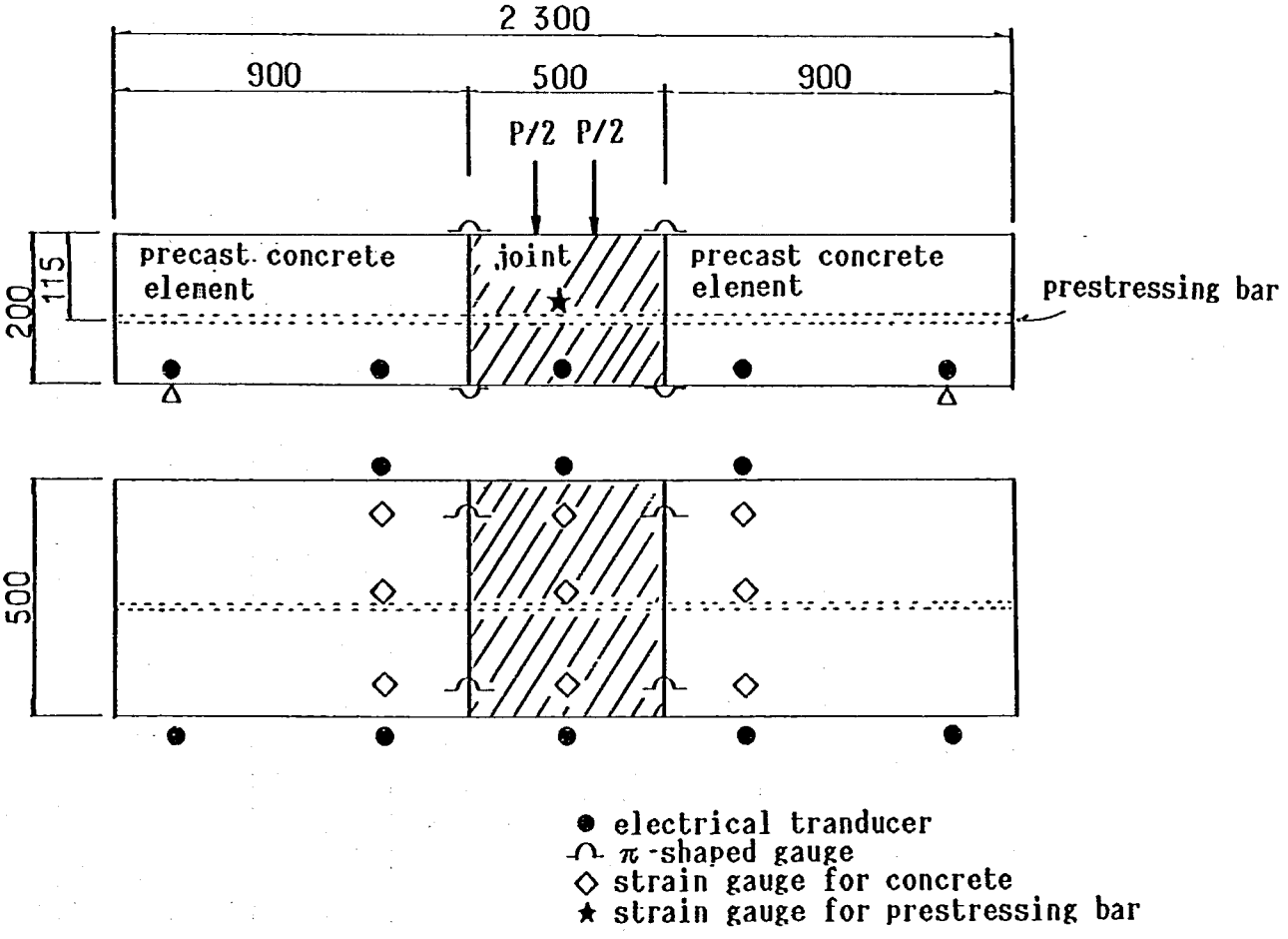


Fig. 2 Dimensions of tested beans (unit:mm)

Table. 1 The naxiun load in Fatigue test

naxiun load	3.0 ton	5.5 ton	7.0 ton	13.0 ton
renarks	design load	65% of static ultinate flexural strength (Pu=8.5 ton)	65% of static ultinate flexural strength (Pu=11.2 ton)	65% of static ultinate flexural strength with steel plate (Pu=19.9 ton)
conditions	deconpression state for nornal beam	using H2-6 $f_{ck}=180kgf/cm^2$ $\sigma_p=20kgf/cm^2$	using H2-7 $f_{ck}=180kgf/cm^2$ $\sigma_p=40kgf/cm^2$	using H3-5, 6 $f_{ck}=180kgf/cm^2$ $\sigma_p=20kgf/cm^2$

Table. 2 Details of test variables and test results

specimen No.	fck' (kgf/cm²)	σ_p (kgf/cm²)	conditions of concrete	rein-forcement	naximun load(ton)	repeated cycles	failure mode	final deflection / initial deflection
H2-3	300	40	dry	—	3.0	2,000,000	—	1.00
			dry	—	7.0	2,000,000	—	1.58
H2-7	300	40	wet	—	3.0	2,000,000	—	1.00
			wet	—	(11.2)	static test	crushing of concrete	—
H4-1	300	40	wet		7.0	2,000,000	—	1.52
H2-1	180	40	dry	—	3.0	2,000,000	—	1.06
			dry	—	7.0	1,990,000	breaking of PC-bar	2.41
H2-5	180	40	wet	—	3.0	2,000,000	—	1.02
			wet	—	7.0	17,130	crushing of concrete	2.14
H2-4	300	20	dry	—	3.0	2,000,000	—	2.00
			dry	—	7.0	78,000	crushing of concrete	1.20
H2-8	300	20	wet	—	3.0	2,000,000	—	1.10
			wet	—	7.0	2,430	crushing of concrete	1.39
H2-6	180	20	wet	—	3.0	2,000,000	—	1.09
			wet	—	(8.5)	static test	crushing of concrete	—
H3-1	180	20	wet	—	5.5	3,470	crushing of concrete	1.22
H3-5	180	20	dry	steel plate	5.5	2,000,000	—	0.91
			dry	steel plate	7.0			
H3-6	180	20	wet	steel plate	5.5	2,000,000	—	1.00
			wet	steel plate	(19.9)	static test	peeling off of plate	—
H3-7	180	20	dry	—	5.5	39,000	crushing of concrete	1.38
H3-3	180	10	dry	—	3.0	2,000,000	—	2.04
			dry	steel plate	7.0	2,000,000	—	1.02
			dry	—	13.0	1,026,000	breaking of steel plate	1.18
H3-4	180	10	wet	—	3.0	197,000	crushing of concrete	2.11
H4-2	180	10	wet	steel plate	3.0	2,000,000	—	1.18
			wet	steel plate	7.0	2,000,000	—	1.06

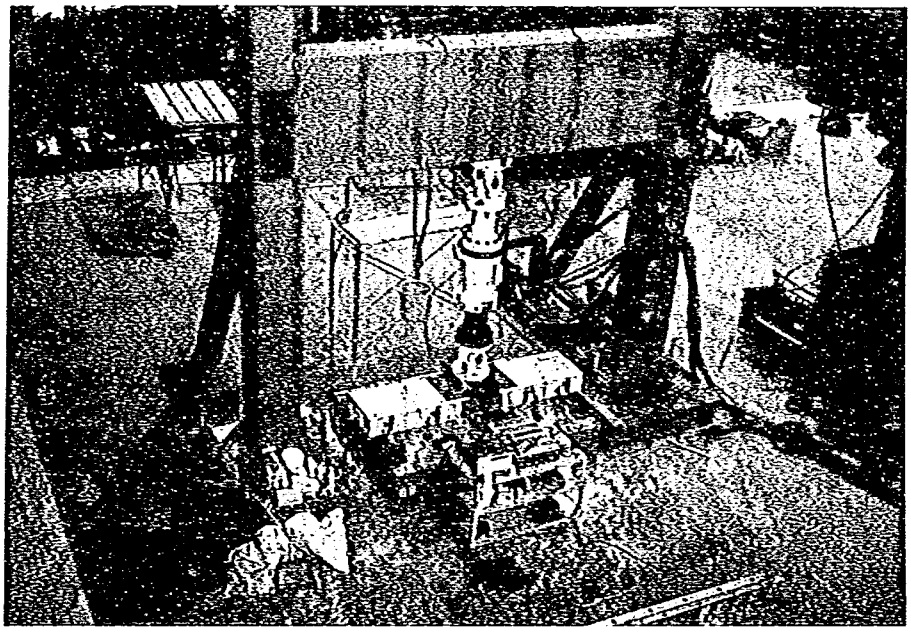


Photo. 1 View of Fatigue tast

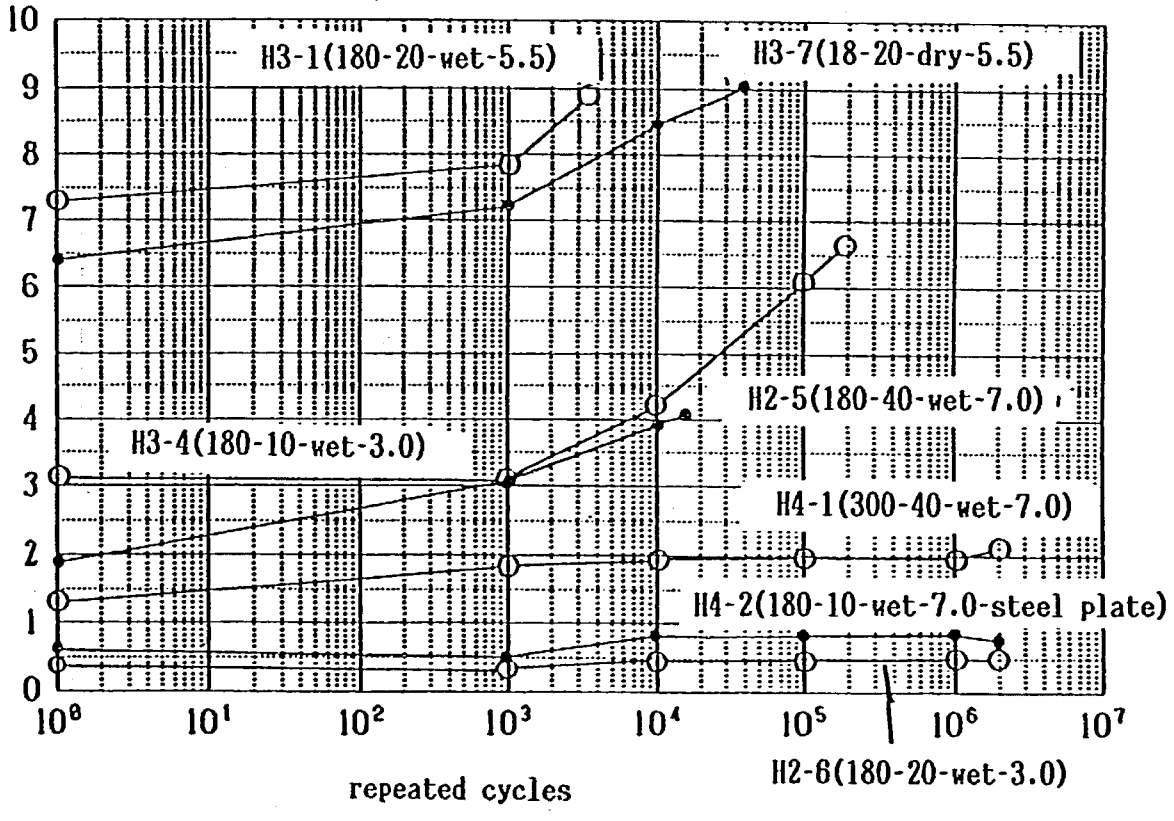


Fig. 3 Relation between midspan deflection and repeated cycles

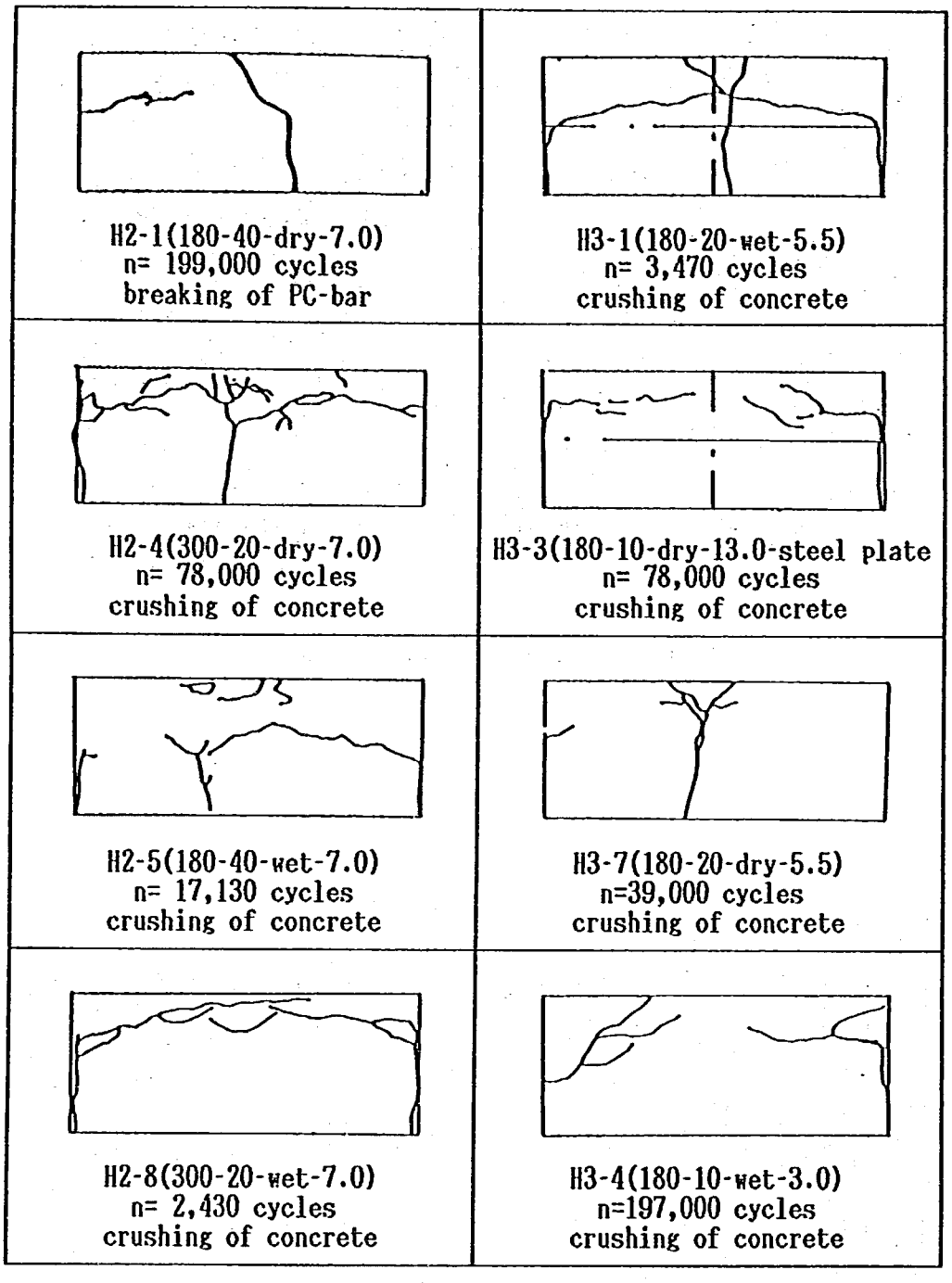


Fig. 4 Crack pattern of joint part

(3) Session 3

Superstructure (2)

4) Strengthening of Steel-Stringer Bridges by Post-Tensioning
(F.W. Klaiber*, K.F. Dunker, T.J. Wipf and F.S. Fanous)

5) Application of Buried Joint in Cold and Snowy Region
(T. Shirono*, H. Nishi, O. Nakano and K. Kumagai)

STRENGTHENING OF STEEL-STRINGER BRIDGES BY POST-TENSIONING

F. W. Klaiber, K. F. Dunker, T. J. Wipf, F. S. Fanous

Department of Civil and Construction Engineering
Iowa State University
Ames, Iowa

ABSTRACT

The need to upgrade a large number of understrength bridges in the United States has been well documented in the literature. Through several research projects which involved testing of strengthening schemes on scale model bridges in the laboratory as well as the testing of strengthening systems on existing bridges, the concept of strengthening simple-span and continuous-span bridges by external post-tensioning has been developed. A post-tensioning strengthening design manual for simple span bridges has been developed for use by practicing engineers. A similar manual for continuous-span bridges is currently being developed. In addition to the post-tensioning system, the authors have developed superimposed trusses which currently are being tested on a continuous steel-stringer bridge. This paper will briefly review these strengthening procedures which have been successfully employed in the field.

INTRODUCTION

Of the large percentage of the nation's bridges classified as deficient and in need of rehabilitation or replacement, many are deficient because their load-carrying capacity is inadequate for today's traffic. Strengthening can often be used as a cost-effective alternative to replacement or posting for restricted loads.

For the past 12 years, the authors have been investigating the use of external post-tensioning for strengthening existing steel-stringer bridges. Although this work involved numerous projects, for clarity in this paper, it will be presented as two projects with several phases:

Project I: Strengthening of Existing Single-Span, Steel-Stringer, Concrete-Deck Bridges: Phases I-1, I-2, and I-3.

Project II: Strengthening of Existing Continuous-Span, Steel-Stringer, Concrete-Deck Bridges: Phase II-1, II-2 and II-3.

This paper briefly describes the laboratory portions of the study (Phases I-1 and II-1) and emphasizes implementation and testing of the post-tensioning strengthening systems on existing structures. References are provided on all phases of the investigation (except Phase II-3 which is still in progress) for those desiring additional details.

PROJECT I

As previously noted, Project I consisted of three separate phases: Phase I-1--Laboratory Investigation, Phase I-2--Field Study, and Phase I-3--Development of a Design Methodology. Results of these three phases will be presented in the following sections.

Phase I-1

One of the objectives of this phase was to determine a procedure for strengthening single-span, composite steel-stringer concrete-deck bridges (Klaiber, et al., 1981, 1982). In most cases, only the exterior stringers of these bridges required strengthening. After reviewing several possibilities, post-tensioning the exterior stringers was determined to be the most promising. The feasibility of this strengthening technique was verified analytically and experimentally through the testing of various post-tensioning schemes on a half-scale model bridge [L = 26'-0" (7.925 m), W = 15'-8 3/8" (4.785 m)]. Various post-tensioning schemes were investigated to obtain data on the lateral distribution in the bridge; as previously noted, in most cases only the exterior stringers actually required post-tensioning to reduce the overstress. Due to lateral distribution, when the exterior stringers are subjected to post-tensioning, significant stress reduction results in the interior stringers. The bridge model was fully instrumented for determination of strains and deflections at critical locations. Excellent agreement was found between measured strains and deflections and the respective theoretical values.

Phase I-2

As a result of the success of the Phase I laboratory investigation (Phase I-1), Phase I-2 (Klaiber, et al., 1983; Dunker, et al., 1985b) of the investigation was undertaken. This phase consisted of field strengthening and monitoring two existing bridges. One of the bridges, [Bridge 1: L = 52 ft (15.849 m), W = 31 ft - 10 1/2 in. (9.715 m)] (see photograph of bridge and bracket used in Fig. 1) was a prototype of the model bridge tested during Phase I-1. The other bridge, [Bridge 2: L = 72 ft (21.945 m), W = 31 ft - 10 1/2 in. (9.715 m)] (see photograph of bridge and bracket used in Fig. 2), was considerably longer and had a 45° skew. In both these bridges, the exterior stringers are smaller than the interior stringers.

Theoretical analyses indicated Bridge 1 needed two, high strength tendons [2 - 1 1/4 in. (32 mm) in diameter] and Bridge 2 needed four high strength tendons [2 - 1 1/4 in. (32 mm) in diameter plus 2 - 1 in. (25 mm) in diameter] for the required post-tensioning force. Post-tensioning brackets were attached to the stringers using high strength bolts as shown in Figs. 1 and 2. The concern that the type of steel in some bridges requiring strengthening is unknown prompted the decision to use bolts rather than welding. Although only the exterior stringers in both bridges were post-tensioned, significant stress reduction was also obtained in the interior stringers because of lateral distribution.

For composite action, both bridges had angle-plus-bar type shear connectors. Analyses indicated that for the bridges to carry additional live load, the exterior stringers of Bridge 1 and all the stringers of Bridge 2, needed additional shear connectors. The unknown type of steel concern previously noted prompted the decision to add shear connectors by bolting rather than by welding. High-strength bolt shear connectors tested in the laboratory were found to be slightly stronger than shear studs of equivalent size (Dedic and Klaiber, 1984; Klaiber, et al., 1983). In the field, cores [4 in. (102 mm) in diameter] were drilled in the

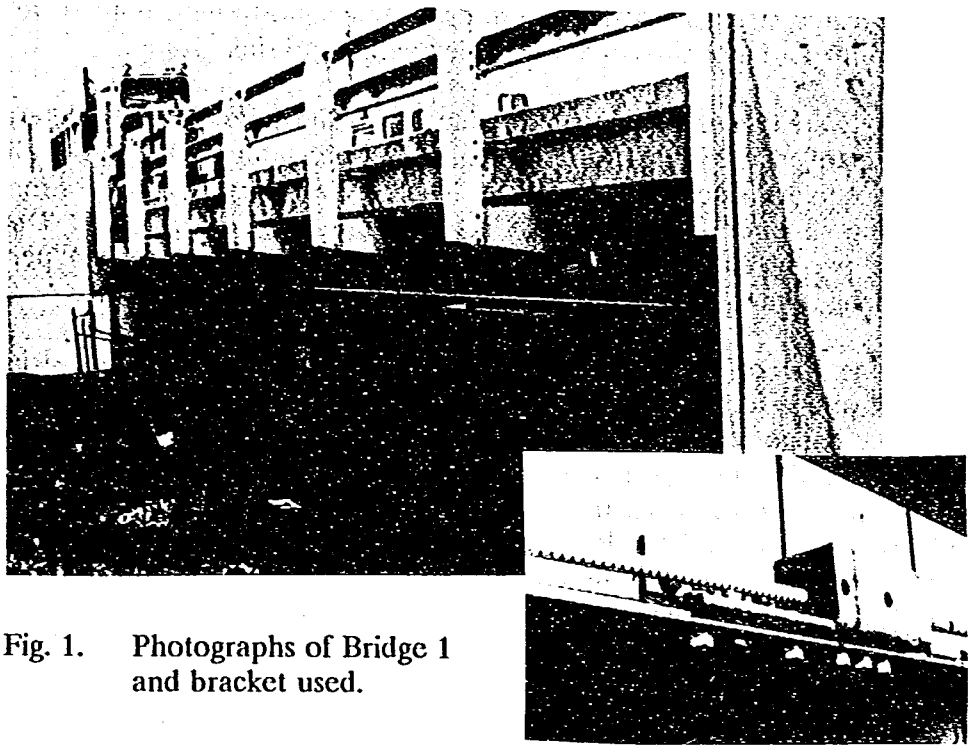


Fig. 1. Photographs of Bridge 1 and bracket used.

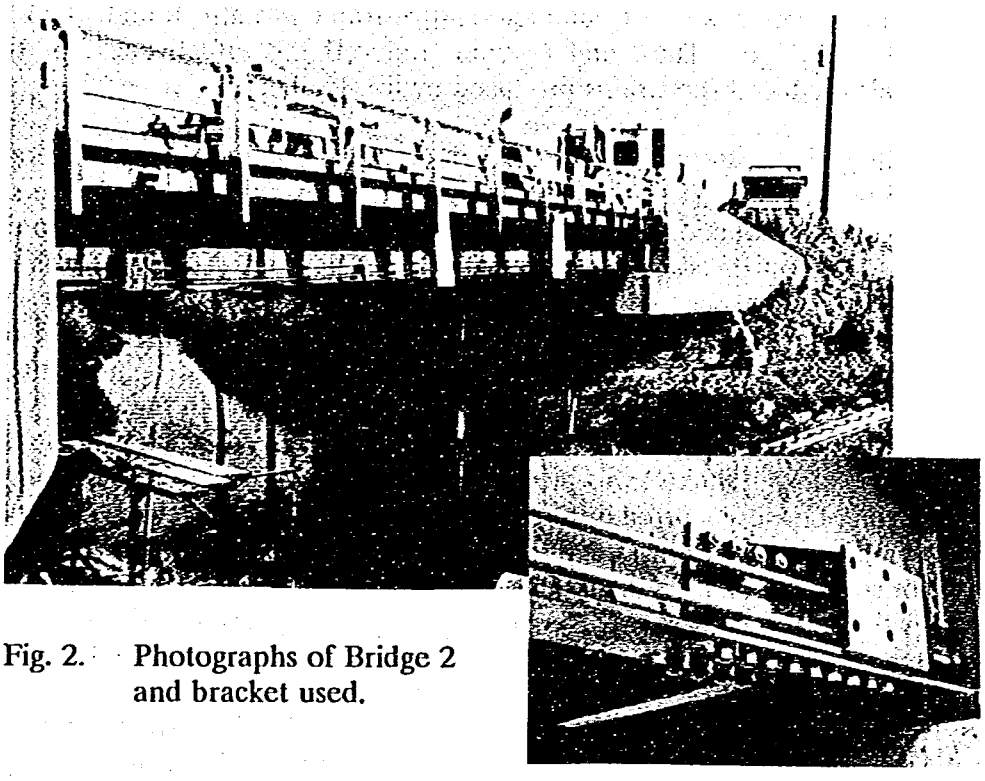


Fig. 2. Photographs of Bridge 2 and bracket used.

bridge deck above the stringers in the two bridges, and high-strength bolts were double-nutted to the stringers. Later the cores were filled with nonshrink grout.

Both bridges were instrumented to determine strains and deflections. To determine the bridges' response to post-tension strengthening, they were both load tested with heavily loaded trucks prior to and after post-tensioning. The two bridges were initially strengthened and tested during summer 1982 and were retested during summer 1984. During the intervening time period and the time period since, the bridges have been periodically inspected; no changes have been noted in either bridge.

Bridge 1: During the original post-tensioning of Bridge 1, each exterior stringer was subjected to an average force of 182.0 kips (810 kN), to produce a strain reduction of 218 MII in the lower flange coverplates of the exterior stringers. However, because of the presence of end restraint, a strain reduction of only 145 MII was obtained. When the post-tensioning force was removed from the bridge during summer 1984, a magnitude of 172.0 kips (765 kN) was measured. This decrease in force (5.5%) is primarily due to a decrease in the amount of end restraint present, however, a small percentage of the decrease is due to relaxation of the post-tensioning tendons. A post-tensioning force of 196.8 kips (875 kN), which produced an average upward displacement of 0.18 in. (5 mm) in the exterior stringers, was reapplied to each exterior stringer during summer 1984. The midspan bottom flange coverplate strains resulting from this post-tensioning force are shown in Fig. 3. Also shown in the figure are theoretical curves, obtained from finite element analysis, for both simple support and fixed end conditions. The measured strains are essentially midway between the two theoretical curves, thus indicating the presence of significant end restraint. An additional verification of the presence of end restraint is the sizable magnitude of strains that were measured at instrumented sections 9 in. (229 mm) from the centerline of supports. Although the desired strain reduction was not obtained, end restraint was also found when live load was placed on the bridge. Thus, end restraint reduced the effectiveness of the post-tensioning and also reduced the strains produced by live load.

Bridge 2: Initially, each exterior stringer of Bridge 2 was subjected to an average post-tensioning force of 305.6 kips (1359 kN) that, based on the assumption of simple supports, was to produce a strain reduction in the lower flange of 212 MII. However, when this force was applied, a reduction of slightly less than half that amount (102 MII) was obtained because of the skew effect and the presence of end restraint. During summer 1983, this bridge was resurfaced and had major portions of the curb sections removed and replaced. Because the post-tensioning forces were still in place, large upward displacements were visible upon removal of the dead load and the associated reduction in the effective section. When the post-tensioning force was removed from the bridge during summer 1984, a magnitude of 271.5 kips (1206 kN) was measured. This decrease of 11.2% is thought to be primarily the result of losses incurred during the rehabilitation of the bridge which took place the previous summer. A post-tensioning force of 371.2 kips (1651 kN) was then reapplied to each exterior stringer, resulting in an upward displacement of 0.33 in. (8 mm). Shown in Fig. 4, along with the theoretical curves assuming simple supports and fixed ends, are the midspan bottom flange coverplate strains resulting from this post-tensioning force. Because of the skew, the end restraint present in this bridge was greater than that observed in Bridge 1. Note, the measured strains on the exterior stringers shown in Fig. 4 are closer to the fixed end theoretical curves than to the simple span theoretical curves. As in Bridge 1, significant strains were measured in the vicinity of the supports which verified the presence of end restraint. End restraint again reduced the effects of live load. In effect, the live load tension

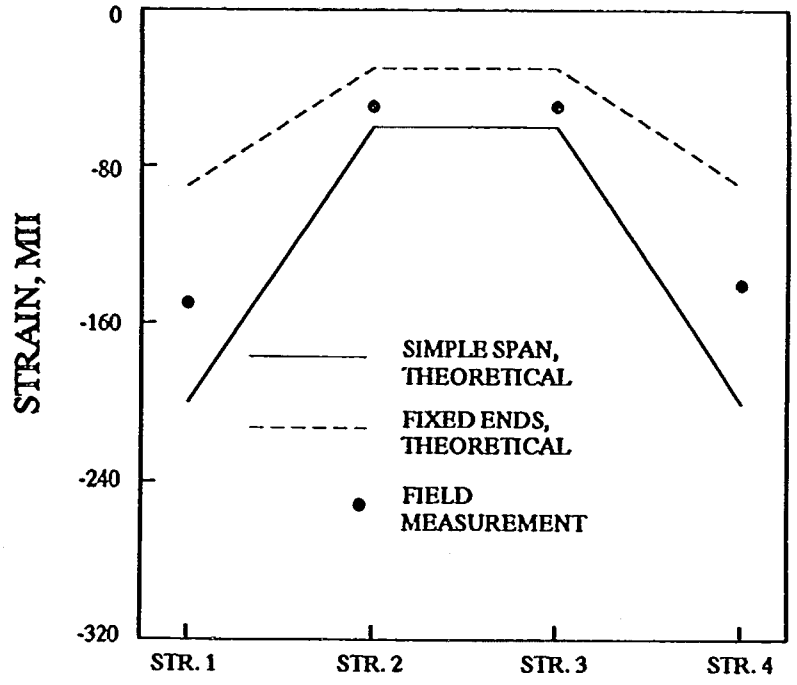


Fig. 3. Post-tensioning midspan, bottom flange stringer strains - Bridge 1.

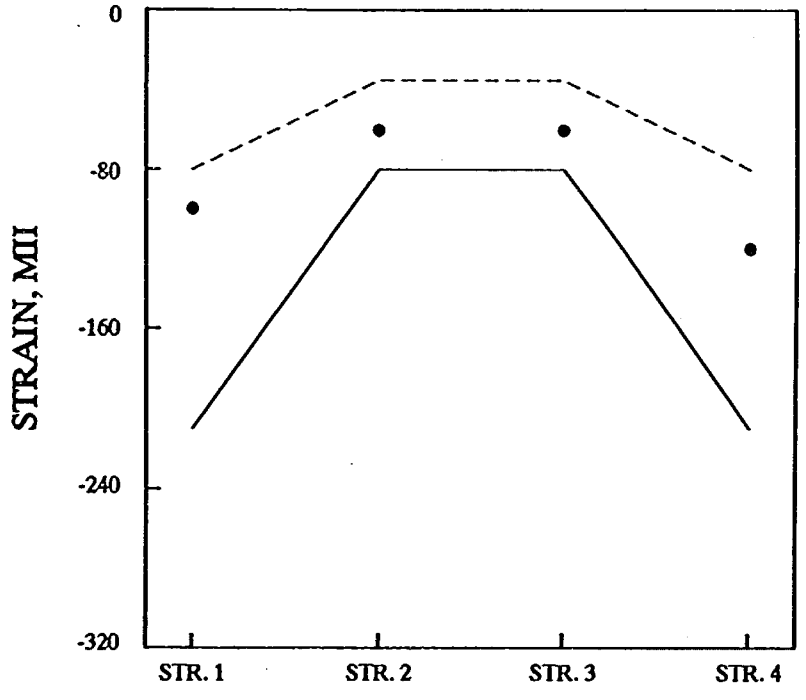


Fig. 4. Post-tensioning midspan, bottom flange stringer strains - Bridge 2.

strains, which were lower-than-expected, compensated for the lower-than-expected post-tensioning compression strains.

Phase I-3

The third phase of the investigation (Dunker, et al., 1985a, 1986) involved the development of a simplified design methodology for practicing engineers so that they could avoid use of orthotropic plate theory and/or finite-element analysis.

By analyzing an under-capacity bridge, an engineer can determine the overstress in the interior and exterior stringers. This overstress is based on the procedure of isolating each bridge stringer from the total structure. The amount of post-tensioning required to reduce the stress in the stringers can then be determined if the amount of post-tensioning force remaining on the exterior stringers is known; this force can be quantified with force and moment fractions. A force fraction, FF, is the ratio of the axial force that remains on a post-tensioned stringer at midspan to the sum of the axial forces for all bridge stringers at midspan, while a moment fraction, MF, is the moment remaining on the post-tensioned stringer divided by the sum of midspan moments for all bridge stringers. Knowing these fractions, the required post-tensioning force may be determined by utilizing the following relationship:

$$f = FF\left[\frac{P}{A}\right] + MF\left[\frac{Pec}{I}\right]$$

where f = desired stress reduction in stringer lower flange.
P = post-tensioning force required on each exterior stringer.
A = cross-sectional area of exterior stringers.
e = eccentricity of post-tensioning force measured from the bridge's neutral axis.
c = distance from neutral axis of stringer to lower flange.
I = moment of inertia of exterior stringer at section being analyzed.

Distribution factors were determined by a finite element analysis, the accuracy of which was determined through use of the data obtained in the laboratory and field tests. A series of experiments was conducted with the finite element model to determine the sensitivity of the distribution factors to the various bridge variables. These experiments demonstrated that variables such as the stiffness of shear connectors, cover plate length, bridge skew, and deck crown had no significant effects. Those variables having significant effects on the distribution factors are end restraint, span and anchorage location, and relative beam stiffness:

- Through analysis it was found that end restraint increased the amount of post-tensioning force and moment retained by the exterior stringers. However, because of the difficulty in quantifying end restraint existing in actual bridges, partial end restraint was conservatively neglected in the design methodology.

- Span length was found to be the most significant variable in the moment fractions; exterior stringers were found to retain less moment as the span length was increased. The distribution was also determined to be dependent on the length of the stringers subjected to post-tensioning (i.e., distance between anchorages).

- Moment distribution was found to be dependent on relative stringer stiffness; stiffer exterior stringers retained more post-tensioning moment. Thus, if the exterior stringers were smaller than the interior stringers, the exterior stringers retained considerably less of the post-tensioning moment than if the stringers were all the same size.

Utilizing the finite element model, bridges having various combinations of the previously noted variables were analyzed to determine the midspan force and moment fractions. By using a multiple linear regression procedure, relatively simple equations with high degrees of accuracy were derived for the distribution fractions. For the distribution fractions and other details on the design methodology the reader is referred to Dunker, et al., 1985a.

The strengthening procedure and design methodology just described have been used on several bridges in the states of Iowa, Florida, and South Dakota. In all instances, the procedure was employed by local contractors without any significant difficulties.

PROJECT II

In addition to the problems with single-span bridges that were addressed in Project I, there are a large number of continuous composite bridges that are also structurally inadequate. Some of these bridges are overstressed in the negative moment regions, some in the positive moment region, while a large number are overstressed in both regions.

Phase II-1

On the basis of Project I results, it appeared that post-tensioning could also be used to strengthen continuous bridges. Thus, the primary objective of this phase of the investigation was to determine the feasibility of strengthening continuous span composite bridges by post-tensioning. More specific objectives of the study were to determine: the distribution of post-tensioning forces and moments in the positive and negative moment regions, the best tendon arrangement, and the contribution of the deck to composite action in negative moment regions.

The objectives of this project were fulfilled through testing of a continuous span model bridge (Dunker, et al., 1987, 1990). Because of space limitations in the Structural Engineering Laboratory, it was necessary to limit the size of the bridge model. After reviewing various possibilities, it was decided to construct a one-third-scale four-beam, three-span continuous bridge. The overall dimensions of the bridge are total length = 41 ft - 11 in. (12.776 m), width = 8 ft - 8 in. (2.642 m), deck thickness = 2.25 in. (57 mm), and individual span lengths = 12 ft - 8 in. (3.861 m), 16 ft - 4 in. (4.978 m), 12 ft - 8 in. (3.861 m). To accurately model the stringers, the stringer sections were fabricated from steel sheet and plate. The exterior and interior stringers were 6 in. (15 mm) and 7 in. (18 mm) in depth, respectively.

The bridge model was instrumented for strain and deflection measurements at critical sections; each tendon was strain gaged so that accurate post-tensioning forces could be determined. Post-tensioning continuous bridges is considerably more complex than post-tensioning simple-span bridges because longitudinal and transverse distributions must both be determined. Tendons were mounted on the bridge so that the positive moment regions of all stringers (12 areas) and the negative moment regions of all stringers (8 areas) could

be post-tensioned. This arrangement of tendons made it possible to investigate essentially any combination of post-tensioning.

Experimental strains and deflections measured were found to be in excellent agreement with those obtained in the finite element analyses. Post-tensioning the positive moment regions of the stringers produced beneficial strains (i.e., opposite to those produced by dead load) both at midspan and at interior supports. Similar results were obtained when the negative moment regions of the stringers were post-tensioned. Thus, depending on the bridge, it may be possible to strengthen it (both in the positive and negative moment regions) by post-tensioning only the positive moment regions of the stringers. Because of the presence of the deck, post-tensioning the positive moment regions is obviously simpler than post-tensioning the negative moment regions of a given stringer.

In the strengthening of a continuous span bridge, the engineer has so many variables (stringers to be post-tensioned, regions of stringers to post-tensioned, magnitude of post-tensioning force, post-tensioning length, etc.) that in essentially all cases it is possible to "fine-tune" the bridge--that is, reduce strains at the critical locations the desired amount.

Phase II-2

This phase of the investigation (Klaiber, et al., 1990a, 1990b)--post-tension strengthening of an existing continuous-span bridge--was undertaken as a result of the successful laboratory investigation (Phase II-1). A photograph of the bridge selected for strengthening [Bridge 3: L = 150 ft (45.719 m), W = 26 ft (7.925 m) individual span lengths = 45 ft - 9 in. (13.944 in.), 58 ft - 6 in. (17.831 m), 45 ft - 9 in. (13.944 m)] is shown in Fig. 5. Exterior stringers in this bridge are smaller than the interior stringers. An analysis of the bridge indicated that the bridge required strengthening to reduce flexural stresses; additional shear connectors were also needed to improve composite action. The additional shear capacity was obtained by adding high strength bolt shear connectors which were previously described.

The post-tensioning scheme designed involved post-tensioning the positive moment regions of all stringers: 106 kips (472 kN) for all end span stringers, 138 kips (614 kN) for the exterior middle span stringers, and 160 kips (712 kN) for the middle span interior stringers. This post-tensioning system will reduce flexural stresses to the desired level in all but a few locations. To obtain these forces, two 1 1/4 in. (32 mm) diameter high strength tendons were attached to the positive moment region of each stringer.

Bridge 3 which was instrumented for deflection and strain measurement was originally strengthened and tested during the summer of 1988 and was retested one year later. Shown in Fig. 6 are the bottom-flange strains in an interior stringer (Fig. 6a) and an exterior stringer (Fig. 6b) resulting from the post-tensioning. Also shown in these figures are the theoretical bottom-flange strains (obtained from a finite element analysis) assuming simple end supports. Except for the middle span, bottom-flange strains, there is excellent agreement between the experimental and theoretical strains. Although only the positive moment regions were post-tensioned, strain reduction in the negative moment regions is readily apparent. Also apparent is the presence of end restraint--considerably more at the north abutment (pinned end) than at the south abutment (roller support).

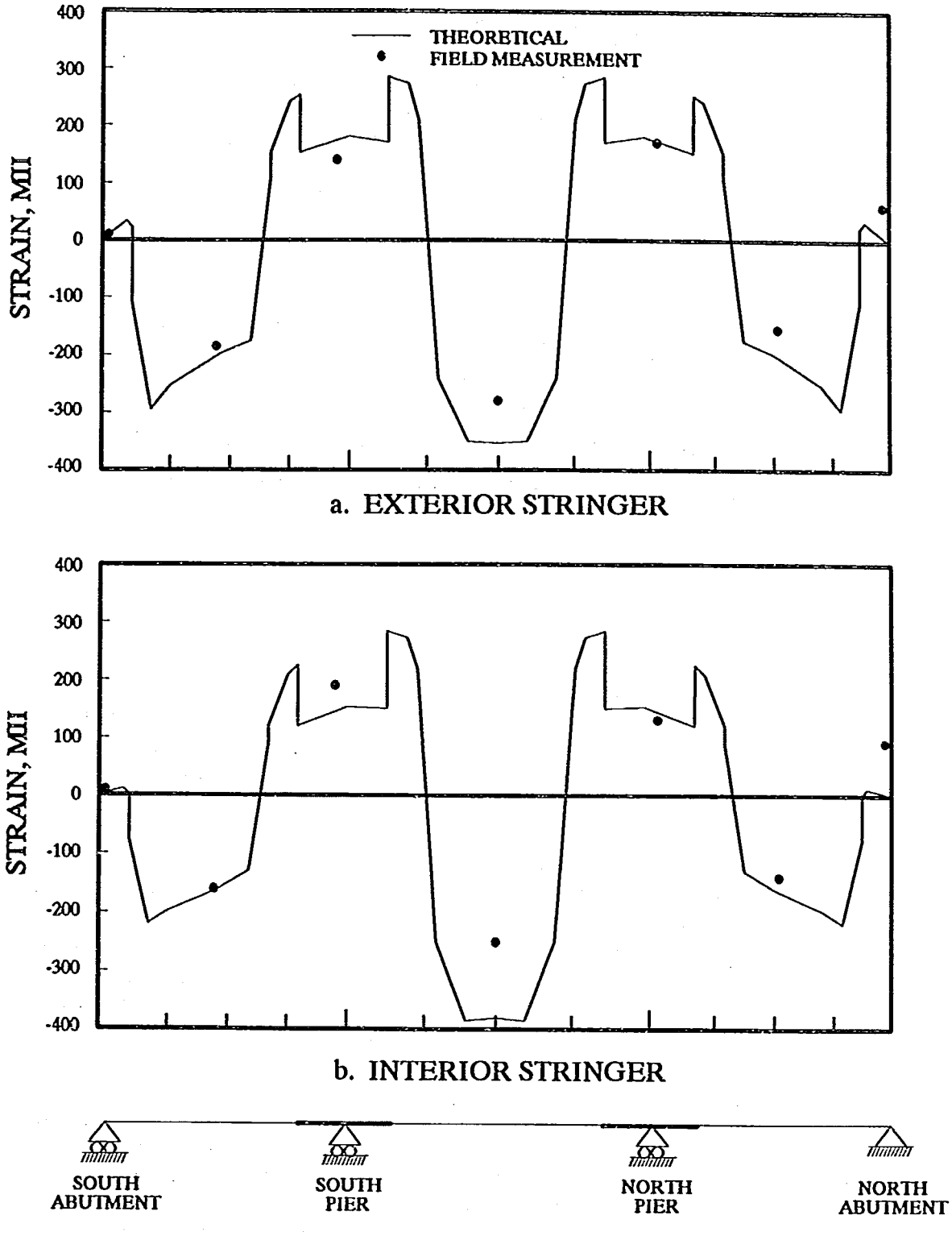


Fig. 6. Post-tensioning bottom flange stringer strains - Bridge 3.

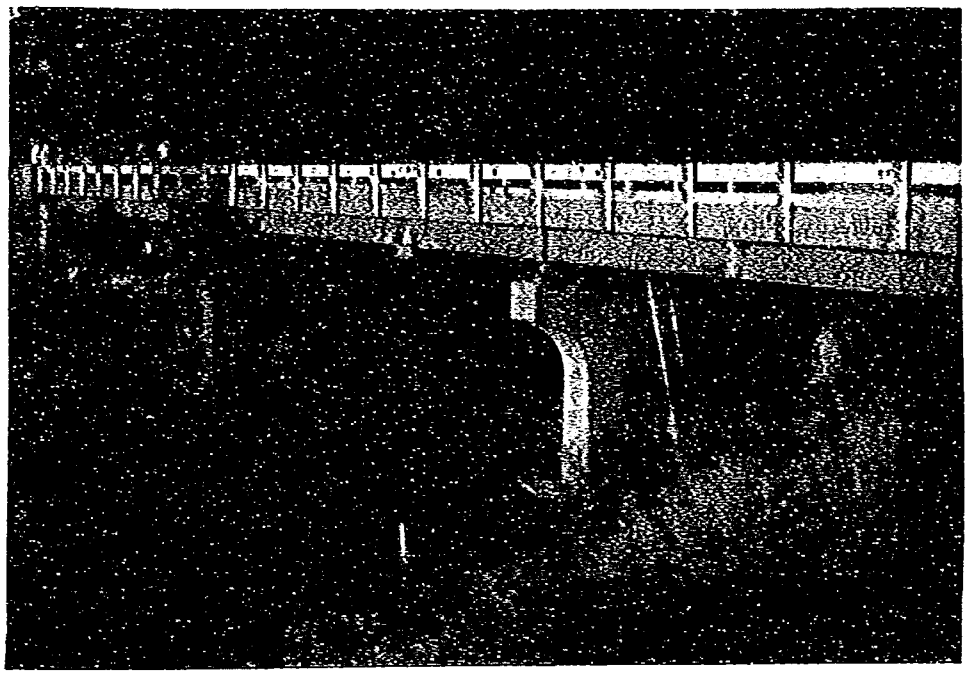
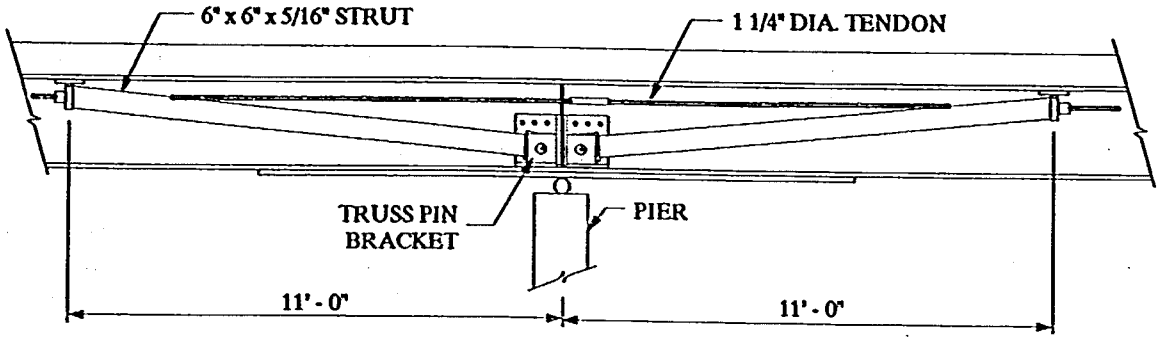


Fig. 5. Photograph of Bridge 3.

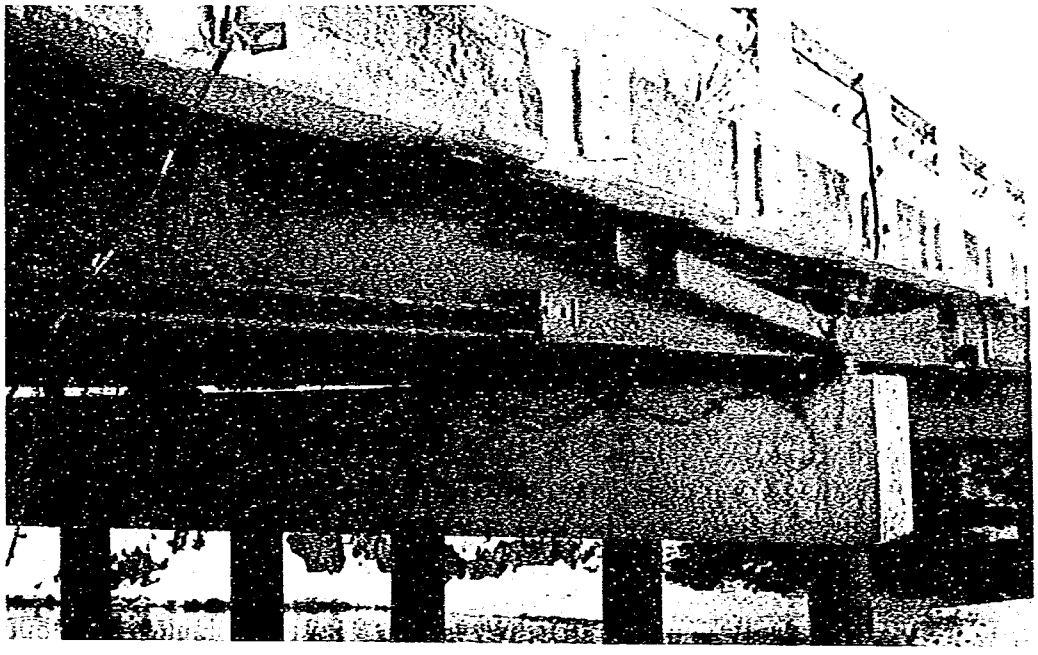
Phase II-3

As previously noted, this phase of the investigation is still in progress and thus will only be briefly discussed. In this phase, a fourth bridge (Bridge 4) is being strengthened and tested; also a continuous span design methodology for practicing engineers is being developed. Bridge 4 is identical to Bridge 3 except for the type and size of diaphragms. During the summer of 1992, post-tensioning tendons were attached to all stringers in the positive moment regions. In addition to the post-tensioning tendons, superimposed trusses, shown in Fig. 7, were installed on the exterior stringers at the piers. At each location, there are trusses on both sides of the beam web for a total of 16 superimposed trusses on the bridge. By tensioning the tendons in the trusses, upward forces are produced at the upper truss joints. The combination of trusses and post-tensioning of the positive moment regions makes it possible to reduce stresses the desired amount at all locations in the bridge. Also, the addition of the trusses significantly reduces the required post-tensioning forces in the positive moment regions. Bridge 4 is fully instrumented and will be strengthened and tested during summer 1993.

Development of the proposed practical design methodology for strengthening continuous span bridges is essentially completed. By using an accurate finite-element analyses, variables which significantly influence the longitudinal and transverse distribution of moment and force between the stringers have been identified. These variables include: stringer spacing, deck thickness, bridge length, ratio of adjacent span lengths, post-tensioning location, degree of skew, and ratio of external and internal beam stiffness. Simplified analysis techniques that provide essentially the same answers as the finite-element analysis have been developed. The simplified analysis, however, requires the use of computer spreadsheets. Depending upon the location and magnitude of the overstresses determined in a given bridge, the engineer using the design methodology and spreadsheets developed will be able to design the required strengthening system. The procedure developed will indicate



a.) Truss details (1 ft = .305 m).



b.) Photograph of trusses in place on Bridge 4.

Fig. 7. Superimposed trusses.

to the engineer the required magnitude and location of post-tensioning, if superimposed trusses are required, or some combinations thereof, to obtain the desired stress reductions.

SUMMARY

The results of the research outlined in this paper indicate that post-tensioning is a viable, economical technique for flexurally strengthening simple-span and continuous-span steel-stringer and concrete-deck composite bridges. The post-tensioning systems employed on the single-span bridges and the continuous-span bridges essentially reduce dead load

strains (stresses) in the bridges, thus making it possible for the bridges to carry additional live loads. Post-tensioning will slightly increase the ultimate strength of the bridge and in most cases induce a small upward camber. It does not, however, significantly reduce live load deflections or significantly influence live load distribution.

ACKNOWLEDGMENTS

The research reviewed in this paper was conducted by the Bridge Engineering Center, Engineering Research Institute of Iowa State University, and was funded by the Highway Research Board and the Highway Division of the Iowa Department of Transportation, Ames, Iowa. The authors thank the engineers at the Iowa DOT, especially William A. Lundquist, Bridge Engineer, and John P. Harkin, Chief Structural Engineer, for their support, cooperation, and counsel. Special thanks are accorded the numerous students who assisted with the various phases of the project. The opinions, findings, and conclusions expressed herein are those of the authors and not necessarily those of the Iowa Department of Transportation or the Highway Research Board.

REFERENCES

Dedic, D. J., and Klaiber, F. W., "High Strength Bolts as Shear Connectors in Rehabilitation Work", Concrete International: Design and Construction, ACI, V. 6, No. 7, July, 1984, pp 41-46.

Dunker, K. F., Klaiber, F. W., Daoud, F. K., and Sanders, W. W., Jr., "Strengthening of Continuous Composite Bridges", Journal of Structural Engineering, ASCE, V. 116, No. 9, Sept. 1990, pp 2464-2480.

Dunker, K. F., Klaiber, F. W., Daoud, F. K., Wiley, W. E., and Sanders, W. W., Jr., "Strengthening of Existing Continuous Composite Bridges", Final Report, ERI Project 1846, ISU-ERI-Ames 88007, Engineering Research Institute, Iowa State University, July, 1987, Ames, Iowa, 220 pp.

Dunker, K. F., Klaiber, F. W., and Sanders, W. W., Jr., "Post-Tensioning Distribution in Composite Bridges", Journal of Structural Engineering, ASCE, V. 112, No. 11, Nov. 1986, pp. 2540-2553.

Dunker, K. F., Klaiber, F. W., and Sanders, W. W., Jr., "Design Manual for Strengthening Single-Span Composite Bridges by Post-Tensioning", Final Report--Part III, ERI Project 1536, ISU-ERI-Ames 85229, Engineering Research Institute, Iowa State University, March, 1985, Ames, Iowa, 102 pp.

Dunker, K. F., Klaiber, F. W., Beck, B. L., and Sanders, W. W., Jr., "Strengthening of Existing Single-Span Steel-Beam and Concrete Deck Bridges", Final Report--Part II, ERI Project 1536, ISU-ERI-Ames 85231, Engineering Research Institute, Iowa State University, March 1985, Ames, Iowa, 146 pp.

Klaiber, F. W., Dunker, K. F., and Planck, S. M., "Strengthening of a Three-Span Continuous Bridge by Post-Tensioning", Bridge Evaluation, Repair, and Rehabilitation, Proceedings of U.S.-NATO Advanced Research Workshop held April, 1990 Baltimore, Maryland, NATO ASI Series, Vol. 187; pp 525-538.

Klaiber, F. W., Dunker, K. F., Planck, S. M., and Sanders, W. W., Jr., "Strengthening of an Existing Continuous-Span, Steel-Beam, Concrete-Deck Bridge by Post-Tensioning", Final Report, ERI Project 3030, ISU-ERI-Ames 90210, Engineering Research Institute, Iowa State University, Feb. 1990, Ames, Iowa, 165 pp.

Klaiber, F. W., Dedic, D. J., Dunker, K. F., and Sanders, W. W., Jr., "Strengthening of Existing Single Span Steel Beam and Concrete Deck Bridges", Final Report--Part I, ERI Project 1536, ISU-ERI-Ames 83185, Engineering Research Institute, Iowa State University, Feb. 1983, Ames, Iowa, 185 pp.

Klaiber, F. W., Dunker, K. F., and Sanders, W. W., Jr., "Strengthening of Single-Span Steel-Beam Bridges", Journal of the Structural Division, ASCE, V. 108, No. 12, Dec. 1982, pp 2766-2780.

Klaiber, F. W., Dunker, K. F., and Sanders, W. W., Jr., "Feasibility Study of Strengthening Existing Single Span Steel Beam Concrete Deck Bridges", Final Report, ERI Project 1460, ISU-ERI-Ames 81251, Engineering Research Institute, Iowa State University, June 1981, Ames, Iowa, 141 pp.

Application of Buried Joint in Cold and Snowy Region

Tadayuki SHIRONO
Hiroaki NISHI
* Osamu NAKANO
** Katsuhisa KUMAGAI

Research Engineers, Structures Section
Civil Engineering Research Institute, Hokkaido Development Bureau
* Head of Structures Section, Civil Engineering Research Institute
Hokkaido Development Bureau
** Head of Development Coordinating Section
Secretariat of Hokkaido Development Bureau

Abstract

Expansion joints of bridges play an important roles to keep the smoothness and the continuity of road surface but they have been worn out due to live loads. They also have been damaged by recent heavy traffic and vehicle vibrations. Especially in snowy and cold region such as Hokkaido, the sharp drops on road surface have spoiled the joints or snowplows. To take measures against these circumstances, buried joints have been improved and applied to real bridges. In this study, the characteristic of the buried joint was investigated under various conditions and a new type superior to customary types in point of strain-diffusing performance was developed in indoor tests.

1. Introduction

The expansion joints of bridges play an important role to keep the smoothness and the continuity of road surface and secure the safety and the amenity for driving, absorbing displacement accompanied by expansion and contraction of the superstructure. However the expansion joints have directly suffered from the influence of live loads of passing vehicles, so that they have been worn out violently. The frequency of repair work or maintenance work has rapidly increased with the recent increase of traffic volume and heavy vehicles, and traffic controls under the repair work have become a factor of traffic jam. Besides the expansion joints in themselves directly influence the amenity for driving and cause various problems such as vibrations and noises to the circumference of them because they are directly set up on road surface. Especially in snowy and cold region such as Hokkaido, the sharp drops or the pot holes on road surface tend to be produced between an expansion joint and the pavement before and behind the joint, by using studded tires in winter. In snow-removing work, a snowplow or the joint itself has been damaged by the sharp drops.

To take countermeasure against present circumstances, a variety of ideas are under consideration. For instance, they are to improve the durability of existing expansion joints, to adopt the bridge structure that has few expansion joints, and to design the buried joint that was reformed in the dummy joint or the cut-off joint [1)-6)]. The buried joint can unify the joint surface itself and the pavement surface before and behind the joint surface, and the expansion and contraction of girders can be absorbed by asphalt mixture in itself because it applies the asphalt mixture as a material covered above the joint. Therefore it has many advantages to secure not only the amenity and the safety for passing vehicles but also the workability and the manageability in snow-removing work during winter. In addition to these facts, it can bring on constructive and economical advantage.

In this paper, the characteristic of customary buried joints was investigated under various conditions and a new type superior to the customary types was developed especially from a viewpoint of strain-diffusing performance.

2. Experimental Outline

2.1 Experimental Devices

The testing machine used in these experiments consists of two units, an actuating unit for expansion and contraction of specimens, and a manipulation panel for control. The allowable temperature rage of the machine is from -30°C to +60°C, the permissible load to the machine is 10,000 kgf, the maximum stroke is ±150mm, the speed for expansion and contraction is 180~0.024mm/min with four gears, and the external size is 1,000mm wide, 780mm high, and 2,438mm long. Photo 1 shows an external appearance of the machine on which was set up specimens and measuring instruments. All the experiments, to make the strict control of temperature, were conducted in a laboratory for low-temperature experiments. This means that the characteristic of asphalt mixture strongly depends on rises and falls of temperature [7)8)9)], so that the temperature of specimens has influence on behavior of expansion and contraction of the specimens [10)11)]. The low- temperature laboratory consists of a prefabricated laboratory at the inside size of 2,000mm wide, 2,000mm high and 4,000mm long, a refrigerator, two supplementary coolers, a control board, a program regulator, and a temperature recorder. Photo 2 shows the external appearance of the laboratory. It is programmable for setting of random repetition and random temperature setting from +5°C to -30°C. As for the temperatures, the refrigerator and the coolers are automatically controlled by the program regulator with the accuracy of ±1°C and defrosting is also automatically executed by a defrost timer.

2.2 Specimens

Eight specimens used in this test were manufactured to compare the characteristic with each specimen from the viewpoint of expansion speeds, setting temperatures, and structures of the joints. Table 1 shows differences between each specimen. The fine-graded asphalt concrete was used as the upper asphalt mixture in all specimens, so that the table shows only the lower mixture in the columns. The each structure of specimens is drawn in figure 1. A customary type was used in specimen A-1 to D-1, and a new type developed for these tests was used in specimen E-1 to F-2. Figure 1 shows the central structure of the specimens. A customary type was adopted as specimen A-1 to D-1 and the new type, reflected test results for the past two

years, used as specimen E-1 to F-2. Here the specimen E-1 and E-2 to F-2 used asphalt mixture of 2cm thick and 3cm thick respectively. The feature of this new type, specimen E-1 to F-2, is to install a layer in order to absorb the displacement of joint clearance accompanied by expansion and contraction of girders, and to adopt the bituminous sheet spread on the layer in order to diffuse the strain with the displacement. As for the structure, the rubber sheet that was fixed by anchor bolts and anchor plates at both ends of the sheet was set up on a box dug down to concrete blocks, the rest of the box was filled up by asphalt mixture, and the bituminous sheet was spread on the box in the same way as the customary type. Moreover the asphalt mixture covered with the anchor bolts and anchor plates is effective to supplement the structural defect, and the bituminous sheet is useful to shut down cracks in here and to keep away water intrusion to joint clearance or bearings.

2.3 Experimental detail

The expansion and contraction tests to grasp the behavior of the buried joint and fatigue tests were performed in the refrigerator. First, the expansion and contraction tests were conducted once in contraction of 5mm and in expansion of 5mm, being kept at +5°C (only in specimen B-1 at -10°C). The speed of expansion and contraction was set at 0.10mm/min (only in specimen A-1 at 0.05mm/min). As for this speed setting, it is equivalent to the speed that is about seven times as one cycle of a day, assuming that expansion and contraction revolve once a day in real bridges. This experiment supposes that it takes one cycle a year to make expansion and contraction, so that the value of the speed is approximately 2,600 times as the value of real bridges. Actual bridges rotate the expansion and contraction of a great extent through a year, repeating the motion of a small extent once a day. In addition to that, the bridges repeat random motion under the influence of vibrations by passing vehicles and of expansion and contraction with the change of temperature. Therefore it is difficult to reproduce the complex behavior of real bridges in a laboratory.

Next, a temperature gradient was set up to +0°C to -20°C (+5°C to -25°C only in specimen A-1) at the same speed of expansion and contraction as the first time in the second experiment. In this condition, the temperature gradient was linked up with the speed of expansion and contraction, and was fixed at 12°C/hr (6°C/hr only in specimen F-type). This setting is quite severe because the maximum temperature gradient is 5°C/hr in an intense cold region of Hokkaido.

After the second experiment was finished, the specimen was let alone until they were settled down at +5°C, and the fatigue tests were conducted at the speed of 1.00mm/min (3.00mm/min only in specimen A-1). The fatigue tests were quitted in case that specimens were cracked completely, being anticipated to repeat ten times or more from the test results for past two years. In this measurement, twelve displacement gauges and one load cell were set up on the specimens. The data acquired through a switch-box and a data-logger was read as an ASCII file into a personal computer, also the data was analyzed and visualized by a graphical software. Figure 2 shows the size of the specimens and the arrangement of measuring instruments. The absolute displacement was measured at an observation point on fixed pedestal of the machine, and the relative displacement was observed at the other points except it.

3. Experimental Results

3.1. Comparison with Difference of Setting Speed

The setting speeds of specimen A-1 and D-1 are 0.05mm/min and 0.10mm/min respectively, as shown in Table 1, so the speed of specimen A-1 is a half of the speed of specimen D-1. On horizontal displacement near the center of the joint, specimen A-1 has a smaller burden rate than specimen D-1 in the maximum contraction. On the other hand, there is no conspicuous difference in each observation point between specimen A-1 and D-1 in the maximum expansion. According to Moriyoshi, et al, it is proved that the breaking of asphalt mixture depends on the strain speeds [7)8)], and the dependency was confirmed especially in contraction. From a viewpoint of load, as the strain speed increases, the burdening load on a specimen decreases. Thus the speed control in experiments affects the expansion and contraction behavior of specimens, so that the speed control has to manage severely. Figure 3 shows the strain distribution with difference of setting speed in the maximum contraction and expansion, and Figure 4 shows the change of burdening load with that.

3.2. Comparison with Difference of Setting Temperature

The temperature dependency on breaking strain of asphalt mixture was certified in many dissertations [12)13)14)] and the dependency was also confirmed in the last indoor experiments. As the temperature becomes low, the stress that increases according to the temperature decline remains into asphalt mixture beyond the speed of stress relaxation. When the residual stress exceeds expansion strength of asphalt in itself, visible cracks break out. The invisible micro cracks are produced in an early stage of expansion but the visible cracks occur comparatively late after generation of micro cracks.

Specimen B-1 cracked at 3mm of expansion and the strain burden in the center of the joint is larger than that of specimen D-1 in both maximum contraction and breaking point of expansion. Figure 5 shows the strain distribution with difference of setting temperature in the maximum contraction and the breaking point. Here in the breaking point of expansion, both of them are compared with the values at 3mm of expansion. Also in Figure 6, the change of burdening load with that is shown.

3.3 Comparison with Difference of The Number of Bituminous Sheet

In the strain distribution in the maximum contraction and expansion, specimen A-2 that used two bituminous sheets shares the strain in wide range as compared with specimen D-1 that used one bituminous sheet. Also in a change of burdening load, specimen A-2 showed smaller value than specimen D-1 in contraction and expansion, and it was clearly proved that using two sheets had a good effect on strain diffusing. However distribution of strain itself was irregular, and it happened to be seen that metal fittings became slack especially in expansion. Figure 7 shows the strain distribution with difference of the number of the bituminous sheet in the maximum contraction and expansion . From this comparison between two specimens, it was confirmed that the strain accompanied by expansion and contraction of a girder can diffuse in wide range of the upper asphalt pavement by using a proper structure in the center of the joint. Figure 8 shows the change of burdening load on the number of the bituminous sheet.

3.4 Comparison with Difference of Lower Asphalt Mixture

Through specimen C-1, C-2 and D-1, there is no remarkable difference but specimen C-2 used open-graded asphalt concrete including rubber chips was a little superior to specimen C-1 and D-1 in the elasticity. The same results as this experiment was accepted from the last year's tests [15]. However it was certified that the higher the percentage of void becomes, the more it has a harmful influence on properties of asphalt mixture by freezing and thawing action [16]. Therefore it seems that a rapid application of the open-graded asphalt concrete is too easy going, granted that the elasticity is attached importance. Especially in actual construction of a new bridge, its workability is lost by using different mixture from the pavement before and behind the joint, so that the balance between its workability and its performance such as the elasticity becomes important. Figure 9 shows the strain distribution with difference of the lower asphalt mixture in the maximum contraction and expansion, and Figure 10 shows the change of burdening load with that.

3.5 Comparison with Difference of Structure of Joint

Specimen E-1 and E-2 are newly developed in this test, as stated above, and its structural difference from the customary type, was reflected distinctly upon this experimental result. From a view-point of the strain distribution in each observation point, both of specimen E-1 shows the same behavior as specimen E-2 and the strain was diffused widely in all over the specimen. As for the change of load, both of them were lightened conspicuously as compared with specimen D-1, especially in expansion. Therefore it was certified that a rate of strain burden in the center of the joint was lessened and shared in wide range by installing the strain-diffusing layer. Figure 11 shows the strain distribution with difference of structure of the joint in the maximum contraction and expansion and Figure 12 shows the change of burdening load with that.

By the way, as to the second experimental result of expansion and contraction in which the temperature gradient was set up from +0°C to -20°C, a change of pavement rigidity with a decline of temperature caused a slide on the adhesive surface between a pavement itself and a pair of concrete blocks. The quantity of the slide differs with each specimen, so that it is difficult to compare with all the specimens. Therefore a discussion about that is omitted in here. In regard to the test results of specimen F-1 and F-2 set up at the expansion stroke of 15mm, any visible crack was not observed on the specimens. From these good results, it was estimated that the buried joint of this type can apply to bridges with the span of about 30m long.

3.6 Results of Fatigue Tests

The fatigue tests were carried out in five specimens, A-1, A-2, C-1, C-2 and D-1, and the appearance of visible cracks delayed comparatively in specimen A-2 and D-1. Specimen A-2 made no visible cracks after 25 repetitions but it is hard to say that specimen A-2 has better elastic performance than specimen D-1. Actually some kind of the slack or the slide, as pointed out in 3.3, brought about between metal fittings and concrete blocks. Therefore it is impossible to discuss the fatigue performance of each specimen from these results. Figure 13 shows a histerisis loop of load and displacement in specimen D-1. For a common feature to each loop, a load acted on a specimen remarkably decreased after an end of the first cycle and then the load became smaller gradually. Thus the loops showed the stress relaxation of asphalt mixture well. Figure 14 shows the change of horizontal displacement in the fatigue test of specimen D-1.

4. Conclusions

The results obtained from these experiments and analyses are as follows:

1) According to increase of the expansion speed, the asphalt mixture lost its elasticity and the stress tended to concentrate in the center of the joint.
2) Temperature is the most important parameter to determine the properties of asphalt mixture and its elasticity decreased noticeably accompanied by a decline of temperature, especially in the range below 0℃.
3) Laying two bituminous sheets can improve the elasticity of the buried joint as compared with using one bituminous sheet.
4) In these experiments the same mixture, the fine and gap-graded asphalt concrete was used as an upper asphalt mixture, so that there is no remarkable difference between each specimen. However to pave the open-graded asphalt concrete with rubber chips is a little helpful to improve the elasticity of the buried joint.
5) Adopting the new type to expansion joints is effective to utilize the maximum elasticity that asphalt mixture possesses in itself, and it was confirmed that the new one can apply to expansion and contraction of 15mm stroke even at low temperature.

The buried joint is eventually dominated by the characteristics of asphalt mixture, for that the buried joint has a structure of which expansion joint is installed under the pavement. However, it is possible to delay an outbreak of cracks if a new structure is adopted so that its expansion and contraction can be acted within the rage of breaking strain. To attain this performance considering the workability or the economical advantage, it is essential to take the bituminous sheet superior in the elasticity with the strain-diffusing layer filled up by asphalt mixture. Moreover in actual bridges, the strain speed is so slower than the speed set in these experiments, and the stress relaxation of asphalt and the kneading action by traffic loads interacts advantageously to pavement itself. Therefore application of the buried joint will extend to longer-span bridges from a consequence of which field measurement has been continued in actual bridges. As matter of fact, the buried joint that was stated through this paper is now functioning in real bridges constructed by Hokkaido Development Bureau. In the future, more detailed examination about the effective length of bituminous sheets, the thickness of strain-diffusing layer, and the width of joint clearance is required to promote extensive application of the buried joint.

Acknowledgments

The authors would like to express sincere appreciation to Mr.Shigeki Kumagai and the persons concerned of the Hokkaido branch of Maeda Road Corporation for their valuable advice, and to Mr.Akio Misawa, the chief manager on experiments of structures section of CERI, for his support and cooperation.

References

1) Maeda,Y., Ohgushi, H., Usui, O. and Hama, H. (1992) Propriety Investigation of Buried Joint for Real Bridges, in Proc. 47th Annual Conference of Japan Society of Civil Engineers, I-450, pp.1076-1077.

2) Takahashi, O., Maruyama, T. and Inaba, T. (1992) Study on Buried Joint and Hexarock Joint, in Proc. 47th Annual Conference of JSCE, V-56, pp.142-143.

3) Ohta, S., Morikawa, T., Fukazawa, Y. and Sugiyama, T. (1991) Basic Study on Precasting Expansion Joint for Smooth Pavement Surface, in Proc. 46th Annual Conference of JSCE, I-338, pp.714-715.

4) Fujii, Y. and Ohmori, A. (1987) Development of No-joint Method for PC Girder, in Proc. 42nd Annual Conference of JSCE, I-228, pp.490-491.

5) Obata, H., Satoh T. and Fujiwara, H. (1987) Investigation on Application of Buried Joint, in Proc. 17th Japan Road Conference, No.717, pp. 734-735.

6) Nakamura, I., Kubo, M. and Sekimoto, H. (1991) Development of Easy No-joint Method in Constructed Short Bridges, in Bridge and Foundation, pp.33-41.

7) Moriyoshi, A. and Nitta, N. (1988) Fracture Behavior of Asphalt Mixture in Brittle Zone, in Dissertation of JSCE, No.390 V-8, pp.219-224.

8) Moriyoshi, A., Uejima, S. and Sugawara, T. (1973) Fracture Strength of Bituminous Mixture, in Dissertation of JSCE, No.210, pp.57-64.

9) Matsuo, T. et al. (1968) Study on Temperature of Pavement, in Proc. 12th Annual Presentation of Hokkaido Development Bureau, pp.147-159.

10) Structures Section, CERI (1991) Report on Application of Buried Joint, in Material of Structures Section, pp.13-27.

11) Moriyoshi, A., Tokumitsu, K. and Kawamura, K. (1992) Study of Breaking Strain of Asphalt at Low Temperature, in Proc. 47th Annual Conference of JSCE, V-22, pp.74-75.

12) Maintenance and Management Section, CERI (1986) Report on Crossing Cracks of Asphalt Pavement, in Material of Maintenance and Management Section, pp.4-31.

13) Fukude, T. (1978) Cracks of Asphalt Pavement at Low Temperature, in ASPHALT, Vol.21, No.117, pp.17-23.

14) Moriyoshi, A., Kawamura, K. and Karai, T. (1991) in Proc. Annual Conference of the Hokkaido Branch of JSCE, V-22, pp.973-976.

15) Nakano, O., Yamauchi, T., Shirono, T. and Ono, Y. (1993) Development of Buried Joint Considered Cold and Snowy Region, in Proc. Annual Conference of the Hokkaido Branch of JSCE, I-65, pp.313-318.

16) Sasaki, M., Yoshie, S. and Fujiwara,T. (1992) Influence of Void Percentage to Freezing and Thawing Resistance of Asphalt Mixture, in Proc. 47th Annual Conference of JSCE, V-24, pp.78-79.

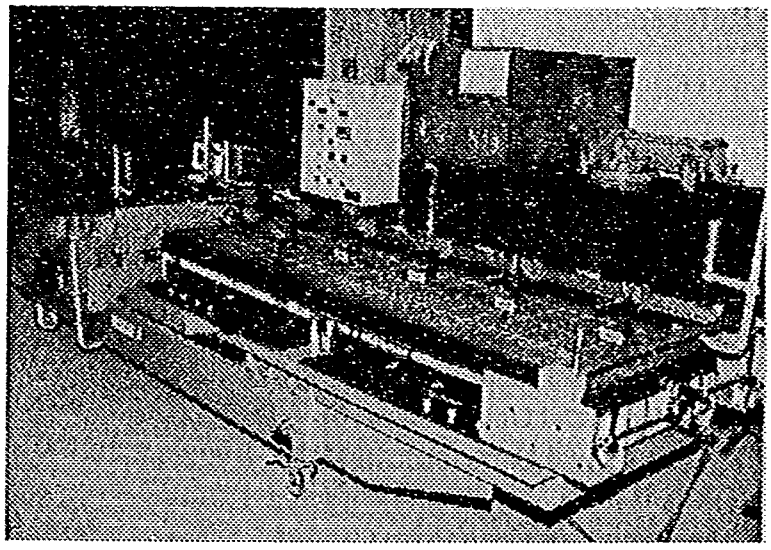


Photo 1 External Appearance of Testing achine used in Expansion and Contraction Experiments

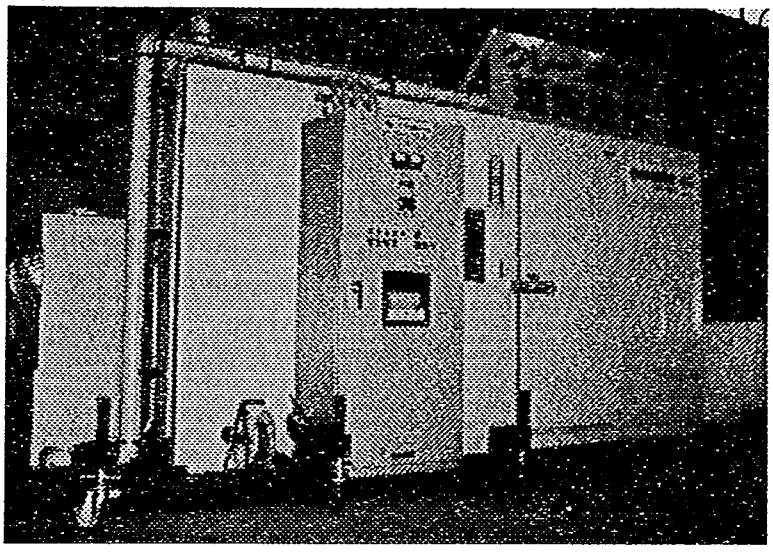


Photo 2 External Appearance of Low-Temperature Laboratory

Table 1 Structural Differences between Each Specimen

Specimen	Lower Asphalt Mixture	Bituminous Sheet	Temperature (Celsius)	Speed (mm/min)	Joint Clearance (mm)	Expansive Stroke (mm)
A-1	Fine and gap-graded	1	5	0.05	15	10
A-2	Fine and gap graded	2	5	0.10	15	10
B-1	Fine and gap-graded	1	-10	0.10	15	10
C-1	Coarse-graded	1	5	0.10	15	10
C-2	Open-graded with Rubber Chips	1	5	0.10	15	10
D-1	Fine and gap-graded	1	5	0.10	15	10
E-1	Fine and gap-graded	1	5	0.10	15	10
E-2	Fine and gap-graded	1	5	0.10	15	10
F-1	Fine and gap-graded	1	5	0.10	20	20
F-2	Fine and gap-graded	1	5	0.10	20	20

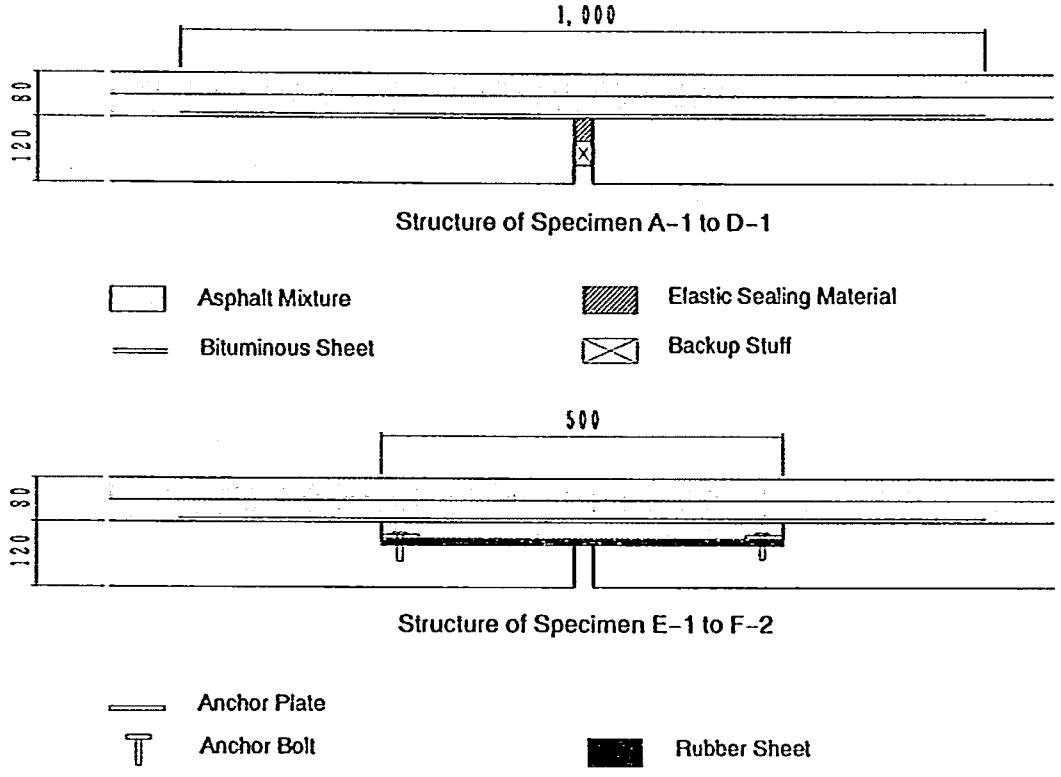


Figure 1 Structure in The Center of The Buried Joint

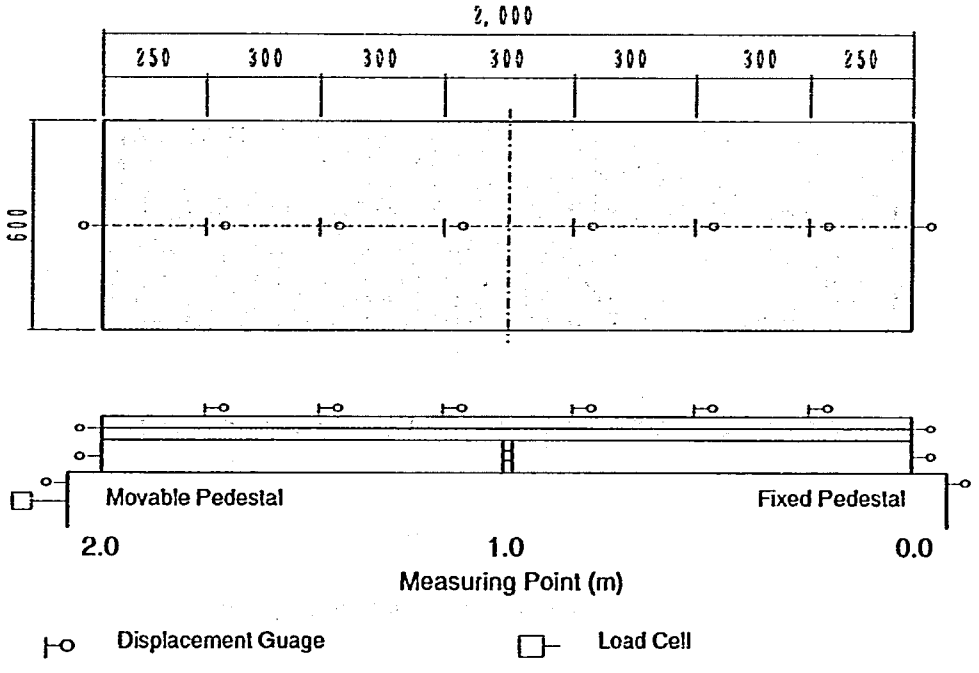


Figure 2 Arrangement of Measuring Instruments

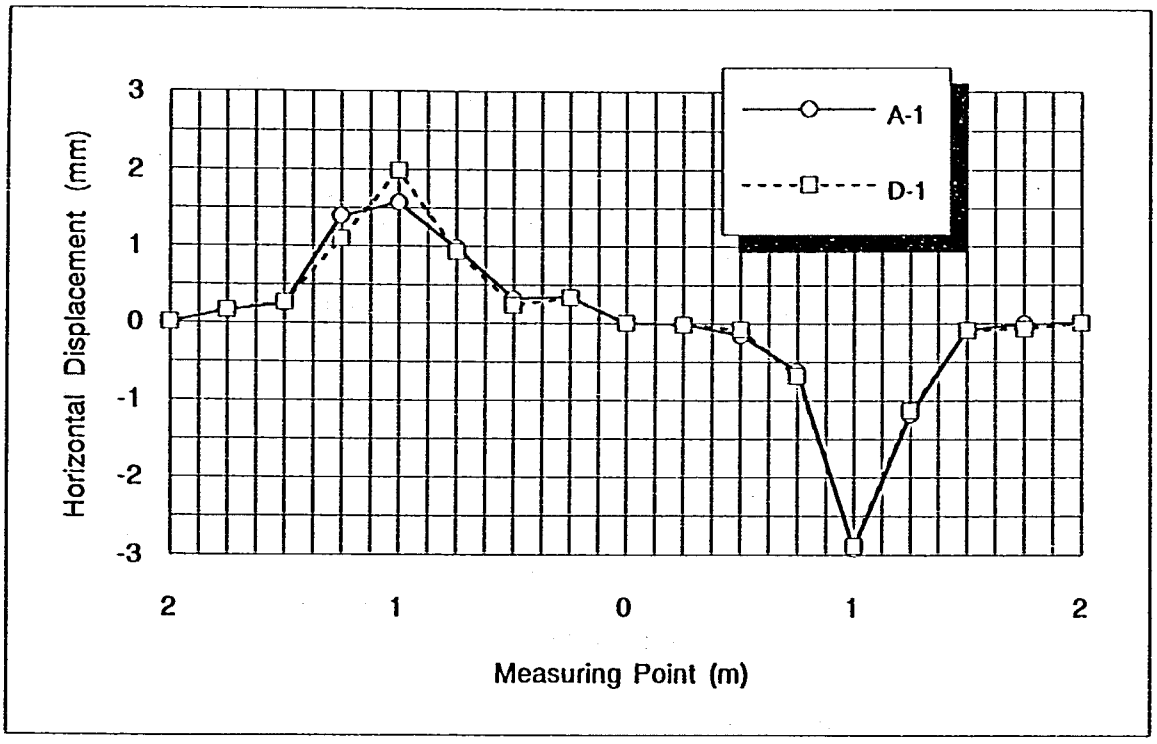


Figure 3 Strain Distribution on Setting Speed

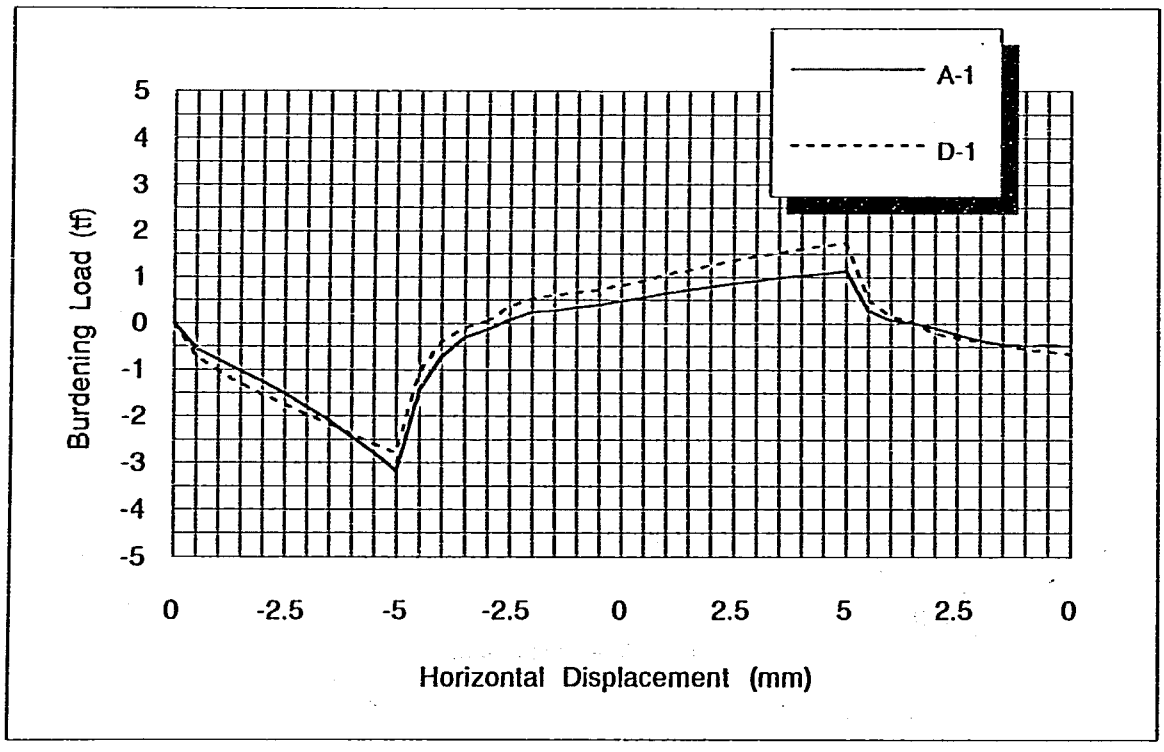


Figure 4 Change of Burdening Load on Setting Speed

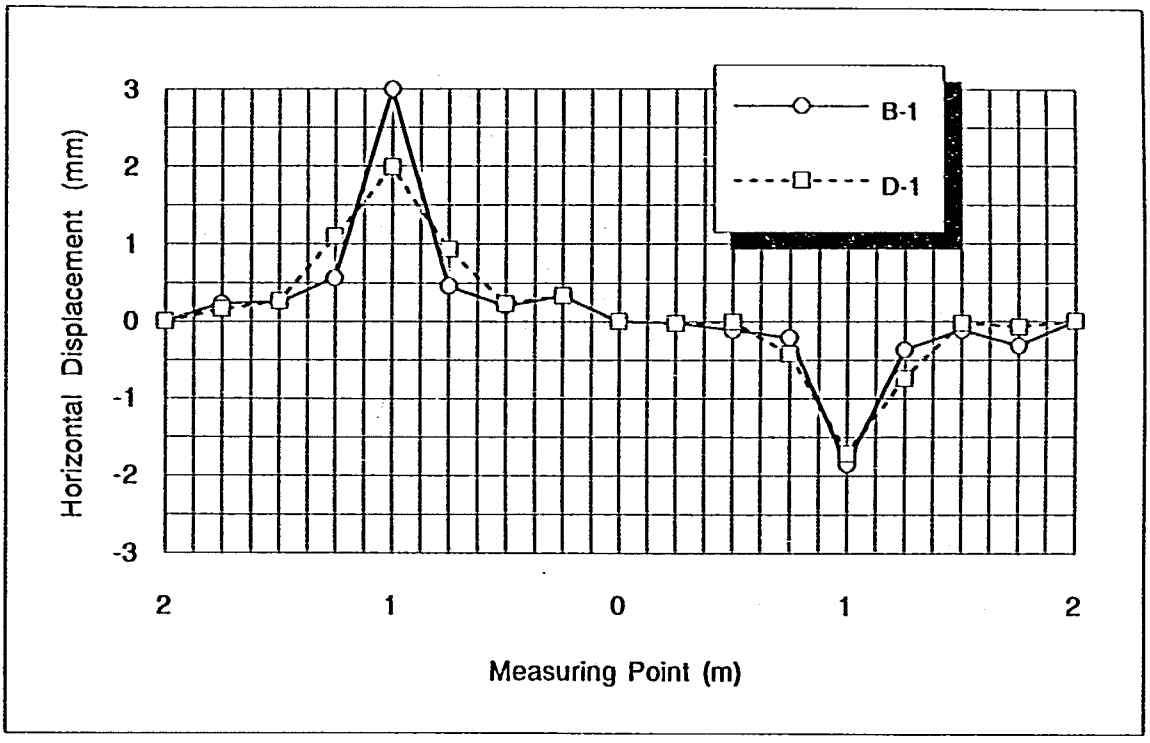


Figure 5 Strain Distribution on Setting Temperature

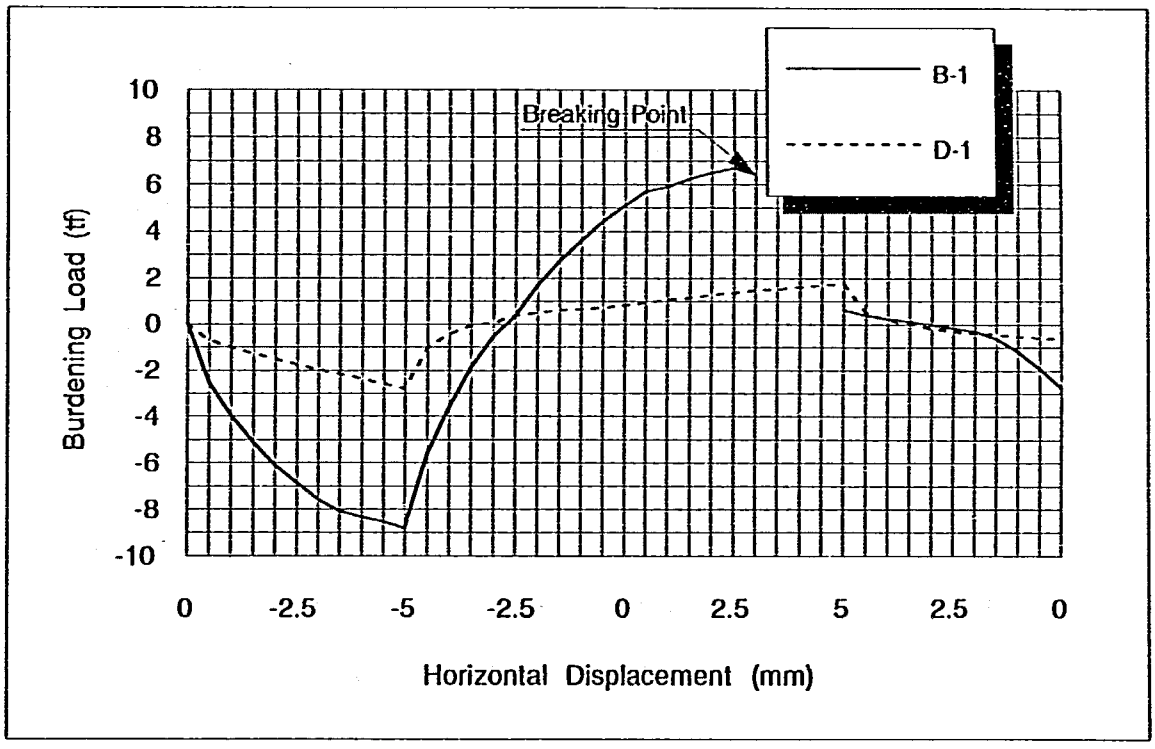


Figure 6 Change of Burdening Load on Setting Temperature

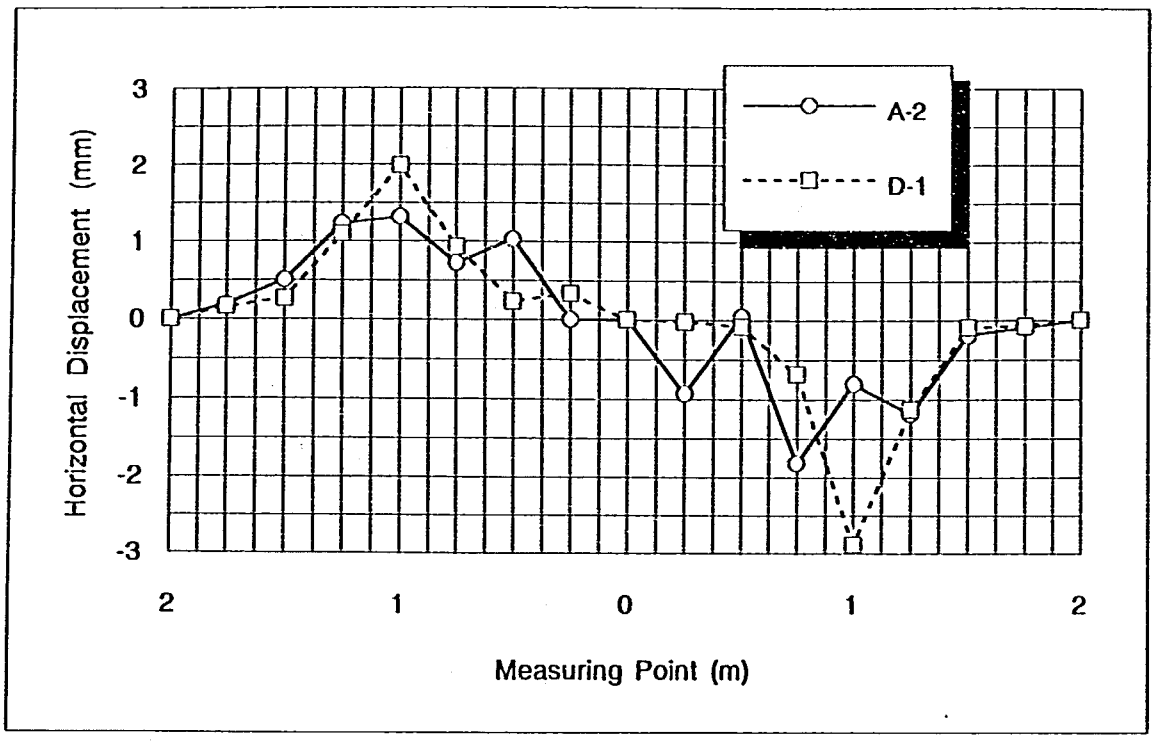


Figure 7 Strain Distribution on The Number of Bituminous Sheet

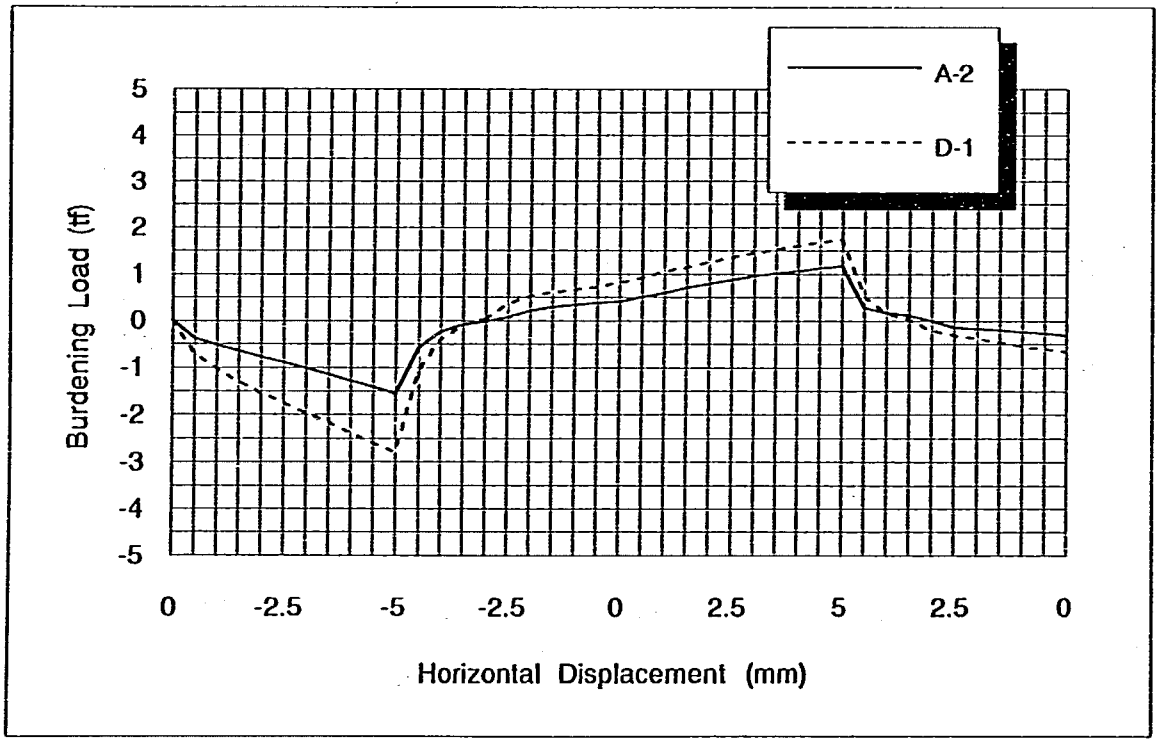


Figure 8 Change of Burdening Load on The Number of Bituminous Sheet

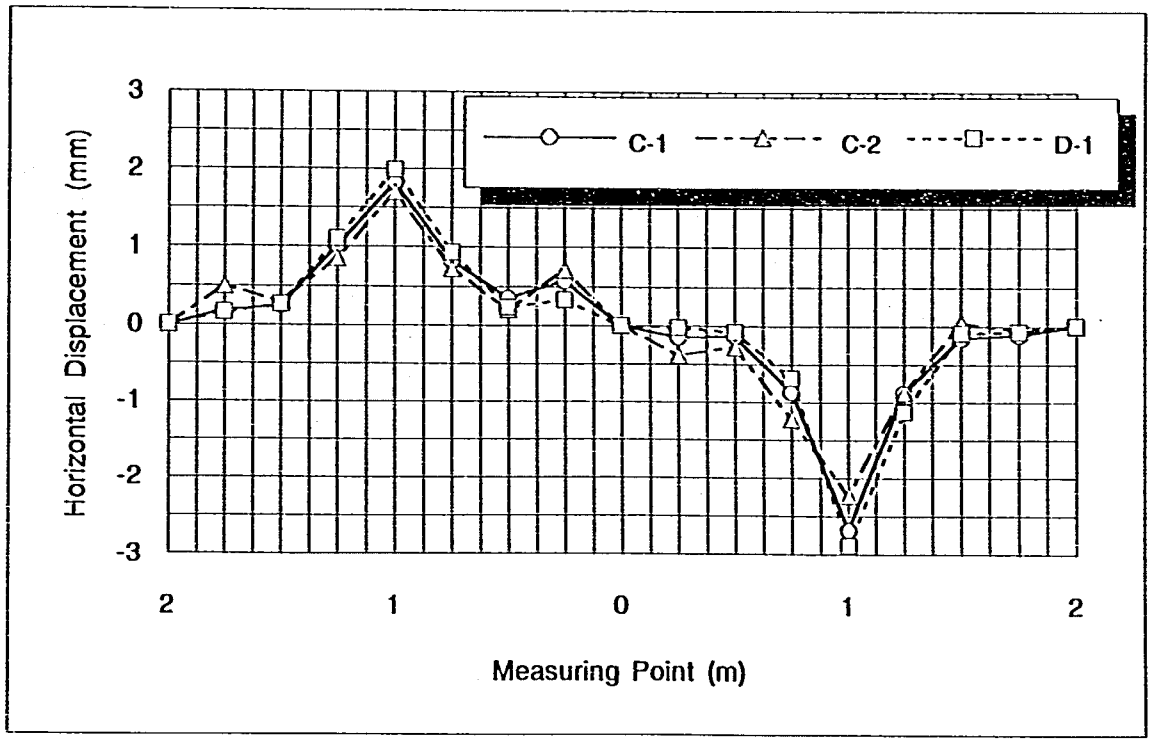


Figure 9 Strain Distribution on Lower Asphalt Mixture

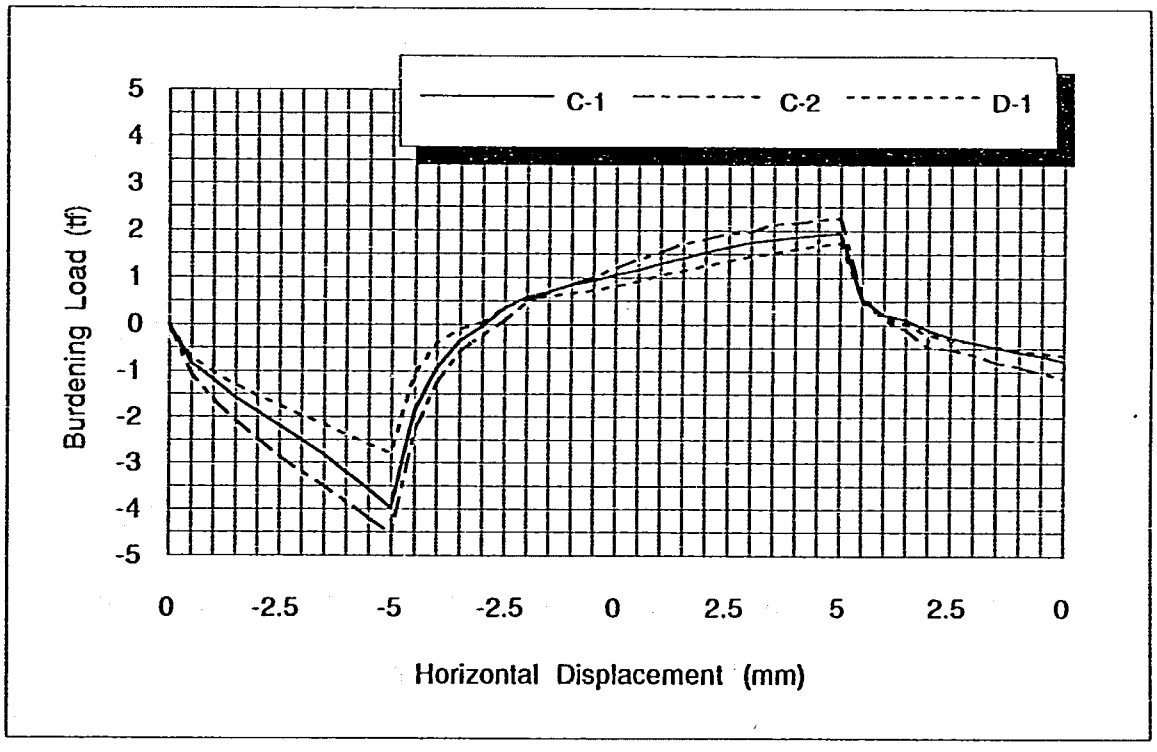


Figure 10 Change of Burdening Load on Lower Asphalt Mixture

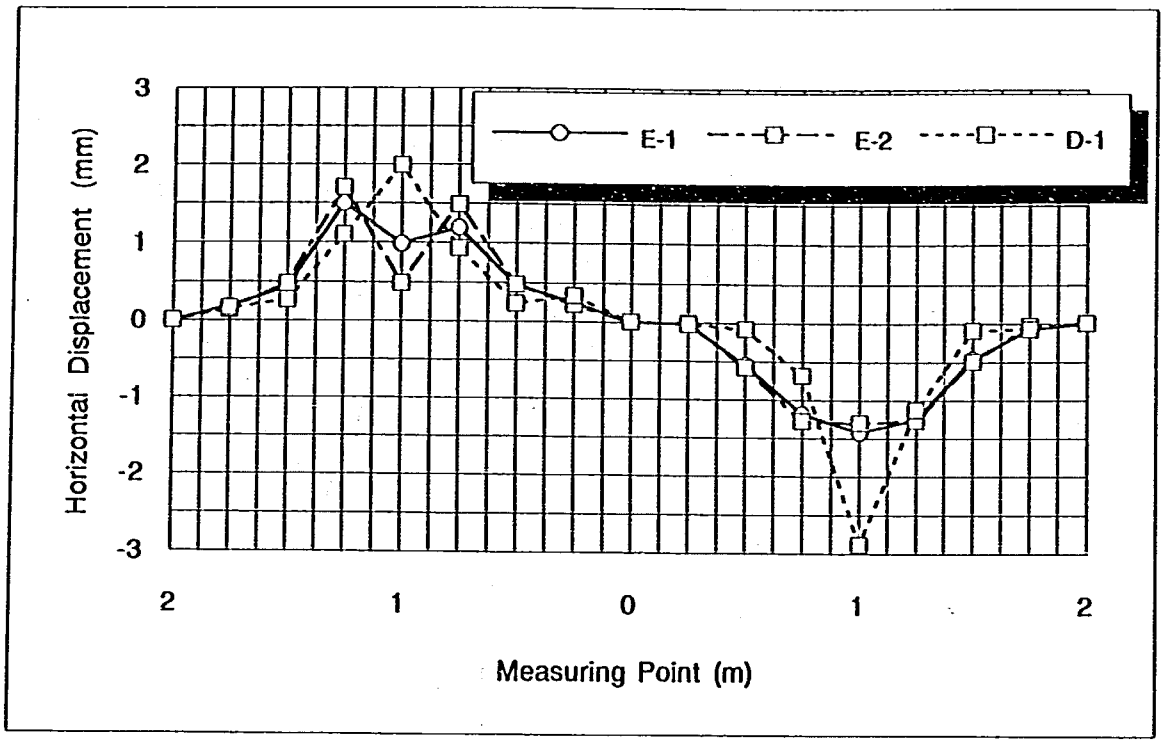


Figure 11 Strain Distribution on Structure of Joint

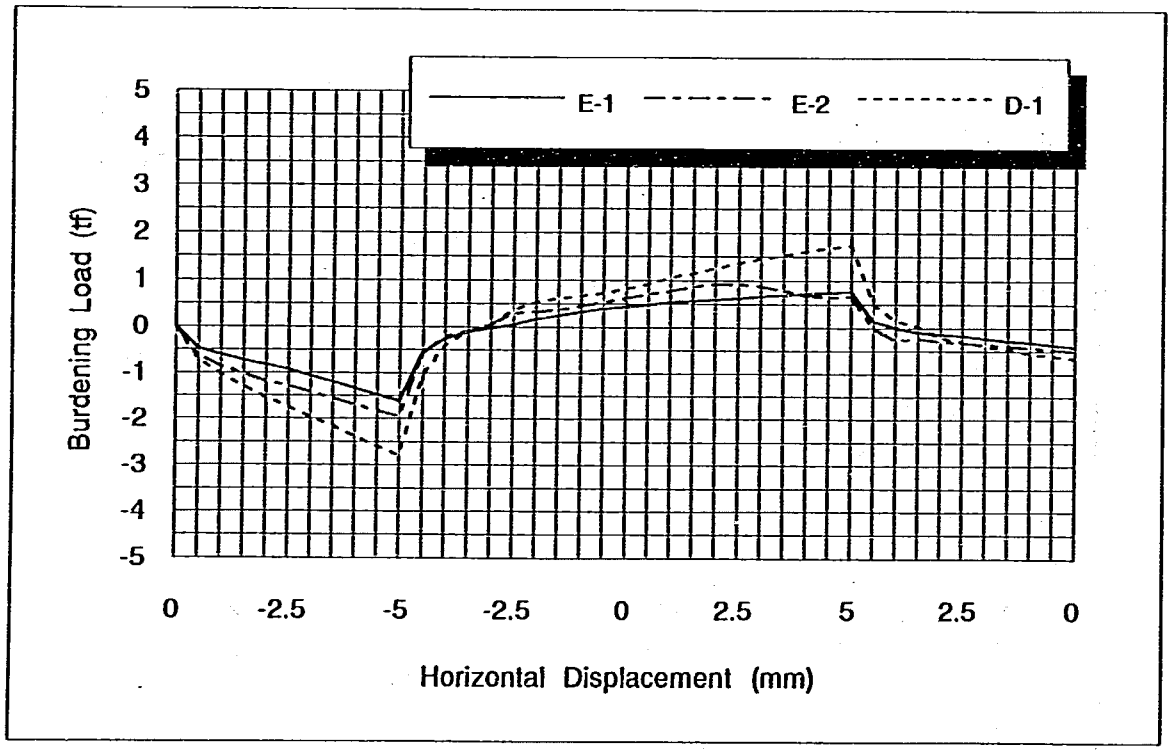


Figure 12 Change of Burdening Load on Structure of Joint

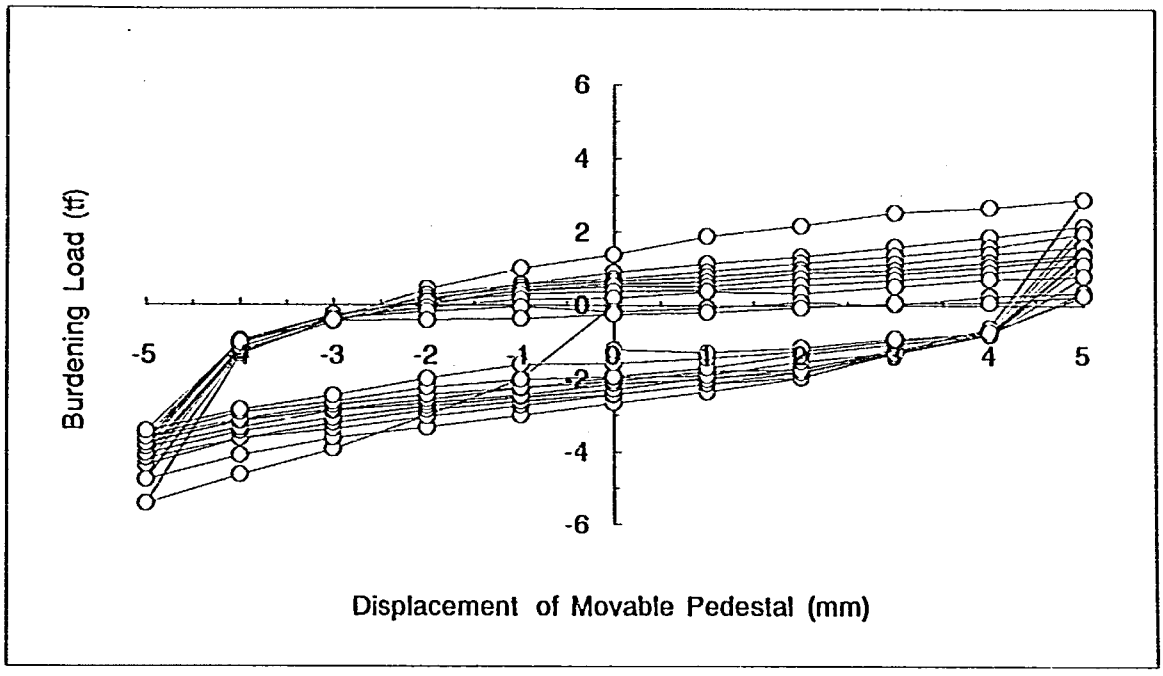


Figure 13 Histerisis Loop of Load and Displacement in Fatigue Test of Specimen D-1

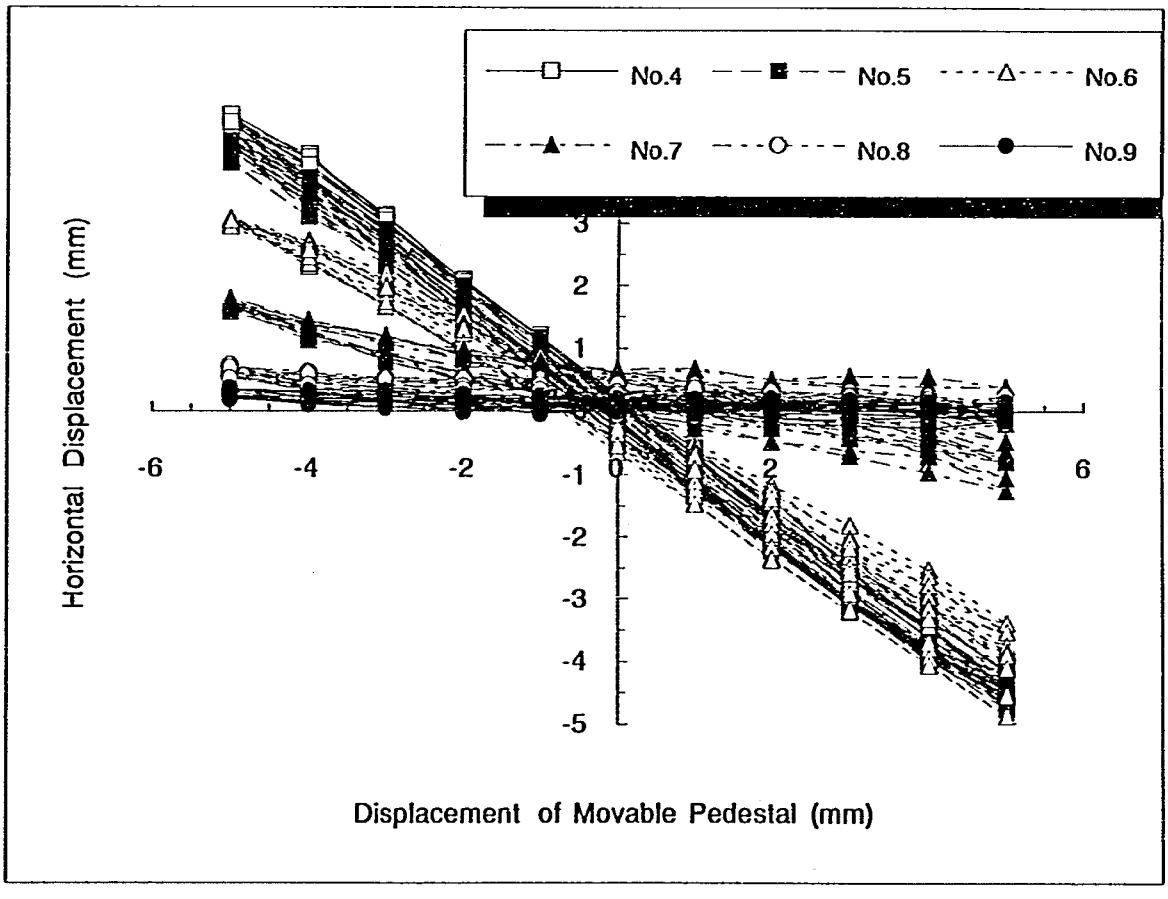


Figure 14 Change of Horizontal Displacement in Fatigue Test of Specimen D-1

(4) Session 4

Wind Resistant Design (1)

6) An Experimental Study on Aerodynamic Sound Generated From Handrails of Flat Plate Cascades
(K. Kimura, Y. Fujino* and S. Hiejima)

7) Simulation Techniques for Bridge Aerodynamic Investigations at the Turner-Fairbank Highway Research Center
(O.U. Onyemelukwe and H.R. Bosch to be presented by J.D. Cooper)

8) Analytical Study on Flutter of Suspension Bridge
(H. Sato and R. Toriumi*)

US-Japan Bridge Workshop May 1993, Tsukuba, Japan

An experimental study on aerodynamic sound generated from handrails of flat plate cascades

K. Kimura, Y. Fujino and S. Hiejima

Department of Civil Engineering, The University of Tokyo, Tokyo 113, Japan

ABSTRACT

To clarify the characteristics of the wind-induced sound from handrails of flat plate cascades, a series of wind tunnel experiments is conducted. Pure loud sound is observed when the wind is oblique to the plates. The relation between the sound frequency and the wind speed as well as the result from the flow visualization experiment suggests the cause of the sound as follows; the flow separated from the windward edge of the plate impinges the other windward edge of the same plate, generating large pressure fluctuations. It is observed that the sound frequencies increase in a step-wise manner as the increase of the wind speed, and they are shown to correspond to the resonant frequencies of acoustic oscillation of the space enclosed by the flat plate cascades. The step-wise increase of the frequencies indicates that there is a feedback between the sound generation and the acoustic resonant oscillation.

1. INTRODUCTION

In flexible structures such as long-span bridges and tall buildings, wind is one of the critical loadings since it potentially induces catastrophic or intolerable vibrations. In these structures, serviceability can be also affected by wind-induced vibrations. Although it is not widely recognized, wind often induces intolerable sound through the interaction between structures (or their elements) and wind. Wind-induced sounds in transmission cables or handrails in tall residential buildings are typical examples. This paper is concerned with one of the wind-induced sounds.

Handrails that consist of many very thin flat stainless steel plates (Fig. 1) have been often used in bridges and buildings. It has been reported, however, that wind-induced sound (noise) is generated in handrails of this type under moderate wind, causing an environmental issue.

There are a few experimental studies dealing with the wind-induced noise in the handrails (Refs. 1 and 2). Their studies seem to place an emphasis on clarifying the characteristics of the wind-induced noise in the prototype handrails mainly using the wind tunnel tests, and parametric experiments have not been made to elucidate the mechanism of the noise induced in the flat plates cascades.

The objective of this study is to conduct a series of wind tunnel experiments of the flat plate cascades and to attempt to clarify the mechanism and characteristics of wind-induced noise.

2. WIND TUNNEL EXPERIMENTS

The model used in the wind tunnel experiments consists of a steel frame and many thin aluminum flat plates as shown in Figs. 2 and 3. The flat plates which have rectangular sections are placed in parallel. The width, b, and the thickness, t, of the plates and the spacing intervals between the plates, p, were parametrically varied in the experiments as shown in Table 1. The length of the plates is 700 mm.

The wind tunnel used has a working section of 16 m width and 1.9 m height, and the smooth flow with the turbulent intensity of less than 1% was employed in the experiments. The wind speed was increased in a step-wise manner from zero to 15 m/s which is the maximum possible in the wind tunnel used. The horizontal angle of wind attack relative to the flat plates, θ, was varied by an interval of 15 degrees.

The sound was measured by a microphone which is covered with a wind shielding. The microphone was placed very close to the plates. The signal was sent through an octave band pass filter. A spectrum analyzer was used to obtain the sound intensity, which was computed from the area under the spectrum peak of the sound.

3. EXPERIMENTAL RESULTS

It was observed that sound is indeed generated from the flat plate cascades under certain horizontal angles of wind attack within a certain wind speed range. The spectrum of the induced sound shows one or two very sharp peaks, indicating that the sound was harmonic or a combination of two harmonics. The sound was felt as a noise since it was loud and very unpleasant.

Two experimental results are presented as examples in Fig. 4 where the sound frequency and the sound pressure level are plotted as a function of the wind speed. In both cases, sound with very high intensity was observed. The frequency of the sound increases as the increase of the wind speed, but the increase is step-wise. We define the Strouhal numbers as

$$S = f \cdot t / U \qquad (1)$$

where U : the wind speed, f : the frequency of the sound and t : the thickness of the plates. The average value of S for each experimental case is computed. Although the value S is somewhat scattered, it is found that S is approximately 0.75 in most cases. In a few cases it is 1.5 and in other few cases S is 0.75 as well as 1.5 as shown in Fig. 4(b). In Eq.(1), if the width of the plates, b, is used instead of the thickness of the plates, t, a consistent value(s) of S can not be obtained. This suggests that the frequency of the sound is associated with the thickness of the plate rather than its width.

The horizontal angle of wind attack, θ, was varied from 0° to 90° by an interval of 15°. The loud sound was not observed when the angle was either 0°,15°, 30° or 90°.

The cases in which the wind-induced sound was observed are presented in Fig. 5. It appears in Fig. 5 that in order that the sound is induced, larger angle θ is required when the ratio of the width to the spacing interval, *b/p*, becomes larger.

4. DISCUSSIONS

As shown in Fig. 4, the sound frequency doesn't increase monotonically as the increase of the wind speed. As well known, the same phenomenon is observed in the vortex-induced vibrations and is called as 'lock-in'. This indicates that there is a feedback between the sound generator and acoustic oscillation which magnifies the sound. We think that the sound from the flat plate cascades can be explained as follows.

Periodic eddies are generated in the flow around the flat plates and consequently periodic pressure fluctuations are radiated. Note that this frequency of generated eddies is basically in proportion to the wind speed unless any disturbance is applied. The pressure fluctuation is magnified in the resonant mechanism if the frequency of the pressure fluctuation coincides with one of the resonant frequencies of the acoustic oscillation. This magnified pressure fluctuation affects the generation of eddies, i.e., sound source. This is a feedback; the eddy frequency becomes so-called the lock-in state, resulting in the step-wise increase of the sound frequency for the increase of the wind speed. In the following, mechanism of the generation of sound from the flat plate cascades is discussed in more detail.

4.1 Sound Generator

Ref. 1 gives an explanation of the generation of the sound source; the eddies separated from a windward edge of a plate are impinging at the leeward edge of the adjacent plate (Fig. 6(a)) and large pressure fluctuation is induced. To confirm this, a flow visualization experiment was conducted in this study and one of the result is shown in Fig. 7. It appears in Fig. 7 that the eddies in the separated flow from the windward edge are conveyed in parallel with the plate rather than are impinging at the leeward edge of the adjacent plate. As aforementioned, Fig. 5 indicates that the wind-induced sound occurred in larger angle θ for larger *b/p* ratios and this fact doesn't support the explanation given in Ref. 1.

Hara (Ref. 4) experimentally studied the sound generation from flat plate cascades. His explanation is that the eddies which are separated at a windward edge of a plate are impinging at the other windward edge of the same plate and this is the source of the sound.

It can be easily accepted that the approaching flow is more distorted as the ratio b/p increases and the separated flow at a windward edge tends to be reattached at the other windward edge of the thin plate as shown in Fig. 6(b). Indeed when the ratio *b/p* is larger, larger angle θ is required to induce the sound; this is consistent with Hara's explanation. As mentioned, the sound frequency is related to the thickness of the plates; this also supports Hara's explanation.

4.2 Acoustic Resonance

Magnification mechanism is necessary to make the generated sound become intense. An enclosed space has many resonant frequencies and the sound can be magnified at these frequencies.

The wind tunnel has a floor and ceiling although the width of the tunnel is very large. A sound-absorber mat was placed on the floor of the wind tunnel and the sound was measured. It was found that the sound induced by the plate cascades was practically not affected by the presence of the sound-absorber mat. This confirms that the wind tunnel itself is not contributing the sound magnification.

The flat plates themselves form enclosed space. The resonant frequencies of the space enclosed by the plates are tabulated in Ref. 5 and are used. Fig. 8 shows an example where the computed resonant frequencies of the enclosed space as well as the measured sound frequencies are plotted. The agreement is good. In order to divide enclosed space between the plates into two, thin plates were horizontally placed at the middle of the flat plates (Fig. 9) and the induced-sound was measured. It was found that the sound frequencies are alternates of those in Fig. 8 and this fact supports that the frequencies of the sound are the resonant frequencies of the acoustic oscillation of the spaces enclosed by the plate cascades.

5. CONCLUDING REMARKS

A series of wind tunnel experiments of handrails which consist of thin flat plate cascades has been conducted under smooth flow; the thickness of the plates, the spacing interval of the plates, the horizontal angle of wind attack and the wind speed were chosen as parameters. It is found that wind-induced sound is indeed generated under certain conditions.

Most important finding is that, when the plates are densely spaced, larger horizontal angle is required to induce the sound. This as well as the results from the experiment of the flow visualization suggest that the sound source is due to the flow which is separated from the windward edge of a plate and impinging at the other windward edge of the same plate. It is also suggested that the sound is magnified by the resonances of the acoustic oscillation enclosed by the plate cascades. The wind-induced sound is due to the separate flow that is impinging at an edge, and it may be classified as the edge tone (Ref. 5). It is known that the edge tone has a feedback mechanism.

To identify the source mechanism of the sound more clearly needs, more detailed experiments will be made in the near future. To find engineering remedies in order to suppress the wind-induced sound is also an important subject.

Acknowledgments

Nomura, T., University of Tokyo, and Inoue, H., Mitsui Engineering & Shipbuilding Co. Ltd, gave us very useful advice during the course of the study. R. Shimada,

formerly student of University of Tokyo, and H. Murase, formerly student of Tokyo Denki University, assisted the wind tunnel experiments very much.

References

(1) Kaku, J. and Yamasita, M. : Aerodynamic noise radiated from parallel blades of aluminum rail, Tech. Conf. Japan Soc. Noise Control, pp. 129-132,1982. (in Japanese)
(2) Shibata, H. and Mori, H. : On an experiment of noise from bridge handrails, Japan Public Works Tohoku Div. Internal Annual Tech. Conf., pp. 535-540, 1987. (in Japanese)
(3) Hara, S. : A study on the aerodynamic noise from flat plate cascades, Proc. Japan Soc. Mechanical Eng., Vol. 41, No. 346, pp. 1781-1789, 1975. (in Japanese)
(4) Parker, R. : Resonance effects in wake shedding from parallel plates: calculation of resonant frequencies, J. Sound and Vibration, Vol. 5, No. 2, pp. 330-343, 1967.
(5) Blake, W.K. : Mechanics of flow-induced sound and vibration, Academic Press, 1986.

Table 1 Experimental parameters

b (mm)	30, 50, 70
t (mm)	1, 3, 5
p (mm)	15, 30, 50, 70, 100, 150

b : width, t : thickness and p : spacing interval of the plates

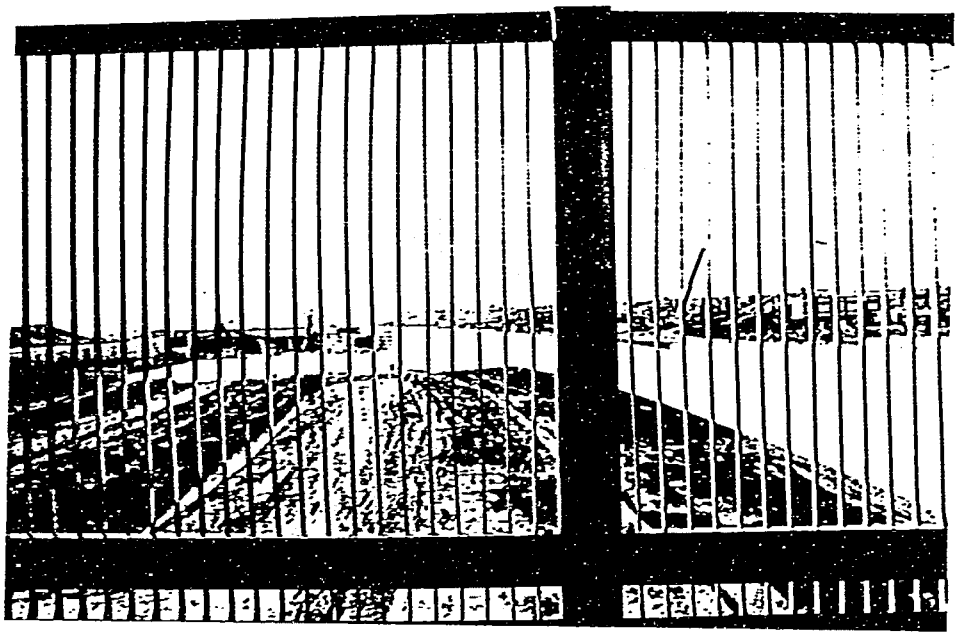


Fig. 1 A handrail of flat plate cascades



Fig. 1 A handrail of flat plate cascades (continued)

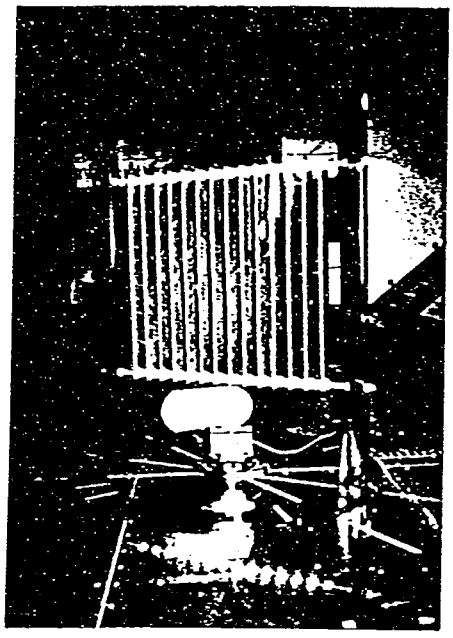


Fig. 2 The flat plate cascades model in the wind tunnel

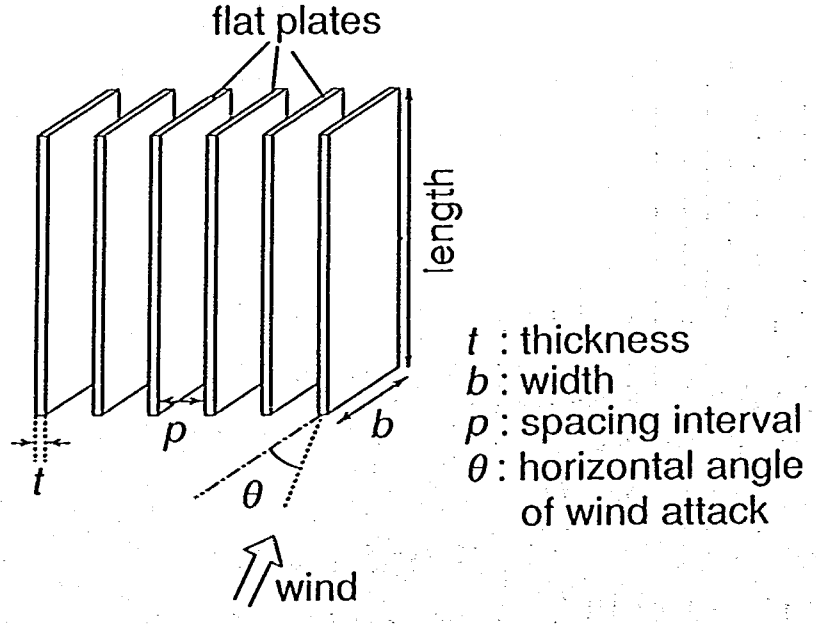
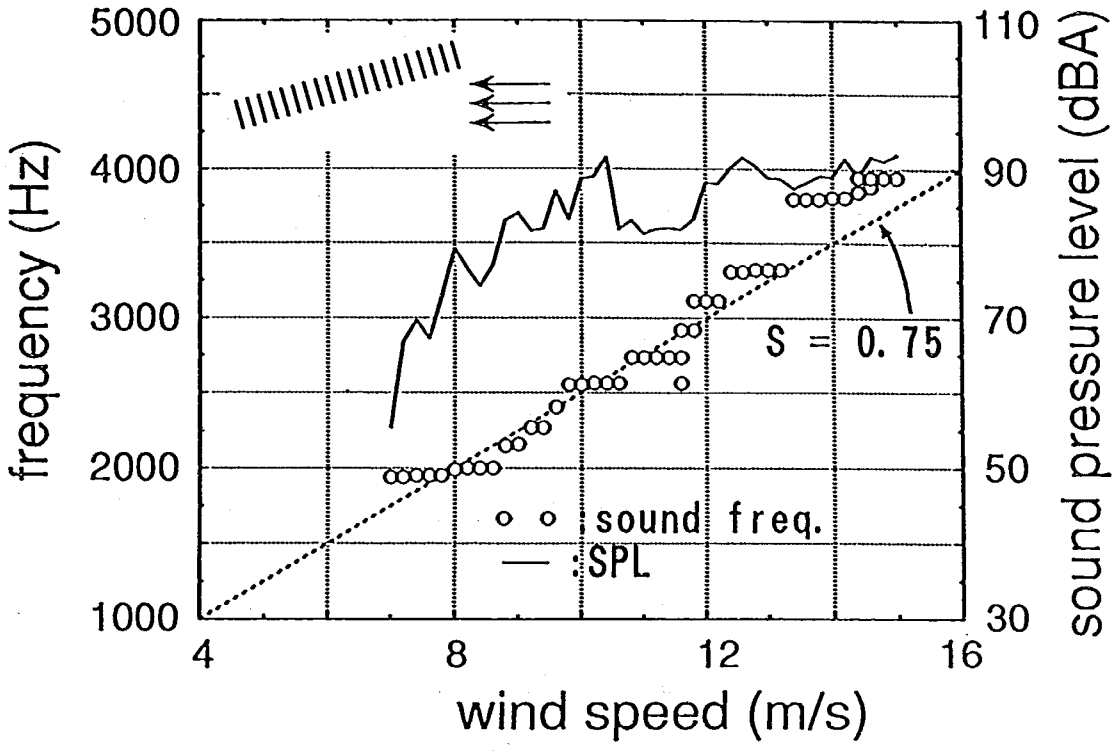
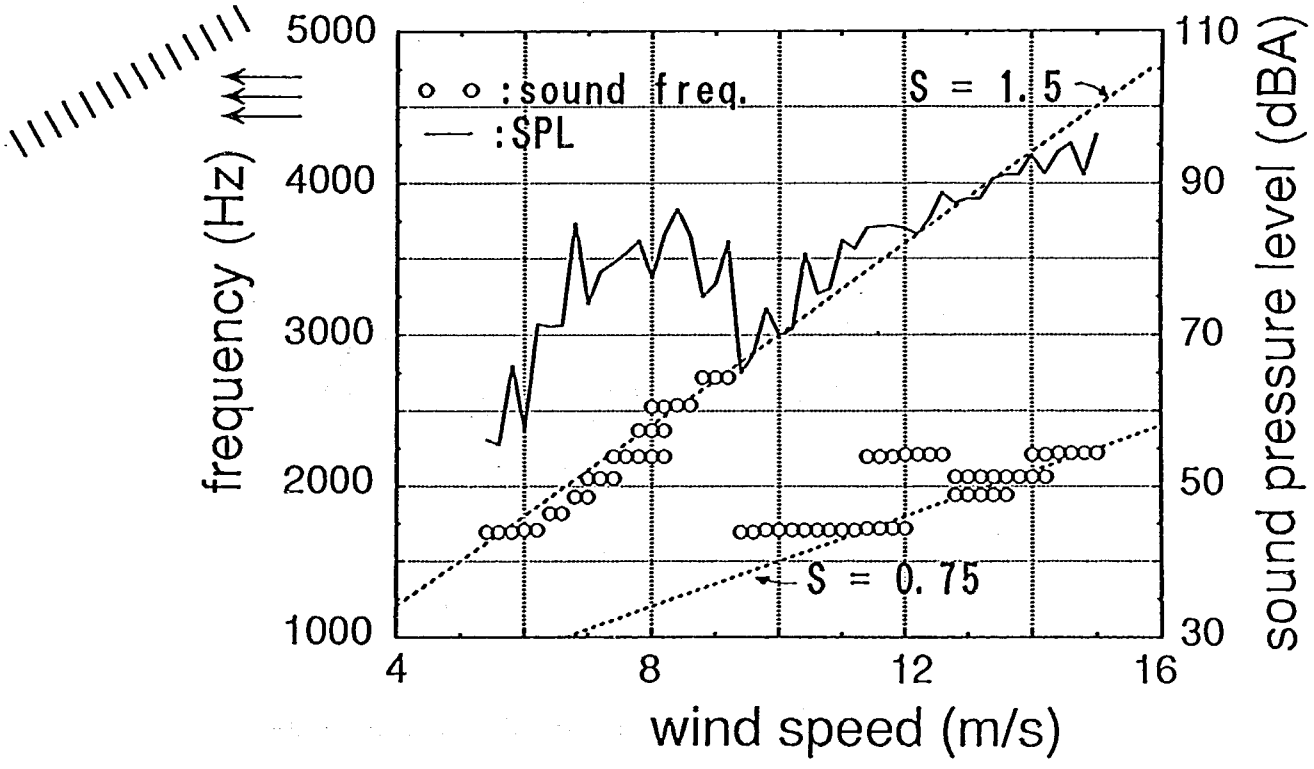


Fig. 3 Parameters of the model



(a) $t = 3$ mm, $b = 70$ mm, $p = 30$ mm, $\theta = 75°$



(b) $t = 5$ mm, $b = 70$ mm, $p = 50$ mm, $\theta = 60°$

Fig. 4 Sound frequency and sound pressure level vs. wind speed

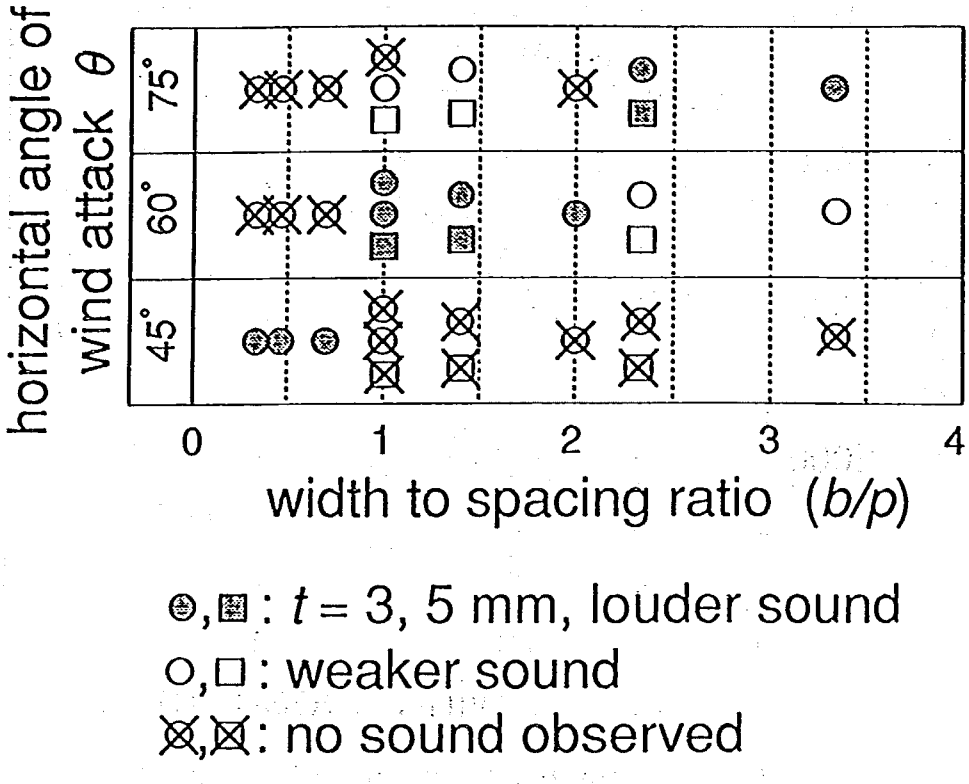


Fig.5 Relationship between sound generation and parameters

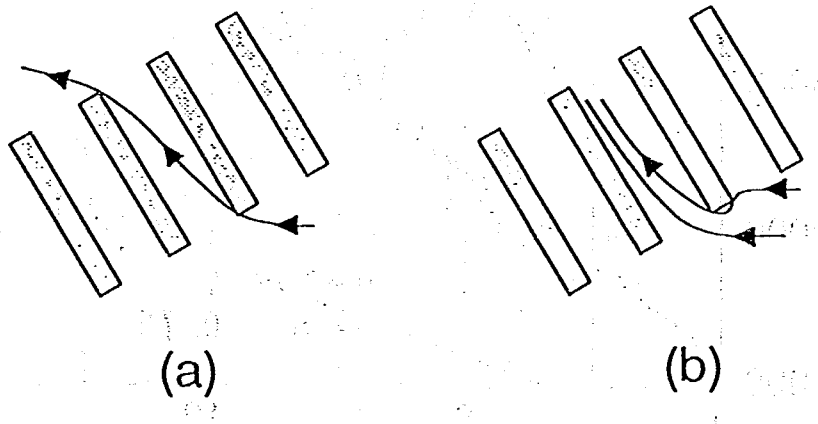


Fig. 6 Suggested flow patterns in flat plate cascades

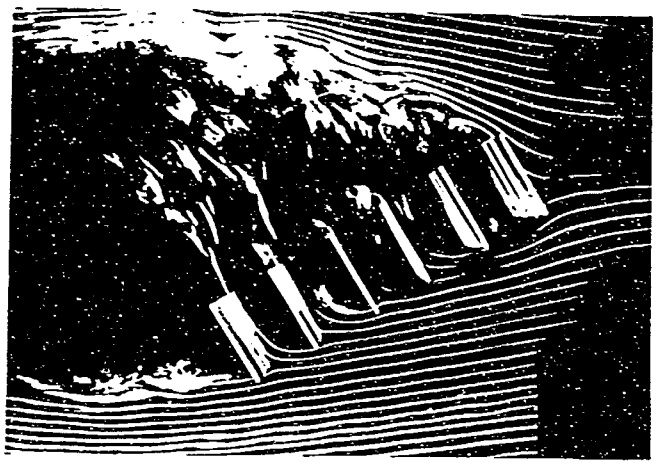


Fig. 7 Flow visualization result ($t = 3$ mm, $b = 70$ mm, $p = 50$ mm, $\theta = 60°$)

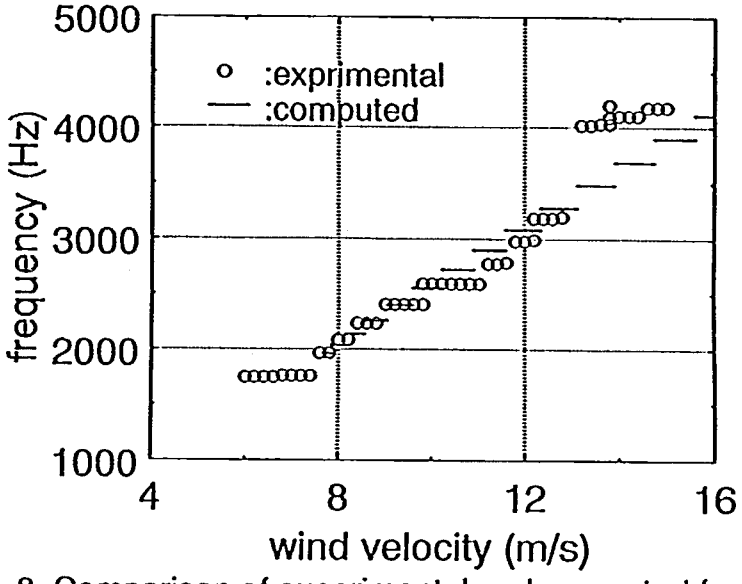


Fig. 8 Comparison of experimental and computed frequencies ($t = 3$ mm, $b = 70$ mm, $p = 50$ mm, $\theta = 60°$)

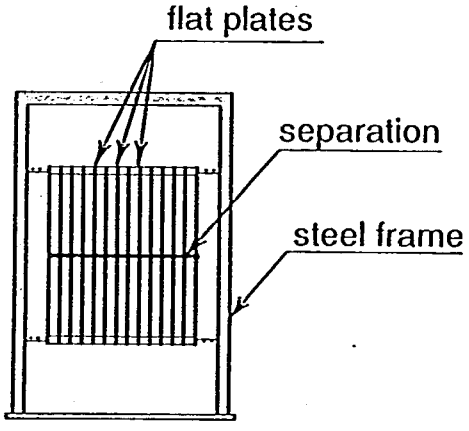


Fig. 9 The model with a separation

Simulation Techniques for Bridge Aerodynamic Investigations at the Turner-Fairbank Highway Research Center.

by

Okey U. Onyemelukwe[1] and Harold R. Bosch[2]

ABSTRACT

This paper presents methods currently employed at the Federal Highway Administration's (FHWA's) Aerodynamics Laboratory, to study wind effects on bridges. The discussion focuses mainly on techniques for investigating the aerodynamic characteristics of long-span bridges, as opposed to the aeroelastic behavior, an area in which researchers at the FHWA's Aerodynamics Laboratory have also made major strides over the past several years.

Two approaches used at the Laboratory, herein dubbed "Experimental Simulation" and "Numerical Simulation", are discussed as they pertain to wind flow around bridge deck sections. For a majority of long-span bridges, the bridge deck is one of the most critical bridge elements (aerodynamically and aeroelastically), and as such, it receives the most attention. First, the more established and widely used experimental simulation technique (model testing in the wind-tunnel) is briefly presented. Next, emphasis is placed on procedures for the more recently developed technique of numerical simulation (computer modeling), which at its current developmental stage is intended to complement wind-tunnel testing.

Finally, the advantages and shortcomings of using either simulation technique are discussed. It is evident from this discussion that the use of both techniques to varying degrees, in a long-span bridge wind design program, is beneficial to the bridge engineer.

---

[1] Post Doctoral Fellow, George Vincent Memorial Aerodynamics Laboratory, Federal Highway Administration, Turner-Fairbank Highway Research Center, Mclean, Virginia, 22101.

[2] Research Structural Engineer, George Vincent Memorial Aerodynamics Laboratory, Federal Highway Administration, Turner-Fairbank Highway Research Center, Mclean, Virginia, 22101.

INTRODUCTION

For almost 4 decades, researchers at the George Vincent Memorial Aerodynamics Laboratory located at the Turner-Fairbank Highway Research Center (TFHRC) in Mclean, Virginia, have focused their efforts primarily on investigating wind effects on bridges. Of course, long-span bridges such as suspension bridges and modern cable-stayed bridges, are most susceptible to wind-induced instability, and have received the most attention. The motion of wind around any body in its flow field produces pressure and velocity variations, which produce aerodynamic forces and moments on the body. If the body moves or deforms appreciably under the induced wind forces, these deflections will affect the wind forces, which will in turn influence the deflection, giving rise to succeeding deflections of oscillatory and/or divergent nature (instability).

It has become common place in wind engineering, to categorize wind-induced effects on structures as being of aerodynamic consequence or aeroelastic consequence. Simply stated, aerodynamic effects relate more to the determination of wind-induced forces on the bridge, and the description of wind flow characteristics around the bridge components. Aerodynamic considerations are highly dependent on the body geometry, and tend to occur wholly within the flow alone. Phenomena such as vortex shedding and galloping, which are characterized by the production of trailing vortices from separation points or a rapidly diverging wake, are aerodynamics related. The wind-induced aerodynamic forces can be expressed in terms of lift, drag, and pitching moments. It is important to note that these aerodynamic forces (lift, drag, and pitching moment) are required, for both static and dynamic wind analysis of long-span bridges. In consideration of the static stability of bridge structures under steady wind, excessive lift or drag forces may cause an unstable bridge to undergo lateral buckling or torsional divergence.

On the other hand, aeroelastic considerations arise when conditions are present which permit interaction between wind forces, structural deflection, structural damping, structural inertia, and stiffness of the bridge. Hence, the aeroelastic classification is a structural response type investigation. Aeroelastic investigation of long-span bridges can either be a random vibration type problem (buffeting), as a result of the turbulence in the wind, or may be concerned with an instability resulting from a self-excited oscillation of growing amplitude called flutter.

However, it is only the simulation procedures associated with aerodynamic considerations that are pursued further in this paper. There are two fundamental approaches to the

simulation of wind flow around bridges namely, experimental and numerical simulations. The correct use of both of these methods requires a proper understanding of the fluid-mechanical descriptions of wind, and the physical description of wind effects, which will be discussed in the sections that follow.

EXPERIMENTAL SIMULATION (MODEL TESTING IN WIND-TUNNEL)

The wind-tunnel at TFHRC is a low velocity, open circuit tunnel designed primarily for study of wind loads on long-span bridges. This wind-tunnel can generate extremely smooth flow (laminar flow condition) at speeds up to 50 ft/s (15.2 m/s). For experiments where turbulent flow simulation is desired, an active turbulence generator is inserted into the circuit, between the wind-tunnel nozzle and the test frame where the bridge model is suspended in the flow.

Modeling Technique

The bridge testing technique almost always used at the TFHRC wind-tunnel is the section model approach. A section model of a long-span bridge superstructure is a small, but geometrically faithful copy of a typical length of the prototype bridge deck. Cables and hangers are generally not modeled, because the aerodynamic effects from their profile are considered negligible relative to the bridge deck. A typical bridge deck section model tested at the TFHRC wind-tunnel is shown in Figure 1a.

In order to construct a truly representative model, the model length and structural properties are usually scaled from the known prototype values. As in most model testing, the first parameter considered is the geometric length scale or ratio, λ_1, model to prototype. To ensure that all significant structural details can be adequately reproduced, the length scale recommended is usually between 1:100 and 1:25 inclusive.

It has been shown that Froude number (Fr) similarity and Reynolds number (Re) similarity between model and prototype conditions, can not be simultaneously satisfied for wind-tunnel simulation [1]. For bluff bodies such as bridge decks though, where drag is primarily pressure drag and flow separation occurs at sharp corners, lift, drag, and moment forces are relatively insensitive to Reynolds number variation, as long as it is beyond the 300-500 range [2]. Experience has shown that for aerodynamic tests of bridge models, Reynolds number similarity criterion may be violated, provided that λ_1 is selected such that local Reynolds numbers do not become too small (less than 300).

Force Measurement

Wind-tunnel force measurements are conducted by placing the section model in the wind flow, with the section model rigidly attached to a high frequency dual force-balance. The two balance mechanisms, which are outside the direct influence of the wind, enable accurate measurement of the 3 force components (in x,y,z directions) at each end of the model. The electronically measured force data is then recorded automatically using a data acquisition system, from which the data is further processed and reduced to mean values of lift (L), drag (D) and pitching moment (M). These static mean drag and lift forces can also be transformed to chord (X) and normal (Z) forces according to Equation (1) :

$$\begin{aligned} X &= D\cos\alpha - L\sin\alpha \\ Z &= D\sin\alpha + L\cos\alpha \end{aligned} \qquad (1)$$

The orientation of these forces is indicated in Figure 1b. All the aerodynamic forces are normally represented in terms of the dimensionless coefficients defined in Equation (2) :

$$\begin{aligned} C_D &= \frac{2D}{\rho V^2 B} \\ C_L &= \frac{2L}{\rho V^2 B} \\ C_M &= \frac{2M}{\rho V^2 B^2} \\ C_X &= \frac{2X}{\rho V^2 B} \\ C_Z &= \frac{2Z}{\rho V^2 B} \end{aligned} \qquad (2)$$

The values in Table 1, are typical force measurements from a wind-tunnel experiment conducted at the TFHRC Aerodynamics Laboratory [3].

Flow Visualization

For experimental aerodynamic studies, smoke jets in air and dye or bubbles water are two commonly used flow visualization methods. In both cases, a small-scale model of the bridge deck is immersed in the flow field (a stream of dye in water, or smoke in air), and the flow patterns or flow

characteristics around the bridge model are captured using various still or motion photographic techniques.

In the past, flow visualization studies have also been accomplished by installing various velocity sensors on a motorized traverse system, and surveying the flow field around the section model. The vectors of the measured velocities are then plotted, and the flow streamlines traced such that they are at all times parallel to the vectors at adjacent data locations. The plot of Figure 2a shows the streamlines obtained by this method, during a wind-tunnel study at the TFHRC Aerodynamics Laboratory [4].

NUMERICAL SIMULATION (COMPUTER MODELING)

This computer simulation approach uses a numerical scheme, that employs the finite-difference procedure in solving the governing 2-D, unsteady, incompressible, laminar, Navier-Stokes equations, in a body-fitted curvilinear coordinate system [5]. The grid generation technique used, the governing equations both in the physical and transformed planes, the finite-difference scheme, and results from application to an actual bridge deck section are now discussed.

Grid Generation Technique

The body-fitted curvilinear coordinate system is one in which, at least one coordinate line coincides with the boundary surface of the body in the flow field [6]. This automatically eliminates the need for interpolation in the finite-difference implementation of boundary conditions for an irregularly shaped body. This grid generation technique involves the solution of an elliptic partial differential system in the physical plane. To solve the system of equations, a coordinate transformation from the physical plane (x,y), to a uniform rectangular computational plane (ξ,η) is necessary. Mathematically, this transformation is stated as,

$$\begin{aligned} \xi &= \xi(x,y) \\ \eta &= \eta(x,y) \end{aligned} \qquad (3)$$

where the transformed coordinates (ξ,η) are the independent variables, and the physical coordinates (x,y) are the dependent variables. The elliptic system of equations solved are either of the Laplace type or the Poisson type, which are both stated below:

Laplace Equation-

$$\nabla^2 \xi = 0$$
$$\nabla^2 \eta = 0 \qquad (4)$$

Poisson Equation-

$$\nabla^2 \xi = P(\xi, \eta)$$
$$\nabla^2 \eta = Q(\xi, \eta) \qquad (5)$$

After transformation of these equations to the computational plane by using the chain rule of differentiation, the resulting form of the Laplace equation that is actually solved for the grid point values are,

$$a x_{\xi\xi} - 2b x_{\xi\eta} + c x_{\eta\eta} = 0$$
$$a y_{\xi\xi} - 2b y_{\xi\eta} + c y_{\eta\eta} = 0 \qquad (6)$$

Dirichlet boundary conditions, consisting of the physical coordinates of the body geometry and the outer flow boundary, must be specified before the solution can proceed. The coefficients a, b, c, are transformation metrics given in terms of the following difference expressions,

$$a = x_\eta^2 + y_\eta^2$$
$$b = x_\xi x_\eta + y_\xi y_\eta \qquad (7)$$
$$c = x_\xi^2 + y_\xi^2$$

The functions $P(\xi,\eta)$ and $Q(\xi,\eta)$ in the Poisson equation are chosen to enable the control of the grid lines within the flow field. Thus, the grid lines can be clustered towards the body surface where high flow gradients exist.

Flow Equations

Physical Plane - In the physical plane, the governing flow equations are the 2-dimensional, incompressible, laminar momentum equations, and the continuity equation. The dimensional form of the flow equations are usually non-dimensionalized with respect to the flow parameters of the undisturbed flow region. The primitive variable form of the non-dimensional flow equations are :

$$u_x + v_y = 0$$
$$u_t + u u_x + v u_y = -p_x + \frac{\nabla^2 u}{Re}$$
$$v_t + u v_x + v v_y = -p_y + \frac{\nabla^2 v}{Re} \qquad (8)$$

Instead of solving the continuity equation, a new poisson equation in pressure form is solved. The need for the poisson pressure equation is to eliminate the pressure-velocity coupling that exist between the momentum and continuity

equations. In the physical plane, the poisson pressure equation solved is:

$$\nabla^2 p = S_p - \delta_t \tag{9}$$

where,

$$S_p = -(u_x)^2 - 2v_x u_y - (v_y)^2$$
$$\delta = u_x + v_y$$

The derivation of this pressure equation ensured the satisfaction of the continuity requirement. However, the temporal term δ is purposely not set to zero, to avoid numerical instabilities that would otherwise occur [7].

Transformed Equations - Before the flow equations can be solved in the computational plane, the equation of motion must be transformed accordingly. After introducing the applicable transformation metrics into the equations, the form of the transformed momentum equations solved are :

u-momentum-

$$u_t + \frac{u(y_\eta u_\xi - y_\xi u_\eta)}{J} + \frac{v(x_\xi u_\eta - x_\eta u_\xi)}{J} = -\frac{y_\eta p_\xi}{J} + \frac{y_\xi p_\eta}{J} + \frac{(au_{\xi\xi} - 2bu_{\xi\eta} + cu_{\eta\eta} + du_\eta + eu_\xi)}{ReJ^2} \tag{10}$$

v-momentum-

$$v_t + \frac{u(y_\eta v_\xi - y_\xi v_\eta)}{J} + \frac{v(x_\xi v_\eta - x_\eta v_\xi)}{J} = -\frac{x_\xi p_\eta}{J} + \frac{x_\eta p_\xi}{J} + \frac{(av_{\xi\xi} - 2bv_{\xi\eta} + cv_{\eta\eta} + dv_\eta + ev_\xi)}{ReJ^2} \tag{11}$$

Pressure Equation-

$$\nabla^2 p = S_p - \delta_t \tag{12}$$

where,

$$\nabla^2 p = \frac{(ap_{\xi\xi} - 2bp_{\xi\eta} + cp_{\eta\eta} + dp_\eta + ep_\xi)}{J^2}$$

$$S_p = -\frac{(y_\eta u_\xi - y_\xi u_\eta)^2}{J^2} - \frac{(x_\xi v_\eta - x_\eta v_\xi)^2}{J^2} - \frac{2(y_\eta v_\xi - y_\xi v_\eta)(x_\xi u_\eta - x_\eta u_\xi)}{J^2}$$

$$\delta = \frac{(y_\eta u_\xi - y_\xi u_\eta - x_\eta v_\xi + x_\xi v_\eta)}{J}$$

Boundary Conditions - The boundary conditions used for the momentum equation at the body surface are the no-slip boundary conditions i.e. u=0, v=0, and u=1, v=0 are specified at the outer flow boundary. For the pressure equation, a Neumann type boundary condition is specified at the wall surface, i.e. specify $\partial p/\partial n$, and p=0 is specified at the outer flow boundary.

Finite-Difference Scheme

The finite-difference formulation is based on an upwind-implicit scheme. A backward difference is used in time, and central difference expression used for the space derivatives, except for the convection terms where a third order upwind-difference expression is used instead [8]. For the u-velocity convection term in the transformed momentum equations, this third order upwind finite-difference expression is :

$$\left(\hat{u}\frac{\partial u}{\partial \xi}\right)_i = \hat{u}_i \frac{-u_{i+2} + 8\,(u_{i+1} - u_{i-1}) + u_{i-2}}{12\,\Delta\xi} + |u_i| \frac{u_{i+2} - 4\,u_{i+1} + 6\,u_i - 4\,u_{i-1} + u_{i-2}}{4\,\Delta\xi} \qquad (13)$$

The $\hat{u}_i$ refers to the transformed form of the non-linear velocity term in the flow equations of motion.

Wind Force Coefficients

The bridge engineer is often interested in obtaining the wind-induced forces on a bridge deck section for design or analysis purposes. The numerical simulation technique just presented, provides the force coefficients in 3 different forms - pressure, mean forces, and instantaneous forces.

First, solving the time-dependent equations of motion enables the instantaneous pressure coefficients, $C_p(t)$, to be computed. The mean pressure distribution, C_p, around the body surface can then be obtained by calculating the time-average of the body surface instantaneous pressures. Integrating the mean pressures along the body surface, yields the so called static mean force coefficients (C_D,C_L). Summing the moment of these forces about a given location on the body produces the mean pitching moment (C_M). On the other hand, integrating the instantaneous pressure coefficients over the body surface, directly yields the corresponding instantaneous force coefficients $C_D(t)$, $C_L(t)$, and $C_M(t)$.

In addition, a fourier analysis of these fluctuating and time-dependent force coefficients, provides the engineer with wind loading frequency data, useful for dynamic analysis in a

frequency domain. The data in Table 2 show an excerpt of numerically computed instantaneous force coefficients, on a bridge deck section model for a proposed cable-stayed bridge across the Chesapeake and Delaware canal.

Computer Flow Visualization

The generation of computer flow visualization plots, provide the bridge engineer with intricate details of the wind flow characteristics at different stages of the flow development. The velocities computed from the numerical modeling are used to generate the flow streamlines, velocity contour plots, and velocity vector plots. The contours of the pressure distribution can also be plotted when this technique is used. This pictorial representation of the distribution of the flow parameters, allows the engineer to make appropriate adjustments and modifications to the bridge model, in order to minimize or possibly eliminate undesirable aerodynamic effects. The plots in Figure 2b show computer simulation of the flow streamlines around the Chesapeake and Delaware canal bridge deck model.

CONCLUDING REMARKS

Both of the wind flow simulation techniques employed at the TFHRC Aerodynamics Laboratory have been presented. Since traditional wind-tunnel testing involves a rigorous process, that can be time consuming and expensive, the researcher must, by necessity, be extremely selective in deciding the model configurations to be investigated. The numerical simulation approach was introduced to take advantage of remarkable advancements in modern computer technology. Thus, providing the engineer with another means for effective and rapid evaluation of bridge model alternatives, and changes in geometric details.

The limited availability of unsteady wind load data over long periods of time from experimental simulation, can be alleviated by the use of numerical simulation techniques. The unsteady wind-induced forces and pressures most useful for dynamic response analysis, are directly provided by numerical simulation. Both techniques yield mean force and mean pressure coefficients, commonly used for static wind analysis of long-span bridge response.

Comparison of the flow streamlines of Figures 2a & 2b, clearly illustrates the inability of the experimental flow visualization procedure to capture the details of the wind flow patterns or wind flow characteristics. This is, perhaps, one of the most useful features of computer simulation. By visualizing the flow patterns on a computer at different

stages of the flow development, the engineer can make appropriate modifications to the bridge model with greater ease.

Since extensive verification of numerically simulated aerodynamic force data has not yet been accomplished, use of this technique is currently limited to a preliminary investigative role. The computer modeling technique is normally used to evaluate a wider range of alternative bridge models, while wind-tunnel tests are reserved for the chosen "final" configurations.

ACKNOWLEDGMENTS

Much of the numerical simulation is from the first author's PhD dissertation. The study was supported by a Federal Highway Administration research grant.

SYMBOLS

x,y,z	physical plane coordinates
$\xi\eta$	body-fitted coordinates
V	velocity vector magnitude
u,v	horizontal & vertical velocity vector components
p	pressure
P,Q	grid clustering forcing functions
B	characteristic length
λ_1	length scale ratio
t	time
NDT	non-dimensional time (V*t/B)
J	Jacobian of transformation
a,b,c,d,e	transformation metrics or scale factors
Re	Reynolds number (ρVB/μ)
g	gravitational acceleration
Fr	Froude number (V^2/B*g)
X	resultant chord force per unit length
Z	resultant normal force per unit length
D	drag force per unit length
L	lift force per unit length
M	pitching moment per unit length
$C_{(L,D,M)}$	static mean force coefficients
$C(t)_{(L,D,M)}$	Instantaneous force coefficients (dynamic)
C_p	mean pressure coefficient ($2\Delta p/\rho V^2 B$)
$C_p(t)$	Instantaneous pressure coefficient
S_p	right hand side of Poisson pressure equation
δ	temporal term in Poisson pressure equation
α	flow angle of attack

REFERENCES

[1] Scanlan, R.H., "Recent Methods in the Application of Test Results to the Wind Design of Long, Suspended-Span Bridges", Report No. FHWA-RD-75-115, Federal Highway Administration, Washington, D.C., 1975, pp. 8-9.

[2] Prandtl, L. and Tietjins, O.G., "Applied Hydro and Aeromechanics", McGraw-Hill, New York, New York, 1934.

[3] Bosch, H.R., "A Wind-Tunnel Investigation of the Deer Isle-Sedgwick Bridge (Phase I)", Report No. FHWA-RD-87-027, Federal Highway Administration, Mclean, Virginia, 1987.

[4] Bosch, H.R., "Aerodynamic Investigations of the Luling Louisiana Cable-Stayed Bridge", Report No. FHWA-RD-77-161, Federal Highway Administration, Washington, D.C.,

[5] Onyemelukwe, O.U. and Bosch, H.R., "Predicting Wind Forces Using Computer Simulation of Air Flow Around Bridges", Preproceeding 24th Joint Meeting of United States-Japan Panel on Wind and Seismic Effects, NIST, Gaithersburg, Maryland, May 19-22, 1992, pg. 1-2.

[6] Thompson, J. F., Thames, F. C., and Mastin, C. W., "Boundary-Fitted Curvilinear Coordinate Systems for the Solution of Partial Differential Equations on fields containing any number of Arbitrary Two-Dimensional Bodies.", NASA CR-2729., 1977.

[7] Harlow, F. H. and Welch, J. E., "Numerical Calculation of Time-Dependent Viscous Incompressible Flow of Fluid with Free Surface." Physics of Fluids, Vol. 8, 1965, pp. 2182-2189.

[8] Kawamura, T. and Kuwahara, K., "Computation of High Reynolds Number Flow around a Circular Cylinder with Surface Roughness." AIAA Paper, 84-0340, 1984.

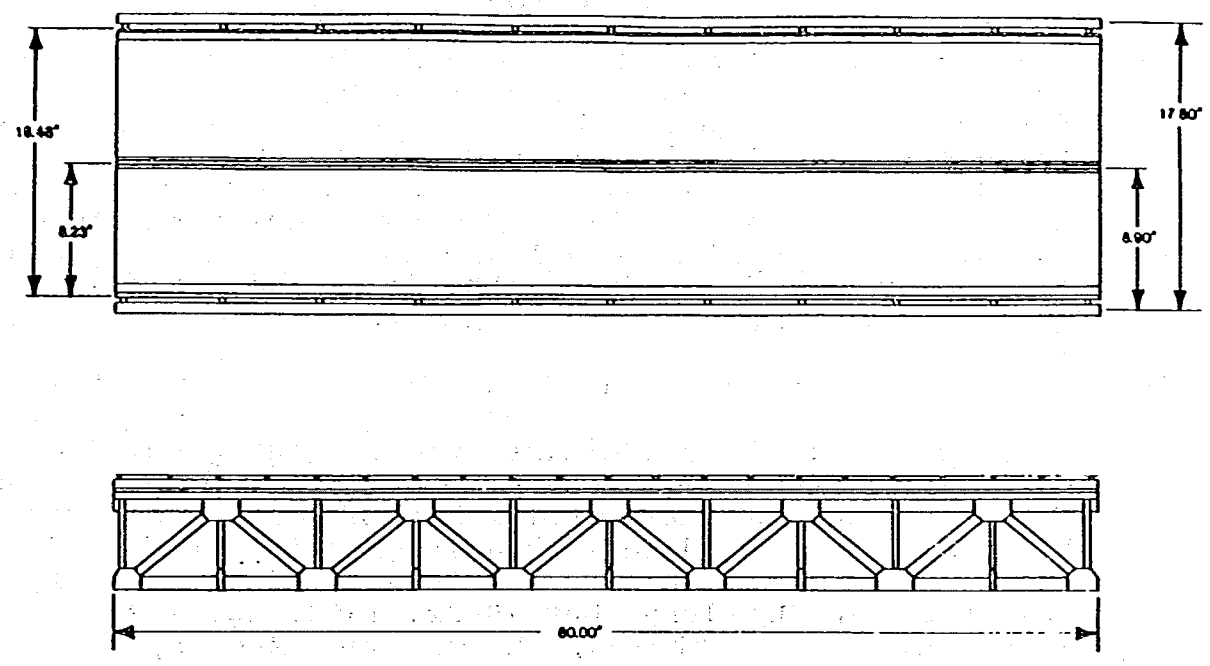


Figure 1a. A Typical Bridge Section Model.

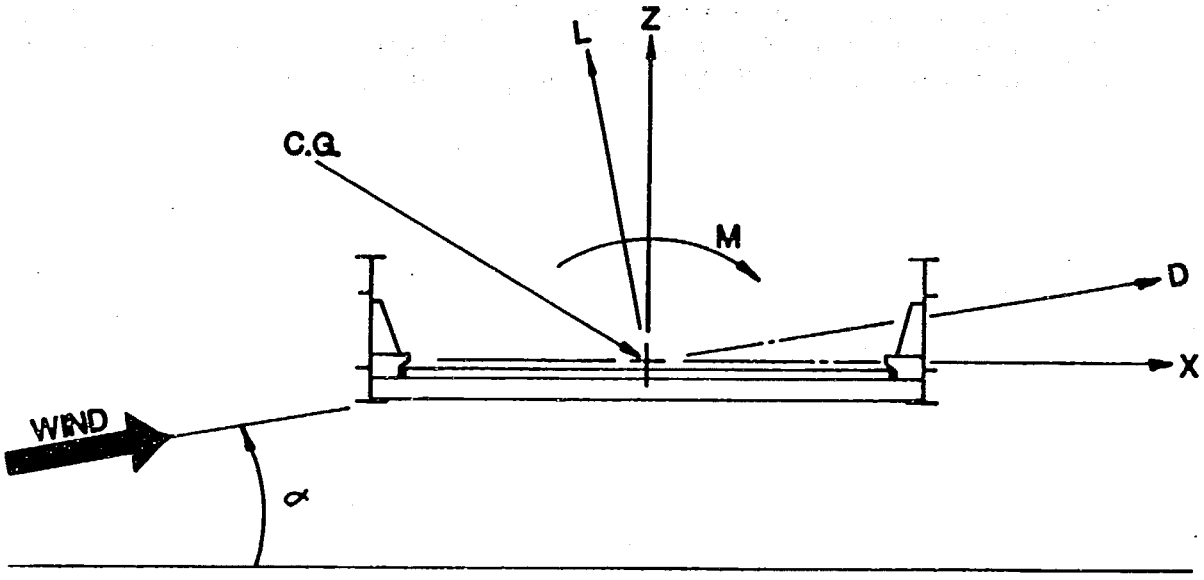


Figure 1b. Orientation of Aerodynamic Forces.

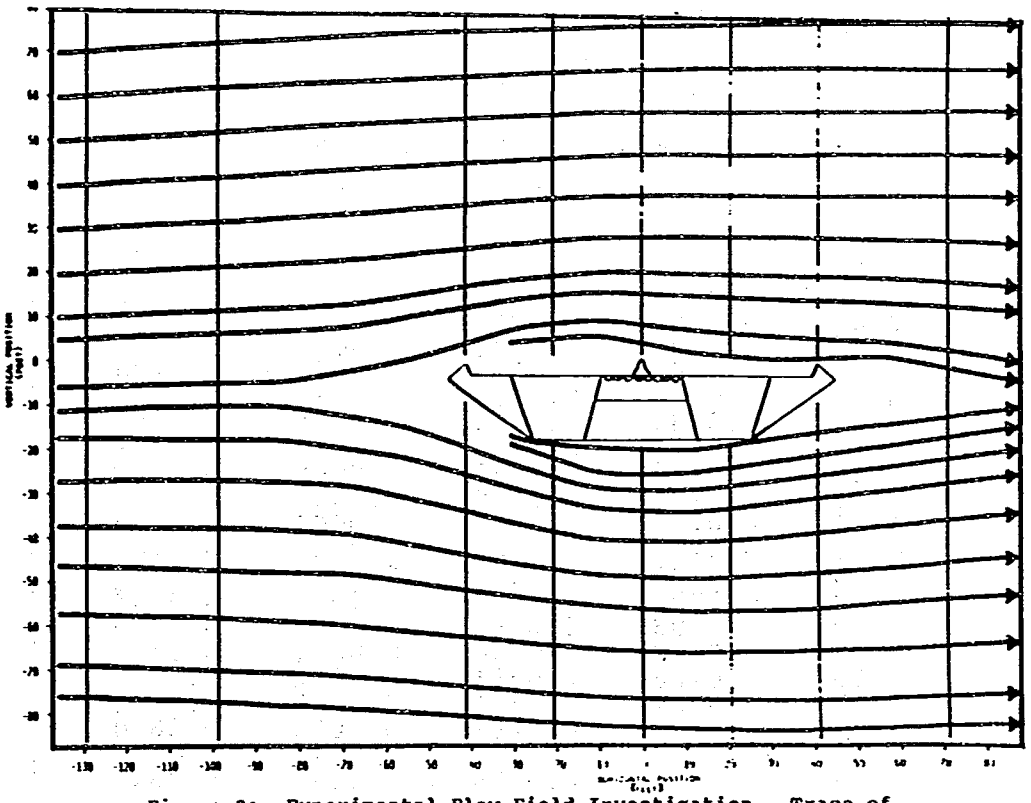


Figure 2a. Experimental Flow Field Investigation - Trace of Streamlines around Luling Bridge Deck (1 ft. = 0.3048 m)

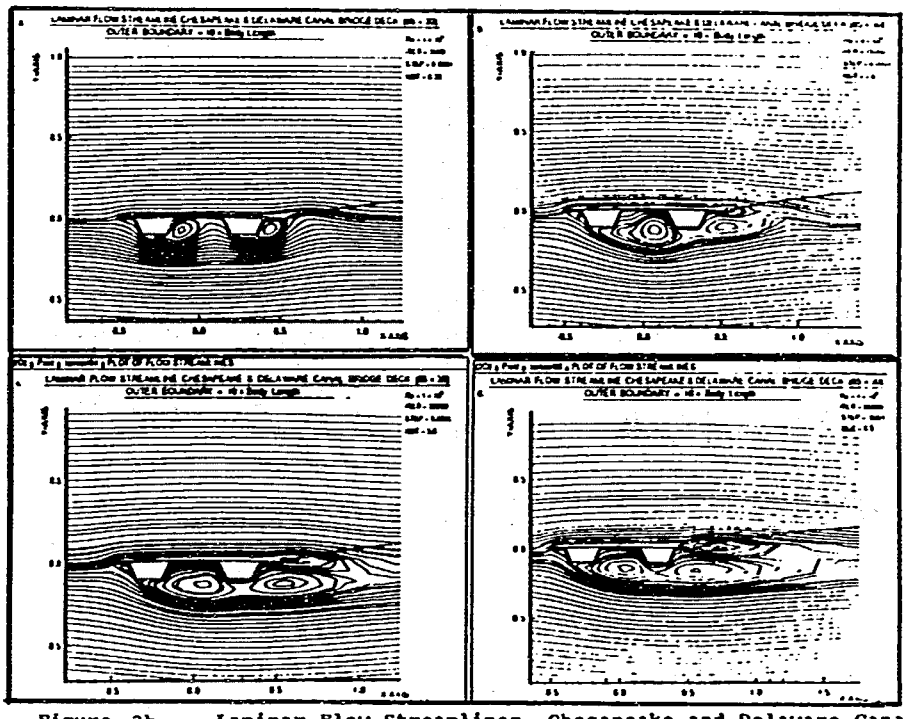


Figure 2b. Laminar Flow Streamlines, Chesapeake and Delaware Canal Bridge Deck, (Re = $1x10^5$, α = 0.0), HDT = 0.30, 1.5, 3.0, 6.5

Table 1. Force Measurements - Existing Shape (Um = 12.8 fps).

DEER ISLE - SEDGWICK BRIDGE

CONFIGURATION---EXISTING

STATIC FORCES AND MOMENTS

SPEED FPS	ANGLE DEG	DRAG #/F	LIFT #/F	MOMENT (F-#/F)	CHORD #/F	NORMAL #/F
12.73	-10.00	0.0839	0.0201	0.0020	0.0861	0.0052
12.74	-9.00	0.0833	0.0256	0.0018	0.0863	0.0122
12.79	-8.00	0.0815	0.0274	0.0015	0.0845	0.0158
12.61	-7.00	0.0764	0.0295	0.0017	0.0795	0.0200
12.82	-6.00	0.0774	0.0303	0.0014	0.0801	0.0221
12.80	-5.00	0.0734	0.0300	0.0016	0.0757	0.0235
12.90	-4.00	0.0744	0.0276	0.0011	0.0762	0.0223
12.66	-3.00	0.0733	0.0226	0.0009	0.0744	0.0187
12.69	-2.00	0.0722	0.0145	0.0002	0.0726	0.0120
12.61	-1.00	0.0702	0.0069	-0.0004	0.0703	0.0056
12.63	0.00	0.0704	0.0007	-0.0006	0.0704	0.0007
13.24	1.00	0.0709	-0.0054	-0.0014	0.0710	-0.0042
13.07	2.00	0.0729	-0.0130	-0.0021	0.0733	-0.0105
12.99	3.00	0.0693	-0.0242	-0.0029	0.0705	-0.0205
12.76	5.00	0.0719	-0.0348	-0.0044	0.0746	-0.0284
12.75	6.00	0.0752	-0.0361	-0.0042	0.0786	-0.0281
12.94	7.00	0.0794	-0.0351	-0.0045	0.0831	-0.0252
12.89	8.00	0.0777	-0.0287	-0.0022	0.0810	-0.0177
12.88	9.00	0.0828	-0.0310	-0.0047	0.0867	-0.0176
12.77	10.00	0.0816	-0.0258	-0.0045	0.0849	-0.0112

STATIC FORCE COEFFICIENTS

SPEED	ANGLE	Cd	Cl	Cm	Cx	Cz
12.73	-10.00	0.4644	0.1113	0.0120	0.4766	0.0290
12.74	-9.00	0.4608	0.1414	0.0106	0.4773	0.0675
12.79	-8.00	0.4471	0.1503	0.0087	0.4637	0.0866
12.61	-7.00	0.4310	0.1663	0.0102	0.4480	0.1125
12.82	-6.00	0.4226	0.1656	0.0083	0.4376	0.1206
12.80	-5.00	0.4016	0.1641	0.0093	0.4144	0.1285
12.90	-4.00	0.4013	0.1487	0.0063	0.4107	0.1204
12.66	-3.00	0.4106	0.1264	0.0056	0.4166	0.1047
12.69	-2.00	0.4018	0.0808	0.0010	0.4044	0.0667
12.61	-1.00	0.3960	0.0387	-0.0027	0.3966	0.0318
12.63	0.00	0.3963	0.0040	-0.0038	0.3963	0.0040
13.24	1.00	0.3631	-0.0279	-0.0078	0.3636	-0.0215
13.07	2.00	0.3829	-0.0684	-0.0119	0.3851	-0.0550
12.99	3.00	0.3685	-0.1286	-0.0162	0.3747	-0.1091
12.76	5.00	0.3960	-0.1918	-0.0259	0.4112	-0.1565
12.75	6.00	0.4153	-0.1995	-0.0246	0.4338	-0.1550
12.94	7.00	0.4257	-0.1881	-0.0260	0.4455	-0.1348
12.89	8.00	0.4194	-0.1551	-0.0127	0.4369	-0.0953
12.88	9.00	0.4481	-0.1676	-0.0268	0.4688	-0.0954
12.77	10.00	0.4490	-0.1420	-0.0264	0.4668	-0.0619

Table 2. Instantaneous Force Coefficients for Cheapeake and Delaware Canal Bridge Deck (Re = $1x10^5$, α = 0.0)

Body shape or Section type	Outer Flow Boundary	Flow Parameters		Computational Parameters			Force Coefficients			
		Angle of attack	Reynolds number	Non-Dim. Time Step	Number of iteration	Non-Dim. Time (NDT)	C_L	C_D	C_M @ $\frac{C}{2}$	Experimental or AASHTO Mean Value
Chesapk. and Delaware Canal Bridge Deck	Circle @ 10 times Body Length	0 Degrees	N/A	N/A	N/A	0^+	-0.166	0.019		
			$1x10^5$	0.0001	3000	0.3	0.011	0.118	-0.011	C_L = -0.360*
					6000	0.6	0.363	0.092	0.028	
					15000	1.5	0.355	0.090	-0.115	
					30000	3.0	0.951	0.052	-0.082	
85x30 GRID					50000	5.0	0.530	-0.010	-0.016	C_D = 0.109*
					65000	6.5	-0.279	-0.004	-0.014	
					80000	8.0	-0.817	0.074	-0.073	
					100000	10.0	0.630	0.115	-0.139	
					125000	12.5	-0.662	0.023	-0.036	C_M = 0.076*
					140000	14.0	0.507	0.120	-0.141	
					150000	15.0	0.760	-0.009	-0.033	

* Mean Force Coefficients from Wind-Tunnel test of same Bridge Section Model.

Analytical Study on Flutter of Suspension Bridge

Hiroshi SATO[1], Ryuichi TORIUMI[2]

ABSTRACT

Flutter of a suspension bridge was numerically analyzed. In this study, multi-mode flutter analysis was used instead of conventional 2-mode (2-degree of freedom) flutter analysis. Unsteady wind forces acting on the deck were taken into account for the analysis. Conclusions are summarized as follows:

(1)By employing multiple modes into analysis, a complicated vibration shape can be expressed.

(2)Critical flutter wind speed can be controlled by a combination of 3 or more modes.

(3)The critical flutter wind speed depends on normal mode shape.

1. INTRODUCTION

When a suspension bridge is designed, aerodynamic stability of the bridge is of the first important item to be checked. Usually, wind tunnel test in use of spring mounted model is used to evaluate the aerodynamic stability of the bridge. Analytically, 2-degree of freedom flutter analysis is used. In these methods, the critical flutter wind speed is evaluated under following assumption:

- Critical flutter wind speed is controlled by combination of the 1st symmetric bending mode and 1st symmetric torsional mode.
- The mode shape of these two modes should be similar to each other.

However, result of full model wind tunnel test shows that the shape of vibration is not so simple. For example, the full model wind tunnel test result of the Akashi-kaikyo Bridge is shown in Fig.1(ref.1). It shows the shape of vertical vibration is not similar to that of 1st symmetric vertical bending mode. In such a case, the critical flutter wind speed can not be evaluated properly through conventional wind tunnel test , nor through 2-degree of freedom flutter analysis. The multi-mode flutter analysis can be applicable to evaluate such aerodynamic characteristics of a suspension bridge because rather complicated vibration shape can be expressed as a result of combination of multiple modes.

This paper outlines the method of multi-mode flutter analysis used in this study, and presents some results of analysis to discuss the effect of coupling of multiple modes.

2. OUTLINE OF MULTI-MODE FLUTTER ANALYSIS

2.1 BASIC EQUATION

The following aerodynamic forces are assumed.

(1) Unsteady aerodynamic lift and moment of deck due to vertical bending and torsional displacement of the deck.

(2) Quasi-steady aerodynamic drag force due to horizontal bending displacement of the deck.

---

1) Dr. of Eng., Head, Structure Division, Structure and Bridge Department, Public Works Research Institute, Ministry of Construction, Japan

2) Ms. of Eng., Senior Research Engineer, ditto

In this analysis, aerodynamic force acting on the cables were not taken into account. So, natural vibration modes where cables' amplitude dominate were eliminated intentionally. Otherwise, very low critical flutter wind speed was calculated because aerodynamic damping due to aerodynamic forces acting on cables were neglected.

Unsteady aerodynamic lift and moment, quasi-steady aerodynamic drag force are expressed as follows:

$$L = \pi \rho B^2 [L_{zR} \omega^2 u + L_{z1} \omega u'] + \pi \rho B^3 [L_{\theta R} \omega^2 \phi + L_{\theta 1} \omega \phi']$$
$$M = \pi \rho B^3 [M_{zR} \omega^2 u + M_{z1} \omega u'] + \pi \rho B^4 [M_{\theta R} \omega^2 \phi + M_{\theta 1} \omega \phi']$$
$$D = -\rho H C_D U v'$$

where L:Lift M:Moment D:Drag
ρ:Air density B:Deck width H:Deck depth
ω:Circular frequency C_D:Drag coefficient U:Wind speed
L_{zR}、L_{z1}、$L_{\theta R}$、$L_{\theta 1}$
M_{zR}、M_{z1}、$M_{\theta R}$、$M_{\theta 1}$:Unsteady aerodynamic force coefficients
' :Differentation with respect to time
u、v、ϕ:Displacement (Vertical, Horizontal, Torsional)

The aerodynamic force coefficients are function of reduced frequency k=fB/U (where f:frequency, U:wind speed) and angle of attack. For this analysis, these coefficients were derived from the Theodorsen functions.

Displacement vector of deck of suspension bridge consists of u,v,ϕ as vertical bending, horizontal bending and torsion of the deck. The displacement vector and the equation of motion are expressed as follows:

$$u = (u, v, \phi)^T$$
$$M u'' + C u' + K u = F$$

where M、C、K : Mass, Damping, and Stiffness matrix
F: Vector of aerodynamic forces (Lift, Moment, Drag)

The analysis method of multi-mode flutter analysis is based on the modal flutter analysis method. For flutter analysis, 3-dimensional model of deck was used. For flutter analysis model, cables and towers were not included.

2.2 PROCEDURE OF THE FLUTTER ANALYSIS

Fig.2 shows a flow chart of this analysis.

At first, the structural data, shapes of natural vibrational modes of the deck, unsteady aerodynamic force coefficients(in this case, Theodorsen function), and range of wind speed to be analyzed are inputted. If necessary, static torsional displacement of the girder due to wind force can be inputted and used so that aerodynamic forces corresponding to the angle of attack may be applied.

After calculation of reduced mass, wind speed is assumed, and static torsional displacement due to the assumed wind is calculated.

Next, circular frequency is assumed. By calculating all the unsteady aerodynamic forces acting on the deck under the assumed circular frequency, all the coefficient of the equation of motion are given. The equation is solved as a complex eigenvalue analysis and results complex frequency and complex normal mode. The real part of the complex frequency gives the circular frequency. If the calculated circular frequency is not equal to or near the assumed one, the assumed circular frequency is changed to the calculated one, and we go back to the step of calculation of aerodynamic forces (loop A). If the calculated circular frequency is equal or near the assumed one, the imaginary part of the complex frequency gives the damping

of the structure under assumed wind speed.

The assumed wind speed is increased step by step (loop B). The lowest wind speed of negative damping gives the critical flutter wind speed.

3. RESULTS OF MULTI-DEGREE OF FREEDOM ANALYSIS

3.1 OUTLINE OF SUSPENSION BRIDGE MODEL

In this study, a single-span suspension bridge with box-girder whose span length is about 1,000m was used as a analysis model (Fig.3). The deck is divided into 85 elements longitudinally. Table.1 and Fig.4 show the structural properties and dynamic characteristics of the model.

3.2 CASES TO BE ANALYZED

Table.2 shows the cases to be analyzed. In the Case 1, 18 modes out of the lowest 25 modes were used. The 7 modes where cables' amplitude dominated were eliminated. In the case 2, only 2 modes were used i.e. 1st symmetric vertical bending mode and 1st symmetric torsional mode. The case 2 is equivalent to conventional flutter analysis with 2-degree of freedom. In the case 3, 2nd symmetric torsional mode were added to the case 2. From case 4 to case 6, some of the mode shapes are changed into sinusoidal shape in order to discuss the effect of mode shapes. From the case 7 to case 9, the frequency of 2nd symmetric torsional mode is changed into 0.25 Hz from 0.21Hz in order to discuss the effect of natural frequency. Fig.4 shows the shapes of natural modes and sinusoidal shapes used in this study.

Table.2 also shows the critical flutter wind speed calculated.

3.3 EFFECT OF CHOICE OF MODES

Fig.5 shows the result of case 1,2, and 3. The critical flutter wind speed of Case 2 , 104.5 m/s is much higher than that of case 1 , 85.2 m/s. The critical flutter wind speed of Case 3, 84.8 m/s is very close to that of case 1. These results indicate that the critical flutter wind speed of this bridge is controlled by the combination of 3 mode, i.e. 1st symmetric torsional mode, 1st and 2nd symmetric vertical bending modes. The flutter vibration shape of casé 1 (Fig.6) also suggests that the 2nd symmetric vertical bending mode dominates together with the 1st symmetric torsional and vertical bending modes. From the flutter vibrational shape shown in Fig.6, it seems that the multi-mode flutter analysis can represent a complicated vibration shape.

3.4 EFFECT OF MODAL SHAPE

Fig.7 shows the result of case 2,3,4,5 and 6. The critical flutter wind speed of case 4, 89.0 m/s is lower than that of case 2. This means the coupling effect of the 1st torsional mode and sinusoidal shaped 1st symmetric vertical bending mode is stronger than that of the 1st torsional mode and 1st symmetric vertical bending mode (original shape). The critical flutter wind speed in case 5, 81.8 m/s, which is lower than that of case 3, indicates that the coupling effect of the 3-modes in case 5 is stronger than in case 3. On the contrary, the critical wind speed of case 6, 89.0 m/s is higher than that of case 3, 84.8 m/s and near that of case 4, 89.0 m/s. This means that the 2nd symmetric vertical bending mode is not effective when the shape of the 1st and 2nd symmetric vertical bending modes are changed into sinusoidal shape.

From these results, it seems that the shape of natural modes are strongly affect the critical flutter wind speed, and affect the combination of modes which control the flutter vibration.

3.5 EFFECT OF NATURAL FREQUENCY

In case 7,8,9, the natural frequencies of the 2nd symmetric vertical bending mode were changed from 0.21 Hz to 0.25 Hz, almost middle of those of 1st symmetric torsional mode and 1st symmetric vertical bending mode. Fig.8 shows the results of case 7,8 and 9.

The differences in critical flutter wind speeds between case 7,(82.4 m/s) and case 3,(84.8 m/s), case 8,(82.0 m/s) and case 5(81.8 m/s) and case 9,(89.0 m/s) and case 6,(89.0 m/s) are small respectively. The modal shapes in the couple of cases compared above are the same.

From these results, it seems that the effect of the natural frequency of 2nd symmetric vertical bending mode on the critical flutter wind speed is not so strong in this case.

4. CONCLUSION

Flutter characteristics of a suspension bridge was evaluated through multi-mode flutter analysis. Through this analysis, the coupling effect of multiple modes, effect of modal shapes, and effect of natural frequency on the critical flutter wind speed were studied. The conclusion obtained are as follows:

(1) Multi-mode flutter analysis can express the complicated vibrational shape as a result of combination of multiple modes.

(2) As far as the suspension bridge analyzed in this study is concerned, the critical flutter wind speed and flutter vibration shape are controlled by coupling of 3 natural modes i.e. 1st symmetric torsional mode, and 1st and 2nd symmetric vertical bending modes.

(3) As far as the suspension bridge analyzed in this study is concerned, the critical flutter wind speed depends on the shape of natural modes.

5. ACKNOWLEDGEMENTS

The development of flutter analysis method reported in this paper was financially supported in part by the Honshu-Shikoku Bridge Authority.

REFERENCES

1) Yokoyama K., Kanazaki T. and Yasuda M.,:Flutter Characteristics of Super Long-Span Suspension Bridge, Proc. of the 24th Joint Panel Meeting on Wind and Seismic Effects, UJNR, 1992

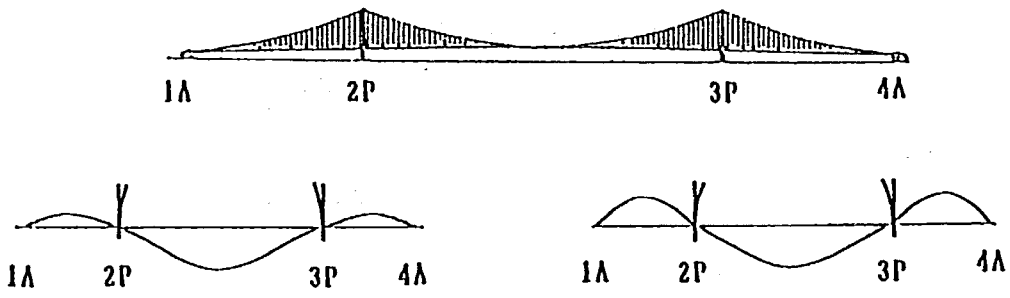
Table 1 Properties of the Model

Span Length	1,030 m
Type of Deck	BOX
Weight of Deck	17.49 ton/m
Width of Deck	32.3 m
Depth of Deck	4.3 m
Natural Frequencies	
Horizontal Bending 1st symmetric	0.068 Hz
Vertical Bending 1st symmetric	0.158 Hz
2nd symmetric	0.211 Hz
Torsional 1st symmetric	0.366 Hz

Table 2 Cases to be Analyzed

	Combination of modes used in analysis			Critical Flutter Wind Speed (m/s)
	Torsional	Vertical Bending		
	1st symmetric	1st symmetric	2nd symmetric	
Case 1	18 modes including above mentioned 3 modes			85.2
Case 2	○	○	–	104.5
Case 3	○	○	○	84.8
Case 4	○	Sine	–	89.0
Case 5	○	Sine	○	81.8
Case 6	○	Sine	Sine	89.0
Case 7	○	○	○ (0.25 Hz)	82.4
Case 8	○	Sine	○ (0.25 Hz)	82.0
Case 9	○	Sine	Sine (0.25 Hz)	89.0

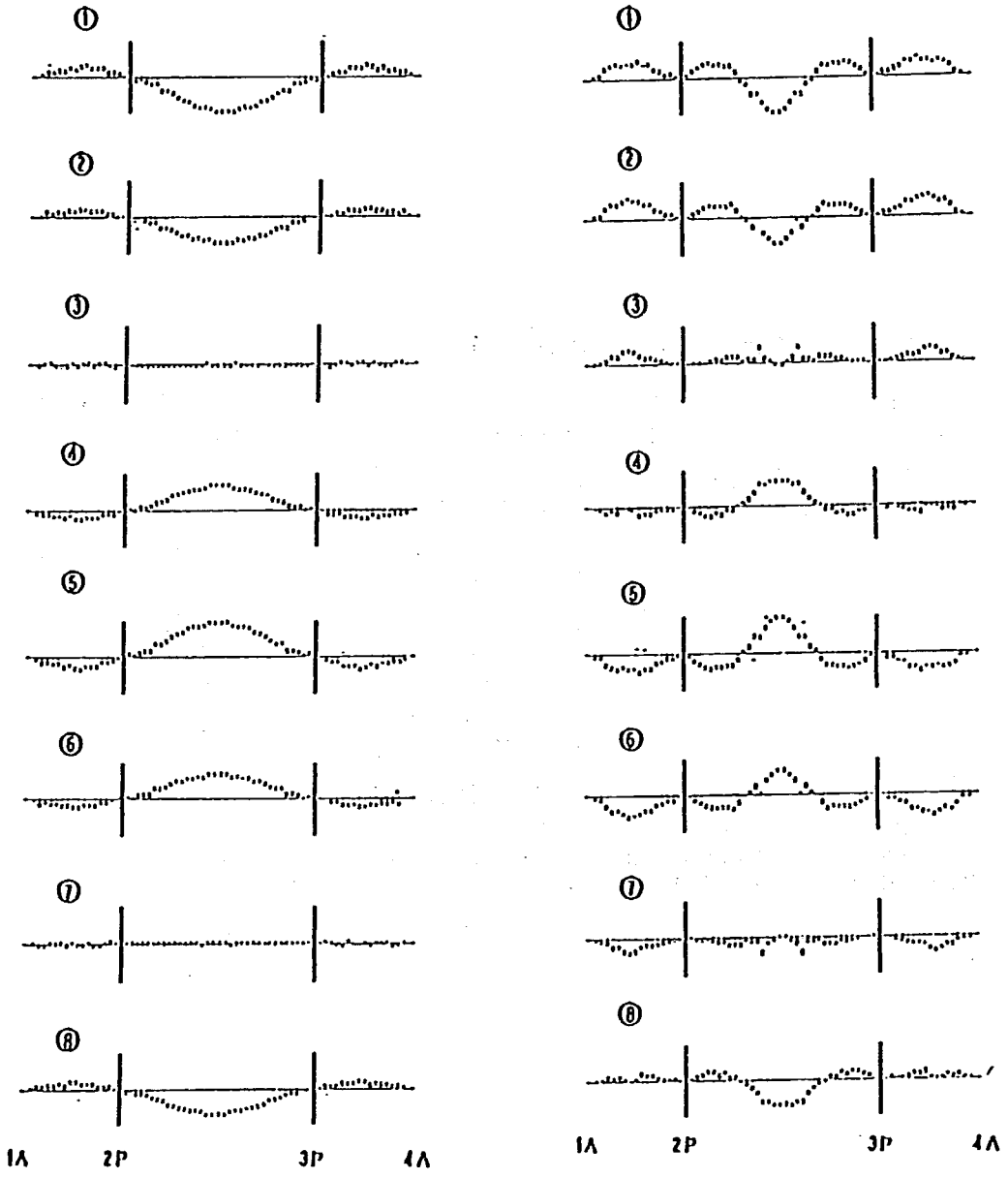
Note ○ : used – : not used
Sine : changed the shape into sinusoidal shape
(0.25 Hz): changed the frequency into 0.25 Hz

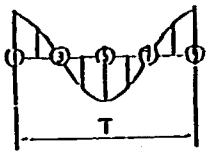


(a) 1st symm. torsion

(b) 1st symm. bending

(1) Mode shapes in windless condition(calculated)





one cycle

(a) torsion

(b) vertical bending

(2) Response during flutter(measured)

Fig. 1 Response of deck in one cycle during flutter[1]

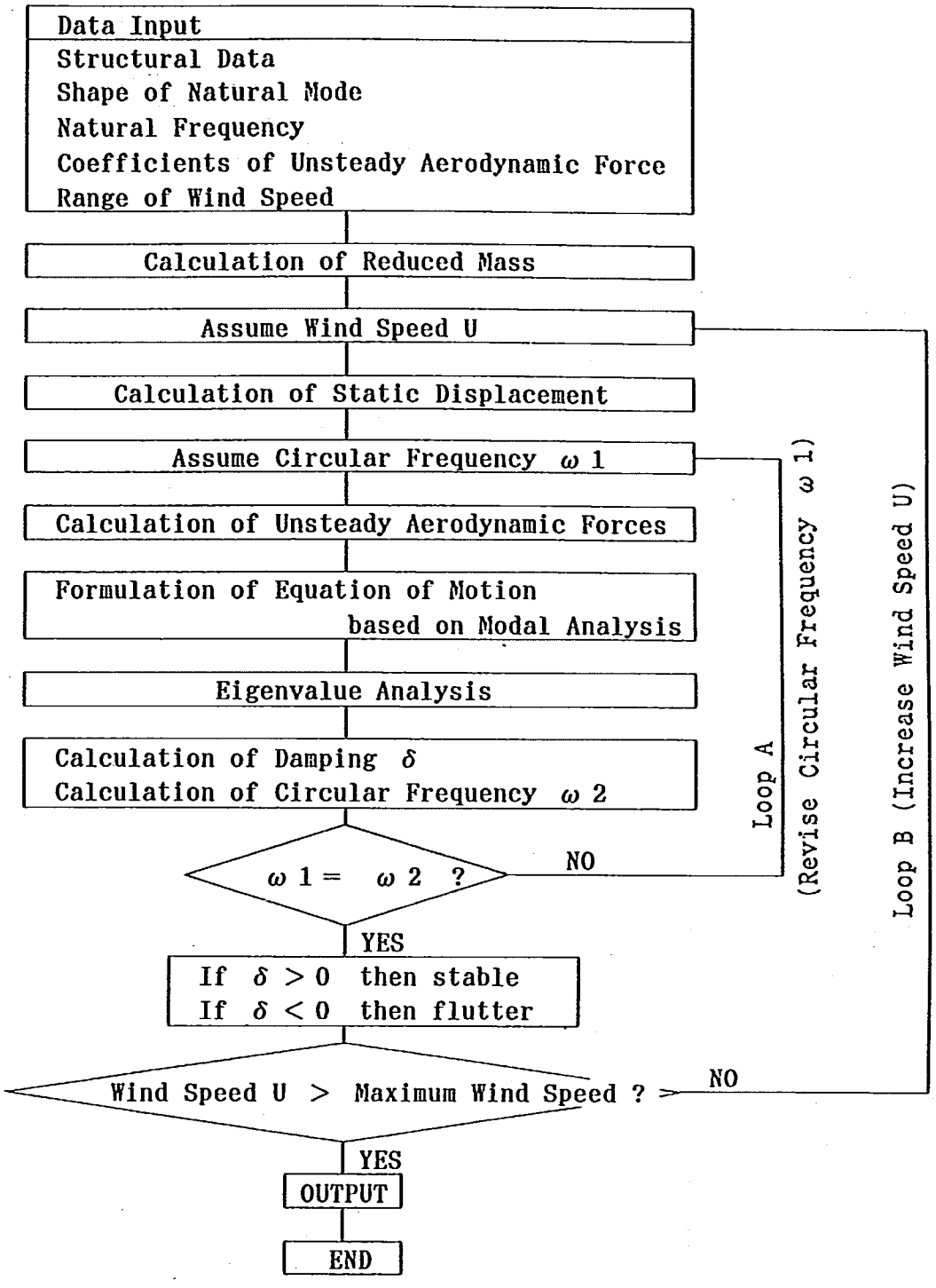


Fig.2 Procedure of Flutter Analysis

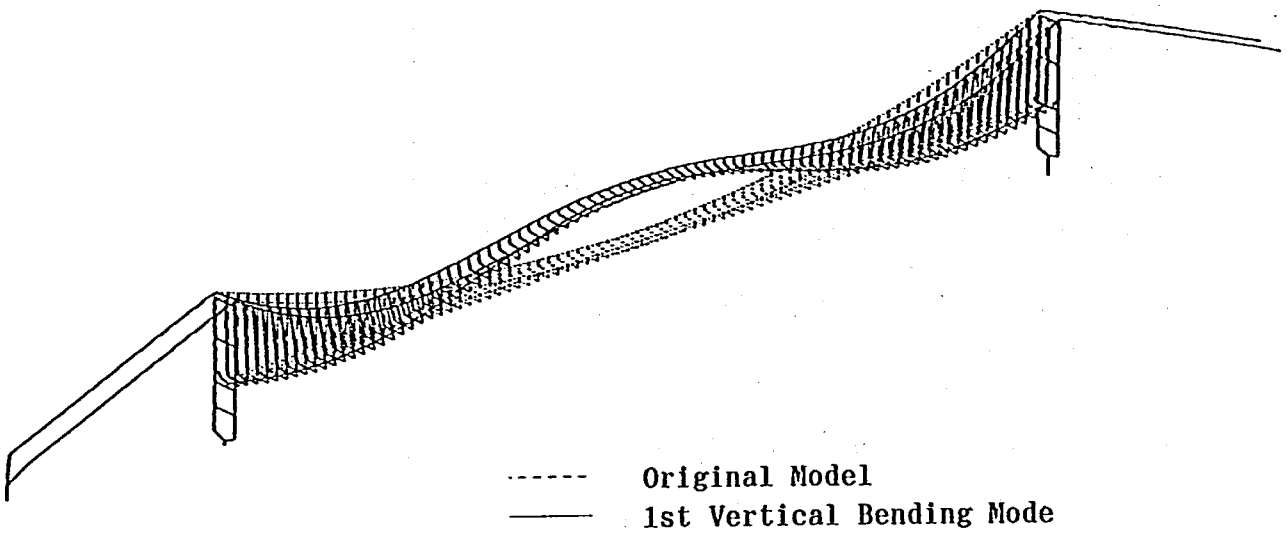


Fig. 3 Suspension Bridge Model

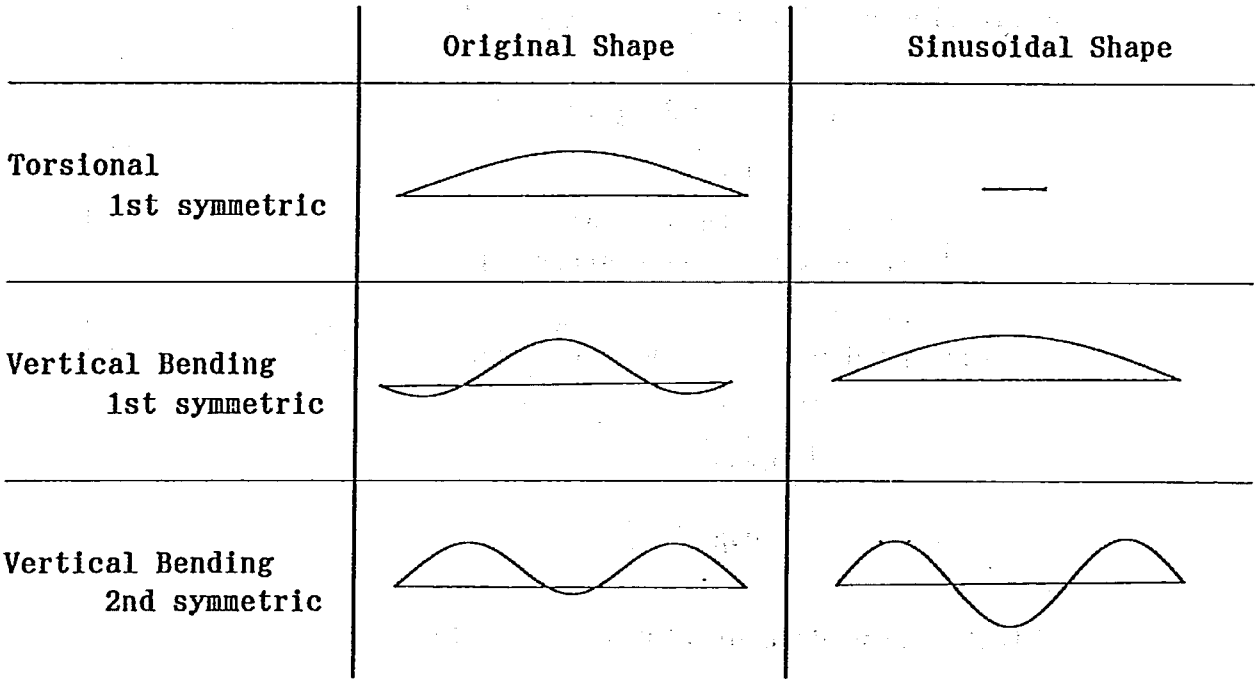


Fig. 4 Shape of Natural Modes

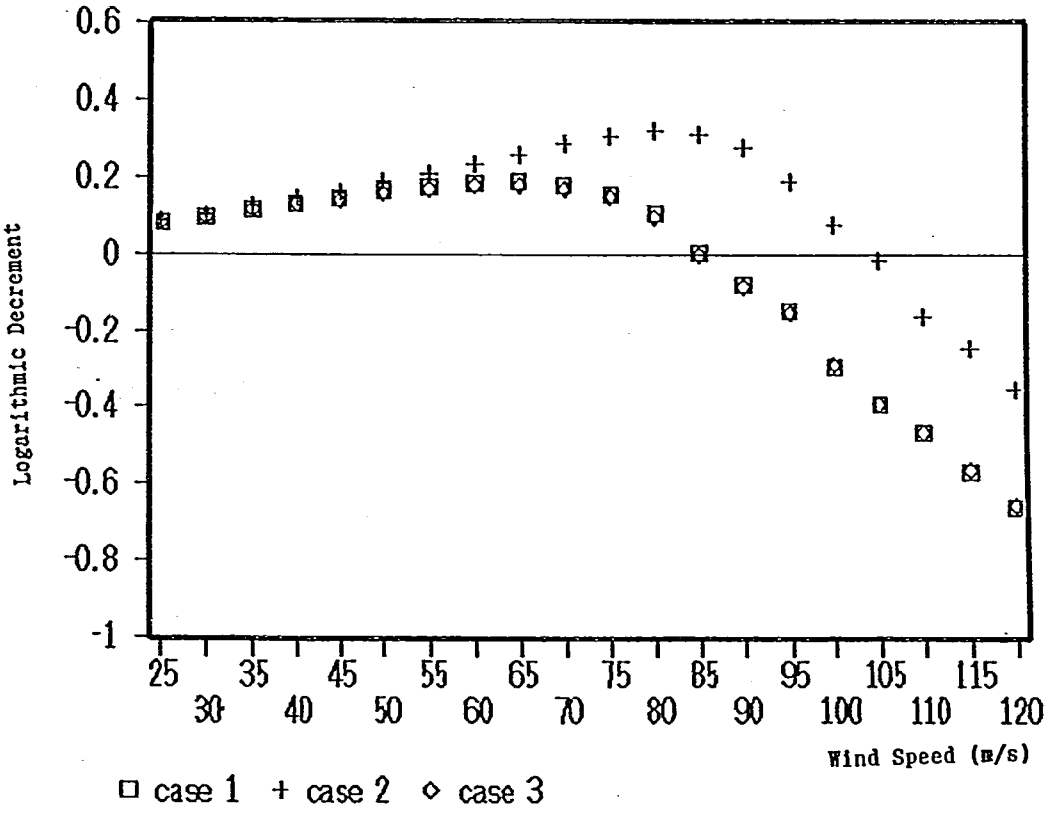


Fig. 5 Wind Speed - Logarithmic Decrement (case 1,2,3)

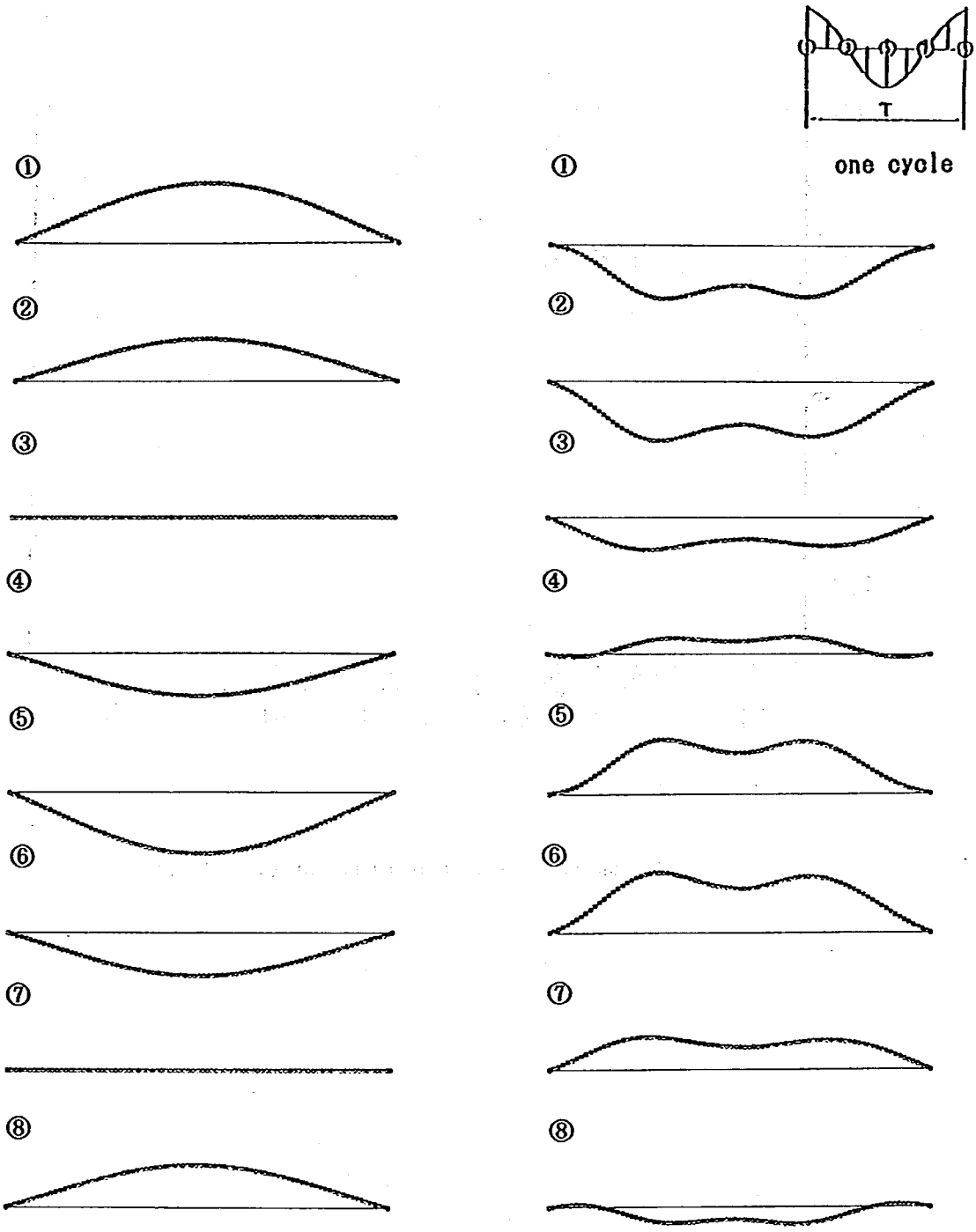


Fig. 6 Vibrational Shape during Flutter (case 1)

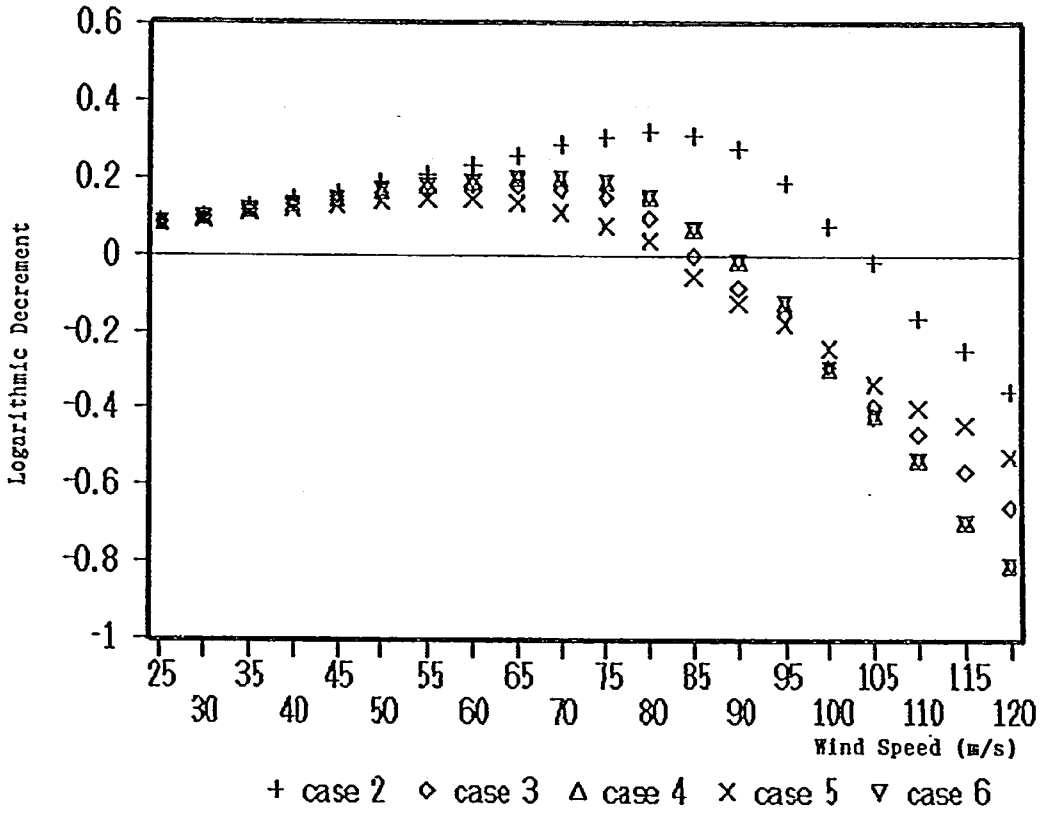


Fig. 7 Wind Speed - Logarithmic Decrement (case 2,3,4,5,6)

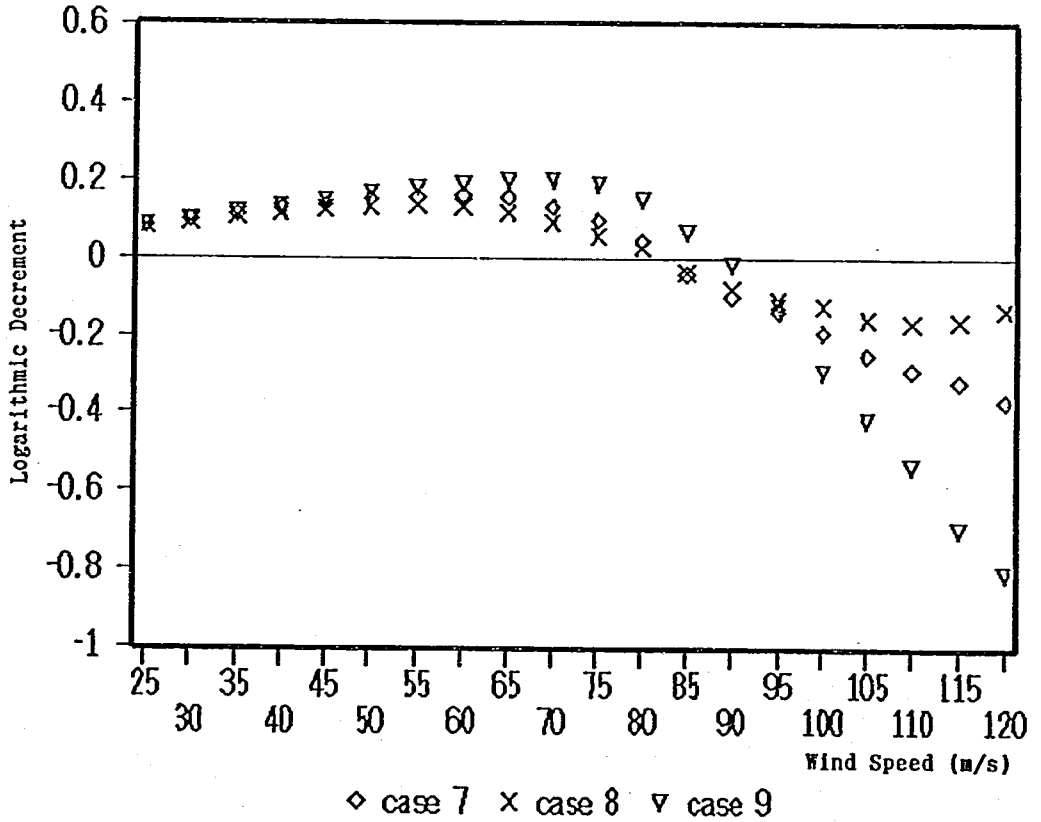


Fig. 8 Wind Speed - Logarithmic Decrement (case 7,8,9)

(5) Session 5

Wind Resistant Design (2)

9) Aerodynamic Stability of Central Nagoya Port Bridge
(K. Nomura*, Y. Suzuki, K. Kuroda and Y. Igase)

10) Aerodynamic Stability of Nakajima Bridge (Provisional Name)
(M. Kamei*, M. Kawakami, K. Ikushima, H. Tanaka and M. Hosomi)

11) Aerodynamic Stability of Trans-Tokyo-Bay Highway Bridge
(Y. Shioi, Y. Yoshida and K. Saga*)

Aerodynamic Stability of Central Nagoya Port Bridge

Kenji Nomura
Engineer, Structural Engineering Section,
JH Nagoya Construction Bureau, JAPAN.

Kenji Kuroda
Engineer, Structural Engineering Section,
JH Nagoya Construction Bureau, JAPAN.

Yuji Suzuki
Chief, Meiko-Central Bridge Project Team,
JH Ise-Bay Highway Construction Office, JAPAN.

Yoshinori Igase
Engineer, Meiko-Central Bridge Project Team,
JH Ise-Bay Highway Construction Office, JAPAN.

Abstract

In Nagoya, Japan, three long-spanned cable-stayed bridges are taking shape. They are named, respectively, West Bridge, Central Bridge, and East Bridge, or collectively Nagoya Port Bridges. The latter two are in the process of construction of their substructures where as West Bridge, or more exactly Second West Bridge to be paired off with First West Bridge completed in 1984 and now in use, is going to be built standing side by side with the senior. All of these bridges are scheduled for completion in 1997.

As for Central Bridge, which is the largest of the three in span length, its aerodynamic stability was carefully evaluated at the design stage through a series of wind tunnel test using the scale models of its girder, tower, and entire bridge structure. This paper reviews specifically the experimental studies made of Central Bridge for the evaluation of its aerodynamic stability.

1. INTRODUCTION

Nagoya is one of the prominent cities in Japan. JH (Japan Highway Public Corporation) is currently engaged in the construction of Nagoya Port Bridges there. They consist of three cable-stayed bridges, named West Bridge, Central Bridge and East Bridge, as shown in Figure 1.

First West Bridge, already in place built back in 1984, is a cable-stayed bridge measuring 405 m in center-span length. In the evaluation of its aerodynamic stability at the design stage, scale-model testing of the girder and tower was carried out in laboratory wind tunnel. In the scale-model testing, the girder was fitted with a parapet equipped with a vortex generator and also the tower of open-top construction was employed as showed in Figure 2. In the process of construction at the site, the bridge stay cables were found to vibrate from the effects of wind accompanied by rain, which phenomena was called as "Rain-Wind Induced Vibration". This stay cable vibration

problem is resolved now by tying with wire the stay cables different in length and hence in mode of vibration.

Second West Bridge, included in the Nagoya Port Bridges construction project now under way and planned to stand side by side with First West Bridge, is to be paired off with the latter bridge and together called simply West Bridge. These two bridges are very similar to each other in their shape.

In designing Central Bridge and East Bridge, the bridge girder was increased in width to accommodate the increase in traffic as well as to provide a space for installing the cable-vibration damper. And as for the tower, the shape is different in these bridges depending on the span length. Then a series of wind tunnel test was to be conducted as described in the following chapters [1].

2. AERODYNAMIC CHARACTERISTICS OF GIRDER

The girder of Central Bridge and East Bridge was planned to have the same shape. To determine the girder design required, the wind tunnel test with a two-dimensional model representing the girder cross section was performed mainly in the uniform air flow. After a series of wind tunnel testing, the girder was designed to have the cross section of the type shown in Figure 3, with due reference to the design employed for Ikuchi Bridge, which had been constructed by Honshu-Shikoku Bridge Authority. Then at the last stage of wind tunnel testing, it was found that a small rail track for the maintenance car would effectively restrain the girder resonance with vortex excitation. This chapter reviews the effect of this small rail track.

2.1. Model for wind tunnel test

The sectional model shown in Figure 4 was employed in the wind tunnel testing was 1/35 in scale, measuring 2.7 m in cross-sectional span. The model was fitted with a side plate at either end and supported by eight coil springs from the wind-tunnel wall outside the path of air flow. Vibration parameters were adjusted as shown in Table 1. The ratio between the torsional frequency and heaving frequency was exclude from simulating conditions employed, because the ratio between the two frequencies with the actual bridge was so large that coupled vibration of these modes was assumed not to occur.

Since it was considered that with the girder cross section of streamlined profile, provision for a small vortex generator on the girder bottom surface would effectively restrain the girder resonance with vortex excitation, the rail track for maintenance car was installed at the bottom of the girder.

2.2. Effect of rail track fitted at the bottom of the girder

Table 2 shows for comparison the response of the girder cross section of basic design and that of the girder modified for restraining the vibration. The cross section of basic design remains free of flutter but resonates with vortex excitation depending on the angle of attack. More specifically, heaving mode of resonance with vortex excitation occurs when the wind blows upward at 0° to 7° in angle of

attack and at the speed of about 7 m/s. Also, torsional mode of resonance with vortex excitation takes place at the wind speeds of about 10 m/s and 25 m/s, with its amplitude reaching 0.2 degrees when the angle of attack is less than 7 degrees upward.

With the maintenance car rail track on the girder bottom surface, however, the resonances with vortex excitation are almost restrained.

3. AERODYNAMIC CHARACTERISTICS OF TOWER

The tower of Central Bridge, measuring about 190 m in height, is of construction flexible in the direction perpendicular to the bridge axis not only in the construction process but in the completed state as well. In the direction of the bridge axis, however, the tower becomes rigid once the stay cable are connected to the bridge girder. Accordingly, the wind tunnel test was performed to determine the tower aerodynamic stability under exposure to wind blowing the direction of the bridge axis in the completed state [2].

3.1. Model for wind tunnel testing

The model employed to represent the bridge tower was 1/100 in scale and of aeroelastic construction as shown in Figure 5. To simulate the modes of vibration of the completed tower, add-on spring was attached to the top of the tower. The logarithmic decrement of the model was adjusted to 0.02.

3.2. Test results

The test results obtained are shown in Table 3. The originally designed tower, which had a rectangular cross section in its column, experienced the galloping vibration when subjected to the wind blowing in the direction of bridge axis at the speed of about 35 m/s.

However, the tower with its column modified to have an octagonal cross section restrained the galloping vibration, and the vortex-induced oscillation was also not observed. Then this type was decided to be adopted for Central Bridge.

3.3. Tower of East Bridge

In East Bridge, its tower is about two thirds the size of that of Central Bridge. The galloping oscillation was also found to occur in this tower, and it was restrained by changing the tower lateral beam position showed as Table 4 [3].

4. AERODYNAMIC CHARACTERISTICS OF CENTRAL BRIDGE IN CONSTRUCTION STAGE

The construction of Central Bridge consists of suspending the bridge girder with cables from the tower on either side and extending the girder length progressively without midway supports and with care for the balancing. At the final stage, the suspended girder length reaches near 300 m on either side of the tower. The entire bridge structure becomes flexible and the natural frequency of the 1st heaving

mode decreases to about 0.1 Hz in this state.

4.1. Model for wind tunnel testing

A 1/120 scale aeroelastic model of the entire bridge structure shown in Figure 6 was used in the wind tunnel test. This model was made up of wooden blocks simulating the bridge-girder structure and a length of metallic rigid bar simulating the girder axial rigidity. Two each of cables used for the actual bridge were bound into one for model application for simulating the cable extensional rigidity and, besides, the cables were covered with the silicon tube for simulating the drag cause on the cable. At the base of the tower, a truss-stiffened support, with attention in greatest possible detail to the model design.

The model vibration characteristics were found to satisfy the Froude Number similarity as well, as shown in Table 5, with the girder deformation being subject to the gravity.

4.2. Turbulence in the wind tunnel

The topography surrounding the Central Bridge construction site is relatively free of undulations. In the wind tunnel test, therefore, two types of air turbulence were generated, one of which was the boundary-layer turbulence produced by means of spires and roughness blocks which were installed up-stream of the model and the other was the active turbulence produced by oscillating into irregular pitching motion the rows of airfoils at the wind tunnel air nozzle [4].

The turbulence characteristics of these two kind of turbulent flow is showed in Table 6. Though these turbulence were almost the same in intensity, the boundary-layer turbulence was slightly smaller in scale than the active turbulence. Figure 7 shows the distribution in height of air speed and intensity of turbulence of the boundary-layer turbulence. The power exponent of the air-speed distribution was adjusted to 1/6 of what actually would be, with due reference to the wind speed measured at the construction site.

The most significant difference between the abovementioned two types of turbulence is in the span-wise correlation of the vertical component of turbulence as shown in Figure 8. The span-wise correlation of the vertical component of boundary-layer turbulence greatly varies with the distance, and when the distance is in excess of 0.5 m in the wind tunnel the region indicating the negative correlation is created.

With the active turbulence, on the other hand, the span-wise correlation of the vertical component can be controlled. That is, oscillating all the rows of airfoils into pitching motion at the same time relative to the entire span of the bridge model produces a high level of correlation whereas oscillating the rows of airfoils independently relative to five spans of the bridge model results in a low level of correlation.

4.3. Response in uniform air flow

As shown in Figure 9, the response in uniform air flow indicates vertical 3rd and 4th modes of resonance with vortex excitation. Any

destructive phenomena characterized by divergence or flutter was not observed.

If the resonance had been the result of exciting force acting on the girder, the 1st and 2nd modes of vortex-excited resonance also should have taken place. According to the estimation of the wind speed of resonance, the 1st mode may occur at the wind speed lower than the minimum value which can be examined in this wind tunnel testing. However, the 2nd mode, whose wind speed of resonance should be high enough to be observed, could not be found. To explore the mechanism of such a resonant vibration, the wooden blocks fitted to the tower were taken away. Then, the vortex-excited resonance did not occur any longer, and it was decided that the cause of the vibration had been the exciting force acting on the tower.

4.4. Response in turbulent flow

Table 7 shows the response that took place in boundary-layer turbulent flow when the horizontal angle of air flow β was changed. The change in horizontal angle of air flow did not cause appreciable change in the amplitude of buffeting that is claimed to occur by Reference [5]. Table 8 shows the response that took place in active-turbulent flow. The span-wise correlation of the vertical component of turbulence was varied to find out its effect on the buffeting response.

The vertical 1st mode of buffeting response in which the girder extensions on both sides of the tower vibrate in the opposite direction was found to decrease with the increase in coefficient of span-wise correlation of the vertical component of turbulence. However, the vertical 2nd mode of buffeting response in which the girder extensions on both sides of the tower vibrate in the same direction was found to increase with the increase in coefficient of correlation.

It was found, in other words, that the amplitude of buffeting response varies with the coefficient of span-wise correlation of the vertical component of turbulence and that the effect of the correlation coefficient also varies especially with the modal shape such as in-phase or out-of-phase mode.

As stated in the foregoing, it was found that the buffeting response would be sensitive to the change in coefficient of span-wise correlation of the vertical component of turbulence. The most important consideration concerns just what natural wind spatial distribution characteristics are like.

In this case, since the topography surrounding the construction site is relatively free of undulations, the bridge buffeting response was calculated employing the Karman's coherence function and taking into account the three-dimensional effect of the admittance function on the girder. The calculated response is shown in Figure 10 together with the results obtained through the wind tunnel testing for comparison.

5. CONCLUSION

1. Through the wind tunnel testing performed to ensure the girder

aerodynamic stability, it was confirmed that appropriately streamlining the girder basic cross-section profile and fitting a small member of rail track to the girder bottom would produce the girder capable of offering a fairly high level of aerodynamic stability.

2. As for the tower aerodynamic stability, it was confirmed that employing the tower column with octagonal cross section would prevent the galloping vibration that could otherwise take place even after the completion of the bridge.

3. The wind tunnel testing with a scale model of the bridge in construction process with the girder extensions on both sides of the tower confirmed that though destructive vibration characterized by divergence or flutter would not occur, the tower could cause the vortex-excited vibration of the whole bridge in smooth flow.

In turbulent flow, the buffeting-vibration amplitude was found to be highly susceptible to the spatial correlation of the vertical component of turbulence, and the wind tunnel testing showed that the vibration amplitude would greatly vary with the boundary-layer turbulence or active turbulence generated in the wind tunnel.

It is also planned that the bridge construction by progressive girder extension be carried out avoiding the typhoon season and that architectural precautions be taken to readily cope with unexpected accidents.

In particular, among others, is deemed as an important consideration for the construction of large cable-stayed bridges now on the drawing board in Japan. In cases where the projected construction site topography features rugged undulations, very careful study in warranted as regards the effect of spatial correlation characteristics of wind on the bridge.

6. ACKNOWLEDGMENT

The authors wish to make a grateful acknowledgment for invaluable advice rendered by Prof. M. Ito of Saitama University and his committee members as well as for highly instructive data given them by Honshu-Shikoku Bridge Authority people.

7. REFERENCES

1 Y. Momiyama et al., Bluff Body Aerodynamics and Applications 2, 1992.
2 M. Yokoyama et al., Proc. of the 46th Annual Conf. of JSCE, I-246, 1991.
3 A. Baba et al., Proc. of the 46th Annual Conf. of JSCE, I-243, 1991.
4 H. Sakata et al., Mitsubishi Heavy Industries, Ltd., Technical Review, Vol. 25, No.1(1988).
5 H. Tanaka et al., Canada-Japan Workshop on Bridge Aerodynamics, Ottawa, 1989.

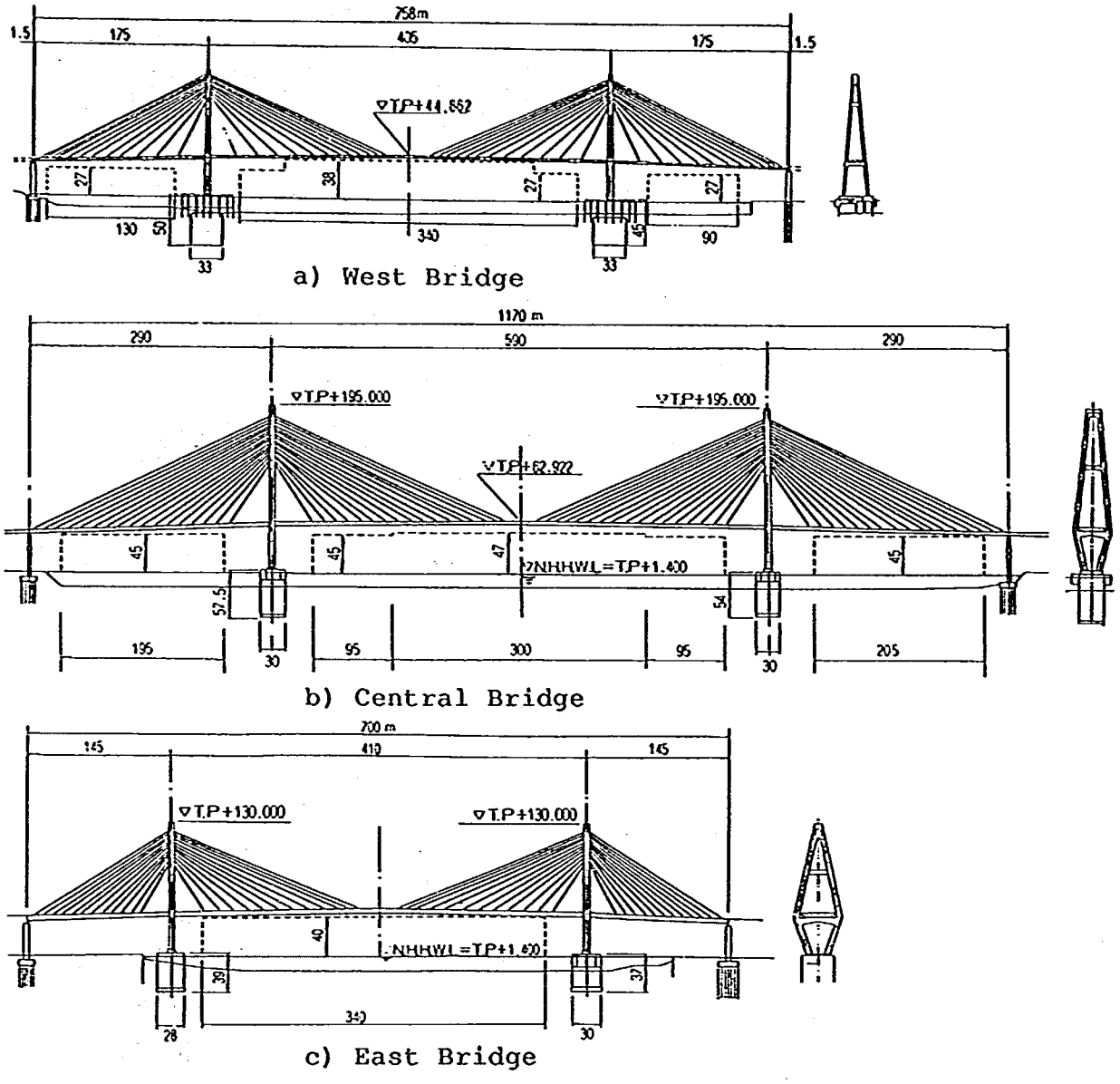


Figure 1. General arrangement of Nagoya Port Bridges.

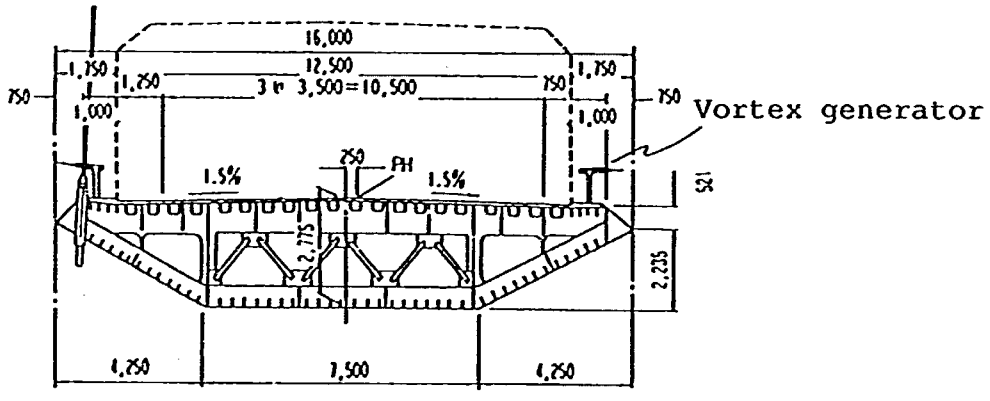


Figure 2. The cross section of girder of First West Bridge

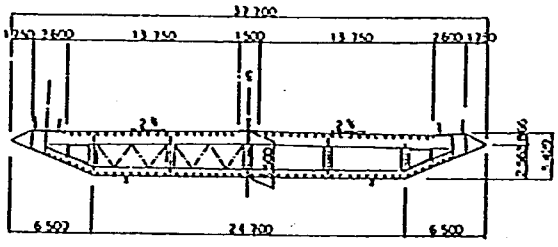


Figure 3. Cross section of girder.

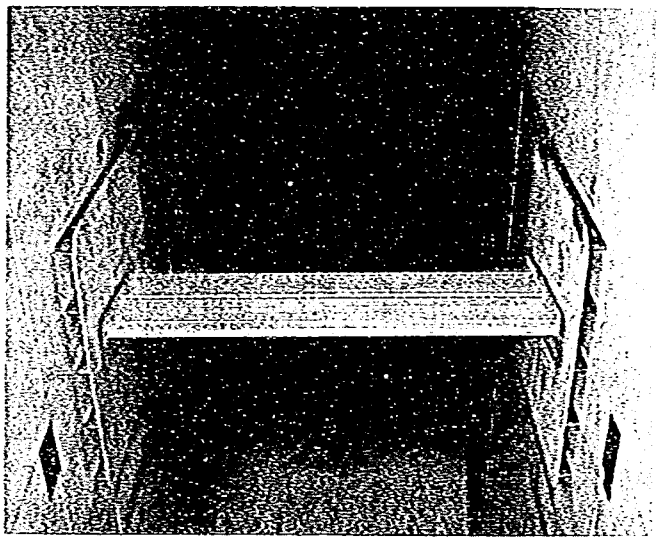
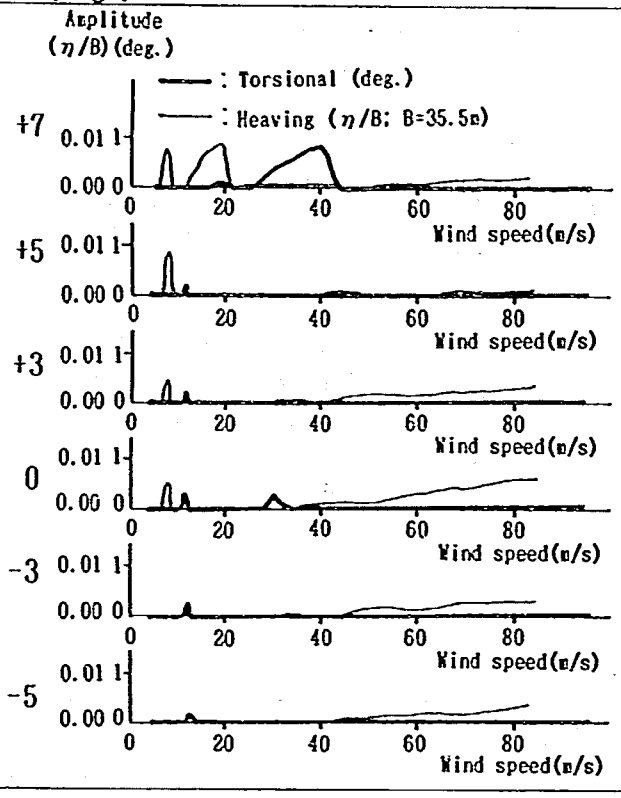
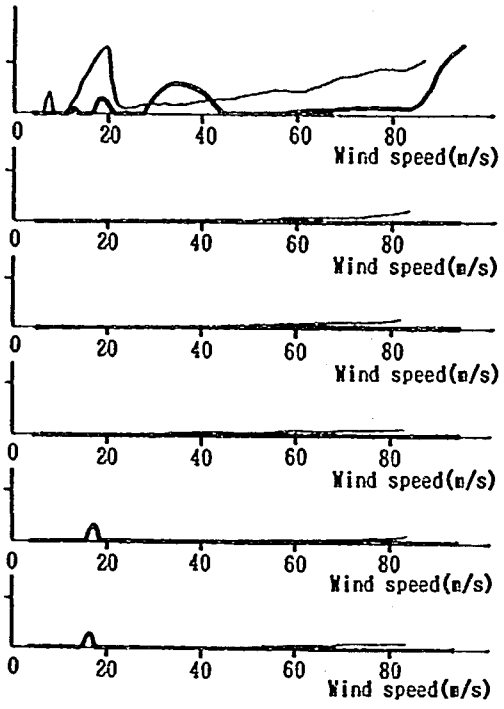


Figure 4. Sectional model of girder.

Table 1
Test conditions of 2D sectional model of girder

Item		Prototype	Model	
		Bridge	Required	Measured
Weight		271.7 kN/m	598.8 N/model	598.9 N/model
Ineteria Moment		27.62 MN·m	49.69 N·m^2/model	49.69 N·m^2/model
Natural Frequency	Heaving	0.177 Hz	———	1.920 Hz
	Torsional	0.668 Hz	———	5.134 Hz
Logarithmic Decrement	Heaving	unknown	0.02	0.02
	Torsional	unknown	0.02	0.02

Table 2
Response of girder sectional model

Angle of attack(deg.)	Basic design	With maintenance car rail track
+7		
+5		
+3		
0		
-3		
-5		

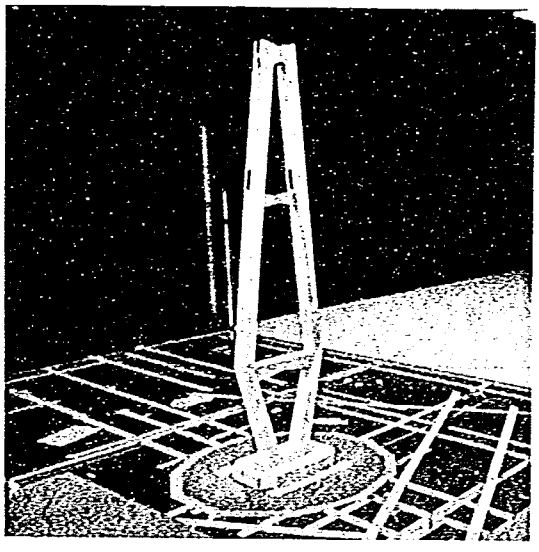


Figure 5. Aeroelastic model for tower.

Table 3
Response of the tower in uniform flow

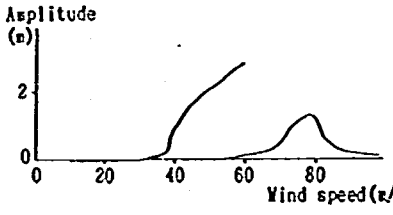
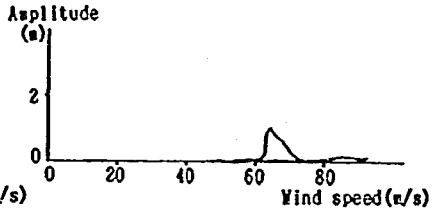
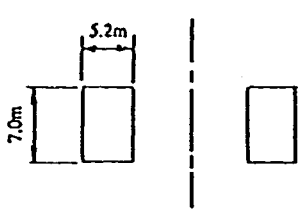
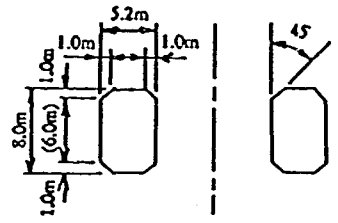
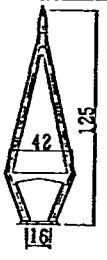
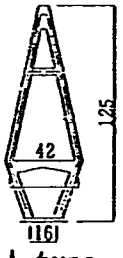
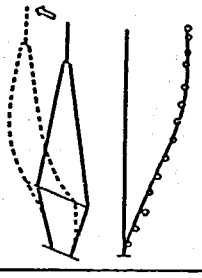
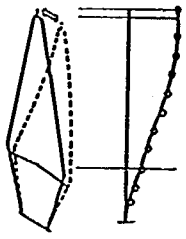
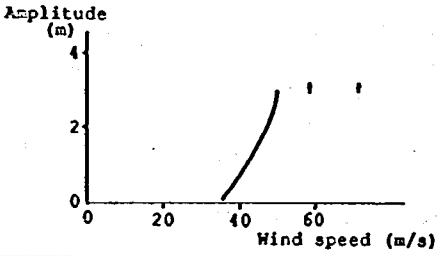
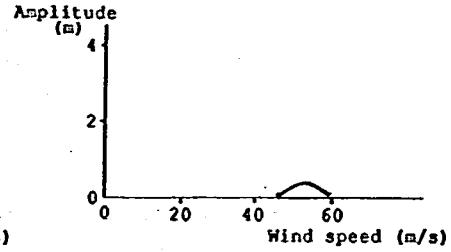
Mode of vibration	Response of the tower	
	Original	Modified
—— : Perpenudicular to the Bridge axis 		
—— : Along the bridge axis 		

Table 4
Response of the tower of East Bridge

Type	Original	Modified
Shape	 Upside down - Y type	 A type
Mode of vibration (free standing state)		
Response (Along the bridge axis)		

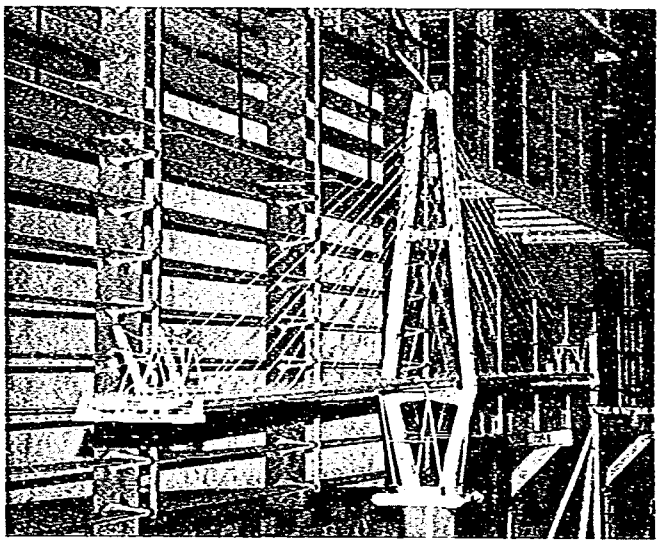


Figure 6. Aeroelastic model.

Table 5
Characteristics of vibration of model

Mode			Natural Frequency (Hz)		Logarithmic Decrement δ
			Prototype	Model measured (Required)	
Vertical	1st		0.0946	1.07 (1.04)	0.023
	2nd		0.4167	4.42 (4.56)	0.015
	3rd		0.4744	4.99 (5.20)	0.017
	4th		0.6465	6.75 (7.08)	0.017
Horizontal	1st		0.1280	1.35 (1.40)	0.016
	2nd		0.2321	2.44 (2.54)	0.010
Torsional	1st		0.5784	6.18 (6.34)	0.015

Table 6
Turbulence Characteristics

Turbulence	Turbulence Intensity (%)		Turbulent Scale (m)	
	Longitudinal	Vertical	Longitudinal	Vertical
Boundary Layer	14	7	130	20
Rotary airfoils	13	7	470	50

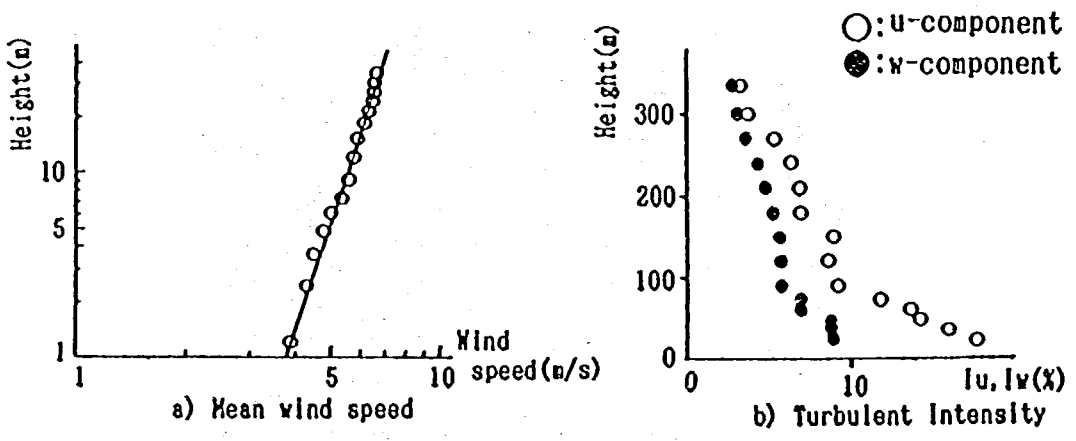


Figure 7. Profile of wind speed and turbulence intensity.

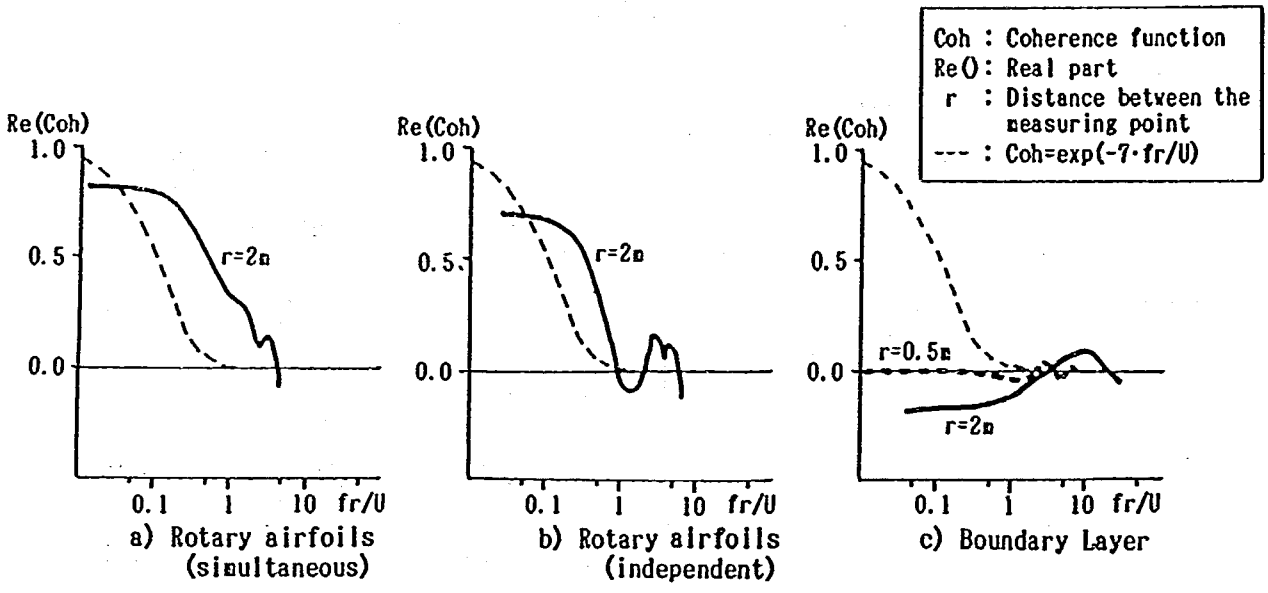


Figure 8. Spanwise correlation of vertical component of turbulence.

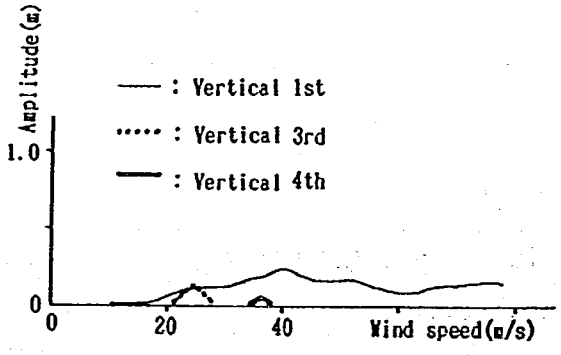


Figure 9. Response in uniform flow.

Table 7
Response in boundary layer turbulence

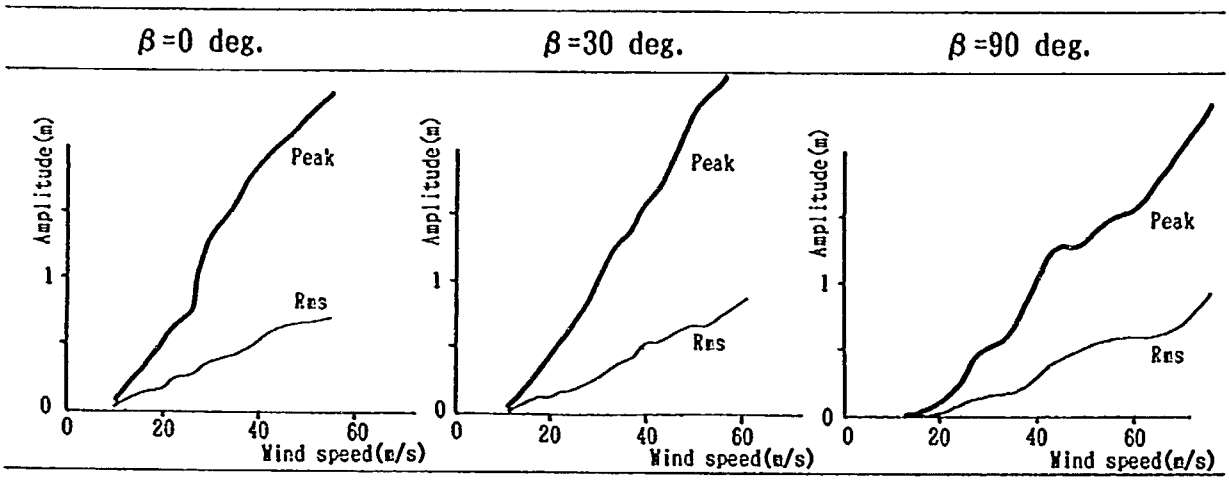
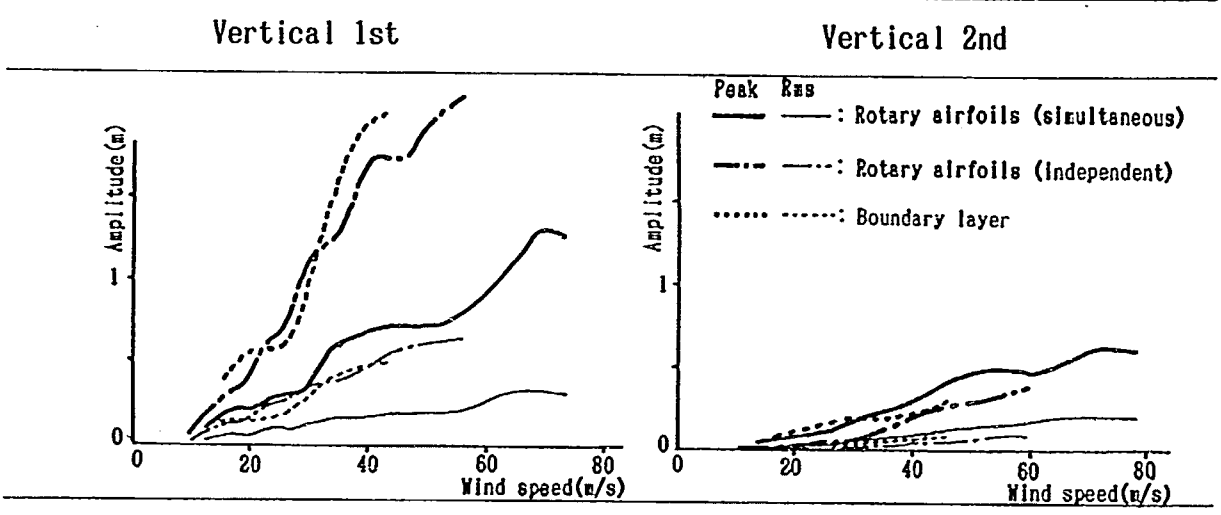


Table 8
Response in turbulence generated by rotating airfoils



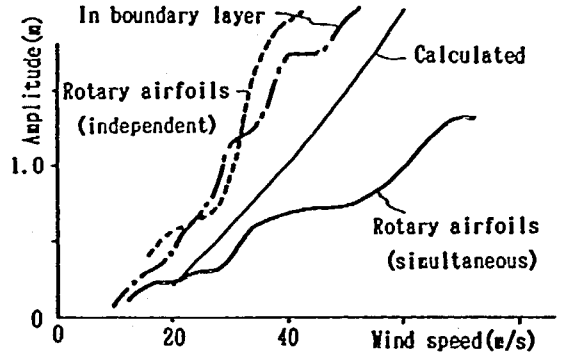


Figure 10. Buffeting response for design.

Aerodynamic Stability of Nakajima Bridge (Provisional Name)

M. KAMEI
Staff Officer, Public Works Bureau, Osaka City Government, Osaka 530, JAPAN

M. KAWAKAMI
Bridge Engineer, Public Works Bureau, Osaka City Government, Osaka 530, JAPAN

K. IKUSHIMA
Bridge Engineer, Public Works Bureau, Osaka City Government, Osaka 530, JAPAN

M. HOSOMI
Bridge Engineer, Bridge Technical Research Dept., Komai Tekko Inc., Osaka 555, JAPAN

H. TANAKA
Bridge Engineer, Bridge Design Dept., Hitachi Zosen Corp. Osaka 554, JAPAN

SUMMARY

An asymmetric girder cross section and an H type tower are employed for the construction of Nakajima bridge (provisional name). From the structural characteristic of the bridge and the condition of the bridge site, wind tunnel tests and natural wind observations were carried out to verify aerodynamic stability of the bridge. The paper describes an outline of the section & full bridge model tunnel tests and field observation of natural wind.

INTRODUCTION

Nakajima Bridge (provisional name) is planned to be built at the mouth of Nakajima River. Its bridge type is a three-span continuous (336.5m = 84.5m + 163m + 89m) cable-stayed bridge (Fig. 1). The characteristics of the bridge are as follows:

1) It may be expected that wind blows at the right angle to the longitudinal direction of the bridge.
2) As the deck is located at about 26m above sea level, there may be less wind turbulence, however the turbulence may become stronger by the surrounding condition of the site.
3) The condition of the bridge site restricts the cable arrangements at certain portion above the center span.
4) The configuration of the girder is asymmetric and the girder height changes in longitudinal direction of the bridge.
5) Bent erection cannot be applied for all spans due to river conditions, adoption of balancing construction method is planned as its alternative.

Considering above conditions, it was planned that aerodynamic stability of the bridge would be confirmed by the wind tunnel tests and natural wind observation should be carried out.

The paper describes an outline of the section & full bridge model wind tunnel tests and field observation of natural wind to verify aerodynamic stability of the bridge [1].

SECTION MODEL TESTS OF THE GIRDER

Section model tests were carried out using 1/40 scale girder models (Fig. 2). Type 1 is an original section with cable anchor brackets and Type 2 is its alternative with fairings. Type 3 is a section of the side span without cable anchor brackets.

Asymmetry of the girder section and discrepancy of the shear center and the gravity center (Fig. 3) may affect the aerodynamic stability. Therefore the aerodynamic responses were examined changing the following test conditions respectively.

1) Configuration of the model (e.g. Type 1, Type 2, Type 3)
2) Position of rotational center (e.g. Rotational center as shear center, gravity center, 1/2 point between shear and gravity center)
3) Direction of the flow (e.g. Upstream, Downstream)
4) Angle of attack (e.g. ±5, ±3, 0 degree)

Fig. 4 shows the typical test results of Type 1. The vortex-induced oscillation of bending mode appeared at about 15m/s and that of torsional mode appeared at about 40m/s. Flutter occurs at the high wind speed of about 90m/s. Following results were obtained from the tests.

1) The larger oscillations appeared in case of the upstream wind and 3 or 5 degrees of angle of attack in Type 1, 2-3, 3.
2) The vortex-induced oscillation for bending mode appeared in Type 1, 2-3, 3.
3) The vortex-induced oscillation for torsional mode appeared in Type 1, 3.
4) Except Type 2-3, fairings could be expected to suppress oscillation sufficiently.
5) Wind tunnel tests were carried out using such kinds of rotational center as shear center, gravity center and 1/2 point between gravity center and shear center. There are few differences in the response among them, therefore shear center was adopted as rotational center.

3-DIMENSIONAL WIND TESTS OF THE TOWER

To investigate the aerodynamic instability and the vibration of the tower for erection stage, 3-dimensional tower model (scale: 1/50) tests were carried out. The effect of structural damping was investigated to use a mechanical damper.

Fig. 5 shows the principal vibrational modes and frequencies of the tower. The first and the 5th mode are out-of-plane modes; the second and the 4th mode are in-plane modes; the third mode is torsional mode.

Fig. 6-(a), (b) show the typical responses of the test. As structural dampings of these tests, 0.01 in logarithmic decrement was employed. The first, second and third mode oscillation were appeared in the wind perpendicular to the bridge axis. The second and 4th mode oscillations were appeared in the wind parallel to th bridge axis. Fig. 7-(a), (b) show the relation between structural damping and responses. Each response was suppressed on condition that structural dumping = 0.04 or more.

The tests were also carried out using the tower model that has one type of aerodynamic damping device as shown in Fig. 6. The Aerodynamic damping device suppresses the second and 4th mode oscillations, however it could not suppress the first and 3rd mode oscillations. It is known that two rectangular cylinders that arranged in tandem have some complex

oscillations. Therefore, the oscillations of the tower of Nakajima Bridge may be affected by the arrangement in tandem.

FULL BRIDGE MODEL TESTS

Test Conditions

The test conditions are as follows:

Model: Full bridge model with scale 1/50 were used.
Fig. 9 shows the girder section and it corresponds to Type 2–2 in Fig. 2.
The dimensions of the model is shown in Table 1.
The frequencies and modes of the model, which are important to verify aerodynamic stability, are shown in Table 2 and Fig. 10, respectively.

Wind: Smooth flow & Boundary layer turbulent flow

Wind direction: Upstream & Downstream (Fig. 2)

System: Bridge completion step and the following erection steps (Fig. 9):
Erection step 1 (maximum canti-lever length in the center span)
Erection step 2 (maximum canti-lever length in the side span)

Facilities: Hitachi Zosen's wind tunnel (W x H x L = 8 x 3 x 23m)

Test Results

Some examples of V-A (i.e., Velocity vs. Amplitude) curve are shown in Figs. 11~14. Fig. 11 shows the 5th mode of vertical bending oscillation of the girder. This vortex excitation occurs only in the upstream flow and it disappears when the fairings are installed along the all edge girders.

Fig. 12 and 13 show the galloping oscillations which contain the first and third in-plain modes evoked by the wind of the bridge axis direction. The oscillation will completely disappear when the corner cut (b/D=1/7) is attached.

The Fig. 14 shows the buffeting oscillation which mainly consists of the vertical bending mode in the turbulent flow. The balancing erection method is used for the erection step 2. The amplitude of the first vertical bending mode was 74cm at the design velocity 38.5 m/s. The stress by the oscillation is not high however the erection machinery on the girder may become unstable. Therefore the oscillation must be reduced.

The following countermeasures are decided to reduce these harmful oscillations: the corner cut is applied for the tower and the active control device with fuzzy control will be installed on the tower top not only to resist tower oscillation during its free-standing stage but also to resist girder oscillation during its erection steps.

NATURAL WIND OBSERVATION

Natural wind has been observed by the ultra-sonic anemometer at the bridge site. The observation hut is installed near the pole with the anemometer. Wind records have been kept in opt magnetic disk files automatically. Observation starts at regular time and at strong wind (above 10 m/s). The observation started from the middle of October in 1991. Measurement items are as follows:

1) maximum wind velocity, 2) mean wind velocity, 3) gust factor, 4) mean wind direction, 5) mean angle of attack, 6) intensity of turbulence (horizontal and vertical) and etc.

RESULTS OF OBSERVATION

Examples of observation results during the period from March 1992 to February 1993 are shown in Figs. 15 ~ 17. Wind possibility of NE direction is high (Fig. 15) therefore careful attention should be paid for wind resistant design. All data were divided into 16 wind directions and for these directions Weibull parameters were identified (Fig. 16). Intensity of turbulence has strong relationship to both wind direction (Fig. 17) and Weibull parameter (C). The relationship between inverse of Weibull parameter (C) and intensity of turbulence (I_u) is shown in Fig. 18. U is along-wind. Fig. 18 indicates that 1/C is proportional to I_u therefore Weibull parameter (C) is influenced by the surroundings of the bridge site.

CONCLUDING REMARKS

Aerodynamic stability of Nakajima Bridge is being assessed by wind tunnel tests and observation of natural wind.

Wind stability of the bridge is confirmed for both the completed bridge and during erection by the section & full bridge models.

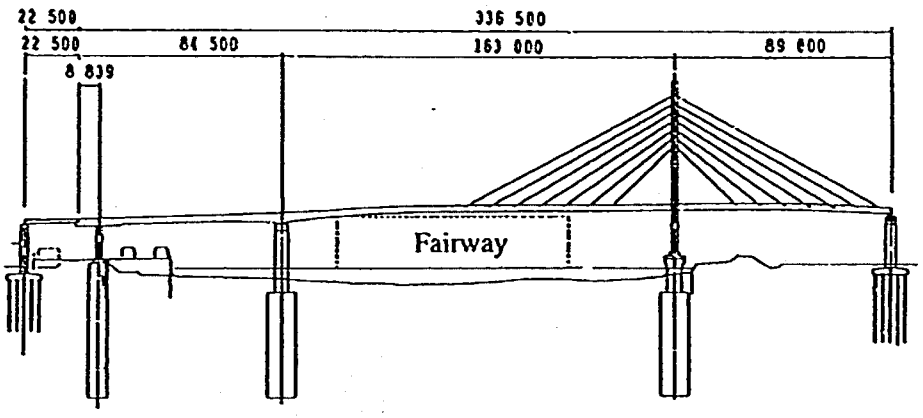
ACKNOWLEDGEMENT

The authors extend sincere appreciation to Prof. N. Shiraishi, Department of Civil Engineering, Kyoto University, for his valuable suggestions on this study.

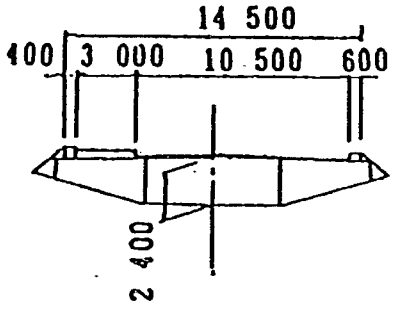
REFERENCE

[1] M. Kamei, M. Kawakami, K. Ikushima, M. Hosomi and H. Tanaka, "Wind Tunnel Test & Natural Wind Observation for Nakajima Bridge" *the Second Japan-Korea Joint Seminar on Steel Bridges*, Tokyo, Japan, July 20-21, 1992, pp.229-234.

Side View



Cross Section



Tower

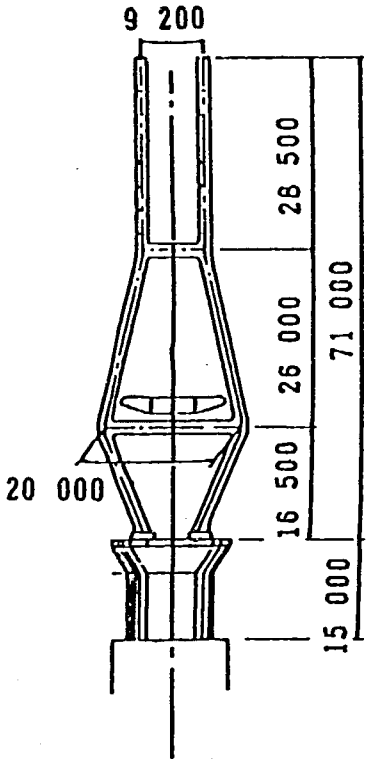


Figure 1 Nakajima Bridge

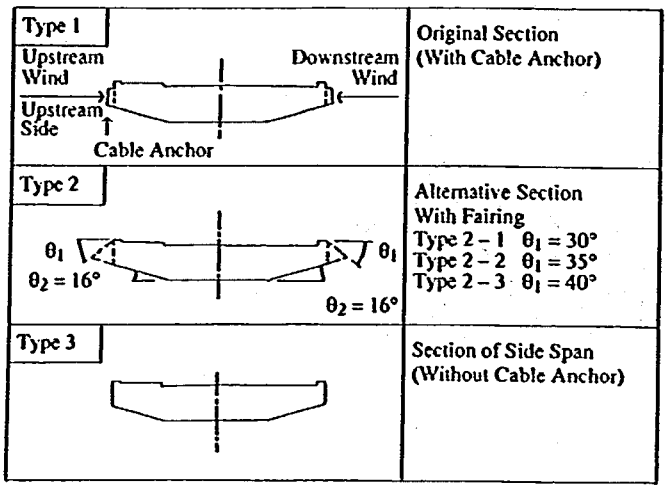
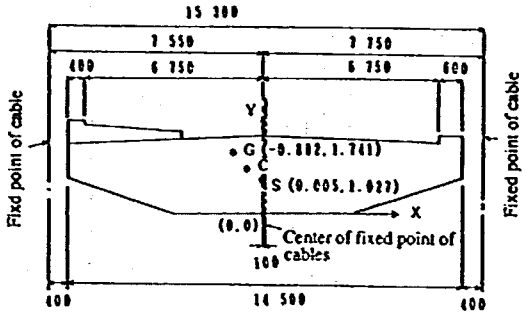


Figure 2 2-D Model Sections



Moment of Inertia (Unit: t·m·s²/m)	
Gravity Center (G)	35.34
Shear Center (S)	37.09
1/2 point between G and S (C)	35.78

Figure 3 Position of gravity and shear center

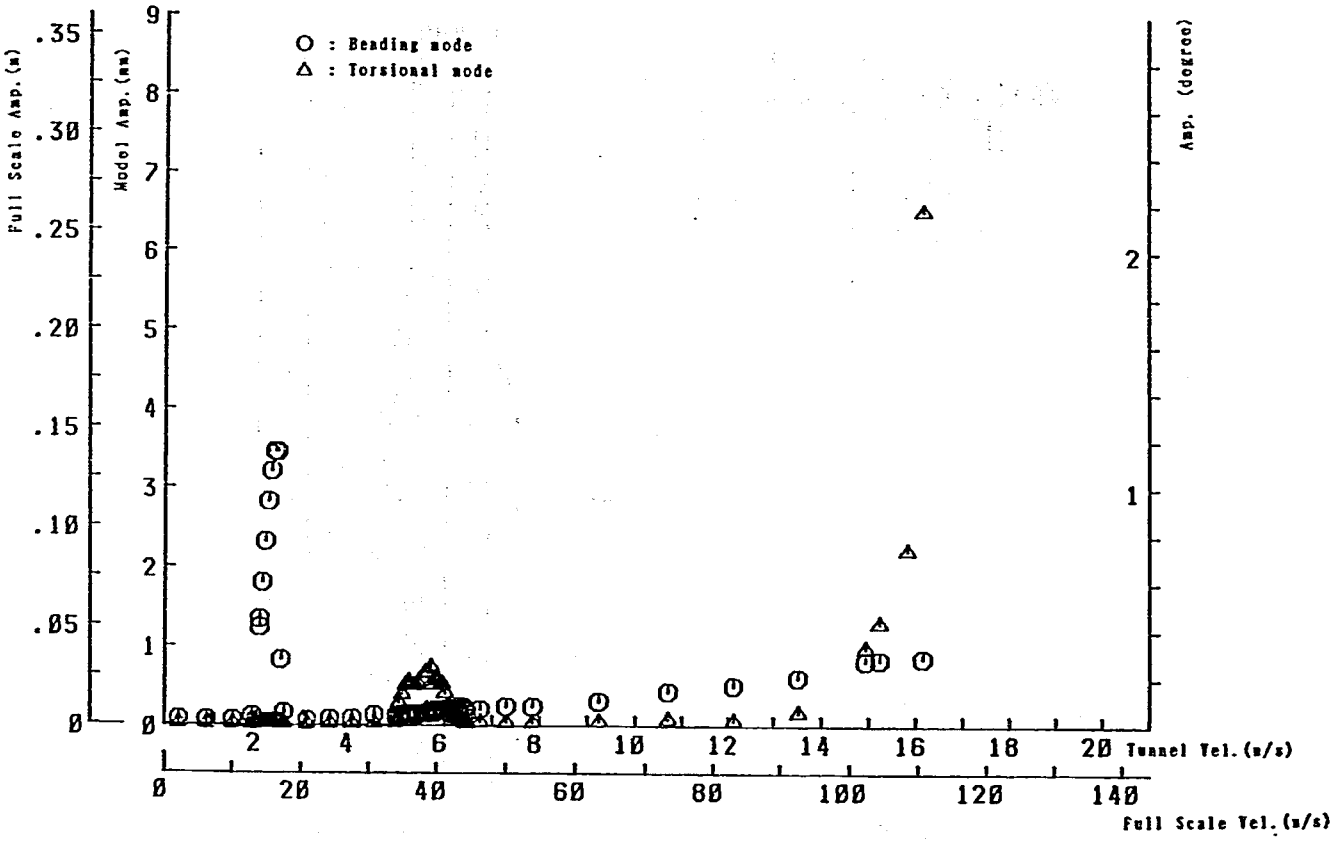


Figure 4 Aerodynamic responses of type 1 model
(Upstream, $\delta = 0.02$, Angle of attack = 5°)

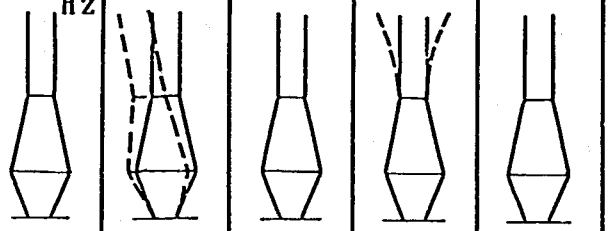
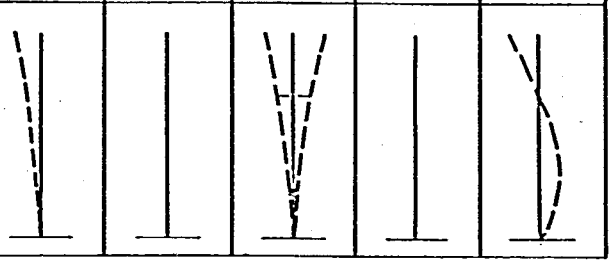
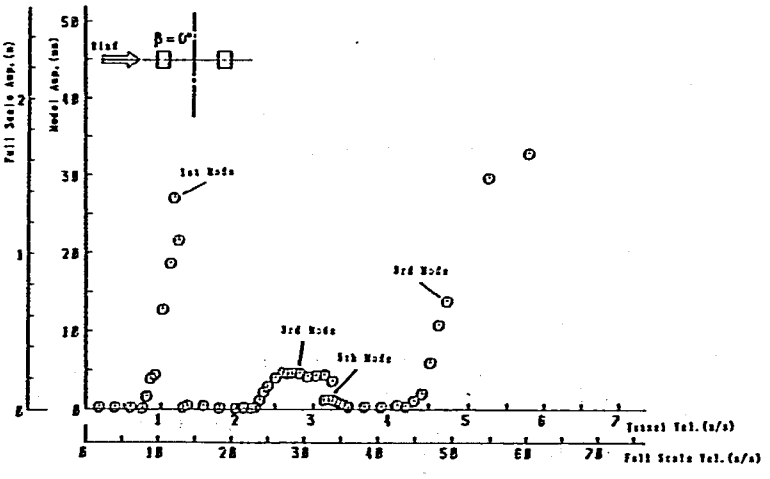
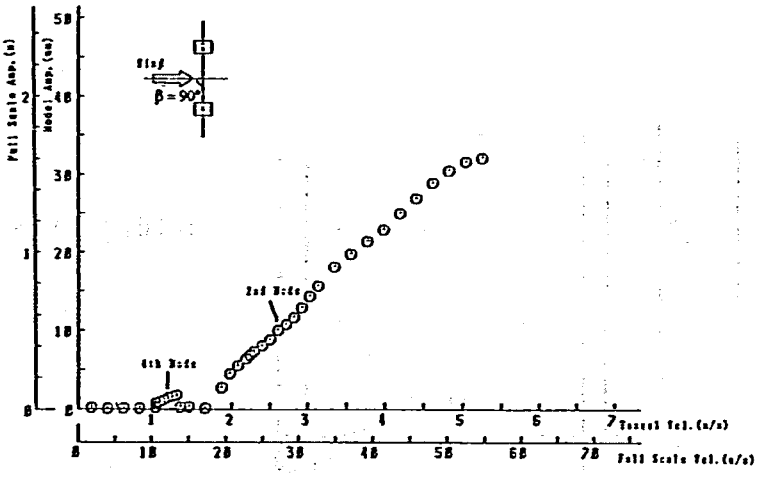
Mode	1	2	3	4	5
Frequency	0.494 Hz	0.998	1.865	2.544	2.999
In-plane					
Out-of-plane					

Figure 5 Vibrational mode and frequency

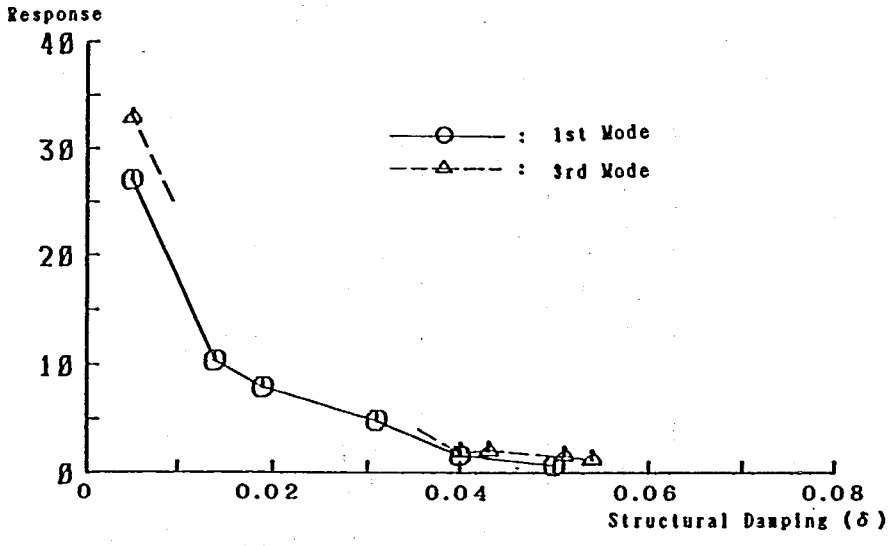


(a) Response by the wind perpendicular to the bridge axis

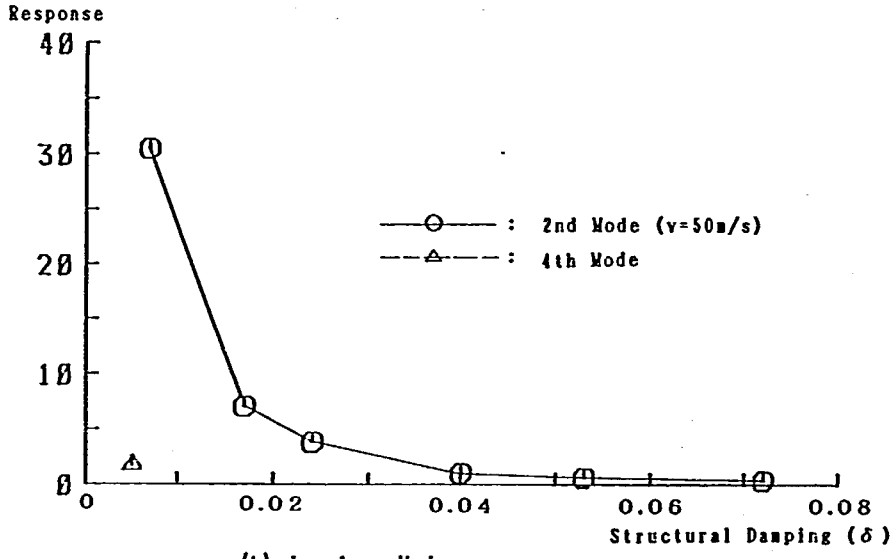


(b) Response by the wind parallel to the bridge axis

Figure 6 Aerodynamic response of the tower ($\delta = 0.01$)



(a) Out-plane Mode



(b) In-plane Mode

Figrue 7 Relation between structural damping and responses

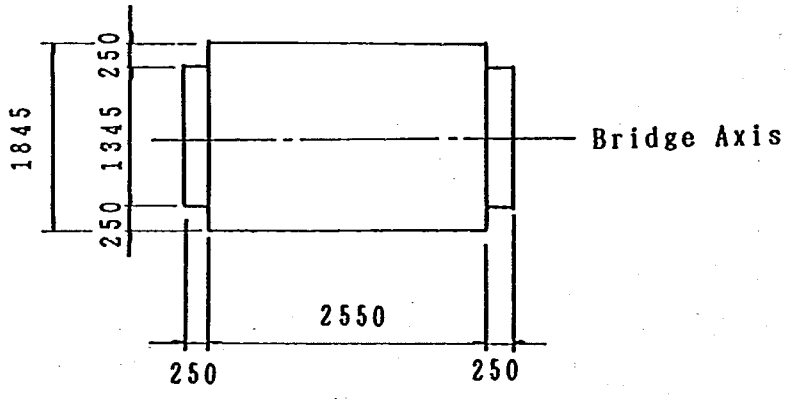
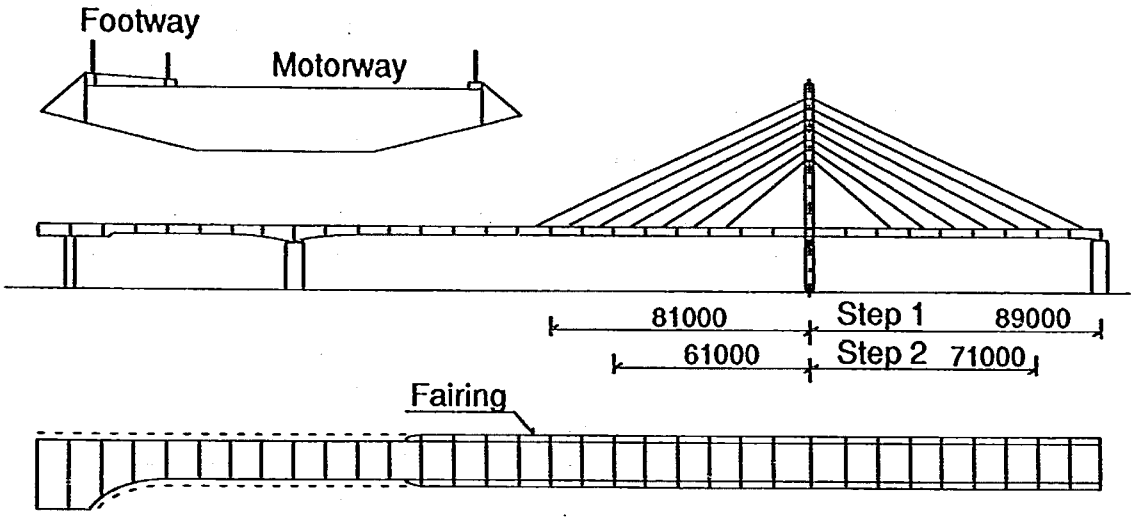


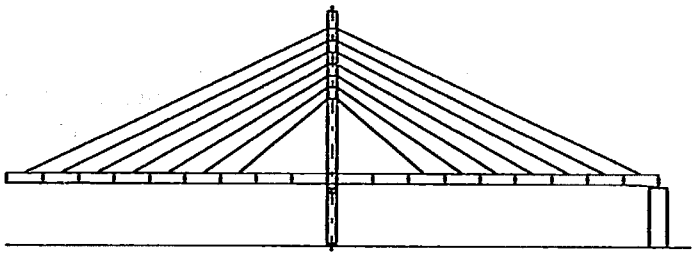
Figure 8 Tower section with aerodynamic damping device

(1) Completion Step



N.B. Dash line denotes fairings which are effective for aerodynamic stability

(2) Step 1



(2) Step 2

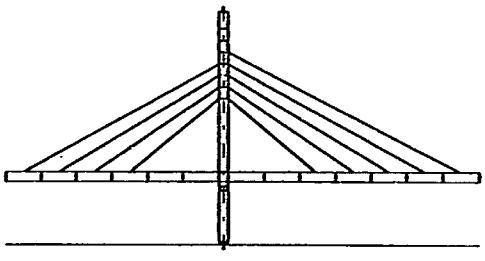


Figure 9 Tests system

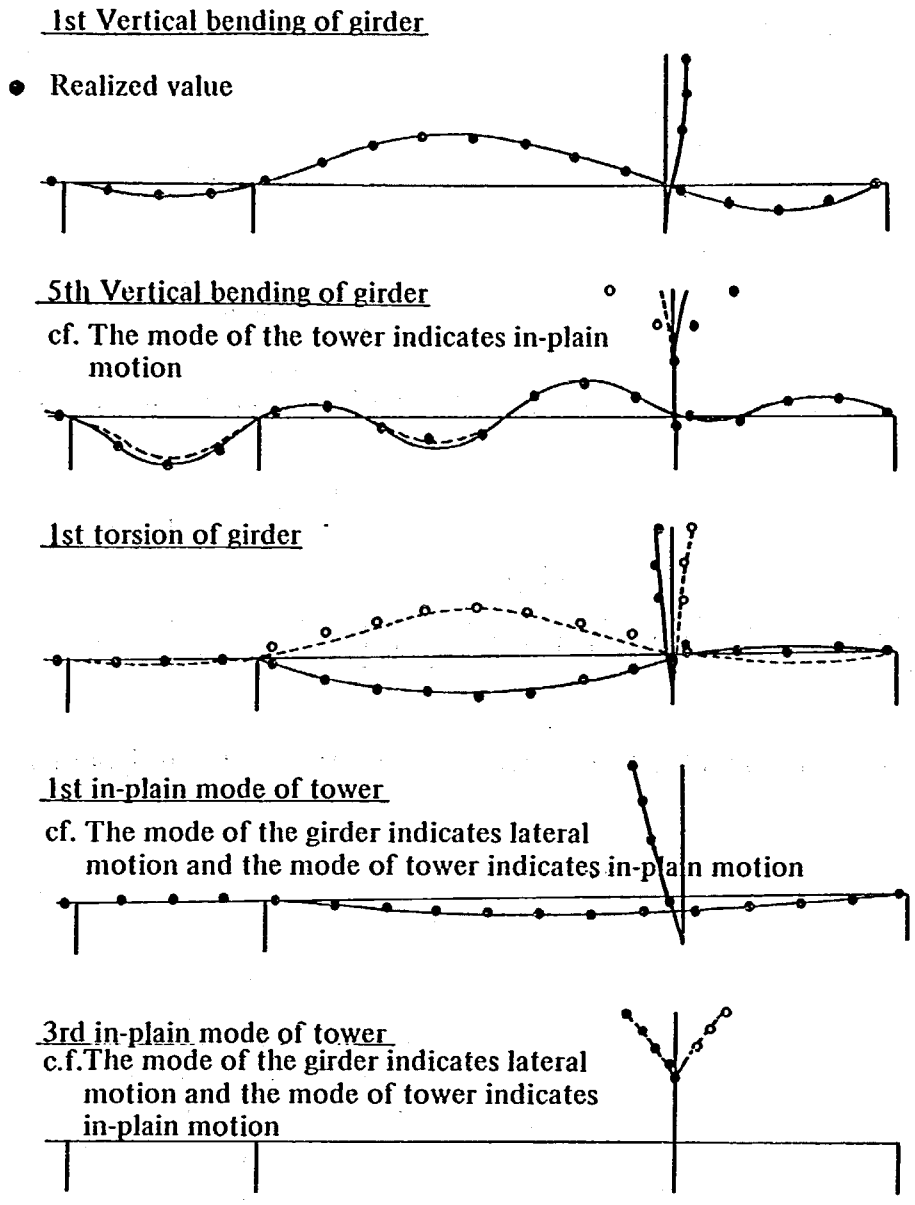


Figure 10 Vibrational modes

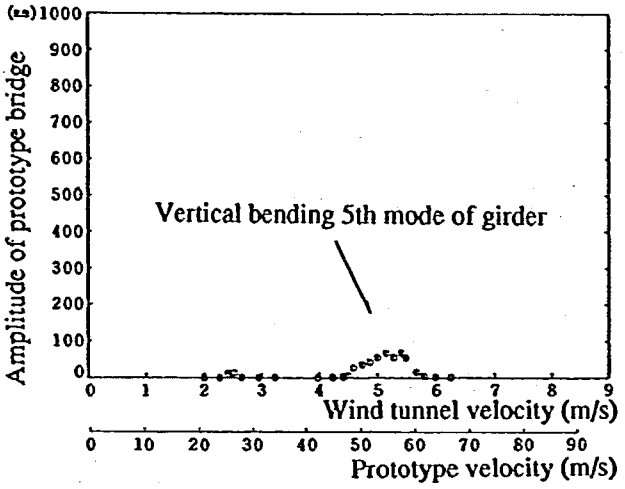


Figure 11 V-A curve of completion step in laminar flow

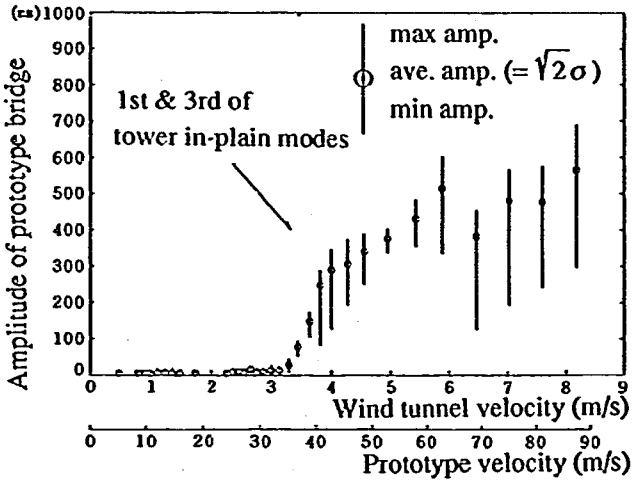


Figure 12 V-A curve of completion step in laminar flow

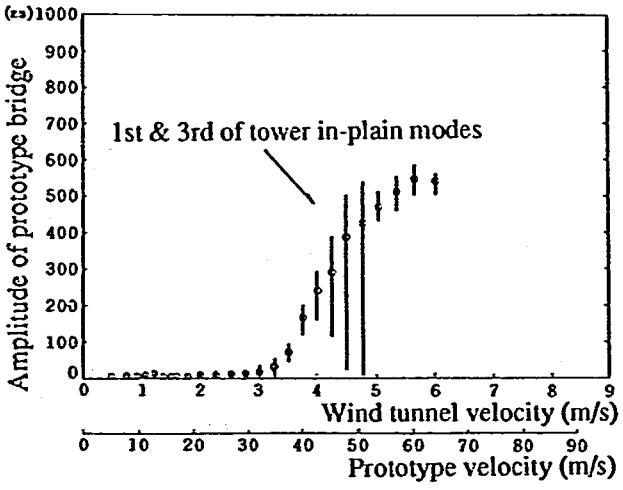


Figure 13 V-A curve of erection step 1 in laminar flow

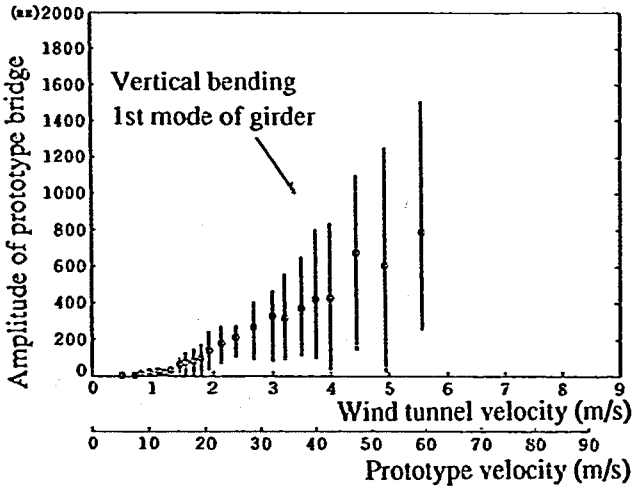


Figure 14 V-A curve of erection step 2 in turbulent flow

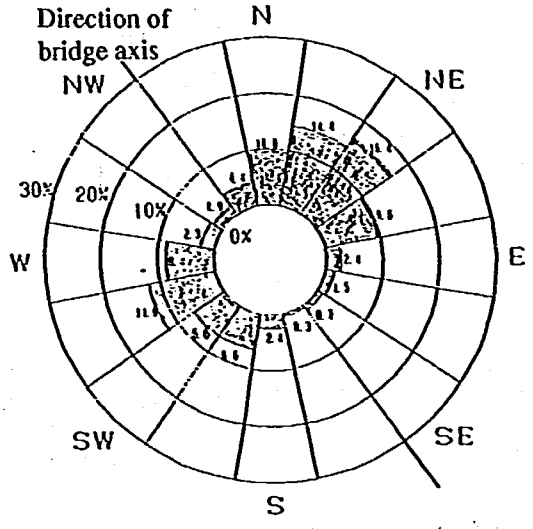


Figure 15 Wind rose at Nakajima Bridge's site

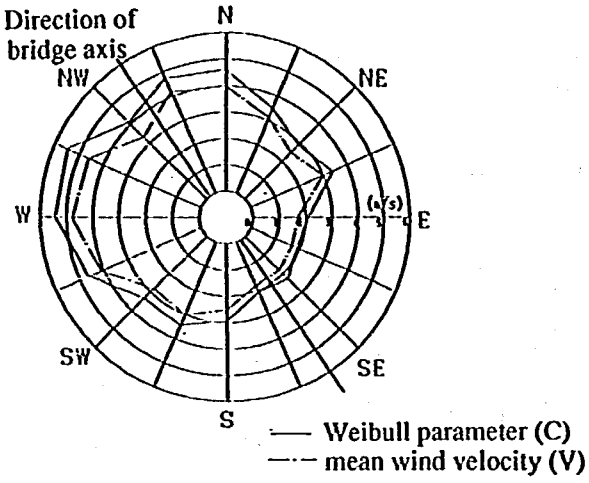


Figure 16 Weibull parameter (C) and mean wind velocity

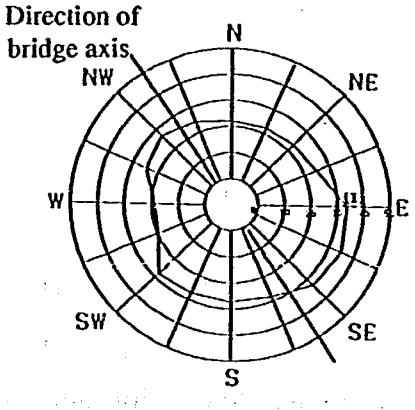


Figure 17 Intensity of turbulence (I_u) and wind direction

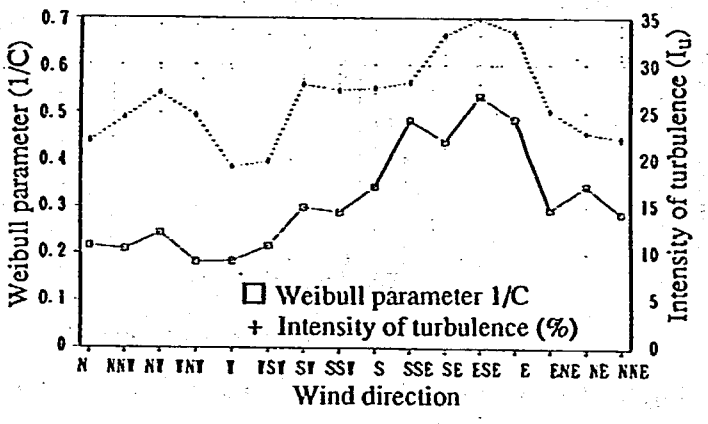


Figure 18 Weibull parameter (I/C) and Intensity of turbulence (I_u)

Table 1 Dimensions of model

	Unit	Required values	Realized values
Length	mm	6.730	6,730
Girder height	mm	48 ~ 80	48 ~ 80
Girder width	mm	290 ~ 306	290 ~ 306
Tower height	mm	1,420	1,420
Girder weight	gf/mm	5.13 ~ 7.81	5.13 ~ 7.81
Girder mass moment	gf·mm^2/mm	47.533 ~ 136,363	47,533 ~ 136,363
Girder vertical stiffness	gf·mm^2	(1.73 ~ 8.52) x 10^{10}	(1.88, 3.13) x 10^{10}
Girder lateral stiffness	gf·mm^2	(3.12 ~ 16.7) x 10^{11}	(4.08, 5.96) x 10^{11}
Girder torsional stiffness	gf·mm^2	(1.43 ~ 9.97) x 10^{10}	(1.60, 2.54) x 10^{10}
Tower mass	gf/mm	0.74 ~ 2.11	0.74 ~ 2.11
Cable (EA)	gf	235,000 ~ 412,000	330,000

Table 2 Frequencies of completion system

	Prototype	Model	
		Required values	Realized values
1st vertical bending mode of girder	0.502	2.37	2.39
5th vertical bending mode of girder	1.841	8.68	8.54
1st torsion mode of girder	2.249	10.60	11.40
1st in-plain mode of tower	0.759	3.58	3.42
3rd in-plain mode of tower	2.219	10.46	9.13

Aerodynamic Stability of Trans-Tokyo-Bay Highway Bridge

Y.Shioi[1], Y.Yoshida[2], K.saga[3]
1) General Manager of Design Department,
Trans-Tokyo Bay Highway Corporation, Tokyo, Japan
2) Manager of Bridge Design Division,
Trans-Tokyo Bay Highway Corporation, Tokyo, Japan
3) Bridge Design Division,
Trans-Tokyo Bay Highway Corporation, Tokyo, Japan

Summary

Trans-Tokyo Bay Highway Corporation carried out an investigtion of aerodynamic stability of 10-span continious steel box girder, which has maximum main span length 240 m and the girders length 1630 m.

A wind tunnel test of 2-dimensional model showed that the galloping and the vortex-induced oscillation shall occor, as had been predicted by computer simulation. In order to obtain more precise data, a wind tunnel test of 3-dimensional aero-elastic model was carried out, representing the entire 10-span box-girder. Contrary to the result of 2-dimensional model test , only the heaving mode of vortex-induced oscilation was observed without galloping vibration. It is considered that the aero-dynamic oscilation of the adjacent span had restrain the main span of the bridge.

Therefore, Tuned Mass-Dumpers are designed to decrease the vibration of the girder. The measurement of aerodynamic response of the actual girder must be done before the opening of the whole Trans-Tokyo Bay Highway, and the TMDs shall be installed into the box girder if such a vibration will occur.

1. Introduction

The Trans-Tokyo-Bay Highway is a 15 km toll highway which runs across the central part of Tokyo Bay from east to west connecting Kawasaki city and Kisarazu city. The Highway consists of an approximate 10km tunnel and a 5 km bridge. Two artificial islands, one at the midpoint of undersea tunnel, another at the junction of the tunnel and the bridge.

The Bridge is 4.4 km long with 42 piers. The navigation areas are where the water depth is about 20 m, and the bridge span is extended up to 240 m. The layout of the bridge is shown in Fig-1 and Fig-2. The steel box girders with orthotropic steel decks have been adopted as super-structure of the bridge, because of its light weight and short construction period. The maximum web height is 10.5 m and the deck width is 22.9 m, which serves dual two lane carriage ways in the first stage, and extra two lanes are planned to be attached in the future. The cross section of the super-structure is shown in Fig-3.

The Bridge is designed to be long continuous girder in order to improve

both seismic stability and road surface smoothness. Then, ultra long 10-spans continuous girder was adopted, culminating 1630 m total length.

The bridge structure may experience strong typhoon wind which may cause aerodynamic problems. So, a series of theoretical and experimental studies have been carried out to investigate the aerodynamic stability of the 10-span continuous girder which has the longest span 240 m. This paper reviews the outline of these theoretical and experimental studies.

2.Site Wind Characteristics

Ultrasonic anemometer was installed near the bridge construction site in Kisarazu, in order to obtain the characteristics of natural wind which would act on the bridge. The wind data measured in the past two years was analyed for tubulence factor. Figure-4 shows that the intensity of turbulence is small and turbulence scale is long when nothern wind blows from the sea. On the other hand, the characteristics of southern wind shows that the turbulence intensity is greater than that of nothern wind. Since the Trans-Tokyo Bay highway bridge is lacated on the sea, it is reasonable to adopt the nothern wind data for examining the aerodynamic stability of the bridge.

In the three dimensional wind tunnel test of the 10-span continuous girder, turbulent air flow is employed simulating the natural wind, in accordance with the site wind measurements.

3.Computer Simulation by Air-Flow Analysis

In the initial design stage, 1-box and 2-box girder structure were compaired by computer simulation, with a stand point of aerodynamic stability.

With these girder cross sections, two types of oscilation shall occur, vortex-induced oscillation and galloping oscillation. The Applied Votex Method was adopted to examine these vibration phenomena. For the vortex-induced oscillation, the air flow around the stationary girder is simulated, and the flucturing lift force is calculated. From the lift force spectrum, the exciting wind speed and the vibration amplitude is estimated. Next for the galloping oscillation, employing the periodic forced displacement, time-averaged exciting is calcurated. The results of the calculations are in Table-1.

Two types of oscillation shall occur with both cross sections of the girder. The difference of the cross section profiles does not become a significant factor, which cause the aerodynamic response. But the 1-box girder system with larger bracket offers a slightly better aerodynamic stability than the 2-box system.

4.Wind Tunnel Test of 2-Dimensional Solid Model

After thorough comparison of designs advanced, 1-box girder system was adopted. The advantages of 1-box girder system are the minimum steel

weight, the minimum painting area, and aesthetic merit. So, wind tunnel test of 2-dimensional solid model was carried out for analyzing the aero -dynamic characteristics of 1-box girder.

4.1 Model Design

The scale of 2-dimensional solid model is 1/30, and the length is 2.7m. Two different cross sections of the longest span were selected, because the girder height progressively varies in the longitudinal direction.The bridge has 4 lanes carriageway with full shoulders at the opening time, and extra 2 lanes shall be attached in the future.The model was arranged to represent both cross section 4 lines and 6 lanes. The test conditions are shown in Table-2. The model was supported by coil springs, and aero -dynamic response was measured in uniform air flow.

4.2 Test Results

Both vortex-induced oscillation and galloping are observed,as have been predicted by air-flow analysis. The vortex-induced oscillation occured at the wind speed of 20m/s, and the galloping at 40m/s. These air speeds are within the range of desighn wind speed. It was found through the test that the galloping can effectively be restrained by fitting small horizontal plate to lower position of each web of the girder. Table-3 shows that the galloping was restrained nearly completely by use of the stabilizing member.Such a additional stabilizer has already been adopted for quite a few box girder bridges in Japan. In case of the expanded 6 -lanes deck, the galloping was found to tend toward the better stability compared with 4-lines case,because of consequential increase of width by height ratio. The vortex-induced oscilation must also be restrained. But it was considered that 3-dimensional model test is more appropriate for detailed studies about the turburence and the effects of dynamic mode form.

5.Wind Tunnel Testing with 3-Dimenional Model

5.1 Model Scale Effect

In the 3-dimensional wind tunnel test, model size must be as large as possible, in order to represent the aeroshape and the dynmic modes of actual bridge. However, the model scale was restricted within 1/170 according to the dimensions of wind tunnel. Therefore, preliminary 2 -dimensional model tests using three different scales 1/30,1/90,1/170, were carried out in order to research the model scale effect.

Figure-5 shows the critical air speed of galloping and maximum ampli -tude of vortex-induced oscillation, in reference to model scale. And it shows each scale models indicated almost no differences.

5.2 Model Design

3-dimensional model was made with aluminum spine and wood blocks, representing the whole 10-spans continuous girder. Aluminum spine represents the rigidity, and wood blocks represents aeroshape of the girder. (Figure-6) Natural frequencies and vibration modes of the 1/170 model are successfully obtained as shown in Table-4.

5.3 Generation of Turbulence

Two types of turbulent air flow were generated in the wind tunnel providing the swinging flaps at the air inlet, in addition to the union air flow. Characteristics of the turbulences are shown in Table-5. Type -A was simulated the minimum level of natural wind turbulence, and Type -B was of average level.

5.4 Test Results

Aerodynamic responses of the 3-dimensional model were measured as shown in Table-6. Contrary to the 2-dimensional model test, the gallopinging did not occur and only the vortex-induced oscillations were observed at each natural modes. This results can be briefly explained by the following logic. The cross section of main span must be aerodynamically excited and adjacent spans effectively serve to reduce the oscillation of main spans. This logic was proved by the fact that the galloping did occur when the adjacent spans were coverd from air flow. Therefore, it was concluded that the galloping oscillation should not occur in actual bridge, and the stabilizer plate should not be attached.

Then the only problem left is the vortex-induced oscillation. The 1st mode of vortex-induced oscillation occurs at the wind speed of 15m/s, and the higher modes occur at each corresponding wind speed. Then, fatigue of bridge structure was examined in case of the vortex-induced oscillation occur, and concluded that the cumulative fatigue damge by the aerodynamic vibration should be under the allowable level. However, if the vibration occurs at the wind speed of 15m/s, driving stability of the vehicles might be effected. So, Tuned Mass Dumpers are designed in order to decrease such an undesired vibration. TMDs are intended to be installed into the box girder if the vortex-induced oscillation is measured on the erected bridge, before the opening of the Trans-Tokyo Bay Highway.

6. Conclusion

Aerodynamic stability of the 10-span continuous box girder of Trans -Tokyo Bay Highway was investigated through a series of theoritical studies and wind tunnel tests. The 2-dimensional wind tunnel test showed the vortex-induced oscillation and galloping occurs at the wind speed of about 20m/s, and 40m/s in each case. Then the 3-dimensional model test was carried out in order to estimate more accurate aerodynamic stability.

The results of 3-Dimensional test showed the galloping did not occur and the vortex-induced oscillations were observed at each natural modes. Tuned Mass-Dumpers are designed to decrease the vibration of the girder. The measurement of aerodynamic response of the actual girder must be done before the opening of the whole Trans-Tokyo Bay Highway, and the TMDs shall be installed into the box girder if such a vibration will occur.

7.Acknowledgement

The authors wish to thank Prof.Narita and Dr.Yokoyama for their helpful advices.

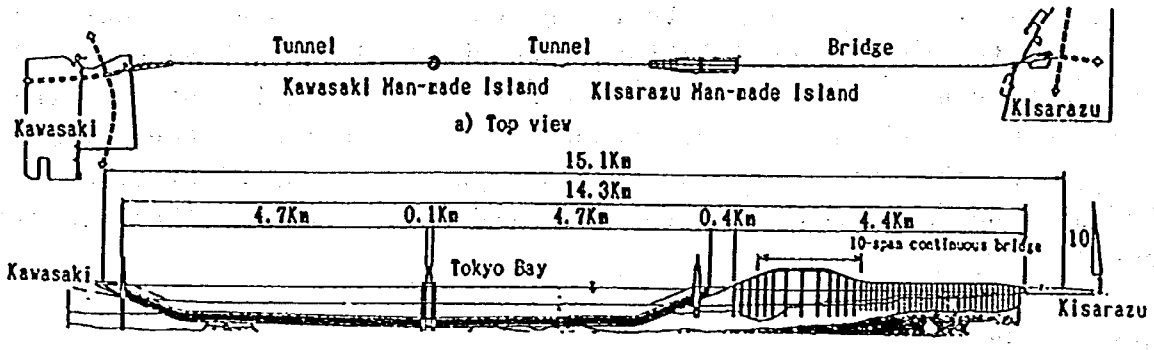


Figure 1. Trans-Tokyo Bay Highway.

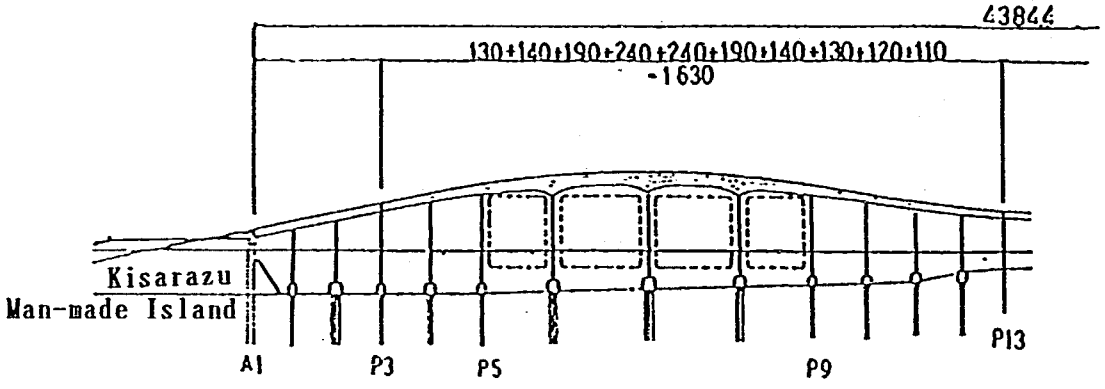
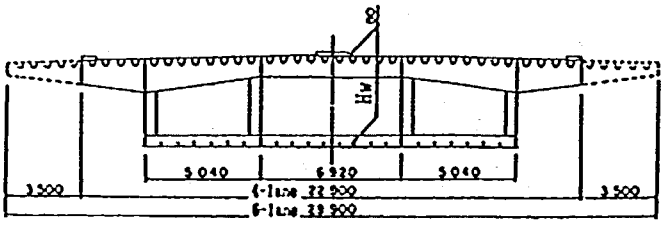
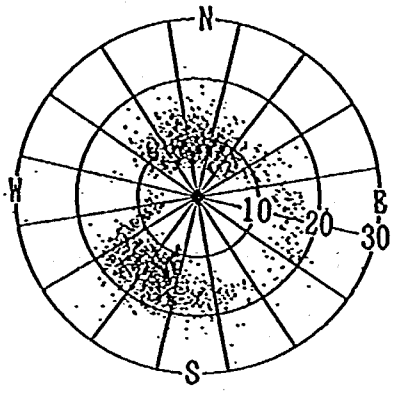


Figure 2. 10-spans contious bridge.

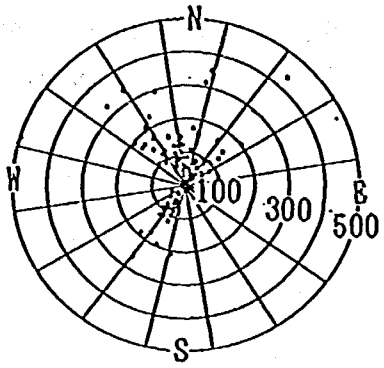


Hw: 3,200 ~ 10,500mm

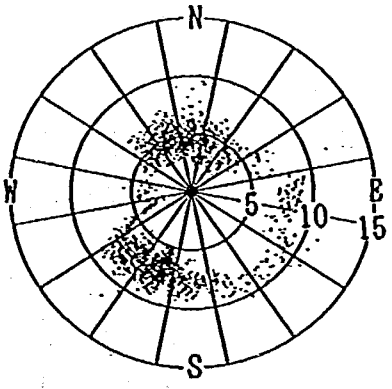
Figure 3. Bridge girder cross section.



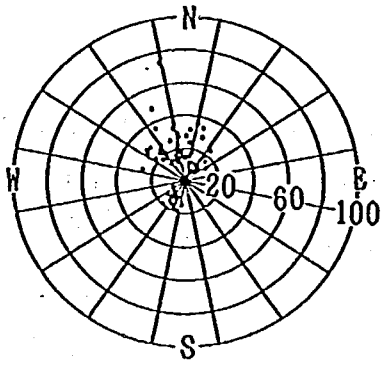
a) Intensity of u-component, Iu(%)



b) Scale length of u-component, Lu(m)



b) Intensity of w-component, Iw(%)



d) Scale length of w-component, Lw(m)

Figure 4. Characteristics of natural wind.

Table 1
Results of Calculation (Section 1, 4-lane)

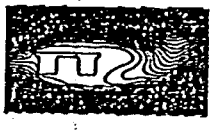
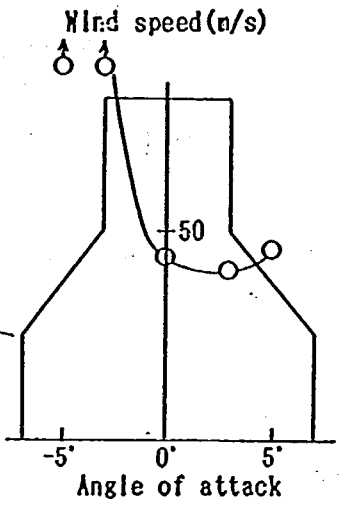
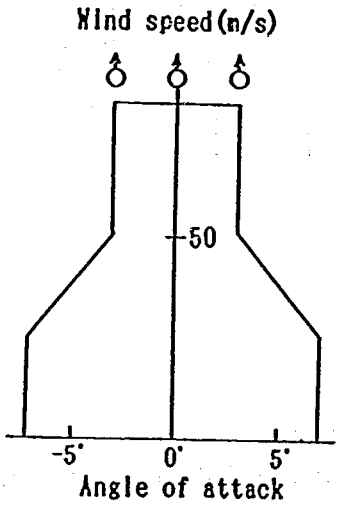
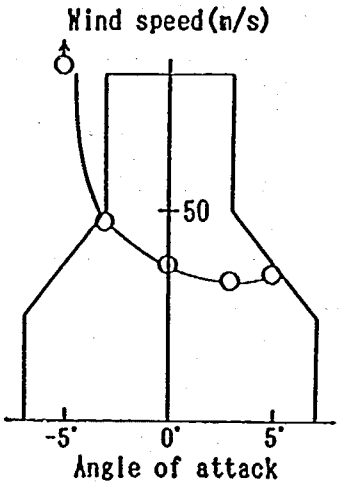
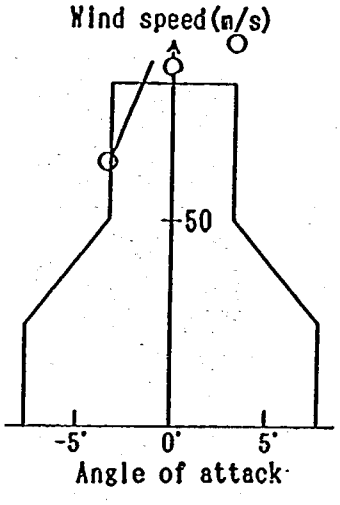
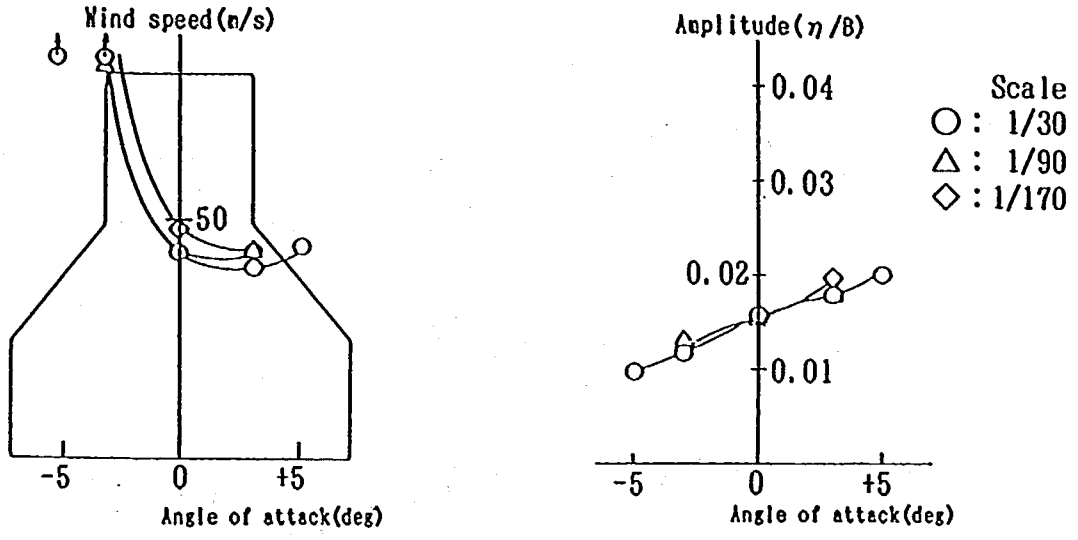
Type	Flow pattern	Vortex-induced oscillation			Galloping		
		Angle of Attack	Wind speed	Amplitude	Critical wind speed	Aerodynamic damping 40 m/s	Aerodynamic damping 82 m/s
One-box		+5°	19 m/s	0.38 m	32 m/s	-0.20	-0.49
		0°	24 m/s	0.65 m			
		-5°	16 m/s	0.14 m		(Logarithmic decrement)	
Two-box		+5°	12 m/s	0.19 m	32 m/s	-0.60	-0.58
		0°	9 m/s	0.12 m			
		-5°	9 m/s	0.05 m		(Logarithmic decrement)	

Table 2
Test conditions of two-dimensional model (Section 1, 4-lane)

Item	Prototype	Model	
		Required	Measured
Scale	1/1	1/30	1/30
Weight	249 kN/m	277 N/m(model)	277 N/m(model)
Natural frequency	0.30 Hz	-----	2.02 Hz
Natural damping (Logarithmic decrement)	-----	0.02	0.02

Table 3
Critical wind speeds of galloping obtained in two-dimensional test (4-lane)

Type of section	Basic section (Without horizontal plate)	With horizontal plate
Section 1		
Section 2		



a) Critical wind speed exciting the galloping

b) Maximum amplitudes of vortex-induced oscillation

Figure 5. Effects of model scale(Section1, 4-lane).

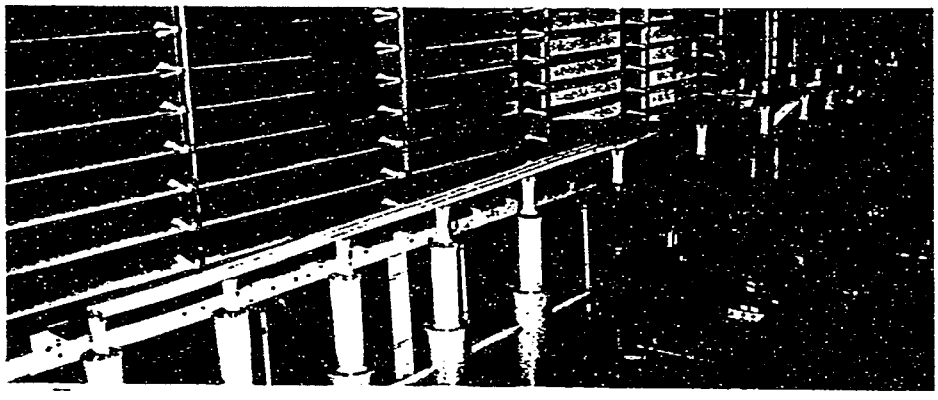
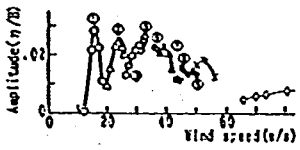
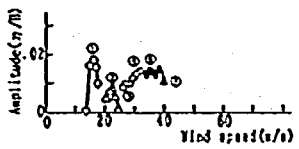
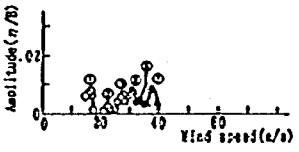
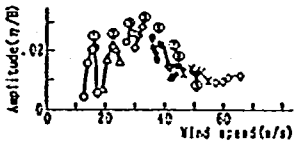
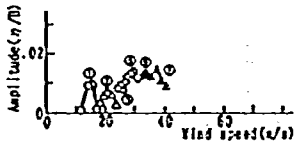
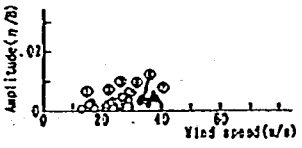
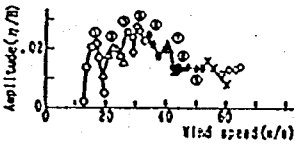
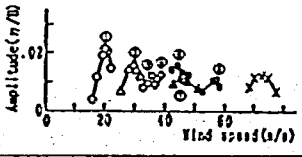
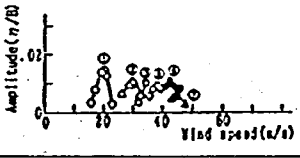
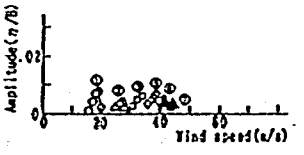


Figure 6. Three-dimensional model

Table 4
Test conditions of three-dimensional model

Mode No.	Natural frequency		Modal shape
	Prototype	Model	(---: calculated, ○: measured)
1st	0.335 Hz	7.76 Hz	
2nd	0.502 Hz	11.48 Hz	
3rd	0.600 Hz	14.51 Hz	
4th	0.628 Hz	15.15 Hz	
5th	0.681 Hz	16.45 Hz	

Table 6
Test results of three-dimensional model

Type	Natural damping (logarithmic decrement, δ)		
	$\delta \fallingdotseq 0.02$	$\delta \fallingdotseq 0.05$	$\delta \fallingdotseq 0.15$
4-lane Uniform flow			
4-lane Turbulent flow (Type A)			
4-lane Turbulent flow (Type B)		—	—
6-lane Uniform flow			

η : Heaving amplitude of oscillation
B : Total width of 6-lane deck (=29.9 m)

Table 5
Turbulence generated in wind tunnel

Type of air flow	Intensity		Scale length	
	u-component	w-component	u-component	w-component
Type A	4.0 %	2.5 %	390 m	140 m
Type B	8.1 %	5.2 %	260 m	110 m

(6) Session 6

Seismic Design (1)

12) An Experimental Study of Horizontal Displacement Behavior Using Large-Size Model Pier
(K. Kosa, Y. Hashimoto and K. Kobayashi)

13) Comparison of the Seismic Design of Highway Bridges in California and in Japan
(M. Sultan* and K. Kawashima)

14) Analysis of Ground Motion Characteristics
(H. Ohtsuka, K. Tokida, K. Tamura, M. Kaneko* and H. Fukada)

An Experimental Study of Horizontal Displacement Behavior Using Large-Size Model Pier

By

Kenji Kosa [1] Yoshiyuki Hashimoto [2] Kazuo Kobayashi [3]

1) Senior Engineer, Design Section, Engineering Department, Hanshin Expressway Public Corporation
2) Section Chief, Design Section, Engineering Department, Hanshin Expressway Public Corporation
3) Professor, Osaka Institute of Technology

ABSTRACT

An experimental study using three types of specimens (1/10 scale and flexural failure, 1/3 scale and flexural failure, 1/3 scale and shear failure) was conducted to assess their deformation behavior and strength, and reinforcement pull-out. The specimens were subjected to reversed cyclic lateral displacement with the axial load kept constant. The results of flexural tests show M-ϕ curve and the ultimate strength are well in agreement with the results based on the non-linear numerical analysis. The results of shear failure tests show the calculated values from the "Specifications for concrete making" can be applied to the large-sized specimens.

1. Introduction

The cross section of reinforced concrete bridge piers is generally determined by an earthquake loading. Japan's current "Specifications for Highway Bridges" specify that the seismic resistance of bridges against general-scale earthquakes shall be achieved by designing with the allowable stress method and against large-scale earthquakes it shall be achieved by designing in accordance with the requirements for lateral inertia force of bridges for seismic design by the bearing capacity method. This means that seismic safety within the plastic range beyond the elastic range, namely, the deformation performance of bridges under severe seismic loadings should be predominately taken into account to make structures earthquake resistant. Therefore, the behavior of RC bridge piers within the plastic range shall properly be grasped, which will eventually lead to the design of structures with sufficient ductility.

To date, a number of experimental studies have been conducted to investigate the ultimate strength and toughness of RC bridge piers under earthquake loadings, and considerably accurate estimation of fracture behavior has already been obtained. However, since most of the experiments were made using small specimens, the derived results were deviated from the results obtained from real structures. The nature of small specimens differ from that of existing bridges in the following points:

(1) The ratio of reinforcement's diameter to the width of column

differ in small specimen from that of a real structure. For example, in a 1/10 model, the diameter of a reinforcement is about 5 % of the 30 cm long width of the specimen. Whereas, in a real pier whose width is, say, about 3 m, the diameter of a reinforcement will be about 1 % of the width of the specimen. This factor may give a serious influence to the pull-out behavior of reinforcements.
(2) Small specimens are made of relatively simple assemblage of reinforcements. However, in the urban-type elevated RC bridge piers like those of the Hanshin Expressway, column reinforcements are multi-layers, and they are placed closely. The formation may be give influence to the fracture patern of the structure.
(3) In a real bridge pier, shearing type fracture induced by the presence of the cut-off point occurs. Shearing type fracture in a small specimen is different from that of large specimen due to the size effect.

In order to investigate the effects the above points may cause, a comparison test was made according to the flow chart in Fig.1. Relatively large-sized RC bridge pier models (1/3 scale) containing the same bar arrangement as the ordinary RC bridge piers of the Hanshin Expressway were produced. And they were compared with a conventional small size model (1/10).

2. Experimental program

2.1 Description of specimens

Experiments were conducted on three bridge pier models produced in accordance with the Hanshin Expressway standard design code. Specimen No. 1 (1/10 model) was made to be equivalent to a conventional model, and was intended to find the characteristics of small specimens. Specimen No. 2 (1/3 model) was a large size model containing the same reinforcement arrangement with a real bridge pier and was designed to let its base area fracture. The comparison between the test results of No. 1 and No. 2 specimens showed the difference associating with fracture behavior and the size effect of reinforcements. No. 3 specimen, whose cut-off point in the axial direction was positioned to be lower by 1d (d: effective width) compared with an actual bridge so that fracture occurred first at the cut-off point. The comparison of the test results of specimens No. 2 and No. 3 revealed the ultimate strength and fracture progress at the cut-off point associating with the difference of failure type.

2. 2 Preparation of specimens

The design concrete strength was 270kgf/cm² for all three specimens, and the actual concrete strength was 289kgf/cm² for No. 1 specimen, 283 kgf/cm² for No. 2 specimen and 304 kgf/cm² for No. 3 specimen. The cement used was high-early-strength portland cement. No. 1 specimen was prepared with ready mixed concrete whose maximum size of coarse aggregate was 20 mm, and No. 2 and No. 3 specimens with microconcrete whose maximum coarse aggregate size was 10 mm. 16 mm-diameter reinforcements were used as

reinforcements in the direction of axis in a 1/10 model and 1: mm-diameter reinforcements were used in a 1/3 scale model. Lateral ties with the diameter of 6 mm, corresponding to SD 35, were used. The 6 mm-diameter reinforcements were used after applying annealing because their quality had severely altered. The main reinforcement ratio is 2.20 %. The tie reinforcements ratio is 0.21 % at the column end and 0.10 % in other areas.

2.3 Method of load application

Specimens were bound to the reaction floor with steel bars. Using two-way actuator, horizontal load was applied at the top of the column. Horizontal load was applied under the load control until a little before reaching the yield point and after that point with displacement being controlled. The specimen were subjected to a series of step-wise increasing symmetric displacement cycles at $\delta y, 2\delta y, 3\delta y, 4\delta y$. At each step, 10 cycles of loading with the same displacement amplitude were applied. The yield displacement (δy) corresponding to ductility factor one was defined as the displacement at loading point at which reinforcing bars at the extreme tension fiber firstly reached yield strain. The experiment was continued until load being applied dropped to either the yield point or 70 % of the maximum load. Fig. 3 shows measurement locations of typical items such as load cell, strain gages and concrete gages.

3.Experimental results

3.1 Experimental results of No. 2 specimen

Experimental results derived from No. 2 specimen are shown in Fig. 4 and Fig. 5. Fig. 4 shows a load-displacement curve and Fig. 5 shows development of cracks. Experimental results derived from No. 1 specimen were excluded in this paper because our results were similar to those hitherto reported in literature. Distinctive behaviors observed in the course of load application were as follows:

(1) Cracks occurred (35.5 t).
(2) Flexural cracks that appeared in the middle area of the column transformed to gentle diagonal cracks (yield load :90.3 t).
(3) Clear diagonal cracks appeared at the bottom area of the column ($2\delta y$).
(4) Load decreased and the spalling of cover concrete increased ($4\delta y$).
(5) Load dropped significantly and concrete spalled off markedly ($5\ \delta y$).

As is shown in these results, No. 2 specimen made a flexural fracture in the bottom end, not making a fracture at the cut-off section. Also, the specimen was confirmed to have an excellent deformation performance with the toughness ratio 5 or 6.

3.2 Experimental results of No. 3 specimen

Fig. 6 shows the load-displacement curve and Fig. 7 shows

the development of cracks derived from No. 3 specimen. Typical behaviors observed during load application were as follows:

(1) Cracks occurred in the corner area (13.3 t).
(2) Flexural cracks that appeared in the cut-off area shifted to diagonal cracks (yield load: 75.2 t).
(3) Spalling off of cover concrete increased at the cut-off area and its range enlarged ($3\delta y$,n=3).
(4) The buckling of column reinforcement ($3\delta y$,n=6).
(5) Marked drop of load at the P- envlopment line and the progress of damage ($4\ \delta y$,n=1).

Tie reinforcements reached the yield point at the cut-off point and the members fractured in the same section. Although the maximum load and ductility decreased in No. 3 specimen compared with No. 2 specimen, the specimen still retained toughness ratio 4 and did not bring a brittle fracture.

4. Analysis of experimental results

4.1 Analysis of ultimate flexural strength

A numerical analysis was conducted on a model in a monotonic loading condition, utilizing material test results of reinforcements and concrete that were used for the preparation of the three specimens. The flexural load-deflection curve was calculated from the stress-strain respone of the compressive concrete and the tensile steel. Then the analytical results were compared with the experimental results derived from the reversed cyclic condition, in order to investigate the validity of the model. A model proposed by Inoue et al. was adopted as a model for the stress-strain response in concrete, for in the test conducted last year on a real bridge and the results using this model well in agreement with experimental results [1]. Their model, shown in Fig. 8, takes into account the effect of lateral confinement of ties. As a stress-strain model for reinforcements, Park-Paulay model that considered strain hardening of reinforcements was adopted. As to the distance from yield point to strain hardening, $8.5\ \varepsilon sy$ was selected from pull-out test results. Table 1 shows the comparison of maximum horizontal load at the time of Mmax between the analysis results and experimental results obtained in both the cut-off area and the bottom area. Fig. 9 shows the growth of bending moment versus horizontal displacement obtained through analysis and in experiment (calculated from the strains of reinforcements measured on compression and tensile sides). Fig. 4 compares the load-horizontal displacement of both experimental and analytical results. According to M-ϕ curve in Fig. 9, the analytical results are well in agreement with the experimental results, and the difference at the time of maximum load remains within a few percent. In contrast, a marked difference is observed in deformation behavior with an increase of load in the $P - \delta$ curve in Fig. 4. This is considered due to a serious effect of a repetitive loading and the pull-out of reinforcements.

4.2 Analysis of ultimate shearing strength

The ultimate strength of No. 3 specimen that had made a shearing failure at the cut-off point was evaluated using shearing strength Vy for the bar members. The value is shown as follows in the "Specifications for concrete making":

$$Vy = Vc + Vs \qquad (1)$$

V c: nominal shear strength attributable to concrete.
V s: nominal shear strength attributable to shear reinforcement.
When safety coefficient (coefficient of materials and members) is 1.0, Vc and Vs are calculated as follows:

$$V\,c = fvc\ bw\ d \qquad (2)$$

bw : the width of web
d : effective depth

$fvc : 0.9 \cdot \beta d \cdot \beta p \cdot \beta n \cdot \sqrt[3]{f'c}$

$\beta d : \sqrt[4]{100/d}$, when $\beta d > 1.5$, βd is taken as 1.5.

$\beta p : \sqrt[3]{100 p_w}$, when $\beta p > 1.5$, βp is taken as 1.5.

$\beta n = 1 + M_o/M_d$, when $\beta n > 2$, βn is taken as 2.

$$V\,s = (Aw\ fwy\ /\ Ss)\ Z \qquad (3)$$

Aw : area of shear reinforcement with a distance Ss along a member.
fwy : yield strength of shearing reinforcing bars.
Ss : the interval of the placement of shearing reinforcing bars.
Z : the distance from the acting point of resultant force of compressive stress to the center of compressive reinforcements (=d/1.15).

Table 2 shows shearing strength calculated from material test results. Fig. 10 shows strain-displacement curve of lateral ties in the web area of No. 3 specimen. As is shown in this figure, almost no cracks occurred in lateral ties until reaching Vc point. After reaching Vc, strain increased with an increase of load and came to the yield point at the time of maximum load. This verifies that the value Vc is nearly adequate and the load applied at the maximum strain (104.7 t) is approximately in agreement with the ultimate shearing strength (V y: 105.6 t). Based on the above results, it can be said that an equation for the evaluation of shearing strength described in the "specifications for concrete making" can reasonably be applied to No.3 specimen which is large-sized.

4.3 Evaluation of the pull-out of reinforcements

The present section evaluates the influence of reinforcement pull-out on the horizontal displacement [2, 3]. The rotational angle was first obtained from the displacement curve plotted by a dial gage which was installed near the bottom end of the column. The horizontal displacement at head of the column induced by the rotatory deformation was then obtained. The ratios of

horizontal displacement due to the reinforcement pull-out to the whole horizontal displacement volume are shown in Table 3. The table indicates that No. 1 specimen was significantly affected by the pull-out of reinforcements as is seen from 50 % at the yield point and 70 % at the ultimate state. It can be said that the results of No. 1 specimen are nearly alike to the conventional experimental results. Compared with this big influence, No. 2 and No. 3 specimens as well as the actual bridge test conducted last year show a relatively less degree of influence. One of reasons for such variation is attributed to the difference of reinforcement's diameter versus pier's width, a big ratio in No.1 specimen and a small ratio in No. 2 and No. 3 specimens and the real bridge pier. As to the degree of the pull-out effect during the period from the yield point to the ultimate state, it increased in No. 1 and No. 2 specimens with the increase of load, but it decreased in No. 3 specimen and the real bridge test in the past. The contrasting behavior shown in Fig. 11 is presumed to be resulted from the difference of fracture position. In the case of fracture at the cut-off section, when load was continued to apply after the yield point, the displacement occured concentrated around the cut-off section, making the displacement ratio due to the pull-out conversely small. In contrast, in the case of fracture at the column's bottom area, the displacement occured around the bottom area, and the pull-out of reinforcements also increased, bringing a relatively large displacement ratio compared with that at the time of yield point. In this way, the influence of reinforcements' pull out increased on the whole in all three specimens up to the point of yield strength, although a small variation was observed. However, after the yield point, the influential ratio increased in case of a fracture at the bottom area while showing a decreasing tendency in case of a fracture at the cut-off section, indicating that the difference lay in the position of fracture.

5. Conclusion

The following conclusions can be drawn from the present experimental study conducted with large-size model piers.

(1)The M-ϕ curve and the ultimate strength obtained from experiments are nearly in agreement with the analytical results that were derived using stress-strain curve based on the strength tests of materials such as reinforcements and concrete.

(2)The yield strength of a specimen that was induced a shearing failure is approximately equivalent to values Vc and Vy that were calculated from the "specifications for concrete making." This indicates that the above-mentioned equation can be applied to large size specimens.

(3)The ratio of the displacement due to pull-out to the total horizontal displacement was 10 strong percent up to the yield point. However, after the yield point, the ratio increased in the case of a fracture at the bottom area and in the case of fracture at the cut-off section the ratio showed a decreasing tendency, indicating that the tendency varies depending on the

area of fracture.

Acknowledgements

The authors are grateful to the members of research committee on ductilities of RC bridge piers for their practical advice and support throughout this study from experiment to numerical analysis.

References

1)Nakabayashi, S; Hamada, K; and Hayashi, H, "An Experimental Study on the Displacement Performance of RC Bridge Piers," Technical Report of Hanshin Expressway, Vol. 11, March 1991, pp. 21-28.
2)Ozaka, Y; Suzuki, M; Kuwasawa, S; and Ishibashi, T, "Load-deflection Characteristics of Reinforced Concrete Columns under Static Alternating Cyclic Loads," Proceedings of JSCE, No. 372, Vol. 5, Feb. 1988, pp. 45-54.
3)Ishibashi, T and Yoshino, S "Study on Deformation Capacity of Reinforced Concrete Bridge Piers Under Earthquake" Proceedings of JSCE, No. 390, Vol. 5, Feb. 1988, pp. 57-66.

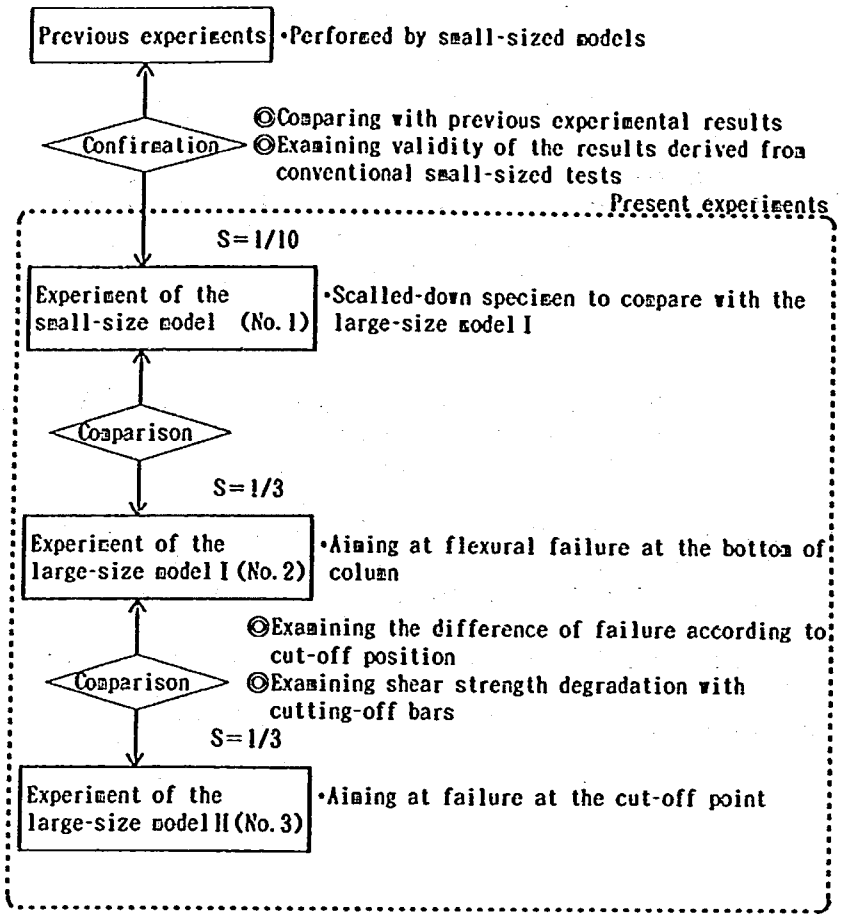


Fig. 1 Arrangement of experimental models

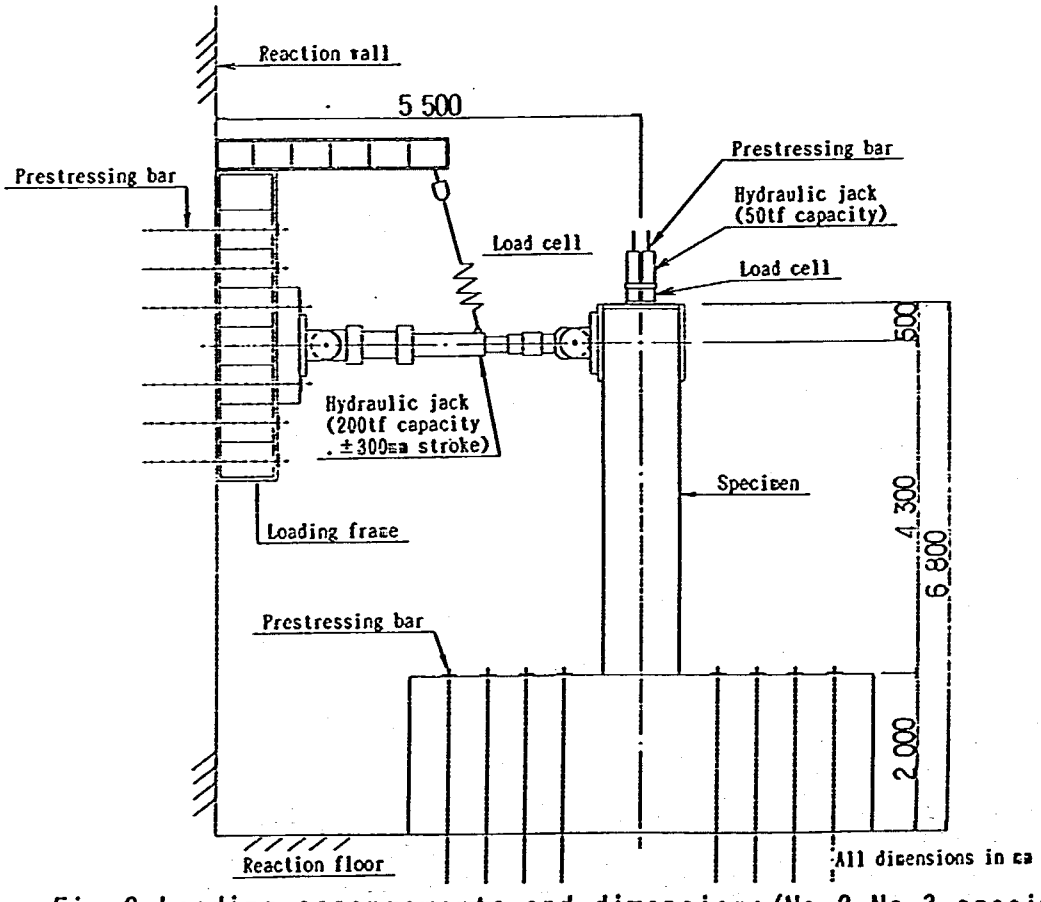


Fig. 2 Loading arrangements and dimensions (No. 2, No. 3 specimen)

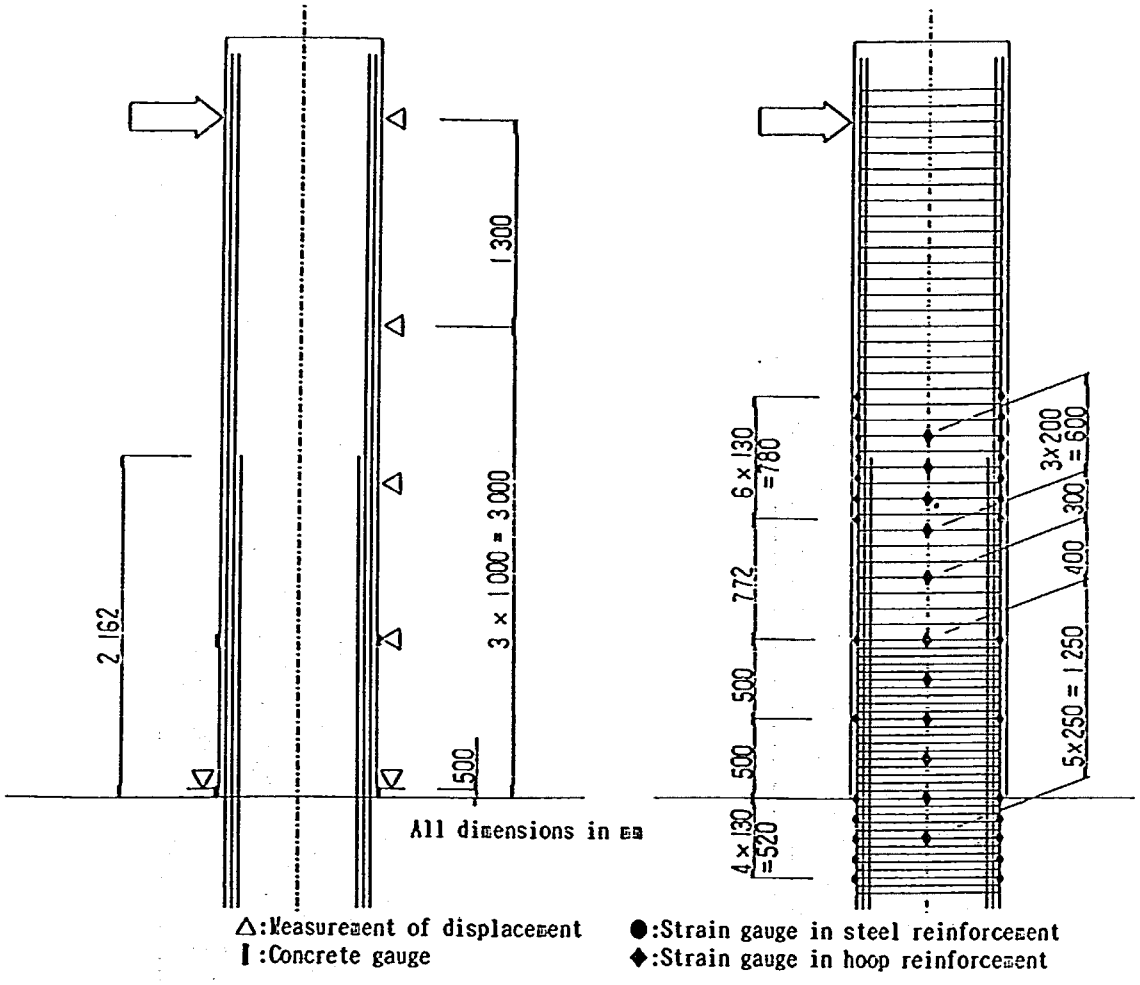


Fig. 3 Measurement locations

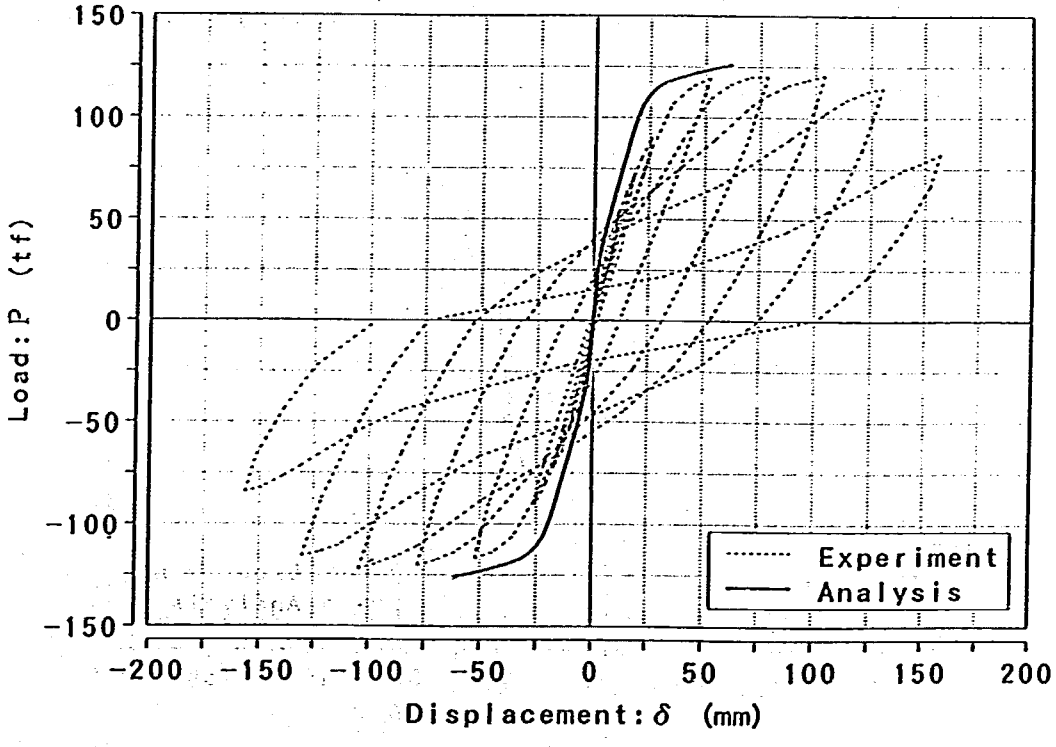


Fig. 4 Load-Displacement curves (No. 2)

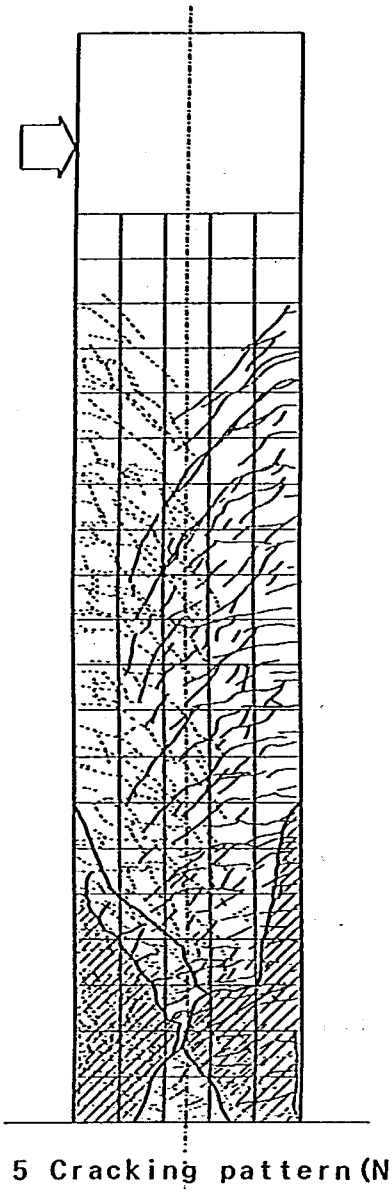


Fig. 5 Cracking pattern (No. 2)

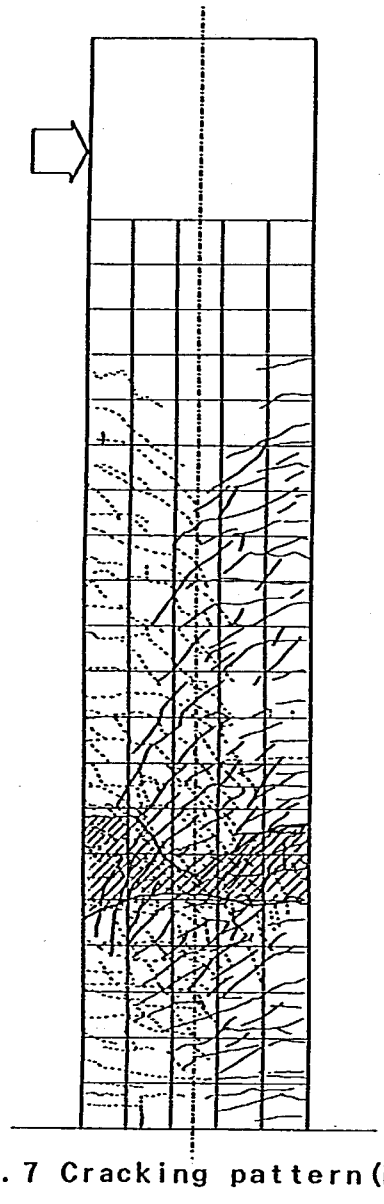


Fig. 7 Cracking pattern (No. 3)

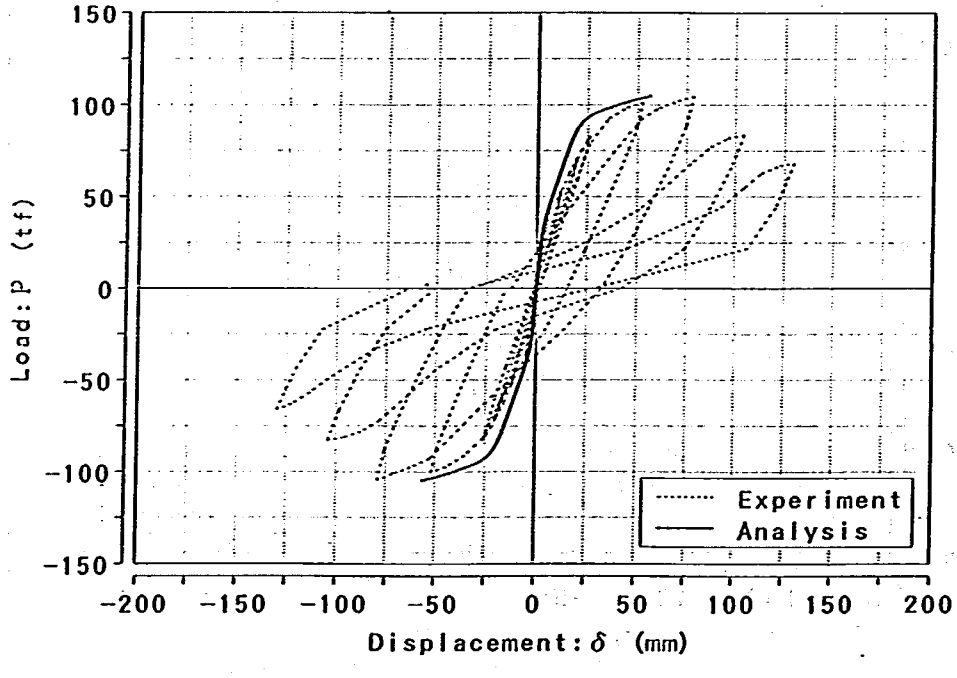


Fig. 6 Load-Displacement curves (No. 3)

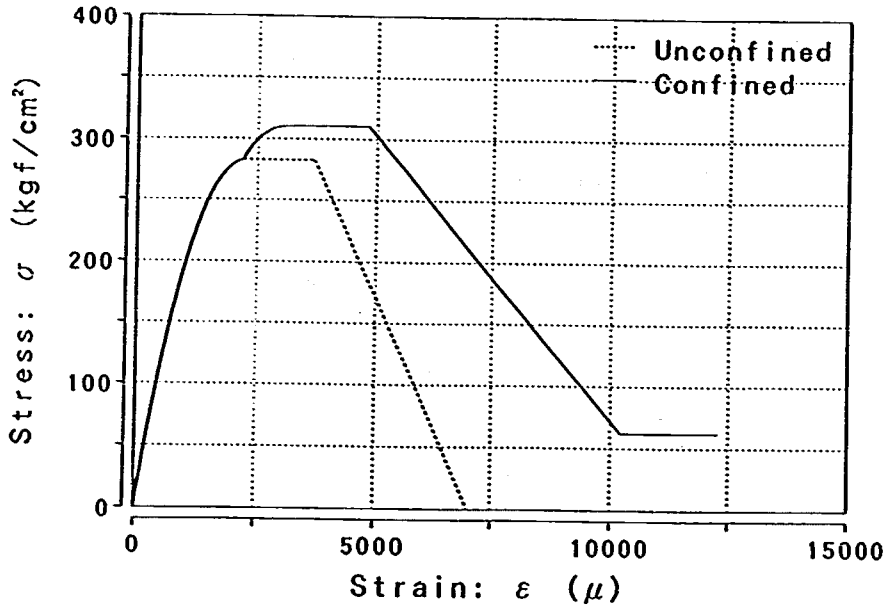


Fig. 8 Stress-Strain relationship of concrete

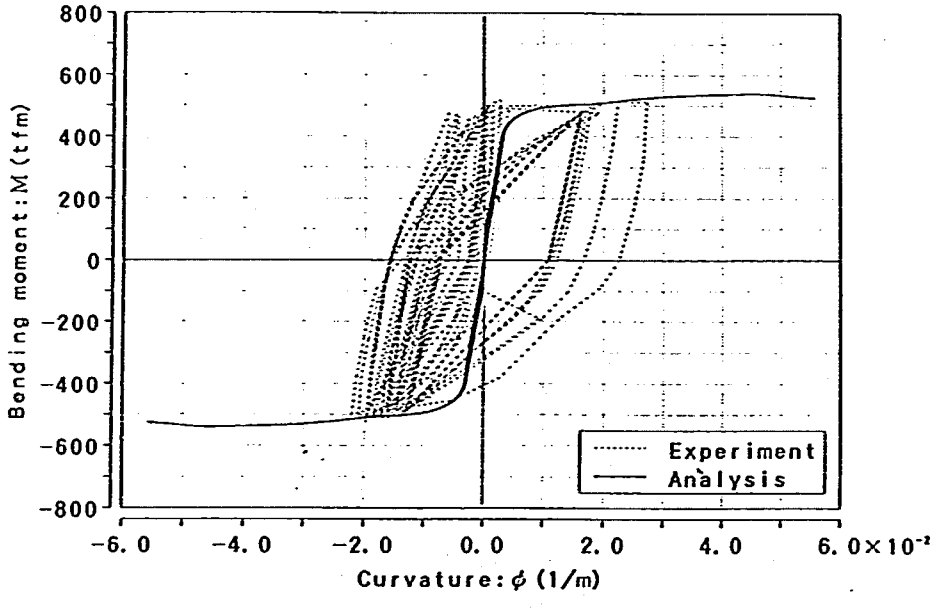


Fig. 9 Moment-Curvature loops (No. 2)

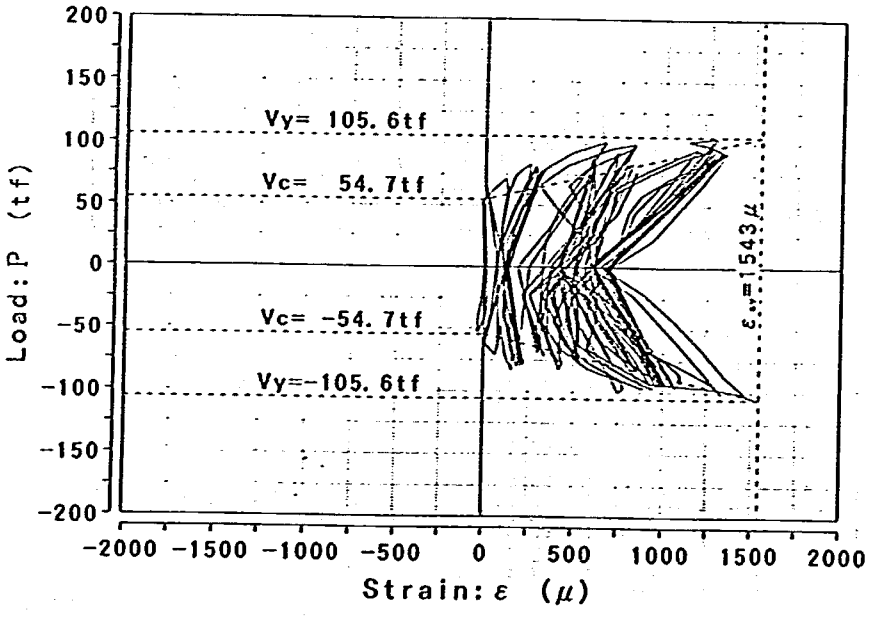


Fig. 10 Load-Strain curves for hoop reinforcement (No. 3)

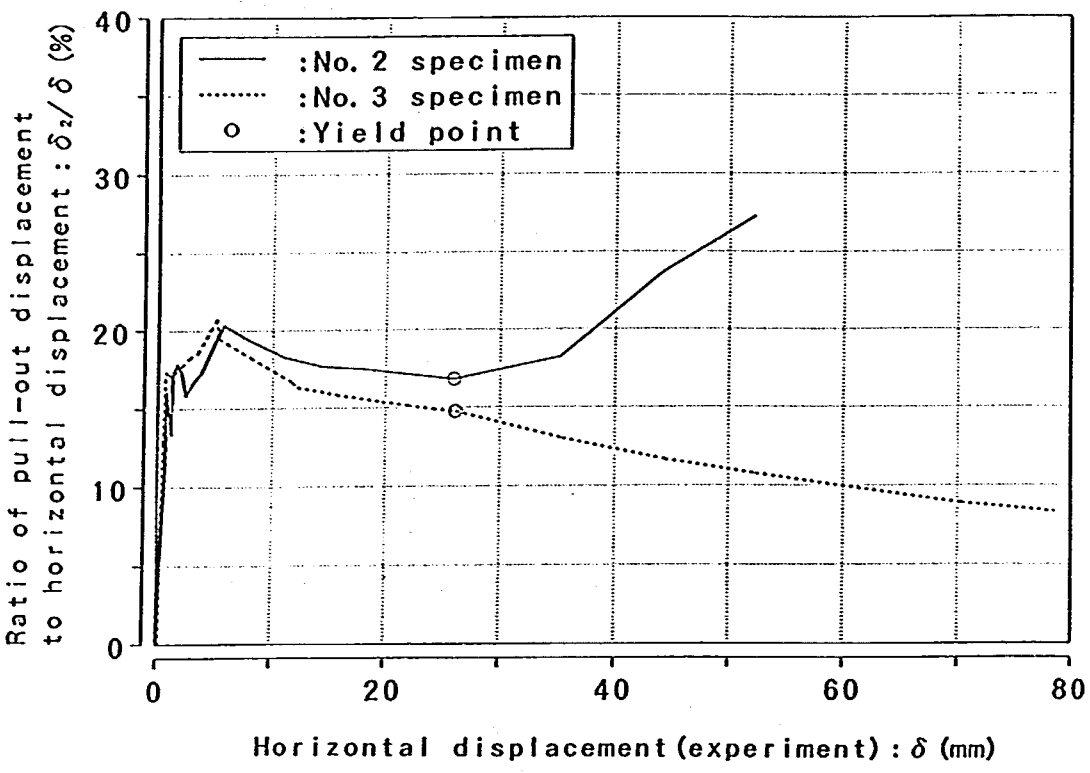


Fig. 11 Influence of pull-out displacement on horizontal displacement

Table 1 Horizontal load at the ultimate flexural strength(unit:tf)

Specimen		No. 1	No. 2	No. 3
Cut-Off	Analysis	—	155.8	99.1
	Experiment	—	—	104.7
Column base	Analysis	9.95	117.7	118.3
	Experiment	10.51	122.1	—

Table 2 Calculated shear strength (unit:tf)

Specimen	No. 1		No. 2		No. 3	
	V_c	V_y	V_c	V_y	V_c	V_y
Cut-Off	—	—	57.4	108.0	55.0	105.9
Column base	8.00	13.67	64.4	163.9	65.9	165.4

Table 3 The ratio of pull-out displacement to horizontal displacement

	Yielding	Ultimate
No. 1	50 %	70 %
No. 2	18 %	30 %
No. 3	16 %	13 %
Actual pier	12 %	9 %

COMPARISON OF THE SEISMIC DESIGN OF HIGHWAY BRIDGES IN CALIFORNIA AND IN JAPAN

By

Mohsen Sultan, P.E.
Senior Bridge Engineer
Division of Structures
California Dept. of Transportation
Sacramento, California, U.S.A

and

Kazuhiko Kawashima, D. Eng.
Head, Earthquake Engineering Division
Public Works Research Institute
Tsukuba Science City, Japan

1. INTRODUCTION

This paper presents preliminary results of a study on the comparative seismic design of highway bridges designed using both the California Department of Transportation (Caltrans) and Japanese seismic design specifications. Such comparison is aimed at providing a better understanding of the two seismic design methods and structural differences. The research project this paper is based on included two bridge design examples. A typical California highway bridge was designed using the Caltrans Bridge Design Specifications (BDS), and keeping the superstructure unchanged, it was redesigned using the Japanese specifications. Similarly, a typical Japanese bridge was first designed using the Japanese specifications, then was redesigned using the California method. Where appropriate, this paper highlights basic seismic design considerations and differences between the two design methods. In this paper, an emphasis on the Caltrans design details and seismic loading is provided.

2. GENERAL ASSUMPTIONS

Differences in the seismic design approach for highway bridges, between California and Japan, include the predominant structure type, the design method and seismic force levels. California bridges typically consist of a moment resisting frame system with monolithic joints connecting the superstructure to the substructure, whereas, in Japan, bearing type supports are typically used for those connections. Load factor (ultimate strength) design with force reduction, based on displacement or curvature ductility and risk factor, is the California approach. In Japan, the seismic force coefficient method based on allowable stresses is utilized. The ultimate capacity check of reinforced concrete piers or columns is performed using a ductility approach, where force levels of up to 1.0 g are applied to vertical support members.

In the process of redesigning the U.S. bridge using the Japanese method, the superstructure is kept unchanged, whereas, substructure components can be different, i.e. column or pier size, and their reinforcement, footings, number of piles, including size and capacity, and abutments are all permissible changes. The focus is to narrow the differences down to a minimum and concentrate on the seismic approach of both Japan and California. The maximum traditional design seismic force in both places is assumed, i.e. ground acceleration of 0.7 g in California, and force coefficient $k = 0.3$ in Japan.

3. BRIDGE DESCRIPTION

The California bridge as shown in Fig. 1, referred to in this paper as the U.S. bridge, is assumed to be a freeway connector having straight alignment and the following span configuration: 130 ft, 3 spans at 175 ft, 130 ft. It consists of a five span continuous, prestressed concrete box girder with single column bents. The girder is 7'-0" (2.13 m) deep and 42'-6" (12.95 m) wide as shown in Fig. 2.

Columns are fixed-fixed (top-bot) and are 65 feet long (to C.G.) supported on pile footings. Abutments are "seat type" supported on pile caps. As for foundations, driven piles with 100 ton service load capacity (Caltrans Class 100) for the bents and 70 ton capacity (Class 70) for the abutments were assumed, although the size in the equivalent Japanese bridge may differ. Only vertical piles are used, as battered piles are rare in Japan.

Soil type, as shown in Fig. 3, used in the design was based on soil conditions found in the vicinity of the Los Angeles area. It consists of a mixture of sand and silt slightly compact to dense with unit weight of 115-125 pcf. Standard penetration index ranges from 11 to 70. The internal friction angle is 25-35 degrees, cohesion is 0 - 1000 psf and the shear strength is 2.0 - 2.9 tsf. The predominant period of vibration of the ground is 0.35 second and the depth to rock like material is greater than 300 feet.

To increase the ultimate moment capacity of the box girder, the typical section is flared over a distance of 20 ft (6.10 m) to reach its maximum at the face of supports. This is done only at the bents not the abutments, since seat type abutments do not resist moments. Table 1 below shows the section properties at those locations. Fig. 4 shows the global axis designation.

Table 1- TYPICAL SECTION PROPERTIES

Location	Area (ft^2)	IZZ (ft^4)	IYY (ft^4)
At Supports	83.77	634.93	10086.61
Minimum Section	74.69	554.79	9449.00

Columns are round 8 feet in diameter, with the area A= 50.27 ft^2 and Izz=Iyy= 201.06 ft^4. Since column size is a permissible change in the redesign, the Japanese version utilizes a 9'- 2" by 19'- 7" (2.8X6 m) rectangular cross section with an area A= 180.74 ft^2 (16.8 m^2).

Table 2 lists dead load reactions. Trial (0) refers to the dead load portion present at time of prestressing, trial (1) refers to added dead load, such as overlay and barrier rail. These numbers do not include the bent cap portion that is not necessarily modeled in the static model. The Caltrans terminology utilizes the terms "column" and "bent" where the Japanese version refers to the same thing as "Pier". The term "Pier" has a specific definition according to Caltrans and therefore will only be used where appropriate.

Table 2- Dead Load Reactions* (Kips)

Loading	Abut 1	Bent 2	Bent 3	Bent 4	Bent 5	Abut 6
Trial (0) Top	566	2058	2138	2138	2058	566
Trial (0) Bot	-	2548	2629	2629	2548	-
Column Weight	-	490	490	490	490	-
Trial (1)	64	229	238	238	229	64

(*) Does not include additional dead load due to bent cap weight at the bents.

4. SEISMIC LOADING

In designing the column (Fig. 5), all load cases prescribed by the specifications are analyzed at all critical locations. The loading at the top of column did control the Caltrans design with the maximum longitudinal seismic load case being the controlling group (Grp. VII case 2). A summary of seismic load input is presented in Table 3.

Table 3- SEISMIC LOADING

(a) Top of Column

	ARS UNREDUCED FORCES	
	CASE 1	CASE 2
MY trans	116257	34877
MX Long	28339	94465
P Axial	104	347

P/S Moment = 3325 k-ft, P (DL)= 2589 k

(b) Bottom of Column

	ARS UNREDUCED FORCES	
	CASE 1	CASE 2
MY trans	61520	18456
MX Long	27423	91432
P Axial	104	347

P/S Moment = 4472 k-ft, P (DL)= 3079 k

Earthquake forces were reduced by the ductility and risk factor Z=5.30. Applied factored moments (reduced) and axial loads are summarized in Table 4.

Table 4- Applied Earthquake Loads

Grp	My	Mx	Comb M	P	Mu	Mu/M
VII-I	21935	8974	23700	2693	24603	1.04
VII-2	6581	21451	22437	2936	24942	1.11

Boundary conditions are essential to the modal behavior of the structure. In the Caltrans design for the subject bridge, all column connections are modeled as fixed top (to the

superstructure) and bottom (to the footings). Abutments possess transverse fixity which means they are restricted only in the transverse direction. However, soil stiffnesses in the longitudinal and transverse directions are used to model the embankment behind the abutment wall.

5. RESPONSE SPECTRUM ANALYSIS RESULTS

Generally, Caltrans utilizes a linear multi-modal dynamic analysis method in calculating maximum forces and displacements, where, an appropriate ARS curve is selected depending on the foundation conditions at the proposed site. The designer may choose the number of vibration modes to be utilized in combining modal maxima and thus computing maximum displacements and forces. The Caltrans analysis is based on the Complete Quadratic Combination (CQC) method as reported by the program "SEISAB". The U.S. bridge dynamic results are concluded from 15 modes of vibration. The Japanese bridge results are reported as 15 modes in the longitudinal direction and 15 modes in the transverse direction. Table 5 summarizes the modal response of the U.S. bridge.

Table 5- Bridge Modal Response (Caltrans Method)

MODE	PERIOD (sec)	SPECTRAL VALUE (g)	DIRECTION
1	1.344	0.84	Transverse
2	1.014	0.93	Longitudinal
3	0.737	1.01	N.P.
4	0.547	1.08	Vertical
5	0.463	1.08	Longitudinal
6	0.400	1.07	Transverse
7	0.382	1.06	Vertical
8	0.301	1.01	Longitudinal
9	0.296	1.01	Vertical
10	0.247	0.96	N.P.
11	0.167	0.88	Longitudinal
12	0.166	0.88	Transverse
13	0.166	0.88	Vertical
14	0.151	0.86	Vertical
15	0.137	0.85	Longitudinal

Table 6 lists the maximum displacements (in feet) at various locations of the structure using the Caltrans method. Design displacements are derived from this list and combined in accordance with the loading combination criteria.

Table 6- DISPLACEMENTS (CALTRANS METHOD)

Direction	Abut 1	Bent 2	Bent 3	Bent 4	Bent 5	Abut 6
Max Lng	0.791	0.788	.0.786	0.786	0.788	0.791
Max Tra.	0.019	0.811	1.521	1.521	0.811	0.019

Table 7 shows the natural period and mass participation factors of the Japanese design.

Table 7- BRIDGE MODAL RESPONSE (JAPAN METHOD)

A- LONGITUDINAL DIRECTION

MODE	PERIOD (sec)	Ratio of Mass Participation
1	0.685	76.14
2	0.452	0.00
3	0.424	0.20
4	0.396	0.00
5	0.300	0.00
6	0.298	2.21
7	0.178	0.00
8	0.127	0.45
9	0.123	0.00
10	0.113	9.70
11	0.108	0.00
12	0.079	0.03
13	0.056	0.00
14	0.044	0.01
15	0.040	0.00

B-TRANSVERSE DIRECTION

MODE	PERIOD (sec)	Ratio of Mass Participation
1	0.661	64.25
2	0.539	0.00
3	0.370	7.54
4	0.254	0.00
5	0.173	3.73
6	0.140	0.00
7	0.121	2.18
8	0.108	0.00
9	0.097	2.14
10	0.080	7.37
11	0.080	0.00
12	0.069	0.00
13	0.066	1.85
14	0.059	0.00
15	0.059	1.78

Design of the footings by the Caltrans method was controlled by the probable plastic moment (Mp), when applied at 45 degrees angle to the footing. The maximum pile compressive load is 335 kips (max allowable 400 k)and maximum uplift force is -163 kips (max allowable -200 k). For pile layout see Fig. 6.

Table (8) below summarizes the resultant design

Table 8- COLUMN DESIGN COMPARISON

DESCRIPTION	CALTRANS METHOD	JAPAN METHOD
COLUMN SIZE	8'-0" Φ	2.8X6.0 m (Rectangular)
COL GROSS AREA	50.27 sq. ft (4.67 sq. m)	16.8 sq. m (180.74 sq. ft)
COLUMN REINFORCEMENT	#14 total 44 A_S= 99 in² (1.368 %) #6 Spiral @ 4 1/4 " (0.45 %)	
FOOTING DEPTH	4'-3" (1300 mm)	2200mm minimum
FOOTING SIZE	21'X21' (6400mmX6400mm)	9000mmX9000mm
FOOTING REINFORCEMENT	Top #6 total 52 (both ways) Bottom #10 total 65 Transverse #10 total 48 Longitudinal	
PILES	40 -15" Diam. Piles/Length (60') 100 Ton Capacity	28 Piles Φ 600X18.3 m

The abutment footing required a total of 24, 15 inch diameter, piles with 70 ton capacity (Class 70) using the Caltrans method (Fig. 8). By comparison, it required 8, 600 mm diameter, piles using the Japan method. Under the California method, abutments are designed such that no earthquake loads can be transferred into their foundation. Therefore, abutment footings and piles are not designed to withstand seismic forces .

6. CONCLUSION

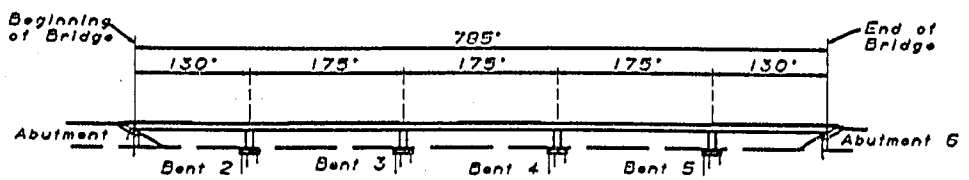
Design data for an example bridge were presented along with factors affecting the final design. One of the most obvious results of the comparison is the size of substructure components (columns), size of foundations (footings), and the natural period of the structure. In this example, the Japanese bridge uses a rectangular pier three times larger than the Caltrans round column. The Japanese footing area and depth are approximately 75 % larger than the Caltrans footing. Length of piles used with both approaches is very similar. Finally, primarily due to the larger substructure, the Japanese bridge has about half the natural period of its Caltrans equivalent, and as such, is twice as stiff.

7. ACKNOWLEDGMENT

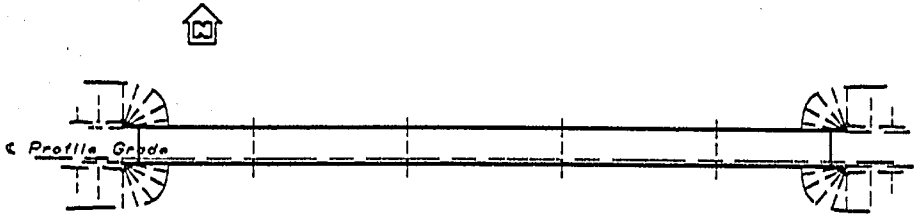
The authors wish to acknowledge the Japan Science and Technology Agency (STA), the U.S. National Science Foundation (NSF), the Public Works Research Institute (PWRI) in Tsukuba, Japan, and the California Department of Transportation for their support and cooperation with the authors and who made their collaboration possible.

8. REFERENCES

1. Kawashima, K. and Hasegawa, K., "Evaluation of Lateral Inertia Force of Bridges for Seismic Design", Seventh US-Japan Bridge Workshop, Tsukuba Science City, Japan. May 8 and 9, 1991.
2. Iwasaki, T., Kawashima, K. and Hasegawa, K., "New Seismic Design Specifications for Road Bridges in Japan.", 22nd Joint Meeting, US-Japan Panel on Wind and Seismic Effects, U.J.N.R, Gaithersburg, Maryland, May 1990.
3. "Standard Specifications for Highway Bridges", Thirteenth Edition, 1983, by the American Association of State Highway and Transportation Officials, Inc. (AASHTO) with Revisions by Caltrans through June 1990.
4. "Abutment Investigation", Bridge Design Aids by Caltrans, January 1988.
5. "Dynamic Model Assumptions and Adjustments", Bridge Design Aids by Caltrans, October 1989.
6. Sultan, M. "Countermeasures at Caltrans following the Loma Prieta Earthquake", Proceedings of the Nineteenth Japan Road Conference, Japan Road Association, Tokyo, Japan, October 1991.



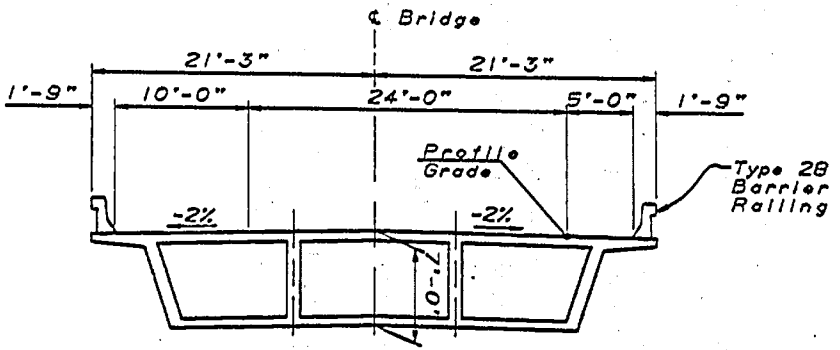
ELEVATION

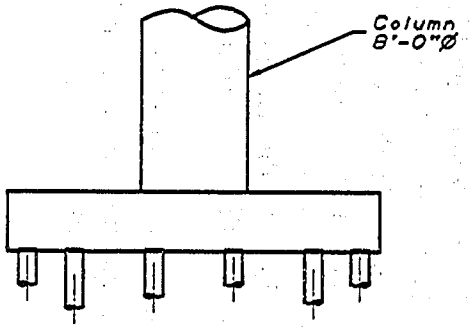


PLAN

GENERAL PLAN - CALTRANS METHOD

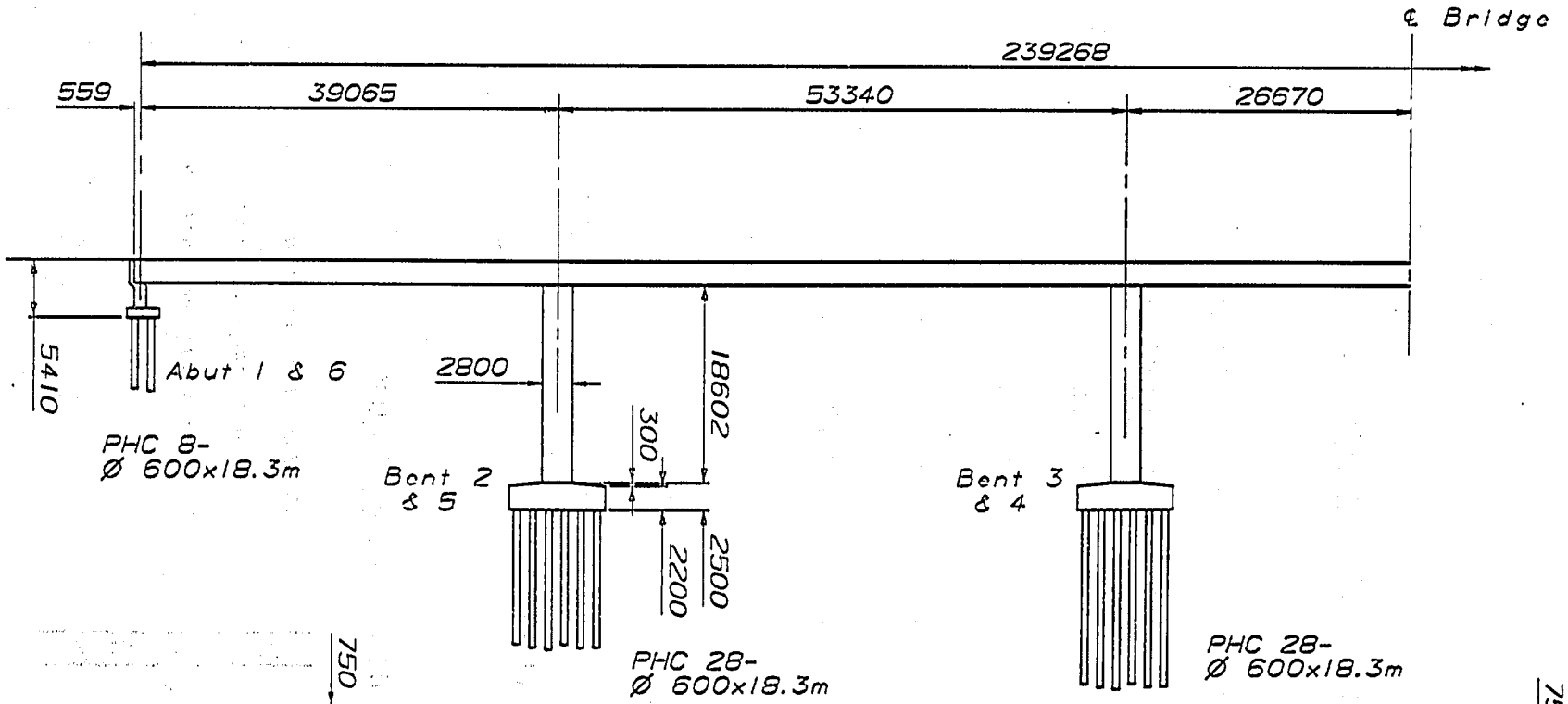
Fig 1 (a)



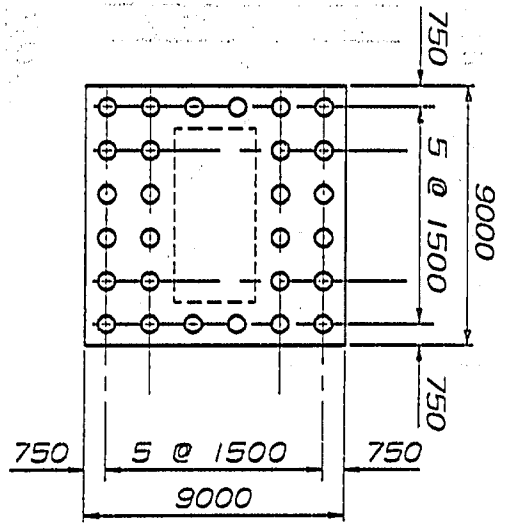


TYPICAL SECTION - CALTRANS METHOD

Fig 2

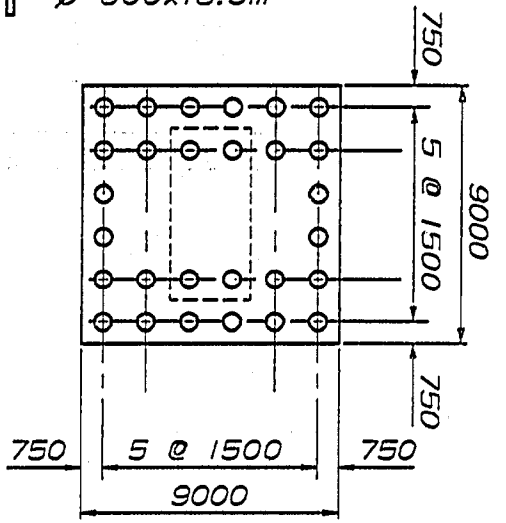


ELEVATION
NO SCALE

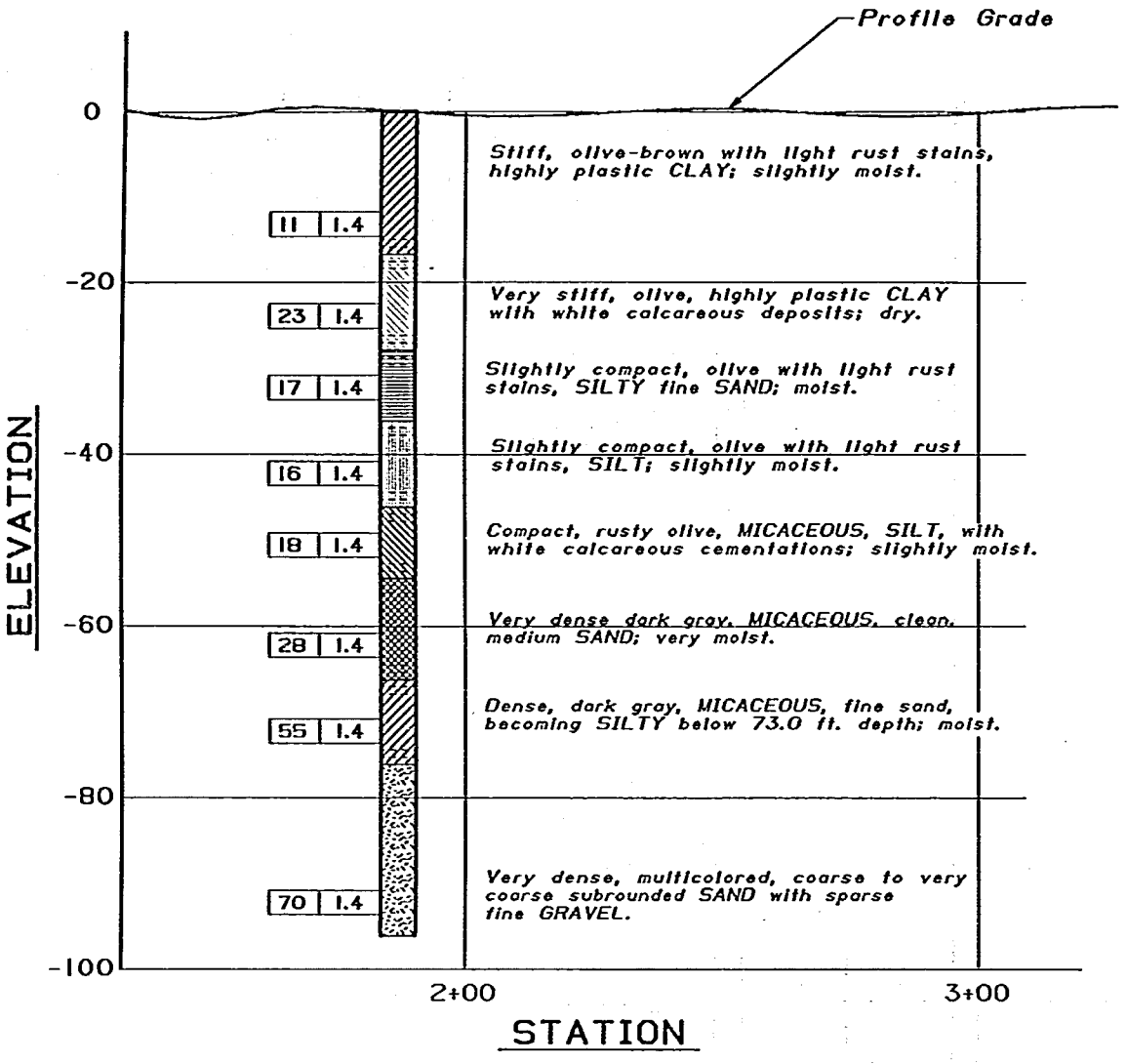


(BENT 2 & 5)
PILE LAYOUT
NO SCALE

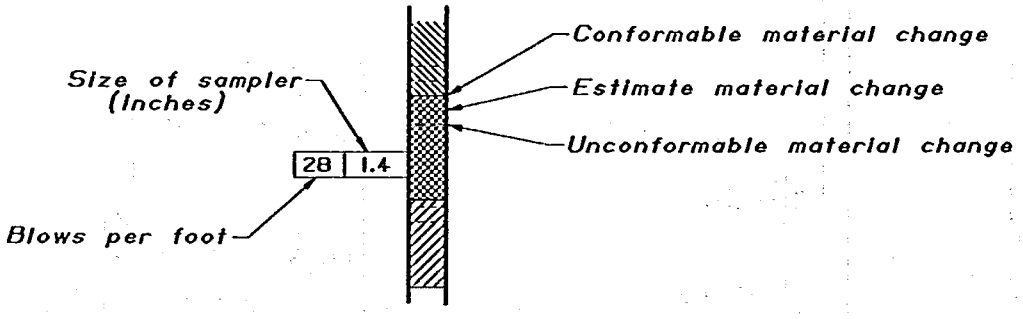
GENERAL PLAN - JAPAN METHOD
Fig 1 (b)



(BENT 2 & 5)
PILE LAYOUT
NO SCALE

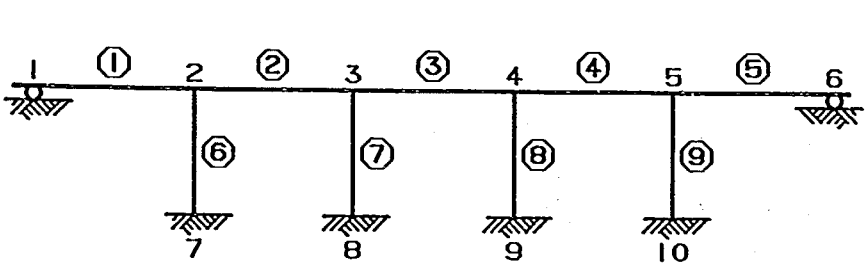


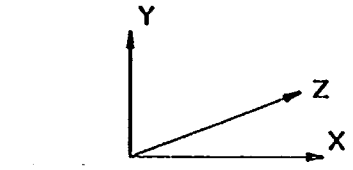
LEGEND OF BORING OPERATIONS



SOIL PROFILE

Fig 3





LEGEND

(1) Denotes Member Number

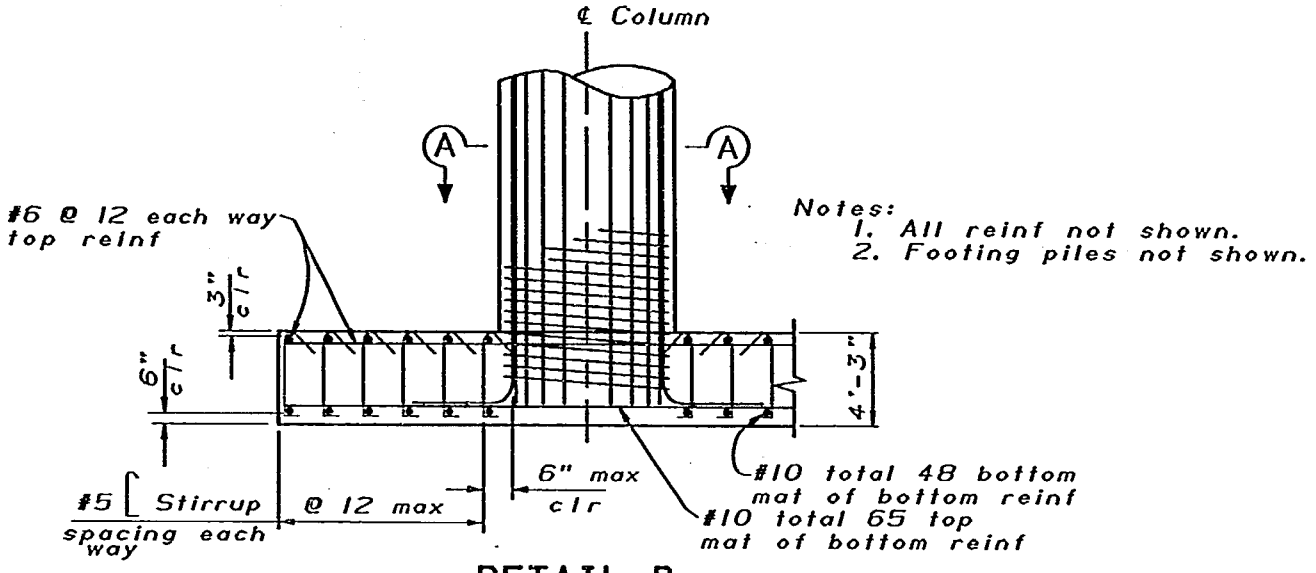
1 Denotes Node Number

Roller Connection

Fixed Connection

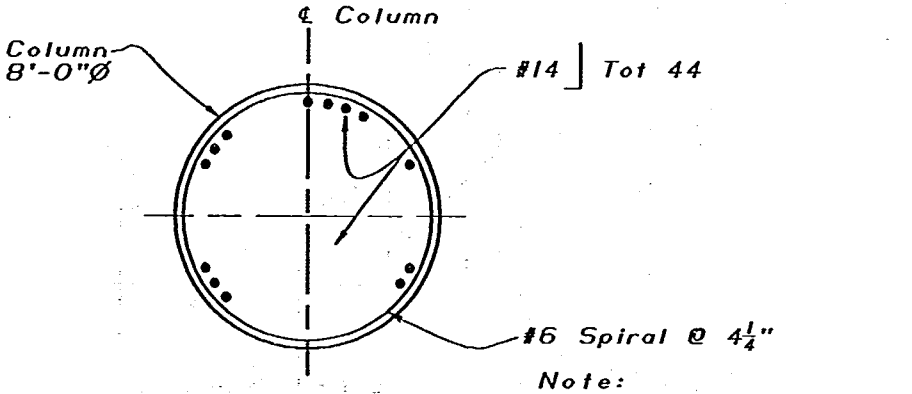
STATIC MODEL - CALTRANS METHOD

Fig 4



Notes:
1. All reinf not shown.
2. Footing piles not shown.

DETAIL B

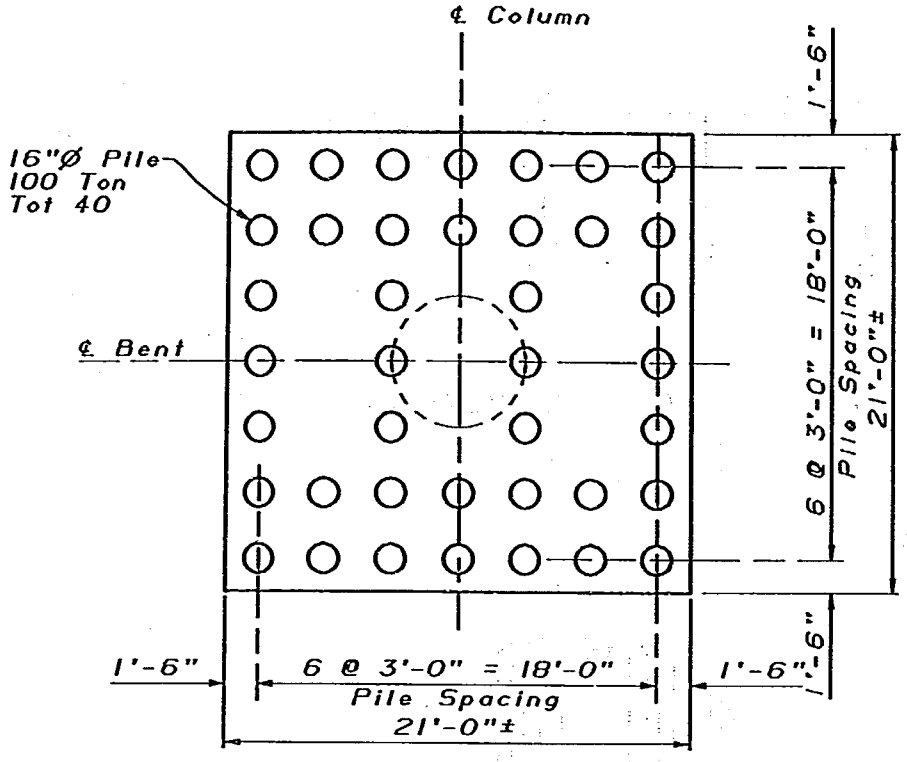


Note:
All reinf not shown.

SECTION A-A

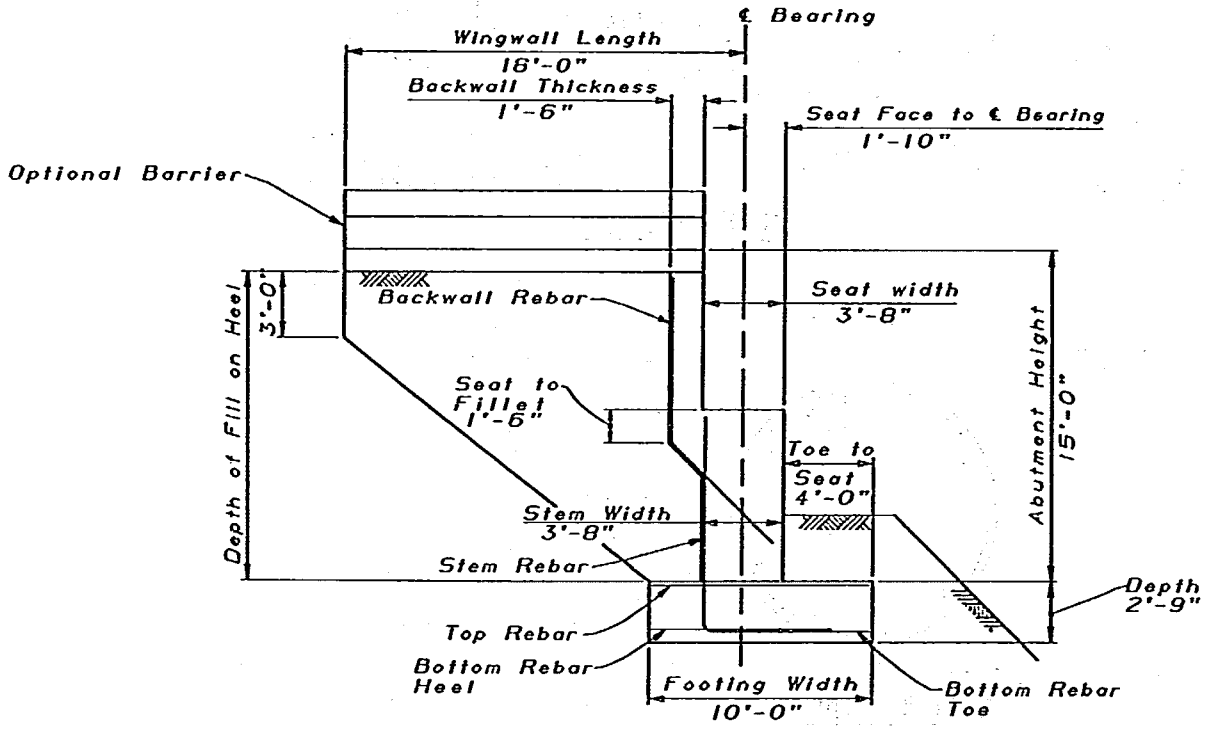
COLUMN & FOOTING DETAILS - CALTRANS METHOD

Fig 5



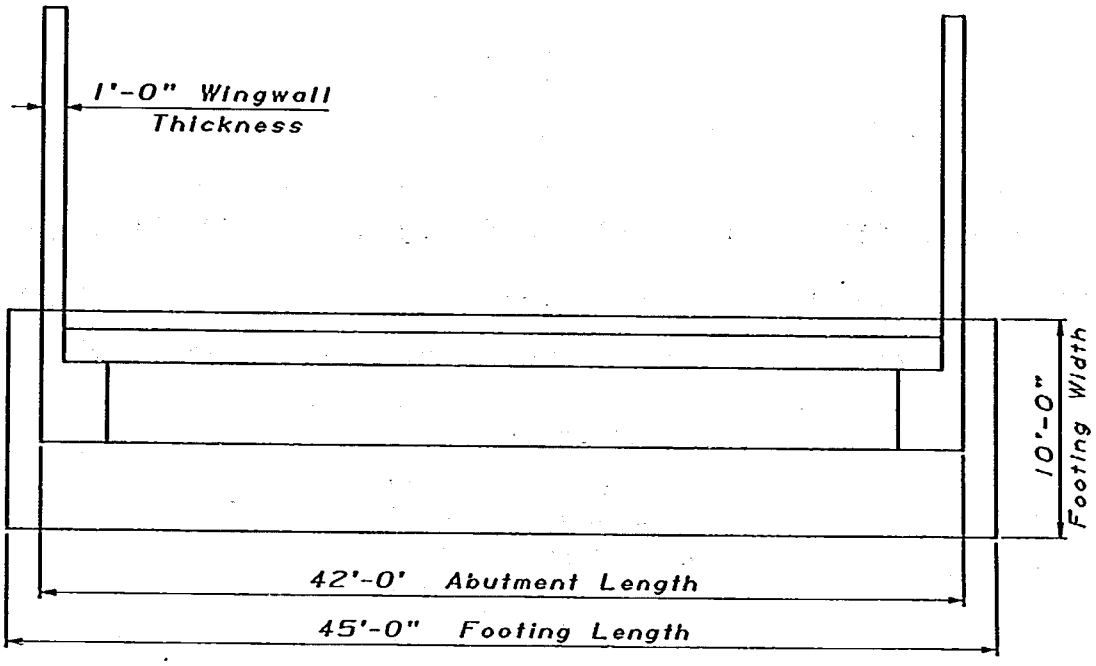
FOOTING PLAN & PILE LAYOUT - CALTRANS METHOD

Fig 6



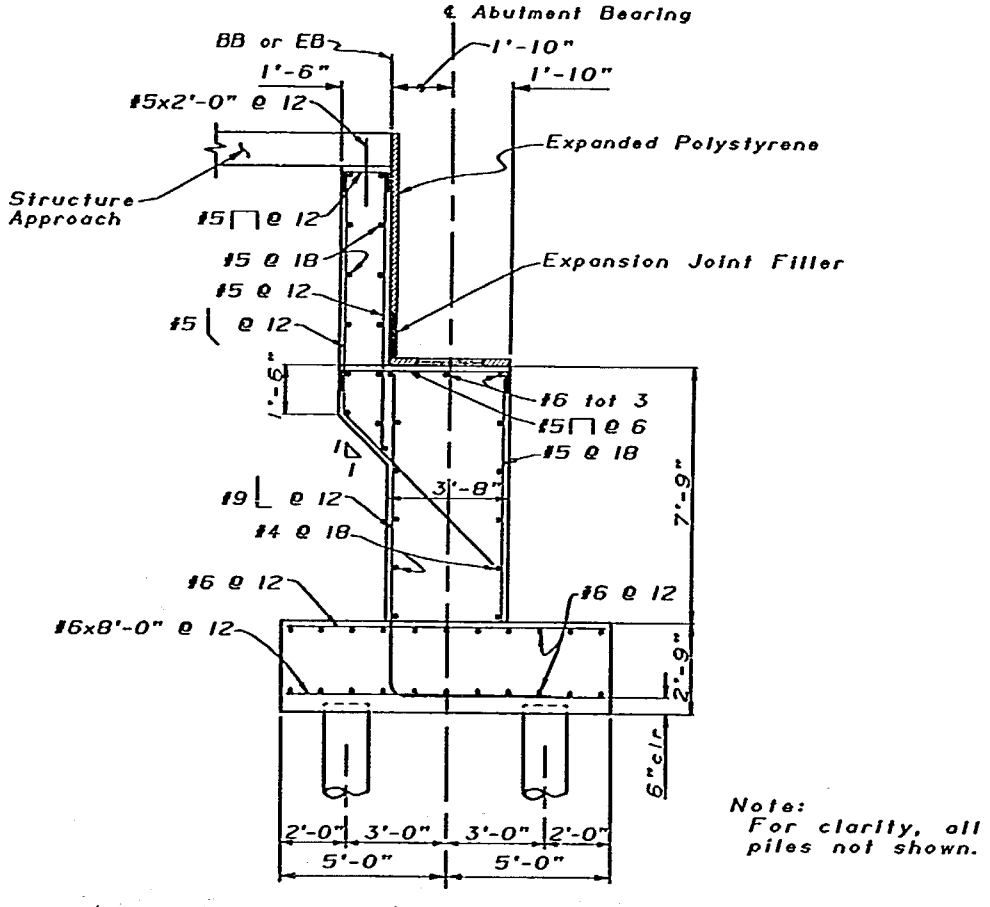
ABUTMENT ELEVATION - CALTRANS METHOD

Fig 7 (a)



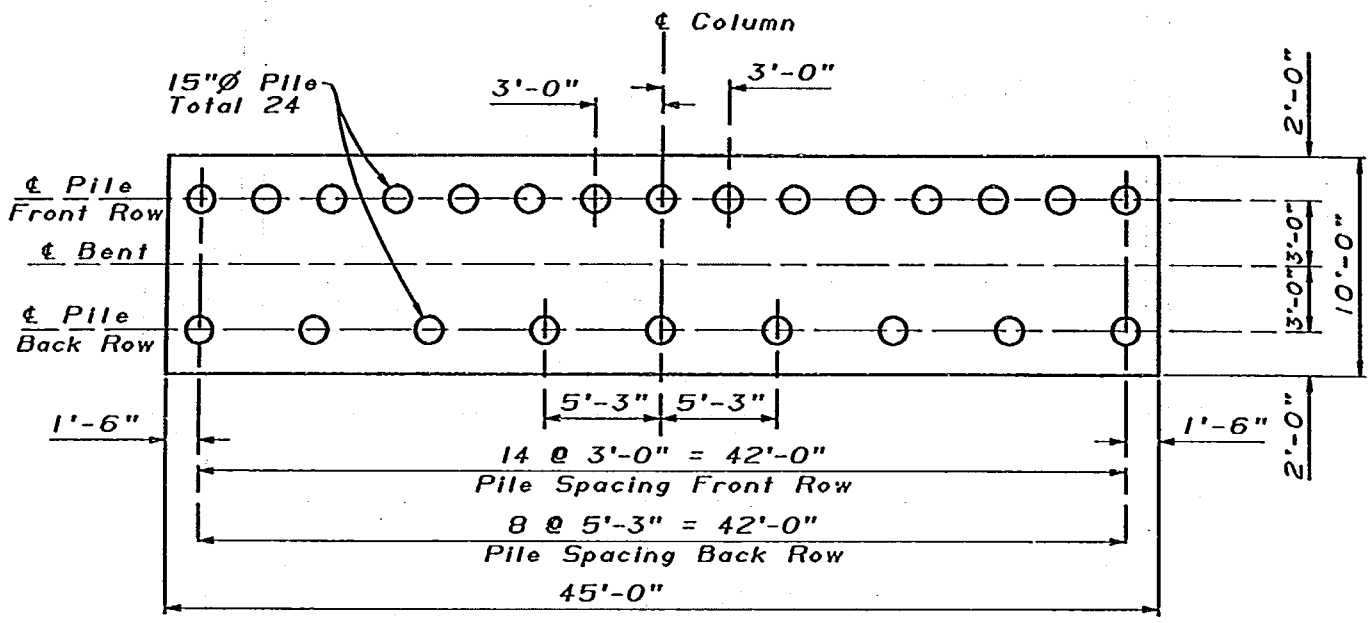
ABUTMENT PLAN - CALTRANS METHOD

Fig 7 (b)



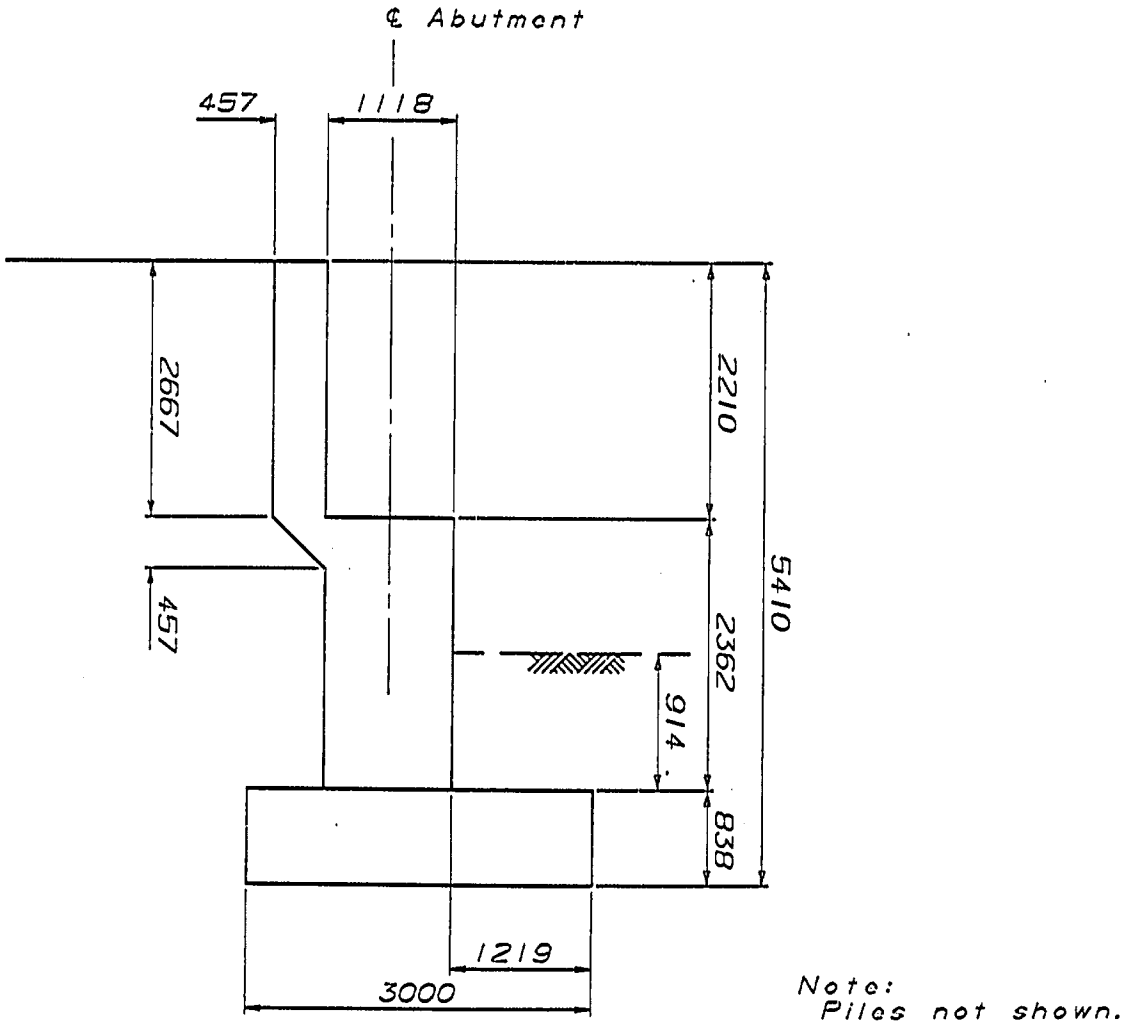
ABUTMENT SECTION - CALTRANS METHOD

Fig 7 (c)



ABUTMENT PILE LAYOUT - CALTRANS METHOD

Fig 8



ABUTMENT DETAIL - JAPAN METHOD

Fig 9

Analysis of Ground Motion Characteristics

H. Ohtsuka Head, Ground Vibration Division, PWRI
K. Tokida Director, Kanazawa Work Office
K. Tamura Road Administration Division, Road Bureau
M. Kaneko Research Engineer, Ground Vibration Division, PWRI
H. Fukada Sendai Work Office

Ministry of Construction

ABSTRACT

Two dimensional response analyses of ground are conducted to study the effects of geometric irregularities of subsurface layers on the seismic ground motion characteristics. The relation between the maximum acceleration, displacement and acceleration response spectrum on the ground surface and their distribution and geometric irregularities of surface layers is discussed and two dimensional responses are compared with one dimensional ones of the horizontally stratified layers.

INTRODUCTION

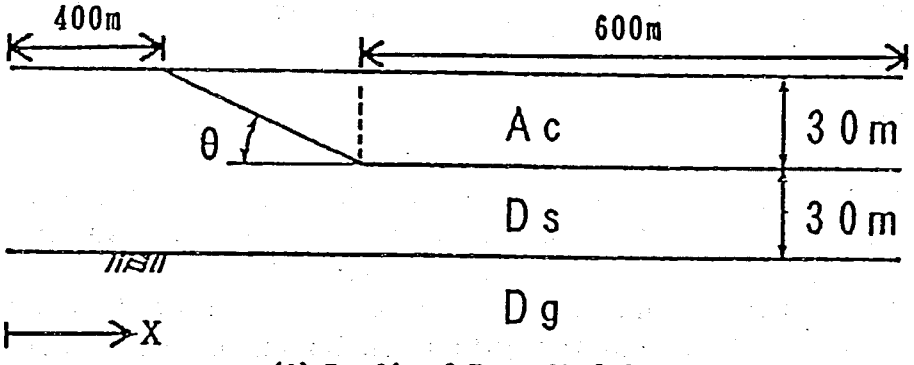
The seismic ground motion characteristics in the surface strata were mainly studied by one-dimensional approaches, assuming vertical propagation of shear waves. However, it has been well recognized that the ground motions are strongly affected by two- or three-dimensional ground irregularities basing on the recent accumulation of strong motion records and development of analytical procedure. For example, it was reported that the ground motion in the Mexico City was much amplified by the soft basin sediment in the 1985 Mexico Earthquake [1] .

From this point of view, two-dimensional earthquake response analyses for subsurface ground models are conducted to study the ground motion characteristics induced by irregular soil profiles. A computer program FLUSH [2] is employed in numerical calculations for tow-dimensional ground models. Two kinds of subsurface ground models are considered; Inclined Base Model and Basin Model, and the dimensions of geometric irregularities: inclined base gradient and spread of surface layer are parametrically changed. The maximum acceleration, displacement and acceleration response

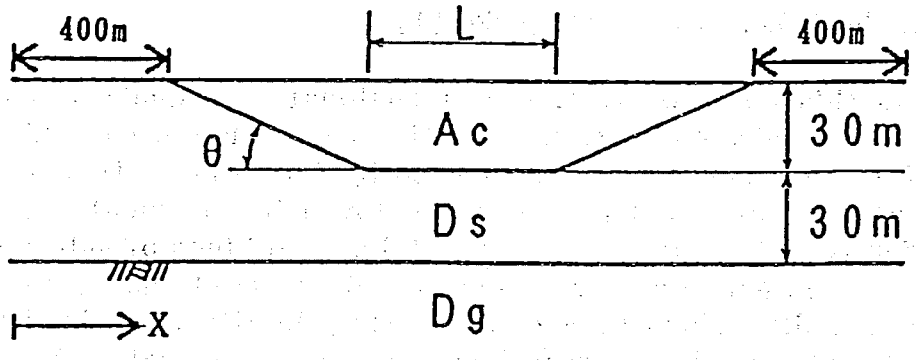
spectrum are considered as representatives of ground motion characteristics. The distribution characteristics of these quantities on the ground surface are studied considering the effects of geometric irregularities, and furthermore two-dimensional responses are compared with the one-dimensional ones of horizontally stratified layers using a computer program SHAKE [3] .

ANALYTICAL GROUND MODELS

The two ground models shown in Figure 1: Inclined Base Model and Basin Model are considered for two-dimensional response analysis of ground. They are designated to simulate typical soft alluvial soil profiles with geometric irregularities. The Ac, Ds and Dg layers represent the alluvial clay, diluvial sand and diluvial gravel layers, respectively. As shown in Figure 1, the thickness of the Ac layer and As layer is ranging from 0 to 30 m and 30 to 60 m, respectively, according to the inclined base gradient: $\tan\theta$. The length of the As layer with equivalent thickness from the right-hand boundary of the ground model is assumed constant to be 600 m, and the one of the Ds layer with equivalent thickness from the right- and/or left-hand boundaries of the ground model



(1) Inclined Base Model



(2) Basin Model

Figure 1: Analytical ground models

Table 1: Soil properties for modeled layers

Layer	Unit Weight [gf/cm^3]	Shear Wave Velocity [m/s]	Poisson Ratio
Ac	1.60	150	0.45
Ds	1.85	270	0.40
Dg	2.10	500	0.40

Table 2: Input ground motions recorded in past earthquakes

Record	Earthquake	Date	Magni -tude	Epicentral Distance [km]
PWRI	Ibaraki-Ken Nanbu	2/27/83	6.0	22
Kaihoku	Miyagi-ken Oki	6/12/78	7.4	83
Kannon-zaki	Chiba-ken Towho-Oki	12/17/87	6.7	69
Rincon Hill	Loma Prieta	10/17/89	7.1	95

is assumed constant to be 400 m. The horizontal coordinate: X indicates the length from the lefthand boundary of each ground model. The gradient of the inclined base of the As layer: θ is changed for three cases in the case of Inclined Base Model: $\tan\theta$ = 1/5, 1/2 and ∞. In the case of Basin Model, the gradient (θ) is changed same with the Inclined Base Model, and the length of central horizontal base of the As layer: L is changed for two cases: 150 and 300 m. The Dg layer is considered the base layer for earthquake response analyses, and the viscous boundary is attached between the Ds and Dg layers. Vertical moving is restrained for the nodal points on the lateral boundaries. The soil properties assumed for modeling layers are listed in Table 1.

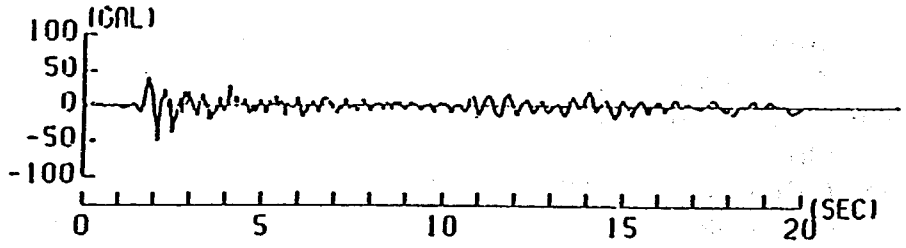
INPUT GROUND MOTIONS

The four recorded ground motion data shown in Table 2 are employed as input motions for the analyses in this paper. The PWRI record was obtained in the diluvial gravel layer at the depth of 46 m from the ground surface [4], and the other three records were obtained on the rock sites: the Kaihoku record [5], the Kannonzaki record [6] and Rincon Hill record [7]. Figures 2 and 3 show acceleration time histories and acceleration response spectra of these four records, respectively. As seen from these figures, strong motion records with different predominant fre-

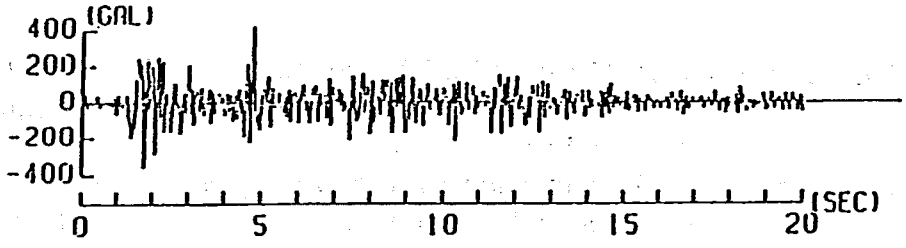
quencies are selected as input motions. In the following seismic response analyses, the maximum peak acceleration of recorded motions is modified so that the peak acceleration at the bottom of Ds layer is 100 gals or 150 gals.

SEISMIC RESPONSE ANALYSES OF GROUND

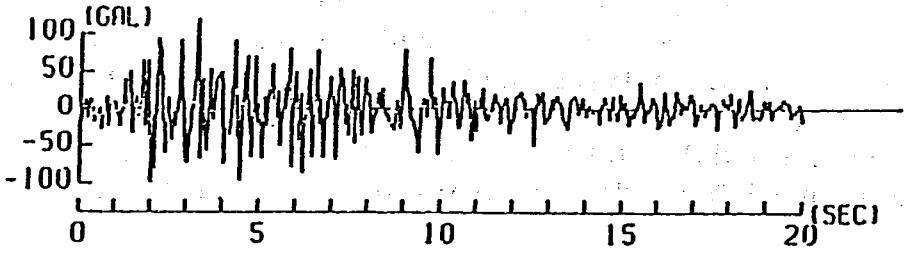
Computer program FLUSH [2] and SHAKE [3] are employed for two-dimensional and one-dimensional response analyses of ground models, respectively. Nonlinear behavior of soils are considered by the equivalent linear method. Figures 4(1) and 4(2) show the shear modulus reduction and damping ratio relationships with shear strain for the Ac layer and As layer, respectively [8,9] .



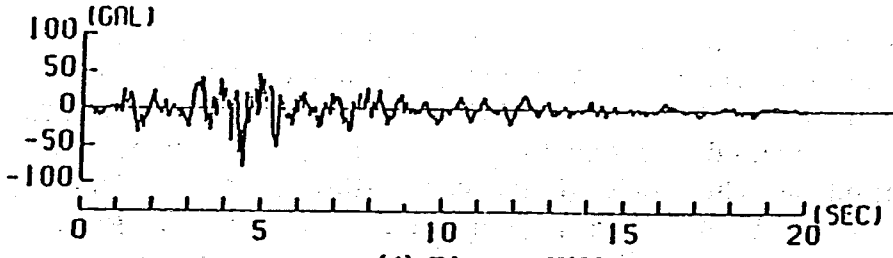
(1) PWRI



(2) Kaihoku

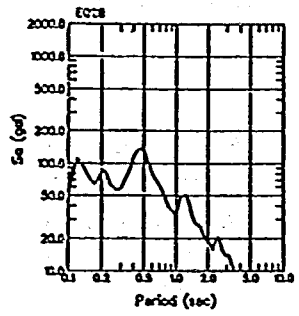


(3) Kannonzaki

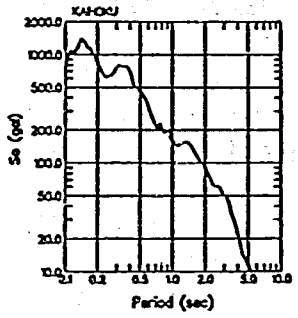


(4) Rincon Hill

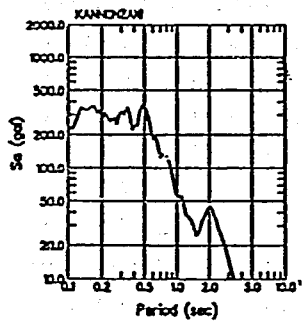
Figure 2: Time histories of input ground motions



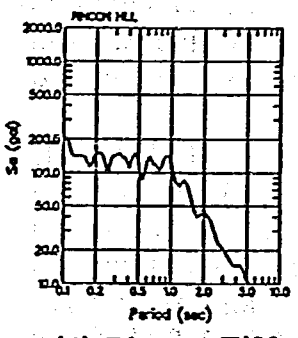
(1) PWRI



(2) Kaihoku

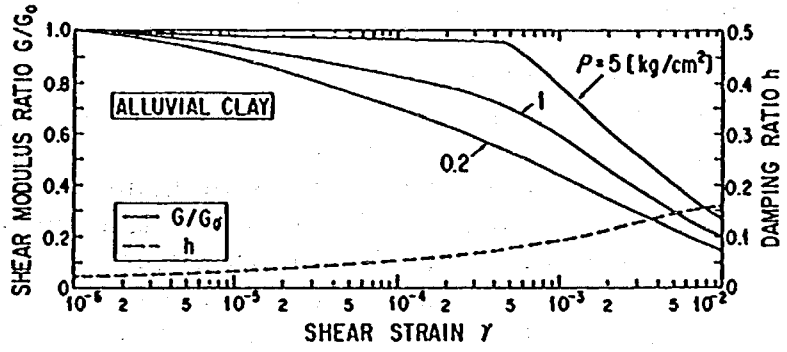


(3) Kannonzaki

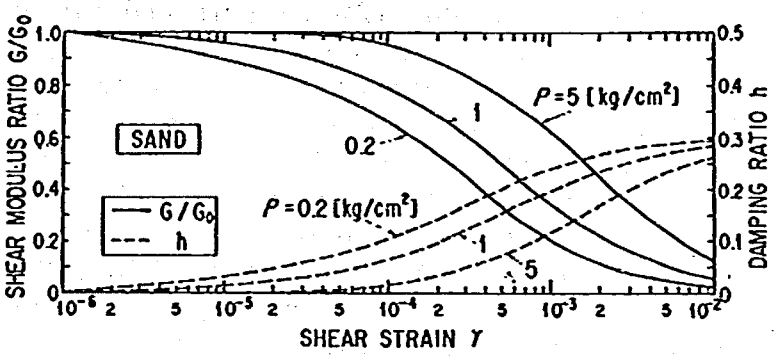


(4) Rincon Hill

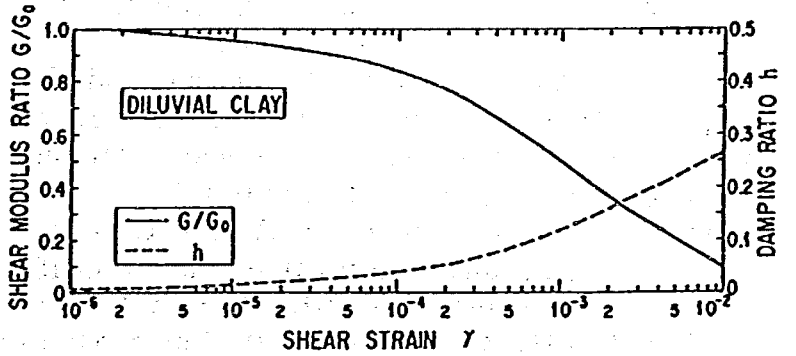
Figure 3: Acceleration response spectra of input ground motions



(1) Ac layer



(2) As layer



(3) Ds layer

Figure 4: Assumed dynamic properties of modeled layers

DISTRIBUTION OF MAXIMUM GROUND ACCELERATION ON GROUND SURFACE IN TWO-DIMENSIONAL ANALYSES

Inclined Base Model

The upper figures of each Figure 5(1), 5(2) and 5(3) show the distribution of maximum ground acceleration on the ground surface calculated by four kinds of input motions using maximum acceleration amplitude of 100 gals in the case of Inclined Base Models with $\tan\theta = \infty$, 1/2 and 1/5, respectively. On the other hand, the lower figures of each Figure 5(1), 5(2) and 5(3) show the distribution of the mean and the standard deviation: S.D. of four different maximum ground acceleration ratios normalized using the maximum ground acceleration at the point of X = 200 m.

From these figures, it can be seen that the maximum ground accelerations on the ground surface are affected by the geometric irregularity of subsurface layers and the characteristics of each result are shown as follows:

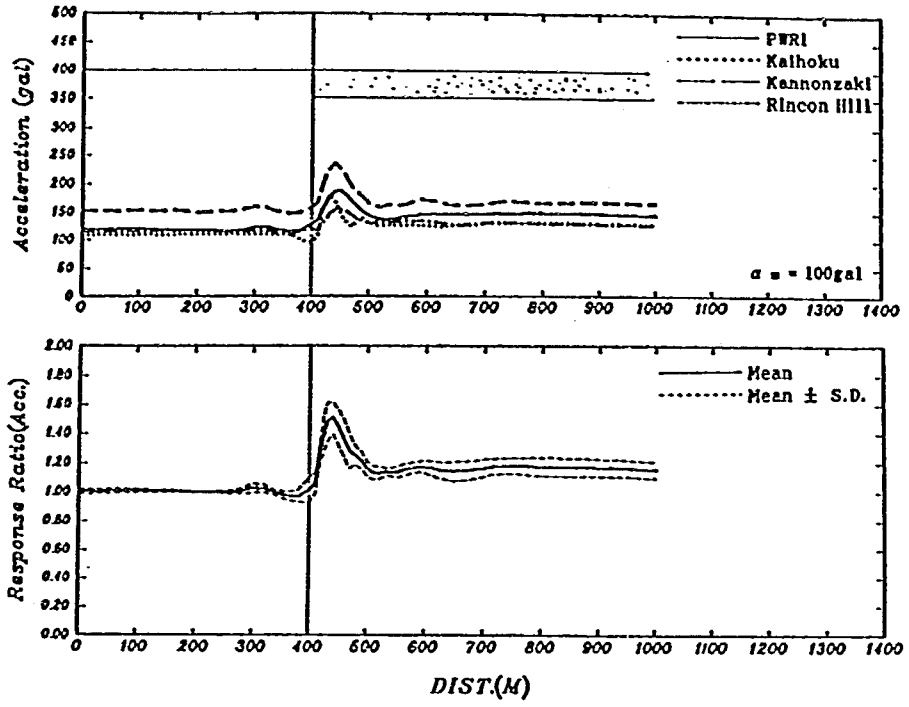
1) In the case of ground model with $\tan\theta = \infty$ as in Figure 5(1), the maximum ground accelerations are amplified largely in the region of ground surface neighboring the boundary between Ac layer and As layer: horizontal coordinate X of about 400 to 490 m. The maximum ground acceleration ratios on the ground surface composing by both Ac and As layers: X = 490 to 1000 m are almost constant and about 1.1 to 1.2 times as large as those composing by As layer alone: X = 0 to 400 m. The peak value of maximum ground acceleration ratio on the ground surface: X = 400 to 490 m is about 1.5.

2) In the case of ground model with $\tan\theta = 1/2$ as in Figure 5(2), the maximum ground accelerations are amplified largely in the region of the inclined base with the horizontal length of 60 m and neighboring it: X = 400 to 520 m. The maximum ground acceleration ratios on the ground surface composing by both Ac and As layers: X = 520 to 1060 m are almost constant and about 1.1 to 1.2 times as large as those composing by As layer alone: X = 0 to 400 m. The peak value of maximum ground acceleration ratio on the ground surface: X = 400 to 520 m is about 1.4.

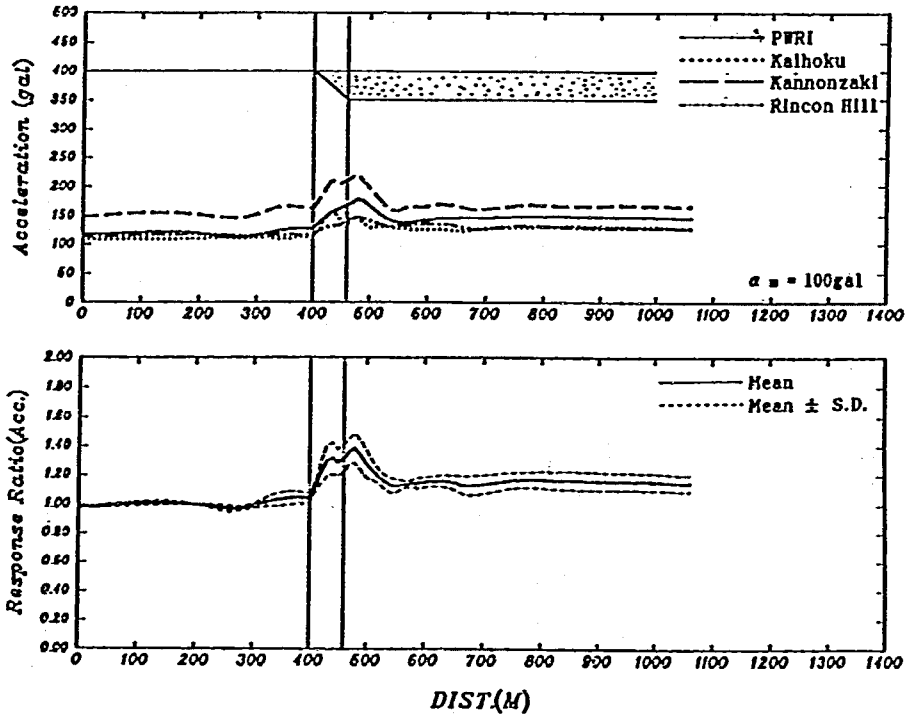
3) In the case of ground model with $\tan\theta = 1/5$ as in Figure 5(3), the maximum ground accelerations are amplified largely in the region of the inclined base with the horizontal length of 150 m and neighboring it: X = 400 to 580 m. The maximum ground acceleration ratios on the ground surface composing by both Ac and As layers: X = 580 to 1150 m are almost constant and about 1.1 to 1.2 times as large as those composing by As layer alone: X = 0 to 400 m. The peak value of maximum ground acceleration ratio on the ground surface: X = 400 to 580 m is about 1.4.

Basin Model

The upper and lower figures of each Figure 6(1), 6(2) and 6(3) also

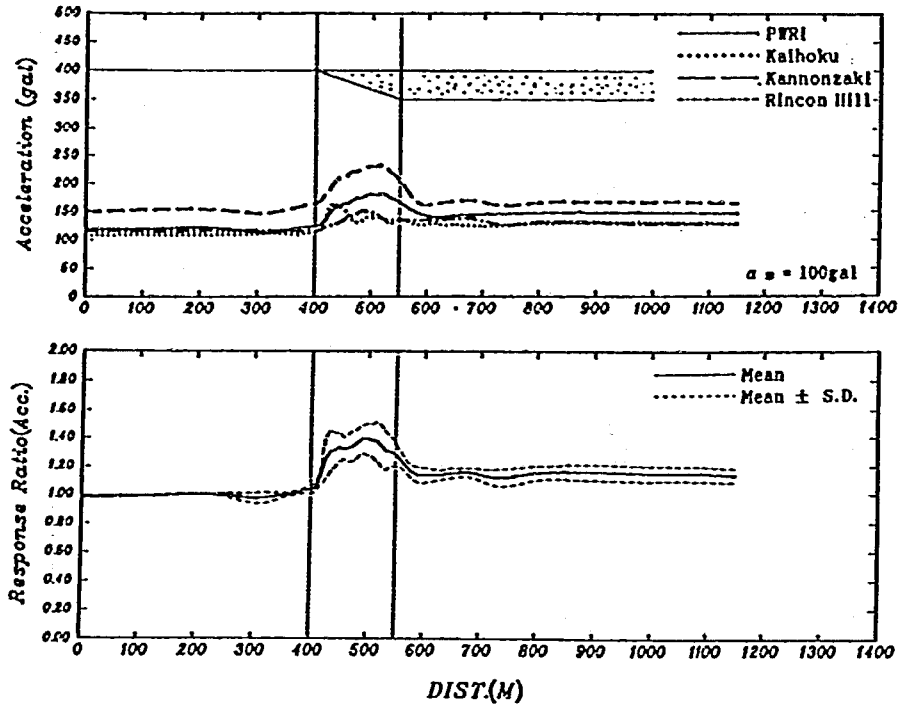


(1) $\tan\theta = \infty$



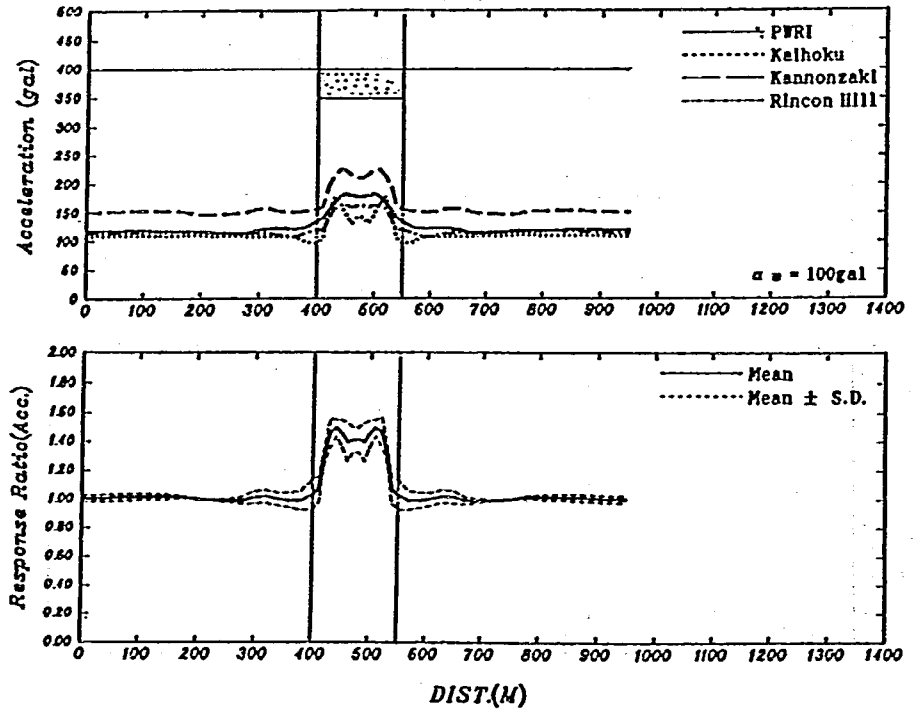
(2) $\tan\theta = 1/2$

Figure 5: Distribution of maximum acceleration and normalized ratio at ground surface for Inclined Base Model: Max. Base Acc. (α_B) = 100 gal



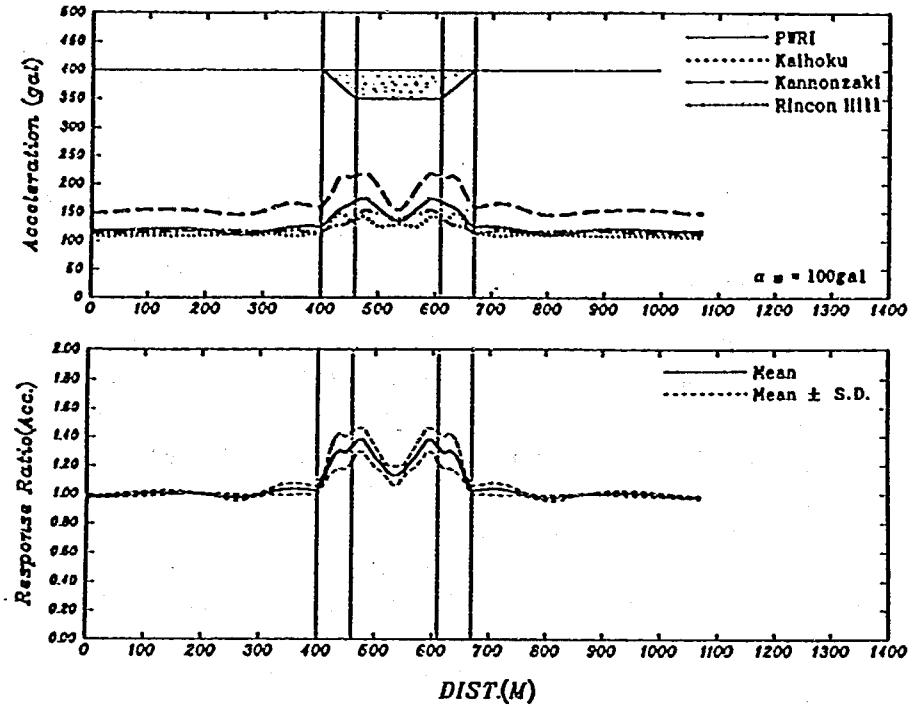
(3) $\tan\theta = 1/5$

Figure 5:(continued)

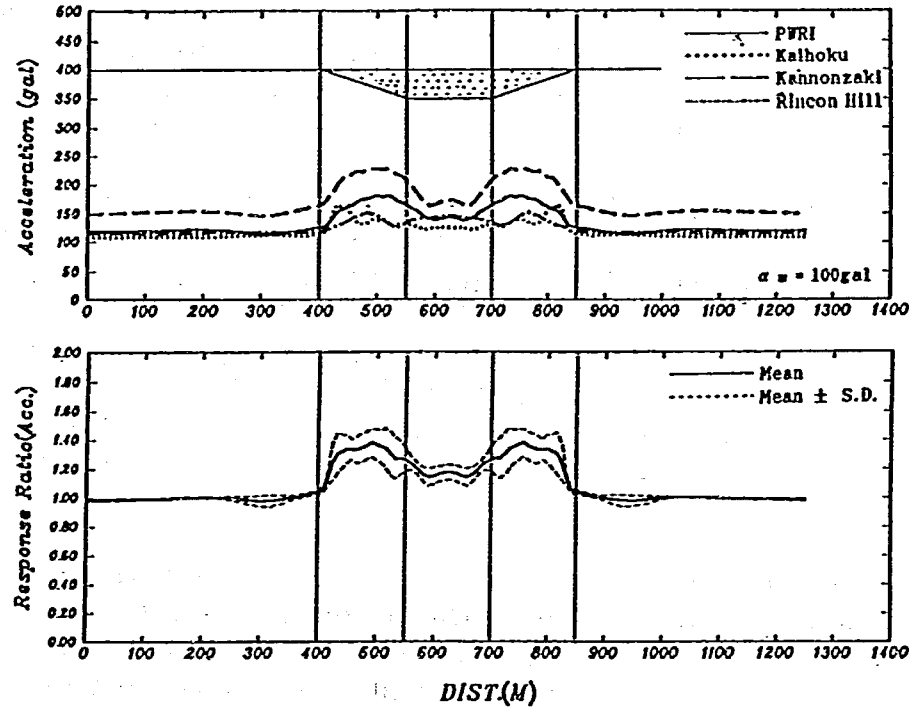


(1) $\tan\theta = \infty$

Figure 6: Distribution of maximum acceleration and normalized ratio at ground surface for Basin Model: Base Length L = 150 m, Max. Base Acc. (α_B) = 100 gal



(2) $\tan\theta = 1/2$



(3) $\tan\theta = 1/5$

Figure 6: (continued)

show the distribution of maximum ground acceleration and their ratios similar to Figure 5 in the case of Basin Models with the basin bottom length of 150 m and $\tan\theta = \infty$, 1/2 and 1/5, respectively.

From these figures, it can be seen that the maximum ground accelerations on the ground surface are affected only in the region of the basin and the characteristics of each result are shown as follows;

1) In the case of ground model with $\tan\theta = \infty$ and the basin surface length of 150 m as in Figure 6(1), the maximum ground accelerations are amplified largely and symmetrically in the region of the basin: X = 400 to 550 m. The peak value of maximum ground acceleration ratio on the ground surface in the basin region composing by Ac layer alone: X = 400 to 550 m is about 1.5. Although the maximum ground acceleration ratio in the center of the basin decreases, the rate of the decrease is very small and its ratio is about 1.4.

2) In the case of ground model with $\tan\theta = 1/2$ and the basin surface length of 270 m as in Figure 6(2), the maximum ground accelerations are amplified largely and symmetrically in the region of the basin: X = 400 to 670 m. The peak of maximum ground acceleration ratio on the ground surface in the basin region: X = 400 to 670 m appears outside of the inclined region and its value is about 1.4. The maximum ground acceleration ratio decreases in the center of the basin: X = 535 m and its minimum value is is about 1.1 to 1.2.

3) In the case of ground model with $\tan\theta = 1/5$ and the basin bottom length of 150 m as in Figure 6(3), the maximum ground accelerations are amplified largely and symmetrically in the region of the basin: X = 400 to 850 m. The peak of maximum ground acceleration ratio on the ground surface in the basin region: X = 400 to 850 m appears inside of the inclined region and its value is about 1.4. The maximum ground acceleration ratio decreases in the center part of the basin and its minimum value is about 1.1 to 1.2: X = 580 to 670 m.

Considering the maximum ground acceleration ratio on the ground surface composing by both Ac and As layers as shown in Figure 5(3): about 1.1 to 1.2, the results of Figure 6(3) indicates that the influence of geometric irregularity by the inclined base appears in the ranges of X = 400 to 580 m and X = 670 to 850 m, and the center part of X = 580 to 670 m is not influenced by the geometric irregularity.

Figure 7 shows the case of ground model with $\tan\theta = 1/2$ and the basin bottom length of 300 m. The maximum ground accelera-

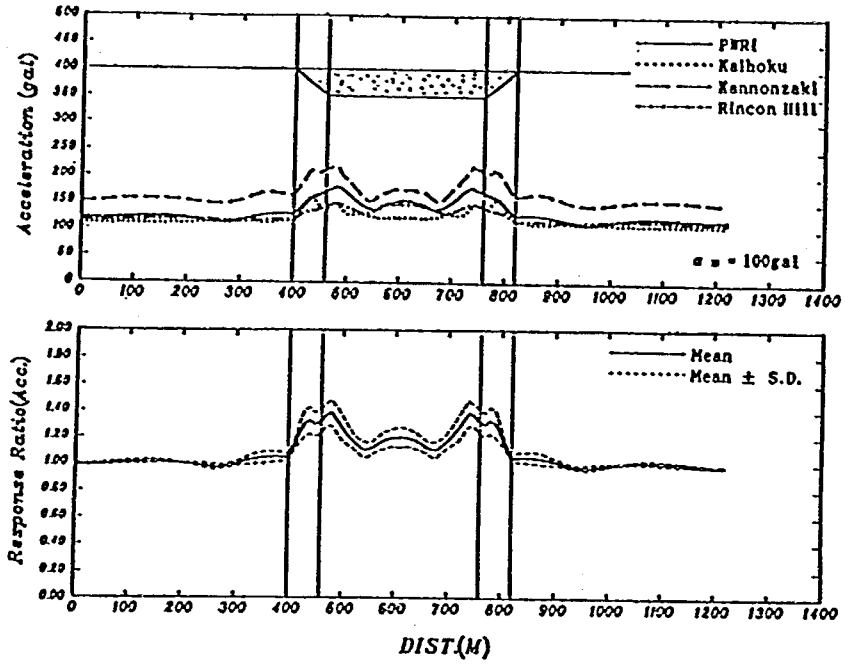


Figure 7: Distribution of maximum acceleration and normalized ratio at ground surface for Basin Model: $\tan\theta$ = 1/2, Base Length L = 300 m, Max. Base Acc. (α_B) = 100 gal

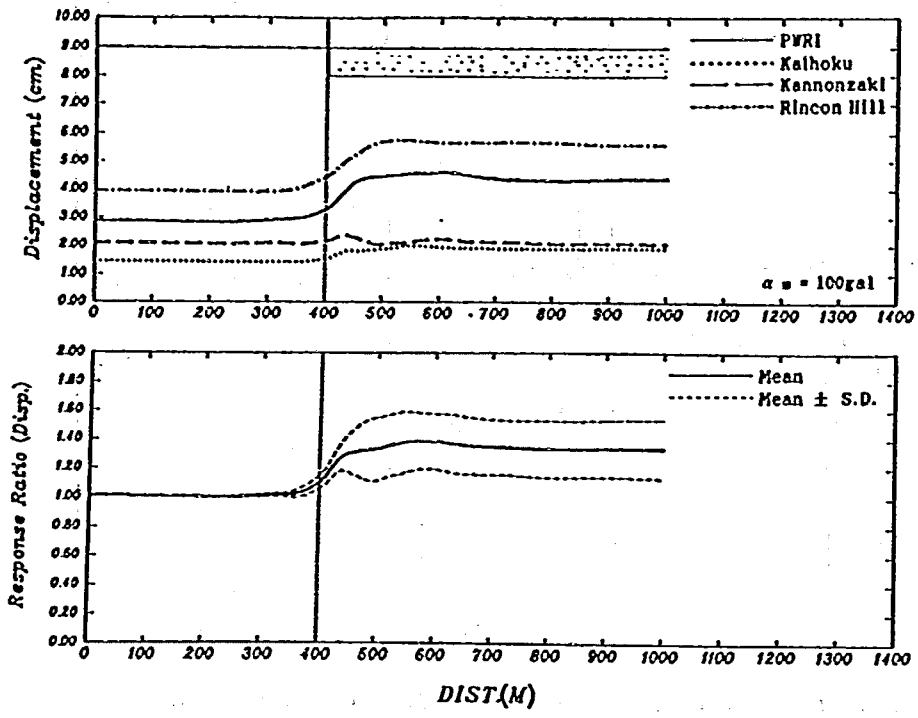
tions are amplified largely and symmetrically in the region of the basin: X = 400 to 820 m. The peak of maximum ground acceleration ratio on the ground surface in the basin region: X = 400 to 820 m appears inside of the inclined region and its value is about 1.4. The maximum ground acceleration ratio decreases in the center part of the basin and its minimum value is is about 1.1 to 1.2 in the range of X = 520 to 700 m.

DISTRIBUTION OF MAXIMUM GROUND DISPLACEMENT ON GROUND SURFACE IN TWO-DIMENSIONAL ANALYSES

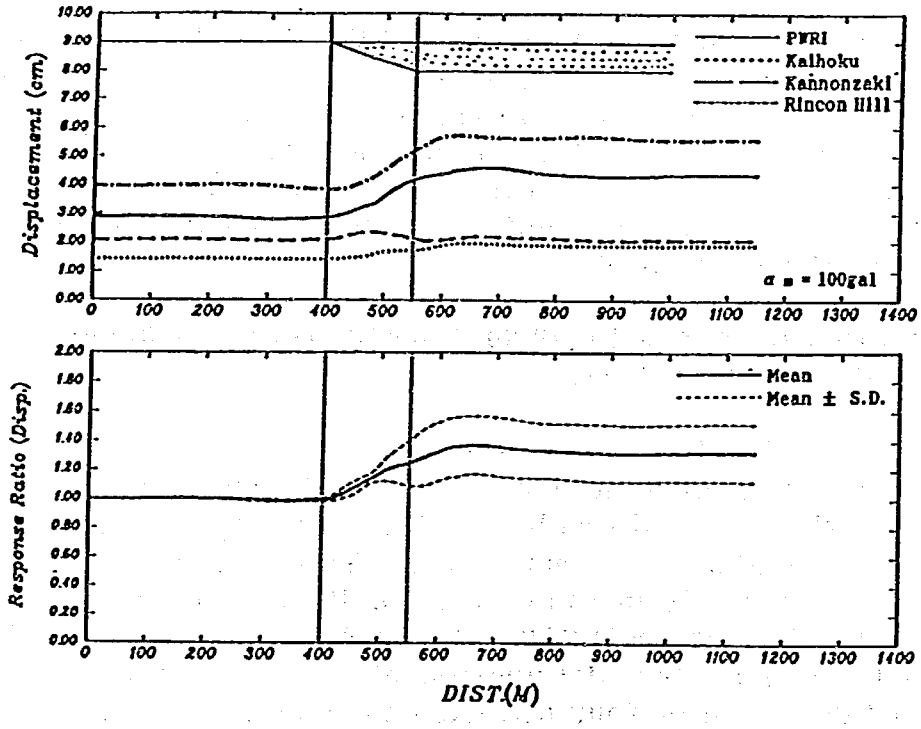
Inclined Base Model

The upper figures of each Figure 8(1) and 8(2) show the distribu tion of maximum ground displacement on the ground surface calculated by four kinds of input motions using maximum acceleration amplitude of 100 gals in the case of Inclined Base Models with tan θ = ∞ and 1/5, respectively. The lower figures of each Figure 9(1) and 9(2) show the distribution of the average/mean and the standard deviation of four different maximum ground displacement ratios normalized using the maximum ground displacement on at the point of X = 200 m on the As layer.

As is evident from Figure 8, the maximum ground displacements and its ratios are not affected clearly by the geometric irregularity of the subsurface layers comparing with the maximum ground



(1) $\tan\theta = \infty$



(2) $\tan\theta = 1/5$

Figure 8: Distribution of maximum displacement and normalized ratio at ground surface for Inclined Base Model: Max. Base Acc. (α_B) = 100 gal

acceleration as in Figures 5 to 7. The maximum ground displacement ratios on the ground surface composing by both Ac and As layers are almost constant and about 1.35 to 1.4 times as large as those composing by As layer alone: X = 0 to 400 m.

Basin Model

The upper and lower figures of Figure 9 also show the distribution of maximum ground displacements and their ratios using maximum acceleration amplitude of 100 gals in the case of Basin Models with $\tan\theta$ = 1/5 and the basin bottom length of 300 m, respectively. Although the maximum ground displacement ratios on the ground surface are large in the basin region and the peak value appears not at the inclined Ac layer but at the horizontal one composing by Ac and As layers, the peak value is about 1.4 times as large as that composing by As layer alone:X = 0 to 400 m and 1000 to 1400 m.

Considering the maximum ground displacement ratio on the ground surface composing by both Ac and As layers as shown in Figure 9: about 1.35 to 1.4, the results of Figure 9 indicate that the influence of geometric irregularity by the basin base is very small.

COMPARISON WITH ONE-DIMENSIONAL ANALYSES ON ACCELERATION RESPONSE SPECTRA

Figure 10 show the ground acceleration response spectrum ratio:

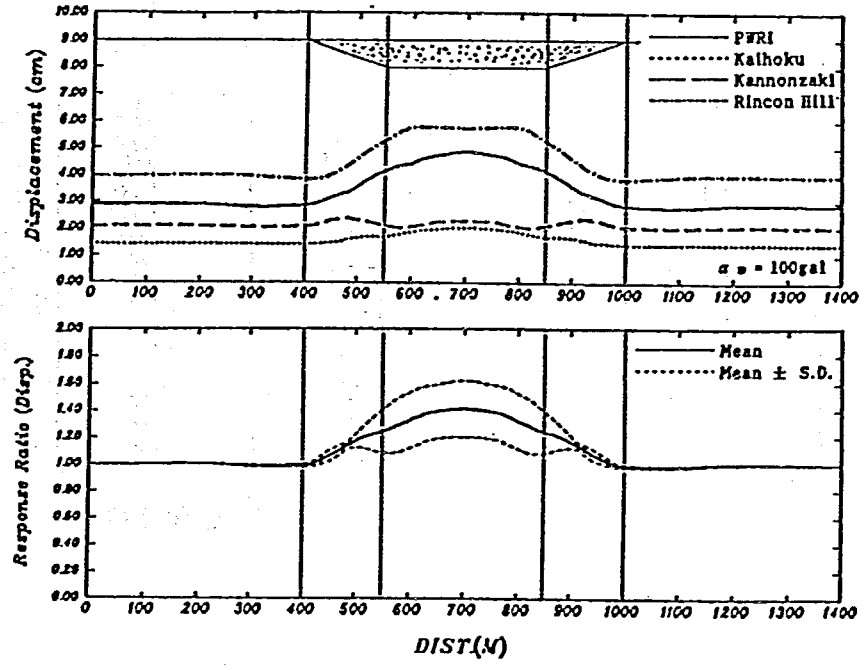


Figure 9: Distribution of maximum displacement and normalized ratio for Basin Model: $\tan\theta$ =1/5, L= 300m, α_B=100 gal.

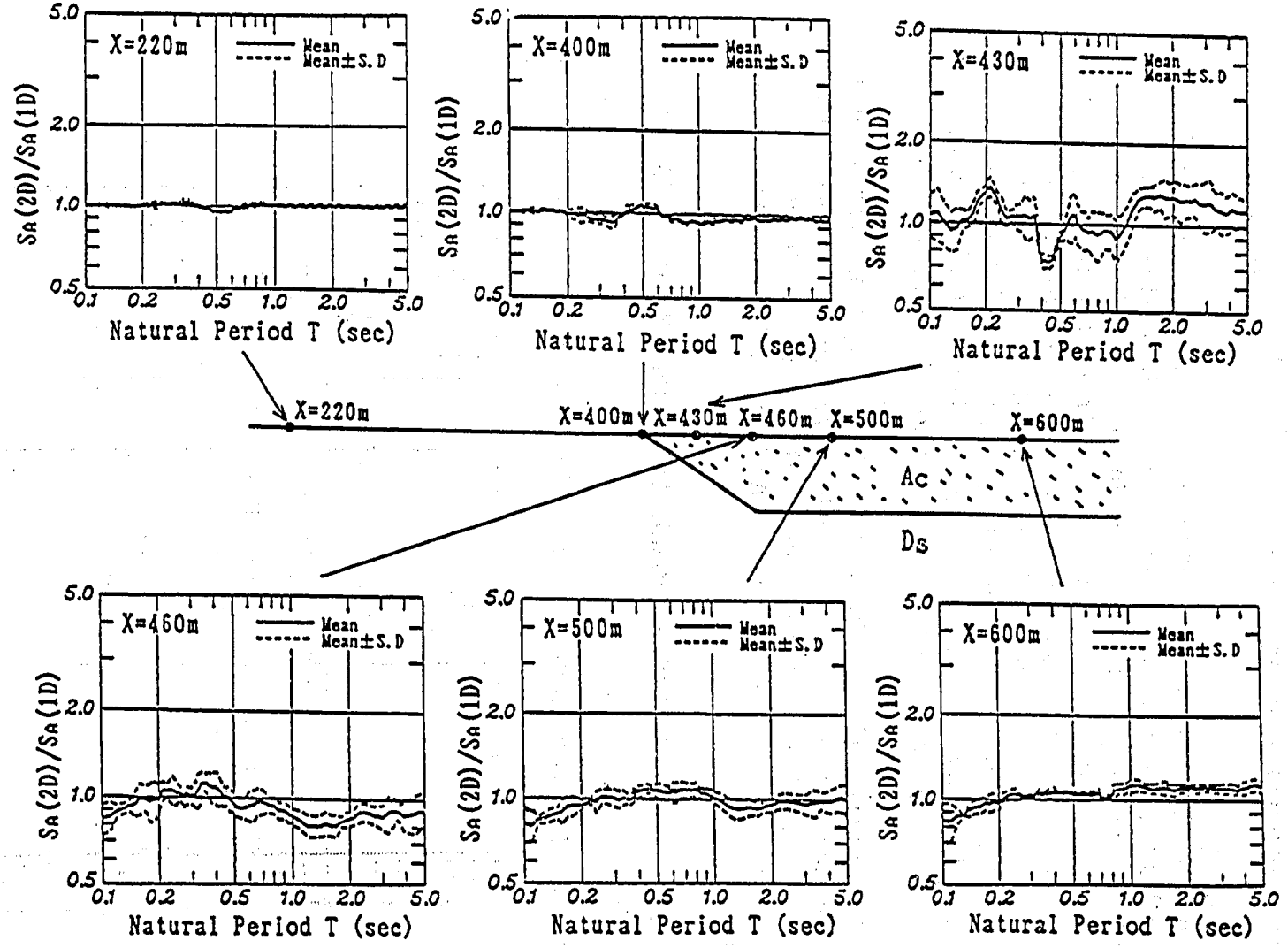


Figure 10:Typical acceleration response spectrum ratio between 2-D analysis and 1-D analysis [Sa(2D)/Sa(1D)] at ground surface for Inclined Base Model:tan θ = 1/2, α_B=100 gal.

$S_A(2D)/S_A(1D)$ basing on the results of one-dimensional analysis and two-dimensional analysis for the Inclined Base Model with tan θ = 1/2 at the typical points of ground surface: X = 220 m, 400 m, 430 m, 460 m, 500 m and 600 m, respectively. The points of X = 220 m and 500 m, 600 m locate on the surface of Ds layer and Ac layer, respectively. The point of X = 430 m locates on the surface of Ac layer at the inclined base, and the two points: X = 400 m and 460 m locate at the boundaries of the inclined base.

As in Figure 10, the acceleration response spectrum ratios are different each other according to the location of points and the natural periods: T. For example, the acceleration response spectrum ratio is about 1.3 to 1.4 at the point of X = 430 m for the natural period of around 0.2 and 1.3 to 2.5 sec. This result indicates that because the acceleration response spectrum is applied in the seismic design for such structures as highway bridges basing on one-dimensional ground model, it is necessary to consider the two-dimensional influence of geometric irregularity of subsurface layers for practical design methods in the future.

CONCLUSION AND FUTURE REMARKS

From the analytical studies in this paper, the following results have been obtained;

1) The maximum ground accelerations on the ground surface are affected by such geometric irregularities of subsurface soft layers as the inclined base ground or the basin ground.
2) The inclined base gradient of a soft surface layer is important factor to discuss the influences of geometric irregularities on maximum ground accelerations: the location of a point where the peak ground acceleration appears and the spread of influenced region.
3) Roughly estimating, the influences of the inclined base gradient can be classified into two types as follows:
(1) In the case of small inclined base gradient: $\tan\theta$ = 1/5, the peak ground acceleration appears inside of inclined base region and the influenced region spreads at the inclined base region and neighboring soft layer within the spread almost same with the thickness of a soft layer.
(2) In the case of large gradient of inclined base: $\tan\theta = \infty$ to 1/2, the peak ground acceleration appears outside of inclined base region and the influenced region spreads at the inclined base region and neighboring soft layer within about 2 to 3 times the spread of inclined base region.
4) The maximum ground displacements on the ground surface are not affected clearly by the geometric irregularity of the

subsurface layers comparing with the maximum ground acceleration in this studies.

5) The acceleration response spectrum at the ground surface obtained using two-dimensional analysis considering the geometric irregularities of subsurface layers are different from that obtained using one-dimensional analysis. The two-dimensional influence of geometric irregularities of subsurface layers should be discussed for practical design methods of structures.

REFERENCES

1. Sanchez-Sesma, F. J. et al., "The Mexico earthquake of September 19, 1985 - On the seismic response of the valley of Mexico", Earthquake Spectra, Vol.4, 1988.

2. Lysmer, J., Udaka, T., Tsai, C. and Seed, H.B., "FLUSH - A computer program for approximate 3-D analysis of soil-structure interaction problems", Earthquake Engineering Research Center Report, No.EERC 75-30, 1975.

3. Schnabel, P.B., Lysmer, J. and Seed, H.B., "SHAKE-A Computer Program for Earthquake Response Analysis of Horizontally Layered Sites", Earthquake Engineering Research Center Report, No.EERC 72-12, December, 1972.

4. Tokida, T., Tamura, K. and Aizawa, K., "Attenuation Characteristics of ground strains induced during earthquake", Proc. of Second International Conference on Recent Advances in Geotechnical Earthquake Engineering and Soil Dynamics, St. Louis, 1991.

5. Iwasaki, T. et al., "Strong-motion records from public works in Japan (No.2)", Technical Note of Public Works Research Institute, Vol.33, 1978.

6. Sasaki, Y. et al., "Strong-motion records from public works in Japan (No.15)", Technical Note of Public Works Research Institute, Vol.52, 1989.

7. Shakal A. et al., "CSMIP Strong-motion records from the Santa Cruz Mountains (Loma Prieta)", California Earthquake of 17 October 1989, Report No.OSMS 89-06, 1989.

8. Iwasaki, T., Tokida, K. and Yoshida, S., "Dynamic Deformation and Strength Characteristics of Alluvial Clay", Proceedings of 15th Annual Conference of Japanese Society of Soil Mechanics and Foundation Engineering, June, 1980. (in Japanese)

9. Iwasaki, T., Tatsuoka, F. and Takagi, Y., "Experimental study on dynamic deformation characteristics of soils", Report of Public Works Research Institute, No.153, 1980. (in Japanese)

10. Tokida, T., Tamura, K. and Fukada, H., "Effects of geological irregularities on ground motion characteristics", Tenth World Conference on Earthquake engineering, Vol.2, pp.669-672, Madrid, July, 1992.

(7) Session 7

Seismic Design (2)

15) Seismic Base Isolation of Curved Highway Bridges
(K.H. Chen and D.A. Foutch*)

16) Evaluation of Modal Damping Ratio of Bridges Based on Strain Energy Proportional Method
(K. Kawashima*, H. Nagashima and H. Iwasaki)

17) Developments in Seismic Prioritization of Bridges in California
(A.D. Gilbert*)

SEISMIC BASE ISOLATION OF CURVED HIGHWAY BRIDGES

K. H. Chen[1] and D. A. Foutch[2]

1.0 Introduction

The collapse of several highway bridges during the San Fernando earthquake of February 9, 1971, demonstrated the potential for damage and loss of life associated with modern highway bridges during earthquakes. This was further demonstrated in the October 17, 1989, Loma Prieta earthquake which resulted in the collapse of the Cypress Street Viaduct with a loss of 70 lives (Nim et al, 1989).

One method of improving seismic performance is to increase the strength of the piers and provide more ductile details. Another is to provide passive control such as base isolation. For this method, special devices are needed to reduce seismic forces taken by piers.

Most of the world's isolated structures are bridges. In the United States, at least six bridges are constructed by using isolation systems, such as the Sierra Point Overhead, the Santa Ana River bridge, the Eel River bridge, the Main Yard and Shop access bridge, the All American Canal bridge in Southern California, and the Sexton Creek bridge in Illinois (Buckle and Mayes, 1989). All of these bridges adopted the lead rubber isolation system. In addition, the Foothill Communities Law and Justice Center in Rancho Cucamonga, California is the first building in the United States to use a base isolation system. At present, there are 26 buildings in the United States (Kelly, 1993) where base isolation has been or will be used to control response during earthquakes. In New Zealand, energy dissipation systems and full isolation systems, such as steel dampers or lead rubber devices, are widely used in highway bridges. New Zealand is probably the leading country in the world in the development and implementation of isolation and energy dissipation systems.

The objectives of this investigation are as follows:

1) Develop a time history method for seismic analysis of curved bridges under uniform and variable earthquake ground motion;

2) Investigate the feasibility of using various base isolation strategies for curved highway bridges;

3) Develop a response spectrum method for predicting the response of isolated curved bridges to simplify the design procedures.

This paper is a research-in-progress report. The purpose is to outline the objectives and the approach that the research will take. No results for curved bridges are available yet, but some preliminary results for straight bridges have been obtained in our pilot study.

---

[1]Graduate Research Assistant, Department of Civil Engineering, University of Illinois at Urbana-Champaign, Urbana, Illinois.

[2]Professor of Civil Engineering, University of Illinois at Urbana-Champaign, Urbana, Illinois.

2.0 Transient Dynamic Analysis of Curved Highway Bridges

2.1 Description of Bridges and Isolation/Dissipation Systems to be Studied

Typical bridges will be studied in this investigation. The bridges adopted here have span numbers from two to six with span lengths of 30 m per span and a pier height of 5 m for short piers and 15 m for tall piers. Both straight and curved bridges will be examined. The ratio of radius-to-span length from 1 to 3 will be used for the curved bridges. The bridge deck will be assumed to be rigid in its plane, but flexibility in the vertical direction will be considered. Effects of pier and support flexibility also will be investigated. Schematics of several bridge configurations are shown in Figure 1.

The performance of standard bridges, bridges without isolation but with energy dissipation devices and those with both isolation and dissipation devices will be evaluated. Several isolation and/or energy dissipation systems, shown schematically in Figure 2, will be included in this research. The three isolation systems to be studied are the lead rubber bearing system (LRB), the high damping rubber system (HRB) and the sliding bearing with helical steel spring system (SHSS). We also plan to include a sliding bearing to be used in conjunction with different energy absorbing systems such as the tapered steel system. The energy dissipation devices that will be considered in this study are the tapered steel system (TS), the lead extrusion system (LE), the viscous damping system (VD) and the shape memory alloy system (SMA) in addition to the LRB and HDR systems. All isolation systems use multi-direction isolators in the horizontal direction. The LRB system is the most widely used for bridges and buildings. The LRB system includes a laminated rubber bearing which serves as a recentering force device and a lead core which dissipates energy through hysteretic action (Turkington, 1989). The HDB system is a low modulus and high damping laminated rubber bearing (Kelly, 1991). The HDB system, like all isolation systems, would lengthen the entire system natural period to avoid resonance damage. This has been demonstrated to be effective even for long period excitation forces such as the 1985 Mexico City earthquake. The TS system uses mild steel to dissipate the input energy by yielding hysteretic action. The TS system has been effectively used in the Dunedin bridge in New Zealand (Tyler, 1978). The SHSS system consists of a teflon disc bearing and helical steel springs. The helical steel springs act as a recentering device. According to results of experiments, this system has been proven to be insensitive to frequency of ground motion (Constantinou et al, 1991). The lead extrusion system (Robinson et al, 1975) and the shape memory alloy system (Witting et al, 1992) dissipate energy through hysteretic force-displacement behavior.

Generally, there are two types of arrangements of isolator systems in highway bridges (Buckle and Mayes, 1990). One method is to only attempt to achieve energy dissipation for the bridge. The other is to achieve full isolation, with or without energy dissipation, for a continuous bridge. For full isolation, the isolators are arranged so that the deck is isolated from all piers and abutments. In the systems that use only energy dissipaters, the isolators are placed only at the abutments to dissipate energy through the isolators.

2.2 Modeling of Earthquake Ground Motions

Both artificial earthquake and real earthquake records will be used as input excitation. The artificial earthquake is based on the Levy-Wilkinson model (Levy and Wilkinson, 1976). This model uses a given horizontal design response spectrum as the target response spectrum. Then, with iterations, the response spectrum of the simulated ground motion in the horizontal direction can match well with the target response spectrum. After the first time history in the horizontal direction has been generated, the second time history in the horizontal direction can be easily generated with low correlation to the first one by the mid-frequency shift approach (Levy and Wilkinson, 1976). The same procedure may be used to simulate vertical motions. For the real earthquake records, several recorded motions will be used including the high frequency 1940 El Centro earthquake and low frequency 1985 Mexico City earthquake.

For variable ground motion as the excitation force to the bridge, the system response may be significantly different from the response to the uniform ground motion. First, the anti-symmetric modes are unable to be excited by uniform ground motion excitation. Second, quasi- or pseudo-static responses only appear in variable ground motion excitation. (Johnson and Galletly, 1972; Abdel-Ghaffar and Nazmy, 1991).

2.3 Bridge Models and Analysis Method

The initial pilot study will include only two-span straight highway bridges. These will be modelled using the simple mechanical systems shown in Figure 3. A bilinear degrading hysteresis model (Saiidi, 1979) will be used to model the piers. Simple elastic springs will be used to model the soil structure interaction. Combinations of elastic springs and nonlinear springs will be used to model the isolators and energy dissipators. Schematics of some of these are shown in Figure 3.

All of the isolation systems, except for the friction system, have recentering capacity. The modelling of restoring helical springs in the teflon friction systems uses a hardening bilinear model. This model has been shown from the experiment to exhibit no interaction between the helical springs and the teflon friction system (Constantinou et al, 1991).

Upon completion of these preliminary studies of one-dimensional behavior of straight two-span bridges, more realistic models will be used to study the more complicated three-dimensional behavior. A bi-axial hysteresis model will be used for the piers. Two to six span straight and curved bridges will be studied. Some of the energy dissipation systems and/or isolation systems will require two or three dimensional hysteretic rules for their behavior. Others will only require one dimensional response rules.

3.0 A response spectrum method for predicting the response of isolated curved bridges

The response spectrum methods are widely used by engineers to reduce the calculation effort. Three main techniques have been developed to do response spectrum analysis. These are the square-root-of-sum-of-square (SRSS), the complete quadratic combination (CQC) (Wilson, Kiureghian, and Bago, 1981), and the multiply-supported excitation spectrum method (MSES) (Kiureghian and Neuenhofer, 1991). The SRSS method leads to erroneous results when the structure has closely spaced natural frequencies or when it is highly asymmetric. The CQC method will give reasonable results by comparison with response from time history analysis. The CQC method differs from the SRSS method by accounting for the additional response that will come from the cross-mode term which is a function of the duration of earthquake, modal frequencies, and damping ratio. Unfortunately, the SRSS and the CQC methods only consider uniform ground motion. As for the variable ground motion, the MSES method may be used to calculate the response from spatially varying ground motions.

For base isolated structures, the response spectrum for bridges has been developed for preliminary design purposes (Turkington et al, 1989). This method considers effects of period shift and additional hysteretic damping resulting from the inelastic deformation of lead-rubber bearings. After these two modification factors have been applied, the procedure is the same as the regular structural analysis by the response spectrum method. The limitation of this method is that it is only valid for the fundamental mode response and for uniform ground motion. Therefore, the response spectrum method with isolation and with varying ground motion will be developed for design.

4.0 Results of preliminary studies

The mechanical models of a straight two-span bridge are shown as in Figure 3. The two-span bridges with span lengths of 30m and a pier height of 5m and with sliding in longitudinal direction at the abutments will be used to study the efficiency of various isolation systems, described above. The excitation force is the 1940 El Centro earthquake. The linear acceleration method is used in the time history analysis. The bridge decks are assumed to

be rigid in the longitudinal direction. The total weight of superstructure is 5100kN. The inelastic behavior of the piers is represented with a bilinear model. The yielding force of the pier is 1307kN, which approximately equals to 25.6% of the weight of the superstructure. The bilinear model is also used for modeling the post-yield behavior of the isolators and the energy dissipaters. The yielding forces of the isolation and the energy dissipation systems are at least 5% of the weight of the bridge deck. In AASHTO, the choice of yielding forces of isolators is open to the designer (AASHTO Subcommittee, 1990). However, 5% of the weight of the bridge deck has been demonstrated to be an optimal value for the yielding force of isolators in the lead rubber full isolation systems (Ghobarah, 1988). This is used to resist minor forces, such as wind, minor earthquake, and traffic braking forces. Both energy dissipater systems and full isolation systems will be used to compare the efficiency of the different hazard mitigation systems.

The performance criteria for evaluating the four systems is based on the maximum displacements of the bridge deck, the minimum yielding forces of the isolators, and the amount of yielding in the piers. First, the constraint of maximum bridge deck displacement is to avoid the large displacement of the deck which might result in the failure of the back wall of the abutment through impact. In addition, the maximum 100% shear strain of isolators and energy dissipaters is used to avoid the roll-out failure of the isolators and damage to energy dissipaters. Also, the minimum yielding force of the isolators is set to fuse only under the excitation forces greater than the minor forces such as wind forces, minor earthquake excitation, and traffic braking forces. Finally, one of the major objectives of isolation systems is to limit damage to the piers so that the bridge may be repaired shortly after an earthquake. Therefore, the displacement limitation of the bridge deck, the minimum yield force of the isolators and the pier damage limitation are used to determine the number of isolators and energy dissipaters that are required.

4.1 Shear demands in piers

The main effects of energy dissipation and/or full isolation are to reduce the shear forces in the piers. The maximum responses of several structures with non-isolation, energy dissipation and/or full isolation are presented in Table 1. These results indicate that plastic hinges occur in the piers in the non-isolation systems, whereas no plastic hinges appear in the pier if a full isolation system or an energy dissipation lead rubber system is used. The displacement ductility factors of the piers are 1.85 for the non-isolation system, whereas the displacement ductility factors of the pier varies from 0.89 to 1.62 for the energy dissipation systems and from 0.20 to 0.31 for the full isolation systems. The damage of the pier depends on the ductility of the pier and the hysteretic energy dissipated by the pier (Park et al, 1986). In addition, the shear demands in the pier are reduced by using the four different devices from 0.89 V_y to 1.03 V_y (V_y = the yielding force of the pier) with energy dissipation systems and from 0.20 V_y to 0.31 V_y with full isolation systems. The yielding forces of energy dissipaters used 14.07%, 13.80%, and 13.50% of the weight of the bridge deck for the lead-rubber systems, the high damping rubber system, and the tapered steel system, respectively. The yielding forces of the isolators in the full isolation systems used 5.45%, 5.50%, and 4.50% of the weight of the bridge deck for the lead-rubber systems, the high damping rubber system, and the tapered steel system, respectively. With these yielding forces for the isolators and energy dissipaters, the shear strains of the isolators in both systems are less than 100%, and vary from 8% to 23% in the energy dissipation systems and from 24% to 33% in the full isolation systems. The low shear strain in the energy dissipater systems, 8% and 23%, are smaller than those of the isolated systems because the pier limits the displacements of the deck. The cost of this, however, is damage to the piers as demonstrated by the ductility factor greater than one.

4.2 Effects of period shift and additional damping in full isolation systems

The period shift that results from the full isolation system lengthens the original natural periods of the structures and reduces the shear carried by the piers. The results of time history analyses, presented in Figure 4 and Figure 5, indicate that the non-isolated bridge pier will yield under the El Centro 1940 earthquake. The ductility demands shown in Figure 6 are the result. However, in the full isolation system, the natural periods of the bridge shifts about 120%, from 0.681 sec. (non-isolation elastic structure) to 1.501 sec. (post-yielding isolation structure), and the demand ductility of the pier is reduced as shown in Figure 7.

The natural periods of the bridges with full isolation systems are continuously changing during an earthquake due to the nonlinear behavior. The exact period shift is not a fixed value but depends on the intensity of the input excitations, the flexibility of the piers, and the post-yield stiffness of the isolators. The additional damping from the inelastic deformation of isolators is also varied from one time step to another time step. Therefore, simplified methods have been developed to take into account the two main effects: effective period and effective equivalent viscous damping. A schematic illustrating this simplified model is shown in Figure 8. The advantages of the simplified approach allowed these new devices to be incorporated into the conventional response spectrum methods and to reduce the cost of computation in the preliminary design.

The simplified methods have been used in AASHTO subcommittee (1990) and by Turkington et al (1989) for bridge design and Andriono et al (1991) for building design. The common assumptions of these three approaches use the maximum displacement to define effective stiffness of isolators and the area of corresponding hysteretic loop as the equivalent viscous damping, as shown in Figure 8. In the AASHTO approach, the effective periods of vibration are obtained from the effective linear stiffness of all bearings supporting the superstructure, as presented in Figure 8. The effects of flexibility of piers are not considered in this approach, so that significant errors may occur for tall piers. In the Turkington approach, the effects of the piers have been included, but design curves of additional period shift and additional equivalent damping are only valid for specific earthquakes and specific isolators. In Andriono's approach, the maximum displacement is obtained by an assumed displacement ductility for the isolators, then the corresponding effective period and equivalent viscous damping are estimated. Finally, the response is read from the conventional response spectrum to evaluate and compare the calculated displacement ductility of isolators with the assumed value. If the bias is not within the tolerance, iterations are required to approximate the maximum response of the isolators. Results can usually be obtained within one or two cycles of iterations. Unfortunately, this method assumes that the isolators are on rigid foundations. For a bridge with flexible foundations the effect of this flexibility on the response should be included in the analysis.

4.3 Proposed simplified method

The proposed method will use an iteration scheme to determine the effective period and effective equivalent viscous damping. Some assumptions in the proposed method are made to simplify the analytical model. First, the response of the pier is assumed to contribute only to the first mode response, as depicted in Figure 9. This can be demonstrated in Figure 5 with the deck and pier having in-phase vibrations. Second, the effective mass is the summation of the first modal mass of the pier and the mass of the superstructure. The mass of the isolators is neglected in comparison with the total mass. Third, the deck is rigid in the longitudinal direction and the effective stiffness of isolators is affected by the flexibility of foundation as shown in Figure 9. The effective stiffness of the system is the combination of the effective stiffness of isolators and the elastic pier. The stiffness of the abutment is rigid, but this is not mandatory. The abutment can be modelled as the elastic foundations if the flexibility of abutments needs to be incorporated into the analysis. Fourth, the effective equivalent viscous damping is proportional to the energy dissipated as represented by the area of the hysteretic loop as shown in Figure 9. The advantage of the proposed method is that it is similar to conventional structural analysis. The only required design chart is the response spectrum. This has been widely implemented in the design of non-isolated structures.

References

Andriono, T. and Carr, A. J. (1991) "A Simplified Earthquake Resistant Method of Base Isolated Multistory Structures," Bulletin of the New Zealand National Society on Earthquake Engineering, Volume 24, No. 3, pp. 238-250.

Abdel-Ghaffar, A. M. and Nazmy, A. S. (1991) "3-D Nonlinear Seismic Behavior of Cable-Stayed Bridges," ASCE, Journal of Structural Engineering, ST11, Volume 117, pp. 3456-3476.

AASHTO Subcommittee on Bridges and Structures (1990) "Proposal and Commentary for Adoption of Provisions for Seismic Isolation Design," 1990 Committee Meeting, Ocean Beach, Florida.

Buckle, I. G. and Mayes, R. L. (1989) "The Application of Seismic Isolation to Bridges," Proceedings of the ASCE Structures Congress: Seismic Engineering Research and Practices, ASCE, pp. 633-642.

Buckle, I. G. (1986) "Development and Application of Base Isolation and Passive Energy Dissipation: A World Review," Proceedings of the ATC-17 Seminar on Base Isolation and Passive Energy Dissipation, San Francisco, California, pp. 153-174.

Buckle, I. G. and Mayes, R. L. (1990) "Seismic Retrofit of Bridges Using Mechanical Energy Dissipators," Proceedings of the 4th U.S. National Conference on Earthquake Engineering, May 20-24, Palm Springs, California, Volume 3, pp. 305-314.

Constantinou, M. C.; Mokha, A. S.; and Reinhorn, A. M. (1991) "Study of Sliding Bearing and Helical Steel Spring Isolation System," ASCE, Journal of Structural Engineering, ST4, Volume 117, pp. 1257-1275.

Ghobarah, A. and Ali, H. M. (1988) "Seismic Performance of Highway Bridges," Engineering Structures, Volume 10, pp. 151-166.

Johnson, N. E. and Galletly, R. D. (1972) "The Comparison of the Response of a Highway Bridge to Uniform Ground Shock and Moving Ground Excitation," Shock and Vibration Bulletin, Volume 42, Part 2, pp. 75-85.

Kelly, J. M. (1986) "A Seismic Base Isolation: Review and Bibliography," Soil Dynamics and Earthquake Engineering, Volume 5, No. 4, pp. 202-216.

Kelly, J. M. (1991) "A Long-Period Isolation System Using Low-Modulus High-Damping Isolators for Nuclear Facilities at Soft-Soil Sites," UCB/EERC-91/03.

Kelly, J. M. (1993) "State-of-the-Art and State-of-the-Practice in Base Isolation," Proceedings of Seminar on Seismic Isolation, Passive Energy Dissipation, and Active Control, ATC 17-1, San Francisco, California, March 11-12, pp. 9-28.

Kiureghian, A. D. and Neuenhofer, A. (1991) "A Response Spectrum Method for Multiple Support Seismic Excitations," UCB/EERC-91/08.

Levy, S. and Wilkinson, J. P. D. (1976) "Generation of Artificial Time Histories, Rich in All Frequencies From Given Response Spectra," Nuclear Engineering and Design, 138, pp. 241-251.

Nims, D. K.; Miranda, E.; Alken, I. D.; Chittaker, A. S.; and Bertero, V. V. (1989) "Collapse of the Cypress Street Viaduct as Result of the Loma Prieta Earthquake," UCB/EERC-89/16.

Park, Y. J.; Wen, Y. K.; and Ang, A. H-S. (1986) "Random Vibration of Hysteretic Systems Under Bi-Directional Ground Motion," Earthquake Engineering and Structural Dynamics, Volume 14, pp. 543-558.

Robison, W. H. and Greenbank, L. R. (1975) "Properties of an Extrusion Energy Absorber," Bulletin of the New Zealand National Society on Earthquake Engineering, Volume 8, Number 8, pp. 187-191.

Saiidi, M. and Sozen, M. A. (1979) "Simple and Complex Models for Non-Linear Seismic Response of Reinforced Concrete Systems," Structural Research Series, Number 465, University of Illinois at Urbana-Champaign, August 1979, 200 pages.

Turkington, D. H.; Carr, A. J.; Cooke, N.; and Moss, P. J. (1989) "Seismic Design of Bridges on Lead-Rubber Bearings," Journal of Structural Engineering, Volume 115, Number 12, ASCE, pp. 3000-3016.

Tyler, R. G. (1978) "Tapered Steel Energy Dissipators for Earthquake Resistant Structures," Bulletin of the New Zealand National Society on Earthquake Engineering, Volume 11, No. 4, pp. 282-294.

Wilson, E. L.; Kiureghian, A. D.; and Bayo, E. P. (1981) "A Replacement for the SRSS Method in Seismic Analysis," Earthquake Engineering and Structural Dynamics, Volume 9, pp. 187-194.

Witting, P. R. and Cozzarelli, F. A. (1992) "Shape Memory Structural Dampers: Material Properties, Design and Seismic Testing," National Center for Earthquake Engineering Research, State University of New York at Buffalo, NCEER-92-0013.

Table 1. Comparison of response of bridges with and without isolation and/or energy dissipation

(1) abutments with energy dissipaters

system	non-isolation	(a) high damping rubber	(b) lead-rubber	(c) tapered steel
max. disp. (cm.)	5.40	4.72	2.61	4.69
max. vel.(cm/sec.)	54.91	39.91	33.29	34.81
max. accel. (g.)	0.53	0.71	0.66	0.66
max. shear in pier (kn)	0.27 W 1.05 V_y	0.26 W 1.03 V_y	0.23 W 0.89 V_y	0.26 W 1.03 V_y
displ. ductility factor	1.85*	1.62*	0.89	1.61*
shear strain of energy dissipaters		23%	10%	8%

(2) pier and abutments with full isolation and energy dissipation

system	non-isolation	high damping rubber	lead-rubber
max. displ. (cm.)	5.40 (deck) 5.40 (pier)	7.46 (deck) 0.59 (pier)	6.83 (deck) 0.92 (pier)
max. vel. (cm/sec.)	54.91 (deck) 54.91 (pier)	38.33 (deck) 7.14 (pier)	41.68 (deck) 15.27 (pier)
max. accel. (g.)	0.53 (deck) 0.53 (pier)	0.43 (deck) 0.57 (pier)	0.43 (deck) 1.08 (pier)
max. shear in pier (kn)	0.27 W 1.05 V_y	0.05 W 0.20 V_y	0.08 W 0.31 V_y
displ. ductility factor	1.85*	0.20	0.31
shear strain of isolators		33%	24%

(W = the weight of the superstructure = 5100 kn, V_y = the yielding force of pier = 1307 kn)

*pier yielding (yielding displacement = 2.92 cm.)

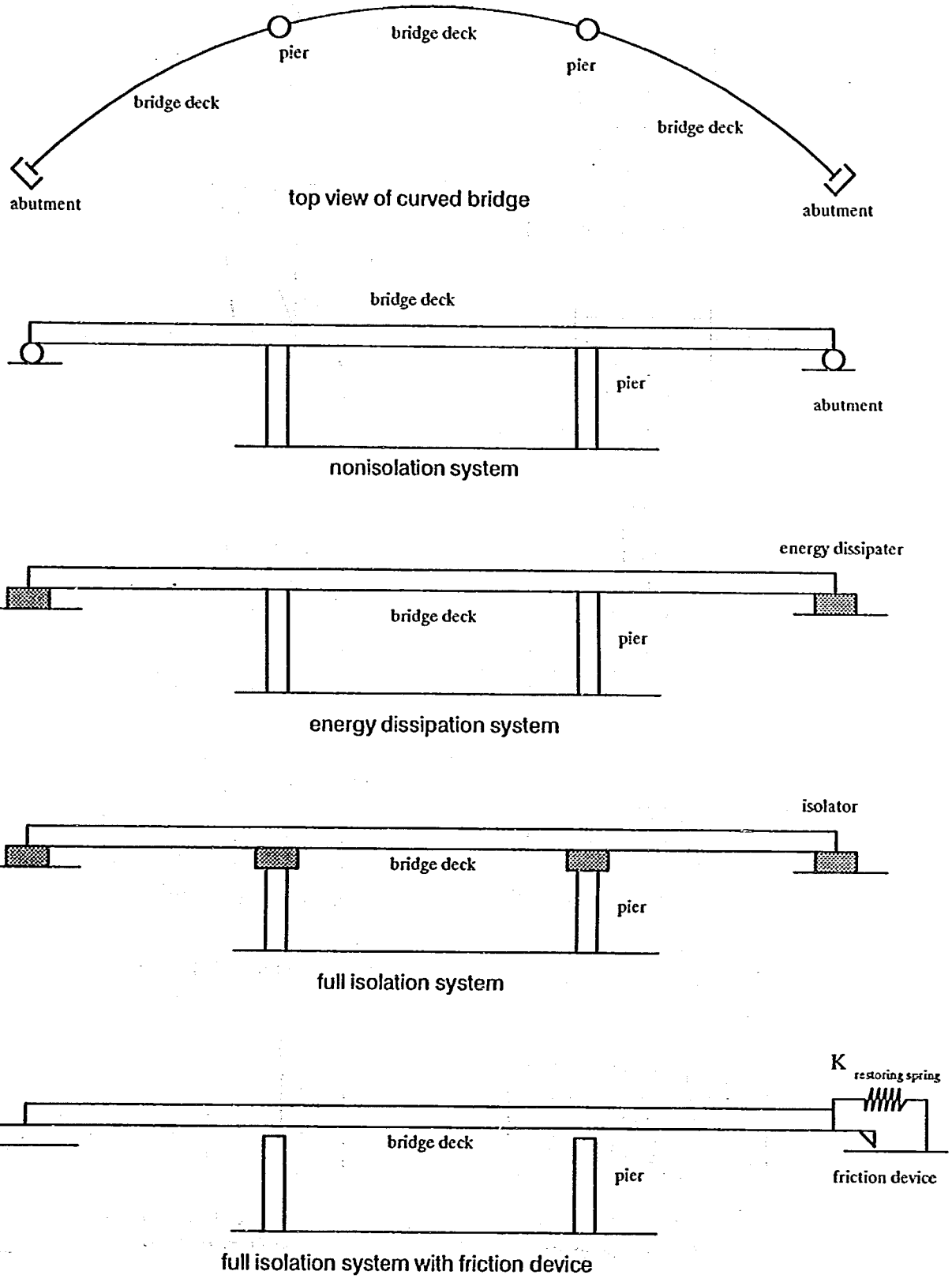
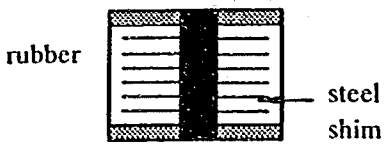
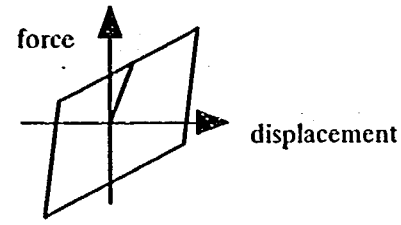


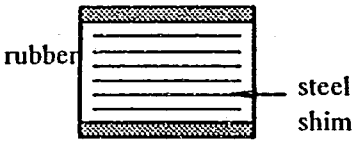
Fig. 1 Non–isolation, full isolation, and energy dissipation systems



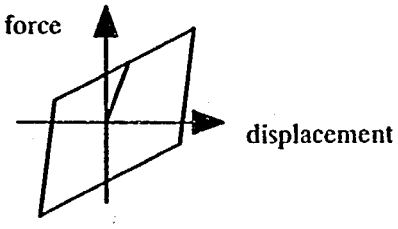
LEAD RUBBER BEARING
(1989 Turkington et al)



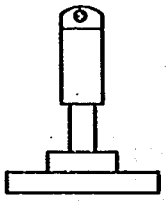
SHEAR PROPERTY OF
LEAD RUBBER BEARING



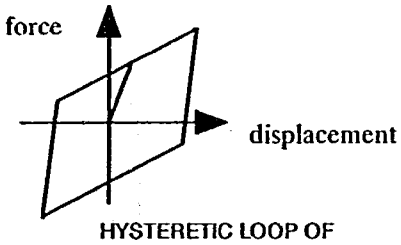
HIGH DAMPING RUBBER BEARING
(1990 Kelly)



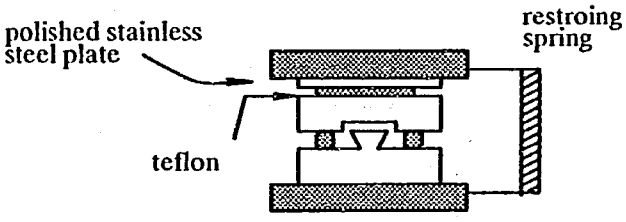
SHEAR PROPERTY OF HIGH
DAMPING RUBBER
BEARING



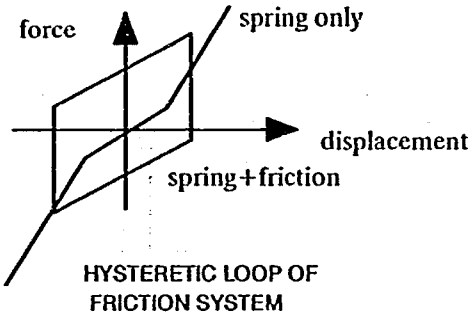
ROUND CANTILEVER DAMPER
TAPERED STEEL ENERGY DISSIPATERS
(1978 Tyler)



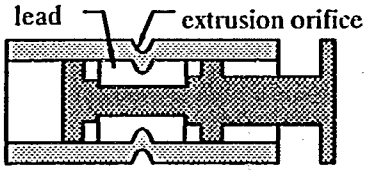
HYSTERETIC LOOP OF
TAPERED STEEL
DAMPERS



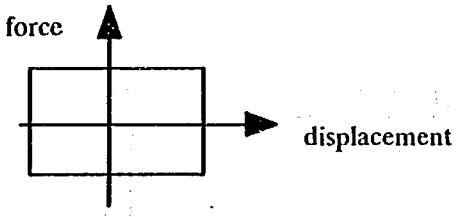
SLIDING BEARING WITH
HELICAL STEEL SPRING
(1991 Constantinou et al)



HYSTERETIC LOOP OF
FRICTION SYSTEM

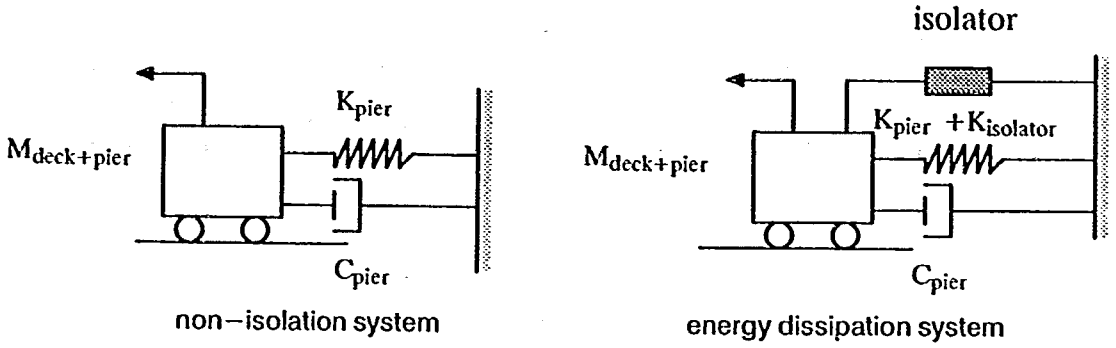


LEAD EXTRUSION DEVICE
(1975 Robinsion et al)



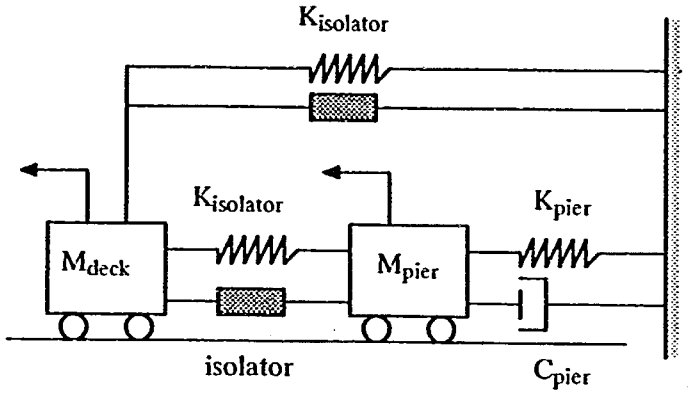
HYSTERETIC LOOP OF
LEAD EXTRUSION
DEVICE

Fig. 2 Isolators and Energy dissipaters

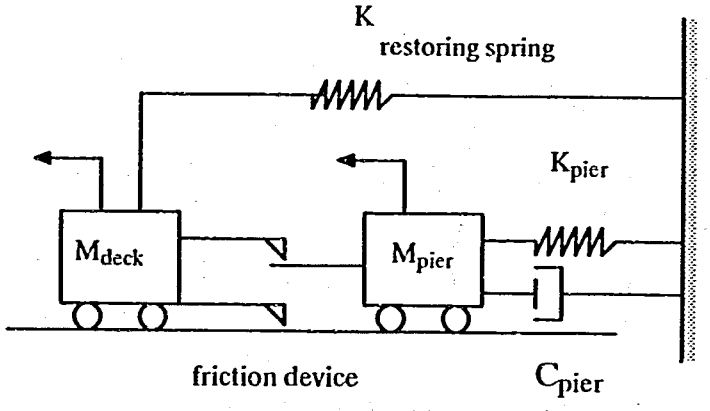


non−isolation system

energy dissipation system



full isolation system



full isolation system with friction device

Fig. 3 Mechanical model of various systems

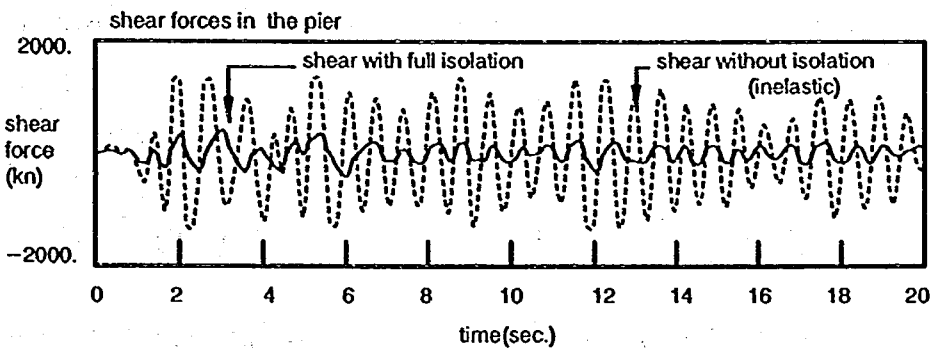


Fig. 4 Shear in the pier for a bridge with and without isolation and/or energy dissipation

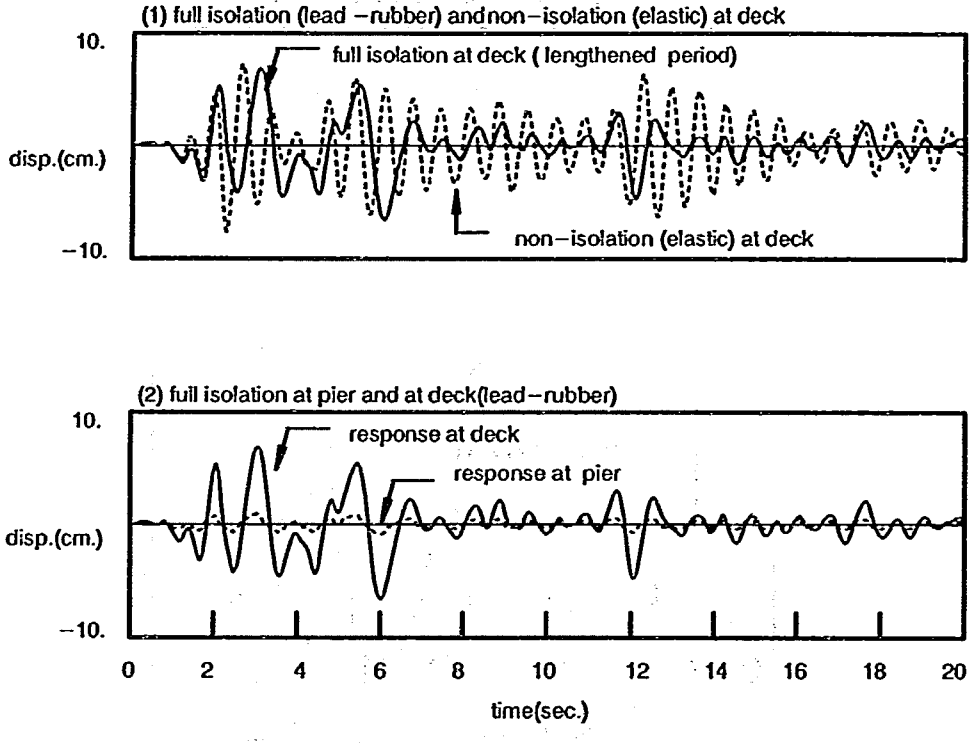


Fig. 5 Displacement of non−isolation energy dissipaters and full isolation lead rubber isolators

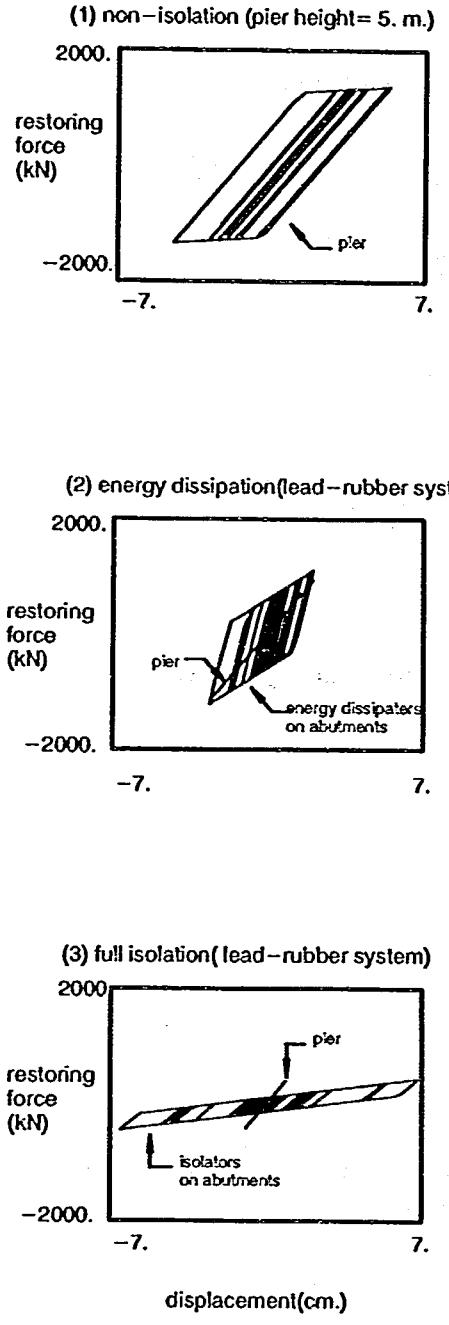


Fig. 6 Hysteretic behavior of piers and of energy dissipaters and isolators on abutments

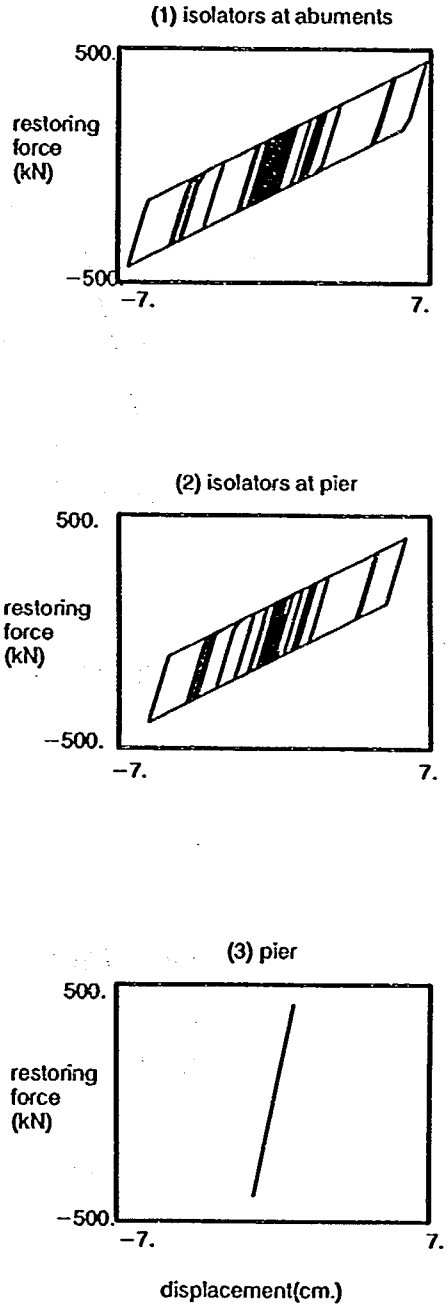


Fig. 7 Hysteretic behavior of isolators and pier with full isolation lead−rubber system

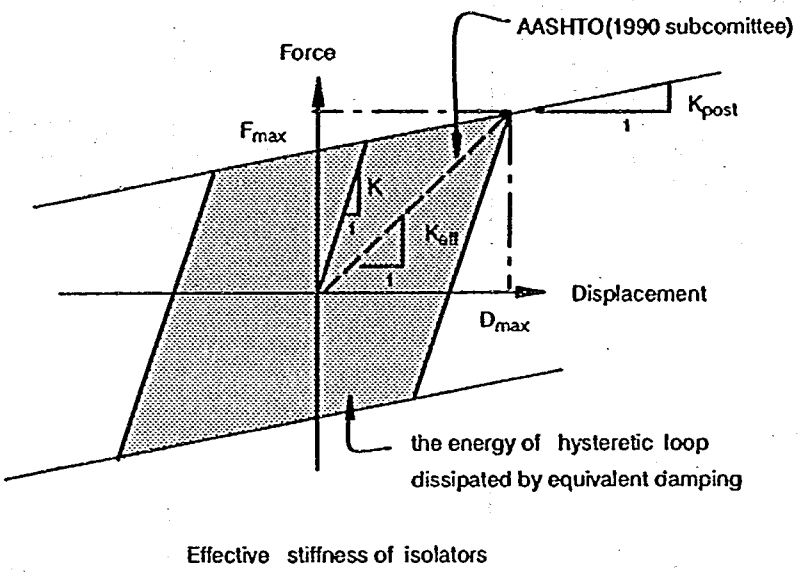


Fig. 8 Simplified effective stiffness and damping model

Notation for Fig. 9

Δ_s=max. displacement of superstructure

Δ_p= displacement of pier

Δ_i = displacement of isolator

F_{max}= max. shear force of isolator with rigid pier

F^*_{max}= max. shear force of isolator with elastic pier

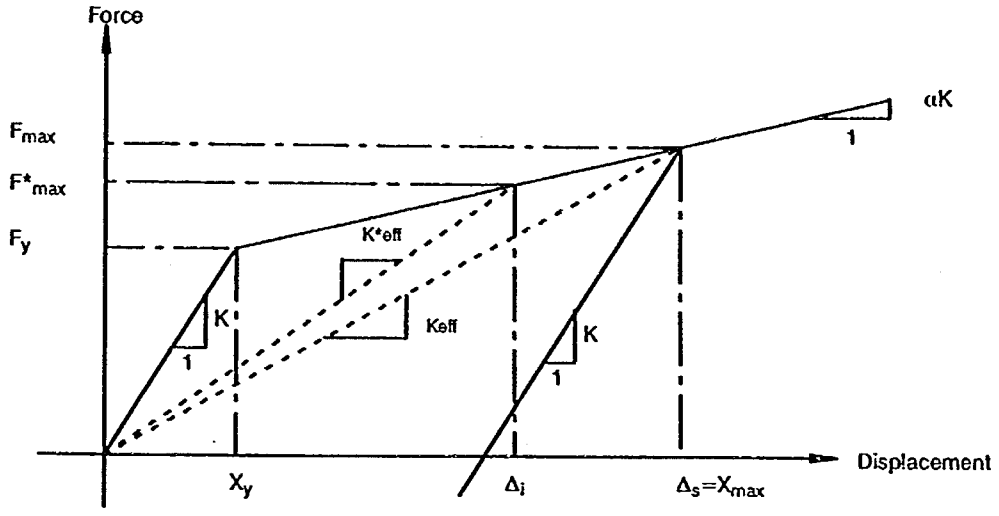
F_y= yielding force of isolator

K= initial stiffness of isolator

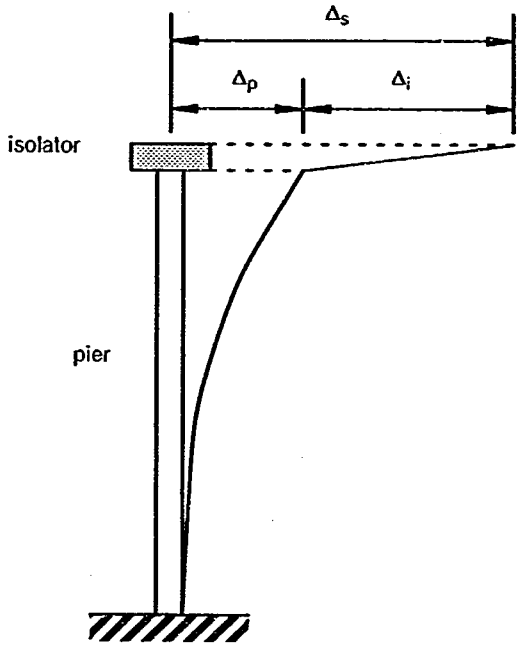
αK= post-yielding stiffness of isolator

K_{eff}= effective stiffness of isolator with rigid pier

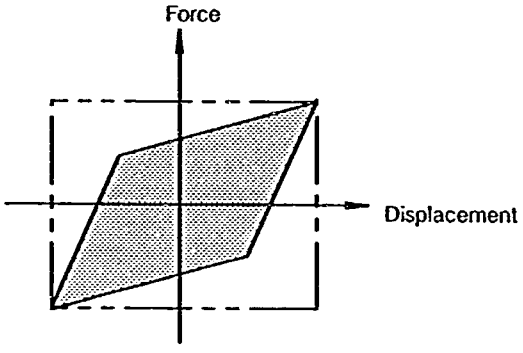
K^*_{eff}= effective stiffness of isolator with elastic pier



Force–displacement relationship of isolators



Displacement of the first mode of sub–stucture



Hysteretic loop ratio

Fig. 9 Proposed simplified model for full isolation of a bridge

EVALUATION OF MODAL DAMPING RATIO OF BRIDGES BASED ON STRAIN ENERGY PROPORTIONAL METHOD

by

Kazuhiko KAWASHIMA[1], Hiroyuki NAGASHIMA[2] and Hideaki IWASAKI[3]

1) Head, Earthquake Engineering Division, Earthquake Disaster Prevention Department, Public Works Research Institute
2) Former Research Engineer, ditto
3) Research Engineer, Ground Vibration Division, ditto

ABSTRACT

Presented in this paper is a model free oscillation test and an analysis for clarifying the strain energy proportional damping method which is widely adopted for evaluating modal damping ratio of structures. Because damping ratio of structural components is sometimes different even in the same structure, it is required in the modal dynamic response analysis to evaluate the damping ratio for each mode. In this paper it is presented from the experiment and analysis that the strain energy proportional method is quite accurate for evaluating the modal damping ratio of structures for seismic analysis.

Key Words : Seismic Design, Damping Ratio, Energy Dissipation, Bridges

INTRODUCTION

Damping ratio is an important parameter for evaluating seismic response of structures. Although the mass and stiffness can be accurately computed from mass and stiffness distribution of structures, the damping ratio can not be evaluated in the similar manner because prediction of energy dissipation in structures is very complex. Therefore instead of directly evaluating energy dissipation in structures it is generally adopted to evaluate the energy dissipation of structures in terms of damping ratio. The damping ratio is an appropriate parameter for assigning the damping characteristics of structures. But it should be keep in mind that the damping ratio can be defined only for a single-degree-of-freedom oscillator. From the analogy of the orthogonal condition of modal matrix with respect to stiffness and mass matrix, the damping ratio has been assumed for seismic analysis of structures.

Damping ratio is sometimes different depending on structural components even in the same structure. Therefore it is required to evaluate the modal damping ratio based on the different damping ratio assigned for each structural component. The strain energy proportional method has been

widely used for such purpose[1]. Because most of energy dissipation is developed due to deformation of structures, it has been considered reasonable to assume this method. But theoretical verification was not yet fully made.

This paper attempts to verify the strain energy proportional method for application to seismic design of structures. Based on a model oscillation test which is carefully made for evaluating energy dissipation of structural components as well as whole structure, accuracy and application of the strain energy proportional method is clarified. A bridges is considered for analysis.

ENERGY PROPORTIONAL DAMPING

For a linear discrete structure, the equations of motion may be written as

$$\mathbf{M}\ddot{\mathbf{u}} + \mathbf{C}\dot{\mathbf{u}} + \mathbf{K}\mathbf{u} = \mathbf{M}\{1, 0, 0, \cdots 1, 0, 0\}^{T}\ddot{z}_{gx} \tag{1}$$

where

M : mass matrix
C : damping matrix
K : stiffness matrix
$\ddot{\mathbf{u}}$, $\dot{\mathbf{u}}$, $\mathbf{u}$: displacement, velocity and acceleration vector
$\ddot{z}_{gx}$: ground acceleration in x axis

Denoting ω_i and ϕ_i as the undamped angular natural frequency and mode shapes for i-th mode, $\ddot{\mathbf{u}}$, $\dot{\mathbf{u}}$, $\mathbf{u}$ may be expressed as

$$\begin{aligned}
\ddot{\mathbf{u}} &= \sum_{i=1}^{K} \boldsymbol{\phi}_i \ddot{q}_i(t) \\
\dot{\mathbf{u}} &= \sum_{i=1}^{K} \boldsymbol{\phi}_i \dot{q}_i(t) \\
\mathbf{u} &= \sum_{i=1}^{K} \boldsymbol{\phi}_i q_i(t)
\end{aligned} \tag{2}$$

in which q_i represents the generalized coordinate for i-th mode and K represents number of freedom.

From the orthogonal condition, the stiffness matrix K and mass matrix M become as

$$\begin{aligned}
\boldsymbol{\phi}_m^{T}\mathbf{K}\boldsymbol{\phi}_n &= 0 \\
\boldsymbol{\phi}_m^{T}\mathbf{M}\boldsymbol{\phi}_n &= 0
\end{aligned} \qquad (m \neq n) \tag{3}$$

Assuming that the damping matrix C can be also orthogonalized as

$$\phi_m^T C \phi_n = 0 \qquad (4)$$

one can have k sets of uncoupled equation of motion as

$$\ddot{q}_i + 2 h_i \omega_i \dot{q}_i + \omega_i^2 q_i = -\Gamma_{ix} \ddot{z}_{gx} \qquad (5)$$

in which h_i and Γ_{ix} represent the modal damping ratio and mode participation factor for i-th mode, respectively.

It is important to note here that the modal damping ratio h_i which is defined only for a single degree of freedom oscillator has been adopted in a dynamic response analysis of multi-degree-of-freedom system in the form of Eq. (5) because there is not a practical definition for energy dissipation for multi-degree-of-freedom system.

It is then required to evaluate the modal damping ratio of Eq. (5) based on the energy dissipation mechanism of the structure. For such purpose it is assumed to divide a structure into several structural segments in which energy dissipation has the same mechanism as shown in Fig. 1[2)3)]. The segment is designated hereinafter as a substructure. The substructure may be a deck, a pier and a foundation as shown in Fig. 2 in the analysis of a bridge.

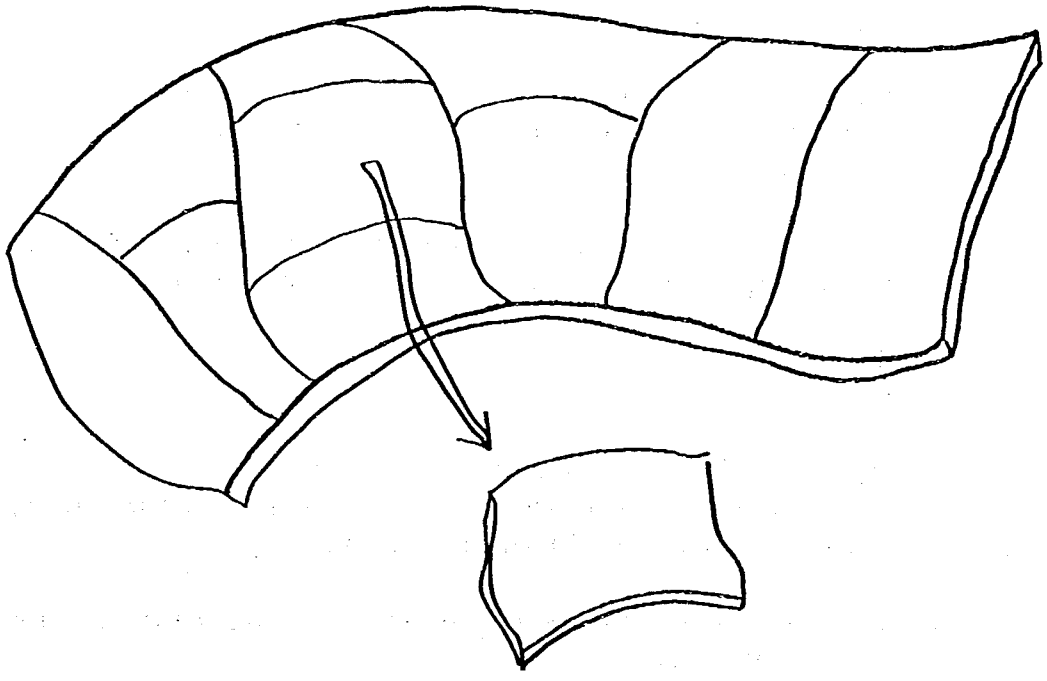


Fig.1 Substructures

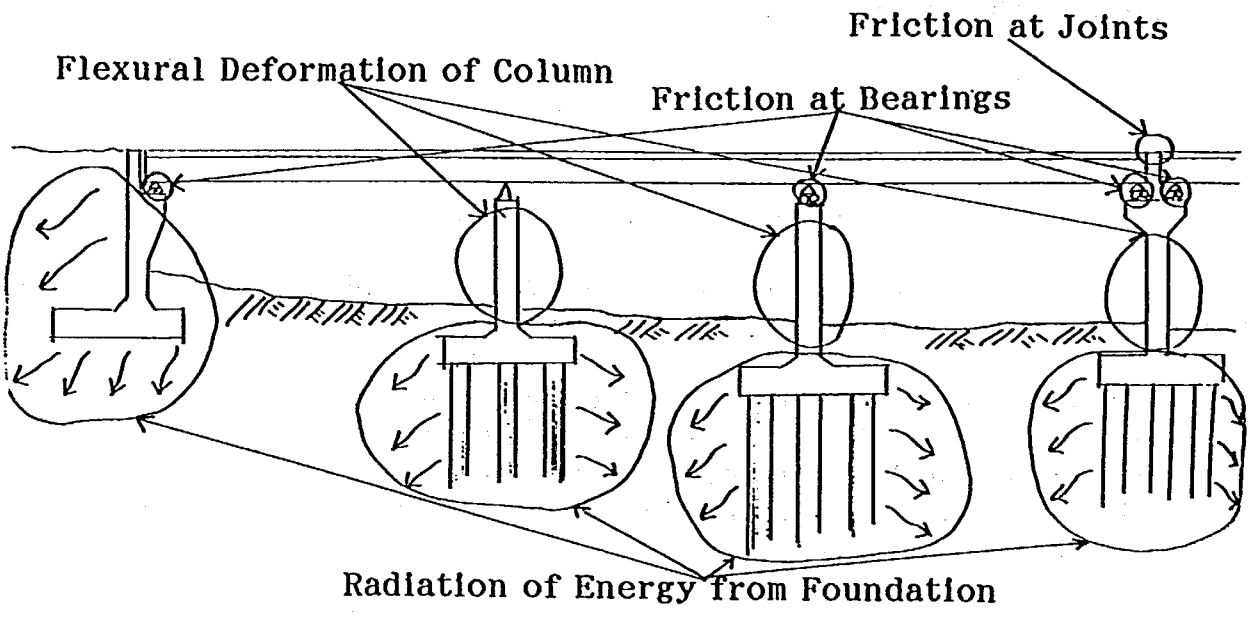


Fig.2 Substructures for Bridges

Strain energy in j-th substructure for i-th mode may be evaluated as

$$E_{ij} = \Sigma \ \phi_{ij}^{T} \cdot k_j \cdot \phi_{ij} \qquad (6)$$

where

E_{ij} : strain energy of j-th substructure for i-th mode
ϕ_{ij} : mode shape of j-th substructure for i-th mode
k_j : stiffness matrix of j-th substructure

Denoting the energy dissipation in j-th substructure for i-th mode as ΔE_{ij}, the damping ratio of the j-th substructure may be evaluated as

$$h_{ij} = \frac{1}{2\pi} \frac{\Delta E_{ij}}{E_{ij}} \qquad (7)$$

Because the damping ratio of substructures depends on the mode shape and boundary condition, it needs to be the one developed when the substructures deform as a part of the structure in the i-th mode shape.

Then the strain energy and energy dissipation of the whole structure for i-th mode can be evaluated as

$$E_i = \sum_{j=1}^{n} E_{ij}$$

$$\Delta E_i = \sum_{j=1}^{n} \Delta E_{ij} \tag{8}$$

in which n represents number of substructures. The damping ratio of whole structure (modal damping ratio) for i-th mode may be written from Eq. (8) as

$$h_i = \frac{1}{2\pi} \frac{\Delta E_i}{E_i} \tag{9}$$

Substituting Eqs. (7) and (8) into Eq. (9), one obtains an equation for evaluating the modal damping ratio as

$$h_i = \frac{\sum_{j=1}^{n} E_{ij} h_{ij}}{\sum_{j=1}^{n} E_{ij}} \tag{10}$$

Eq. (10) is called as the strain energy proportional damping because the averaged damping ratio over each substructure is taken with the strain energy of the substructure being the weighting function. Substituting Eq. (6) into Eq. (10), Eq. (10) can be modified in the form which is more appropriate for computation

$$h_i = \frac{\sum_{j=1}^{n} \phi_{ij}^T \cdot h_{ij} \cdot k_j \cdot \phi_{ij}}{\sum_{j=1}^{n} \phi_{ij}^T \cdot k_j \cdot \phi_{ij}} \tag{11}$$

MODEL FREE OSCILLATION TEST

Fig. 3 shows the model bridge studied for verifying the effectiveness of the strain energy proportional damping method. Photos 1 and 2 show the bridge model and the bearing. The girder is of a rigid steel plate so that energy dissipation during excitation is negligibly small. The girder has the span length of 2.1 m and the weight of 611.7 kgf. Each column with the height of 95 cm is of four steel plates with the top of each two plates being rigidly connected. The bottom of the columns are rigidly connected to base frame for preventing energy dissipation at the bottom.

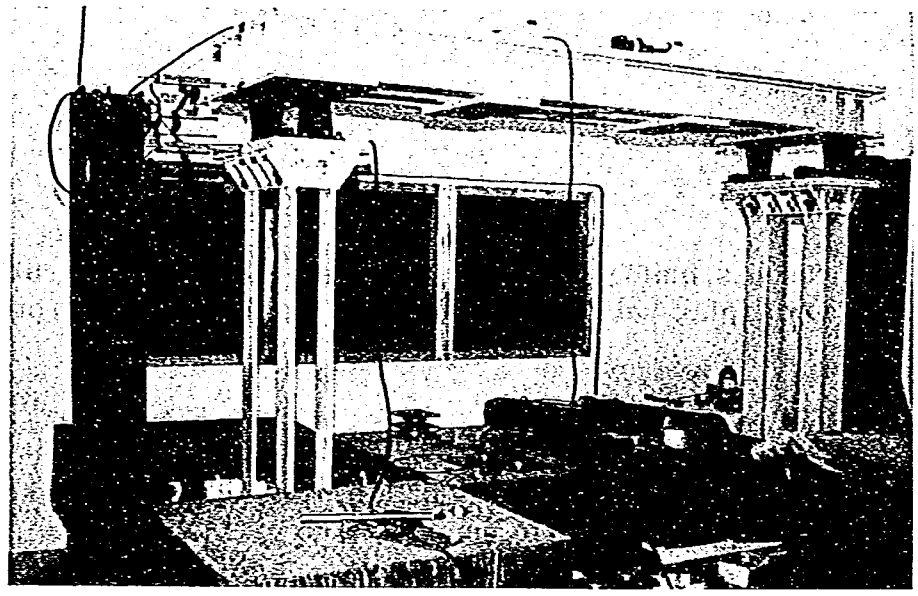


Photo 1 Bridge Model

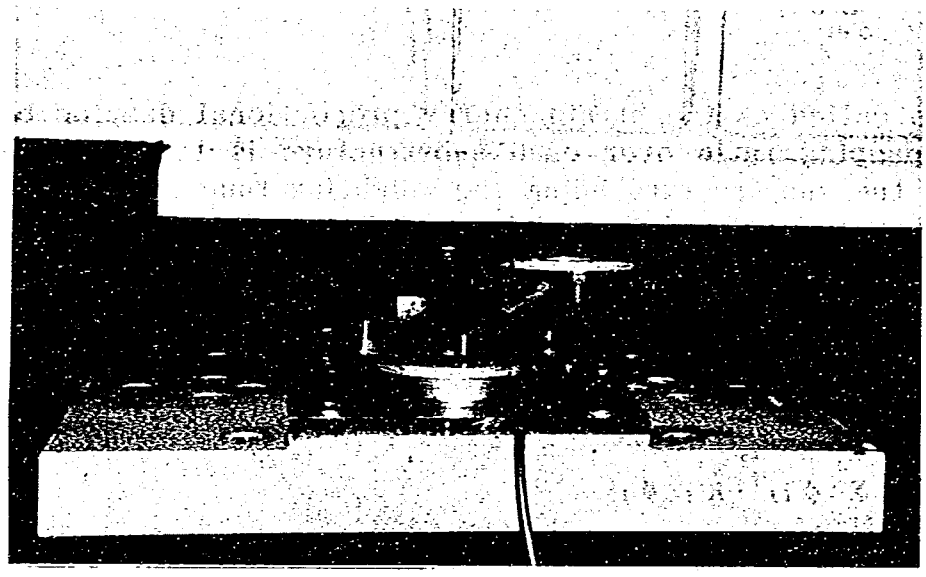


Photo 2 Bearings

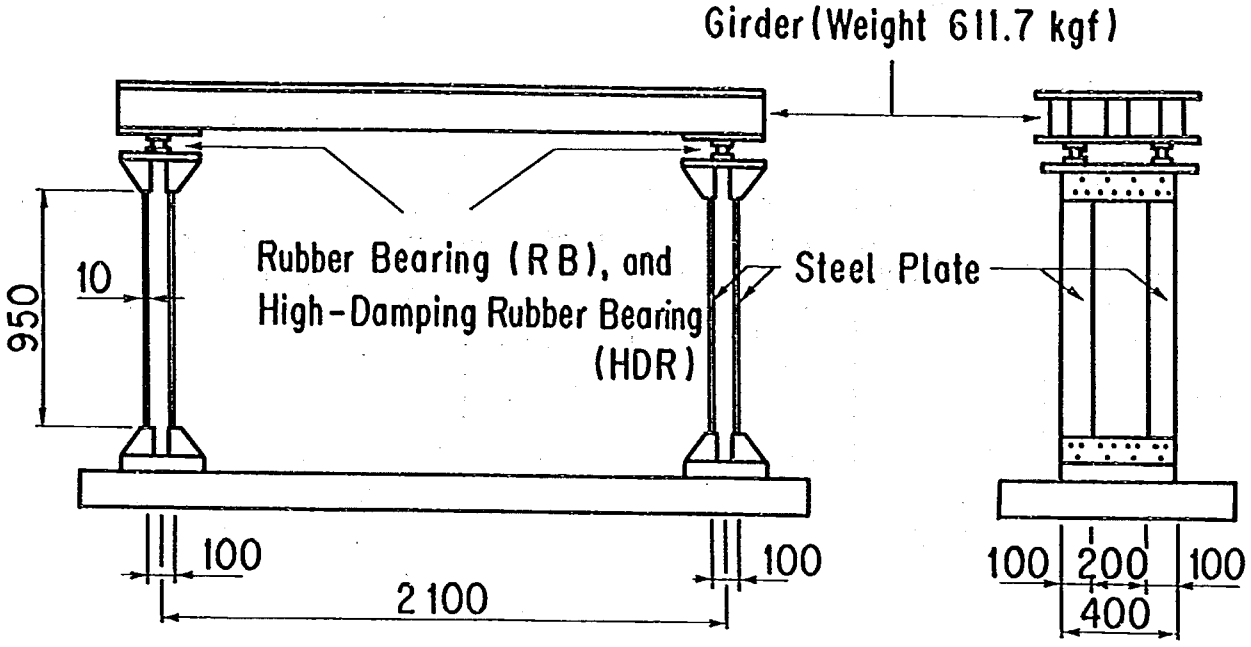


Fig.3 Model Bridge used for Free Oscillation Test

Four bearings were used for supporting the deck. Two types of bearings as shown in Fig. 4 were adopted for the test. One is the laminated natural rubber bearing, which is called hereinafter as RB. This was made by laminating 25 natural rubber plates with thickness of 0.9 mm and 24 steel plates with thickness of 0.3 mm. Total thickness of rubber is 22.5 mm. It has elastic restoring force characteristics. The other is the laminated high damping rubber bearing, which is called as HDR in this paper. This was made by laminating 37 high energy absorbing rubber plates with thickness of 0.5 mm and 36 steel plates with thickness of 0.3 mm. Total thickness of high energy absorbing rubber is 18.5 mm.

In the model bridge, energy dissipation is developed at bearings and columns. Therefore, bearings and columns are regarded as the substructures for evaluating modal damping ratio of the model bridge by Eq. (11). Because little energy dissipation is developed at the rigid deck, it is disregarded in the analysis. The modal damping ratio only for 1st mode is evaluated in the test for making the excitation simple and easy.

For evaluating the damping ratio of each substructure, free oscillation test was made for two types of bearings (RB and HDR) and two columns (Column A and B). Free oscillation test of the model bridge was also made for evaluating the modal damping ratio of whole structure.

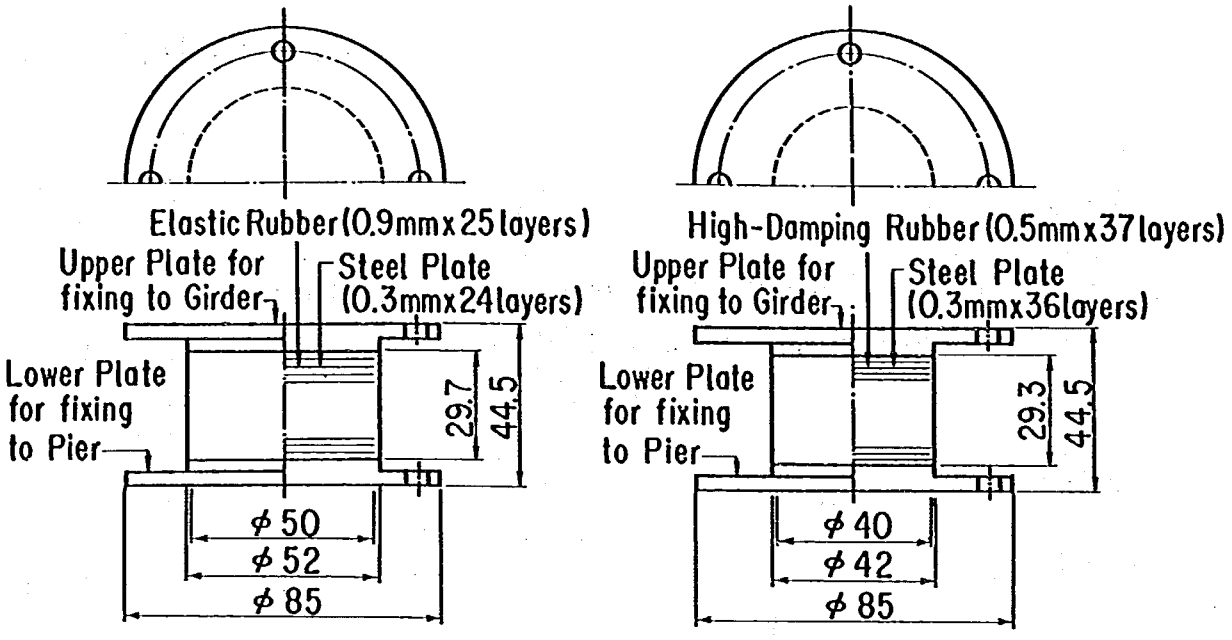


Fig.4 Model Bearings for Free Oscillation Test

In the free oscillation test of the model bridge, the deck was displaced in longitudinal direction, and by releasing it from the displaced position, free oscillation was developed. The 1st mode shape of the model bridge in longitudinal direction is of lateral movement of the deck with flexural deformation of cantilevered columns. Similarly the free oscillation test was made separately for the column A and B. In the free oscillation test of the bearings, four sets of bearings were directly placed on a rigid steel frame and the deck was placed on them. Then the deck was displaced laterally and released smoothly so that shear deformation was developed in the four bearings. Because the steel frame and deck are rigid, energy dissipation developed in this test represents that developed in the bearings. The test was made separately for RB and HDR.

Because the stiffness of the bearing depends on temperature, the tests were made in a room with the constant temperature with 20 ℃. Displacement of the deck and columns was measured. Acceleration was measured so that the inertia force of the deck be evaluated. It will be used to evaluate the stiffness of bearings. Each test was made twice to verify the stableness of the test results.

FREE OSCILLATION OF MODEL BRIDGE

Fig. 5 shows the decay of free oscillation of the bridge model. It is apparent that the free oscillation decays much faster in the model supported by HDR than the model supported by RB. Logarithmic damping ratio δ can be evaluated from the free oscillation as

$$\delta = \log_e (a_m / a_{m+1}) \qquad (12)$$

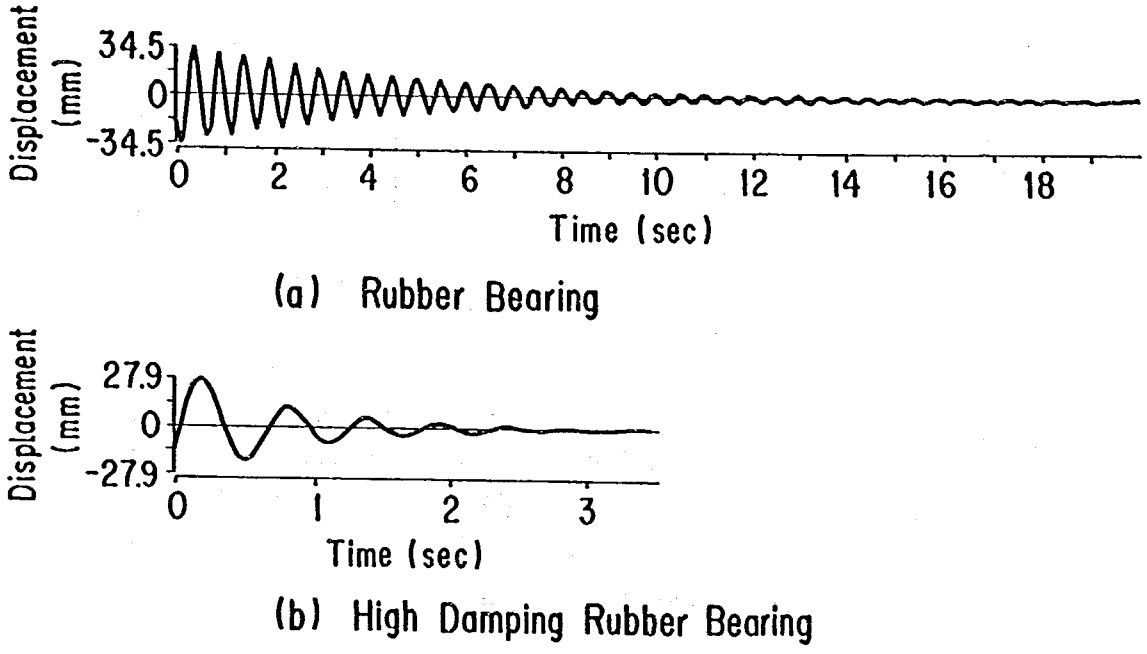


Fig.5 Decay of Free Oscillation of Deck Displacement Amplitude of Bridge Model

where

δ : logarithmic damping ratio

a_m : displacement amplitude of m-th peak of free oscillation

Damping ratio h may be evaluated from the logarithmic damping ratio as

$$\delta = 2\pi h / \sqrt{1 - h^2} \qquad (13)$$

Fig. 6 shows the dependence of the 1st mode damping ratio of the model bridge thus evaluated on the displacement amplitude of the deck. Some scatter is seen at small displacement in the bridge model supported by HDR. HDR shows low damping ratio at small displacement. Therefore disregarding such part, damping ratio was evaluated for the displacement range of 6.3 mm - 27.9 mm in the model supported by HDR and 23.8 mm - 33.0 mm in the model supported by RB. The averaged damping ratio over this range is 11.4 % in the model supported by HDR and 1.69 % in the model supported by RB.

Fig 7 compares the decay of free oscillation of RB and HDR. It is apparent that the oscillation decreases faster in HDR than RB. Fig. 8 shows the dependence of damping ratio of RB and HDR on the lateral displacement developed in the bearings. Decrease of damping ratio at small displacement is seen, especially in HDR. This is the reason for causing the decrease of the damping ratio of the bridge model as shown in Fig. 6. The damping ratio of both RB and HDR has less displacement dependency. The averaged damping ratio over the displacement range developed during the above described free oscillation test of the whole model bridge is 3.27 % in RB and 25.4 % in HDR.

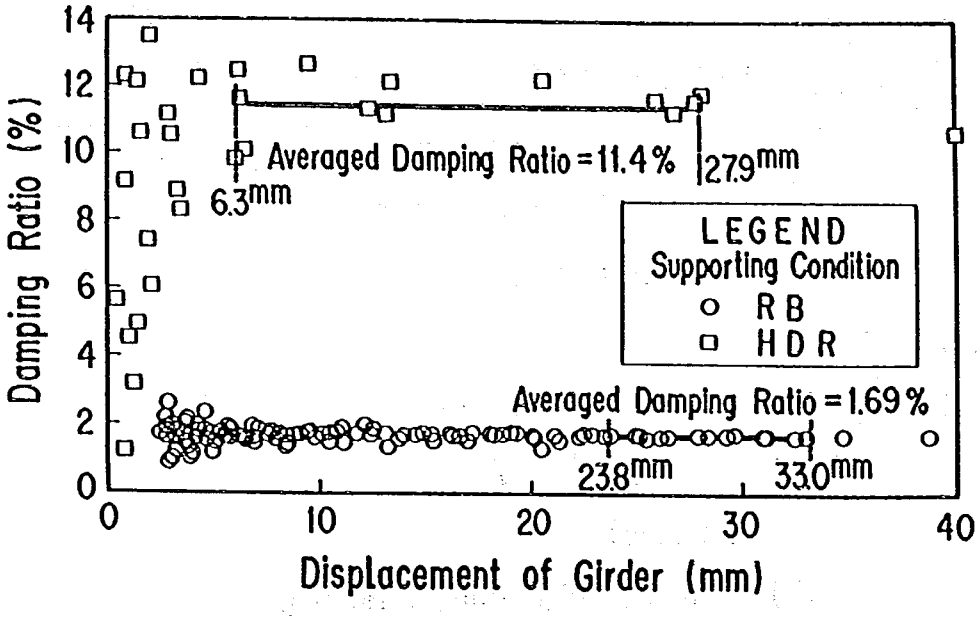


Fig.6 Damping Ratio of Model Bridge vs. Oscillation Amplitude

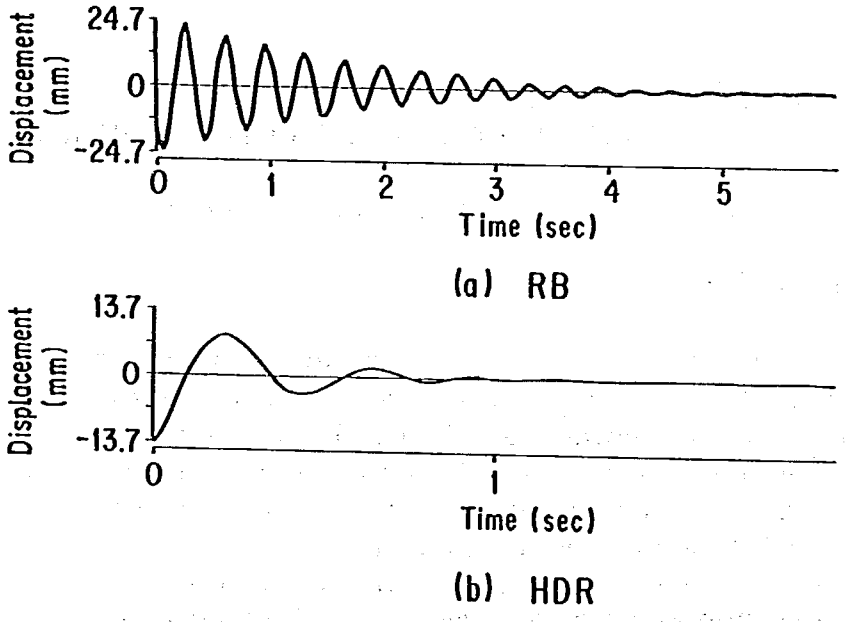


Fig.7 Decay of Free Oscillation of Bearing Displacement

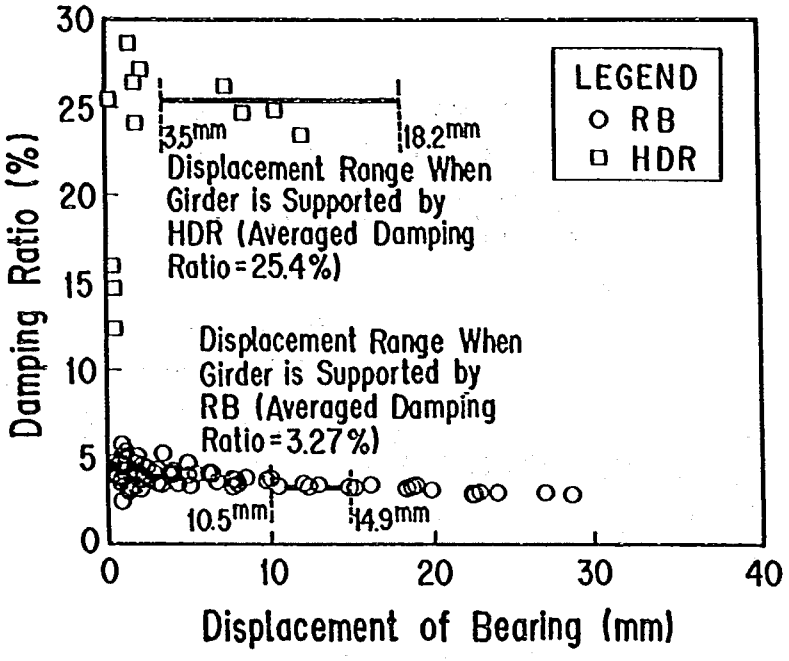


Fig.8 Damping Ratio of Bearing vs. Shear Displacement

Fig. 9 shows the decay of free oscillation at the top of of a column. Fig. 10 shows the displacement dependence of the damping ratio thus evaluated. Because the displacement amplitude developed at the column top during the free oscillation test of the whole bridge model is 13.4 - 18.2 when the deck is supported by RB and 3.0 - 10.9 when the deck is supported by HDR, the damping ratio of the columns A and B is 0.708 % and 0.954 % for RB and 0.459 % and 0.544 % for HDR.

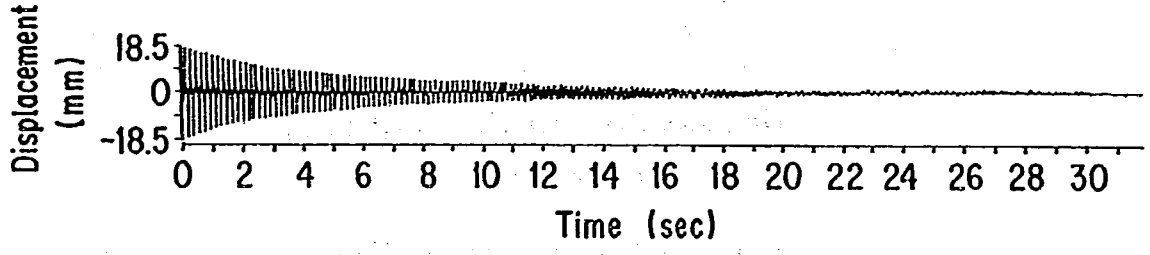
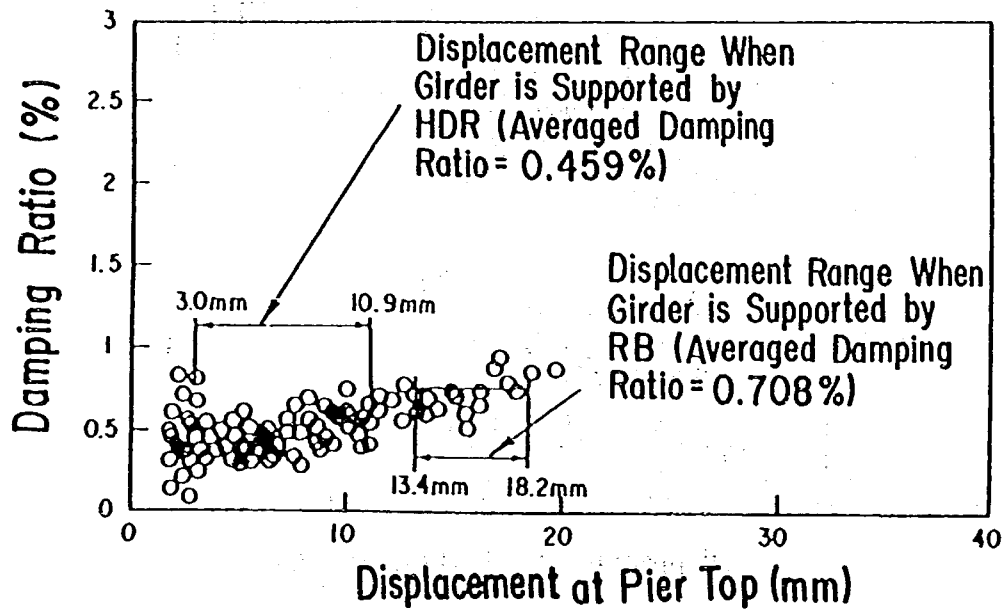
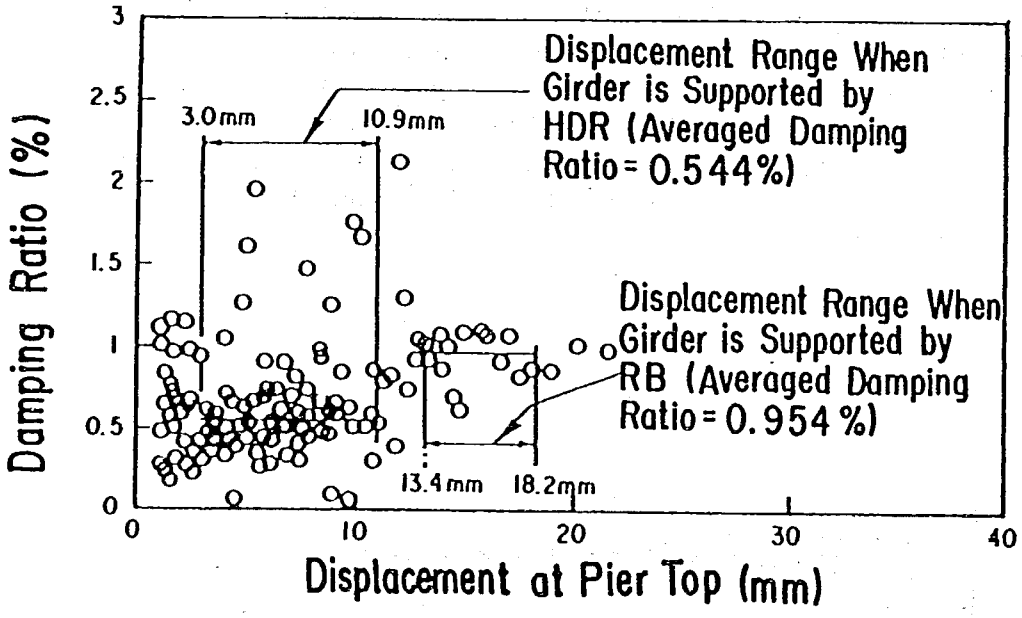


Fig.9 Decay of Free Oscillation of Column



(a) Column A



(b) Column B

Fig.10 Damping Ratio of Column vs. Oscillation Amplitude

ACCURACY OF STRAIN ENERGY PROPORTIONAL METHOD

Because the damping ratio of each substructure was evaluated, the damping ratio h_1 of the the whole bridge model for 1st mode may be evaluated from Eq. (10) as

$$h_1 = \frac{E_{1cA}h_{1cA} + E_{1cB}h_{1cB} + E_{b1}h_{1b}}{E_{1cA} + E_{1cB} + E_{1b}} \tag{14}$$

where

E_{1cA}, E_{1cB} : strain energy of column A and B for 1st mode
E_{1b} : strain energy of bearings for 1st mode
h_{1cA}, h_{1cB} : damping ratio of column A and B
h_{1b} : damping ratio of bearings

Because the damping ratio of the whole bridge model was obtained from the test, accuracy of Eq. (10) is clarified by comparing the damping ratio predicted by Eq. (14) with the one evaluated from the test.

Strain energy of the columns and bearings may be evaluated as

$$E_{1cN} = \frac{1}{2} k_{cN} u_{cN}^2 \quad (N=A, B) \tag{15}$$

$$E_{1b} = \frac{1}{2} k_b u_b^2 \tag{16}$$

where

E_{1cA}, E_{1cB} : strain energy of column A and B for 1st mode
E_{1b} : strain energy of bearings for 1st mode
k_{cA}, k_{cB} : stiffness of column A and B
k_b : stiffness of bearings
u_{cA}, u_{cB} : lateral displacement at top of column A and B
u_b : shear displacement of bearings

The stiffness of the columns k_{cA} and k_{cB} can be evaluated based on the dimension of the columns and elastic modulus. The stiffness of the bearings was evaluated from the hysteresis loop of the force vs. displacement relation as the equivalent stiffness. Fig. 11 shows the stiffness of the bearings thus evaluated vs. shear displacement relation. Because the stiffness of the bearings has some displacement dependency, it was approximated as

$$k_b = 22.7 - 0.2 u_b \quad (RB)$$
$$k_b = 8.0 - 0.2 u_b \quad (HDR) \tag{17}$$

In the free oscillation test of the whole bridge model, the deck displacement can be evaluated as

$$u_d = u_p + u_b \tag{18}$$

where

u_d : deck displacement

u_p : displacement at column top

u_b : shear displacement of bearings

Because u_d and u_p were measured during the test, u_b can be computed from Eq. (18). Then the stiffness of the bearings can be estimated by Eq. (17).

Thus the damping ratio of the model bridge was evaluated from Eq. (14) for several peaks of free oscillations as shown in Table 1. Fig. 12 compares the predicted and measured damping ratio of the bridge model. The predicted values are very close with the measured ones. They are within ± 20 % of the measured damping ratio.

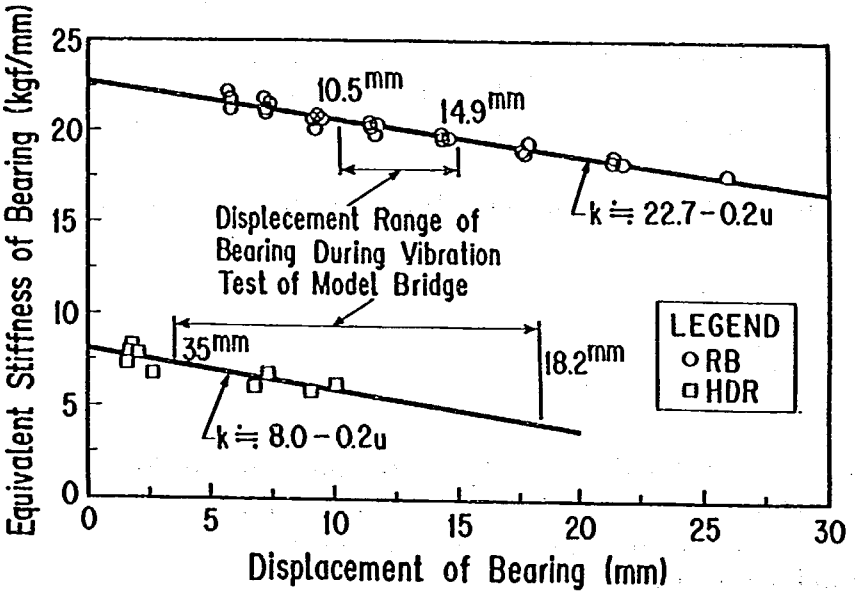


Fig.11 Displacement Dependence of Stiffness of Bearings

Table 1 Comparison of Predicted and Measured Damping Ratio of Model Bridge

Type of Bearing	Number of Free Oscillation	Displacement of Bridge Model			Damping Ratio and Strain Energy of Structural Members						Modal Damping of Bridge	
		Displacement at Girder d_g (mm)	Displacement at Pier Top d_p (mm)	Displacement at Bearing d_b (mm)	Pier A		Pier B		Bearing		Estimated by Eq.(11)	Measured
					h_{pA}(%)	E_{pA}	h_{pB}(%)	E_{pB}	h_b (%)	E_b	h_A	h_E
Rubber Bearing (RB)	1	33.0	18.2	14.9	0.708	1.437	0.954	1.424	3.273	2.192	1.890	1.690
	2	29.6	16.5	13.3	0.708	1.181	0.954	1.170	3.273	1.775	1.881	1.690
	3	26.5	14.8	11.8	0.708	0.950	0.954	0.944	3.273	1.418	1.877	1.690
	4	23.8	13.4	10.5	0.708	0.779	0.954	0.772	3.273	1.137	1.864	1.690
High-Damping Rubber Bearing (HDR)	1	27.9	10.9	18.2	0.459	0.516	0.544	0.511	25.4	0.710	10.7	11.4
	2	13.4	5.7	8.2	0.459	0.141	0.544	0.140	25.4	0.213	11.2	11.4
	3	6.3	3.0	3.5	0.459	0.039	0.544	0.039	25.4	0.045	9.6	11.4

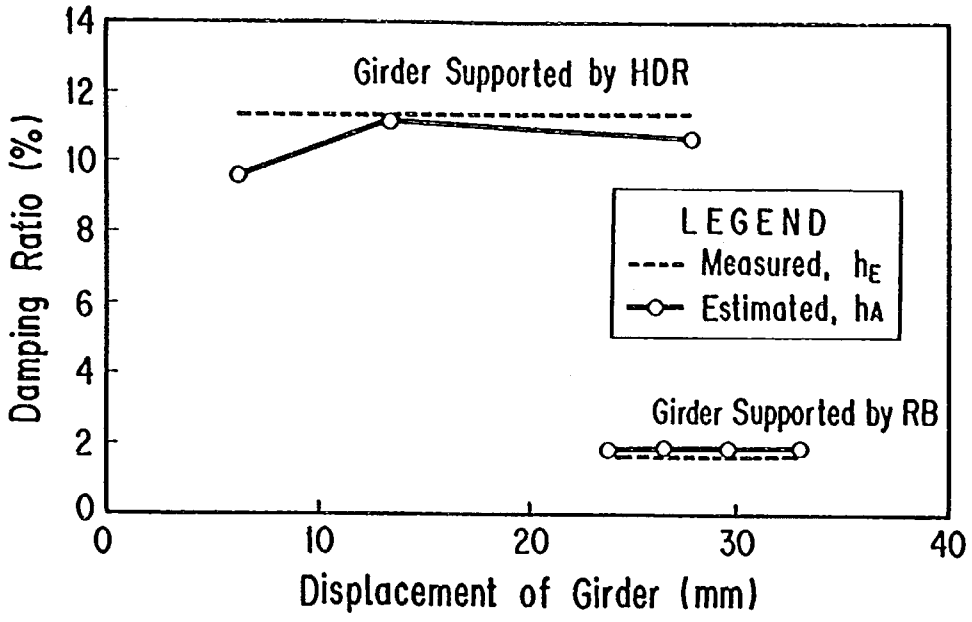


Fig.12 Accuracy of Predicted Damping Ratio

CONCLUSIONS

The effectiveness of the strain energy proportional damping method was verified through the free oscillation test of a model bridge. Damping ratio only for 1st mode was analyzed because of simplicity of the free oscillation test. It became apparent that the damping ratio of the bridge can be predicted by the strain energy proportional method with enough accuracy when the damping ratio of substructures is correctly evaluated.

REFERENCES

1) Japan Road Association : Part V Seismic Design, Design Specification of Road Bridges, February 1990
2) Kawashima, K., Unjoh, S. and Tsunomoto, M. : Damping Characteristics of Cable Stayed Bridges for Seismic Design, Journal of Research, Vol. 27, Public Works research Institute, December 1991
3) Kawashima, K., Unjoh, S. and Tsunomoto, M. : Estimation of Damping Ratio of Cable Stayed Bridges for Seismic Design, Journal of Structural Engineering, Vol. 119, No. 4, April 1993

DEVELOPMENTS IN SEISMIC PRIORITIZATION OF BRIDGES IN CALIFORNIA

ANN D. GILBERT
Caltrans Civil Engineer

California Department of Transportation
Division of Structures

ABSTRACT

Proposed is a risk based methodology to systematically prioritize bridges in California according to their need for seismic retrofit. The proposed procedure is based on the multi-attribute decision theory. Objectives of the prioritization program and procedural details are discussed.

INTRODUCTION

A highway system is a complex network of vulnerable links. Bridge structures are by far the most critical links because of their vulnerability to damage when subjected to earthquake loads. It is crucial that transportation agencies in seismic regions evaluate bridges for potential deficiencies. The California Department of Transportation has an ongoing program to develop risk based methodologies for prioritizing existing bridges according to their need for seismic retrofit. Upgrading efforts to reduce seismic risk have continued at an unprecedented rate since the Loma Prieta Earthquake. A logical procedure to systematically rank all bridges according to their need for seismic hazard mitigation has been an essential tool.

California poses a unique atmosphere with special demands on any prioritization procedure. The California highway system contains over 12,000 bridge structures with a wide variance in the seismic loads and hazards applied to each bridge. Extreme demands are placed on the highway system with usage over 20,000 vehicles per day. Furthermore, bridge types, configurations, and details are inconsistent throughout the state. Engineers must remain cognizant of these challenging issues when developing a seismic prioritization procedure.

This paper presents an overview of the latest developments in the seismic prioritization of bridge structures in California. The recent advances have been significant and will be discussed in terms of overall objectives.

RECENT ACHIEVEMENTS

The seismic retrofit prioritization scheme utilized by Caltrans prior to 1992 employed a simplified judgment based risk assessment. In this scheme, each bridge received an overall score computed as the weighted sum of 12 factors. The real merits of this system was its simplicity and the speed of computation.

This ranking scheme employed an additive approach where the weighted factors affecting the probability of failure were added to the weighted factors affecting the consequences of

failure. The overall ranking score as previously computed may produce inconsistent evaluations of relative risk.

Risk is properly evaluated by multiplying the probability of failure by the consequences of that failure. Recent investigations to revise the prioritization scheme has lead to some significant advances. The development work in this area has meant a redefinition of goals and accompanying limitations. Some cognizant and deliberate trade off decisions were necessary in an effort to make measurable progress and improvements in short periods of time. A conventional seismic risk evaluation for all 12,000 bridges in the 15,000 miles of California state highways, although ideal, would be extremely detailed and time-consuming. It has always been imperative that the screening procedure to prioritize for seismic retrofit be efficient and capable of rapidly assessing a large number of bridges. Thus, it was decided that the merits of the previous scheme in terms of its simplicity and speed of computation should not be compromised for an enhanced methodology.

The objective was to develop a logical framework to systematically combine those factors which evaluate relative risk for ranking purposes. It became essential to migrate toward the proper multiplicative definition of risk as the product of the probability of failure multiplied by the consequences of that failure. These goals have been achieved by the employment of the multi-attribute decision theory [1].

PROCEDURAL DETAILS

The development of a prioritization scheme based on the multi-attribute decision theory has resulted in many positive outcomes. This procedure utilizes a risk-based methodology and therefore provides a rational criteria for evaluating the relative priorities of existing bridges. This procedure does not assess absolute risk but only determines relative risk. It remains simplistic in nature and serves only to produce a preliminary ranking. The resultant ranking provides a framework for selecting bridges to undergo a detailed seismic evaluation and retrofit design. Perhaps the single most important achievement in this prioritization scheme is that it incorporates the advantages of previously developed methodologies while employing a multiplicative formulation. The multi-attribute decision procedure provides a systematic method for treating preferences and values in the prioritization process. The hierarchical nature of this procedure has the distinct advantages discussed below.

The multi-attribute decision procedure assigns a priority rating to each bridge in order to determine those structures which are more vulnerable to seismic activity in their current conditions. The prioritization is based on a two-level approach which separates the seismic hazard from the impact and structural vulnerability criteria. The severity of seismic exposure is considered independently from the vulnerability and importance. The prioritization risk rating estimates the seismic hazard to a bridge from various sources and then subsequently assesses the impact and structural vulnerability resulting from those hazards. The details of this formulation allows a bridge with low seismic hazard to receive a lower overall risk rating than a similar structure with higher seismic hazards. This effect was not as achievable with previous prioritization methods which rely on a point-score summation procedure.

Figure 1 presents an overview of the multi-attribute decision procedure. A priority risk rating is computed for each bridge in the California highway network. It is a two level approach with the first level assessing the seismic exposures to a bridge and the second level assessing the impact and structural vulnerability criteria.

The first level criteria directly assess the seismic activity and hazard to each bridge. The second level criteria jointly define the performance of each bridge and potential losses of a bridge. Each of the following four criteria ($c_1, c_2, \ldots, c_i$): seismic activity, hazard, impact, and vulnerability depend on a set of attributes ($a_1, a_2, \ldots, a_{mk}$). A set of weights ($w_1, w_2, \ldots, w_i$) are assigned to each criterion at every level to reflect their relative importance. Attribute weights ($x_1, x_2, \ldots, x_{mk}$) are also assigned to each attribute to define their relative importance within each criterion [1]. The details are illustrated in Figure 2. The criteria weights and attribute weights are based on a 1991 expert opinion survey work of engineers and managers within Caltrans [2].

A global utility function, $g(a_{mk})$, was created for each attribute. They are essentially weight functions defined between 0 and 1 in Figures 3 through 9. These global utility functions are the same as those used in previous algorithm work.

A prioritization rating, $\mathcal{R}_n$, is thus computed for each bridge such that:

$$\mathcal{R}_1 \geq \mathcal{R}_2 \geq \mathcal{R}_3 \geq \ldots \geq \mathcal{R}_n.$$

The prioritization rating is computed by multiplying the global utility functions with the weights of the attributes. That is:

$$\mathcal{R}_n = \sum_{\text{all } c_i} w_i(c_i) \sum_{j=1}^{mk} x_j(a_j) g(a_j)$$

where,

c_1 = seismic activity
c_2 = hazard criterion
c_3 = impact criterion
c_4 = vulnerability criterion

$w(c_1) = w_1 = 1.0$
$w(c_2) = w_2 = 1.0$
$w(c_3) = w_3 = 0.6$
$w(c_4) = w_4 = 0.4.$

The seismic activity criterion is based on some preliminary assessments and a recently developed activity map by L. Mualchin, Seismologist with the Divisi on of Structures. Fault activity has only recently been incorporated into the prioritization and stems from the recognition that the sources of maximum credible earthquakes [3] have different seismic activities. Since absolute seismic activity is quite difficult to ascertain, relative differences of fault seismic activity were determined utilizing slip rate, seismicity, and recency of movements. The ground shaking effects from each fault were captured by delineating a distance to 0.2g acceleration. The entire state of California was divided into areas affected by high active, active, moderate active, and low active faults. However, only three activity zones resulted because the effects from moderate faults were practically overshadowed by the active and high active faults [4].

The seismic hazard criterion includes three principle components: soil site conditions, peak rock acceleration, and duration of strong ground shaking. The peak rock acceleration is presumed to be produced by maximum credible earthquakes. Duration is a newly considered component and is currently divided into three groups: long (bracketed duration greater than 25 seconds), intermediate (bracketed duration of 15 to 25 seconds), and short (bracketed duration less than 15 seconds). Bracketed duration was employed as the approximate function of magnitude and source distance [4].

The impact criterion utilizes eight attributes to assess the consequences of bridge damage on public safety. The importance of bridge structures as vital lifeline links is determined in

terms of socioeconomic impacts and the effects on the users of the transportation system. In addition to considerations for traffic capacities on and under the structure, potential property damage and loss of life beneath the structure is accounted for by including the residential leased air space and storage leased air space attributes. The importance of each bridge as part of an overall transportation system is evaluated in this criterion.

The final criterion is structural vulnerability. It is defined by six attributes which examine structural details and components to define potential damage. The six attributes generally remain unchanged from previous prioritization procedures [5].

It is useful to compare the ranking which results from the multi-attribute decision procedure with the ranking produced by the previous additive procedure. Figure 10 presents the different ratings for a sample of 100 representative bridge structures. It represents approximately a 30% variation in rank ordering. It is believed that this 30% change produces a more consistent and accurate ranking.

FUTURE OBJECTIVES

There are several areas to address when considering potential enhancement issues. Some efforts are currently underway and others are only potential long term goals. Any refinements which can be achieved have merits in optimizing the allocation of retrofit funds and serve to enhance the prioritization tools which need to be in place in the event of a major earthquake.

Each enhanced prioritization method which has been adopted over the past several years has continually brought Caltrans closer to a methodology based on structural reliability theory. This is a very important concept and provides a defensible and theoretically sound approach to prioritization. Consideration is being given to the application of rigorous structural reliability principles to specific critical bridges with the eventual extension to all structures. A key component will be the development of empirical fragility curves. The ATC-13 [6] structural classifications currently available are inadequate. Work needs to be done in the area of extrapolating extremely limited damage data and correlating it with ground acceleration.

The California highway system is a complex network of critical and potentially vulnerable bridges. It is increasingly important to evaluate the seismic reliability of the lifeline from a network systems point of view. Each critical element, or bridge, must be considered as part of a global system. Some modest attempts have been made to address this concept in the current work. However, additional work is needed.

Further refinements of the current method may eventually include subdividing each attribute into sub-attributes. Possible correlation and interrelationships between attributes must also be addressed. A few of the global utility functions need to be reevaluated, modified, and subjected to a sensitivity analysis. Also, an investigation is needed to evaluate the possibility of saturation of several of the global utility functions. Seismic duration is a complex function of soil conditions, characteristics of sources, and propagation paths. The necessity of improving duration assessments has already been recognized but needs to be implemented.

Improvements in the seismic hazard definitions including refinement of the soil condition attribute and seismic activity maps need to be addressed. Likewise, continued emphasis should be placed on data development efforts. This includes further documentation of leased air space sites and other collocation issues.

Finally, an additional level of sophistication should incorporate a cost-benefit analysis. In this way, the overall highway system vulnerability can be reduced by optimally allocating limited resources. Consideration needs to be given to the fact that a sequentially ordered prioritization list provides an imperfect framework in which to optimally select retrofit projects. The selection of alternatives and optimization exercises must be formalized.

CONCLUSION

Relative seismic risk computations for bridge structures are currently based on a large number of assumptions and judgment. The origin of much of this is the uncertainty and randomness of the earthquake process, as well as, the absence of defensible fragility curves. Yet, the current multi-attribute decision procedure has proven to be a successful tool for prioritization. The heavy reliance on empirical experience through past seismic damage of highway bridges coupled with a logical decision process has served Caltrans well in meeting its current challenges. With research efforts already in place empirical experience can be combined with statistical data to advance towards state-of-the-art structural reliability procedures.

ACKNOWLEDGEMENTS

The author wishes to acknowledge the continued support and contributions from James H. Gates, California Department of Transportation, Divison of Structures. His commitment and recognition of the merits of risk based prioritization procedures have made the recent advances possible in California.

REFERENCES

1. Keeney, Ralph L. and Raiffa, Howard. Decisions with Multiple Objectives: Preferences and Value Tradeoffs. New York: Wiley Publishing. 1976.

2. Gilbert, Ann D. "Expert Opinion Survey". California Department of Transportation, Division of Structures. 1991.

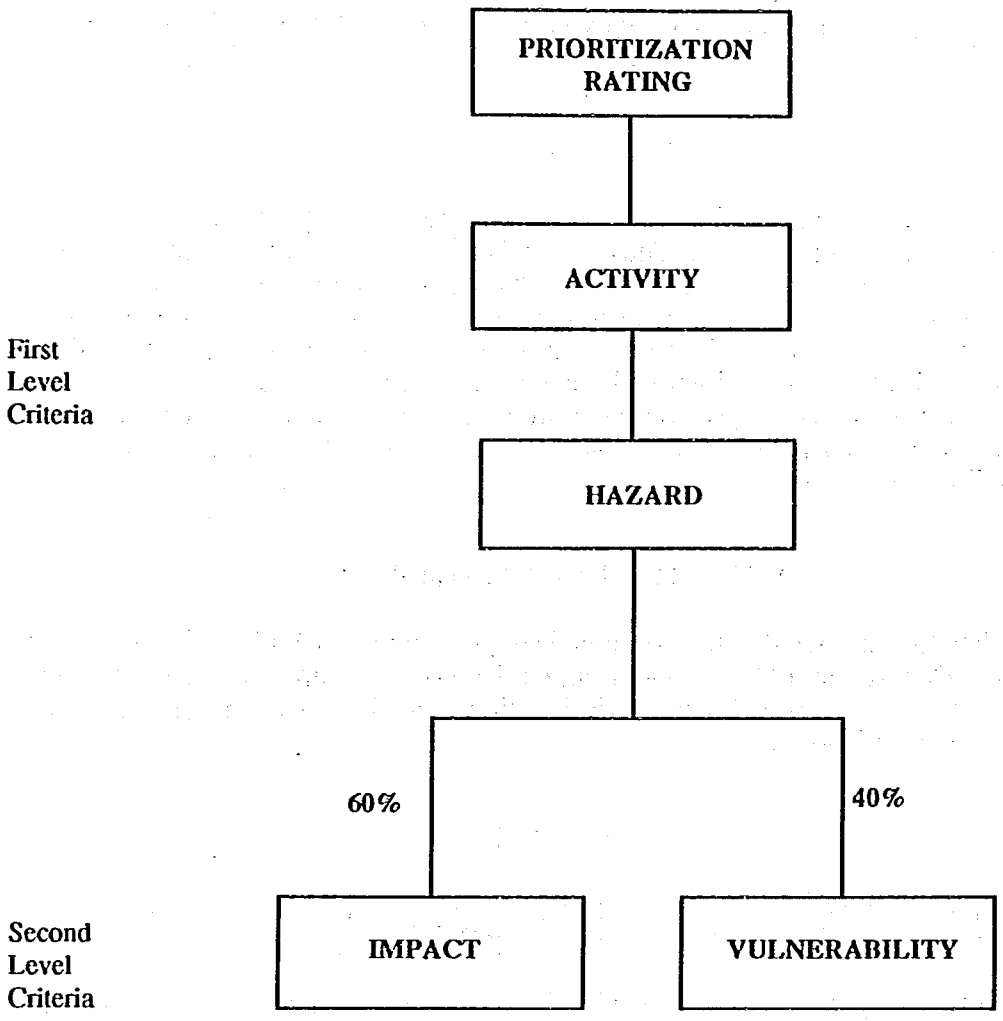
3. Mualchin, Lalliana and Jones, Allen Lynn. "Peak Acceleration from Maximum Credible Earthquakes in California (Rock and Stiff-Soil Sites)". Prepared for internal use by Caltrans. California Department of Conservation, Division of Mines and Geology Open-File Report 92-1. 1990.

4. Mualchin, Lalliana. "Seismic Hazard Components in the Caltrans Prioritization Algorithm". California Department of Transportation, Division of Structures. 1992.

5. Maroney, Brian. "Caltrans Seismic Risk Algorithm for Bridge Structures". California Department of Transportation, Division of Structures. 1990.

6. Applied Technology Council. "Earthquake Damage Evaluation Data for California". Report ATC-13. Also published by Federal Emergency Management Agency EMW-C-0912. 1985.

MULTI-ATTRIBUTE DECISION PROCEDURE



Prioritization Rating = (Activity)(Hazard) [(0.60)(Impact) + (0.40)(Vulnerability)]

Where,

$$\text{Activity} = \text{(Global Utility Function Value)}$$

$$\text{Hazard} = \sum \text{(Attribute Weight)(Global Utility Function Value)}$$

$$\text{Impact} = \sum \text{(Attribute Weight)(Global Utility Function Value)}$$

$$\text{Vulnerability} = \sum \text{(Attribute Weight)(Global Utility Function Value)}$$

Figure 1

CRITERIA AND ATTRIBUTE DETAILS

c_1 = ACTIVITY CRITERION:

Activity Attributes	Activity Weights
a_{11} = Seismic Activity	x_{11} = 100%

c_2 = HAZARD CRITERION:

Hazard Attributes	Hazard Weights
a_{21} = Soil Conditions	x_{21} = 33%
a_{22} = Peak Rock Acceleration	x_{22} = 38%
a_{23} = Seismic Duration	x_{23} = 29%

c_3 = IMPACT CRITERION:

Impact Attributes	Impact Weights
a_{31} = ADT on Structure	x_{31} = 28%
a_{32} = ADT Under/Over Structure	x_{32} = 12%
a_{33} = Detour Length	x_{33} = 14%
a_{34} = Leased Air Space (Residential, Office)	x_{34} = 15%
a_{35} = Leased Air Space (Parking, Storage)	x_{35} = 07%
a_{36} = Rte Type on Bridge	x_{36} = 07%
a_{37} = Critical Utility	x_{37} = 10%
a_{38} = Facility Crossed	x_{38} = 07%

c_4 = VULNERABILTY CRITERION:

a_{41} = Year Designed (Constructed)	x_{41} = 25%
a_{42} = Hinges (Drop Type Failure)	x_{42} = 16.5%
a_{43} = Outriggers, Shared Column	x_{43} = 22%
a_{44} = Bent Redundancy	x_{44} = 16.5%
a_{45} = Skew	x_{45} = 12%
a_{46} = Abutment Type	x_{46} = 08%

Figure 2

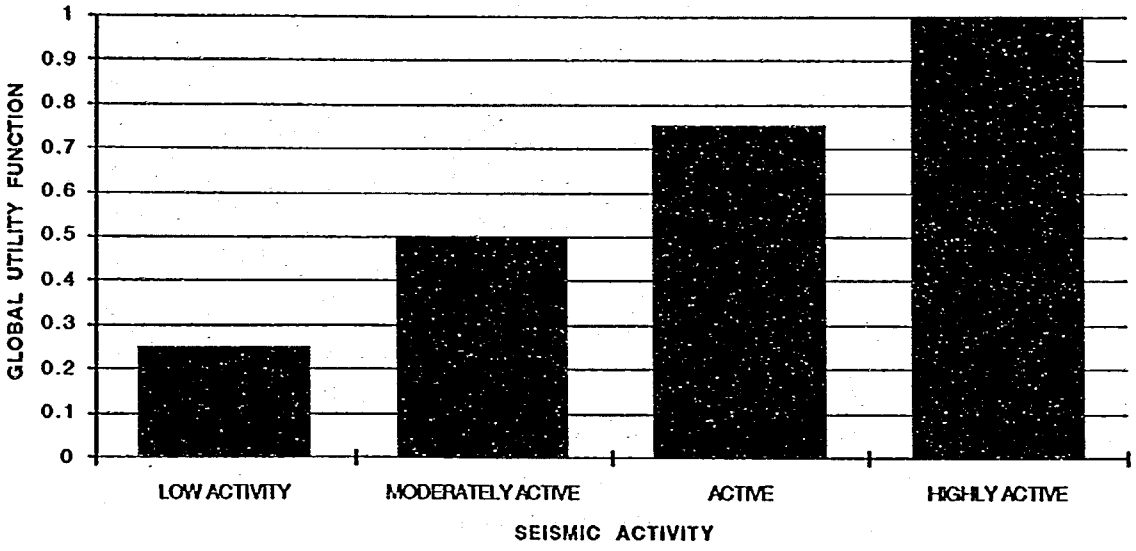
GLOBAL UTILITY FUNCTION DEFINITIONS

ACTIVITY CRITERION	
Seismic Activity	1.00*(0.25=low;0.50=moderate;0.75=active; 1.00=high)
HAZARD CRITERION	
Soil Conditions	0.33*(1=high risk zone; else 0)
Peak Rock Acceleration	0.38*(linear, normalized to 0.7g)
Seismic Duration	0.29*(0.5=short;0.75=intermediate;1=long)
IMPACT CRITERION	
ADT on Structure	0.28*(parabola for a max ADT of 200000)
ADT Under/Over Structure	0.12*(see ADT above)
Detour Length	0.14*(linear, normalized to 100 miles)
Leased Air Space (Residential, Office)	0.15*(1=present; else 0)
Leased Air Space (Parking, Storage)	0.07*(1=present; else 0)
Rte Type on Bridge	0.07*(1.0=interstate; 0.8=US , ST rte, or stream; 0.7=RR; 0.5=fed funded Co rte or city str; 0.2=nonfed funded Co rte of city str; 0.0=fed land, ST land, other)
Critical Utility	0.10*(1=present; else 0)
Facility Crossed	0.07*(see Rte Type on Bridge)
VULNERABILITY CRITERION	
Year Designed (Constructed)	0.25*(0.5=yr<1946; 1.0=1946≤yr≤1971; 0.25=1972≤yr≤1979; 0.0=yr>1979)
Hinges (Drop Type Failure)	0.165*(0.0=no hinge; 0.5=1 hinge; 1.0=2 or more hinges)
Outriggers, Shared Column	0.22*(1=present; else 0)
Bent Redundancy	0.165*(0.0=no col.;0.25=pier walls;0.5 multi-col bents;1.0=single col bents)
Skew	0.12*(linear, normalized to 90)
Abutment Type	0.08*(0=monolithic;1=nonmonolithic)

Figure 3

GLOBAL UTILITY FUNCTIONS

SEISMIC ACTIVITY



PEAK ROCK ACCELERATION

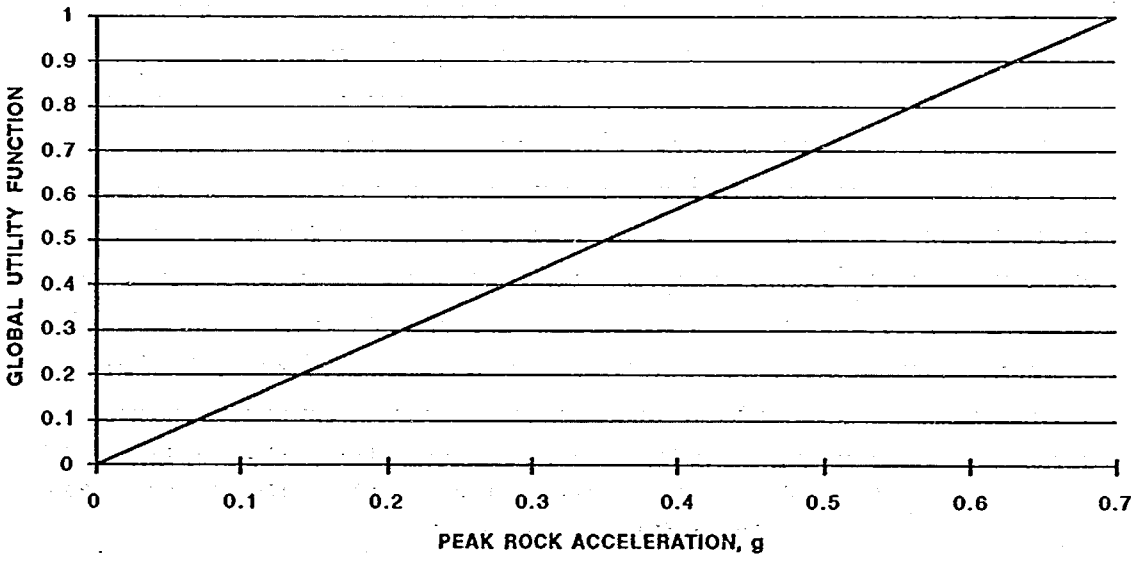
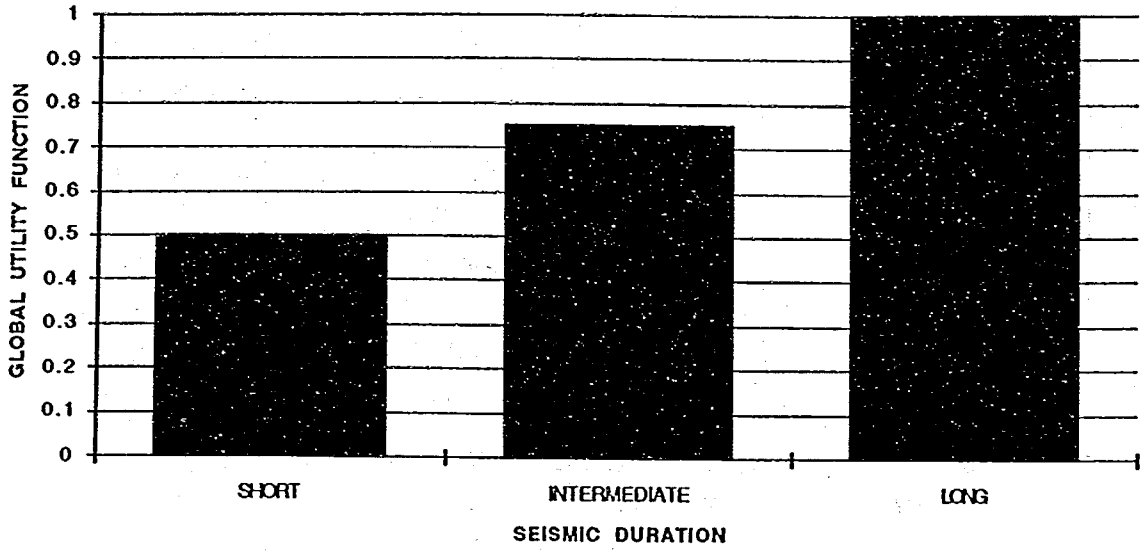


Figure 4

GLOBAL UTILITY FUNCTIONS

SEISMIC DURATION



AVERAGE DAILY TRAFFIC

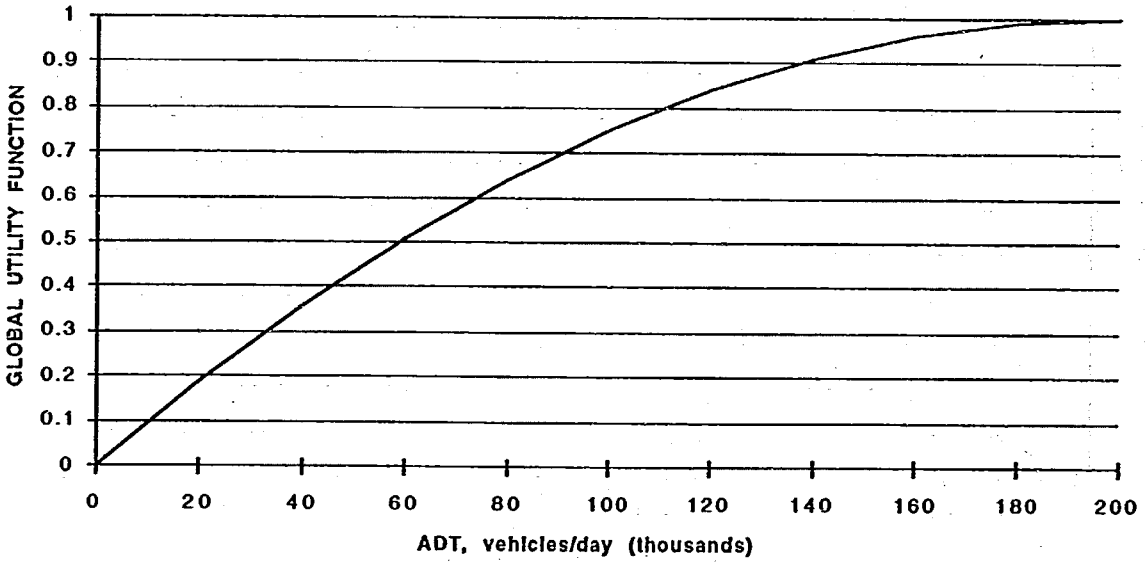
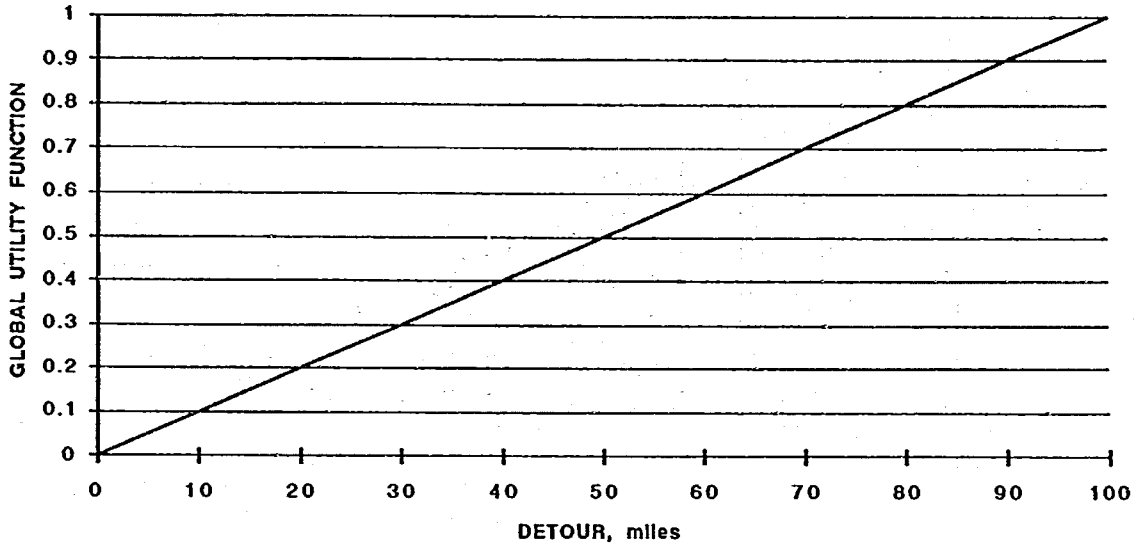


Figure 5

GLOBAL UTILITY FUNCTIONS

DETOUR



ROUTE TYPE

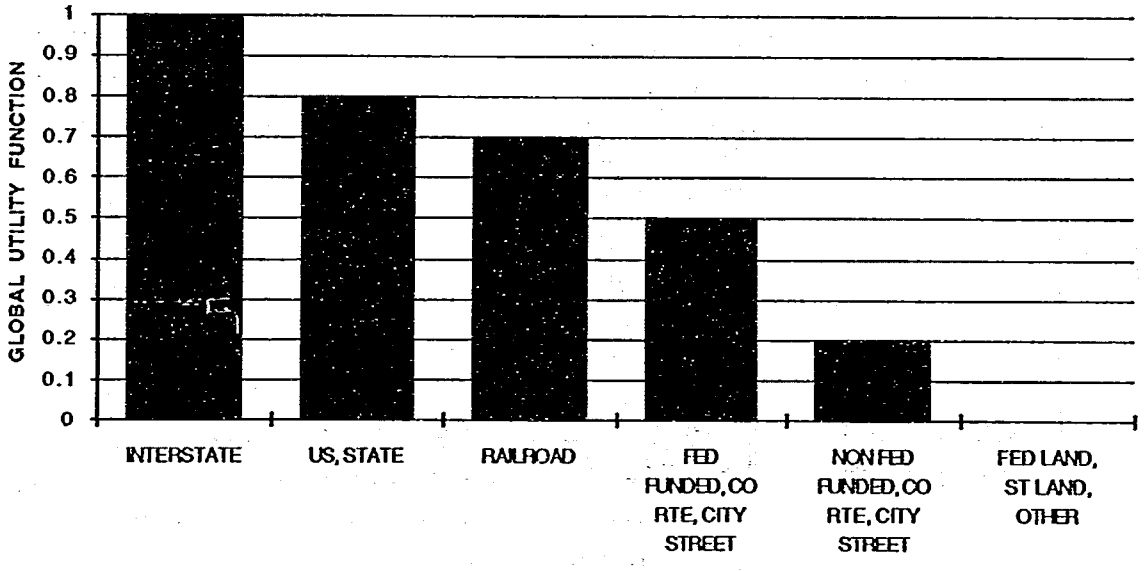
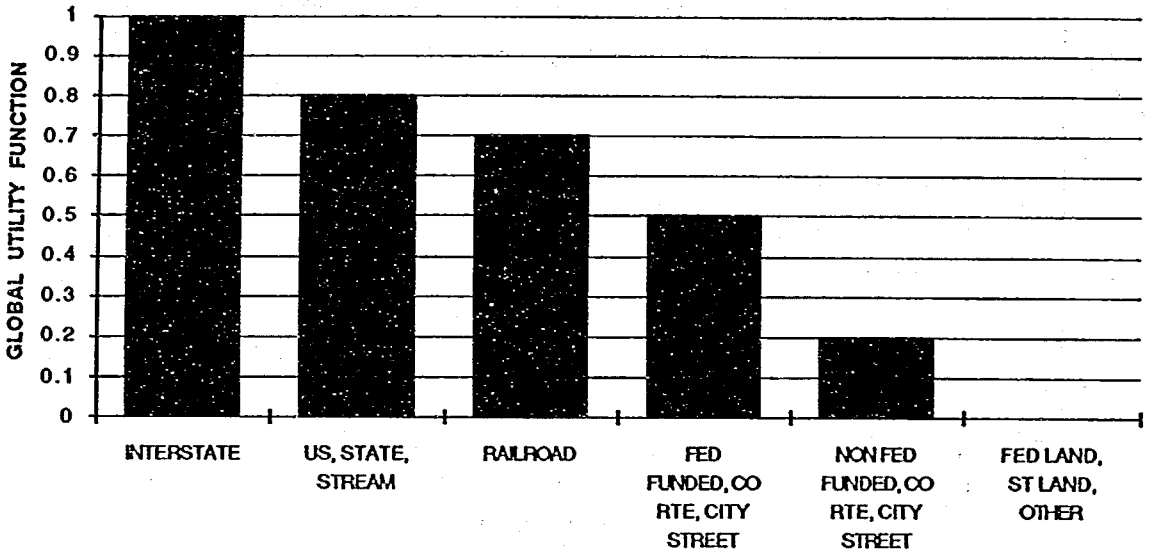


Figure 6

GLOBAL UTILITY FUNCTIONS

FACILITY CROSSED



YEAR CONSTRUCTED

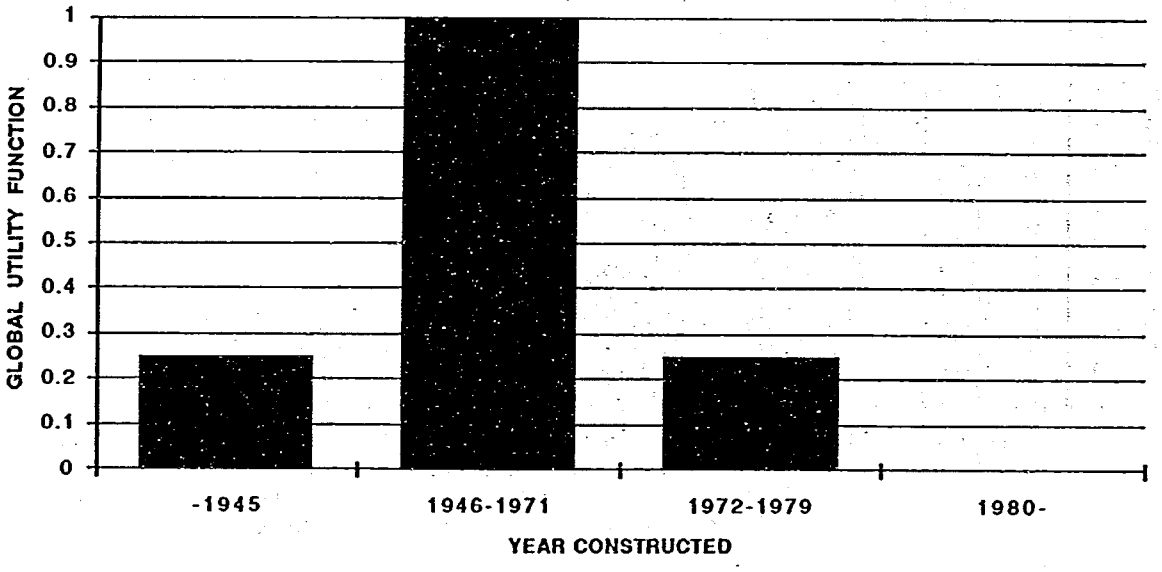
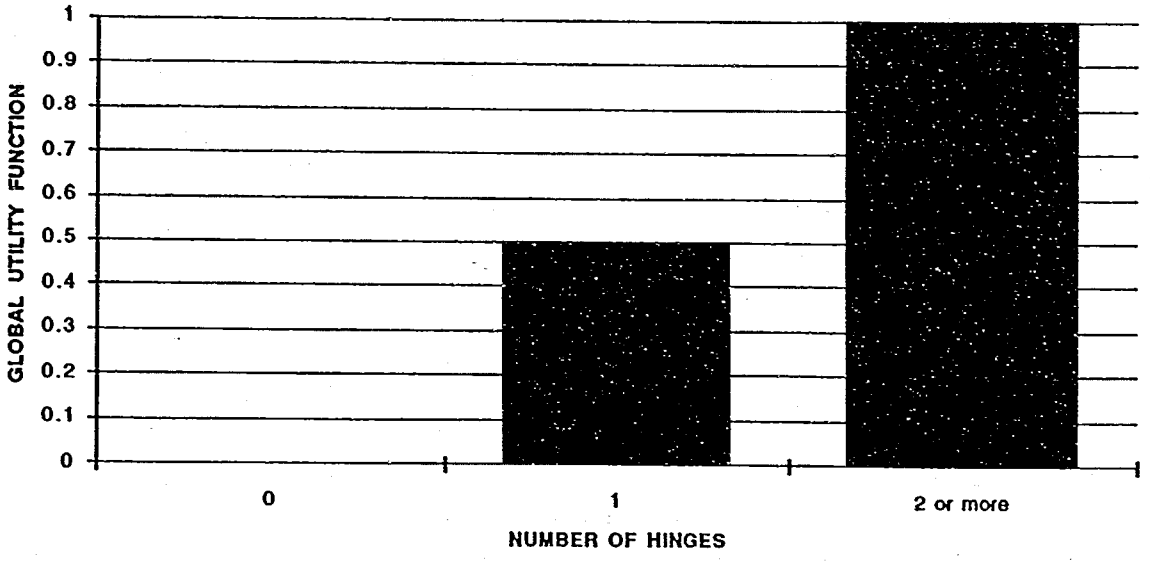


Figure 7

GLOBAL UTILITY FUNCTIONS

HINGES



BENT REDUNDANCY

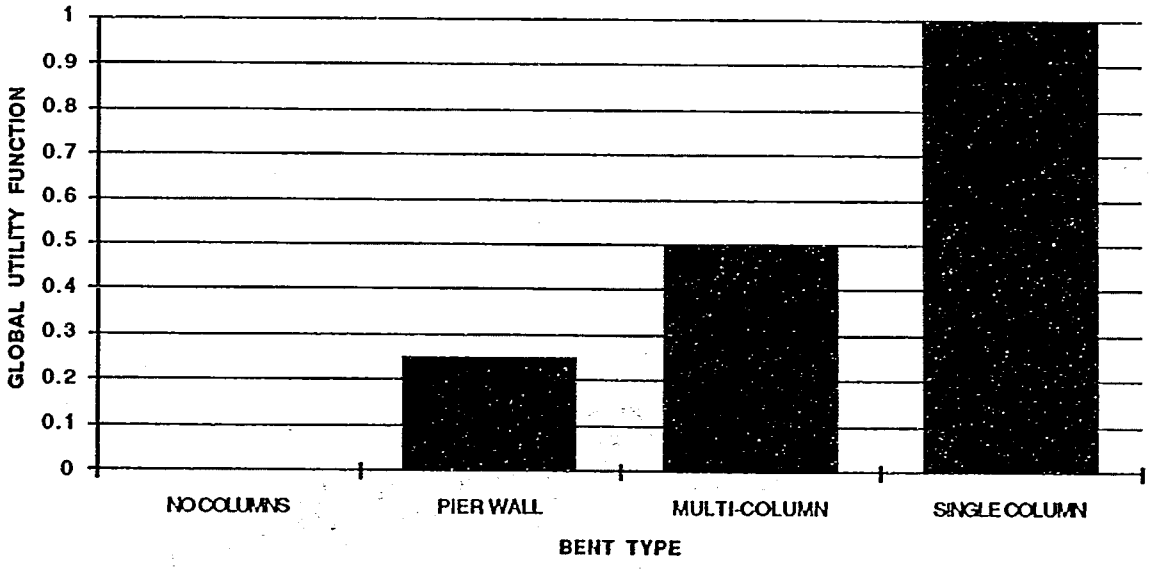


Figure 8

GLOBAL UTILITY FUNCTIONS

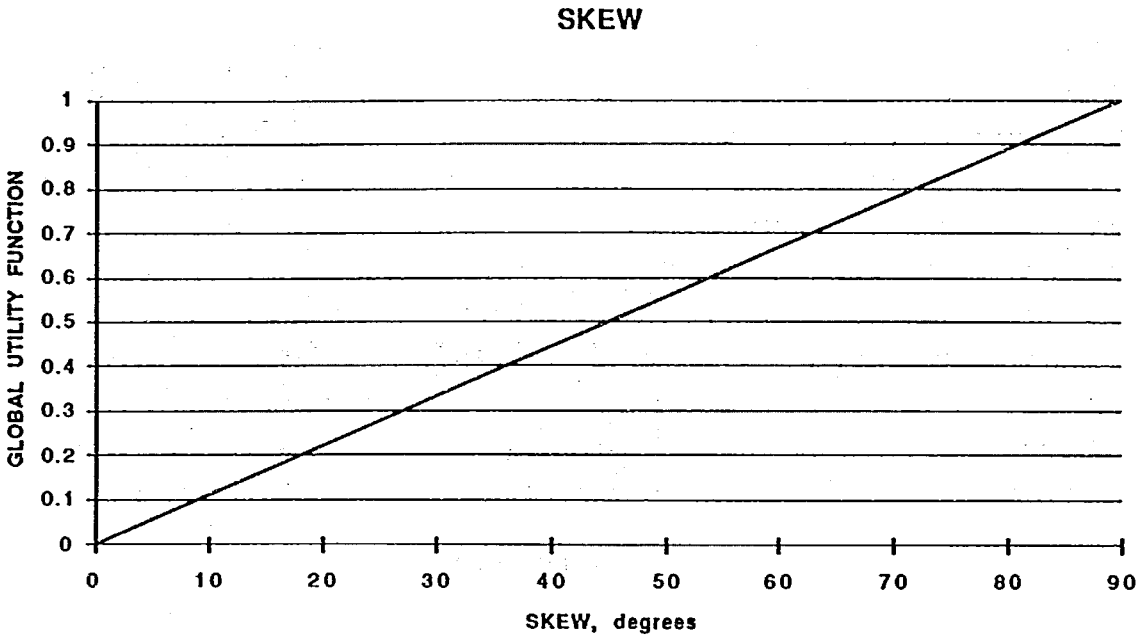


Figure 9

MULTI-ATTRIBUTE DECISION THEORY

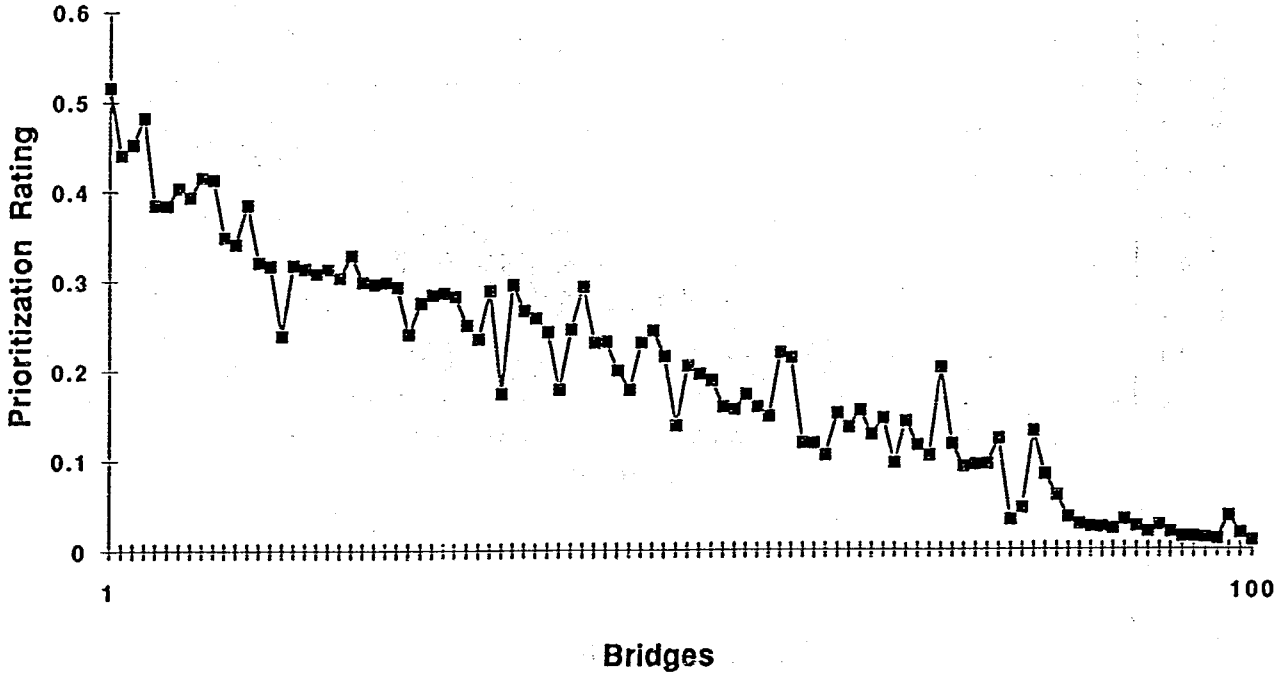


Figure 10

(8) Session 8

Seismic Design (3)

18) Structural Modeling Implications from Snap-Back Tests on a Slab-on-Girder Bridge
(S.S. Chen*, J.B. Mander, D.S. MacEwan and D.K. Kim)

19) Seismic Response of Reinforced Concrete Bridge Piers subjected to Eccentric Loading
(K. Kawashima, S. Unjoh* and H. Mukai)

20) Evaluation of the Seismic Response of Bridges with Hinge Restrainers
(E. Maragakis*, M. Saiidi, S. Feng, S. Abdel-Ghaffar and D. O'Connor)

21) Dynamic Strength and Ductility Characteristics of Steel Bridge Piers
(K. Kawashima, H. Sugita* and T. Nakajima)

Structural Modeling Implications from Snap-Back Tests on a Slab-on-Girder Bridge

by

S. S. Chen
J. B. Mander
D. S. MacEwan
D-K. Kim

Dept. of Civil Engineering
State University of New York at Buffalo

Abstract

A new type of self-equilibrating snap-back (quick-release) test setup is employed to investigate the transverse dynamic response of a two-span continuous slab-on-girder highway bridge. Stick-slip behavior of the expansion bearings was observed to have a measurable effect on the frequency content of the dynamic response of the structure and should be accounted for in inelastic modeling of bridges supported on such bearings. Experimental results from field tests are compared with predictions from both a detailed elastic 3D finite element model of the bridge and a nonlinear *quasi-3D-2DOF* model. Both models account for the field-observed frequencies and mode shapes of the structure under the transverse snap-back excitation. The *quasi-3D-2DOF* nonlinear model also provides reasonable agreement with observed displacement and acceleration amplitudes and time-histories. It can thus be utilized directly in inelastic time-history studies of bridge response to various earthquake ground motions. Both field and analytical results indicate that the current across-the-board recommendation of single-mode analysis and design methods for this class of bridge needs to be re-examined.

Introduction

For common highway bridges in the US, current recommended seismic analysis procedures for bridges [ATC-6, 81] and computer programs such as *SEISAB* [Imbsen 84] have been formulated based on research performed mostly with Californian-type bridges in mind. Such bridges are often characterized by concrete superstructures with a monolithic connection between superstructure and substructures. The modeling recommendations suggested in ATC-6 are based on this type of construction and are thus of questionable relevance to bridges, common to many eastern states and Japan, whose superstructures are composed of concrete deck slabs on steel girders and seated on a variety of bearings. Especially now that the ATC-6 approaches and philosophy have been applied nationally via the 1991 (and subsequent) AASHTO specifications, it is essential that they be re-evaluated in the light of behavior that might be expected from typical slab-on-girder (SOG) bridges that were not necessarily designed for seismic loads.

The need for full-scale validation of analytical modeling assumptions has led to the development of the quick-release method of field experiment [Buckle et. al. 87, Douglas and Reid 82, Douglas et. al. 90, Werner et. al. 90]. Such tests are of importance not just to fine-tune the transverse dynamic behavior predictions of detailed analytical models but also to evaluate the appropriate level of detail to

recommend in analytical methods suitable for design office use. Current code-based provisions stipulate that for "regular" bridges in any Seismic Performance Category (SPC), only a single mode method of analysis is required [Buckle 92].

Regular two-span continuous slab on plate girder structures are often used for overpass bridge replacements due to the use of autostress design methods for the superstructure and the elimination of shoulder piers near the traffic lanes passing beneath the bridge. The bridge examined in this paper is an example of a new structure of this type. The focus of this study is on the appropriateness of a *quasi-3D-2DOF* nonlinear model proposed by the authors. It is shown that this approach gives a reliable prediction of the transverse linear and inelastic dynamic behavior of this bridge when subjected to a new self-equilibrating method of snap-back field testing. Since most previous snap-back tests have been conducted on bridge types other than the SOG type, new insight is also gained into the transverse dynamic behavior of this class of bridge.

Bridge Description and Field Test Setup

The Hopkins Road bridge over Interstate 990, shown in Fig. 1, is a two-span continuous right SOG structure. Located in western New York (SPC B), the bridge was constructed with an 8-1/2 inch (216 mm) thick reinforced concrete deck cast compositely on four 60-inch (1.52 m) deep steel plate girders spaced at 10 ft (3.05 m) centers. The central pier consists of twin reinforced concrete 3 ft (910 mm) square columns supporting a transverse cap beam. The pier and abutments are seated on reinforced concrete pile caps which are founded on battered steel piles. The piles are driven to a depth of 33 ft (10.0 m) at the pier, and 50 ft. (15.2 m) to 56 ft. (17.1 m) at the north and south abutments, respectively. Site test borings indicate the presence of generally firm soil conforming to AASHTO soil type III down to the level of the bedrock at the base of the piles. The bridge appears to have been designed and detailed in accordance with the 1983 AASHTO Seismic Guide Specifications [AASHTO 83]. Constructed in 1990, the bridge was less than two years old at the time of testing in August 1992.

Accelerometers were placed on the pier and superstructure in all three global directions as shown in Figs. 1a and 1b. Static and dynamic transverse displacements of the pier and deck were measured against the reference frame shown in Fig. 1c. An accelerometer was also placed on the reference frame to record its movement during the test and to enable noise-filtering adjustments of the displacement readings from those instruments placed on the reference frame.

The snap-back jacking system used to load the structure is shown in Figs. 1c and 1d. The apparatus was erected in a modular fashion to utilize the mechanical advantage of the lever beam and avoid permanent attachments to the structure. The base bearing wedge, constructed of concrete, was clamped to the west column and included a bearing pivot for the bottom lever beam. The loading beam at the top of the pier rested freely on the end of the cap beam against the pedestal under the fascia girder.

The mechanical advantage achieved by the lever beam magnified the applied diagonal jack force by 6.4 times. This permitted the use of a small 60 kip center-hole

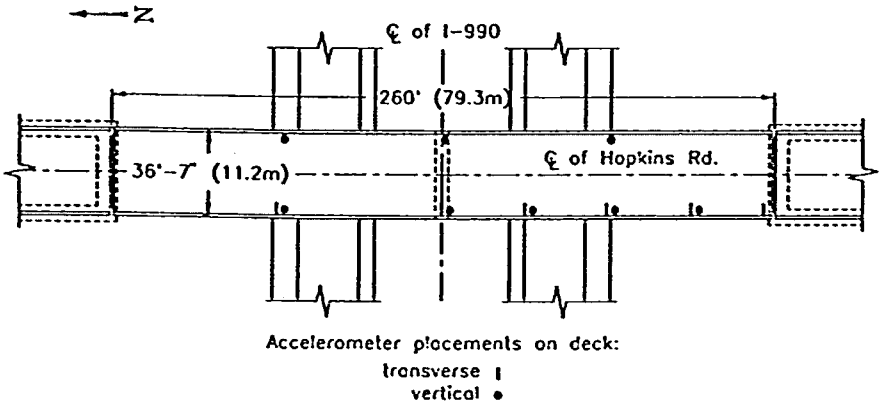


Fig. 1a Plan

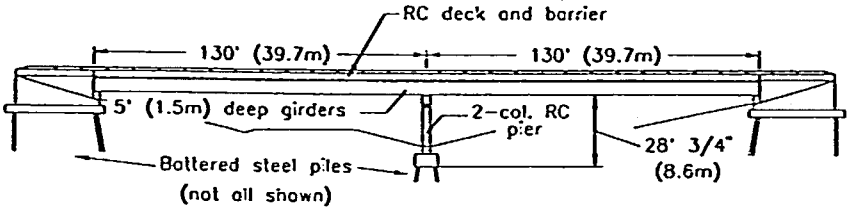


Fig. 1b Elevation

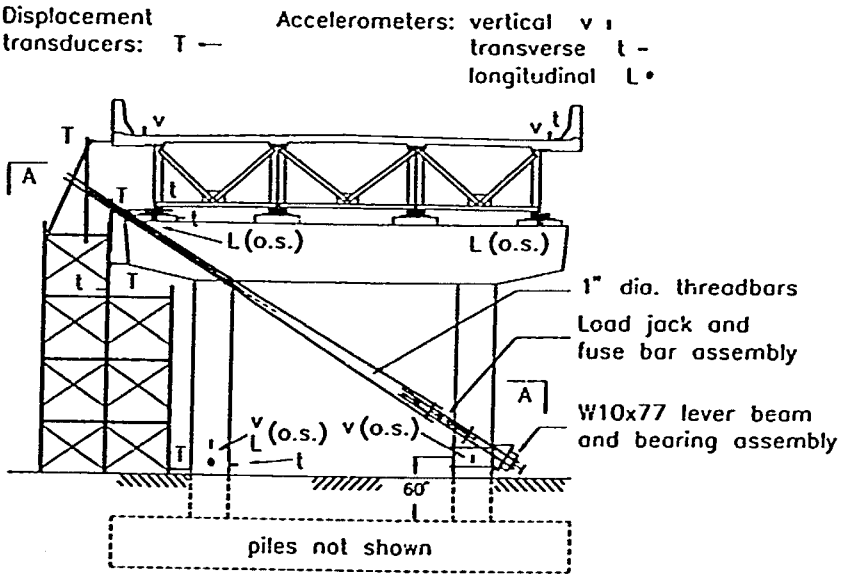


Fig. 1c

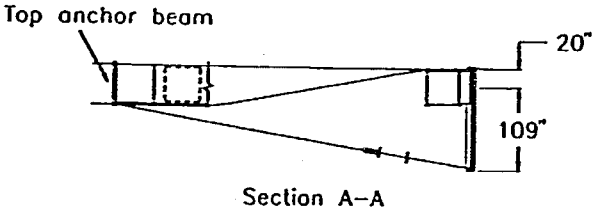


Fig. 1d

Fig. 1 The Hopkins Rd. Bridge over the I-990 Highway Showing the Instrumentation.

hydraulic jack, potentially delivering up to 324 kips diagonal load. Instantaneous release of the static applied load was provided by a fuse-bar connected in series with the jack, as shown in Fig. 1c. Machined to a specified diameter, the fuse bar was designed to break at a prescribed load, allowing subsequent transverse free vibration of the structure. A principal advantage of this type of quick-release setup is that it is self-equilibrating. The complications of soil-structure interaction are thus conveniently avoided in the investigation reported herein, with the focus placed on the above-ground structural response. Two snap-back tests were conducted; one with an equivalent horizontal load of 122 kips, the other with 82 kips; the results of the latter test are reported herein.

The superstructure is supported on fixed bearings at the pier and expansion bearings at the abutments. Bearings over the pier are of the circular elastomeric "pot" type, which consist of an elastomeric pad sealed completely between the piston and the pot. Abutment bearings are shown in Fig. 2 and consist of stainless steel plates on PTFE (Teflon) sliding surfaces supported by elastomeric pads identical to those at the pier. The construction drawings for the bridge called for the fixed pot bearings to supply a 10% horizontal bearing load capacity and the coefficient of friction not to exceed 5% at the expansion bearing locations, while the manufacturer's specifications indicate that the coefficient of friction will be less than 2%. The outer girders at the expansion end were instrumented for displacements as shown in Fig. 2.

During the free vibrations excited following the "snap" of the fuse bar, horizontal and vertical motions were measured at various points in the bridge superstructure and substructure, as shown in Fig. 1. Accelerometer and displacement transducer results were recorded at a sampling rate of 200 Hz in two synchronized PC-based data acquisition systems, one located near the pier and one near the abutment. This system minimized wiring and noise corruption.

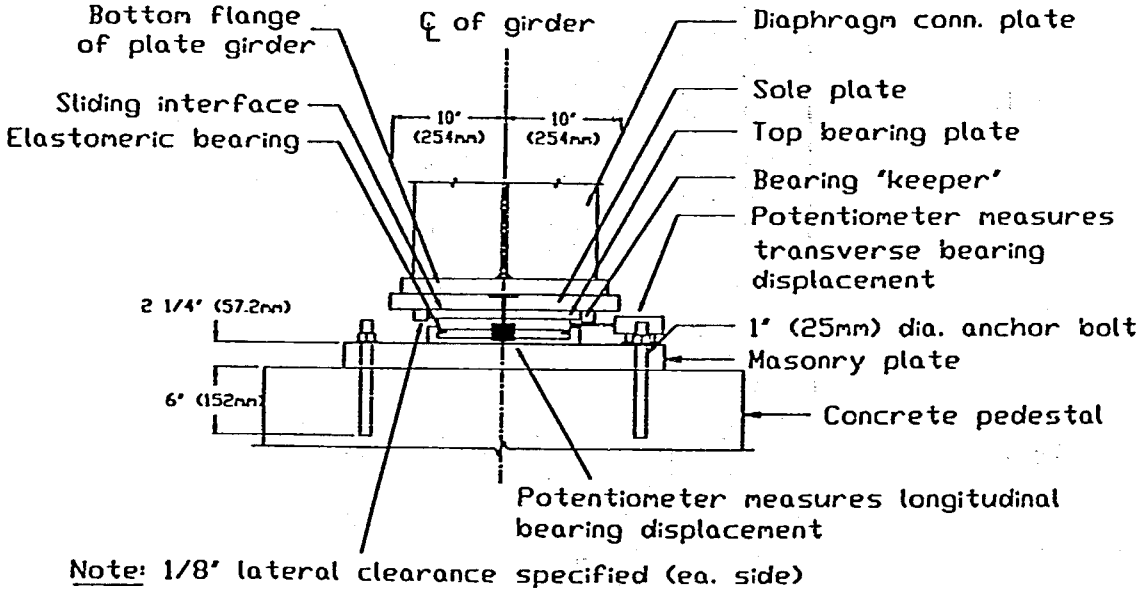


Fig. 2 Expansion Bearings and Displacement Instrumentation

Experimental Results

Fig. 3 presents sample time histories of accelerations and displacements obtained from the field records. It is immediately evident from the acceleration time histories of the deck and pier that more than one mode is present and that different modes dominate the transverse vibration of the deck and pier, respectively. Peak transverse accelerations achieved by the 82 kip snap are approximately 0.065g at the deck, 0.25g at the pier cap, and 0.03g at the girder end above the expansion bearing. The displacement records at the expansion bearings indicate in the transverse direction that some movement occurs within the confines of the side shear key/keeper plates shown in Fig. 2, while movement in the longitudinal direction indicates mobilization of the expansion bearing. While confirming that these relatively new bearings had not yet frozen, this behavior also indicates the inherently nonlinear behavior alternating between "pinned" and "fixed" abutment support conditions that have been assumed in the companion stick-slip analytical modeling.

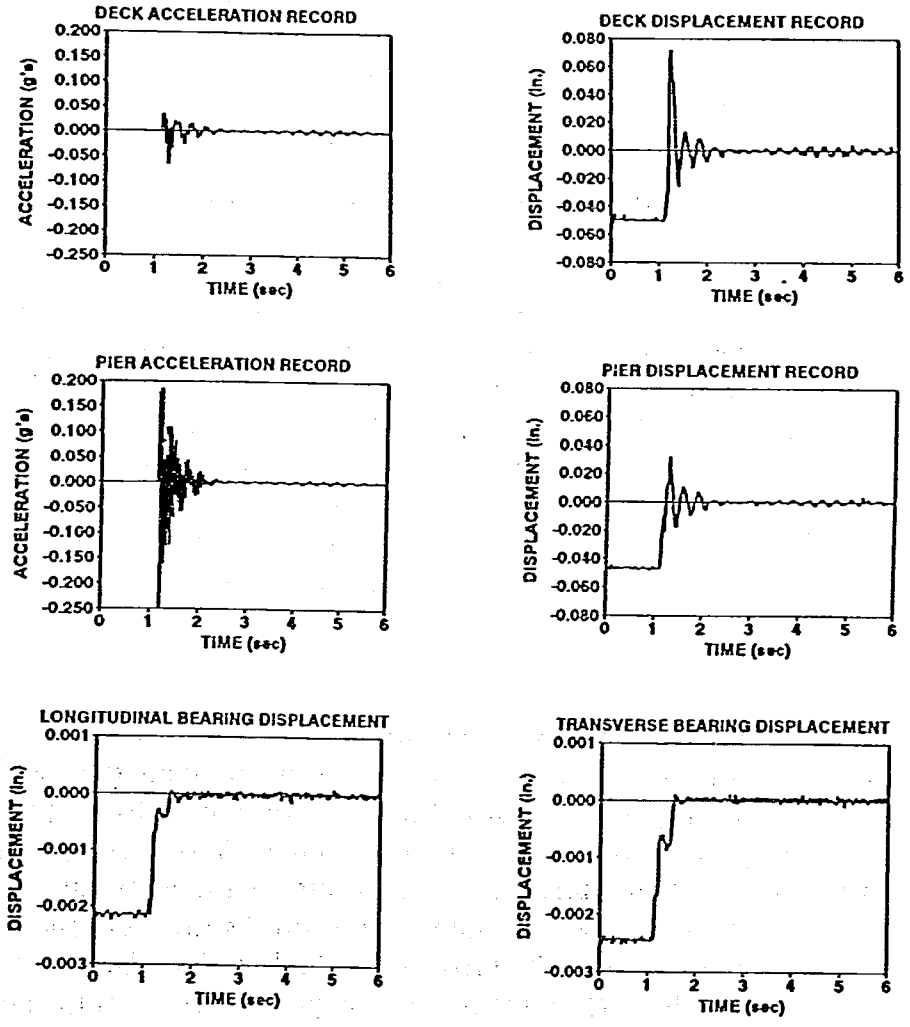


Fig. 3 Sample Snap-Back Time Histories

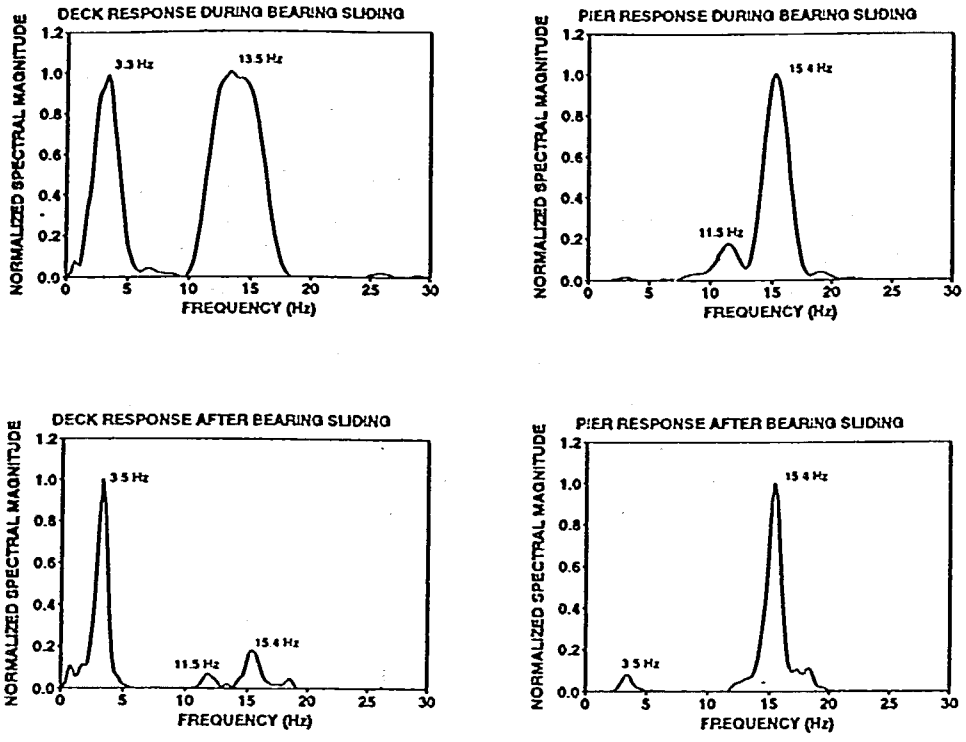


Fig. 4 Sample Snap-Back Frequency Spectra

Fig. 4 shows these selected time histories converted into normalized frequency domain autospectra. This figure shows the spectra for transverse accelerations at the deck and pier, respectively, for the brief period while the bearings were in motion. As suggested by the acceleration records in Fig. 3, higher mode effects are more dominant in the pier, with a frequency of 15.4 Hz. Also shown in Fig. 4 are the frequency spectra for transverse accelerations at the same locations based on the decaying portion of the time history occurring after bearing seizure occurred. Stiffening of the bridge deck due to sticking of the bearings is indicated by an increase in the fundamental frequency from 3.3 Hz to 3.5 Hz.

Rigorous Analytical Modeling

Two distinct models are developed for comparison with the snap-back experimental results. Both models were generated from the construction drawings. Geometry and section properties information was obtained from these, while concrete material properties were obtained from actual 28-day cylinder test data whose results were averaged and increased to account for the approximately 2 year period elapsed since the cylinders were tested. The flexural stiffness of the reinforced concrete piers was based on 60% of the gross uncracked section. Zero displacement clearance is assumed in the transverse shear keys/keepers provided at the abutments, while longitudinal translation at the expansion bearings is permitted. The abutments and foundation below the pile cap are considered to be rigid.

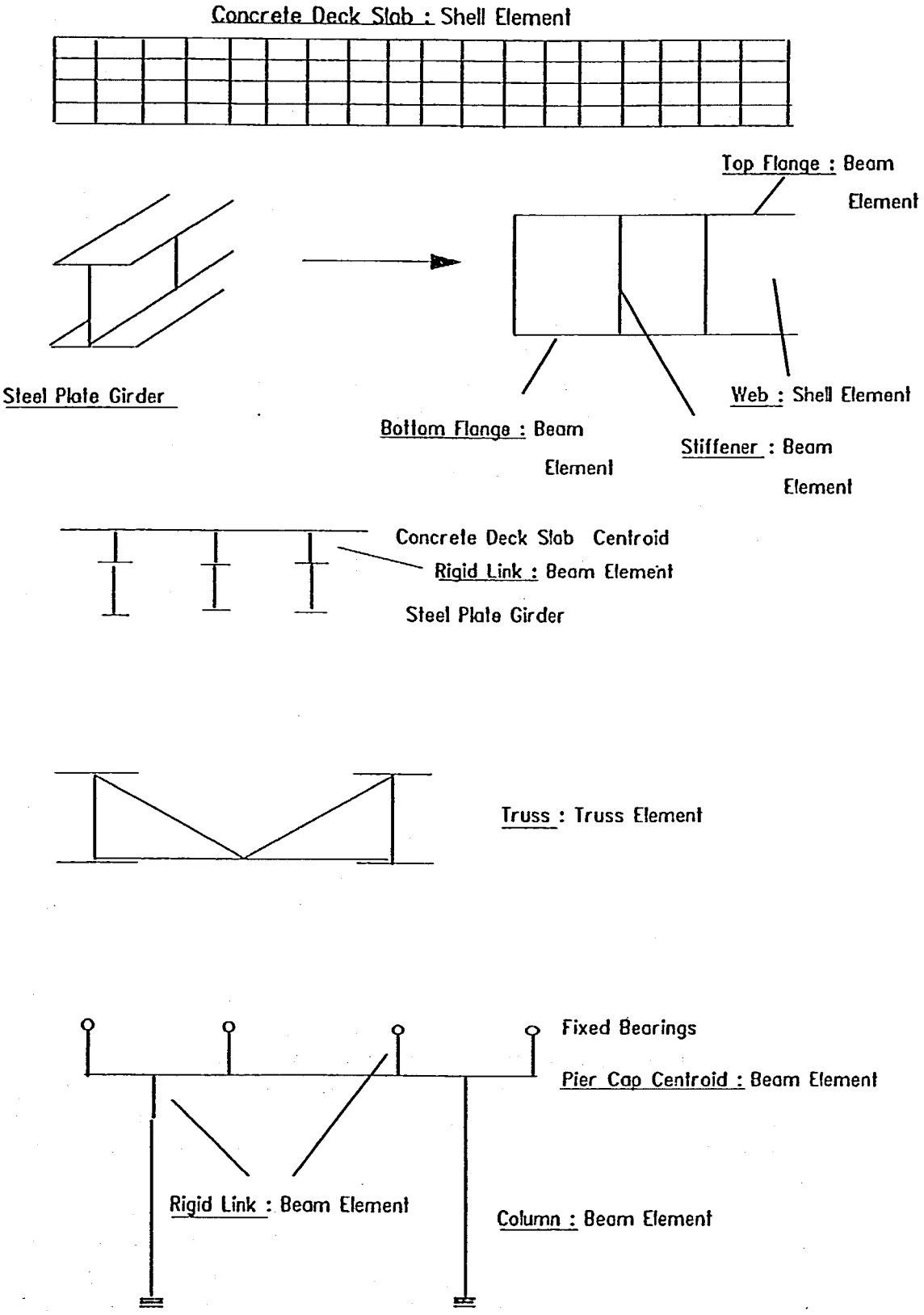


Fig. 5 Detailed Analytical Model 1

Model 1, shown in Fig. 5, is a rigorous 3-D finite element model intended to capture any effects of nonzero member depths while investigating the dynamic characteristics of the bridge. Tetrahedral shell elements are used to model the concrete deck slab and steel plate girder web, while 3-D truss elements are used for the diaphragm trusses and 3-D beam elements are used for the pier cap beam, pier columns, steel plate girder flanges and stiffeners. Rigid link beams account for the finite depth of the concrete deck and pier cap beam. Full composite action is assumed between the deck and top flange of the girder. Masses are lumped at every node using the weight density option. The complete model of the Hopkins Rd. bridge consists of 185 truss elements, 213 beam elements and 108 shell elements, resulting in a total of 1358 degrees of freedom.

Although Model 1 is much more detailed than currently required for code-based seismic evaluation of structures of this type, the distinction between response at the deck level and response at the pier cap level can be striking, as shown in Fig. 6. This figure shows the mode shapes determined from modal analysis for Model 1 along with the experimental modal amplitudes obtained from the actual field test. As is evident, the first mode presents reasonable agreement between analytical prediction and the field experiments. The predicted 2nd, 3rd, and 6th modes were not observed in the field, probably due to the method of excitation utilized. The predominant higher mode observed in the field appears to correspond most closely to either the 4th or 5th mode predicted by Model 1 and the second principal mode in Model 2, described below.

Modeling Simplifications

There are, of course, unavoidable tradeoffs between modeling simplicity and prediction accuracy. It is desirable to provide analysis methods which are highly simplified but also reliable for seismic evaluation of SOG bridges. The common simple models, however, have the following serious drawbacks:

(i) In the "lollipop" method ([Imbsen et. al. 79], [ATC6-2]), the in-plane stiffness of the deck is ignored and the analytical model is based on the resulting simple SDOF idealization.

(ii) In the single mode method advocated by AASHTO, the in-plane stiffness of the deck is considered, but no distinction is made between the superstructure DOF and the substructure DOF. Thus, diaphragm flexibility is not accounted for, and evaluation of diaphragm strength is problematic since the diaphragm does not even exist in such a simplified model. Furthermore, the magnitude of the lateral inertia forces to be transmitted between the deck and the substructure via the bearings is not considered.

The second model, Model 2, is shown in Fig. 7a. It is an intentionally simplified *quasi-3D-2DOF* analytical model for linear and nonlinear time-history analysis in the transverse direction, intended to address the above two principal drawbacks of the lollipop and single mode analysis methods. The principal two degrees of freedom correspond to the transverse displacement at the deck and the pier cap beam, while the stiffnesses K_1, K_2, and K_2^* correspond to the stiffness of the pier, the stiffness of the pier diaphragm, and the in-plane stiffness of the deck, respectively. Deck

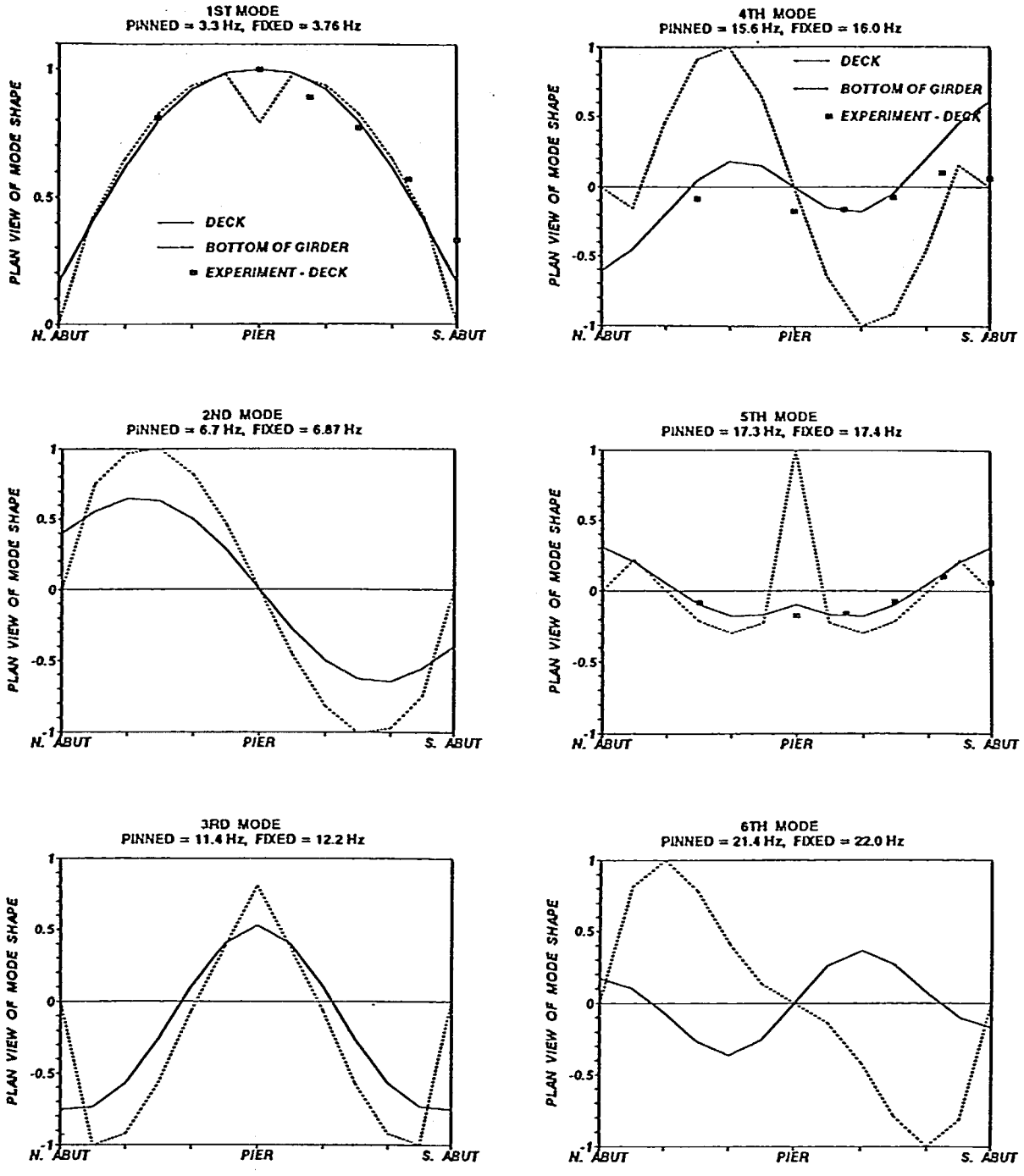


Fig. 6 Theoretical and Experimental Mode Shapes

stiffness K_2^* is obtained based on beam theory including the effects of shear deformation. From solving the eigenproblem, the frequencies obtained from Model 2 are 3.5 Hz and 15.0 Hz, in substantial agreement with the field-observed values shown in Fig. 4.

Model 2 needs only slight modification, as shown in Fig. 7b, in order to evaluate nonlinear response using either a seismic limit (push-over) analysis or a nonlinear dynamic time-history analysis. Such analyses are considered to be preferable to the code-based elastic R-factor approach, which does not account for redistribution of forces due to nonlinear behavior and does not predict the areas of

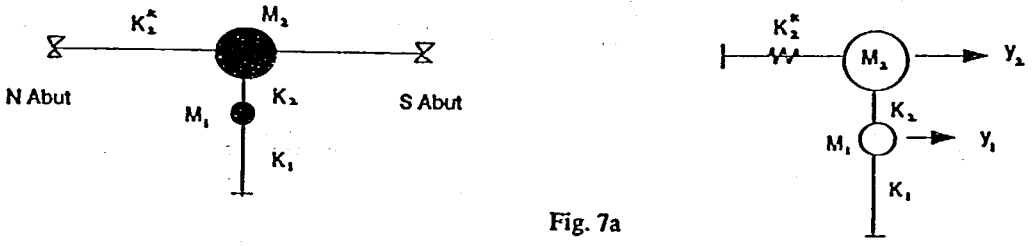


Fig. 7a

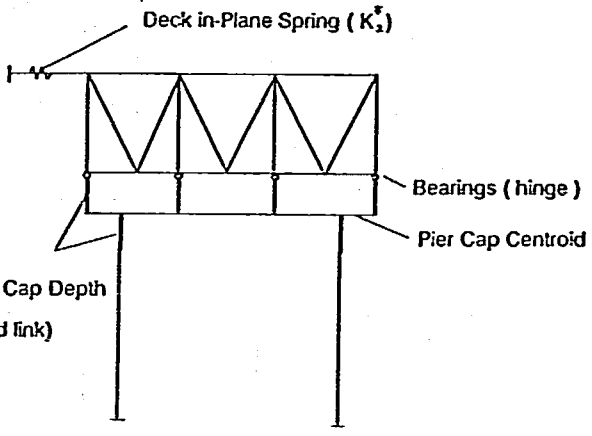


Fig. 7b

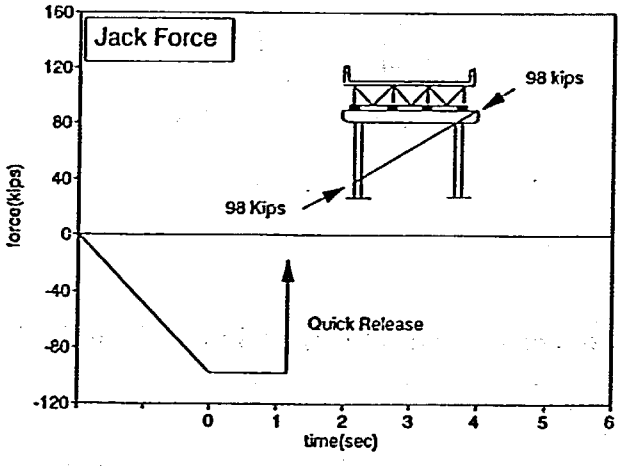


Fig. 7c

Fig. 7 Simplified Analytical Model 2

maximum ductility demand. Programs such as *DRAIN-2DX* [Powell et. al. 92] adequately account for relevant nonlinearities such as bearing stick-slip, diaphragm truss member yielding or buckling, and pier column plastic hinging.

In Model 2, a bi-linear truss element with stiffness K_2^* accounts for the in-plane deck flexibility. The non-sliding fixed condition stiffness is given by

$$\left(K_2^*\right)_{stick} = \left(\frac{AE_{eff}}{L}\right)_{stick} = \frac{12EI_{deck}}{L^3} \qquad (1)$$

and the during- sliding condition by

$$\left(K_2^*\right)_{slip} = \left(\frac{AE_{eff}}{L}\right)_{slip} = \frac{3EI_{deck}}{L^3} \qquad (2)$$

where I_{deck} has been modified to include the effects of shear displacements. A post-yield to elastic stiffness ratio $\left(K_2^*\right)_{slip} / \left(K_2^*\right)_{stick} = 0.25$ is implied in this analysis.

The ultimate capacity can be determined for this Model 2 analysis using a pseudo-static seismic limit analysis based on a static collapse (push-over) mechanism. Following expansion bearing slippage at a transverse load of 5 kips, a pier mechanism forms with four column hinges at a transverse load of 230 kips. Theoretically, structural collapse does not occur until the complete formation of a deck mechanism; a hinge forms in the middle of the deck when the transverse inertia load reaches 1800 kips. These three lateral loads represent base shear capacities of 0.5%, 21%, and 169% respectively, of the gravity load on the pier foundation. Due to a lack of capacity design procedures, it is apparent that the bearing anchorages would fail prior to the formation of the complete mechanism.

A comparison of frequencies obtained from the field test and the various models is given in Table 1. Substantial agreement is evident between the simplified *quasi-3D-2DOF* model (Model 2) and the field-observed mode shapes and frequencies.

Transient Analyses

The program *DRAIN-2DX* is used in conjunction with Model 2 to simulate the effects of the snap-back test conducted in the field, as shown in Fig. 7c. Comparison of the predicted and measured time-history response is presented in this section.

Fig. 8 presents a comparison of the transverse time-history response of the pier cap and deck for both the Model 2 (*DRAIN-2DX*) prediction with 5% damping and the field-measured response. Substantial agreement is obtained in the displacement response and the pier accelerations. The computer simulation somewhat overestimates the acceleration response at the deck level, but still adequately reflects the frequency content of the response. This difference is attributed to the simplifications inherent in the Model 2 analysis.

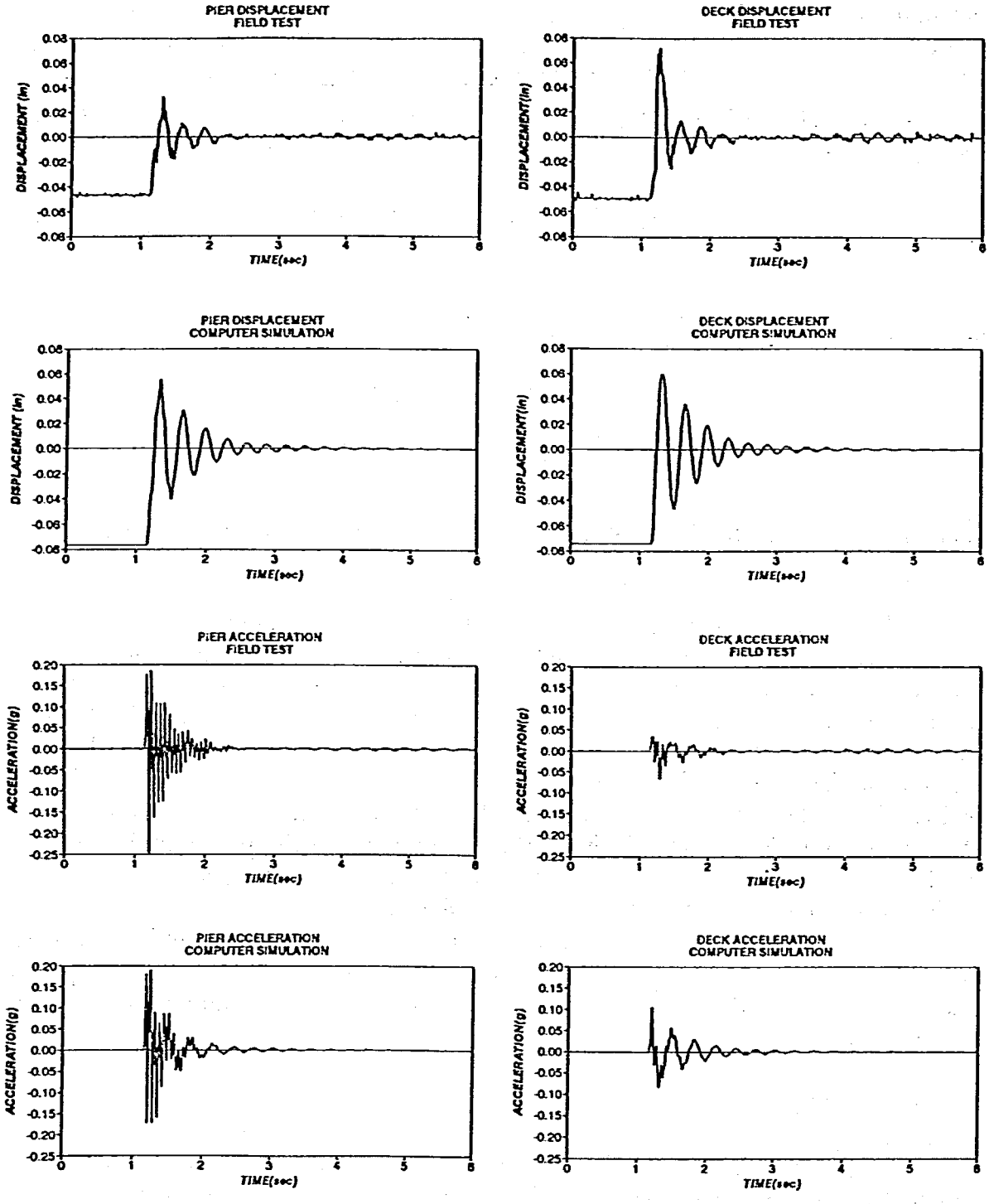
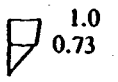
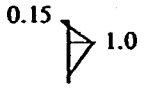
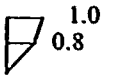
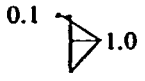
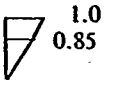
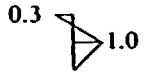
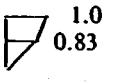
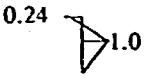


Fig. 8 Model 2 vs. Field-Observed Time Histories

Table 1

	1st mode	2nd mode
Field Test	 3.3 - 3.5 Hz	 15.5 Hz
3-Dimensional Modeling	 3.3 Hz	 17.3 Hz
Lollipop	3.1 Hz	-
Uniform Load	3.7 Hz	-
Half Sine Wave Load	3.2 Hz	-
2 DOF for Modal Analysis	 3.5 Hz	 15.0 Hz
2 DOF for Plastic Analysis	 3.5 Hz	 15.0 Hz

Conclusions

The self-equilibrating test setup provides a useful way of performing transverse snap-back tests of SOG bridges supported by pier bents, although some vibration modes predicted from a rigorous 3D finite element model do not appear in the experimental results.

Reasonable agreement is achieved between the transverse displacement and acceleration predictions of the simplified analytical model (Model 2) and the snap-back field test results at both the deck and pier cap beam levels. The *quasi-3D-2DOF* model accounts for field-observed frequencies and mode shapes as well as displacement and acceleration amplitudes. It is thus shown that the *quasi-3D-2DOF* analytical model accounting for both deck stiffness and diaphragm flexibility is necessary and reasonably sufficient for prediction of both linear and nonlinear aspects of dynamic response of a 2-span continuous slab-on-girder steel bridge. A clear implication of this result is that the current across-the-board recommendation of single-mode analysis methods for this class of bridge needs to be re-examined.

The following avenues for further investigation are also recommended:

1. Although the self-equilibrating experiment setup precluded the mobilization of additional soil strains prior to the snap, dynamic (post-snap) soil-structure interaction effects should be considered in a more refined analysis.
2. Pier and abutment diaphragms in SOG bridges should be designed and/or evaluated for transverse seismic loading, as should their connections.
3. Modal participation of the higher mode(s) needs to be quantified for purposes of capacity evaluation of the diaphragms, bearings, piers, and foundations.

Acknowledgements

The funding support of the National Center for Earthquake Engineering Research is greatly appreciated. Access to the Hopkins Rd. bridge for instrumentation and field testing was enabled by the New York State Dept. of Transportation, and traffic control during the testing was provided by the Town of Amherst Police Department and the Erie County Dept. of Public Works.

References

_____ AASHTO (1983), American Association of State Highway and Transportation Officials, "Guide Specifications for Seismic Design of Highway Bridges."

_____ ATC-6 (1981), Applied Technology Council, "Seismic Design Guidelines for Highway Bridges," Report ATC-6, Applied Technology Council.

Buckle, I. G., Douglas, B. M., Saiidi, M., Richardson, J. A., and Butterworth, J. W. (1987), "Field Tests of Ramp B, Dominion Road Interchange Using Simulated Earthquake Loads," Proceedings of the Pacific Conference on Earthquake Engineering, Wairakei, New Zealand, New Zealand National Society for Earthquake Engineering, August, Vol. 2, pp. 243-255.

Buckle, I. G., Mayes, R. L., and Button, M. R. (1987), "Seismic Design and Retrofit Manual for Highway Bridges," Technical Report No. FHWA-IP-87-6, US Dept. of Transportation, Federal Highway Administration, May.

Buckle, I. G. (1992), "Proposed Revisions to the AASHTO Seismic Design Criteria for Highway Bridges in the United States," Proceedings of the 8th US-Japan Bridge Engineering Workshop, UJNR Panel on Wind and Seismic Effects, Chicago, Ill., May, pp. 81-92.

Douglas, B. M., and Reid, W. H. (1982), "Dynamic Tests and System Identification of Bridges," Journal of the Structural Division, ASCE, Vol. 108 No. ST10, October 1982, pp. 2295-2312.

Douglas, B. M., Maragakis, E. A., Vrontinos, S., and Douglas, B. J. (1990), "Analytical Studies of the Static and Dynamic Response of the Meloland Road Overcrossing," Proceedings of the Fourth U.S. National Conference on Earthquake Engineering, May 20-24, EERI, pp. 987-996.

Imbsen, R. A., Nutt, R. V., and Penzien, J. (1979), "Evaluation of Analytical Procedures Used in Bridge Seismic Design Practice," Proceedings of a Workshop on Earthquake Resistance of Highway Bridges, Applied Technology Council, November, pp. 467-496.

Imbsen, R. A., Lea, J., Kaliakin, V., Perano, K., Gartes, J., and Perano, S. (1984), "SEISAB-I - SEISmic Analysis of Bridges: User Manual and Example Problems," Engineering Computer Corporation, Sacramento, CA, January.

Powell, G. H., et. al. (1992), "DRAIN-2DX Version 1.03 User's Guide," Report No. UCB/SEMM-92/29, Dept. of Civil Engineering, University of California, Berkeley.

Werner, S. D., Beck, J. L., and Nisar, A. (1990), "Dynamic Tests and Seismic Excitation of a Bridge Structure," Proceedings of the Fourth U.S. National Conference on Earthquake Engineering, May 20-24, EERI, pp. 1037-1046.

SEISMIC RESPONSE OF REINFORCED CONCRETE BRIDGE PIERS SUBJECTED TO ECCENTRIC LOADING

by

Kazuhiko KAWASHIMA[1] Shigeki UNJOH[2] and Hideki MUKAI[3]

1) Head, Earthquake Engineering Division, Earthquake Disaster Prevention Department, Public Works Research Institute, Ministry of Construction, Tsukuba Science City, Japan 305
2) Senior Research Engineer, ditto
3) Assistant Research Engineer, ditto

ABSTRACT

Presented are the seismic response characteristics of C-shaped reinforced concrete bridge piers which is subjected to eccentric loading by the dead weights of superstructure and cantilevered beam. The shaking table test and dynamic loading tests of model piers were made to investigate the seismic response characteristics. It is found that the response of pier increases only in one direction in which the bending moment increases and that the excessive residual displacement was developed. It is also found that the ductility significantly decreases with increase of bending moment by the eccentric loading.

1. INTRODUCTION

Recently, new types of structures have been constructed in urban areas by land use restriction and other construction conditions. A C-shaped reinforced concrete (RC) bridge pier as shown in Fig.1 is one of the typical examples. However, the seismic response characteristics of this type of RC piers have not yet been studied. The C-Shaped RC piers is subjected to eccentric loading by the dead weights of superstructure and cantilevered beam to support the superstructure. Therefore, since it is anticipated that the seismic response increases only in one direction during a severe earthquake, it is an important subject to investigate the strength and ductility characteristics and to develop the seismic design method against large-scale earthquakes.

This paper presents the seismic response characteristics of C-shaped reinforced concrete bridge piers through the shake table test and dynamic loading tests of model piers.

2. DEFINITION OF ECCENTRIC LOADING

When RC piers are C-shaped and subjected to eccentric loading in the transverse direction to the bridge axis, the load-displacement relation of RC piers may be illustrated as shown in Fig.2, in which load-displacement relation is assumed as tri-linear. In case in which dead weights of superstructure is concentrically loaded, displacement by seismic loading is developed from the

origin. The pier is deformed in nonlinear region as crack and yielding and ultimate stages with increase of the seismic loading. However, when the dead weights of superstructure is loaded eccentrically, the pier is initially deformed and the origin of displacement developed by the seismic loading is shifted. Therefore, it is anticipated that the seismic response increases only in one direction during a severe earthquake.

In order to define the amount of the eccentric loading, bending moment ratio is assumed as

$$r_M = \frac{M_E}{M_D + M_E} \quad (1)$$

where

r_M : bending moment ratio
M_E : bending moment by design seismic load, and
M_D : bending moment by eccentric loading of superstructure and cantilevered beam

Eq.(1) shows that when the eccentric loading increases r_M deceases, on the other hand, when the eccentric loading decreases r_M increases. r_M = 1 means concentric loading.

Fig.3 shows distribution of the bending moment ratio r_M based on the survey of 45 existing C-shaped RC bridge piers in Metropolitan area, bending moment ratio r_M is in the range of 0.4 - 0.9. Averaged bending moment ratio r_M is 0.55.

3. SEISMIC RESPONSE CHARACTERISTICS OF C-SHAPED RC PIER BASED ON SHAKING TABLE TESTS

3.1 Bridge Pier Model Studied

In order to investigate the seismic response characteristics of a C-shaped RC pier, shaking table test was made at the Public Works Research Institute. Objective of the shaking table test is to investigate how the C-shaped pier responds and behaves in the transverse direction to a bridge axis during an actual earthquake.

Fig.4 shows a C-shaped bridge pier model used for the shaking table test. Details of the pier model was determined based on the actual bridge pier. The actual pier with average bending moment ratio, r_M, of 0.55 was selected as a prototype. The height of pier is 10.2m and the height of girder is 1.5m. The similarity ratio of the pier model with the prototype pier was assumed as 1/4.6.

The specimen has an effective height, h, of 2.55m and cross section of 52cm × 42cm (width in bridge axis : 52cm). The shear span ratio h/d, which is defined as the effective height divided by the effective depth, d, of the cross section of 37cm, is 6.9. Longitudinal reinforcing bars are arranged by 5 reinforcing bars with diameter of 16mm (D16) in the initial compression side by the eccentric loading, 5 reinforcing bars with that of 22mm (D22) in the tension side, and 3 reinforcing bars with that of 16mm (D16) in the other sides. The reinforcement ratio is 0.45, 1.06 and 0.27, respectively. Tie reinforcement was arranged by 17.3cm pitch by reinforcing bars with diameter of 10mm (D10). Tie reinforcement ratio is 0.16. Averaged yielding stress of the longitudinal and tie reinforcement was 3,608kgf/cm^2 for D16, 3,500kgf/cm^2 for D22 and 3,552kgf/cm^2 for D10. Averaged compression strength of the concrete was 335kgf/cm^2. It

should be noted here that since weight of the superstructure supported by the pier model is 40.1tf, seismic coefficient of the pier model can be regarded as 0.27. Axial stress by the dead weight of superstructure was 9.2kgf/cm^2. Computed yield displacement, δ_y, corresponding to one displacement ductility factor and yield strength of the pier in the direction in which the bending moment increases are 7.7tf and 20.5mm computed from the shifted origin. On the other hand, in the direction in which the bending moment decreases they are 11.8tf and 91.3mm, respectively.

3.2 Shaking Table Test

Photo 1 shows the set up of shaking table test. A pier model is fixed at the center of the shaking table and two spans of simply supported girders with total weights of 40.1tf and length of 15m were placed on the pier model. Because two ends of the girder could not be supported by the shaking table, they are supported by the two steel frames placed outside of the table. The pier model and girders were connected by fixed bearings. The steel frames and girder were connected by movable roller bearings so that inertia force developed at the girder during excitation be directly applied to the pier model. It should be noted here that although the direction of the eccentric loading is assumed to be transverse direction, the girder axis was set up in parallel direction with transverse direction of the pier model. However, since the two girders was to load the weight of superstructure and to simulate the inertia force, the direction of the girders is not important.

The shaking table was excited along transverse direction to bridge axis (direction to the girder axis of model bridge). An acceleration record triggered at the Hachirogata during the Nihon-kai-chubu, Japan, Earthquake of 1983 was used as an input motion by reducing the time axis one half so that the predominant frequency of the record matches with the fundamental natural frequency of the pier model. Intensity of the record was assumed as 3.5 times the original.

Extensive instrumentations were made to measure basic parameters including accelerations at the foot of pier and at the girder as well as relative displacement of the girder with reference to shaking table. Inertia force of the superstructure was computed by multiplying the acceleration developed at the girder by the mass of girder.

3.3 Seismic Response Characteristics

Fig.5 shows acceleration of shaking table, response acceleration and displacement of girder. Although measured peak acceleration of shaking table is 812cm/s^2, this is spike-like response and effective seismic intensity to excite the pier model is about 0.35G as assumed. The pier model developed residual lateral displacement with an amount of 16cm at the pier crest in the direction in which eccentric weight is loaded. However, the stopper for preventing falling-off of girders worked at this moment. If the stopper was not installed the larger residual displacement would be developed. Such a permanent displacement is clearly observed in Fig.5 from biased inelastic response displacement. The drift of response displacement was developed at time 12sec when the first large excitation, which exceeded the yielding displacement, loaded. However, after the excitation with larger displacement at time 17sec, the residual displacement reached to about 16cm. Therefore, accumulation of

drifting of response displacement after the first large excitation seems to be less significant. It should be noted here that although the residual displacement was developed in the shaking table test of RC pier model subjected to concentric loading, the amount was much smaller than that mentioned above. Photo 2 shows the residual deformation of the pier model after excitation.

Fig.6 and Photo 3 show the failure mode of the pier model after the excitation by shaking table. Compression failure was found in the compression side by the eccentric loading. Only horizontal tension crack was found in the tension side.

Fig.7 shows the hysteresis loop of the load-displacement relation obtained through the shaking table test. The biased displacement response was clearly developed after the first significant excitation with larger displacement exceeding the yield displacement. The degradation of the stiffness in accordance with nonlinear response can be clearly observed.

4. DYNAMIC LOADING TEST OF RC PIER MODELS

4.2 Bridge Pier Models Studied

In order to investigate the strength and ductility characteristics of C-shaped RC pier, dynamic loading tests were made. Fig.8 shows a C-shaped bridge pier model used for the dynamic loading test. The pier models are basically the same as the shaking table test as mentioned in the above. Five pier models in total were tested, in which bending moment ratio, r_M, and loading direction was varied as a parameters to be investigated.

All pier models have a loading effective height, h, of 2.55m and cross section of 52cm × 42cm (width in bridge axis : 52cm). The shear span ratio, h/d, is 6.9. The bending moment ratio, r_M, was assumed as 0.69 (P-60; small eccentric loading), 0.55 (P-62; medium eccentric loading) and 0.51 (P-64; large eccentric loading), in which the specimen number is the serial number of pier models tested at the Public Works Research Institute. P-62 has the same condition as one used for the shaking table test. More two piers (P-65 and P-66) are for the purpose to investigate the effect of longitudinal loading. The detail of the piers is the same as P-62. Eccentric weight in transverse direction was not loaded for P-65. Axial loading was assumed as 20tf which is the same as the shaking table test. Therefore, axial stress by the axial loading is 9.2kgf/cm^2. It should be noted here that the axial force to P-60 was assumed as 13tf (axial stress is 6.0kgf/cm^2) because of limitation of loading apparatus.

4.2 Dynamic Loading Test

Photo 4 shows the set up of the pier model for the dynamic loading tests. The pier model was anchored to the reaction wall with bolts. The large-stroke dynamic actuator, which was installed to the reaction wall in such a manner, was fixed to the head of the pier model. Also, axial loading apparatus was fixed to the head of the pier models so that the necessary eccentric loading be applied. At the pier crest the steel-made apparatus was set for the purpose to eccentrically impose the axial force.

Fig.9 shows the pattern of loading displacement for dynamic loading tests. The yield displacement corresponding to one ductility factor was assumed as an

unit loading displacement. However, the pier models subjected to eccentric loading is initially displaced by displacement of δ_0. Therefore, unit loading displacement, $\delta 1$, was assumed with the assumption of that the origin is shifted to the initial point as

$$\delta 1 = \delta_y - \delta_0 \qquad (2)$$

where

$\delta 1$: unit loading displacement
δ_y : yielding displacement
δ_0 : initial displacement by eccentric loading

The pier models were subjected to a series of step-wise increasing symmetric displacement cycles as shown in Fig.9. At each step, 10 cycles of loading with the same displacement amplitude was carried out. It should be noted here that the yield displacement was determined by computation with the strain of main reinforcement at the base. The loading velocity was assumed as 1cm/s. The loading direction was assumed as transverse and longitudinal directions depending on the test objectives.

4.3 Failure Mode of Pier Models

Fig.10 and Photo 5 show the failure mode of P-62 (r_M = 0.55; medium eccentric loading). Damage of a side parallel to the loading direction is shown. During δ_1 to δ_2 loading cycles, only small horizontal cracks were found on the concrete surface. This is by the loading in the plus side (the loading in which bending moment increases, this side is referred to A-side), no cracks was found at the minus side (the loading in which bending moment decreases, this side is referred to B-side). After δ_3 loading cycles the cracks was initiated to be developed in B-side. During δ_4 loading cycles, diagonal cracks were developed from the bottom of A-side to B-side. With increase of loading cycles, the significant cracks were developed at the bottom of B-side and cover concrete was spalled-off. During δ_6 loading cycles, concrete of the bottom of pier was failed with a triangular wedge shape and 2 reinforcing bars were fractured in the B-side. During δ_7 loading cycles, deformation of pier was significantly extended at the base and the pier was inclined. It should be noted here that comparing of the failure mode with the shaking table test result, the failure mode was significantly different between two tests. Although the diagonal crack was developed in the dynamic loading test, such diagonal crack was not developed during the shaking table test. This is because that although displacement in the minus side was forced to be loaded to the pier in the dynamic loading test, displacement during shaking table test was developed in one direction in which the bending moment increases.

Figs.11 and 12 show the failure modes of P-60 (r_M = 0.69; small eccentric loading) and P-64 (r_M; large eccentric loading). In case of P-60, from δ_1 loading cycles, crack was developed also in the B-side. Then the crack increased in both A-side and B-side. During δ_6 loading cycles, cover concrete was spalled-off in the both sides of the bottom. During δ_7 loading cycles, 3 longitudinal reinforcing bars were fractured. The difference in the failure mode between P-62 and P-60 is that the damage was developed in both sides and the progress of the damage of P-60 with loading cycles became slower than that of P-62.

On the other hand, in case of P-64 (r_M = 0.51; large eccentric loading), during δ_3 loading cycles the diagonal crack was developed. The cover concrete in the B-side of the bottom was spalled-off during δ_4 loading cycles. During δ_5, concrete at the bottom of B-side was failed by compression and one longitudinal reinforcing bar was fractured. Comparing with the failure mode of P-62, the progress of damage of P-64 became faster than P-62.

Figs.13 and 14 show the failure modes of the P-65 (no eccentric loading, longitudinal loading) and P-66 (eccentric loading). The compression side by the eccentric loading was shown. During δ_5 and δ_6 loading cycles cover concrete was spalled-off. Then during δ_8 loading cycles, 5 reinforcing bars in total were fracture in the both sides for two model piers. The slight difference between two pier models was found in the failure mode. In P-66 in which eccentric loading was applied, the diagonal crack was found more remarkably than P-65 with no eccentric loading.

4.4 Strength and Ductility Characteristics

Fig.15 shows the effect of bending moment ratio, r_M, on load-displacement relation. In the plus side in which the bending moment increases, the displacement range in which load reaches to peak and the displacement increase stably was shorter as the bending moment ratio is smaller. Therefore, the bending moment ratio is smaller, the ductility becomes smaller.

Fig.16 shows the effect of longitudinal loading on the load-displacement relation. The load-displacement relations of two piers are almost the same even if the eccentric loading was applied. Therefore, there is small effect of eccentric loading when seismic load was applied in the longitudinal direction.

Fig.17 shows the comparison of load-displacement relation between shaking table test and dynamic loading test results. The load-displacement relation was the almost close. However, in the shaking table test, the load did not decrease suddenly with increase of displacement. This is because of the difference of loading methods. In the dynamic loading test, forced displacement was applied by the 10 cycles loading.

Table 1 shows the strength and ductility of the tested pier models. The ductility was almost same when r_M is 0.69 and 0.55, but when the r_M is 0.51 the ductility decreases to one of half of those. The ratio of peak strength by yield strength of the P-64 decreases by 10% than P-60 and P-62.

5. CONCLUDING REMARKS

In order to investigate the seismic response characteristics of C-shaped reinforced concrete bridge piers which is subjected to eccentric loading in the transverse direction to bridge axis by the dead weights of superstructure and lateral beam, the shaking table test and dynamic loading tests of model piers were made to investigate the seismic response characteristics.

According to the above results the following conclusions may be deduced:

(1) When the pier model subjected to eccentric loading, the displacement was developed only in one direction in which the bending moment increases. The large amount of residual displacement was finally developed.

(2) When the bending moment ratio is 0.51, the ductility decreases to one half that greater than 0.55. Therefore, the bending moment ratio is smaller, ductility becomes smaller.

REFERENCES

1. Kawashima, K., Hasegawa, K., Koyama, T. and Yoshida, T. : Hysteretic Behavior of Reinforced Concrete Bridge Piers by Dynamic Loading Tests and Shaking Table Tests, Ninth World Conference on Earthquake Engineering, Tokyo-Kyoto, Japan, August 2 - 9, 1988
2. Kawashima, K., Hasegawa, K., Koyama, K. and Yoshida, T. : Experimental Investigation on Dynamic Strength and Ductility of Reinforced Concrete Bridge Piers, (Part.1), Technical Memorandum of PWRI, No.2232, 1985
3. Kawashima, K., Hasegawa, K., Koyama, K. and Yoshida, T. : Experimental Investigation on Dynamic Strength and Ductility of Reinforced Concrete Bridge Piers, (Part.3), Technical Memorandum of PWRI, No.2504, 1987
4. Iwasaki, T., Kawashima, K., Hasegawa, K., Koyama, T. and Yoshida, T. : Effect of Number of Loading Cycles and Loading Velocity of Reinforced Concrete Bridge Piers, 19th Joint Meeting, Wind and Seismic Effects, UJNR, Tsukuba, Japan, 1987
5. Iwasaki, T., Kawashima, K., Hasegawa, K. and Yoshida, T. : Dynamic Strength and Ductility of Reinforced Concrete Bridge Piers, 20th Joint Meeting, Wind and Seismic Effects, UJNR, 1988
6. Iwasaki, T., Ueda, O., Kawashima, K., Hasegawa, K. and Yoshida, T. : Inelastic Behavior of Reinforced Concrete Bridge Pier, -Effect of Bilateral Loading and Circular Hollow Section-, 21st Joint Meeting, Wind and Seismic Effects, UJNR, Tsukuba, Japan, 1989
7. Kawashima, K., and Koyama, T. : Effect of Number of Loading Cycles on Dynamic Characteristics of Reinforced Concrete Bridge Pier Columns, Structural Eng./Earthquake Eng., Proc. JSCE, Vol.5, No.1, pp.183-191, 1988.4
8. Kawashima, K., and Koyama, T. : Effect of Cyclic Loading Hysteresis on Dynamic Behavior of Reinforced Concrete Bridge Pier, Structural Eng./Earthquake Eng., Proc. JSCE, Vol.5, No.2, pp.343-350, 1988.10

Table 1 Strength and Ductility of Pier Models

	P-60	P-62	P-64	P-65	P-66
Loading Direction	Trans.	Trans.	Trans.	Longi.	Longi.
Bending Moment Ratio r_M (Eccentric Loading)	0.69 Small	0.55 Medium	0.51 Large	0 --	0.55 Medium
Yield Strength Py (tf)	12.7	15.0	22.8	17.2	16.0
Peak Strength Pmax (tf)	14.8	18.3	24.3	21.3	20.1
Pmax/Py	1.17	1.22	1.07	1.24	1.26
Yield Displacement δ y(cm)	1.6	1.3	2.0	1.6	1.8
Ultimate Displacement δ y(cm)	8.8	7.3	5.4	7.3	7.9
Ductility Factor δ y/δ u	5.5	5.6	2.7	4.6	4.4

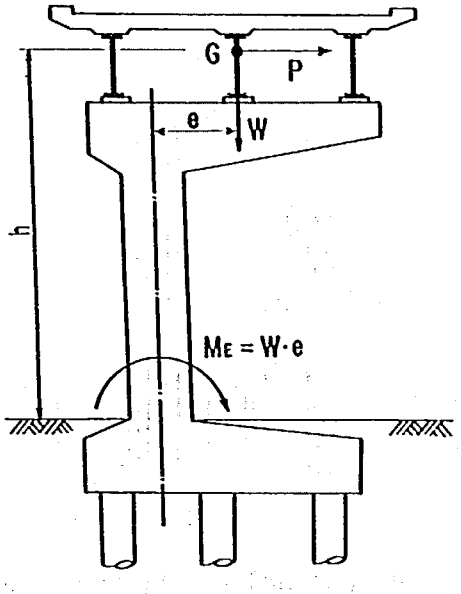


Fig.1 C-Shaped Reinforced Concrete Bridge Pier Subjected to Eccentric Loading

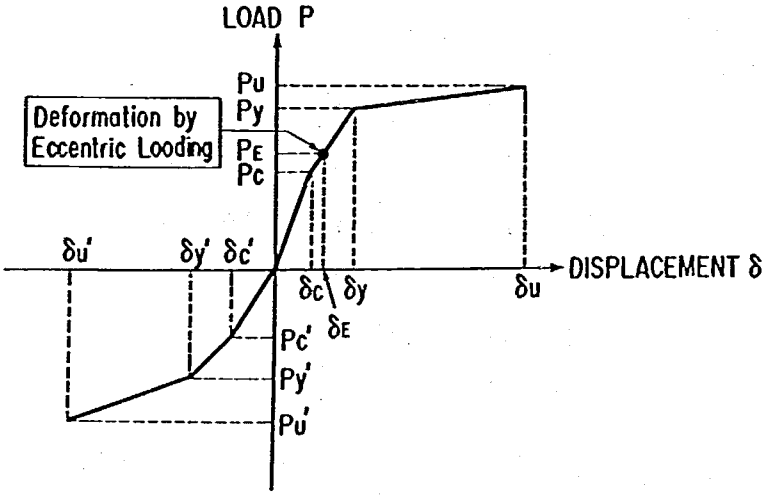


Fig.2 Effect of Eccentric Loading on Load-Displacement Relation

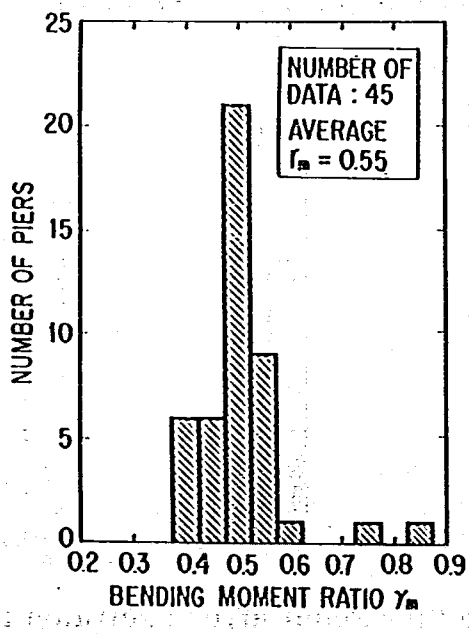


Fig.3 Distribution of Bending Moment Ratio of Actual Bridge Piers Surveyed

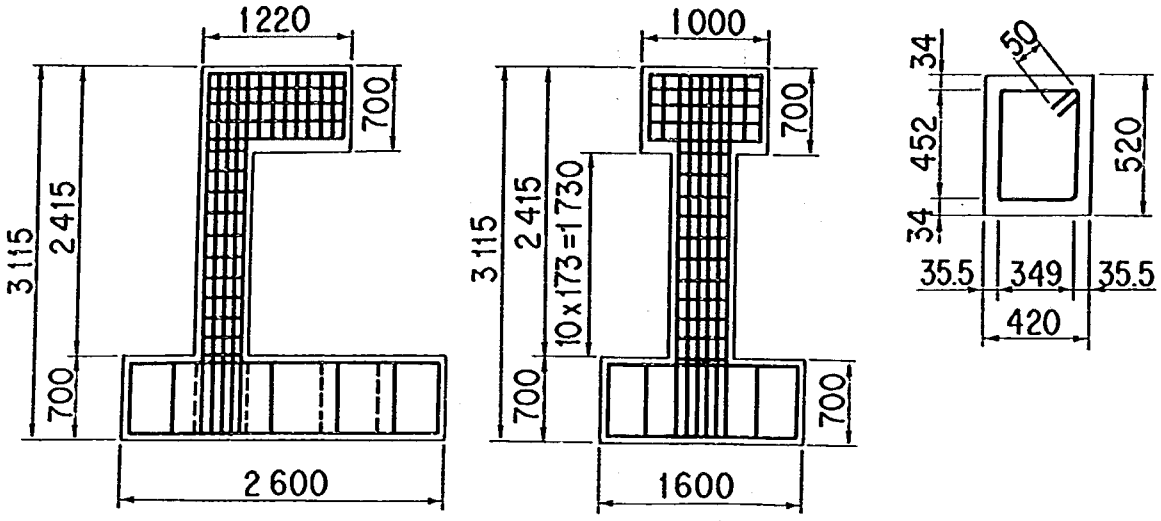


Fig.4 C-Shaped Bridge Pier Model for Shaking Table Test

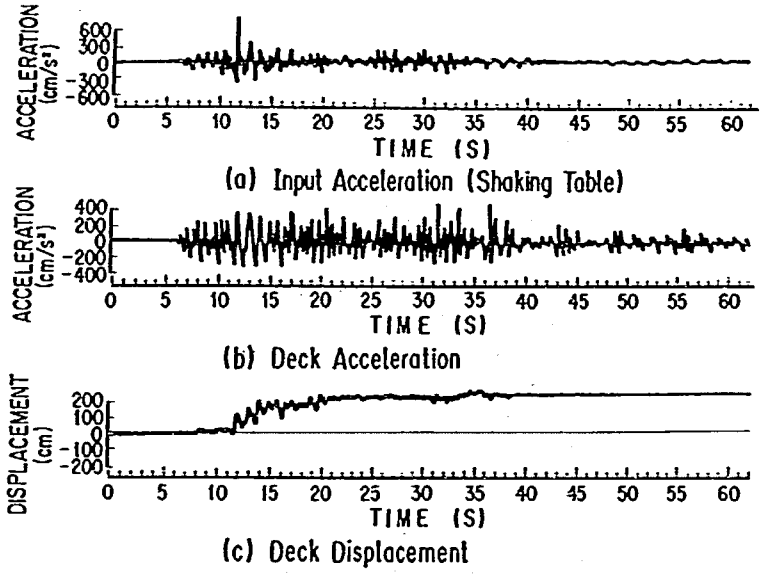


Fig.5 Response Accelerations and Displacement

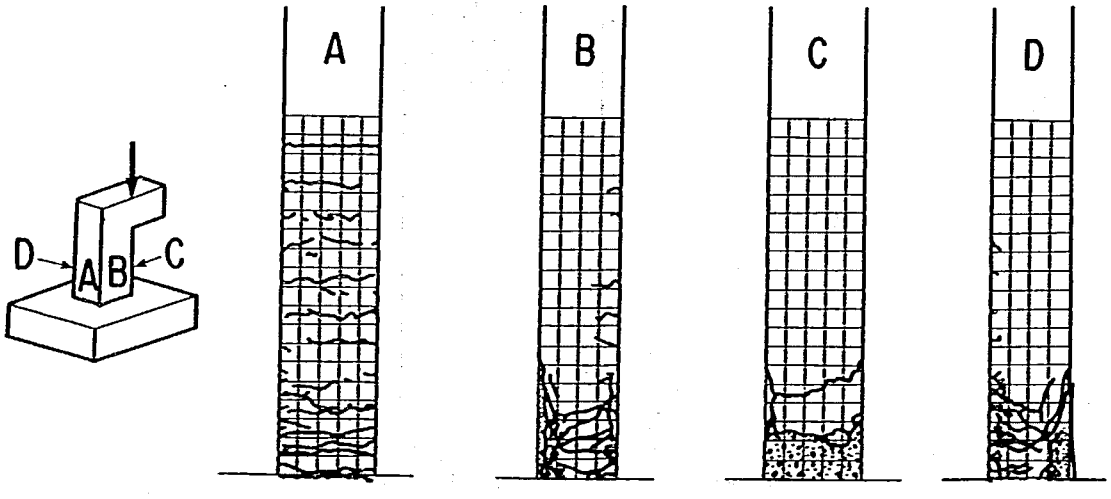


Fig.6 Failure Mode of the Pier Model after Excitaion by Shaking Table

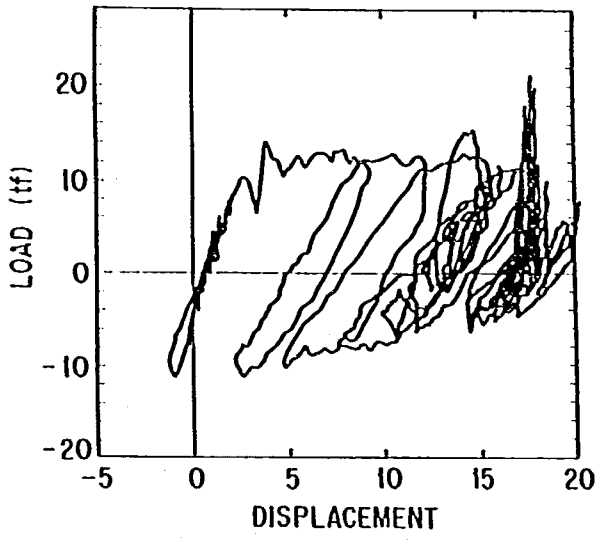


Fig.7 Hysteresis Loop of load-displacement relation obtained through Shaking Table Test

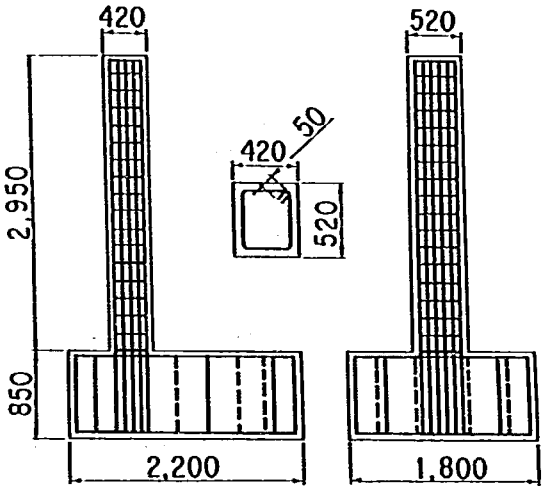


Fig.8 C-Shaped Bridge Pier Model for Dynamic Loading Tests

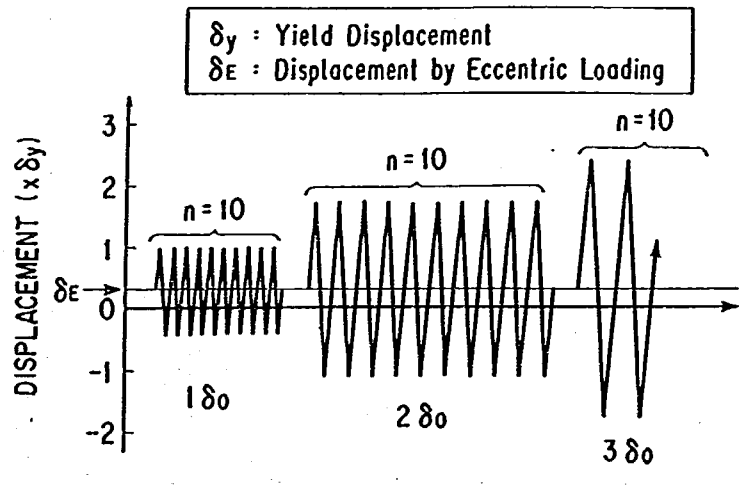


Fig.9 Loading Pattern of Displacement for Dynamic Loading Tests

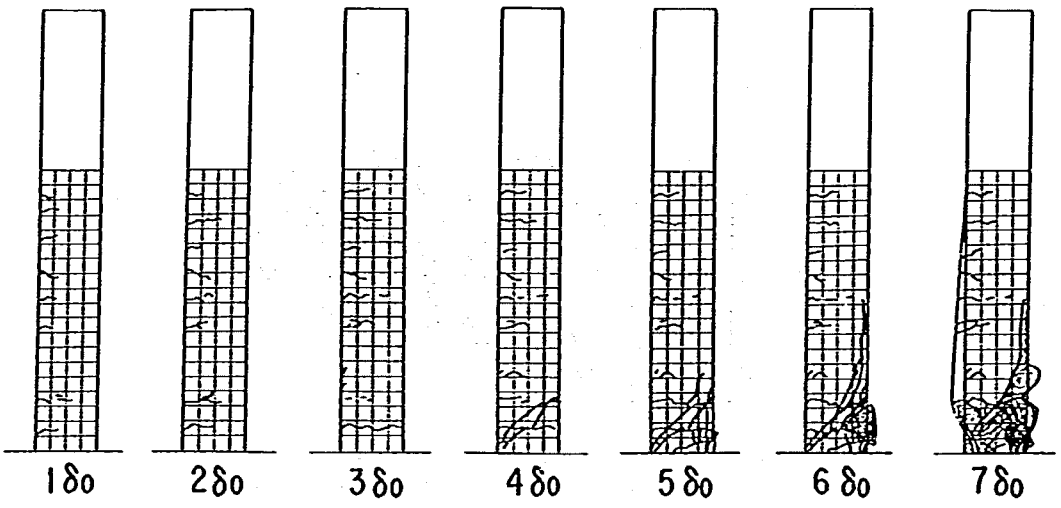


Fig.10 Failure Mode of P-62 (r_M = 0.55)

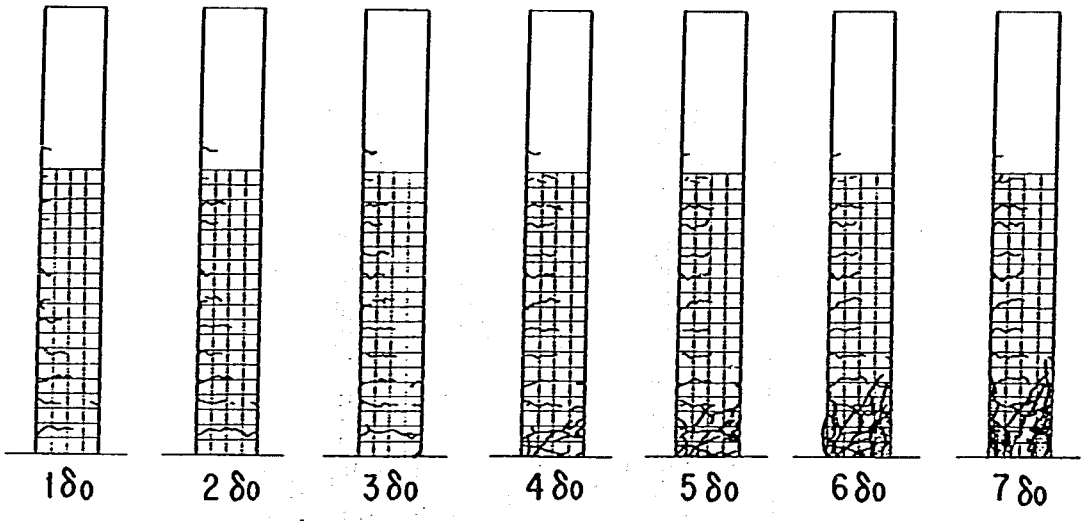


Fig.11 Failure Mode of P-60 (r_M = 0.69)

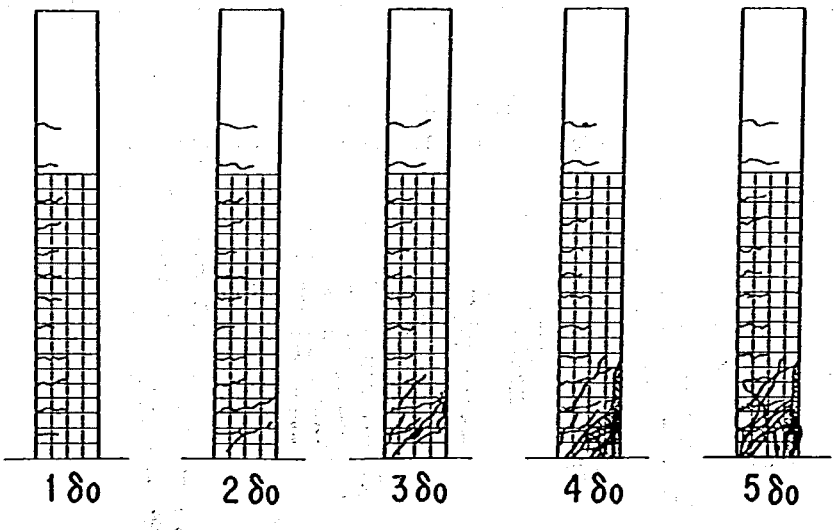


Fig.12 Failure Mode of P-64 (r_M = 0.51)

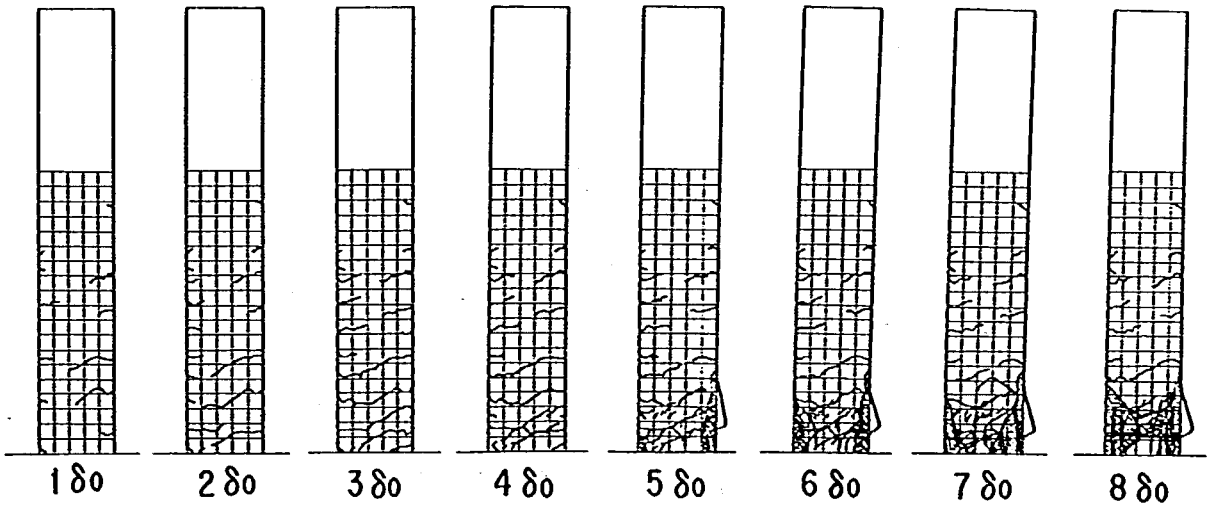


Fig.13 Failure Mode of P-65 (No Eccentric Loading, Longitudinal Loading)

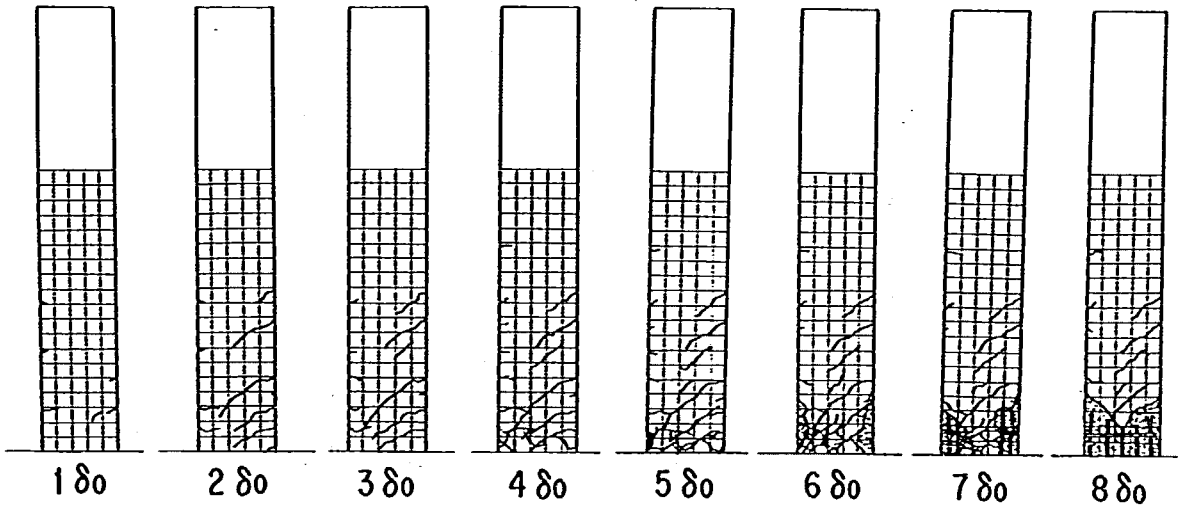


Fig.14 Failure Mode of P-65 (Longitudinal Loading)

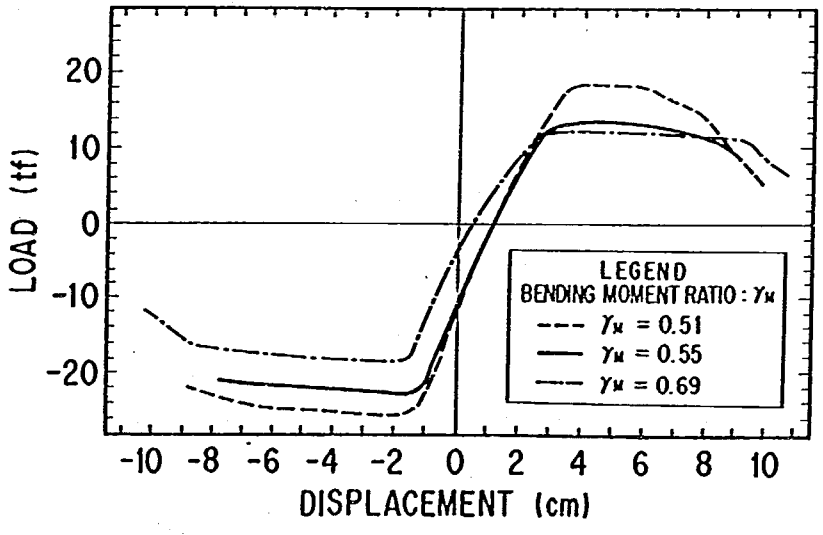


Fig.15 Effect of Bending Moment Ratio r_{M} on Load-Displacement Relation

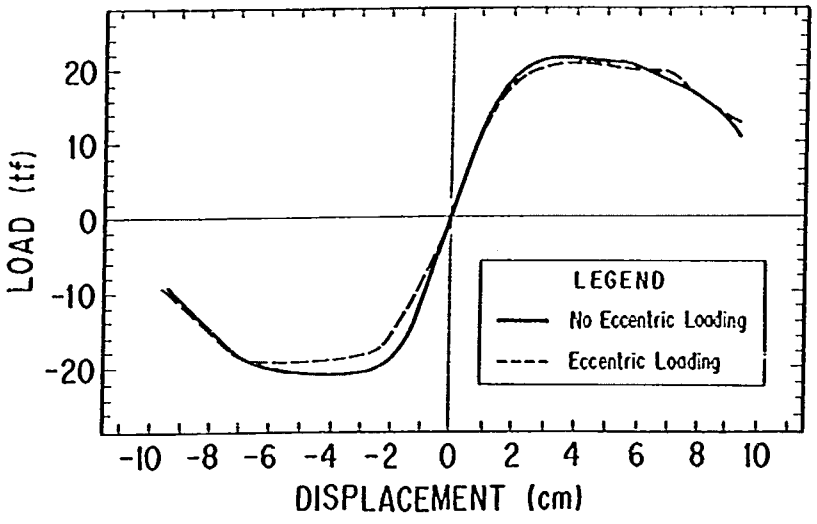


Fig.16 Effect of Loading Direction

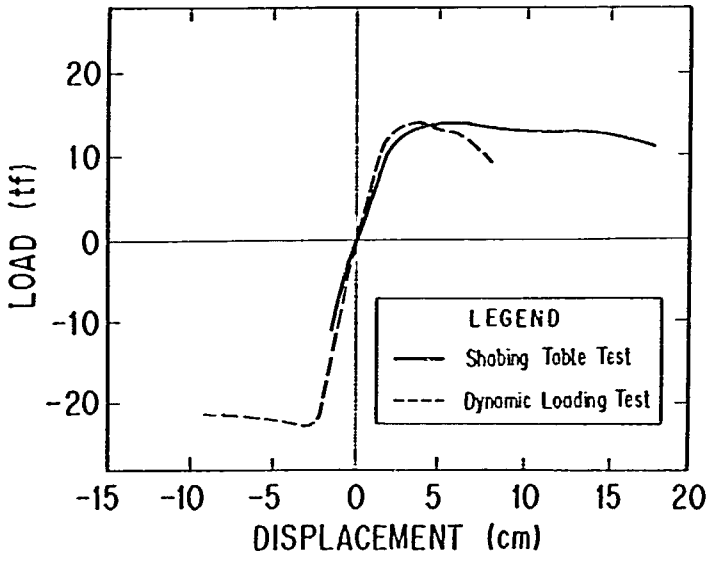


Fig.17 Comparison between Shaking Table Test and Loading Test

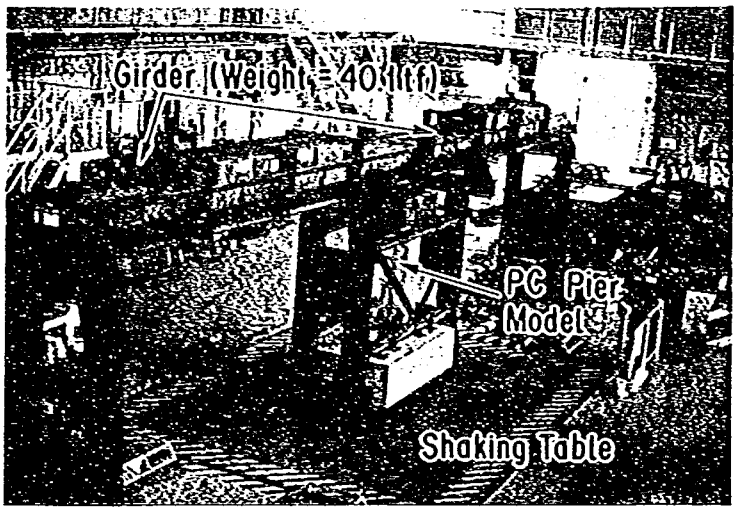


Photo 1 Set up of Shaking Table Test

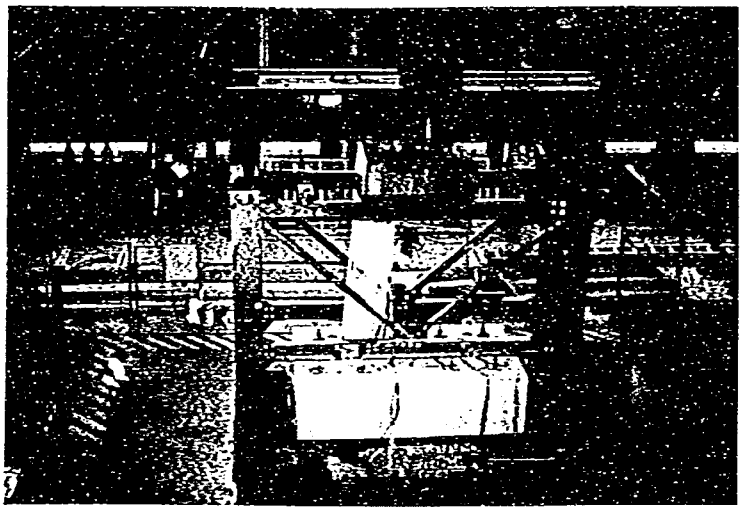


Photo 2 Residual Deformation of the Pier Model

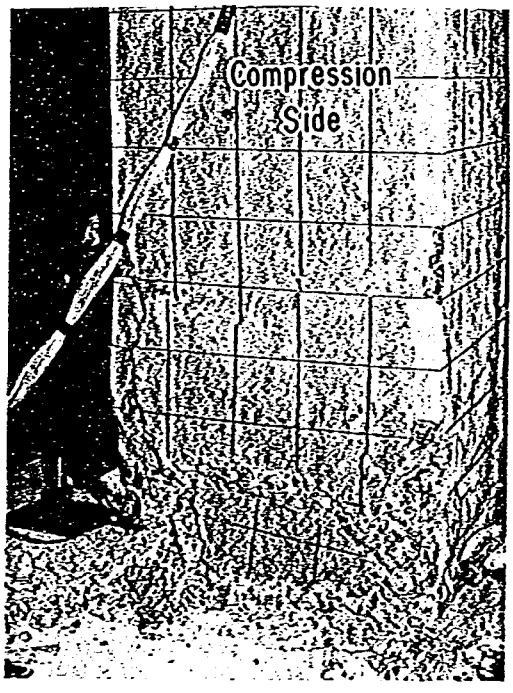


Photo 3 Failure Mode of the Pier Model

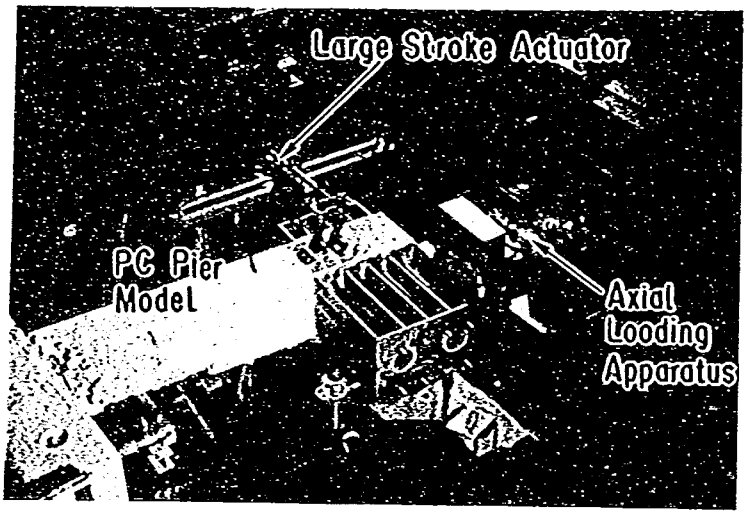


Photo 4 Set up of Dynamic Loading tests

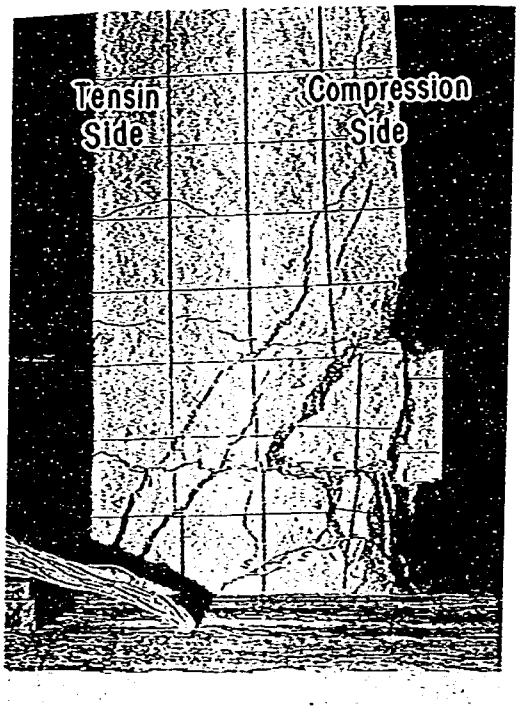


Photo 5 Failure Mode of the Pier Model

EVALUATION OF THE SEISMIC RESPONSE OF BRIDGES WITH HINGE RESTRAINERS

by

E. " Manos " Maragakis, M. " Saiid " Saiidi,
Shiping Feng, Daniel O'Connor, and
Saber Abdel-Ghaffar
Civil Engineering Department
University of Nevada, Reno

INTRODUCTION

The use of longitudinal hinge restrainers has been one of the most common seismic retrofitting techniques used by the California Department of Transportation (Caltrans) in bridges throughout the State of California. The main goal of the restrainers is to prevent the slipping of bridge girders off their supports during strong earthquake shakings.

During the 1989 Loma Prieta earthquake, a significant number of bridges which have been retrofitted with restrainers were subjected to significant ground excitation. This, along with the fact that these bridges were in an area densely instrumented, presented the opportunity for a detailed evaluation of the performance of these structures.

The California Department of Transportation funded a research project entitled "A Comprehensive Evaluation of the Performance of Bridge Cable Restrainers During the Loma Prieta Earthquake" under the direction of the first two authors of this paper. The goals, scope, and budget details of this project are discussed in the First Caltrans Annual Seismic Research Workshop.

To this point, five bridges with hinge restrainers are under analysis. In addition to analyzing the response of these structures to the 1989 Loma Prieta earthquake, the current procedure for restrainer design has been analyzed by using a nine-span example bridge which has pre-1971 design details and was retrofitted with restrainers.

In this paper, some of the most important aspects of the analysis of two of the bridges, the San Gregorio Bridge and the Madrone Drive Undercrossing, are presented along with some of the main points of the parametric study of the effects of the restrainers.

PART A: STUDY OF SAN GREGORIO BRIDGE

BRIDGE DESCRIPTION

The San Gregorio Bridge (Fig. 1) is located in San Mateo County, about thirteen miles south of Half Moon Bay on Highway 84. Built in 1940, the bridge is a five-span reinforced structure with an overall length of 265 feet and a height of 56 feet. Having an average vertical grade of 6 percent, the bridge elevation is higher at the south abutment than at the north abutment.

The deck (Fig. 2) consists of 8.125-inch thick reinforced concrete slab and three 20-inch wide variable depth rectangular girders spaced on 10.5-foot centers. The maximum depth of the girders is 8.25 feet at the center of the span. The two end spans are 42 feet long, and the three middle spans are 59 feet long. The three intermediate expansion joints (Fig. 3) are located in spans 1, 3, and 5.

The three columns at bent 2 are reverse-tapered rectangular columns, with the smallest section at the column base. Each of the bents (3, 4, and 5) consist of three tapered columns resting upon a 15-foot high wall. The walls continue to taper in both the wide and deep dimensions (Fig. 4). The seat-type abutments consist of a concrete seat and a 7.6-foot high backwall. A 2-inch expansion joint gap exists between the abutment backwall and the bridge deck (Fig. 5).

SEISMIC RETROFIT

In 1982, the San Gregorio Bridge was seismically retrofitted. Two sets of restrainer cables were installed at each intermediate hinge. Each restrainer set consists of seven cable units. Each cable unit consists of a 17.2-foot long, 3/4-inch diameter steel cable with swaged ends and a turnbuckle. Also, two 3-inch diameter steel pipes were installed as transverse shear keys at each intermediate hinge. The pipes were filled with concrete and were contained in a 3.75-inch diameter cored hole through the hinge diaphragm.

Three reinforced concrete shear pedestals were installed under the girder ends at each abutment to restrain movement in the transverse direction. Each shear pedestal contains two shear blocks, one on either side of the superstructure girder. An expansion gap of 1 inch exists between the shear blocks and the girders.

DAMAGE FROM THE LOMA PRIETA EARTHQUAKE

The San Gregorio Bridge is located approximately 40 miles from the epicenter of the Loma Prieta earthquake. During the earthquake, both abutments were damaged. There were 1/8-inch diagonal cracks on the face of abutment 1. The left and right wing walls at abutment 1 had diagonal cracks, and the joint set at abutment 1 had

failed. There were ¼-inch wide diagonal cracks on the face of abutment 6. The left and right wing walls at abutment 6 cracked at the top corner. There were no signs of instability or settlement of the abutments (Ref. 1). There was no damage reported to the superstructure of the bridge. Also, the damage report made no mention of any damage at the intermediate hinges or the restrainer cables.

EARTHQUAKE ANALYSIS MODEL

The computer model (Fig. 6) of the San Gregorio Bridge consists of 85 nodes, 82 linear-elastic straight beam elements, 31 expansion joint elements, and 3 five-spring bending elements (Ref. 2). The intermediate hinges were modeled with one expansion joint element representing the actual joint and the cable restrainers and with other elements to model the shear pipes and shear bolts. Because the restrainer element is capable of tensile loading only, two restrainers are required to model a two-way member. The expansion hinge elements were also employed to model the abutment backfill soil, the piles supporting the abutments, the backwalls, and the retrofit shear blocks.

RESULTS OF ANALYSIS

Accelerograms from the nearest strong-motion station, located at Springs Reservoir Pulgas in Upper Crystal, were used as the ground motion input for the earthquake analysis (Ref. 3). Three combinations (0.16g and 0.09g, 0.32 g and 0.18g, and 0.60g and 0.34g) of peak ground acceleration (PGA) were used in study cases. The larger PGA in each combination was applied longitudinally to the bridge, while the smaller was applied transversely. In all of the figures, each combination is shown by the value of the longitudinal acceleration (for example, 0.32g in a figure stands for the combination 0.32g and 0.18g).

Figure 7 illustrates the longitudinal displacement response for three PGA combinations. The peak displacement for the largest PGA is approximately 5.5 inches. Figures 8 and 9 show the maximum response at the hinges and the abutments due to the three PGA combinations. The following remarks can be made.

1) The maximum longitudinal relative displacement, 3.88 inches at hinge 2 due to 0.60g and 0.34g PGA, was very close to the movement limit of 4 inches at the hinges.

2) The maximum cable forces were below the force limit of 492 kips in all cases. However, the maximum cable force at hinge 2 due to 0.60g and 0.34g PGA was close to 96 percent of the limit.

3) The forces at the abutment backfill of both the abutment and the piles at abutment 1 reached the yield limit due to the 0.6g and 0.34g PGA combinations.

4) The forces at both abutments due to the 0.32g and 0.16g PGA combinations were below the yield level, and the abutment movements were relatively small.

5) Since no damage to the intermediate hinges was reported, the analysis with a lower PGA combination such as 0.32g and 0.18g produced a bridge response which is more consistent with the actual behavior of the bridge during the Loma Prieta earthquake.

Figure 10 shows a comparison of displacement response of the San Gregorio Bridge in the cases with and without the seismic retrofit. Figures 11 and 12 show the maximum displacement and force responses of the hinges and the abutments in cases with and without the seismic retrofit due to three PGA combinations. The following remarks can be made.

1) The longitudinal relative hinge displacements were sensitive to the existence of the seismic retrofit. The cable restrainers effectively reduced the longitudinal relative displacements at the hinges regardless of the PGA combination used as input ground motion.

2) In the case without the retrofit, the combination of 0.60g and 0.34g PGA input produced a relative displacement at hinge 2; this exceeded the permissible limit of 4 inches.

3) The seismic retrofit did not play any major role in reducing the abutment forces. In the case of 0.60g and 0.34g PGA, the abutment yielded regardless of the presence of retrofit.

In this paper, some of the most important aspects of the analysis of two of the bridges, the Madrone Drive Undercrossing and the San Gregorio Bridge, are presented along with some of the main points of the parametric study of the effects of the restrainers.

PART B: STUDY OF MADRONE DRIVE UNDERCROSSING

BRIDGE DESCRIPTION

The Madrone Drive Undercrossing (Fig. 13) is located about five miles south of Los Gatos on California State Route 17. Built in 1938, the bridge is a three-span reinforced concrete T-beam structure with an overall length of 134 feet and a width of 59 feet. The bridge lies on a 700-foot radius curve with a superelevation rate of 10.4 percent and has a vertical grade of 7 percent.

The deck (Fig. 14) consists of a 7.25-inch thick reinforced concrete slab and eight 15-inch wide by 41-inch deep rectangular girders spaced on 8.25-foot centers. The south end span is 43 feet long, the center span is 50 feet, and the north end span measures 41 feet long.

The center span is continuous over the two column bents with a short cantilever section at each end. Each end span consists of a simply-supported deck section resting on an intermediate hinge (Fig. 15) at the cantilever end and rocker bearings at the abutment.

SEISMIC RETROFIT

In 1985, the Madrone Drive Undercrossing was seismically retrofitted. Two reinforced concrete shear pedestals were installed at each abutment to restrain movement in both the longitudinal direction and in the transverse direction. Each shear pedestal contains two shear blocks, one on either side of the first interior girder; therefore, four shear blocks act to restrain movement in the longitudinal direction while only two blocks act simultaneously in the transverse direction.

Two sets of restrainer cables were installed at each intermediate hinge. Each cable unit consists of a 12-foot long ¾-inch steel cable with a turnbuckle connector. Two cable units are looped through holes cored through the girders and diaphragms on opposite sides of the hinge and connected to form a restrainer set.

DAMAGE FROM THE LOMA PRIETA EARTHQUAKE

The Madrone Drive Undercrossing is located approximately 8 miles from the epicenter of the Loma Prieta earthquake. Ground acceleration at the bridge site was estimated at 0.65-g, and was strongly transverse (Ref. 4).

During the earthquake, the north abutment underwent slight rotation, as evidenced by pavement cracking at the backwall, and the rocker bearings were knocked out of plumb. All of the retrofitted end-span shear blocks were severely damaged, producing large spalls and exposing the reinforcing steel (Ref. 5). The retrofit, however, appears to have contained the structure and prevented a catastrophic collapse of the end spans. The damage report makes no mention of any damage to the intermediate hinges or the restrainer cables.

EARTHQUAKE ANALYSIS MODEL

The earthquake analysis for the Madrone Drive Undercrossing was performed using *NEABS* (*N*onlinear *E*arthquake *A*nalysis of *B*ridge *S*ystems) computer software (Ref. 6).

For ease in implementing the computer model, the bridge was assumed to be straight, with no superelevation, and with no vertical grade. The model (Fig. 16) consisted of 43 element nodes, 20 auxiliary (direction) nodes, 34 beam elements, 4 five-spring bending elements (Ref. 7), 6 foundation spring elements, and 18 expansion joint elements.

The abutment joints are modeled by three expansion joint elements each, one acting in the longitudinal direction and two acting in opposite transverse directions. A disadvantage

of using separate restrainer elements in the longitudinal and transverse directions is that coupling effects cannot be modeled.

The intermediate hinges were modeled with one expansion joint element representing the actual joint and the cable restrainers, and other elements to model the shear bolts. Because the restrainer element is capable of tensile loading only, two restrainers are required to model a two-way member. Thus, two expansion joints each were required to model longitudinal and transverse shear in the bolts.

RESULTS OF ANALYSIS

Accelerograms from the nearest strong-motion detector station, Aloha Avenue in Saratoga, were used as the ground motion input for the *NEABS* earthquake analysis (Ref. 3). The east-west component of this record was scaled to 0.65-g and applied to the bridge in both longitudinal and transverse directions.

Two models were used to determine the effects of the retrofit restrainer cables: one model included the cables, the other did not. A comparison of the structure's response give an indication of the effectiveness of the restrainers.

Fig. 17 illustrates the longitudinal displacement responses for both models. The peak displacement for the model without restrainer cables is approximately 4 inches, compared to 2.5 inches for the model with cables. In this figure, a positive displacement represents northward travel while a negative displacement represents southward travel.

Fig. 18 shows a comparison of the shear block longitudinal deformation histories at the north abutment. In the case with restrainer cables, the damage is greater than actually observed after the Loma Prieta earthquake. The earthquake was estimated to have been strongly transverse; therefore, the 0.65-g acceleration record applied to the models both longitudinally and transversely appears to have been conservative. Cursory analyses with the acceleration history scaled to 0.5-g produced bridge responses which are more consistent with the observed damage.

The longitudinal relative displacement histories for the north intermediate hinge are shown in Fig. 19. A positive value indicates a widening of the hinge gap. A negative value of 0.5 inch indicates closure of the gap; negative values beyond 0.5 inch are the artificial results of impact modeled with a finite stiffness. Relative displacements are comparable for the two models up to the last few peaks of the record; however, the maximum relative displacement for the model without restrainer cables is nearly 6 inches. Since the width of the hinge is 4.5 inches, the north-end span would have dropped off its seat if the restrainers were not present. Cable force for the north hinge restrainer cables is illustrated in Fig. 20. Note that the cables reach their yield load several times. In the 0.5-g studies, the restrainer cables still reach the yield load; however, the north span is not in danger of dropping-off its seat.

PART C: PARAMETRIC STUDY OF THE EFFECTS OF RESTRAINERS

The design of restrainers has been based on a relatively simple equivalent static analysis method that incorporates many of the primary factors affecting the seismic response of bridges (Ref. 8). The purpose of this part of the paper is to present some of the results of a parametric study of the nonlinear response of a nine-span bridge subjected to several input earthquake records. Details of the study are presented in Ref. 9. Only the longitudinal response of straight bridges was considered to be consistent with the Caltrans design method.

EXAMPLE BRIDGE

Figure 21 shows the elevation of the example bridge which is the subject of the study. No span lengths are specified in Ref. 8 because only the superstructure weight and not the length enters the calculations. The span lengths shown in the figure were estimated for the purpose of nonlinear analyses which are presented in this paper. The hinges are numbered from left to right. The method to determine initial stiffnesses and yield forces are the same as those used in Ref. 8. It is assumed that the bridge is at an alluvium site with a peak bed rock acceleration of sixty percent of gravity. The example bridge represents the pre-1971 designs in which typical hinge width was 6 in. (150 mm). The hinge gap and the restrainer gap are both assumed to be 0.75 in. (19 mm).

NONLINEAR MODELING

Because the properties specified in Ref. 8 for the example bridge were suited only for an equivalent static analysis, many assumptions had to be made about the geometric and section properties of different bridge components in order to perform the nonlinear analyses. The nonlinear response history analysis of the bridge was performed using computer program NEABS-86 (Ref. 2). Different time intervals for numerical integration were attempted on a sample case until the results converged. It was found that a time interval of 0.005 second is appropriate. Three earthquake records were used in the nonlinear analyses. These were the north-south component of the 1940 El Centro earthquake, the north-south component of the Eureka earthquake of 1954, and the east-west component of the 1989 Loma Prieta earthquake recorded at the Saratoga station. All the records were normalized to a peak ground acceleration (PGA) of 0.6g which is the same as that used in the example bridge. The response spectra for these records showed notable differences.

Variation of Parameters

Two parameters were studied. One was the hinge restrainer cross sectional area and the other was the restrainer initial gap. Because only 3/4-in. (19-mm) diameter 7-ft. cable restrainers were considered, the first parameter was studied by changing the number of restrainers (Table 1). The restrainer gaps included in the study represented the condition of the bridge during the extreme high and extreme low ambient temperatures. The

specified restrainer gap of 0.75 in. (19 mm) in Ref. 8 is for the "hottest ambient temperature." The corresponding hinge gap is assumed to be 0.75 in (19 mm). During the extreme low ambient temperature, the restrainer gap is expected to become very small and even approach zero. Under this condition, the hinge gap will reach 1.5 in. (38 mm).

RESULTS OF STUDIES WITH RESTRAINER GAP=0.75 IN.

Hinge Movements - Shown in Fig. 23 are the maximum relative displacements of the two segments of the superstructure adjacent to each hinge. Note the following:

1) The relative hinge displacements were insensitive to the changes in the number of cables including Case 6 in which no restrainers had been used. This was true regardless of the input ground motion.

2) The maximum relative movement at hinges varied depending on the earthquake.

3) Hinge 2 experienced the largest relative displacement in all earthquakes. This is because the proximity of the two other hinges to the abutments helped reduce their movement and because Hinge 2 has the smallest number of restrainers.

4) The permissible relative displacement at the hinges when restrainer gap is 0.75 in. (19 mm) is 2.25 in. (57 mm). It can be seen that this limit was not reached even when no restrainers were used.

Restrainer Stresses - Figure 24 shows the maximum restrainer stresses. It can be seen that the restrainer stresses were generally insensitive to the number of cables. The maximum restrainer stress was well below the yield stress of 176.1 ksi (1214 MPa) in all cases.

RESULTS OF STUDIES WITH RESTRAINER GAP=0

All the computer analyses discussed in the previous section were repeated for bridge models without any gap for the restrainers. A reduction in the restrainer gap led to an increase in the hinge gap to 1.5 in. (38 mm). Because the total seat width is 6 in. (150 mm) (Fig. 22), to maintain a minimum of 3 in. (75 mm) bearing (a criterion set in the design example in Caltrans, (Ref. 8), the maximum permissible relative displacement between the two segments of the superstructure adjacent to each hinge is 1.5 in. (38 mm) when restrainer gap is zero.

Hinge Movements - Shown in Fig. 25 are the maximum relative superstructure movements at different hinges. The following general observations can be made on this figure:

1) In most cases, the relative hinge displacements increased as a result of reduction

in the number of cables. When no restrainers were used (Case 6), the displacements in Hinges 2 and 3 exceeded the permissible limit. This was true regardless of the input ground motion.

2) The maximum relative movement at Hinge 1 varied depending on the earthquake.

3) Hinge 2 experienced the largest relative displacement in all earthquakes.

Restrainer Stresses - Figure 26 shows the maximum restrainer stresses. The results indicate that the restrainer stresses generally increased as the number of cables was reduced. This is because of the reduction in cross sectional area of the restrainers and the increase in the relative displacements. The maximum restrainer stresses were below the yield stress of 176.1 ksi (1214 kN) in all cases. However, the maximum cable stress in Case 5 was approximately 85 percent of this limit.

CONCLUDING REMARKS

The results presented in Part C of this paper pointed out the need to consider the extreme low ambient temperature condition (zero restrainer gap) to determine critical restrainer stresses. The maximum relative superstructure displacements at hinges and abutments, however, may develop for the case of zero or non-zero restrainer gap depending on the number of restrainers. It is therefore recommended that the design of restrainers include both the extreme high and low temperatures conditions.

ACKNOWLEDGEMENTS

The study presented in this paper was part of a project which was mainly funded by the California Department of Transportation. This financial support along with the additional support provided by the National Science Foundation and the Nevada Department of Transportation are gratefully acknowledged. Mr. Mark Yashinsky, the Caltrans project monitor and Mr. R. Obisanya, a staff engineer of Caltrans, are thanked for providing helpful comments.

REFERENCES

1. Herr, H. 1989. "San Gregorio Bridge Supplementary Bridge Report," Sacramento, California Department of Transportation.

2. Saiidi, M., G. Ghusn, and Y. Jiang. 1989. "Five-Spring Element for Biaxially Bent R/C Columns," *Journal of Structural Engineering*, ASCE, Vol. 115, No. 2, February.

3. Shakal, A., M. Huang, M. Reichle, C. Venture, T. Cao, R. Sherburne, M. Savage, R. Darrah, and C. Peterson. 1989. "CSMIP Strong-Motion Records

from the Santa Cruz Mountains (Loma Prieta), California Earthquake of 17 October 1989," Report No. OSMS-89-06. Sacramento: California Department of Conservation, Division of Mines and Geology.

4. Yashinsky, M. 1991. "Performance of retrofit measures on existing older bridges." Sacramento: California Department of Transportation, Division of Structures.

5. Nagai, E. 1989. "Madrone Drive Undercrossing supplementary bridge report." Sacramento: California Department of Transportation, Division of Structures.

6. Imbsen, R. A., and R. A. Schamber. 1983. "Earthquake resistant bridge bearings." *Report No. FHWA/RD-82/166,* Vol. 2. Washington, D.C.: U.S. Department of Transportation, Federal Highway Administration.

7. Saiidi, M., and M. A. Sozen. 1979. "Simple and complex models for nonlinear seismic response of reinforced concrete structures." *Report No. UILU-ENG-79-2013.* Urbana, Ill.: University of Illinois, Department of Civil Engineering.

8. Caltrans (California Department of Transportation), "Seismic Design References" Division of Structure, July, 1990, and the Restrainer Design Example Update, July 1991.

9. Saiidi, M., E. Maragakis, S. Abdel-Ghaffar, and D. O'Connor, "Effect of Hinge Restrainers on the Response of Highway Bridges during the Loma Prieta Earthquake," Proceedings, Third Workshop on Bridge Engineering Research in Progress, San Diego, California, November 1992.

10. Saiidi, M., E. Maragakis, and S. Feng, "An Evaluation of the Current Caltrans Seismic Restrainer Design Method," Civil Engineering Department, Report No. CCEER-92-8, University of Nevada, Reno, October 1992.

Table 1 - Number of Cables in Different Cases

CASE NO.	NUMBER OF CABLES		
	HINGE 1	HINGE 2	HINGE 3
1	8X10	6X10	10X10
2	7X10	5X10	9X10
3	6X10	4X10	8X10
4	5X10	3X10	7X10
5	4X10	2X10	6X10
6	0	0	0

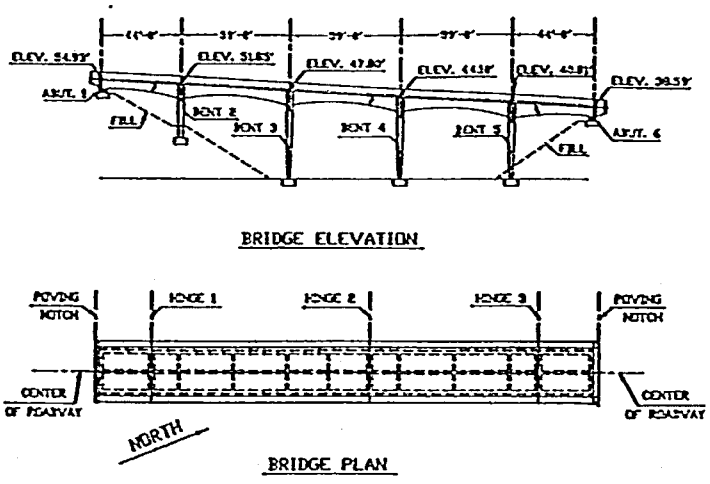


Fig. 1. San Gregorio Bridge

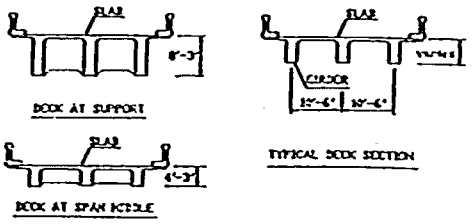


Fig. 2. Deck Section of San Gregorio Bridge

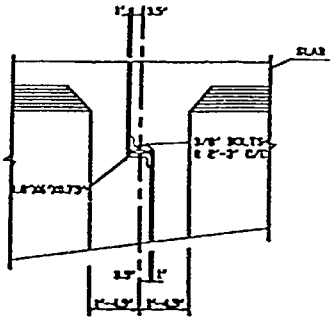


Fig. 3. Detail of Intermediate Hinge

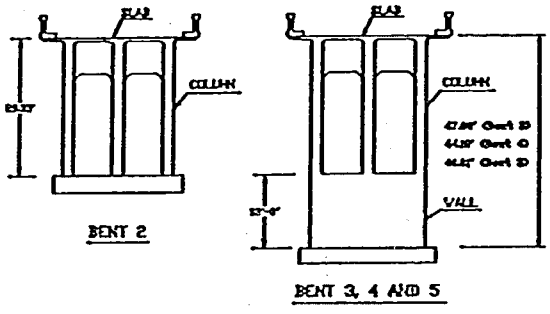


Fig. 4. Bent Elevation of San Gregorio Bridge

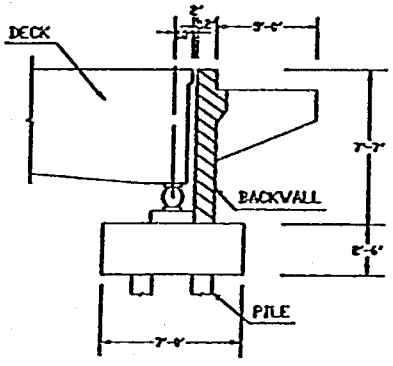


Fig. 5. Abutment Detail

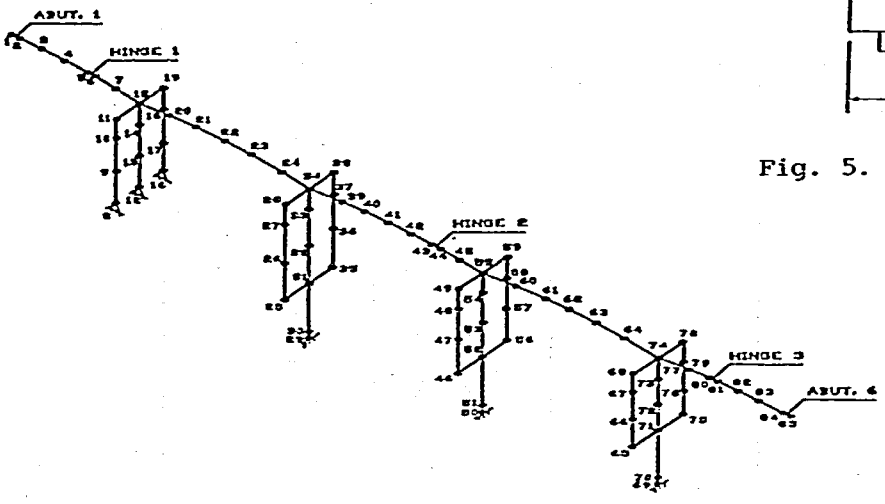


Fig. 6. Computer Model for San Gregorio Bridge

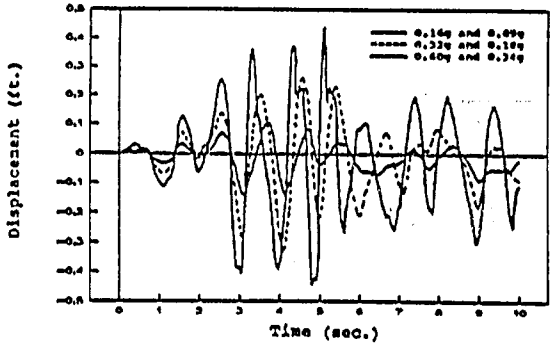


Fig. 7. Longigudinal Displacements Due to Three PGA Combinations

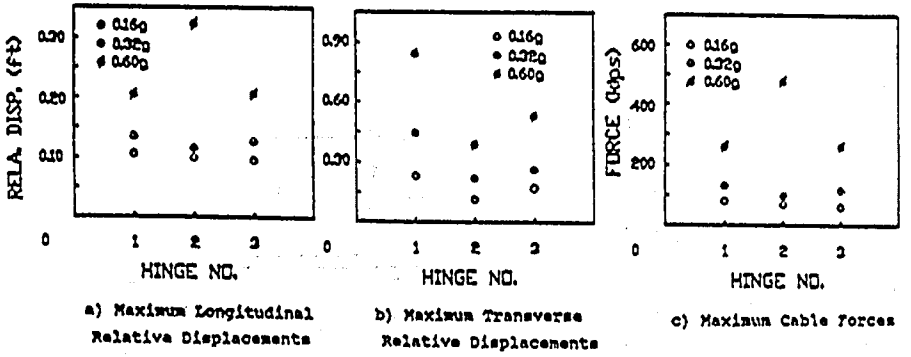


Fig. 8. Maximum Response of Hinges Due to Three PGA Combinations

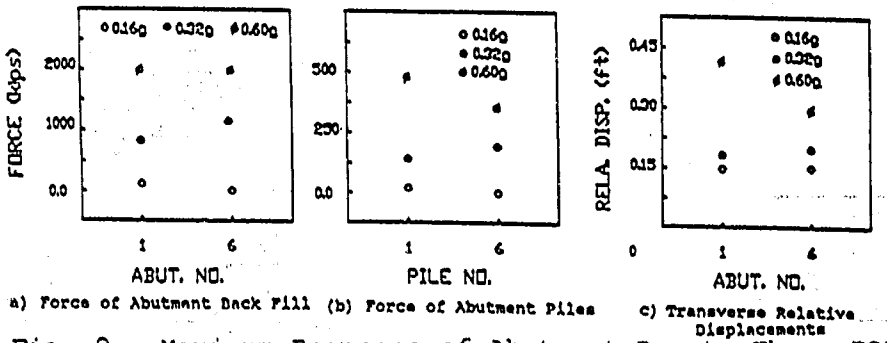


Fig. 9. Maximum Response of Abutment Due to Three PGA Combinations

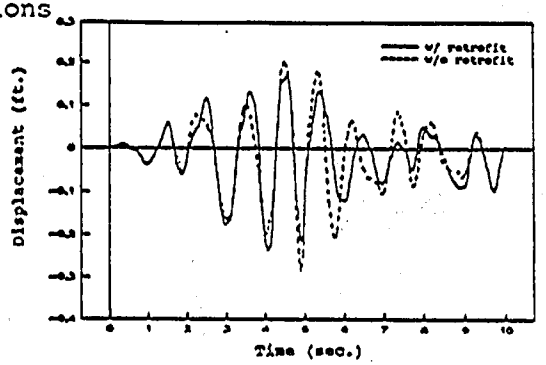


Fig. 10. Longitudinal Displacements (with and without retrofit)

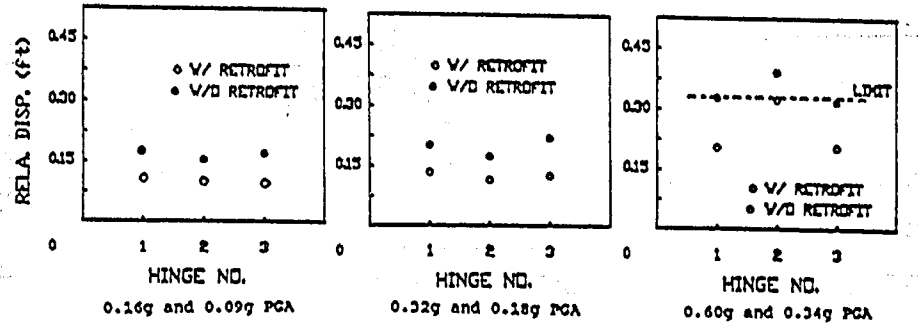


Fig. 11. Maximum Response of Hinge (with and without retrofit)

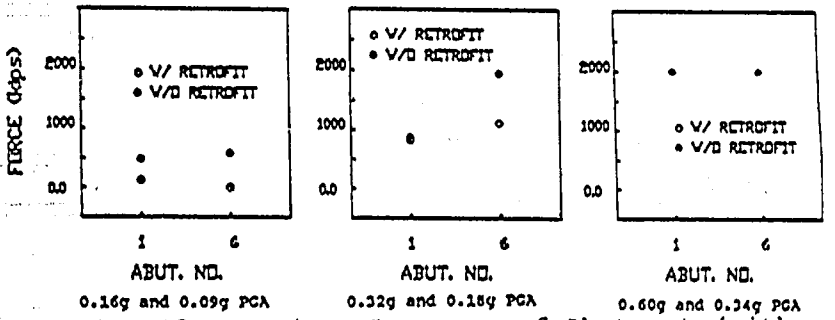


Fig. 12. Maximum Response of Abutment (with and without retrofit)

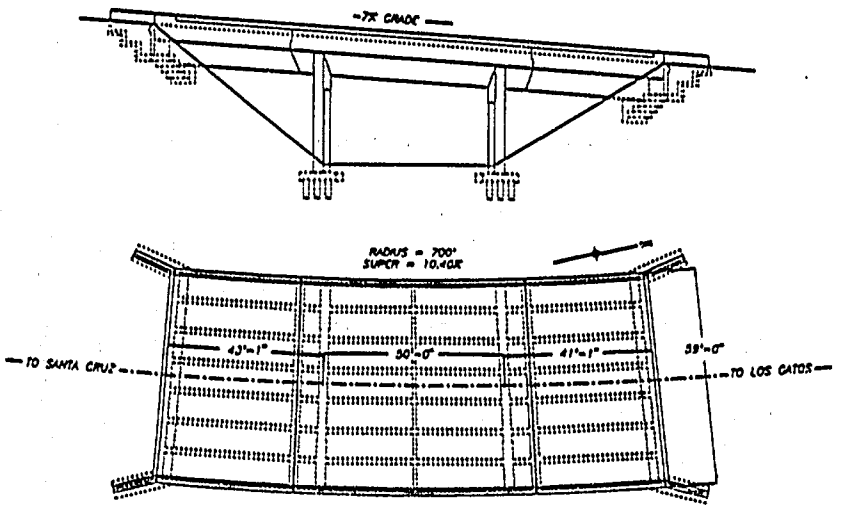


Fig. 13. Madrone Drive Undercrossing

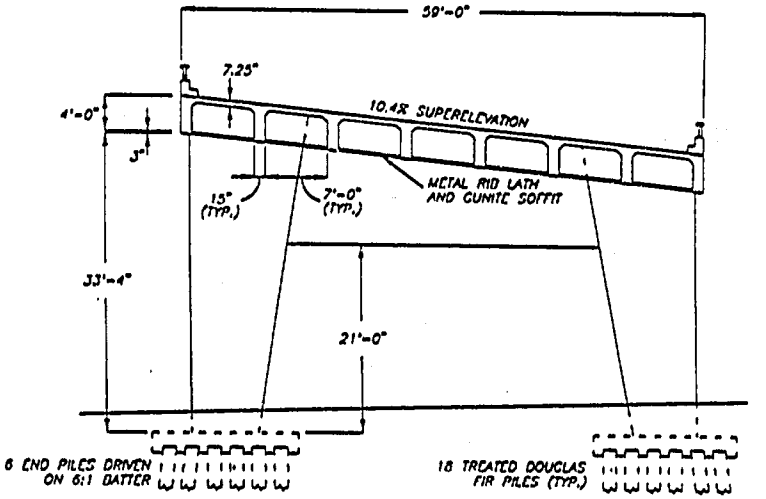


Fig. 14. Cross-Section of Madrone Drive Undercrossing

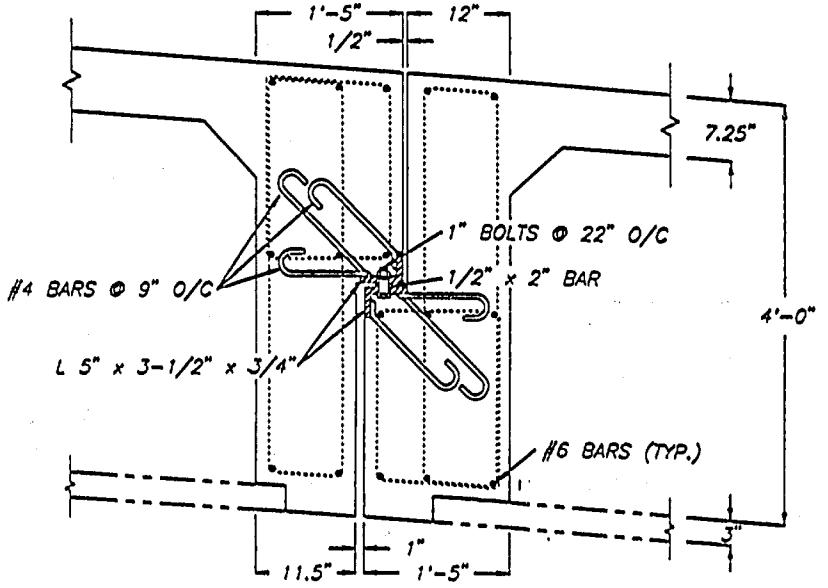


Fig. 15. Detail of Hinge Joint

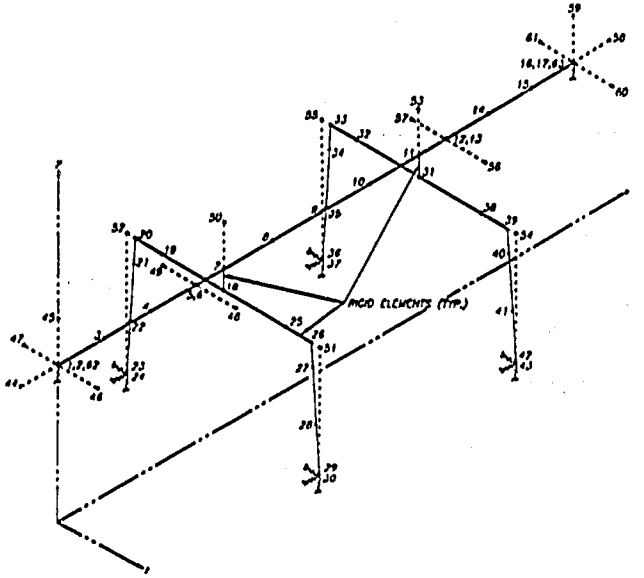


Fig. 16. NEABS Finite Element Mesh for Madrone Drive Undercrossing

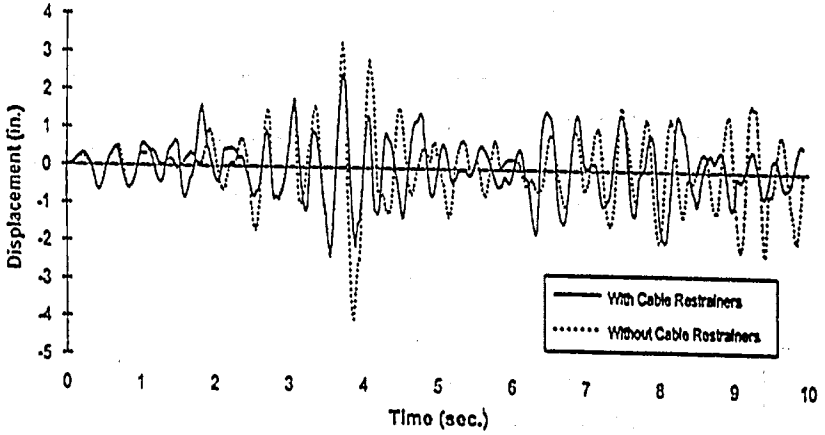


Fig. 17. Longitudinal Response to 0.65g Acceleration Record

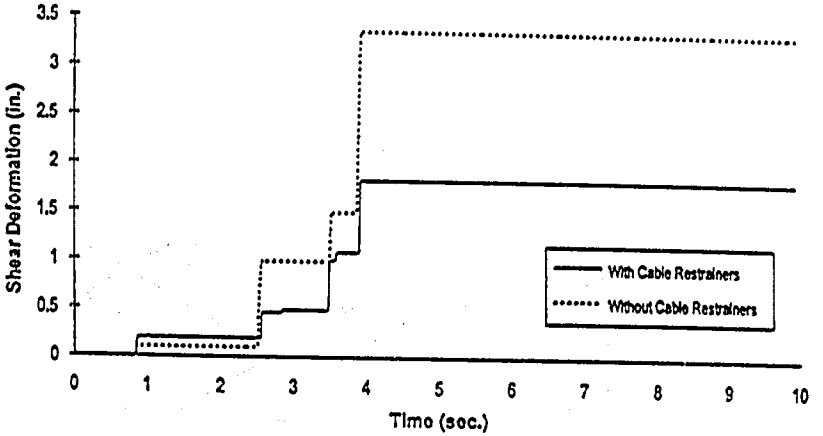


Fig. 18. Longitudinal Deformation of Retrofit Shear Blocks at North Abutment

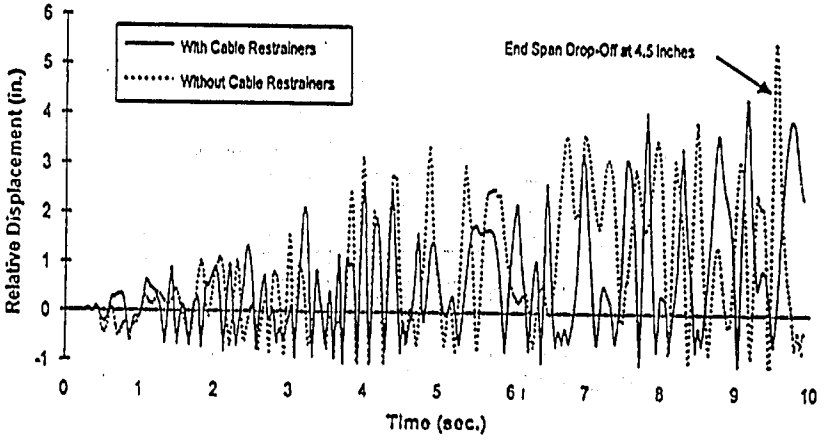


Fig. 19. Longitudinal Response of North Hinge

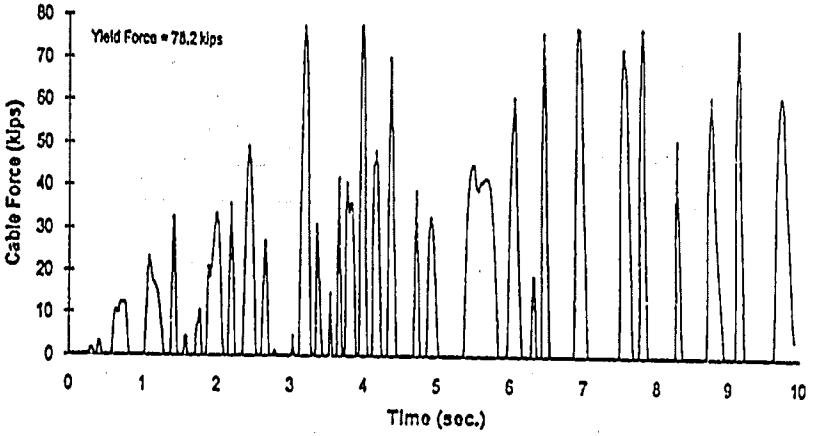


Fig. 20. Restrainer Cable Force at North Hinge

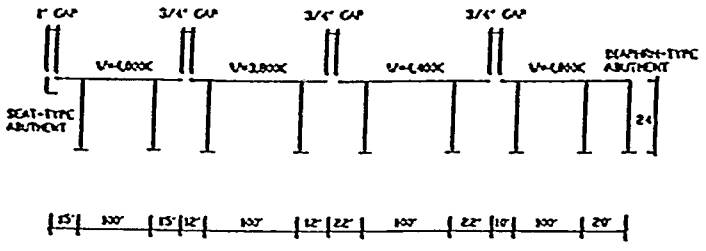


Fig. 21. Elevation of the Example Bridge (Ref. Caltrans 1990, 1991)

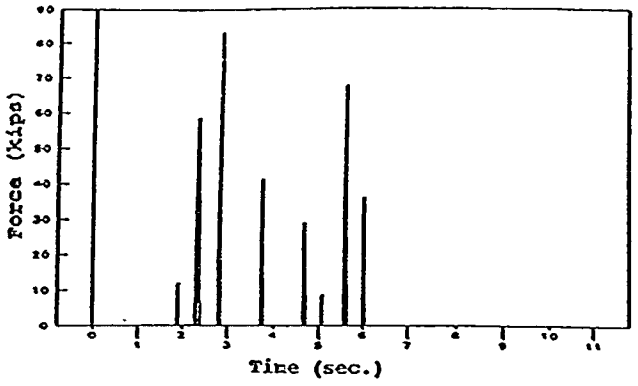


Fig. 22. Restrainer Force at Hinge 2 Due to El Centro Earthquake

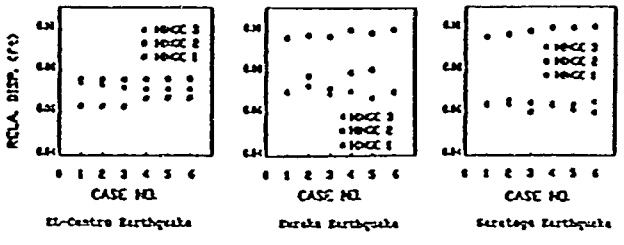


Fig. 23. Maximum Relative Displacements at Hinges (Restrainer Gap = 0.75 in.)

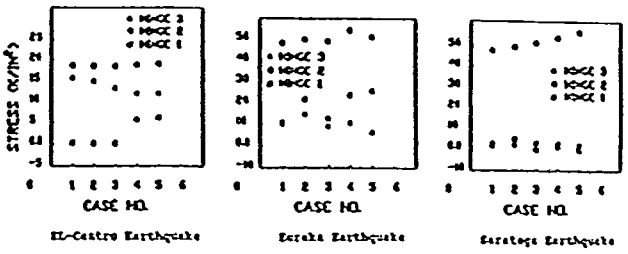


Fig. 24. Maximum Restrainer Stresses (Restrainer Gap = 0.75 in.)

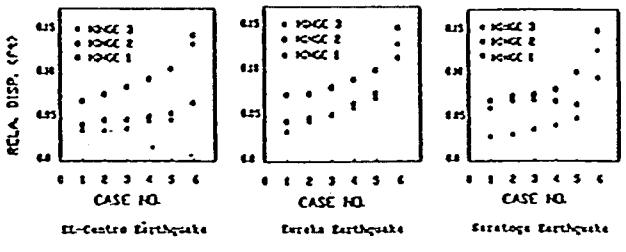


Fig. 25. Maximum Relative Displacements at Hinges (Restrainer Gap = 0 in.)

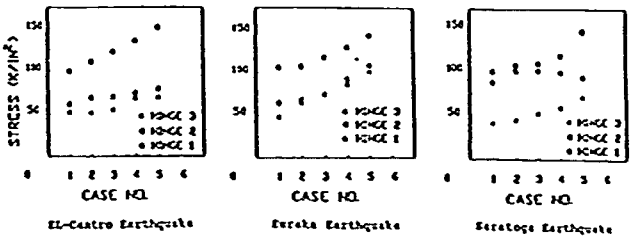


Fig. 26. Maximum Restrainer Stresses (Restrainer Gap = 0 in.)

DYNAMIC STRENGTH AND DUCTILITY CHARACTERISTICS OF STEEL BRIDGE PIERS

Kazuhiko KAWASHIMA1), Hideki SUGITA2) and Tomoru NAKAJIMA2)

ABSTRACT

This paper presents a series of loading test results of steel bridge piers constructing for highway bridges. Even for a significant earthquake, the bridge has to avoid critical failure. Because the steel pier is the most important member for preventing critical failure of bridge, it is desirable to check bearing capacity for lateral load to prevent brittle failure. Failure mechanism and effect of longitudinal stiffeners on strength and ductility of steel bridge piers are presented.

INTRODUCTION

Steel bridge piers, constructed by the welding together of thin plate, have been used over past 30 years for constructing highway bridges. Because the section size of steel piers is significantly less than that of reinforced concrete piers, it is ideal to use in city locations where there are various restrictions derived from land use and construction space.

In the 1990 JRA specification for seismic design of highway bridges, ductility check for the design of reinforced concrete piers was introduced in addition to the standard design force requirements. In this check, it is required that reinforced concrete piers be able to resist a level of earthquake acceleration which is significantly greater than the level of standard earthquake acceleration by a combination of strength and ductility.

The steel pier is the most important member for preventing critical failure of bridge. It is desirable to check bearing capacity for the acceleration of significant earthquake. Because actual damage has not been observed in recent earthquakes and few tests for earthquake resistance have been carried out, strength and ductility of steel bridge piers are still unknown.

For aiming to study the strength and ductility of steel bridge piers, a series of loading tests was made. This paper presents the effect of longitudinal stiffeners on strength and ductility of steel piers through the loading tests.

DYNAMIC LOADING TESTS OF STEEL BRIDGE PIERS

Test Specimens

As shown in Fig.1 and Table 1, 3 types of specimens of steel bridge piers were used in the dynamic loading tests. Specimen number presented show those used to identify specimens in a series of dynamic loading tests conducted at Public Works Research Institute. Scale of specimens used in this tests was assumed approximately 1/3 in length to typical highway bridge piers. The dimension of the cross section is 80.0cm × 81.6cm. The height of specimens is 7.1m including a footing of 0.7m height at the bottom of the column. Diaphram and rib are used as lateral stiffeners alternatively in longitudinal direction. 3 plates of ribs for each flange and web are used as longitudinal stiffeners.

Spacing of lateral stiffeners, size and plate thickness of longitudinal stiffeners are different in each type of specimens. Spacing between lateral stiffeners is 35cm for specimen S-23 and S-24, and 60cm for specimen S-28. Spacing between longitudinal stiffeners is 20cm for all specimens. Plate thickness of flange, web and lateral stiffeners are 8mm, 8mm and 4.5mm alternatively. Section size of longitudinal stiffeners are 6 × 64mm for specimen S-23, 10 × 64mm for specimen S-24 and 6 × 59mm for specimen S-28. SM490A steel material is used for all flange, web and stiffeners. Average yield strength and strain derived from tests of materials are shown in Table 2.

Panel and stiffener were designed according to the Design Specification for Highway Bridges-part II Steel Bridge(JRA). The stiffness of longitudinal stiffeners must be sufficient to ensure that wall buckling does not prematurely decrease the strength of piers. In the specification, both sectional area and sectional second moment of a longitudinal stiffener should be satisfy the certain values given in equation (1) and (2).

$$I_l \geq \frac{bt^3}{11} \cdot \gamma_{l \cdot req} \qquad (1)$$

$$A_l \geq \frac{bt}{10n} \qquad (2)$$

where

b: the width of the section(mm)
t: plate thickness(mm)
n: number of panels divided by longitudinal stiffeners
$\gamma_{l \cdot req}$: relative stiffness required

Relative stiffness of longitudinal stiffeners γ_l presents the ratio of sectional second moment between a longitudinal stiffener and a panel. γ

$\gamma_{1\cdot req}$ means the minimum γ_1 required not to develop overall wall buckling but local panel buckling which is, as shown in Fig.2, local buckling of each panel between the longitudinal stiffeners. Whether the buckling mode of panel is overall wall buckling and local panel buckling can be estimated by the gamma ratio($\gamma_1/\gamma_{1\cdot req}$). In the case if gamma ratio is greater than 1.0 then buckling mode would be expected to be local buckling. In the case if gamma ratio is less than 1.0 then overall wall buckling is expected. Because gamma ratios of specimen S-23, S-24 and S-28 are calculated as 4.1, 6.0 and 1.1 respectively, the buckling mode of all specimens is expected as local panel buckling.

The box shaped section consists of 4 major plates to which stiffeners and diaphrams are welded from the inside. Fig.3 shows the weld way between each materials. Weld between web and flange was carried out by a combination of fillet weld with leg length of 6mm and V-shape weld with leg length of 5mm. Longitudinal stiffeners were welded onto both web and flange by fillet weld with leg length of 3mm. Although there are various way to connect both web and flange with upper base plate, in these specimens both web and flange go through upper base plate and are welded onto lower base plate which is the way adopted in piers of Metropolitan Expressway Publish Corporation. Weld between upper base plate and both web and flange was carried out by butt-weld.

Dynamic Loading Test

Fig.4 shows the experimental set-up of specimen. Specimens were fixed on the steel footing which was attached on the reaction wall with bolts. The dynamic actuator installed on the reaction wall was set at the crest of specimens. 10% of yield load associate with dead weight was applied in the axial direction with use of static actuator. Dynamic loading test was carried out by controlling the lateral displacement of the dynamic actuator.

Fig.5 shows the loading hysteresis loop of specimens. Because the reaction wall and steel footing are not completely rigid, it is desirable to estimate the lateral displacement developed at the crest of specimens due to their deformation. So, in the first, to determine the loading displacement δ, 75% yield load which was calculated from the result of material test was statically applied to the specimen. Against the yield load, Lateral displacement developed at the crest can be estimated in equation(3).

$$\delta_D = \delta_y + \delta_E \qquad (3)$$

where

δ_y: yield displacement, is defined as the displacement at which yielding first occurs in the extreme fiber of the section(cm)

δ_E: lateral displacement developed at the crest due to deformation of

reaction wall and steel footing(cm)

δ_o: loading displacement at the crest(cm)

Because δ_E is in proportion to the lateral load, δ_E can be calculated in equation(3). Loading displacement δ_o which is desirable for applying lateral displacement $1\delta_y$ to the specimen can be also calculated in equation(3) with use of δ_E. But, because δ_E becomes larger according with the increment of lateral load, loading displacement for applying over $2\delta_y$($2\delta_y, 3\delta_y \cdots$) can not be determined. In this study, loading displacement $n\delta_o$ for applying $n\delta_y$ is calculated in equation(4) based on an assumption that lateral load does not increase after yielding of specimen.

$$n\delta_o = n\delta_{py} + \delta_E (n=1,2,3\cdots) \qquad (4)$$

where

$n\delta_o$: standard loading displacement at the crest(cm)

δ_{py}: calculated yield displacement of specimen(cm)

δ_E : lateral displacement developed at the crest due to deformation of reaction wall and steel footing(cm)

Calculated yield displacement δ_{py} are 56mm, 57mm and 53mm for specimen S-23, S-24 and S-28 respectively. δ_E is 19mm for both specimen S-23 and S-24, and 22mm for specimen S-28.

As shown in Fig.5, loading displacement was increased by $1\delta_y$ step. Although the number of cyclic loading for each δ_y($1\delta_y, 2\delta_y, 3\delta_y, \cdots$) should effect on the deformation characteristics of steel piers, 10 times cyclic loading which is the way adopted in the past loading tests at PWRI was carried out. Lateral displacement was increased up to the ultimate displacement that was defined as the displacement at which maximum load become smaller than yield load. Because the effect of loading speed on the deformation characteristics seemed to be small enough, an unified 0.04Hz loading was carried out for every specimens.

PROGRESS OF FAILURE

3 types of specimens commonly deformed up to $1\delta_y$ lateral displacement loading. Lateral thin lines which means the yielding of material were developed on the flange plates. The lines were developed at the section between upper base plate and neighboring diaphram, which section is designated hereinafter as the panel. The 4 panels of each specimen is designated hereinafter as shown in Fig.6. After $2\delta_y$ lateral displacement loading, deformation characteristics and progress of failure of each specimens were as follows.

Specimen S-23 (gamma ratio of 4)

Fig.7 shows the failure mode after $2\delta_y$ lateral displacement loading. Out-of-plane residual deformation was developed. The residual deformation was extremely large at the section of 20cm from the upper base plate. Typical point was the buckling mode at the section between 2 longitudinal stiffeners, i.e., concave deformation and convex deformation developed alternatively at each 2 sections neighboring a lateral stiffener. The deformation mode seemed similar to the local panel buckling mode. Also, concave deformation and convex deformation generally developed alternatively at each 2 sections neighboring a longitudinal stiffener. Although residual deformation was larger at the section between longitudinal stiffeners, deformation of 2~3mm was developed at longitudinal stiffeners. The amount of residual deformation was about 30mm toward outside of specimen and about 25mm toward inside of specimen. According to the residual deformation at the panel, 8mm decreace of specimen height was developed.

Fig.8 shows the failure mode after $3\delta_y$ lateral displacement loading. Typical point on this stage was the transition of the deformation mode. According to the deformation of longitudinal stiffeners, overall wall buckling turned from local panel buckling was developed. Overall wall buckling was developed on 3 panels of specimen. Picture 1 and Picture 2 show the residual deformation of face-2 and face-4 at which local panel buckling and overall wall buckling were developed alternatively. Picture 3 shows the residual deformation of longitudinal stiffeners welded on face-2. Large deformation of longitudinal stiffeners was developed at the section at which large deformation of panel was developed. Maximum amount of residual deformation was about 70mm toward outside of specimen and about 85mm toward inside of specimen.

Most important point on this stage was the fracture of panels. Fracture of panels was developed at the following section.
(1) Welded section at which large difference of deformation between web and flange was developed due to the difference of each out-of-plane deformation. (Fig.8 ①④⑥)
(2) Knuckle section of buckling mode on which longitudinal stiffener was welded. (Fig.8 ②③)
(3) Crest section of buckling mode (Fig.8 ④⑥)
In these sections fracture of panel was developed by the alternative tension and compression according with the cyclic lateral displacement loading.

Specimen S-24 (gamma ratio of 6)

Fig. 9 shows the failure mode after $2\delta_y$ lateral displacement loading.

Amount of residual out-of-plane deformation developed at face-4 was about 20mm toward outside of specimen and about 12mm toward inside of specimen. On the other panel, amount of residual deformation was about 5~6mm toward both outside and inside of specimen. So, amount of residual deformation developed at specimen S-24 seems smaller than that of specimen S-23. Although local panel buckling between 2 longitudinal stiffeners could be seen, local panel buckling of sections neighboring longitudinal stiffener which was shown on specimen S-23 on this stage could not be seen. Because the stiffness of longitudinal stiffeners are larger than that of specimen S-23, local panel buckling knuckled by longitudinal stiffeners could hardly be developed rather than overall wall buckling. decreace of specimen height was much smaller than that of specimen S-23.

Fig.10 shows the failure mode after $3\delta_y$ lateral displacement loading. Residual deformation toward outside of specimen was developed at almost all panels excepting small part of face-2 and face-4. Residual deformation was developed in the overall wall buckling mode. As shown in Picture 4, according to the large deformation of panel, fracture of weld between panel and longitudinal stiffeners was developed. There were few sections where fracture at weld between longitudinal stiffeners and upper base plate was developed. Maximum amount of residual deformation was about 60mm toward outside and about 35mm toward inside of specimen. Fractures at weld between web and flange developed on the 4 corners of specimen could almost progress up to the lowest lateral stiffener. Decreace of specimen height was 44mm, which was about 40% smaller than that of specimen S-23.

Specimen S-28 (gamma ratio of 1)

Fig.11 shows the failure mode after $2\delta_y$ lateral displacement loading. Residual out-of-plane deformation was developed at the lower panel which was about 60cm height section from upper base plate. Amount of residual deformation developed at face-1 was about 32mm toward outside and about 40mm toward inside of specimen. Residual deformation was much larger than that of the other specimens. Major buckling mode was overall wall buckling. In the small section of face-1 and face-3, local panel buckling at sections neighboring with lateral stiffener could be seen. Because the stiffness of longitudinal stiffener was smaller than that of the other specimens, local panel buckling knuckling by longitudinal stiffeners could not hardly be developed.

Fig.12 shows the failure mode after $3\delta_y$ lateral displacement loading. All of the residual deformation was developed in overall wall buckling mode. Almost all of the residual deformation was developed toward inside of specimen excepting small part of face-1 and face-3. Maximum amount of residual deformation was about 85mm toward outside and about 110mm toward

inside of specimen.

Picture 5 shows the fracture at weld between web and flange. The fracture at weld was developed at 4 corners with fracture length of 10～40cm. Fracture of panel at the crest of buckling mode was also developed with fracture length of 3～5cm.

STRENGTH AND DEFORMATION CHARACTERISTICS

Fig.13 shows the comparison of loading hysteresis loops among 3 specimens. First hysteresis loop for each loading displacement($1\delta_y$,$2\delta_y$,$3\delta_y$) are presented. Because of the large stiffness of longitudinal stiffeners, maximum strength for each loading displacement is larger in the order as $1\delta_y$,$2\delta_y$,$3\delta_y$. But any difference among 3 specimens can not be seen on the shape of the loading hysteresis loop.

Fig.14 shows the decline of strength due to the 10 times cyclic loadings for each specimen. The characteristics of decline of strength for each specimen was as follows.

Specimen S-23 (gamma ratio of 4)

Maximum strength P_{max} of 61.2tf was shown in the first hysteresis loop for loading displacement of $2\delta_y$. Because any decline of strength due to cyclic loadings could not be seen for loading displacement of $1\delta_y$, it should be pointed out that specimen deformed elastically in this stage. For loading displacement of $2\delta_y$, remarkable decline of strength occurred after third cyclic loadings. The reason why should be the residual out-of-plane deformation developed at lowest panel as was mentioned above. The maximum strength of 61.2tf for the first cyclic loading was about 30% decreased to 43.0tf after 10 times cyclic loadings.

Specimen S-24 (gamma ratio of 6)

The hysteresis loop for loading displacement of $1\delta_y$ was similar with that of specimen S-23. Maximum strength of 67.3tf was shown in the first hysteresis loop for loading displacement of $2\delta_y$. In this stage, maximum strength of 67.3tf was about 10% decreased to 60.4tf after 10 times cyclic loadings. The extent of decrease was about 20% smaller than that of specimen S-23. The reason why should be the large stiffness of stiffeners, i.e., large stiffness of stiffeners could prevent the residual out-of-plane deformation to be developed, and could reduce the decrease of strength due to cyclic loadings. But for the loading displacement of $3\delta_y$, decrease of strength due to cyclic loadings had become larger. The maximum strength of 57.8tf for the first cyclic loading was about 85% decreased to 8.7tf after 10 times cyclic

loadings. The extent of decrease was rather larger than that of specimen S-23. In this stage, large stiffness of stiffeners caused concentration of stress onto the weld between web and flange, and caused fracture at this section.

Specimen S-28 (gamma ratio of 1)

The hysteresis loop for loading displacement of $1\delta_y$ was similar with that of both specimen S-23 and S-24. Maximum strength of 51.8tf was shown in the first hysteresis loop for loading displacement of $2\delta_y$. In this stage, maximum strength of 51.8tf was about 76% decreased to 12.5tf after 10 times cyclic loadings. The extent of decrease was the largest of all specimens. The reason why should be the smallest stiffness of stiffeners, i.e., the smallest stiffness of stiffeners caused the overall wall buckling to be developed at the panel, and caused the largest residual out-of-plane deformation.

Table 3 shows the comparison of strength and ductility for each specimens. The extent of strength increase after yielding (maximum load P_{max}/ yield load P_y), which is 1.34 for specimen S-23, 1.38 for specimen S-24 and 1.18 for specimen S-28, is smallest on specimen S-28. The reason why is related with the smallest section area of longitudinal stiffeners on specimen S-28. Because the maximum strength of specimen would be developed just after complete yielding of longitudinal stiffeners, smaller the section area of longitudinal stiffeners are, smaller the energy absorbed due to yielding becomes. For developing the extent of strength increase after yielding, it seems important to study the section shape of longitudinal stiffeners for developing energy absorbed due to yielding.

The ductility (yield displacement δ_y/ maximum displacement δ_u) is 2.35 for specimen S-23, 2.71 for specimen S-24 and 1.90 for specimen S-28, respectively. The ductility of specimen becomes small according to the decrease of gamma ratio. The reason why seems to be related with both maximum strength and the extent of strength decrease due to panel buckling. Smaller the gamma ratio is, both smaller the maximum strength and larger the extent of strength decrease would be developed. So, it should be noted that increase of gamma ratio is quite effective to increase the ductility of steel piers.

CONCLUDING REMARKS

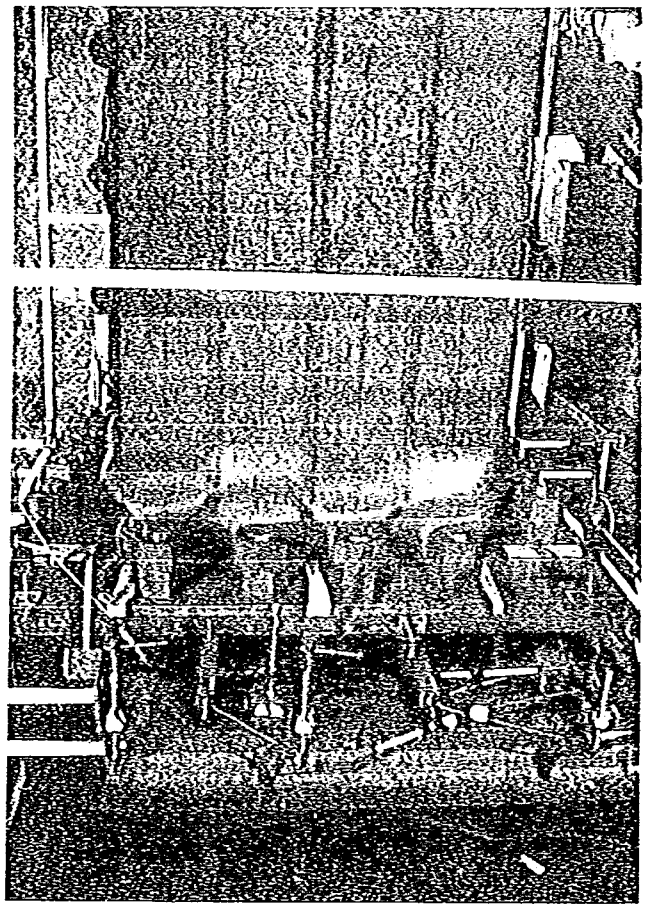
Dynamic loading tests were made on 3 types of steel pier models to study the effect of longitudinal stiffeners on strength and ductility of steel bridge pier. From the results presented, following conclusions may be deduced.

(1) Residual out-of-plane deformation of panels were developed at the

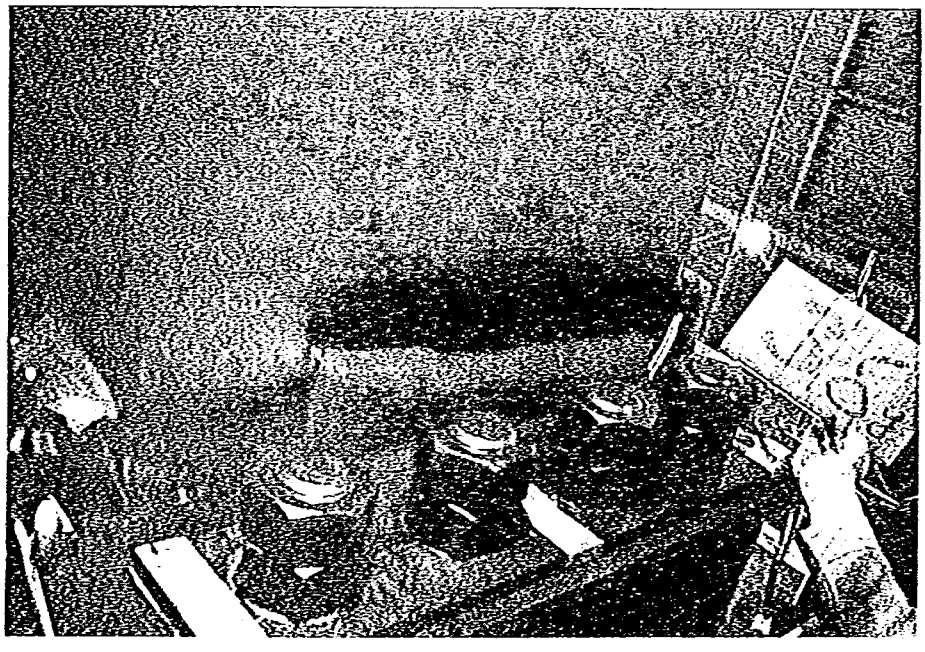
section between upper base plate and lowest diaphram. The buckling mode was local panel buckling for specimen with gamma ratio of 4, and overall wall buckling for specimens with gamma ratio of 6 and 1.
(2) Major failure of specimen was fracture at weld. Major fracture was developed at weld between web and flange. Fracture of panels at the crest and knuckle part of the buckling mode were also developed.
(3) According to the development of panel buckling and fracture at weld, decline of maximum strength due to the cyclic loadings was increased.
(4) As the gamma ratio became larger, the extent of strength after yielding was increased. And as the gamma ratio became larger, the decrease of strength according to the cyclic loadings was reduced. For these reasons, the ductility of specimen was increased as the gamma ratio became larger.

REFERENCES

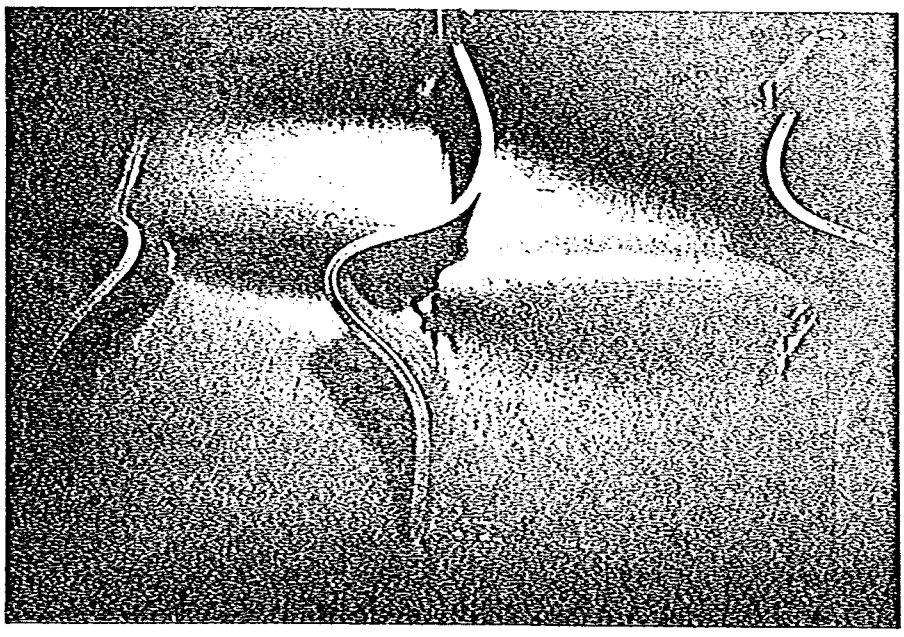
(1) Japan Road Association: Design Specifications for Highway Bridges, Part II Steel Bridges, English Edition, 1987
(2) Subcommittee on Stability Design: Guidelines for the stability of Steel Structures, Japan Society of Civil Engineering, 1987
(3) K.KAWASHIMA, G.A.MacRae and K.HASEGAWA: The Strength and Ductility of Steel Bridge Piers Based on Loading Tests, PWRI Journal of Research, Vol.29, March 1992



Picture 1 Failure Mode of Specimen with Gamma Ratio of 4 (Face-2)



Picture 2 Failure Mode of Specimen with Gamma Ratio of 4 (Face-4)



Picture 3 Residual Deformation of Longitudinal Stiffeners



Picture 4 Fracture at Weld Between Web and Flange (Specimen S-24, Gamma Ratio of 6)



Picture 5 Fracture between Panel and Longitudinal Stiffeners (Specimen S-24, Gamma Ratio of 6)

Table 1 Characteristics of Specimens

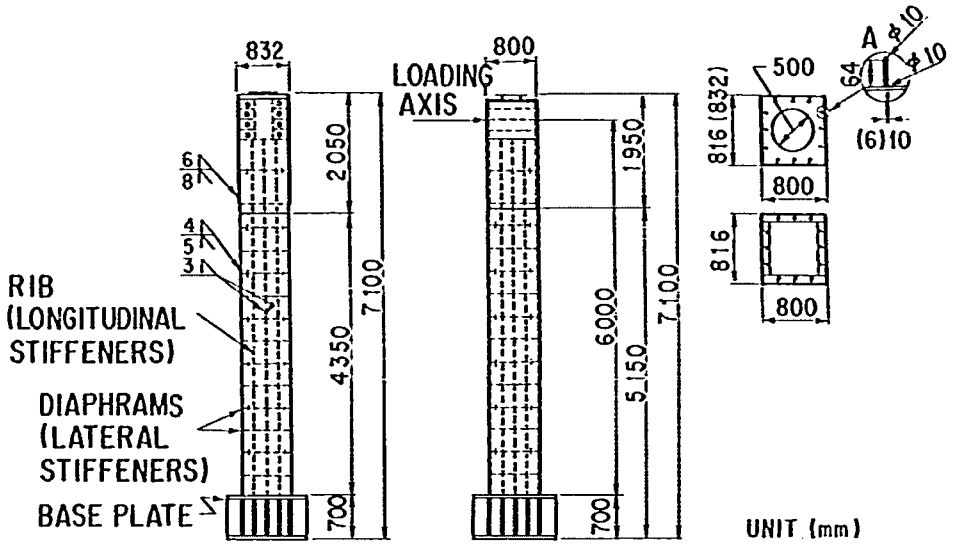
SPECIMEN		S-24	S-23	S-28
LONGITUDINAL STIFFENER	SECTION SIZE (mm)	10 x 64	6 x 64	6 x 59
	NUMBER OF PANEL	4		
LATERAL STIFFENER	PLATE THICK (mm)	4.5		
	SPACING (mm)	350		600
RERATIVE STIFFNESS γ_ℓ		23.46	14.08	11.03
RERATIVE STIFFNESS $\gamma_{\ell\cdot req}$		3.94	3.45	10.38
GAMMA RATIO $\gamma_\ell / \gamma_{\ell\cdot req}$		5.95 ≒ 6	4.08 ≒ 4	1.06 ≒ 1

Table 2 Average Yield Strength and Strain

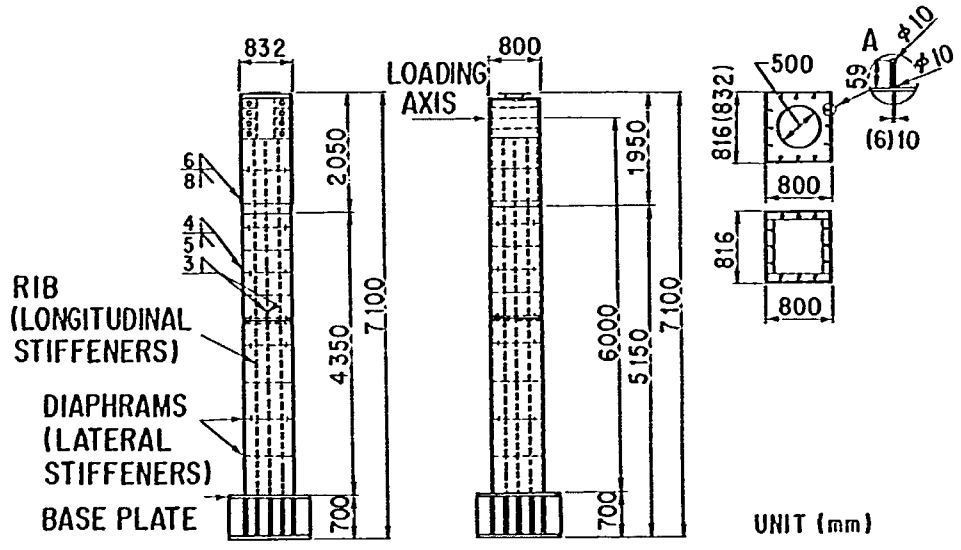
	LONGITUDINAL STIFFENERS		WEB AND FLANGE	
THICKNESS (mm)	10	6	8	
STANDARD	SM490A			
YIELD STRENGTH (kgf/cm^2)	3872	4021	3920	3946
YIELD STRAIN(μ)	1850	1920	1870	1880

Table 3 Strength and Ductility of Specimen

SPECIMEN	S-24	S-23	S-28
GAMMA RATIO $\gamma_l / \gamma_{l\cdot req}$	6	4	1
YIELD LOAD Py (tf)	48.8	45.6	43.8
MAXIMUM LOAD Pmax (tf)	67.3	61.2	51.8
Pmax / Py	1.38	1.34	1.18
YIELD DISPLACEMENT δy (mm)	65.0	66.0	75.1
MAXIMUM DISPLACEMENT δu (mm)	176.3	155.3	143.0
DUCTILITY $\delta u / \delta y$	2.71	2.35	1.90

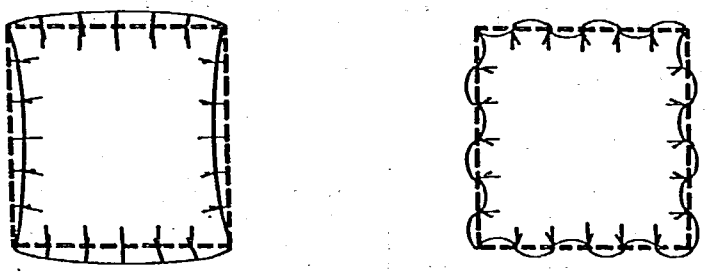


(a) Specimen S-23 and S-24



(b) Specimen S-28

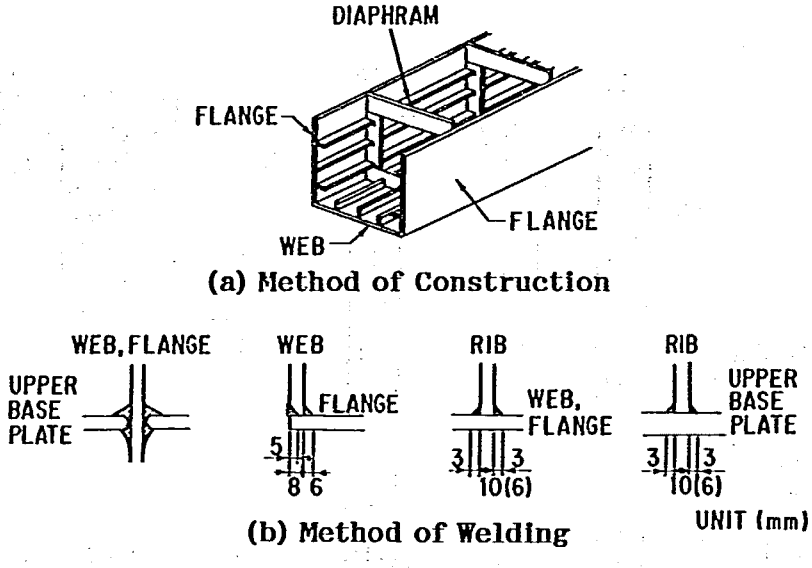
Fig.1 Specimens



(a) Overall Wall Buckling ($\gamma_A / \gamma_{2\cdot req} < 1.0$)

(b) Local Panel Buckling ($\gamma_B / \gamma_{2\cdot req} \geqq 1.0$)

Fig.2 Buckling mode of Box-shaped Section



(a) Method of Construction

(b) Method of Welding

Fig.3 Method of Construction and Welding

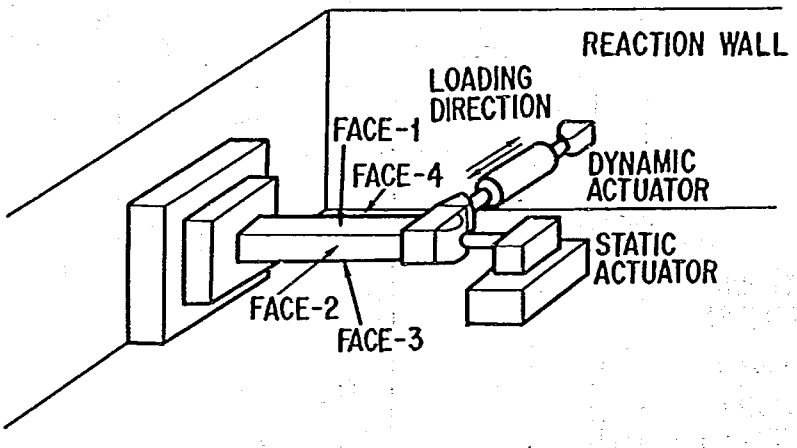


Fig.4 Experimental Set-up of Specimen

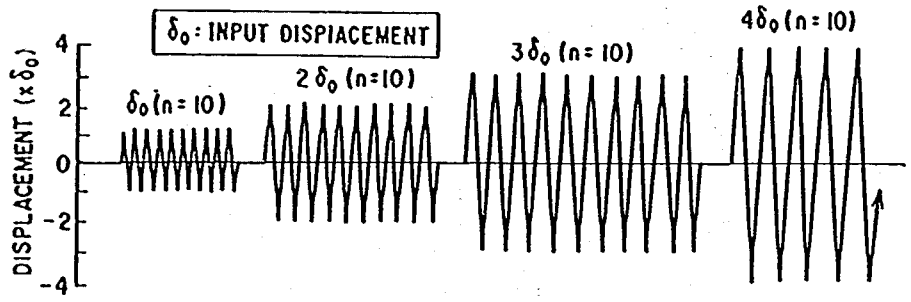


Fig.5 Loading Hysteresis Loop

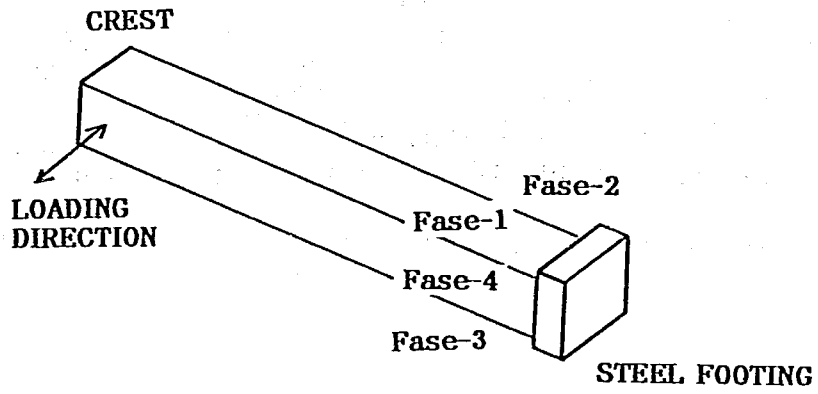


Fig.6 4 Panels of Specimen

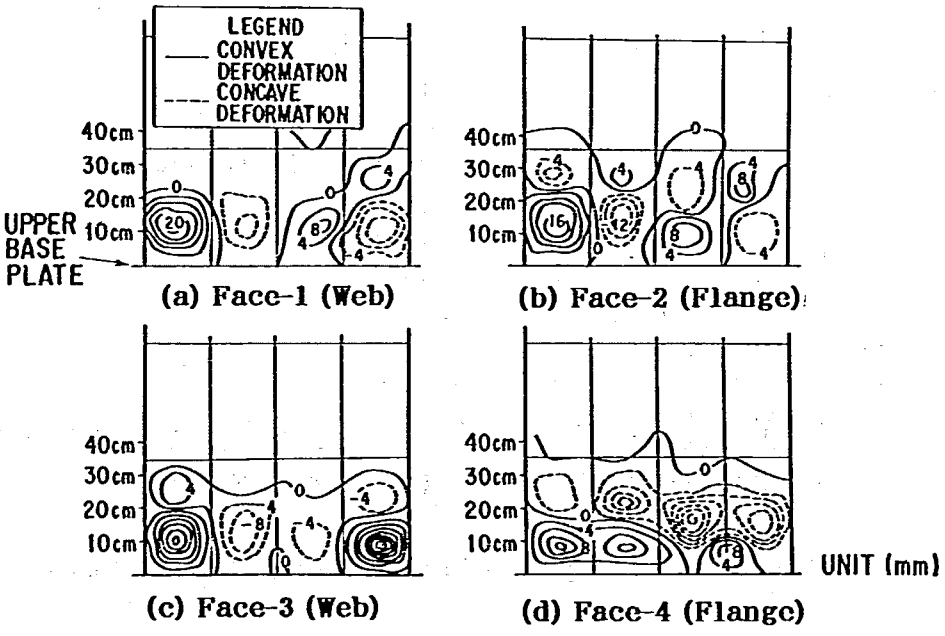


Fig.7 Buckle Contours after 2δ y Loading (Specimen S-23, Gamma Ratio of 4)

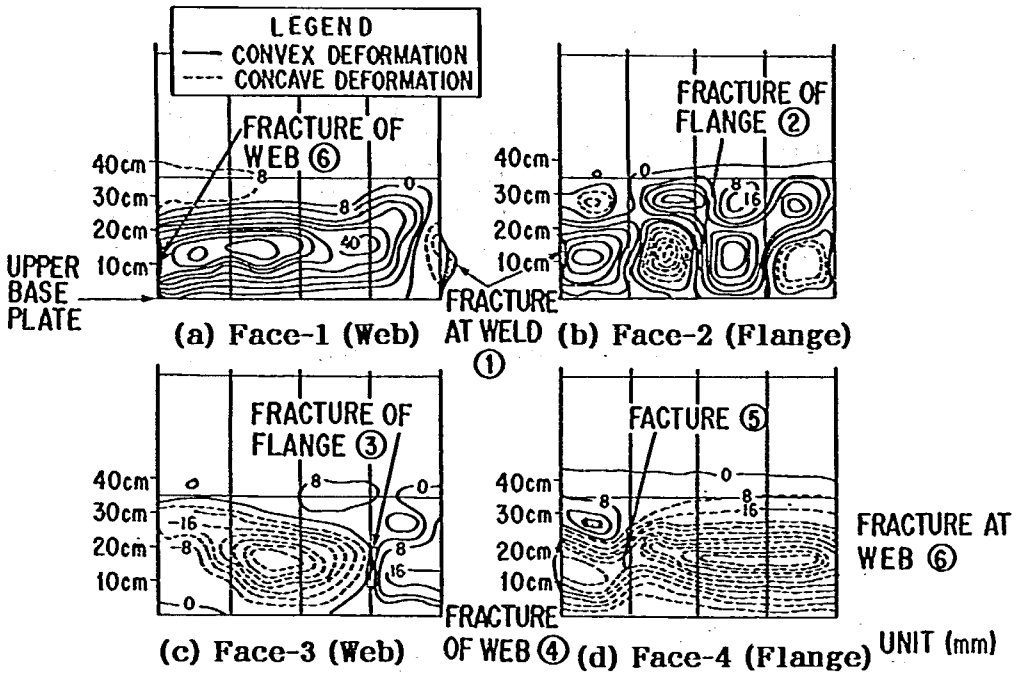


Fig.8 Buckle Contours after 3δ y Loading (Specimen S-23, Gamma Ratio of 4)

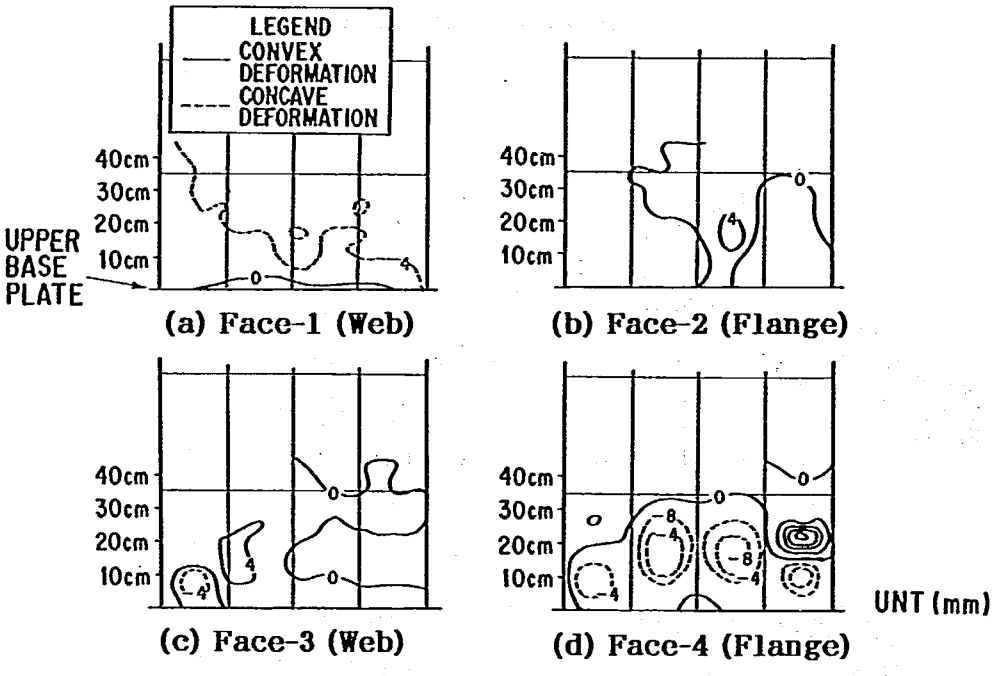


Fig.9 Buckle Contours after 2δ y Loading (Specimen S-24, Gamma Ratio of 6)

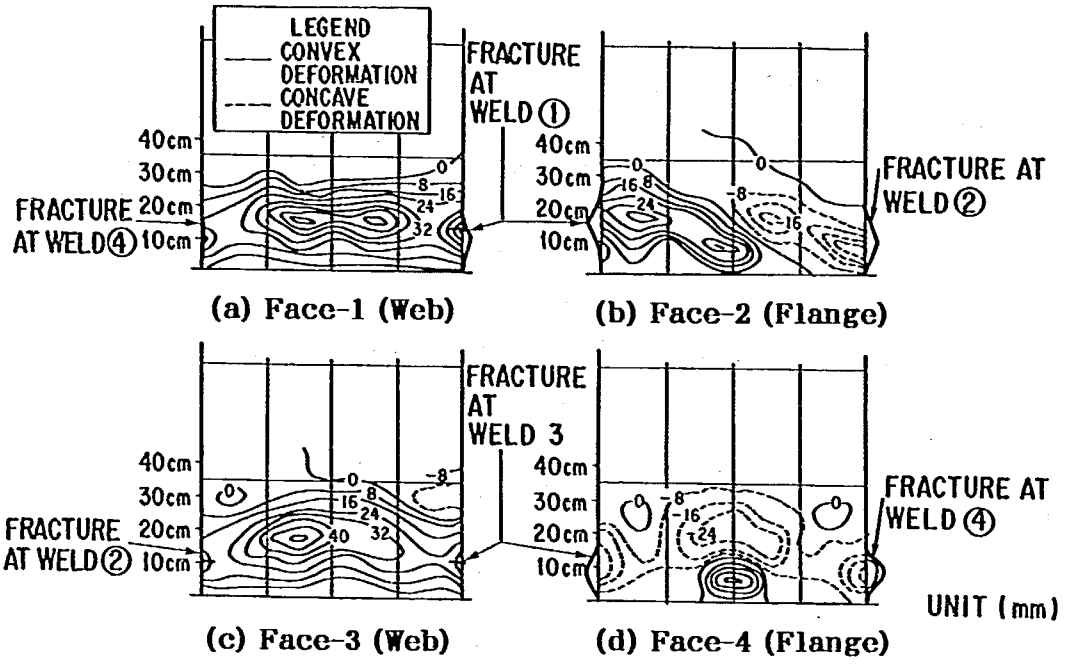


Fig.10 Buckle Contours after 3δ y Loading (Specimen S-24, Gamma Ratio of 6)

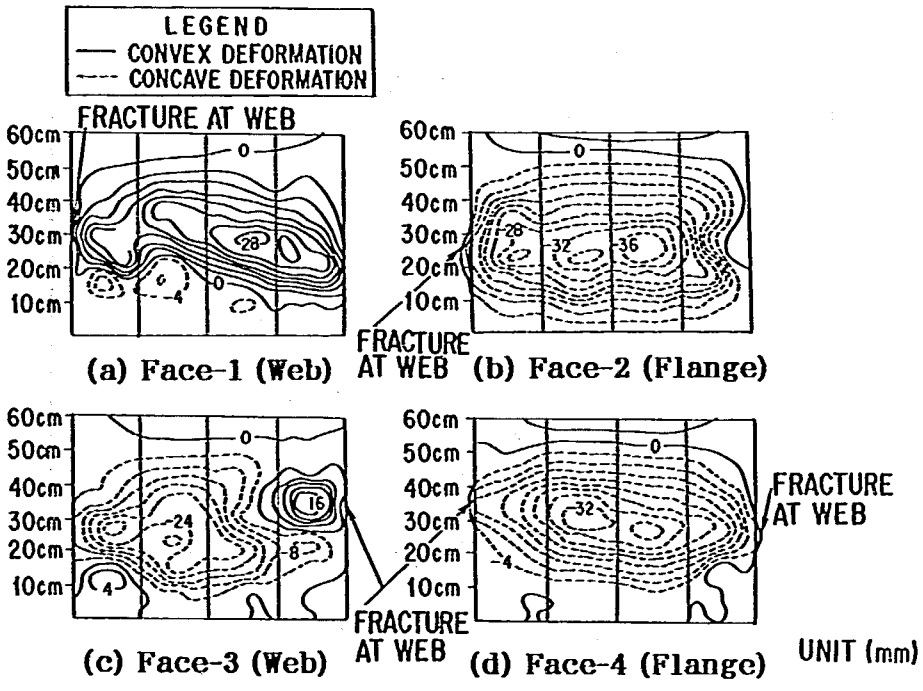


Fig.11 Buckle Contours after 2δ y Loading (Specimen S-28, Gamma Ratio of 1)

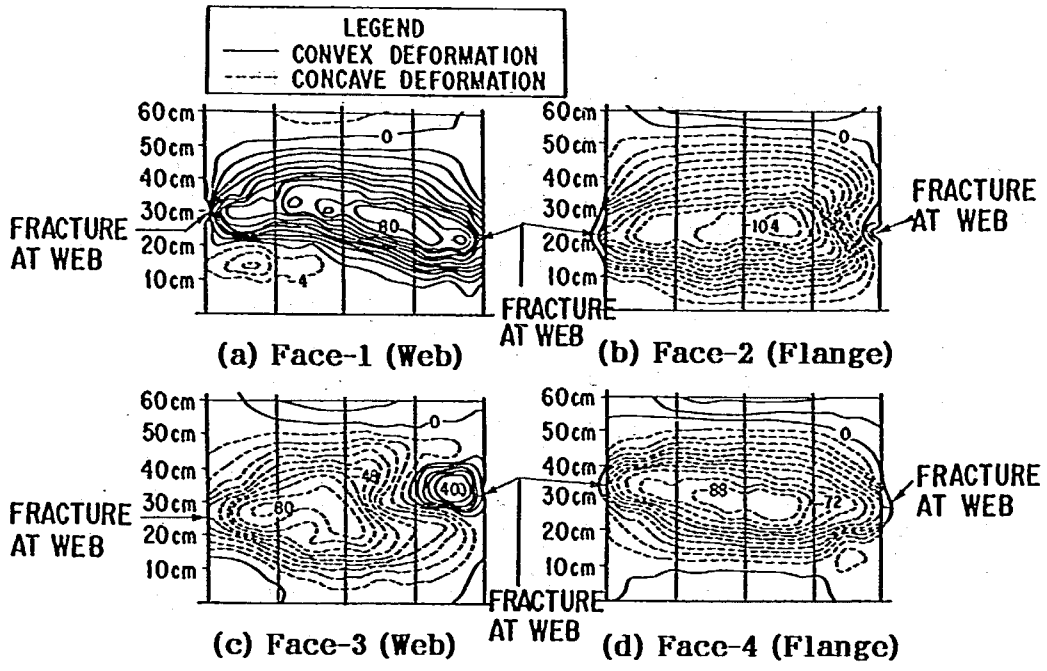


Fig.12 Buckle Contours after 3δy Loading (Specimen S-28, Gamma Ratio of 1)

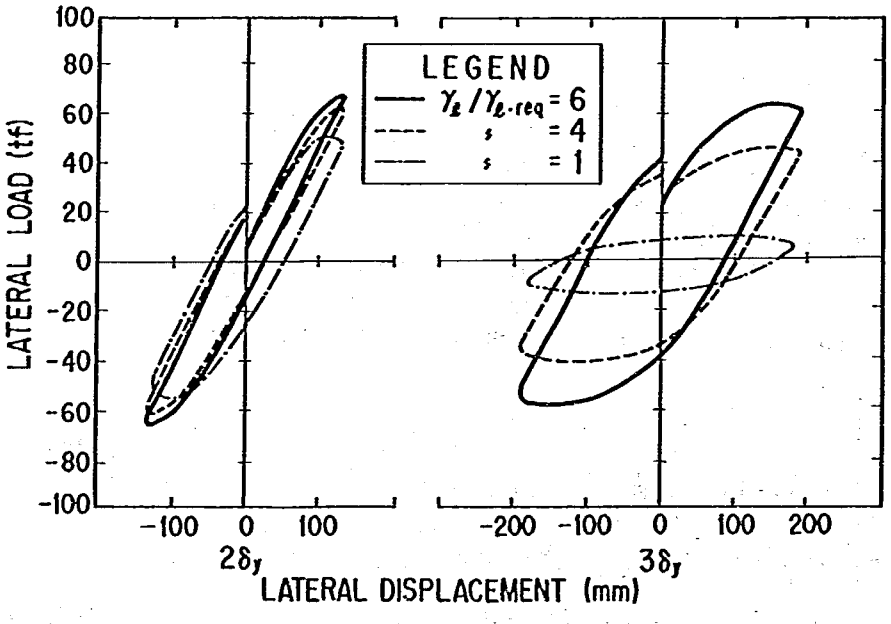
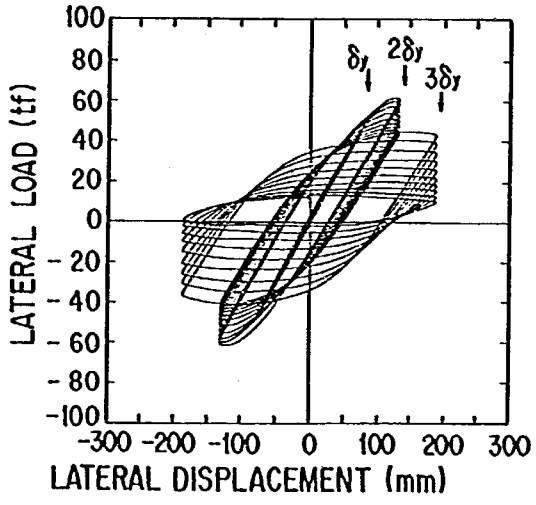
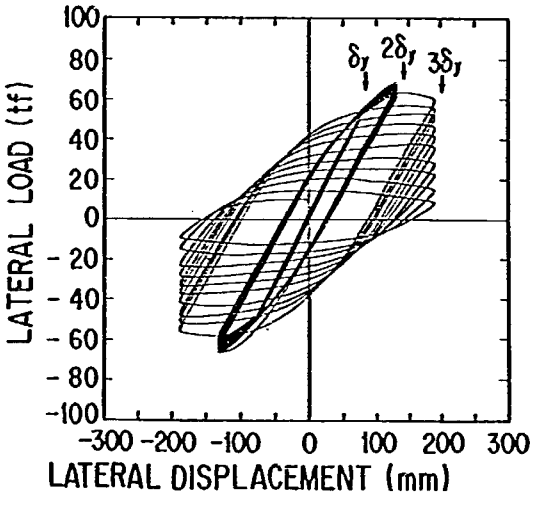


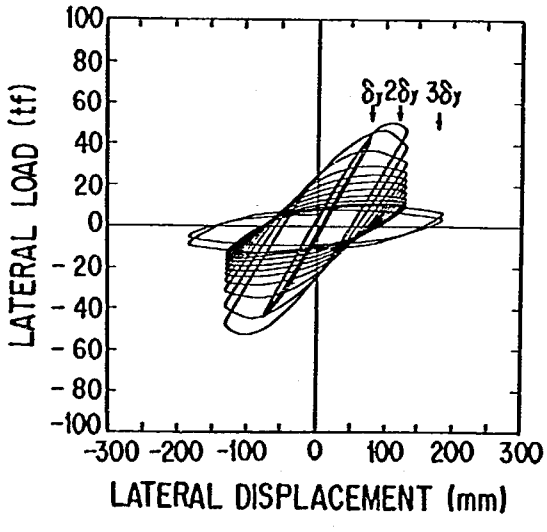
Fig.13 Comparison of Loading Hysteresis Loop among 3 Types of Specimens



(a) Specimen S-23 with Gamma Ratio of 4



(b) Specimen S-24 with Gamma Ratio of 6



(c) Specimen S-28 with Gamma Ratio of 1

Fig.14 Loading hysteresis Loop of Specimen

(9) Session 9

Seismic Design (4)

22) SR5 Lake Washington Ship Canal Bridge Seismic Vulnerability Assessment
(J.H. Clark*)

23) Research on Adoption of Vane-Dampers for the Tsurumi Fairway Bridge
(N. Ito* and M. Okada)

24) Seismic Performance and Retrofit of the Golden Gate Bridge
(C. Seim*, S. Rodriguez and T. Ingham)

25) Lateral-Load Response Models of a Reinforced Concrete Bridge
(M. Eberhard)

SR5 LAKE WASHINGTON SHIP CANAL BRIDGE SEISMIC VULNERABILITY ASSESSMENT

Dr. John H. Clark, Vice President and Chief Bridge Engineer
ANDERSEN BJORNSTAD KANE JACOBS, INC
Seattle, Washington

9th US-Japan Bridge Engineering Workshop
May 1993

Introduction

The Loma Prieta earthquake of October 1989 strongly reinforced the need for responsible agencies to assess the seismic vulnerability of existing bridges, particularly those whose design pre-dated current seismic design codes. This paper describes the seismic vulnerability assessment undertaken for the SR5 Lake Washington Ship Canal Bridge in Seattle. The structure and the seismicity of the site are described, criteria for assessment is presented, analysis methodology described, and the results of analyses and assessments to date (May 1993) described.

Description of the Structure and Site

This critical bridge carries twelve lanes of highway traffic on the principal north-south route in the State of Washington. Annual average traffic on the structure is in excess of 160,000 vehicles per day. The structure was designed in 1958 and constructed between 1959 and 1961. The American Association of State Highway and Transportation Officials (AASHTO) design code at the time (1958) required only a pseudo-static design for seismic response loads.

The total structure length of 1350 meters (4430 feet) is divided into the south approach units (352 m 1156 ft), the truss units (700 m 2294 ft), and the north approach units (299 m 980 ft). See Figure 1. The north and south approach units are similar and are continuous reinforced concrete box girder rigid frames. Three of these units are double decked. The box girder units are typically three span units (27.4-36.6-27.4 m 90-120-90 ft or 27.4-36.6-37.4 m 90-120-90 ft). The south approach has two 4 span continuous flat slab units (10.4-17.1-17.1-10.4 m 34-56-56-34 ft). End columns are monolithic with the superstructure with thermal expansion and contraction accommodated by "split" columns at the juncture between units.

The truss units are two simple spans, a three span continuous unit and a simple span (2 x 106-106-168-106-106 m 2 x 349-348-552-348-349 ft). The simple span trusses are typically supported on rocker bearings at one end and pinned bearings at the other end. The continuous spans have rocker bearings at the exterior piers and pinned bearings at the interior piers. The piers supporting the trusses are typically portal frame reinforced concrete piers. Each pier carries a pair of pinned bearings and a pair of rocker bearings except for the two interior piers of the continuous span unit and the end piers. Some of the existing portal frame and bearing details are shown in Figure 2.

Site soil conditions are generally good. Foundations are typically spread footings founded on glacially consolidated sands and gravels at maximum bearing pressures of approximately 4 tons per square foot. There are a few foundations on short (35 ft) reinforced concrete piles on the south approach where some clayey soils were encountered. The piles are probably point bearing in the glacially consolidated material.

Seismicity

A site specific seismicity study was performed to confirm that the AASHTO spectrum with a_{max} = 0.29 g and soil type II adequately describes the input motions. The source regions for earthquakes can be divided into three specific areas.

Shallow (focus < 20 km) earthquakes up to M7.0 have occurred in the State within the last century although the fault has never been successfully identified. It is believed that these events produce typical strike-slip motions. It has been assumed that an event up to M7.5 could occur anywhere in the region in the shallow crustal zone.

Deep (focus > 50 km) earthquakes up to M7.2 have occurred in the Puget Sound Basin in the past 50 years. These events are believed to be the result of tension rupture of the down-going slab. Motions have tended to be of moderate (~ 30 seconds) duration with sizeable vertical components with the peak vertical acceleration up to two-thirds of the peak horizontal acceleration. Seismologists estimate that events up to about M7.5 could occur in the deep crustal zone. Evidence indicates that a warping fold in the down-going slab concentrates these events in the southern part of the Puget Sound Basin or within 50 to 80 km of the bridge site.

There is good geological evidence to support the occurrence of large subduction zone earthquakes off the western Washington coast. Events of M8 to M9+ are believed possible depending upon the length of fault rupture involved. Geological evidence indicates a return period of 300+ years for such an event but the recurrence interval has not been conclusively established at this time. The source zone for this type of event would probably be greater than 100 km from the bridge site. These events would be expected to produce the long duration motions typical of thrust fault type earthquakes even though the peak accelerations at the site might not be greater than for the other two type events.

The spectrum adopted for this seismic vulnerability assessment was the AASHTO spectrum with a_{max} = 0.29 g and soil type II or

$$C_{sm} = \frac{1.2 a_{max} S}{T^{2/3}}$$

where C_{sm} = response coefficient for the m^{th} mode
S = soil type modifier = 1.2 for soil type II
T = period of the m^{th} mode.

This spectrum is considered to represent the motions resulting from a deep focus, near source earthquake of M7.5 and is considered to have a 90% probability of non-exceedance in 50 years.

Liquefaction of the foundation soils does not seem to be possible at this site. There is some evidence of prior landslides on the south bank but these deposits are not deep and the age of movement is not known.

Design (Ca 1958)

This structure was designed according to the 1957 AASHTO design specifications. These specifications required design for 3% of gravity applied as a static horizontal load for structures founded on spread footings and 6% for structures founded on piles. The latter value was used for this structure.

Minimum specified concrete strength was typically 28 MPa (4,000 psi) and reinforcing steel yield strength 275 MPa (40,000 psi). Reinforcing bar sizes through #18 were used in the project. Structural steel for the trusses was both 248 Mpa (36,000 psi) and 345 Mpa (50,000 psi) yield strength material.

Working stress design methods were used for concrete design with allowable concrete stresses of f_c = 11 Mpa (1,600 psi) and steel stresses of f_s = 138 Mpa (20 ksi). Allowable over-stress up to 133% was accepted for seismic loadings. Main vertical reinforcing in the columns was size #10 through #18 bars. Lap splices of 20 to 30 bar diameters were typical. Confinement reinforcement in the columns was minimal as was the practice of that time. According to present day standards there is effectively no confinement reinforcing.

Dynamic Analysis Modelling

"Local" models of the individual concrete units between expansion joints were prepared from existing record plans. The dynamic analysis program selected was GTSTRUDL. Models are assemblages of frame members (3D beams). Finite joint lengths were modelled since the member depth/span ratios were not large. Columns were assigned flexural inertia properties corresponding to the cracked section. Flexibility of the foundations were explicitly accounted for by providing springs at the bases of the columns and on the columns where the depth of overburden was significant. These assumptions were believed to be appropriate for evaluation of maximum seismic displacements.

In the existing condition, the truss units are separated by expansion joints at each pier except for the three span continuous unit. A portal frame type pier supports a common bolster which carries the pinned bearing from one truss span and the rocker bearing for the other. At the joint between the trusses and the concrete approach units, the rocker bearing is supported on a partially split column. The truss units were locally modelled to account for each individual member with the associated concrete piers and foundation springs. The concrete deck was not considered capable of contributing to the transverse flexural or shear stiffness of the trusses due to the presence of cold joints over each floor beam and expansion joints at every third floor beam. Transverse shear was assumed to be carried entirely by the lateral system.

A "global" model was constructed by linking the "local" units together with rigid links to model the condition where seismic response motions had brought the units into contact (i.e. expansion joints completely closed). Figure 3 shows such a model for the north approach. The truss units could be replaced by equivalent single beam members for the global models.

A response spectrum analysis was carried out on each "local" model as well as on the "global" model to obtain elastic response forces and displacements. Both cracked section stiffness and gross section stiffness models were analyzed.

A "push-over" analysis was performed on each "local" model of the concrete units to evaluate ductility requirements. This analysis is conducted by applying a static horizontal loading (in direct proportion to dead load) in increments while monitoring selected members for possible plastic hinge formation. As soon as a hinge has formed, the stiffness matrix of the model is altered and the analysis continued until a plastic collapse mechanism is formed. The resulting force-displacement relationship is used to perform a single mode dynamic analysis to predict maximum seismic response displacements. Assessments are then made of the ability of individual members to sustain the indicated flexural curvatures and shears as well as the ability of splices to develop the required bar forces. Joint shear is also investigated for premature brittle failure or limited ductility. The ability of the foundation to develop the plastic hinge moments in the columns was also investigated.

The steel truss units were analyzed using a response spectrum analysis with the seismic motions applied directly to the truss bearings to determine indicated steel stresses due to seismic motions. A similar analysis was conducted with the model supported on the piers to check for possible amplification of ground motions.

Assessment Criteria

Assessment of seismic vulnerability is measured against the collapse state. Importance classification is I (essential bridge). Major damage is anticipated; however, access for emergency vehicles is required immediately after the design event. Therefore, the damage which can be accepted is limited.

The methodology for assessment is taken from the work of Priestley and Seible [1] and Priestley, Seible and Chai [2].

Concrete strengths are increased from the design minimum to account for statistical variation and age of the concrete. The strengths used in calculating nominal strengths, specified minimum strengths, and cement content were:

Concrete Class	f'_c Nominal	f'_c Minimum	Cement Content
AX	41 MPa (6,000 psi)	28 MPa (4,000 psi)	360 kg/m^3 (6.5 sacks/cy)
A	34 MPa (5,000 psi)	25 MPa (3,600 psi)	335 kg/m^3 (6.0 sacks/cy)
B	31 MPa (4,500 psi)	21 MPa (3,000 psi)	307 kg/m^3 (5.5 sacks/cy)

Reinforcing steel yield strengths were increased from the design minimum to account for statistical variation. The values used in calculating nominal yield strengths and the specified minimum yield strengths were:

Steel Grade	f_y Nominal	f_y Minimum
40	303 MPa (44,000 psi)	275 MPa (40,000 psi)
60	455 MPa (66,000 psi)	414 MPa (60,000 psi)

Structural steel yield strengths were increased from the design minimum to account for statistical variation. The values used in calculating nominal yield strengths and the specified minimum yield strengths were:

Steel Grade	f_y Nominal	f_y Minimum
ASTM A36	275 MPa (40,000 psi)	248 MPa (36,000 psi)
ASTM A242	380 MPa (55,000 psi)	345 MPa (50,000 psi)

Ultimate bearing capacity of soils is 0.96 kPa (20 ksf) for Piers 10 through 17 and 2.4 kPa (50 ksf) for all others. The ultimate axial load capacity (based on the soil) of the reinforced concrete piling under Piers 10 through 15 is 890 kN (100 tons) and the ultimate tensile capacity of these piles is 445 kN (50 tons). The piles are not positively connected to the footings, therefore, it was assumed that the footings cannot transfer tensile loads to the piles. A nominal tensile capacity was assumed for checking the need for top mat reinforcing in the pile cap.

The applicable shear modulus for calculating stiffness of soil springs were taken from the geotechnical report and are summarized as follows:

Pier Number	Vertical	Translation Torsion Rocking	
1-9,23-35	103 MPa (15 ksi)	103 MPa (15 ksi)	
10,11*,12*	41 MPa (6 ksi)	41 MPa (6 ksi)	* Spread footings at 11 & 12
12-15	31 MPa (4 ksi)	31 MPa (4 ksi)	Pile foundations
13,15*,16,17	21 MPa (3 ksi)	21 MPa (3 ksi)	* Spread footings at 15
18-20	62 MPa (9 ksi)	62 MPa (9 ksi)	
21	90 MPa (13 ksi)	90 MPa (13 ksi)	
22	138 MPa (20 ksi)	138 MPa (20 ksi)	

Adjustment of foundation springs for embedment considered embedment into the glacial till only. (i.e., unconsolidated overburden was neglected for purposes of evaluating foundation springs).

Piers which had a depth of overburden greater than 2 times the column width above the top of the pedestals were modelled with translational springs representing the overburden. Typically, these springs were placed one-half of the distance between the ground line and the top of the pedestal. Where the depth of overburden was large, more than one horizontal spring was used. Piers 21 and 22 have an additional spring at mid-depth of the tremie seal.

Flexural strength, M_n, of concrete section was based on nominal (phi=1.0) strength of member as shown on the plans and axial load corresponding to nominal dead load plus (or minus) seismic overturning loads. It is necessary to use trial and error to evaluate the correct axial load depending upon the frame condition (i.e. number and location of plastic hinges).

Available flexural strength may also be limited by lap splices and bar development length unless retrofit measures are taken to provide confinement. At locations where bars are terminated, an

assessment of the development of the bar was made by determining the force which could be developed in the bar at the point where cracking of the concrete cover was initiated. Potential splitting crack surfaces are shown in Figure 5. The maximum force capable of being developed in the longitudinal bar is:

$T_s = f_t l_s p$

where l_s = splice length

$f_t = 4 (f'_c)^{0.5}$ direct tensile strength of the concrete (in English units)

p = perimeter of splitting crack $= 2(c + d_b) + s$

c = clear cover

d_b = bar diameter

and s = spacing between bars.

If the force capable of being developed in the bar is greater than the ultimate force then the full plastic moment can be developed. If the force capable of being developed in the bar is greater than the yield force but less than the ultimate force, then only the moment at first yield can be developed and ductility is limited. The minimum length of splice for nominal bar diameter "d_b" is given as follows:

$$l_{s\,min} = 0.025\, d_b \frac{f_y}{\sqrt{f'_c}}$$

This expression gives the length necessary to develop ultimate strength of bar. This minimum length assumes confinement by tensile stress in the concrete or transverse reinforcing steel crossing the fracture planes. If the actual splice (or development) length is less than $l_{s,min}$, the nominal moment strength (M_n) will be reduced proportionately.

The residual flexural strength (M_n) of columns with lap splices in unconfined potential plastic hinge regions is taken as the value which can be sustained by the maximum eccentricity of the axial compression force in the column, using the reduced section defined by the inside of the layer of longitudinal reinforcement. For rectangular sections, the residual moment capacity based on axial load alone is

$$M_r = N \left(\frac{h'}{2} - \frac{a}{2}\right)$$

where N = axial load

h' = depth of reduced section

a = depth of equivalent rectangular stress block

$a = N/(0.85\, f'_c\, b')$

b' = width of reduced section.

This residual strength is assumed to be developed at a displacement ductility factor of 3.

The shear strength of the columns should be capable of developing the nominal flexural strength (allowing for 20% over-strength). The shear strength for rectangular columns is calculated as the contribution of the concrete

$$V_c = \beta \sqrt{f_c}\, b\, d$$

where beta = a function of the required displacement ductility (See Figure 6)
b = section width
d = section effective depth.

plus the contribution of the transverse steel

$$V_s = A_v\, f_y \frac{d}{s} \cot \theta$$

where theta = angle between the shear crack and the axis of the member
A_v = area of transverse steel
s = spacing of the transverse steel.

The transverse reinforcing provided by the hairpin bars typical on this project is considered as effective shear reinforcing only outside of plastic hinge regions since the legs of opposing bars did not lap nor did they extend far enough to be considered anchored in the compression region.

Joint shear strength is assessed by examining equilibrium conditions at a joint when flexural hinges have formed in the members framing into the joint. The assessment was carried out separately in each of the two mutually perpendicular planes. Joint shear strength is given as the minimum of

$$V_{jh} = maximum(f_t\, h_c\, b\ ,\ A_{vh}\, f_y)$$

or

$$V_{jv} = maximum(f_t\, h_b\, b\ ,\ A_{vv}\, f_y)$$

where:

$$f_t = \frac{f_a}{2} - \sqrt{(\frac{f_a}{2})^2 + v_q^2} \le 3.5\sqrt{f_c'}$$

h_c = column width in plane of flexure
h_b = beam width in plane of flexure

b = joint width perpendicular to plane of flexure
V_{jv} = vertical joint shear
V_{jh} = horizontal joint shear
f_a = axial stress at mid height of joint
f_y = yield strength of joint reinforcement
A_{vv} = area of vertical joint reinforcement
A_{vh} = area of horizontal joint reinforcement

Contribution of joint reinforcing steel may be considered only when such steel is fully developed at the middle of the joint.

Joints in which a joint shear failure occurs prior to formation of the plastic hinges in the beams or columns are capable of limited ductility as illustrated in Figure 7.

Ductility demands of individual frames (units between expansion joints) are assessed by applying static loads at deck levels in each direction to calculate force-displacement relationship up to the formation of the collapse mechanism. This force-displacement relationship is then used in a trial and error procedure to predict seismic response displacement. The displacement ductility demands of the individual columns are then assessed. The displacement demand/capacity ratio is determined as

$$\frac{d}{c} = \frac{\textit{Seismic ductility demand}}{\textit{Member displacement ductility capacity}}$$

In some cases member displacement ductility capacity was limited by member shear capacity, joint shear capacity, bar development, or curvature ductility capacity. Curvature ductility demand is assessed from the member length to the point of inflection and an assumed plastic hinge length.

$$l_p = 0.08\, l + \chi\, d_b$$

where l_p = the length from the point of inflection
chi = 6 (for Grade 40 reinforcing steel)
d_b = bar diameter of longitudinal reinforcement.

The relation between displacement ductility and curvature ductility is given by

$$\mu_\phi = 1 + \frac{(\mu_\Delta - 1)}{3\,\frac{l_p}{l}\left(1 - \frac{l_p}{2\,l}\right)}$$

where mu_{phi} = curvature ductility
mu_{delta} = displacement ductility.

Limiting curvature ductility is assessed from a strain compatibility analysis of the section considering the axial load present. Ultimate curvature for a lightly confined section is taken as the curvature where the maximum concrete strain is 0.4%. Yield curvature is taken as the curvature at first yield times the ratio of the nominal ultimate moment to the moment at first yield. The curvature ductility capacity is then the ratio of ultimate curvature to the yield curvature.

This assessment is made for both longitudinal and transverse seismic motions.

The force-deflection relationship for the double deck units assumes that forces at each deck level are in proportion to the distribution of mass and act in the same direction.

Results of dynamic analysis

Natural periods of the linear elastic structure units range from approximately 0.20 seconds to 2.50 seconds. The short period structures are the small flat slab bridges at the ends which have deeply embedded short columns. The longest period units are the main truss piers in the longitudinal direction. Indicated seismic displacements range from 0.20 inches to 8 inches for these same units. The indicated ratio of elastic moment demand to nominal moment capacity ranges from approximately 5 to 2 for the results to date. The "push-over" analyses of the structural units have not yet been completed.

Summary

The seismic vulnerability assessment of one of the most important bridges in the Seattle area will serve as an important guide for policy making decisions in arriving at a retrofit strategy. The assessment criteria proposed herein attempts to provide a means for assuring adequate safety while recognizing all the potential capacity of the existing structure by employing the latest research results.

References:

[1] Priestley, M.J.N. and Seible, F., Seismic Assessment and Retrofit of Bridges, Structural Systems Research Project, University of California, San Diego, July 1991 Report SSRP-91/03.

[2] Priestley, M.J.N., Seible, F. and Chai, Y.H., Design Guidelines for Assessment Retrofit and Repair of Bridges for Seismic Performance, Structural Systems Research Project, University of California, San Diego, August 1992 Report SSRP-92/01.

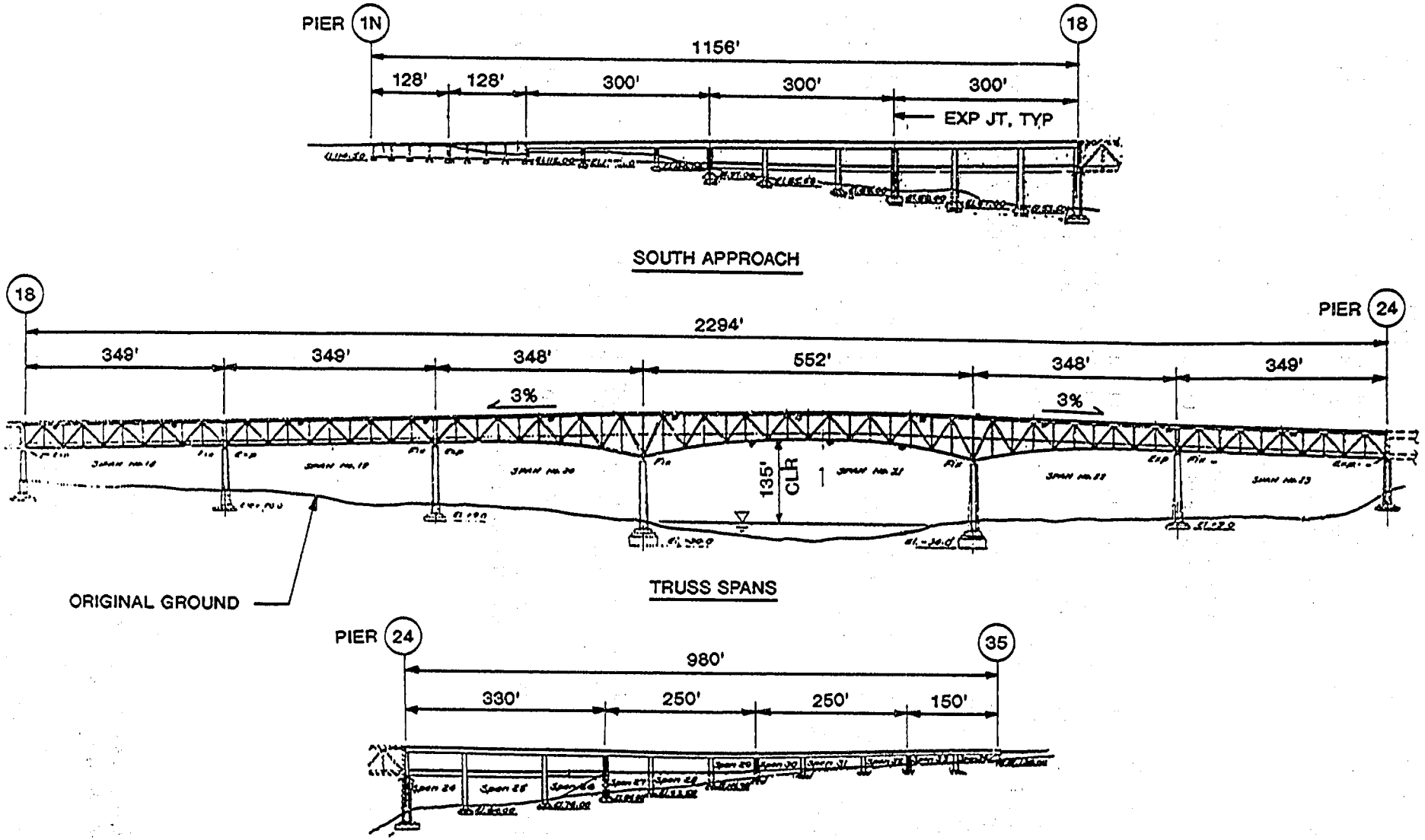


FIG. 1 LAKE WASHINGTON SHIP CANAL BRIDGE

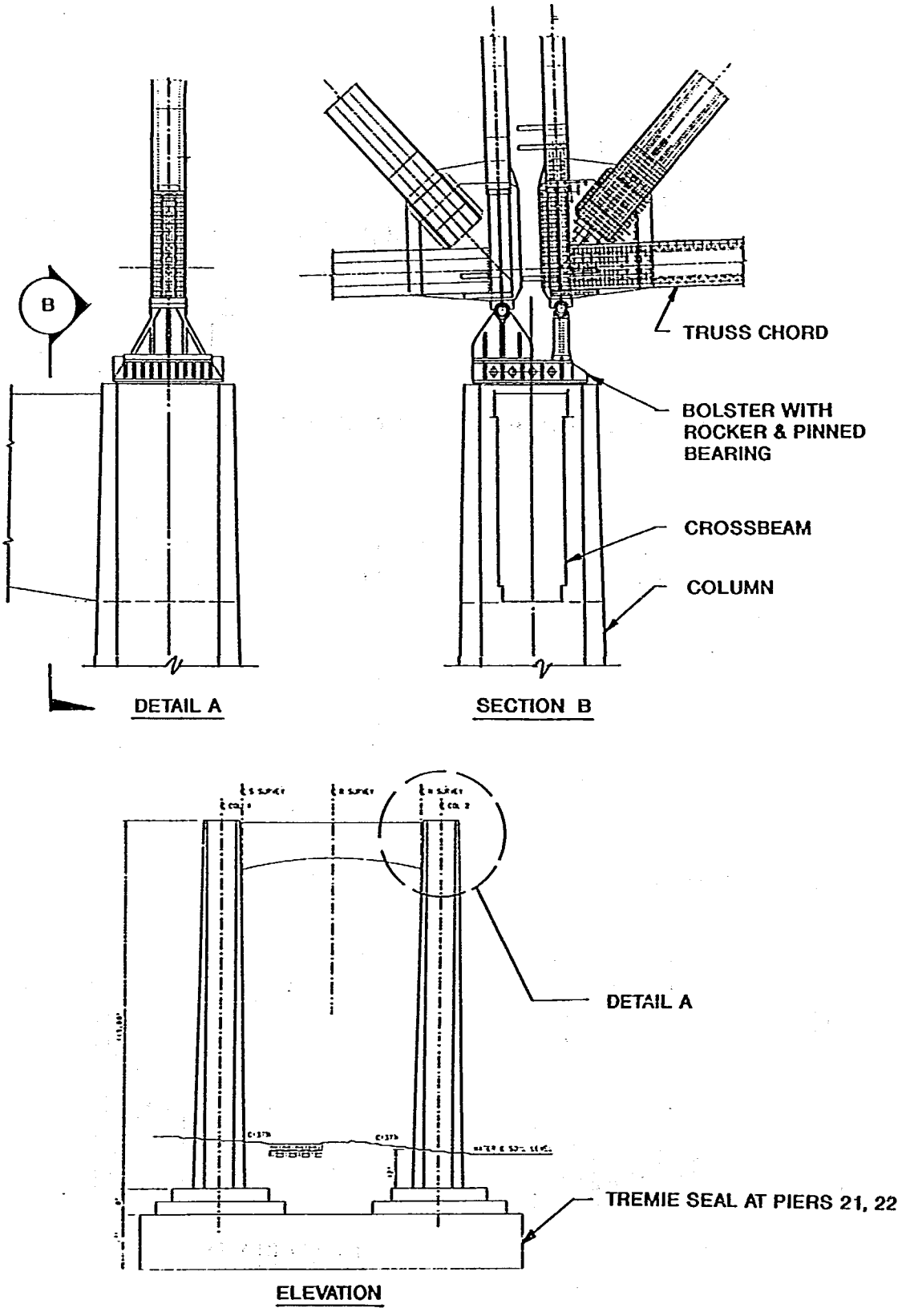


FIG. 2 TYPICAL CONCRETE PORTAL AT TRUSS SPANS

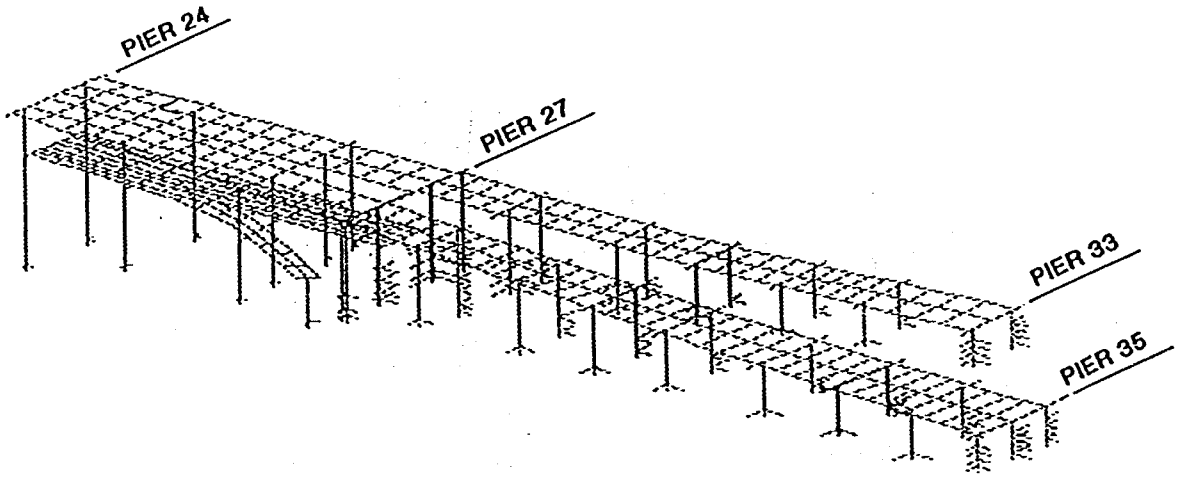
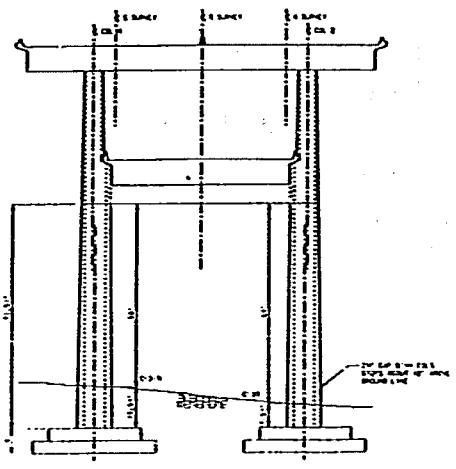
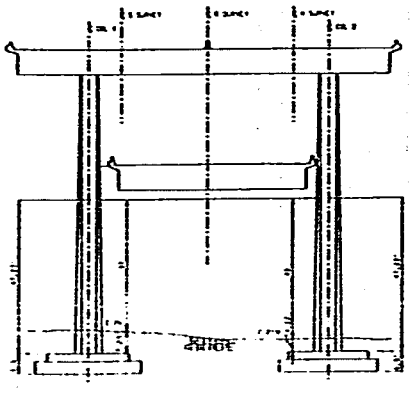


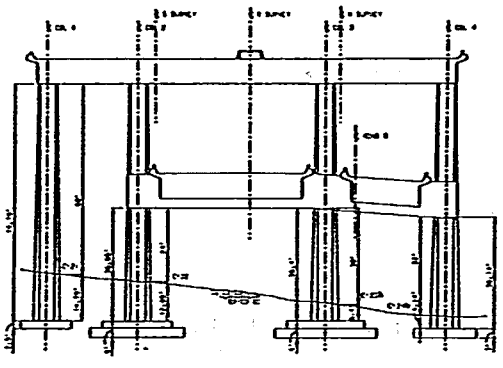
FIG. 3 GLOBAL GTSTRUDL MODEL OF NORTH APPROACH



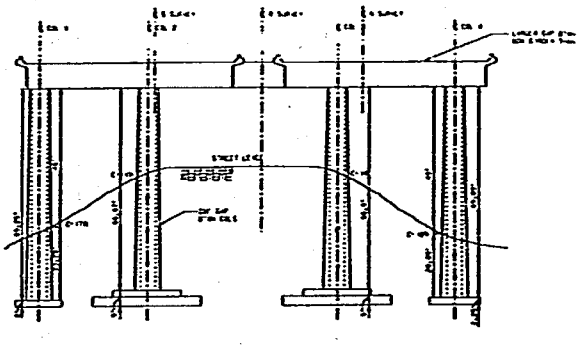
PIER 24 (N 1/2)



PIER 25



PIER 26



PIER 27 (N 1/2)

FIG. 4 PIER ELEVATIONS AT NORTH APPROACH

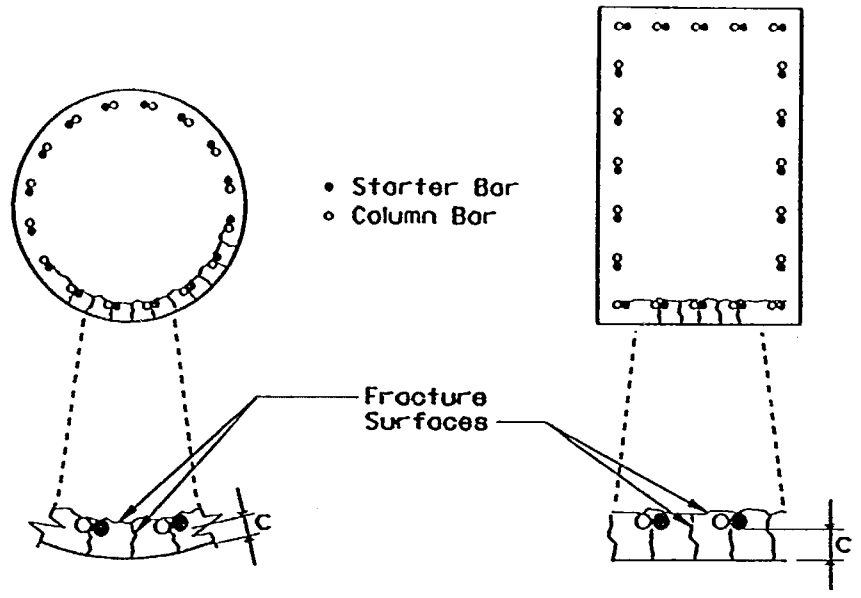


FIG. 5 LAP SLPICES IN COLUMNS

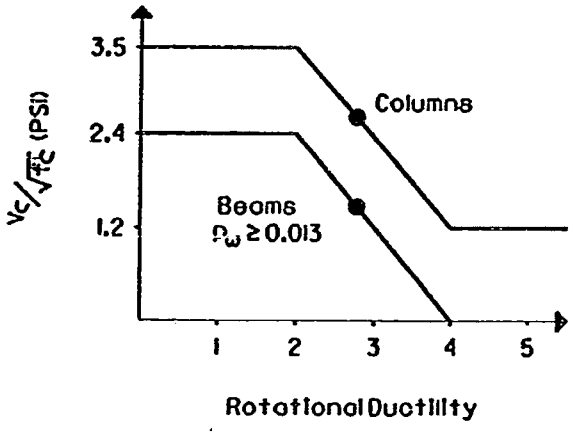


FIG. 6 CONCRETE SHEAR STRENGTH / DUCTILITY RELATIONSHIPS FOR PLASTIC HINGES

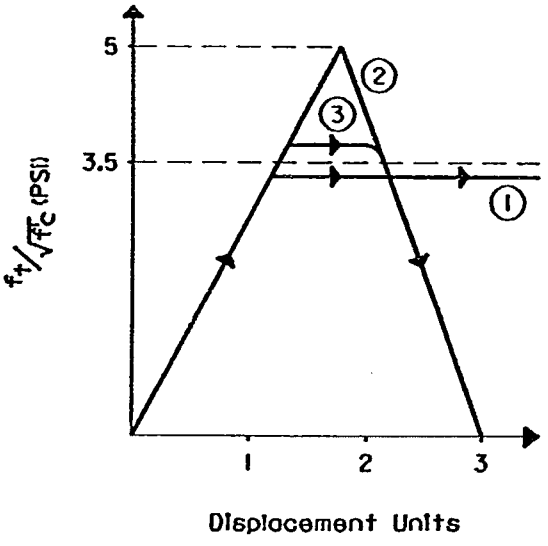


FIG. 7 JOINT TENSION STRENGTH FAILURE MODEL

Research on adoption of Vane-Dampers for the Tsurumi Fairway Bridge

By Noboru Ito[1] and Masasumi Okada[2]

1) Senior Engineer, Special Structural Design Division, Kanagawa Construction Bureau, Metropolitan Expressway Public Corporation
2) Civil Engineer, Special Structural Design Division, Kanagawa Construction Bureau, Metropolitan Expressway Public Corporation

ABSTRUCT

Connection between the girder and the tower of the Tsurumi Fairway Bridge, a long span cable-stayed bridge on Metropolitan Expressway Bay Shore Route, is elastic support using 'Attachig Horizontal Cables'. For stable use of the Cables during large earthquakes, Vane-Dampers have to be installed. Reaction of the damper is proportional to square of the relative velocity between the girder and the tower and the maximum reaction is controlled by the reaction control valve. From the time-history response anaysis, the adoption of the dampers have benefitial effects on the bridge. The characteristics of the valve and the half-scale model of the damper was confirmed from experiments. Tests for the real dampers are also planned.

1. INTRODUCTION[1]

The Tsurumi Fairway Bridge is one of the major bridges on Metropolitan Expressway Bay Shore Route, a part of the Tokyo Bay Ring Road which, as shown in Figure 1, will extend approximately 185 km along the Tokyo Bay Coastline. As shown in Figure 2, the Bridge is a single plane, three span continuous cable-stayed bridge composed of 510 m center span and two 254 m side spans. The center span length was determined from requirements of the Fairway for over 400 vessels including 50,000 GT class use the Fairway daily. In the future the same type bridge for National Highway Route 357 will be constructed along the bridge parallelly and they will become the twin bridges as shown in Figure 3.

Configurations of the cables, the towers and the girder were determined from aerodynamic stability, requirements for durability and aesthetical consideration at the twin bridges completion stage. Single plane cable type was recommended as they would not appear to be entangled at the time of twin bridges. Basic wind tunnel test results supported the decision. Seventeen cables from each side of the tower were arranged as semi-fan type. Streamlined shape of the girder with fairings, determined from requirements of wind resistance and stability, also expected to help adding a slender image upon the bridge. Shape of the tower, an inverted Y shape, was also adopted after aesthetical research utilizing computer graphics based on the decision of single plane cables. Cross section of the tower is determined as the combination of two trapezoids and a rectangle to add more slender impression. For lower part of the tower is thought to be affected from splash of tides and sea salts, a durable steel reinforeced concrete (SRC) structure is chosen. Therefore, middle part of the tower, a transient part between steel structure and concrete structure, is designed as a steel shell structure with inserted dowel bars based on results of model experiments. Shape of the concrete structure of the tower and the end pier is determined as octagonal shape based on aesthetical research utilizing computer graphics.

Type of the foundations of the bridge is a pneumatic caisson supported by the diluvial formation some 30 or 40 m under the sea level. Because the water depth is about 12 m, floating construction method utilizing the steel caisson chamber was chosen as the most economical and suitable method. For excavation, overhead crawler shovels controlled from the remote operation room were adopted to minimize the amount of work under high pressure and to maintain safety.

2. ANALYTICAL STUDY ON ADOPTION OF VANE-DAMPERS

2.1 Study of the Supporting Condition at Towers

Supporting conditions at towers or connections between girders and towers have remarkable effects on vibrational modes and natural frequency of the cable-stayed bridges. For the Tsurumi Fairway Bridge various supporting conditions, as shown in Figure 4, were studied and comparison is made as Table 1.

For the fixed connection, although longitudinal displacement can be minimized, acting forces at the lower end of the tower due to thermal displacement and those due to earthquakes are extremely large. Dimensions of piers and foundations have to be larger than others to withstand such large forces and, hence, the structure is thought to be uneconomical.

The floating type, on the other hand, moment of the lower end of the tower is almost half as the fixed type, however, longitudinal displacement due to live load is about 30 times larger than that of fixed type. Expansion joints will be, therefore, extremely large and give drivers unpleasant feelings. Since the Tsurumi Fairway Bridge is a single-plane cable-stayed bridge, as large displacement due to live load seems undesirable, floating type is thought to be unsuitable.

For the Yokohama Bay Bridge[2], located near the site of the Tsurumi Fairway Bridge, the tower and the girder were connected by tower links, similar to the one used for suspension bridges. The connection type is thought to be as 'floating but elastically constrained'[3]. Adopting the link type for the Tsurumi Fairway Bridge, acting forces at the lower end of the tower is almost same as the floating type and longitudinal displacement is rather small than the floating type. For this conncetion type, however, width of the tower have to be widened because tower links have to be placed between the tower and the girder. The fact is crucial because only about 3 m clear space between the twin bridges is specified in the urban plan for the case without tower links and, therefore, provided space is thought to be insufficient for tower links.

For elasic connection utilizing 'Attaching Horizontal Cables', which was adopted for the Meiko Central Bridge[4], acting forces are almost same as the link type and longitudinal displacements due to both of live loads and earthquakes are rather smaller than those of the link type. As the Attaching Horizontal Cables are installed inside the girder, the width at the tower is same as floating type. For longitudinal displacement due to live loads is relatively small, dimension of expansion joint is not so large.

Considering the above results, supporting type at the towers of the Tsurumi Fairway Bridge was determined as elastic fixing type utilizing 'Attaching Horizontal Cables'.

2.2 Attaching Horizontal Cables

The Attaching Horizontal Cables for the Tsurumi Fairway Bridge are prefabricated parallel wire strands of 167 mm diameter, the same type as the main cables. Each cable is composed of 367 galvanized high strength wires of 7 mm diameter and covered with polyethlene in a factory. Two pairs of 117 m cables are attached from the tower to both the center and side spans and supported on rollers at 1.8 m intervals.

Attaching Horizontal Cables were designed under following conditions;

① Although stresses of cables are increased for one side and decreased for the other side, both sides of cables are maintained in tension due to the combination of live loads and temperature changes.

② 'EA/L' have to be maintained to prevent excessive force due to temperature change.

③ Assuming only one side of cables withstand all the horizontal forces during the earthquakes and the stress of the attaching horizontal cables does not exceed the allowable value, 108.8 kgf/mm^2.

Cross sectional area, length and initial tension, 690 tf, were determined from above conditions.

Earthquake responses were computed using the time-history response analysis for the determined attaching horizontal cables assuming non-linear cable stress-strain relationship with no resisitance to compression. From the results, however, it is found that tension of compressed side of the cables is vanished several times during earthquakes.

Corresponding to this problem with cables only, initial tension must be increased, hence, 'A' must be increased from the requirement ① and, consequently, cable length must be longer to maintain 'EA/L' in certain range. In other words, longer and thicker or more cables must be attached. The method is unrealistic and uneconomical solution because 117 m cables for 254 m side spans are already long enough and, moreover, without doubt, it affects the design of the girder itself.

Installing dampers at the tower to reduce earthquake responce would be another solution and Vane-Dampers, which have been installed at end piers of the Higashi Kobe Bridge[5, 6], are proposed. Unless the excessive reaction does not occur at the tower base, it is thought to be a good countermeasure to correspond slack of the cables. Consequently the connection of the tower and the girder were determined, as shown in Figure 5, as combination of Attaching Horizontal Cables and Vane-Dampers.

2.3 Vane Damper[7, 8]

Structure of the Vane Damper is shown in Figure 6. In order to minimize its size, relative horizontal motion between the girder and the tower is converted to rotational oscillation owing to the vane and the cylinder. When the vane is rotated, oil pressure of the left and right chambers become different and, thus, oil is compelled to pass through the orifices at the center of the damper. Turbulence resistance generated as passing orifices induces horizontal reaction proportional to square of the velocity. To prevent the excessive force to the substructure and to avoid excessive pressure inside the damper itself, pressure control valves are installed in the partition.

Basic property of the damper is shown in Figure 7. As stated above, the

horizontal resistance is proportional to square of the relative velocity between the girder and the tower and after the reaction reaches maximum value, the resistance is constant regardless to the velocity. The maximum reaction was determined as 200 tf for prevention of excessive pressure to the damper. Constant C was determined so as to reduce the horizontal force of the attaching horizontal cables to prevent the cable slack. After some trial, it is found that cable slack can be avoided when $C \geqq 800 kgf/(cm/s)^2$.

Time-history response analysis adopting two dampers for each tower, the horizontal forces of attaching horizontal cables during earthquakes are reduced by 20 to 30 % compared with the case of only attaching horizontal cables. The example of the response is shown in Figure 8. Since the longitudinal displacement is smaller than the value without dampers, the additional damping to the superstructure in longitudinal direction is also found.

After this study, it becomes clear that the installation of dampers with certain property has beneficial effects for the stable use of attaching horizontal cables and also for additional damping of the superstructure.

Design of the damper is to design the orifices and the pressure control valves for the constant C is the characteristic value of the property of the orifice and the maximum horizontal reaction is of the pressure control valve. It is, therefore, necessary to confirm the properties of the damper experimentally.

3. EXPERIMENTAL STUDY ON THE VANE-DAMPER[9, 10]

3.1 General

Two series of basic experiments had to be carried out ahead of the tests for the real dampers in order to confirm the design of Vane-Damper. The first series of experiments were tests of the pressure control valves in order to certify the valves to start opening at the specified pressure. After the function of the valves was verified, the second series tests, the tests for a 1/2 scale model including the pressure control valves, were performed in order to find whether or not the damper has speicfied properties.

3.2 Tests for the Pressure Control Valves

Basic function of the pressure control valves is, shown as the flat part of Figure 7, to avoid excessive pressure for the damper and excessive reaction for the substructures. In order to obtain such character, the valve consists of a cranked orifice, much larger than the orifice of the damper, and a spring to control the pressure to open the cranked orifice. Several springs of different spring constants were tested and, as a result, the valves started to function around the calculated pressure regardless to spring type. In Figure 9, comparison of calcurated pressure and measured pressure to open the valve, it is apparent that both are coincided.

3.3 Tests for a 1/2 Scale Model

1/2 scale damper model, which had been used for the tests for the Higashi-Kobe Bridge[6], was reformed for the tests of the Tsurumi Fairway Bridge and the pressure control valve, which was confirmed in tests described above, was tested in order to confirm the basic character of the damper: i.e.,

① Velocity-Reaction relationship
② The Pressure to open the pressure control valve

③ Properties after opening of the pressure control valve

Setup for the tests is shown in Figure 10. Four types of pressure control valves were installled. The damper was oscillated by adding sine waves using hydraulic actuater and reaction of the damper, displacements and pressures of damper's chambers were measured. Frequency of the sine wave is in the range of 0.02 to 1.0 Hz and amplitudes are ±2 cm and ± 5cm, so that various velocities can be achieved.

Relationship between the velocity and the reaction is shown in Figure 11. In this figure, measured results for various valves are indicated by various plots, the horizontal lines are the desired pressure to open the valves and the curve is the objective property of the 1/2 scale damper; i.e.,

$$F = 200\ v^2$$

Measured results for the damper with four types of pressure controls valves show good agreements of the calculated properties. Pressure control valves started to open around the desired pressure. Slightly increasing tendency in reaction can be seen after the valve opening, however, since 10 % tolerance for the reaction is already counted for the design, the results seem satisfactory.

Durability of the damper was also checked by the experiment adding 500 of ± 5 cm sine waves in 0.25 Hz. As shown in Figure 12, reaction of the damper was almost constant through the experiments and increment in temperature is about 26 degrees. From the results of this test, it will be concluded that properties of the damper are almost constant and temperature rise is negligible for earthquakes expected in the design stage.

4. CONCLUSION

Analytical and experimental studies stated above are summerized as follows.

① For connection type between the girder and the towers of the Tsurumi Fairway Bridge, combination of Attaching Horizontal Cables and Vane-Dampers with certain property is thought to be the most suitable type.

② Vane-Damper has the property that the horizontal force proportional to the relative velocity between the girder and the tower. To avoid excessive pressure for the damper and to prevent excessive reaction for the substructures, the maximum reaction has to be controlled by the pressure control valves.

③ From the experimental results of a half scale model, the desired properties for the model are almost satisfactorily. It is expected that the desired properties will be reappeared for the real dampers.

Based on the results, the real dampers were designed. Confirmational tests for the real dampers will be carried out at Tadotsu Engineering Laboratory of NUPEC using two 250 tf hydrauric actuaters simultaneously. The tests are scheduled at the end of fiscal 1993.

ACKNOWLEDGEMENT

The authers wish to express their appreciation to the members of Investigation Committee on Design and Construction of the Tsurumi Fairway Bridge (Chairperson: Dr. Manabu Ito of Saitama University) for their valuable suggestions and advices.

REFERENCES

1) Yamadera, Morikawa and Ito: "Design of the Tsurumi Fairway Bridge (1)", Kyoryo to Kiso(Bridges and Foundations), Jan. 1993, pp.15-24(in Japanese)
2) Maeda, Otsuka and Takano: "The Design and Construction of the Yokohama Bay Bridge", Cable-Stayed Bridges Recent Developments and their Future, Elsevier Science Publishing Company Inc., pp.377-395, 1991
3) ASCE Committee on Cable-Stayed Bridges: "Guidelines For the Design of Cable-Stayed Bridges", 1992
4) Japan Highway Public Corporation: "Meiko West Bridge", 1985(in Japanese)
5) Kitazawa and Robinson: "White Steel For Osaka Bay", Civil Engineering, Feb. 1991, pp.44-47
6) Yamada, et al.,: "Earthquake-Resistant and Wind-Resistant Design of the Higashi-Kobe Bridge", Cable-Stayed Bridges Recent Developments and their Future, Elsevier Science Publishing Company Inc., pp.397-416, 1991
7) Metropolitan Expressway Technology Center: "Reports of Investigation Committee on Design and Construction of the Tsurumi Fairway Bridge (in fiscal 1990)", 1991 (in Japanese)
8) Okada and Hayashi: "Response Analysis for the long span Cable-Stayed Bridge utilizing both Attaching Horizontal Cables and Dampers", The 46th Technological Presentations of the Ministory of Construction, Road Division General Papers, 1992, pp.41-44 (in Japanese)
9) Metropolitan Expressway Technology Center: "Reports of Investigation Committee on Design and Construction of the Tsurumi Fairway Bridge (in fiscal 1991)", 1992 (in Japanese)
10) Okada and Ito: "Confirmation Experiments for the Vane-Dampers of the Tsurumi Fairway Bridge", Collected Papers of the 48th Annual Technological Meeting, Division 1, Japan Society of Civil Engineers, 1993 (in Japanese)

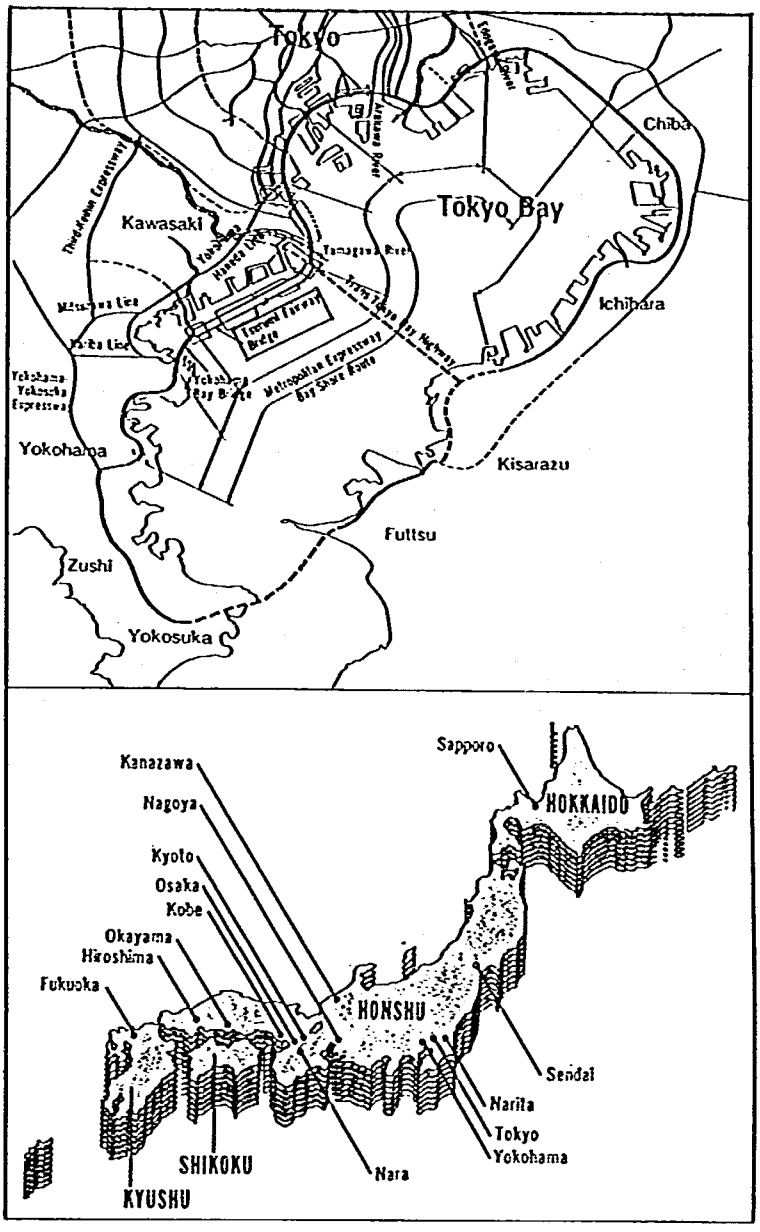


Fig. 1 Tokyo Bay Ring Road

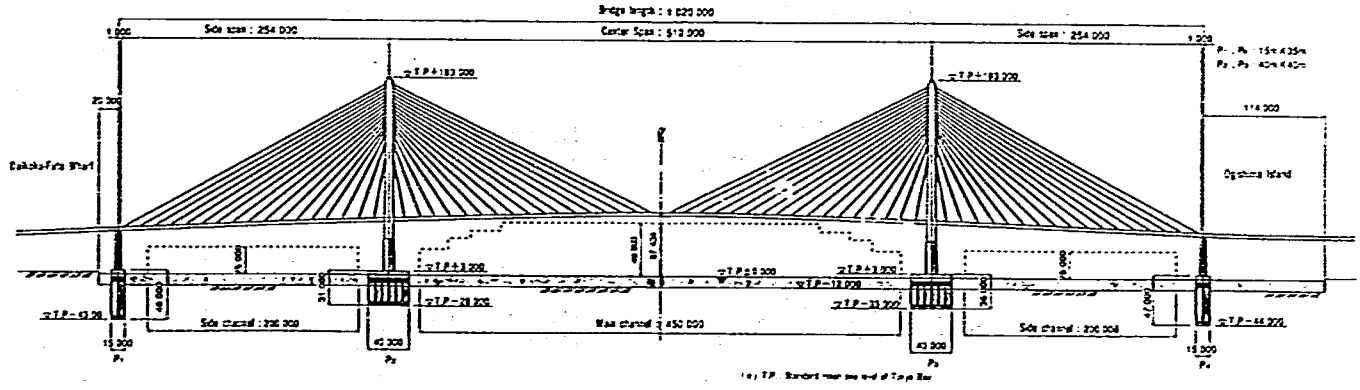


Fig. 2 Side Elevation

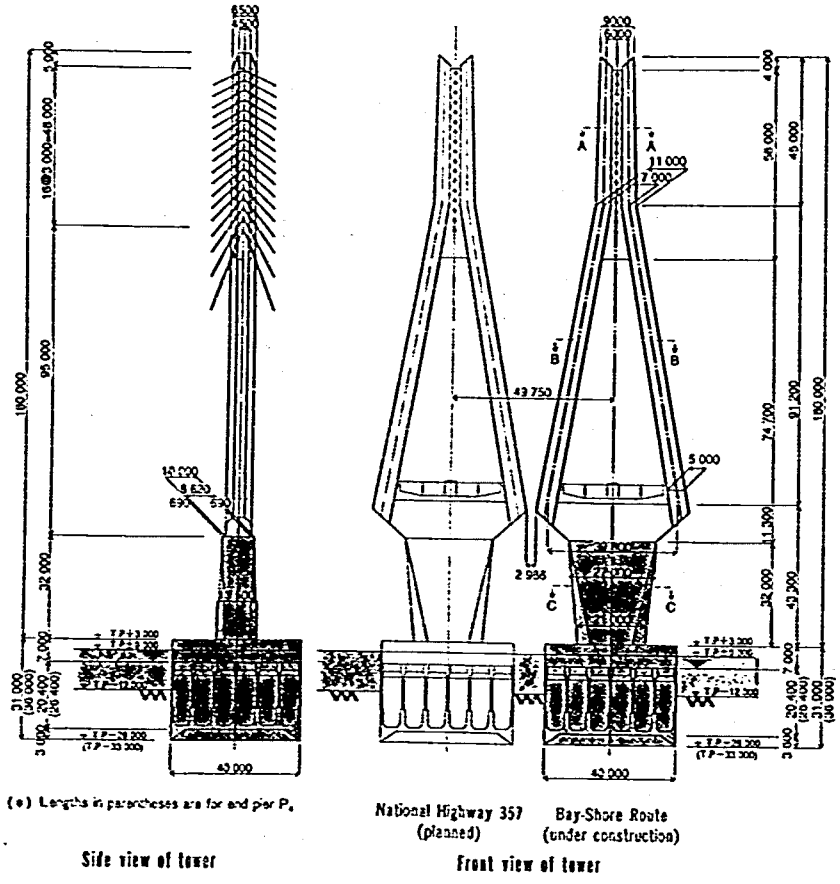


Fig. 3 Front View

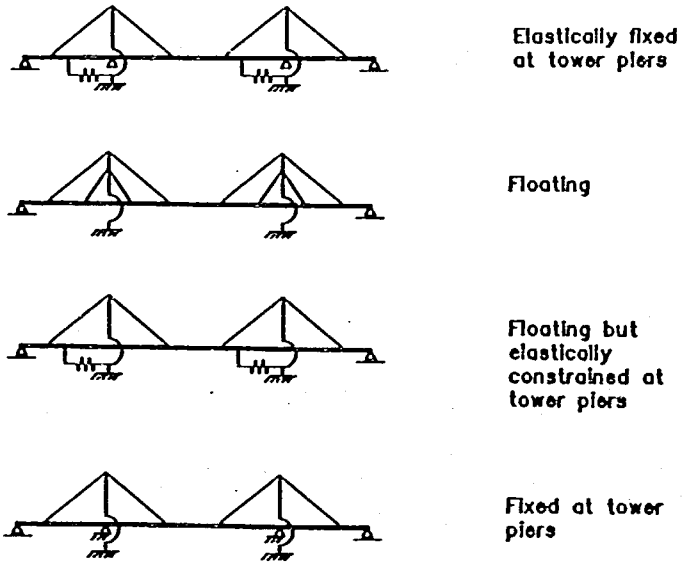


Fig 4. Various Supporting Conditions

Table 1. Comparison of Different Supporting Conditions

			Elastically fixed at tower piers	Floating	Floating but elastically constrained at tower piers	Fixed at tower piers
displacement of girder (m)	deflection	side span	0.503	0.684	0.519	0.450
		center span	0.825	0.830	0.830	0.779
	longitudinal displacement	live load	0.034	0.833	0.279	0.015
		earthquake	0.354	1.514	0.920	0.172
force of the bottom end of the tower pier	thermal forces	M(t·m)	41980	6061	9673	284600
		S(t)	825	40	115	6243
	earthquakes	M(t·m)	229600	226800	220400	434100
		S(t)	6815	6999	7054	10230
period of girder longitudinal diflection (T)			3.05	13.53	8.15	1.55

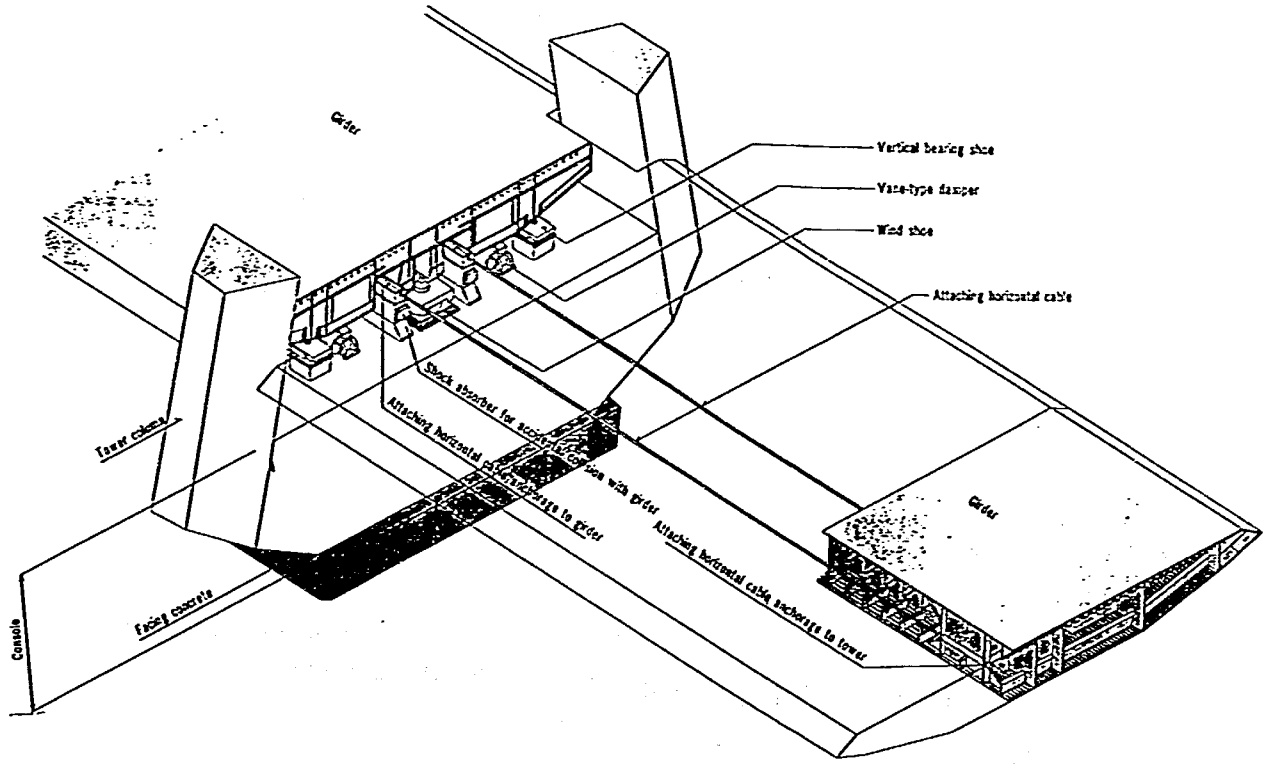


Fig 5. Equipment between the Girder and the Tower

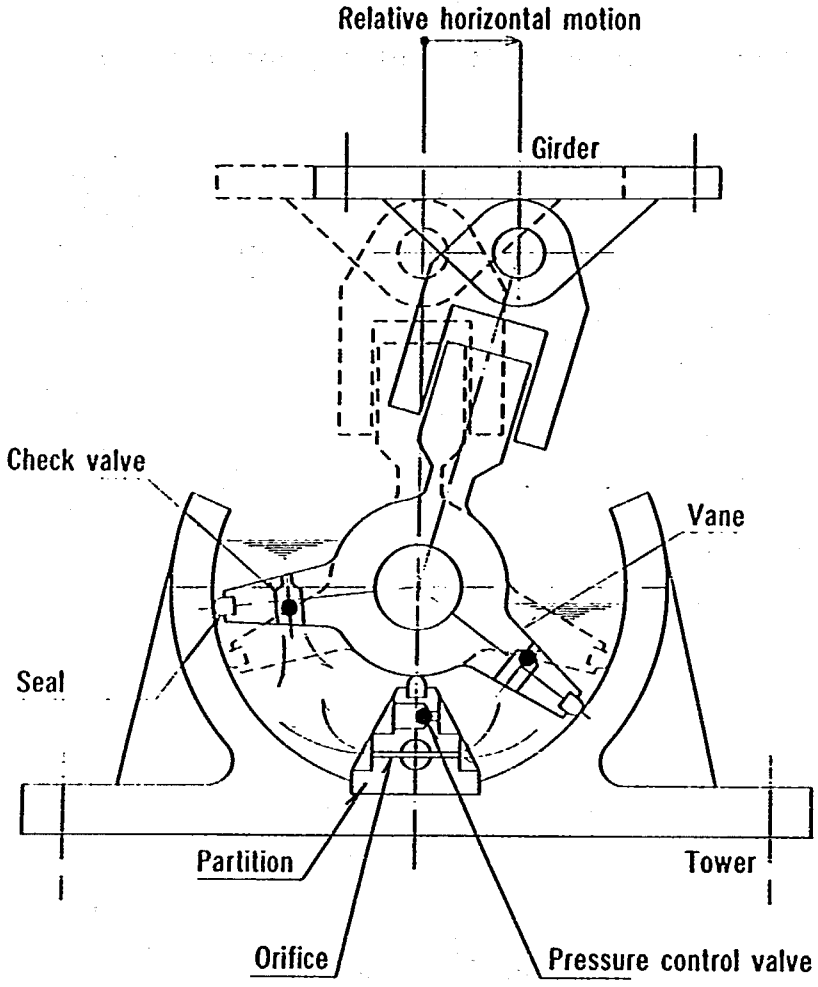


Fig 6. Mechanism of the Vane Damper

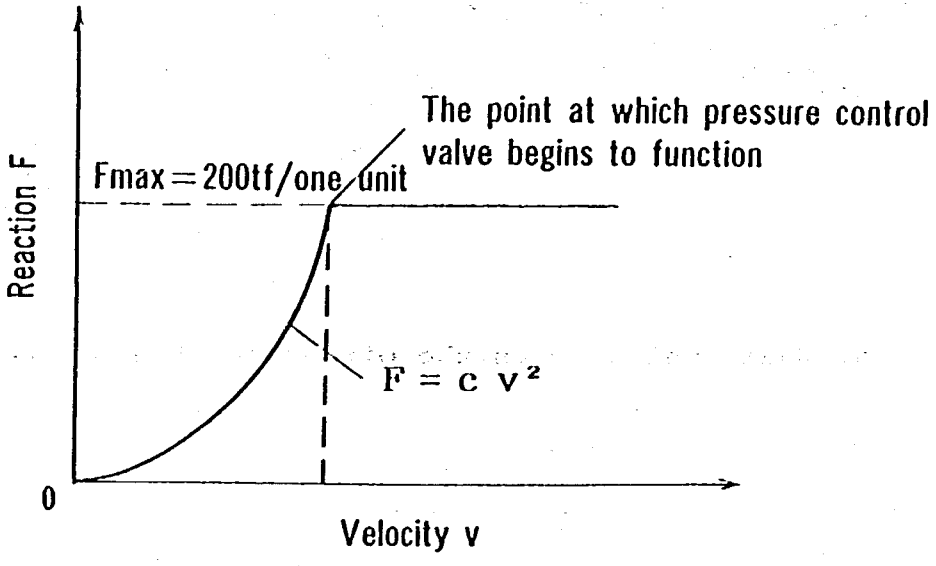


Fig 7. Reaction Property of the Vane Damper

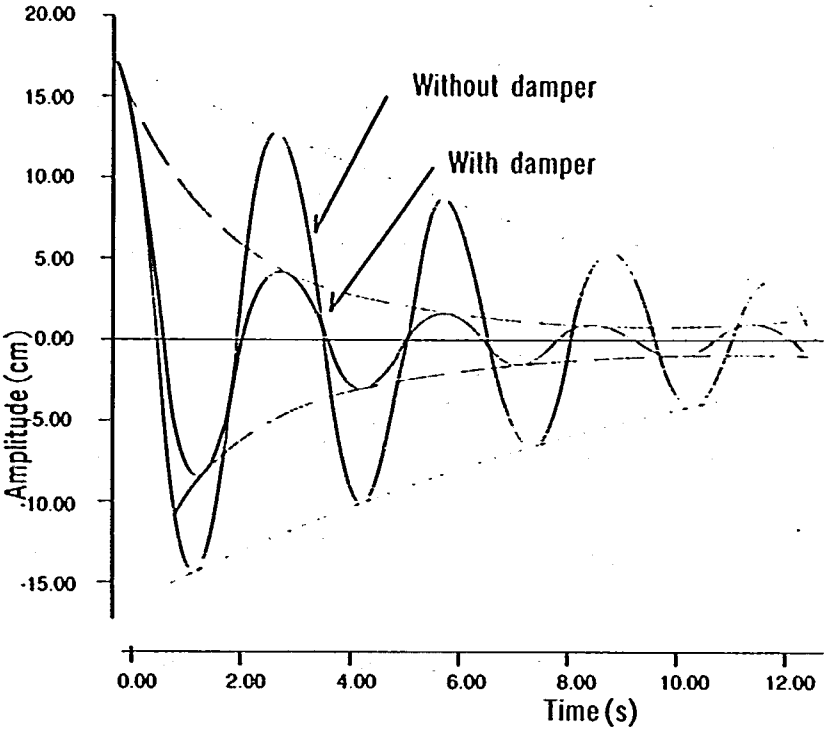


Fig 8. Free Vibration Wave at Girder End

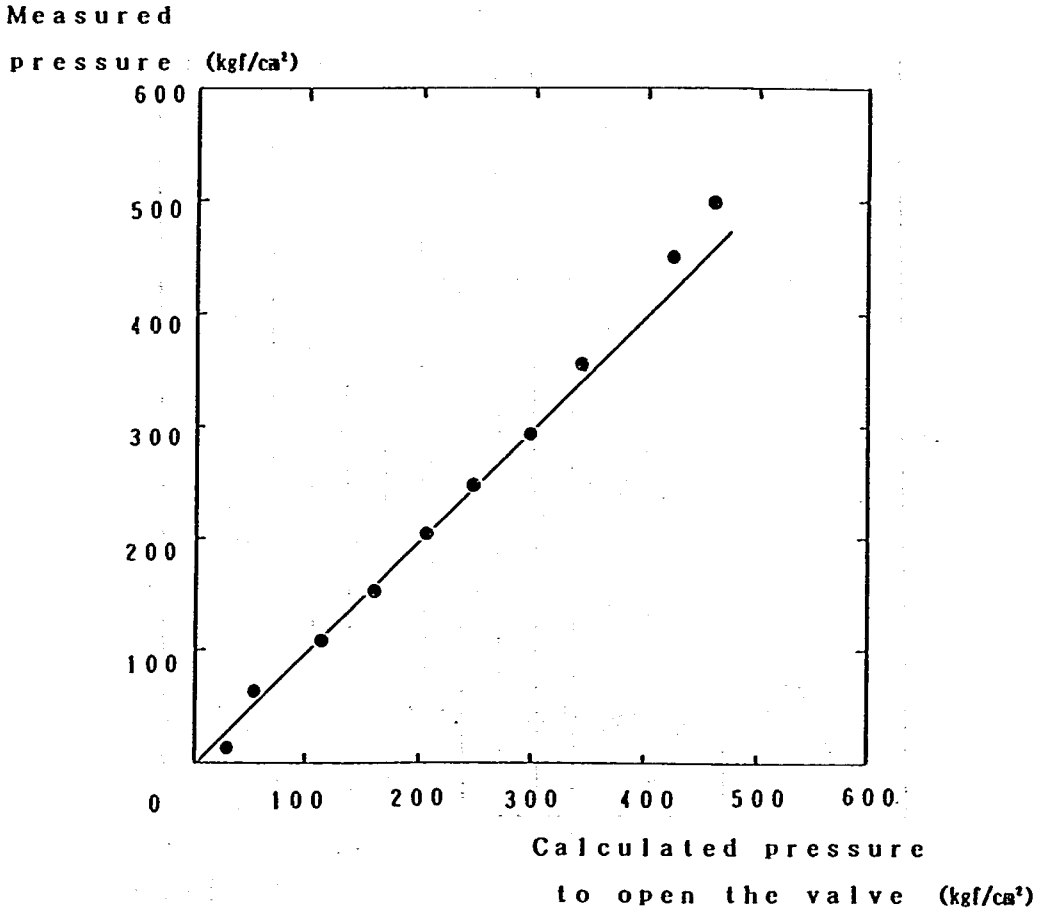


Fig 9. Results of the Pressure Control Valve Experiment

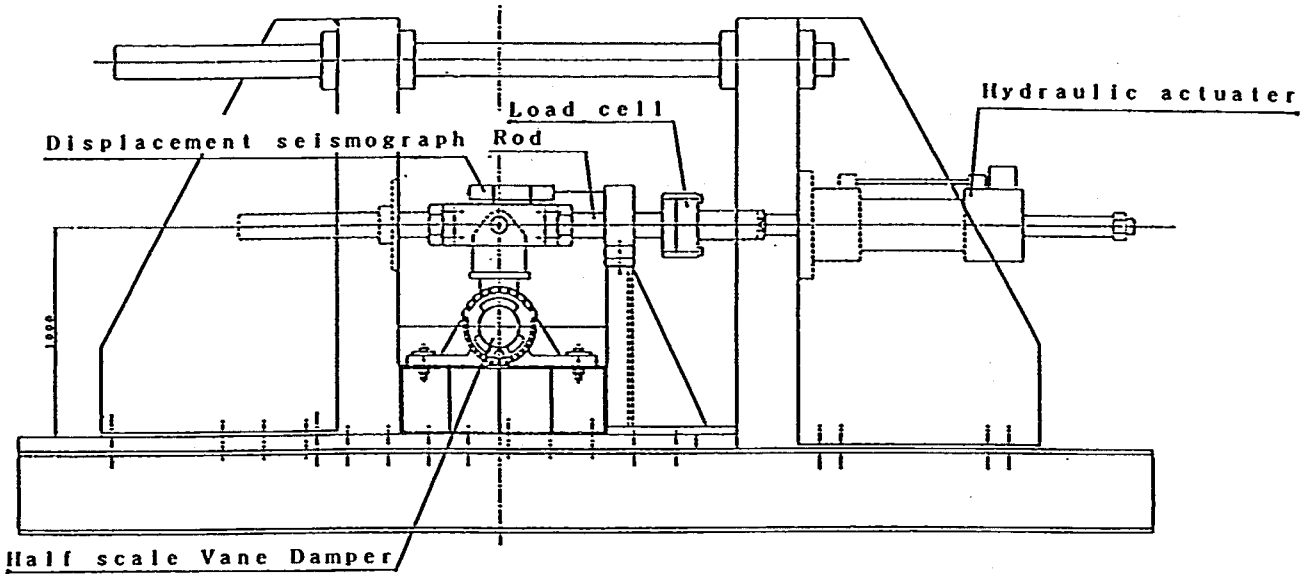


Fig 10. Experiment Equipment

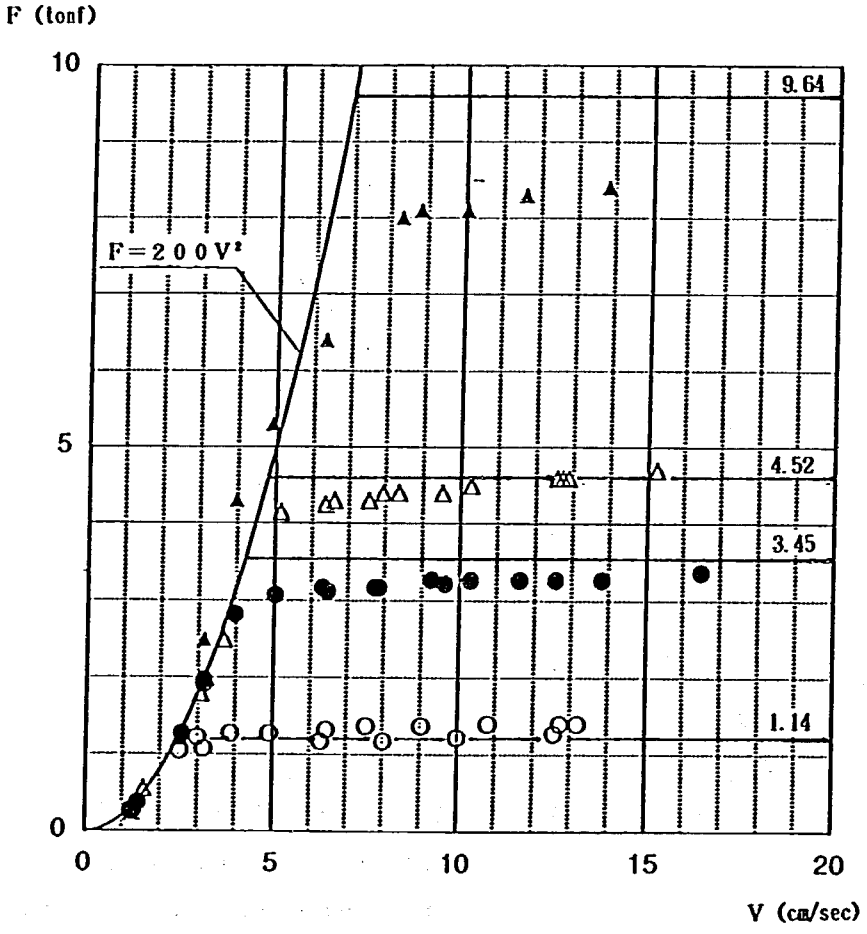


Fig 11. Results of the Half Scale Model Experiments

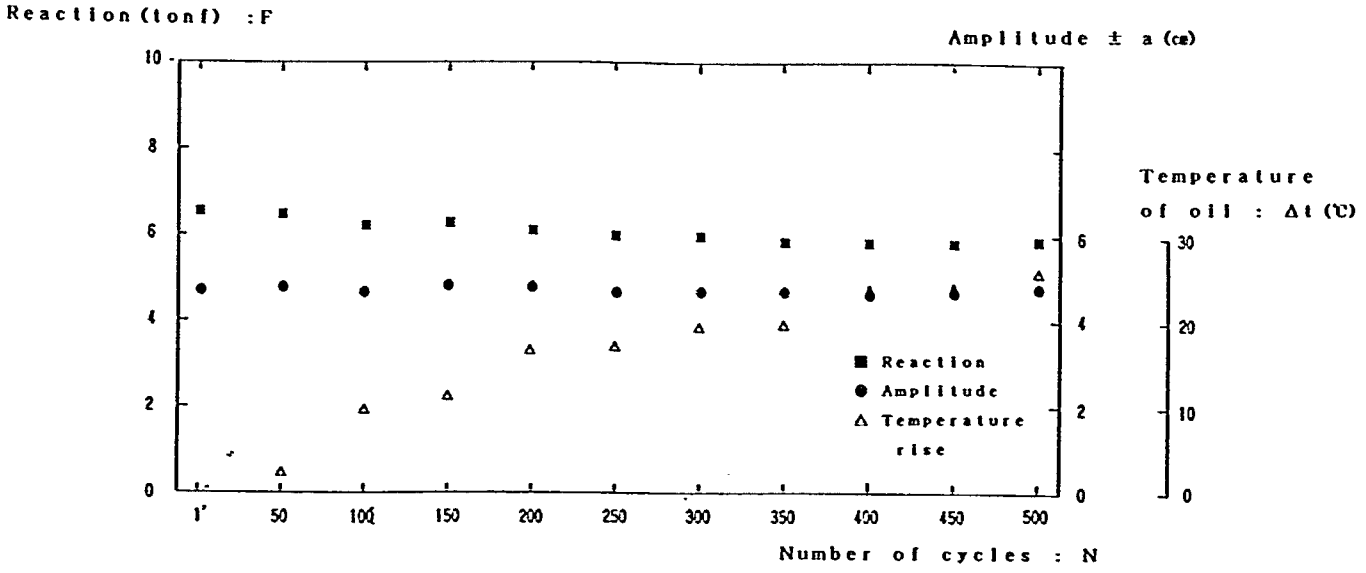


Fig 12. Results of Durability Test

Seismic Performance and Retrofit of the Golden Gate Bridge

Charles Seim, P.E., F. ASCE[1], Tim Ingham, Ph.D., S.E.[2] and Santiago Rodriguez, P.E.[3]

Abstract

The Golden Gate Bridge has served for over fifty years as a vital transportation link connecting San Francisco with the area to the north. The Bridge is owned, operated, and maintained by the Golden Gate Bridge Highway and Transportation District (District). Immediately after the Loma Prieta earthquake, the District engaged T.Y. Lin International (TYLI) to perform seismic evaluation and retrofit studies of the bridge. These studies concluded that a major earthquake could cause severe damage to the bridge and a prolonged interruption of traffic.

The seismic retrofit studies consisted of the following five stages: 1) Evaluating the seismic risk and generation of site specific ground motions and response spectra, 2) defining performance levels and developing design criteria, 3) performing both linear and nonlinear seismic analyses, 4) developing conceptual retrofit designs, and 5) preparing construction plans and specifications. Stages 1 to 4 are completed. Stage 5 is in process and is scheduled to be completed at the end of 1994. Construction is expected to start in early 1995 extending over three years.

Introduction

One of the most renowned bridges in the world, the Golden Gate Bridge opened to traffic on May 28, 1937. Today, the suspension span is greatly admired for its aesthetics as well as the technology of its design. At the time of its design and construction in the 1930s, it set new standards for the engineering of long-span bridges. Until 1964, the bridge had the

[1]Senior Principal, T.Y. Lin International, 825 Battery Street, San Francisco, CA 94111

[2]Senior Project Engineer, T.Y. Lin International, 825 Battery Street, San Francisco, CA 94111

[3]Project Engineer, T.Y. Lin International, 825 Battery Street, San Francisco, CA 94111

longest span of any structure in the world. It is still a famous landmark bridge and stands as the very symbol of the City of San Francisco. The design and construction of the Bridge is well documented in the Chief Engineer's final report [3].

The 2790m overall length of the Golden Gate Bridge consists of a number of different structure types. The bridge's major components are the steel truss approach viaducts, the Fort Point steel arch, the concrete cable anchorage and anchorage housings, the concrete pylons and the steel suspension bridge. All of the foundations for these structures except the northern viaduct are supported directly on rock.

The 1280m suspension bridge span is designed using a sag-to-span ratio of 1-to-9 for the main cable. This ratio requires towers 227m high to support the length of the span. The 1-to-9 ratio 'fits' the setting of the bridge, emerging as it does from hills on both sides of the strait, poised majestically between the Bay and open ocean. Visitors viewing the crossing from the south or north end vistas are uniformly impressed by the beauty of this structure from virtually every angle of sighting.

The four struts above the roadway vary in depth and spacing, being thinner and closer together with height. The two top struts are each approximately 6.7m deep and the lower two are approximately 9.1m deep, giving a ratio of about 1 to 1.36. From the tower top down to the roadway, the vertical strut spacing ratios are 1, 1.1, 1.3, and 1.4, respectively.

A lateral bracing system was added as wind retrofit in 1954. The vertical suspenders were replaced in the mid 1970s. The original concrete deck was replaced in 1985 with a lightweight orthotropic steel deck with a net reduction in weight of about 11,000 tons.

The Loma Prieta earthquake that occurred at 5:04 pm on October 17, 1989 was rated at a magnitude of 7.1 and damaged buildings and bridges throughout the Bay Area. The Golden Gate Bridge was not instrumented, but appeared to be in an area where the bed rock acceleration was recorded at 0.08 of gravity. Immediately following the earthquake, the District engaged TYLI to perform a seismic evaluation and retrofit studies of the bridge. Subconsultants Imbsen & Associates, Inc. and Geospectra, Inc. were also engaged to add their expertise to the TYLI team. The results of the seismic evaluation were presented in *The Golden Gate Bridge Seismic Evaluation* [1] in November, 1990. The evaluation revealed that a major earthquake on a nearby segment of the San Andreas or Hayward Faults would likely cause severe damage to the bridge and could cause interruption of traffic and require significant repairs. The *Golden Gate Bridge Seismic Retrofit Studies* [2] included development and evaluation of concept retrofit measures as well as estimation of their construction costs and schedules.

Governor's 1989 Board of Inquiry

Following the October 1989 Loma Prieta earthquake, the Governor of California appointed a *Board of Inquiry* to investigate the causes and effects of the damage sustained in other Bay Area structures and to recommend methods to prepare for a major earthquake. The Board of Inquiry, chaired by George W. Housner, issued its report, *Competing Against Time* [4], in May 1990. On June 2, 1990, the Governor issued *Executive Order D-86-90* which mandated State agencies to implement all the major recommendations of the report.

A number of recommendations and findings of the Report are particularly pertinent to the evaluation and retrofit of the Golden Gate Bridge. The report and the Governor's Executive Order specifically refer to the vital importance of the Golden Gate Bridge in the Bay Area transportation system because it is an "essentially nonredundant system having no satisfactory alternative."

Seismic Risk and Ground Motions

The determination of seismic risk and site specific ground motions was based on evaluations of the geology and topography of the area surrounding the bridge site, seismic risk analyses, and computer simulations of ruptures on nearby faults. The results of these studies are presented in Geological, Geotechnical and Ground motion studies for seismic retrofit of the Golden Gate Bridge in July, 1992 [5] by Geospectra, Inc., Richmond, CA.

Seismic risk was evaluated by applying a probabilistic assessment of ground motion using the maximum expected earthquake values assigned to the two main faults, the San Andreas and the Hayward, with a magnitude of 8.5 and 7.3 respectively. The peak ground acceleration estimated for a maximum credible event comparable to the 1906 San Francisco earthquake is 0.65g. Site-specific response spectra were developed on the basis of these seismic risk analyses.

Ground Motion Synthesis

The seismic signals from a major earthquake can be divided into three portions:

1. The *onset of motions portion*, triggering the recording instruments.
2. The *peak amplitude portion*, subjecting the structure to strong ground shaking.
3. A much longer *coda portion* of lower-amplitude shaking during which the surface waves and various reflection waves arrive. In the case of magnitude 8 earthquakes, the coda portion may last up to about 80 seconds.

Seismic evaluation of flexible or lightly damped structures such as long-span bridges requires careful consideration of the coda portion. The response of such structures at higher (short-period) modes are excited by the peak amplitude portion of the accelerograms, whereas their lower (long-period) mode are excited by the longer-duration, long-period signals of the coda portion.

Multiple Support Ground Motion Synthesis

Ground motions for multiple support excitation contained proper estimates of the phase delays that are reflective of the wave velocity in the media in which they travel. The ground motion records also contained the proper degree of incoherency that reflects the rupture scenarios and wave travel media.

Seismic Performance Criteria

The seismic performance criteria for a retrofitted suspension bridge presents a compromise between available retrofit measures, constructibility constraints, user expectations, and cost. Current American seismic codes are based on saving life but not

necessarily the structure. The retrofit measures for the Golden Gate Bridge must preserve life and allow the bridge to be used immediately after the largest expected event, first for emergency vehicles and then for the toll paying general public. To guide the designers in developing the seismic retrofit measures of the Golden Gate Bridge, seismic performance criteria were developed based on preserving the use of the bridge after a major earthquake with limited amount of repairs required.

The bridge structures in their current configuration were analyzed first, finding that the structures would not meet the performance criteria. In fact, the structures were at risk of collapse. Retrofit measures were then developed to bring the structures into compliance with the performance criteria. This required the various bridge components capacities to be upgraded. A maximum ductility demand of 1.5 is allowed in general, for elements for which analytical evaluations or testing are not available.

Seismic Analysis

The seismic response of the Golden Gate Bridge Structures to strong earthquakes would be nonlinear due to large deformation effects and inelastic behavior. Only the most important sources of nonlinear behavior were considered in the analysis with the purpose of capturing the dominant behavior modes.

Due to the complexity of the Golden Gate Bridge Structures, the seismic analysis was performed with a combination of global and local models. A total of six global models were created, including the South Viaduct, the South Anchorage Housing, the Fort Point Arch, the Suspension Bridge, the North Anchorage Housing and the North Viaduct. Local models were developed for problematic areas such as the base of the main towers, the stiffening truss, and the horizontal struts between the towers' shafts.

Suspension Bridge

The characteristics of the suspension bridge which most significantly influence its seismic response and the analysis requirements related to those characteristics are summarized below.

Large Displacement Effects

The stiffness of the structure, which is provided mainly by the shape of the cable adjusted to the applied loads, is very sensitive to its geometry. The distortion of its geometry under applied loads causes its stiffness to change as the loads change.

A geometrically nonlinear analysis which considers large displacement effects is required to capture this behavior.

Multiple Support Excitation

Due to the large distance between supports, the ground motion will be different at each support. These differences are caused by both phase delays due to traveling waves and incoherence created by the travel media and the rupture scenario.

The multiple support excitation imposes relative displacements between the towers and the anchorage blocks that induce both static and dynamic stresses and displacements. The analysis must consider the multiple support ground motion in order to obtain the actual earthquake response.

For the Golden Gate Bridge project, additional analyses were performed under uniform support excitation, to evaluate the importance of the multiple-support excitation on the peak structural response. The purpose of these analyses was to provide data on the significance of the multiple support problem in the seismic performance of the bridge. The data revealed that there are some responses that are larger under uniform support excitations.

Dynamic Characteristics

Due to their dimensions and flexibility, suspension bridges have a long fundamental period of vibration. The seismic response for long period structures is characterized by large displacements and low seismic forces.

Obtaining the proper response for long period structures requires an adequate description of the earthquake's long period content. Acceleration time histories should be corrected to assure that they do not have a long period content due to a displacement drift which would cause an unrealistically high displacement response.

Although often ignored, secondary vibration modes with a shorter period make an important contribution to the seismic forces. In a response spectrum analysis based on a mode-superposition procedure, it is necessary to consider a very high number of vibrational modes in order to include the modes with a natural period in the range of the maximum spectral acceleration. The high modes have a small mass participation when compared with the total mass but may actually have a very large participation in the response of local elements such as the towers.

For example, in the seismic analysis of the Golden Gate Bridge, it was found that the first longitudinal mode for the towers, with a period of 1.4 seconds, contributed greatly to the towers' seismic forces. However, this mode is the 67th mode for the bridge as a whole and it would be overlooked in an analysis considering less than 67 mode shapes.

A time history analysis performed by direct integration of the coupled equations of motion avoids the problems associated with the mode-superposition method.

Material Nonlinearity

The main cables and suspenders of the Golden Gate Bridge respond to the maximum credible earthquake in the elastic range. Yielding of structural elements is confined to local areas such as towers, pylons and stiffening truss.

The current practice in earthquake engineering is to design for reduced earthquake loads. This practice is based on the assumption that if the structural members are detailed appropriately, they have significant reserve displacement capacity beyond the initial yielding. This approach has a strong theoretical and experimental basis for structures with fairly uniform distributions of such yielding elements. In the Golden Gate Bridge, however, the

structural steel components are not expected to yield significantly, however, the seismic studies of the reinforced concrete pylons suggest that they will yield.

The effects produced by the yielding of the reinforced concrete pylons in the Golden Gate Bridge were studied by comparing the results of two different analyses. In the first, the pylons were modeled as elastic members. In the second, the yielding in bending was modeled with elasto-plastic rotational springs. The results were very similar as far as global behavior. This fact indicates that an analysis considering elastic material behavior may give a very good estimate of the actual response, although material nonlinearities will be considered for final design.

Displacement Compatibility

Due to the long natural period suspension bridges have, the seismic displacements are large; on the same order of magnitude as the ground displacements. In addition to this, different parts of the structure are subjected to different ground motions thus creating large relative displacements at the expansion joints. When the relative displacement at an expansion joint reaches the maximum displacement capacity, the expansion joint closes and transmits impact forces. A joint closure changes the dynamic properties and the response of the bridge. Thus, it is necessary to consider these effects in the analyses by means of nonlinear gap elements.

Support Conditions

It is also important to watch for changes in the support conditions due to seismic forces. In the case of the Golden Gate Bridge, the towers are weakly anchored to the underlying reinforced concrete piers. For service loads, the towers can be considered to be fixed to the piers because the dead load produces compressive stresses which are not exceeded by the bending stresses due to wind loads. However, uplift of the towers can be expected in strong earthquakes. This uplift can significantly change the towers' response characteristics. The rocking motion of the towers actually reduces the seismic stresses at the towers but increases the deflections. The nonlinear rocking behavior was considered in the seismic analysis of the suspension bridge.

Because of these characteristics, conventional linear theory of structures provides a poor estimate of the structural response. The seismic evaluation of the Golden Gate Bridge was performed by using the analysis technology described in the following sections.

Structural Modeling

Several different mathematical computer models of the suspension bridge were studied. Two-dimensional models of the entire bridge were used for preliminary studies of response to vertical and longitudinal components of ground motions. Three-dimensional models of the entire bridge were used for final studies of response to all three components of ground motions. The underlying idea behind the modeling effort was to attain a global model as simple as possible but yet able to reproduce all the significant linear and nonlinear modes of behavior.

The global model was built with the help of more elaborate local models. A detailed

three-dimensional finite element model of the tower base region was used to study the stress distributions and moment-rotation relationships of this critical part of the bridge. Other local models included the stiffening truss, the horizontal struts between the tower's shafts, and the bridge approaches.

The global computer models include representations of all major structural components of the bridge: the main cables from anchorage to anchorage, the suspenders, the towers, the pylons and the tie-down cables inside, and the stiffening trusses. While most structural members are modeled explicitly, the suspended stiffening truss system is nevertheless modeled using superelements to reduce the size of the numerical problem. The three-dimensional model consisted of 903 nodes and 1,351 elements, which are assembled into a system of 3,030 simultaneous equations.

Analysis Technology

The analysis of the seismic response of the Golden Gate Bridge required the following three steps of increasing complexity: definition of the dead load state, modal analysis and response spectrum analysis assuming linear behavior, and nonlinear time history analysis, considering multiple-support ground motion.

Definition of the Dead Load State

The dead load state was defined starting with the geometry and dead load corresponding to the time the construction was completed. The dead load and the construction procedure determined the initial stresses. A static nonlinear analysis considering large displacement theory was performed to check equilibrium and to fine-tune the original geometry. The result of this analysis yielded the dead load state at the completion of construction.

The change in the structure's dead load due to the addition of the bottom lateral bracing system and the replacement of the deck were superimposed on the original dead load situation. The deformations and stresses of this dead load state, computed by geometrically nonlinear analysis, served as the initial conditions for the dynamic analyses.

The Newton-Raphson method, based on tangent stiffness iteration, was used for this static load analysis to account for the large displacement effects.

Modal Analysis

Once the dead load state was determined, a modal analysis was performed to compute the vibrational properties. The modal analysis assumes linear behavior for small deformations from the dead load state. The natural frequencies and mode shapes computed from the analysis were compared with the ones obtained from ambient vibration tests. This comparison provided a way to verify the computer models.

Following the modal analysis, a response spectrum analysis was performed for the maximum credible earthquake. The response spectrum analysis did not include the effects of the nonlinear behavior or the multiple support excitation. However, it gave an initial insight into the magnitude of the seismic forces, thus redirecting the modeling and analysis efforts towards the problematic areas.

Nonlinear Time History Analysis

The analyses of the global response of the bridge to multiple-support ground motion excitations were performed using a dynamic nonlinear finite element computer program, in which large displacement effects were considered by establishing the static or dynamic equilibrium of the structure in its deformed configuration. The effect of a limited displacement capacity at the expansion joints and the nonlinear uplifting behavior of the tower's bases was examined by using "gap" elements. The yielding of the reinforced concrete pylons was modeled with elasto-plastic rotational springs.

The nonlinear dynamic analyses were performed by integrating the coupled equations of motion in the time domain by using the acceleration implementation of the average acceleration method. This method is unconditionally stable and has second order accuracy. The ground motion excitation was applied as a time-varying displacement boundary condition at each of the supports. In each time step, the nonlinear system of equations relating the effective dynamic loads and the nodal accelerations was solved by using the Newton-Raphson method, based on tangent stiffness iteration. For some models, a modified Newton-Raphson Method that was based on constant stiffness iteration was also used.

Rayleigh damping was assumed, in which the damping matrix is proportional to a linear combination of the mass and stiffness matrices. The proportionality factors were computed to yield a damping ratio of 5% at periods of 0.5 seconds and 20 seconds. The damping ratios for periods between those two values are smaller, with a minimum of 1.5% at a period of 3 seconds. These values are consistent with ambient vibration measurements.

Viaducts and Fort Point Arch

The seismic behavior of the viaducts is less complicated than that of the suspension bridge due to their structural type and dimensions. The large displacement effects can be neglected and a uniform support ground motion gives a good estimate of their seismic response. The structural components have little ability to withstand deformations beyond those which cause yielding or buckling and a linear elastic analysis gives a good estimate of the seismic deficiencies. The viaducts and the arch were modeled as a three dimensional frame structure.

Anchorage Housings

The North and South Anchorage Housings are building-type reinforced concrete structures which consist of exterior reinforced concrete walls braced with pilasters, internal reinforced concrete moment frames supporting the roof, and the reinforced concrete roof slab itself. Linear elastic analysis were performed to assess the ductility demand of the as-built and retrofitted structures.

Vulnerabilities and Retrofit Proposals

The proposed retrofit measures include both tuning the structures, i.e., adjusting the local and overall response of the existing structures so they can better respond to strong ground motions without damage, and strengthening the structures to minimize the damage caused by the structures' responses to strong ground motion.

Suspension Bridge

The vulnerable areas for the suspension bridge and the proposed retrofit are:

1. Connection between Stiffening Trusses and Towers: Impact between the main span stiffening trusses and the towers is predicted since seismic displacements exceed the existing displacement capacity. The proposed retrofit includes the installation of dampers at this location.
2. Reinforced Concrete Pylons: New ductile concrete walls inside the pylons are proposed to increase strength and ductility.
3. Main Towers: Uplift due to rocking motion of the tower would cause high contact stresses at the toe of the uplifting base, requiring strengthening of the steel plates. Because uplifting of the tower bases improves the global seismic performance, it will not be prevented with the retrofit.
4. Side Span Stiffening Trusses: There are high tension and compression stresses in the chords of the side span stiffening trusses. A local nonlinear model of a chord member shows that the required ductility of two is attainable.
5. Piers: The piers supporting the main towers are subjected to high bearing stresses under uplift conditions. The installation of post-tensioning tendons at the top of the piers to provide confinement is proposed.
6. Cable Saddles: The connections of the cable saddles to the tower tops need to be strengthened for shear stresses due to differential cable tension.
7. Deck Panels: The connections of the orthotropic steel plate deck panels to the floor beams need improvement due to high horizontal shear forces.

Viaducts and Fort Point Arch

The retrofit proposal for the viaducts includes replacing the existing cast steel bearing shoes with seismic isolators, connecting each truss span to its adjacent span, strengthening the girders of the plate girder spans, strengthening the chords and diagonals of the truss spans, strengthening bents and their footings, and strengthening the connections between the existing orthotropic steel deck panels and the floor beams.

The proposed retrofit measures for the Fort Point Arch consist of member strengthening, including rib chord members, spandrel columns, and the chords of the trusses below deck level, retrofitting of the inner rib deck truss, installation of new sway bracing members between the inner and outer ribs, installation of energy dissipators, installation of bearing tie-downs, and strengthening of the connections between existing orthotropic steel deck panels and the floor beams.

Anchorage Housings

The anchorage housings have high ductility demands, but they lack the necessary confinement reinforcement to provide ductility. The proposed retrofit measures include installation of new internal framing and shear walls, strengthening the connections between the existing walls and the floor and roof diaphragms, and reinforcing the foundations.

Seismic Deficiencies to Avoid in a New Design

Advances in seismology have also given the engineering community a better understanding of seismic risk. There is more information available regarding ground motions during strong earthquakes and it is thus possible to generate site-specific synthetic ground motions according to local geological conditions. In spite of these advances, there are still many uncertainties regarding the description of future ground motions since they depend on geotechnical conditions that can never be perfectly ascertained, and may be caused by sources which may not previously be known. The long term structural behavior may also be affected by unforseen service conditions or by the degradation of structural materials.

In order to increase the overall seismic performance under unforseen circumstances, suspension bridges should be designed taking into consideration their seismic behavior beginning with the conceptual stages. In addition to providing adequate strength for the predicted seismic forces, the design should be based on the following principles:

1. Ductility: The structural elements, connections and components should be detailed to achieve ductility and avoid brittle failure. The connections should exceed the capacity of the members and yielding should occur before either local or global bucking. The hysteresis behavior of a ductile structure provides an energy dissipation mechanism which minimizes the probability of member failure or collapse.

2. Redundancy: Alternative load paths should be provided so that the structure can adjust to loads larger than expected by redistributing the load.

3. Displacement Compatibility: A suspension bridge consists of elements with different vibrational properties such as cables, stiffening girder, towers, and anchor blocks. The *interface* between different elements may have large relative displacements. The design must address this by either leaving enough free space or by keeping the connections between different elements to a minimum. Energy absorption devices such as dampers provide the option of controlling differential displacements but must always include a fail-safe mechanism.

Conclusion

The seismic retrofit studies for the Golden Gate Bridge have shown that all of the structure types can be adequately analyzed; retrofit measures can be developed, designed and constructed to provide adequate capacity to resist the demands from a major earthquake occurring on the San Andreas fault.

Contract plans and retrofit designs are in preparation and are expected to be completed in late 1994. The three year construction period is scheduled to start in early 1995.

The seismic retrofit studies for the Golden Gate Bridge have also provided a methodology which can be applied to the seismic design of other major crossings. These methodologies consisted of an evaluation of the seismic risk, a generation of site specific ground motions, a definition of performance levels and design criteria, and finally a seismic analysis.

Important factors to consider in the analysis of suspension bridges are: large displacement effects, multiple support excitation, dynamic characteristics, material nonlinearity, the displacement compatibility and support conditions.

The retrofit design must provide for adequate ductility, redundancy and must at the same time insure displacement compatibility between different elements.

Acknowledgements

All of the Golden Gate Bridge studies summarized in this paper were made under the direction of the Golden Gate Bridge Highway and Transportation District. The authors wish to thank the General Manager Carney Campion, District Engineer Daniel Mohn, and Deputy District Engineer Mervin Giacomini for their support.

REFERENCES

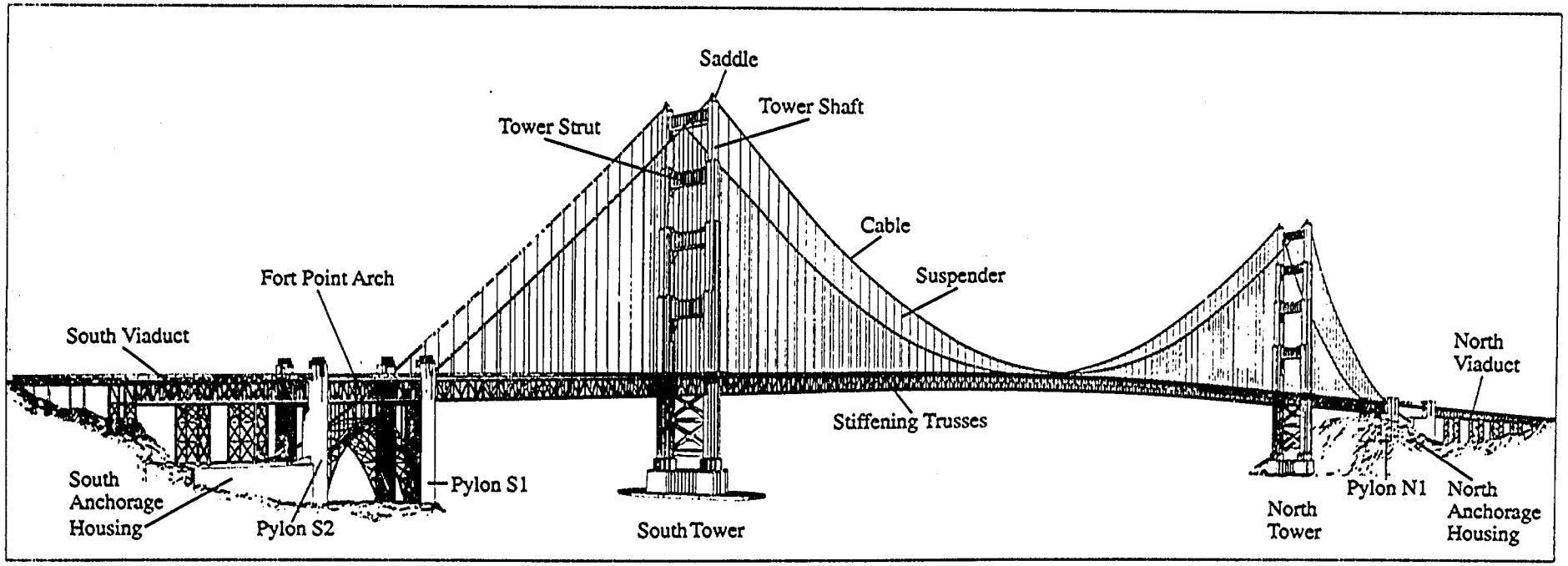
1. Ketchum, M.A. and Seim, C., Golden Gate Bridge Seismic Evaluation, T.Y. Lin International, Golden Gate Bridge, Highway and Transportation District, San Francisco, CA, November 1990.

2. Ketchum, M.A. and Seim, C., Golden Gate Bridge Seismic Retrofit Studies, T.Y. Lin International, Golden Gate Bridge, Highway and Transportation District, San Francisco, CA, July 1991.

3. Strauss, J., The Golden Gate Bridge: Report of the Chief Engineer to the Board of Directors of the Golden Gate Bridge and Highway District, California, 1937, San Francisco, California, Golden Gate Bridge and Highway District, 1938.

4. Housner, G.W., et.al., Competing Against Time, Report to Governor George Deukmejian from the Governor's Board of Inquiry on the 1989 Loma Prieta Earthquake, State of California, Office of Planning and Research, May 31, 1990.

5. Geological, Geotechnical and Ground Motion Studies for Seismic Retrofit of the Golden Gate Bridge, Geospectra, Inc., Golden Gate Bridge, Highway and Transportation District, San Francisco, CA, July 1992.


Saddle
Tower Shaft
Tower Strut
Cable
Suspender
Fort Point Arch
South Viaduct
North Viaduct
Stiffening Trusses
South Anchorage Housing
Pylon S2
Pylon S1
South Tower
North Tower
Pylon N1
North Anchorage Housing

Lateral-Load Response Models of a Reinforced Concrete Bridge

Marc Eberhard
Assistant Professor
University of Washington
Department of Civil Engineering
Seattle, WA 98195
U.S.A.

ABSTRACT

Destructive lateral-load tests of a three-span reinforced concrete bridge were conducted. These tests provided the opportunity to compare measured response with that predicted by various analytical models. On the basis of these comparisons, modeling recommendations are proposed.

INTRODUCTION

Seismic design requirements have changed dramatically since the 1950s and 1960s, when much of the United States interstate highway system was constructed. Bridges built during that period rarely satisfy the prescriptive detailing regulations of modern codes. In comparison with current requirements, common deficiencies in piers of that period include (1) bridge columns that have too little confinement reinforcement, (2) reinforcing splices between the column reinforcement and footing dowels that are too short and are unconfined, and (3) lack of top reinforcement in footings.

To decide whether to retrofit a brittle pier, an engineer needs to estimate the lateral displacement to which the pier is likely to be subjected and the displacement at which the pier will be damaged. Preferably, both of these estimates should be made with models that have been calibrated on the basis of measured response. The opportunity to perform such a calibration was provided by destructive lateral-load tests of a three-span, reinforced-concrete bridge.

DESCRIPTION OF BRIDGE

WSDOT constructed the three-span, reinforced concrete bridge in 1966. The two end spans were 41-feet long, and the center span was 60-feet long (Fig. 1). The abutments and intermediate piers were skewed by 12.8 degrees.

Each abutment consisted of two wingwalls and a combination diaphragm/endwall, which was supported by bearing pads and polystyrene, as illustrated in Figure 2. The bearing pads, polystyrene, and soil contributed to transverse resistance of the abutment. The soil resistance was expected to be large because the superstructure, endwall and wingwalls were monolithic and heavily reinforced.

Each pier consisted of a crossbeam and two 3-foot diameter columns, which were supported on spread footings. Compacted fill surrounded the 25-foot high columns to a height of approximately 12 feet (Fig. 1). A typical pier is shown in Figure 3. The bridge's details are provided in Reference (1)

DESCRIPTION OF TESTS

A first series of static tests (Phase I) focused on the response of the entire bridge, including the superstructure, piers, and abutments. A second phase of static tests (Phase II) focused on the vulnerability of a pair of piers to large, transverse displacements. Concurrent with the static tests, dynamic tests were performed on the structure. This paper discusses only the Phase I static tests and the associated analysis.

During Phase I, researchers imposed six cycles of transverse displacement on the bridge (Fig. 4) by applying loads to the crossbeams of the intermediate bents. The loading system consisted of four principal components: prestressing cables, harnesses, jacking frames and deadmen anchors, as shown in Figure 5. To distribute the load from the cables to the pier, a steel harness was installed on the ends of each crossbeam. Each set of cables was pulled by two hydraulic rams that were installed in a jacking frame located at ground level. Reactions were provided by a second set of prestressing cables that was anchored by a deadmen anchor (one for each loading system). In the horizontal plane, all components of the load train were aligned along the 12.8-degree skew of the bridge. In the vertical plane, components were aligned at an angle of 14 degrees below the horizontal, corresponding to a 4 to 1 slope. The magnitude of the load at each bent was controlled such that the displacements of the bents would be approximately equal.

The first cycle, Test P, was a preliminary test during which researchers checked the loading system and instrumentation without damaging the bridge. The following two cycles, denoted as Test I, had a target bent displacement of 0.15 inches, which corresponded to a drift ratio of 0.05 percent. During Test II, researchers applied the maximum load that could be applied safely with the loading system. This 800-kip force was equal to 65 percent of the superstructure's weight.

The final two tests, EXC and ISO, were conducted to determine the resistance provided by the soil and the bearing pads at the abutments. Test EXC was conducted after the soil behind the wingwalls and along the abutment endwall had been removed. After Test EXC, the abutment endwalls were lifted, and researchers replaced the bearing pads and expanded polystyrene with nylon blocks that rested on greased, polished, stainless-steel plates. The nylon block/steel plate combination was selected to minimize the abutment's resistance. The final cycle, Test ISO, was conducted to measure the resistance of the bents. The stiffness of the soil and pads could be estimated by comparing the results of Tests EXC and ISO with the results of the previous tests.

The researchers measured the applied load; transverse displacements of the piers and abutments; and longitudinal displacements of the four corners of the bridge. Forty-four instruments measured the relative rotations of critical beam and column cross-sections. Additional instrumentation monitored footing translation and rotation for the west pier. The electronic instruments were connected to a data acquisition system located in a trailer near the bridge.

RESPONSE OF BRIDGE

The bridge in its initial state was extremely stiff, as can be seen in Figure 6. In two cycles to a load equal to 45 percent of the bridge's weight, the maximum bridge displacement was 0.15 inches. For a column height of 25 feet, this displacement corresponded to a drift ratio of 0.05 percent. Displacements were recovered fully upon

unloading. Damage in this test was limited to minor flexural cracking at the tops of the columns.

At a load equal to 65 percent of the bridge weight, the pier displacement corresponded to a drift ratio of 0.10 percent. At this load, the stiffness decreased abruptly. This decrease coincided with the formation of a 0.10-inch wide crack in the north-east wingwall. For the three half cycles of Test II, the secant stiffness of the pier-displacement response ranged from 25 to 50 percent of the initial stiffness. Upon unloading, deck deflection was fully recovered, but most of the abutment displacement was not recovered. In Test II, cracking increased at the tops of the columns, but cracking was not visible at the column bases.

After the bridge had been excavated (Test EXC), the stiffness reduced to 15 percent of its initial stiffness (Cycle IS1). The stiffness reduced further to 8 percent of the initial stiffness after the superstructure had been isolated from the abutments (Test ISO). No new damage was observed during tests of the bridge in its excavated and isolated conditions.

ANALYTICAL MODELS

To better understand the lateral-load response of the bridge, the researchers created a series of nonlinear models for the initial, excavated, and isolated conditions (UW models). These models were developed on the basis of the structural plans and the measured material properties. The UW models were compared with the observed response and with finite-element models developed by the California Department of Transportation (CALTRANS) and Washington State Department of Transportation (WSDOT). The CALTRANS and WSDOT models were more objective than the UW analyses because the engineers in these agencies were not aware of the measured response. Also, the CALTRANS and WSDOT analyses were more representative of standard practice because their engineers were not aware of the measured material properties.

UW Model

To perform nonlinear analysis, the researchers combined a series of linear SAP90 analyses (2). The step-by-step combination process was implemented by a Basic computer program. A schematic of a typical finite-element model is shown in Figure 7. Equal horizontal loads were applied along the skew to each pier crossbeam. A total of 278 beam elements modeled the girders; curb and railing; crossbeams; and columns. The bases of the columns were fixed. A total of 444 four-node, shell elements modeled the bridge deck, end diaphragms, and wingwalls.

Initial properties of the reinforced concrete sections were calculated on the basis of gross sections and an elastic modulus of 4,600 ksi. The strength of the wingwall was calculated based on the measured material properties of the concrete and steel. The unit weight of the concrete was assumed to be 150 pcf.

The analyses reflected the expected nonlinear behavior of the bearing pads, polystyrene, isolation system, columns, and wingwalls. Initial friction from the soil behind the abutment endwalls was modeled as perfectly plastic. Linear springs modeled soil compression behind the abutment endwalls, behind the wingwalls, and around the bottom half of the columns. The stiffness of the springs near the columns was the secant stiffness corresponding to the maximum pier displacement.

CALTRANS Model

CALTRANS created a linear finite-element model of the bridge. The model was composed entirely of beam elements and linear springs. Model dimensions were determined from the bridge plans, and the abutment skew was modeled. Gross section properties were assumed. The soil around the base of the columns was not modeled. The resistance of the bearing pads, polystyrene, and soil friction was neglected. To account for possible instability of the soil sloping away from the abutments, only two-thirds of each wingwall was assumed effective in resisting transverse loads.

WSDOT Model

WSDOT also created a linear finite-element model of the bridge. The WSDOT model was similar to the CALTRANS model in that it was composed entirely of beam elements and linear springs. Model dimensions were derived from the bridge plans. The abutment skew was not modeled. Gross-section properties were used in the WSDOT model.

The pier crossbeam and diaphragm were modeled as a single beam. WSDOT modeled only one wingwall to account for the instability of the soil sloping away from the abutments; the contribution was reduced further to only one-third of a wingwall because of the flexibility of the wingwalls. The resistance provided by the bearing pads, polystyrene, and soil friction were neglected.

CALCULATED DISPLACEMENT RESPONSE

Along with the measured load-displacement response for cycles ISOS1, ISON1, EXN1, and IS1, Figures 8, 9 and 10 show the calculated response for the UW, CALTRANS, and WSDOT models. In these figures, the vertical axis is the horizontal component of the total applied load.

The calculated response of the UW model provided a good fit to the measured response of the isolated piers (Fig. 8). The CALTRANS and WSDOT models predicted load-displacement slopes that were 65 and 68 percent, respectively, of the measured slopes.

For the excavated bridge, the UW model was too stiff (Fig. 9). The model indicated that the polystyrene slipped at a total applied load of approximately 200 to 220 kips. The observed reduction in slope of the measured response occurred at a lower load, in the range of 100 to 175 kips. The abutment and bent load-displacement slopes for EXCN1 were 253 and 194 percent, respectively, of the measured values.

All of the analytical models underestimated the stiffness of the bridge in its initial state (Fig. 10). The UW model predicted slip of the polystyrene at an applied load of approximately 320 kips. Though the model predicted a large reduction in stiffness at this load, no such reduction was observed in test IS1. The load-displacement slopes of the UW, CALTRANS, and WSDOT models for cycle IS1 varied from 11 to 62 percent of the measured values.

CALIBRATION OF UW MODEL

In general, if an analytical model is complex, one can easily modify it to reproduce a few measured load-displacement relationships. However, the validity of such a calibration is difficult to establish, because several sets of modifications may

result in similar calculated response. Fortunately, in developing "UW modified" models, the calibration procedure was not arbitrary. The following goals guided the model calibration:

(1) The model should reproduce the measured load-displacement relationship for the isolated piers.

(2) For the excavated bridge, the model should reproduce the pier load-displacement relationship.

(3) For the excavated bridge, the model should reproduce the abutment load-displacement relationship.

(4) For the bridge in its initial state, the model should reproduce the pier load-displacement relationship.

(5) For the bridge in its initial state, the model should reproduce the abutment load-displacement relationship.

(6) The model should predict cracking at the top and bottom of the columns that is consistent with that observed in the test.

(7) The model should predict wingwall failure at a load and displacement that is consistent with that observed in the test.

(8) Only model parameters that have large uncertainty should be modified to reproduce response.

Isolated Conditions

The measured load-displacement response and the observed damage agreed well with those the UW model predicted. Therefore, the researchers did not modify the UW model of the isolated bridge.

Excavated Conditions

Whereas the UW model of the isolated bridge reproduced the observed behavior well, the excavated model was too stiff, particularly for small displacements. The resistance of the abutment bearing pads and polystyrene was the only difference between the UW models for the excavated and isolated conditions. Therefore, it is likely that the model overestimated the resistance the polystyrene and bearing pads provided. Of the two components, it most likely the polystyrene resistance was overestimated because the properties of the polystyrene were the most uncertain.

The UW model was modified by halving the coefficient of friction for the polystyrene. The calculated response from the UW modified model of the excavated bridge provided a good fit to the measured response throughout the load history (Fig. 9). For this model, the polystyrene slipped at a total applied load of approximately 100 kips. The calculated abutment and bent load-displacement slopes were within 15 percent of the measured values.

Initial Conditions

For the bridge in its initial state, the UW models were too flexible, particularly for loads larger than 350 kips. The halving of the polystyrene friction (to fit the excavated bridge response) further reduced the stiffness of the model and, correspondingly increased the discrepancy between the measured and calculated responses. To match measured response, the stiffness of one or more components had to be increased.

The only differences between the UW bridge models for the excavated and initial conditions were; the amount of pier column cracking (in cycle IS1, the columns were assumed to be uncracked initially); and the stiffness of the soil at the abutments. It was not reasonable to resolve the discrepancy by increasing the stiffness of the bents because the bent behavior was modeled successfully in cycle ISO. Further, the bent stiffness was too small to greatly affect the calculated response for the bridge in its initial state.

The amount of soil friction was not a good candidate for modification either. Though soil friction is accompanied with great uncertainty, an increase in soil friction would primarily affect the calculated response for small displacements. In contrast, the discrepancy was largest for large displacements.

An underestimate of the stiffness of the soil behind the wingwalls and abutment was a more reasonable cause of the discrepancy in cycle IS1. The original UW model was based on Douglas and Davis (3) solution for a rigid plate that was free to rotate. In the field, the wingwall and endwall rotation was restrained. Further, the model depended on the laboratory measurement of compressive modulus of the soil, E_S. The measured E_S was surprisingly low for a silty sand with an internal angle of friction equal to 38 degrees. It is likely that soil disturbance resulted in a low value of E_S. To model the bridge without using E_S, the researchers followed recommendations proposed by Bowles (4). For a medium-dense silty sand, Bowles suggested that a typical value for the modulus of subgrade reaction, k_S, is 175 lb/in.^{3} (4). This choice of k_S increased the stiffness of the soil at the wingwalls and endwalls by an order of magnitude from that of the UW model.

The calculated response from the UW modified model for the bridge in its initial state provided a good fit to the measured response, particularly at the abutments. The model predicted slip of the polystyrene at an applied load of approximately 240 kips. Consistent with the observed response, there was not a great decrease in stiffness at this load. The UW modified model abutment load-displacement slopes were within 7 percent of the measured values. The UW modified model bent load-displacement slopes were within 25 percent of the measured slopes.

DISCUSSION

Important parameters from the UW, UW modified, CALTRANS, WSDOT, and UW simplified finite element bridge models are summarized in Table 1. Significant differences among the models include the abutment stiffness, bent stiffness, superstructure flexural rigidity, EI, and rotational resistance at the abutments.

The UW, CALTRANS and WSDOT models underestimated the stiffness of the bridge in its initial state (Cycle IS1). It is likely that the UW model overestimated the resistance of the polystyrene at the abutments and underestimated the stiffness of the soil at the wingwalls. The CALTRANS model was too flexible because the resistance

of the bearing pads and polystyrene was neglected. The WSDOT model was too flexible because the resistance of the bearing pads and polystyrene was neglected; and the soil stiffness was underestimated.

CONCLUSIONS

Recommendations must be tempered by acknowledging some of the tests' limitations. During the tests, a slowly varying, transverse load was applied to the bridge. In reality, earthquake response involves higher loading rates; and longitudinal, vertical, and torsional ground accelerations. In addition, since only one bridge was tested, the reproducibility of the results was not established. Nevertheless, the test results provide a good benchmark with which to calibrate analytical models.

An engineer needs reliable estimates of abutment stiffness to decide whether piers should be retrofitted. If one neglects components that provide substantial resistance, such as the polystyrene, the evaluation may be unnecessarily conservative.

For abutment configurations similar to that of the test bridge, the calculated abutment stiffness depends greatly on the estimated soil stiffness. When combined with simple soil tests, relatively simple models provided reasonable estimates of soil stiffness for the test bridge. In this study, soil stiffnesses for the wingwalls were calculated using a tabulated modulus of subgrade reaction. The soil resistance at the columns was modeled as if the column was a pile. Complex methods of modeling the soil resistance may not be justified if soils test data is not available.

Even for relatively low loads, some bridge components have nonlinear force-deflection relationships. Column cracking; bearing pad and polystyrene resistance; soil friction; and soil compression are example of such nonlinear phenomena. Though the benefits of performing nonlinear analysis may not outweigh its costs, the analyst should be aware of these nonlinear effects.

ACKNOWLEDGMENTS

Tom O'Donovan directed site construction activities. M. Lee Marsh was in charge of instrumentation and data acquisition. Jeff MacLardy and Gaukur Hjartarson performed much of the analyses presented in this paper. Special thanks are given to H. Coffman of WSDOT, as well as J. Gates, T. Cartner, and G. Reyes-Gutierrez of CALTRANS for providing independent analyses of the bridge.

The project was funded primarily by the WSDOT and the Federal Highway Administration. E. Henley served as the technical contact at the WSDOT Office of Bridges and Structures.

REFERENCES

1. Eberhard, M.O., Marsh. M.L., O'Donovan, T.O. and Hjartarson, G., "Lateral-Load Tests of a Reinforced Concrete Bridge," *Transportation Research Record*, No. 1371, March, 1993, pp 92-100.

2. Wilson, E.L. and Habibullah, A., "Sap90 Users Manual," Computers and Structures, Berkeley, California, 1989.

3. Douglas, D.J. and Davis, E.H., "The Movement of Buried Footings Due to Moment and Horizontal Load and the Movement of Anchor Plates," *Geotechnique*, vol. XIV, no. 2, June, 1964.

4. Bowles, J.E., *Foundation Analysis and Design*, 3rd edition, McGraw-Hill Book Company, 1988.

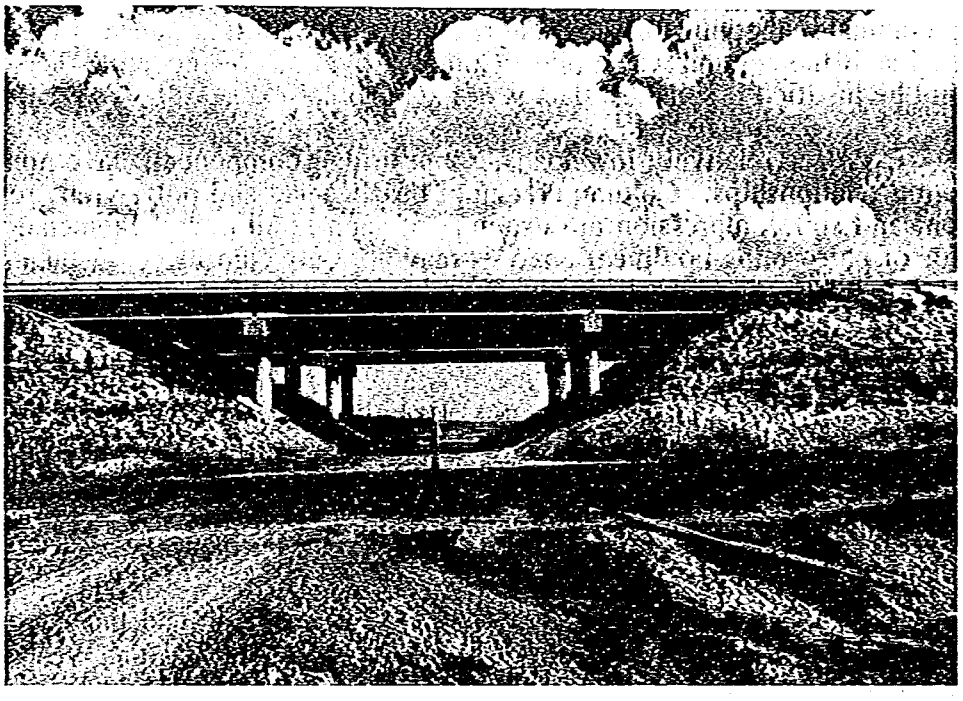


Figure 1. Photograph of Bridge

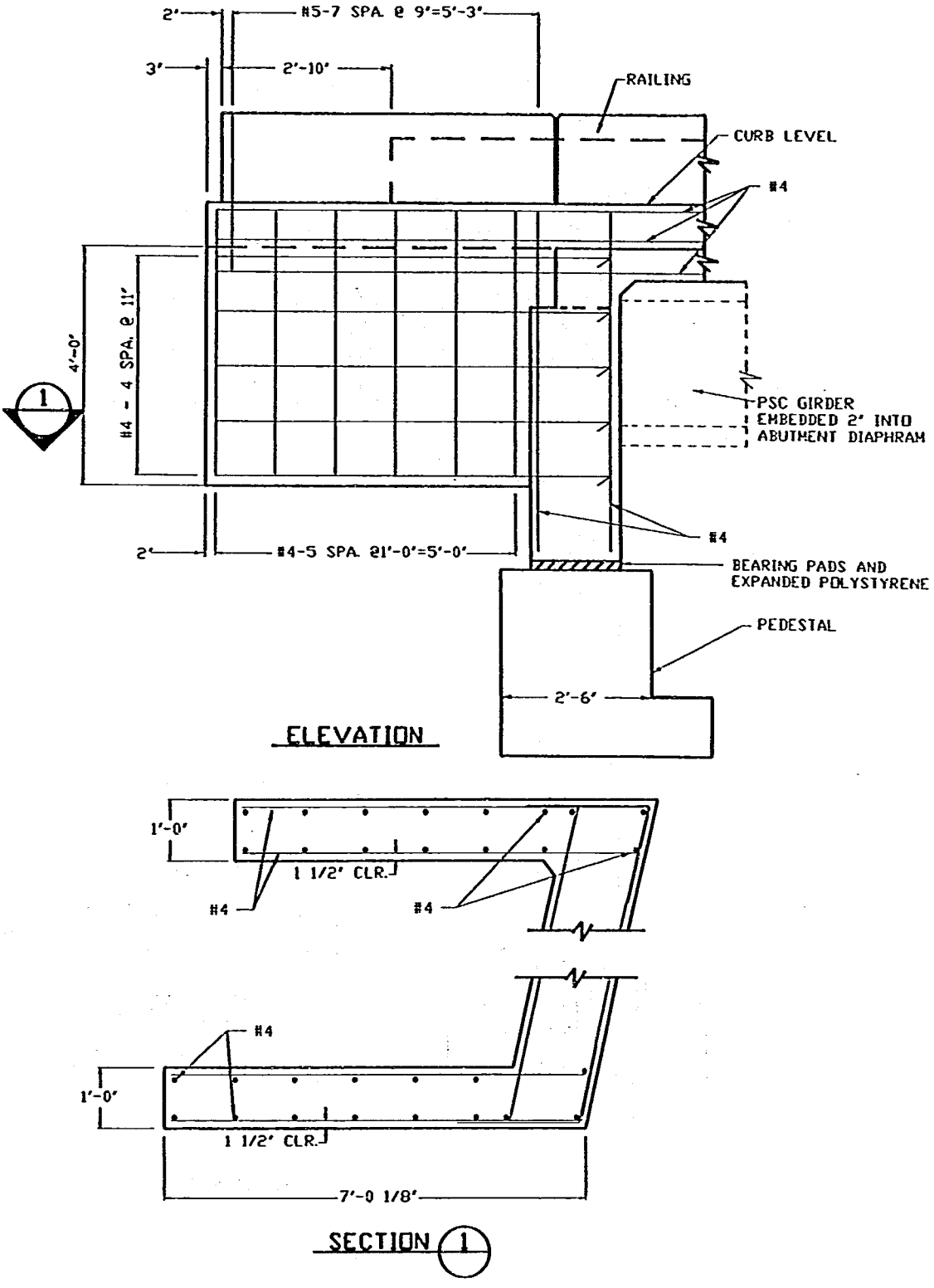


Figure 2. Abutment Detail

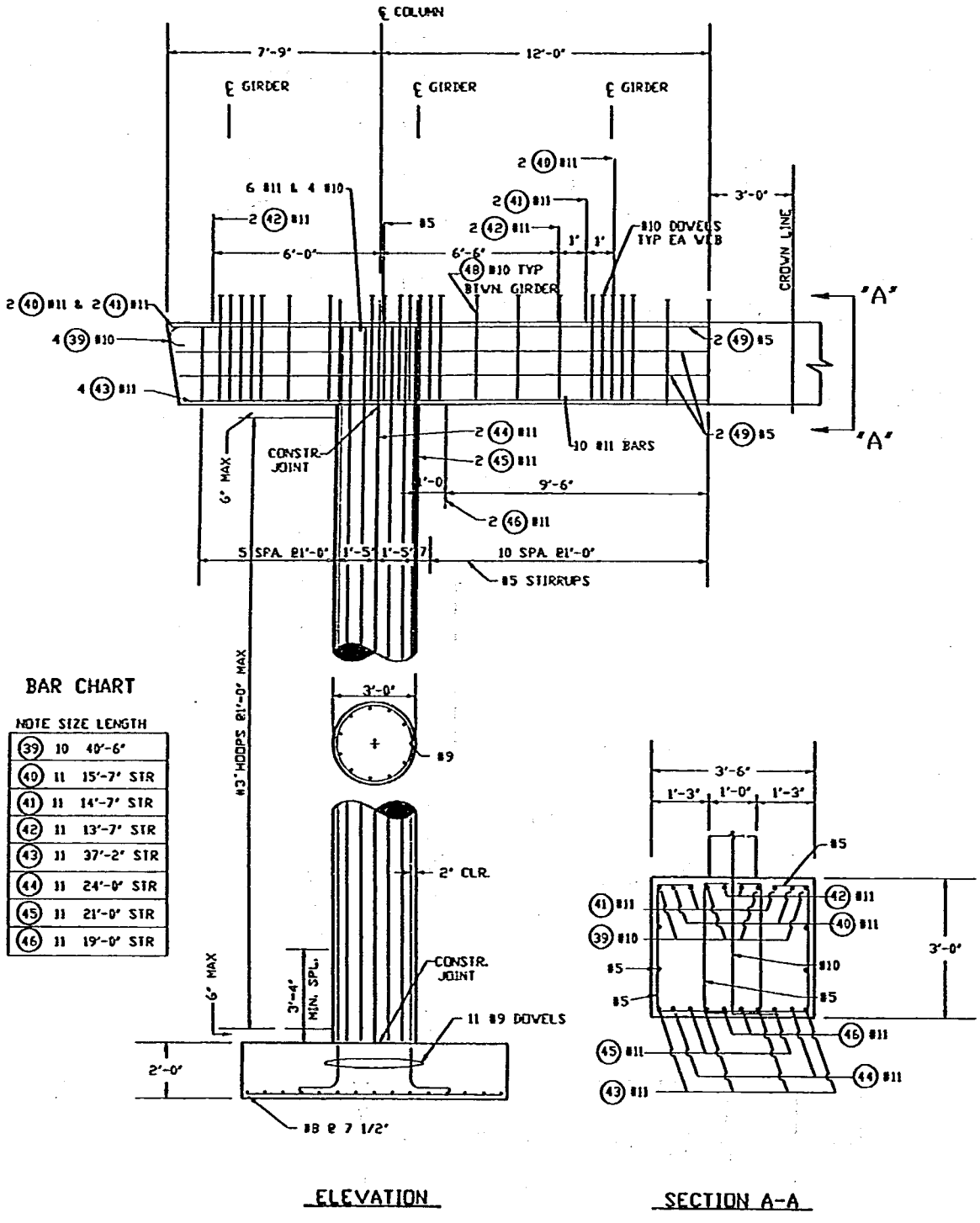


Figure 3. Pier (Bent) Detail

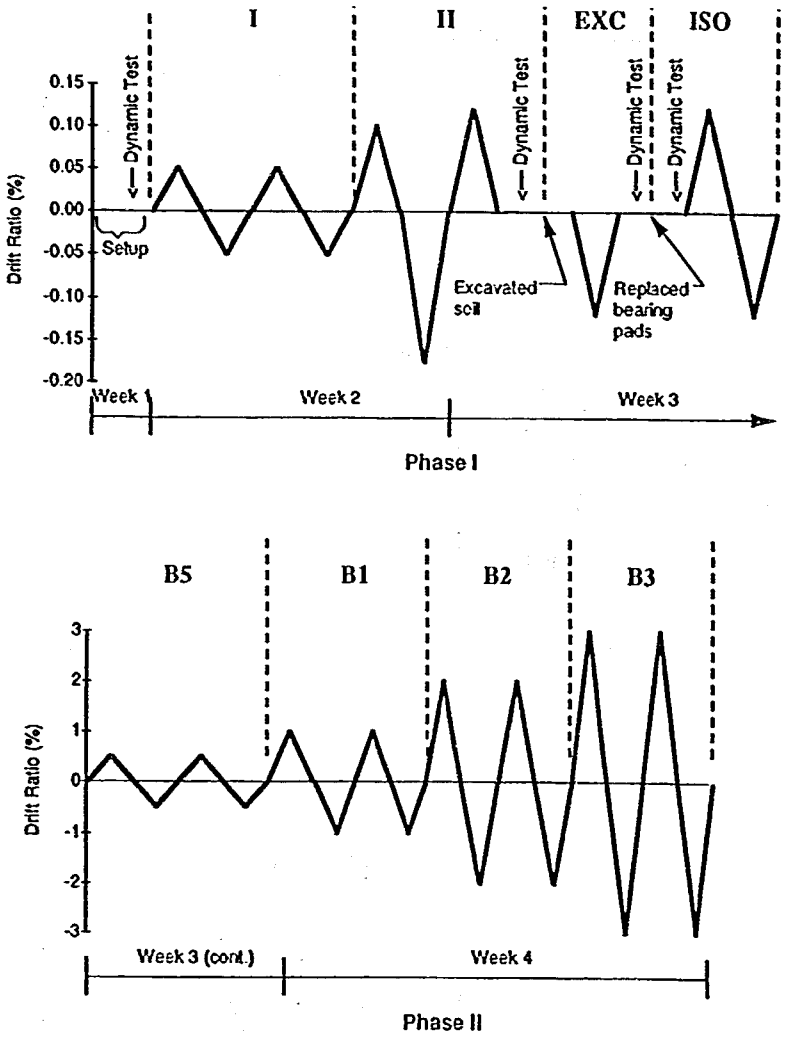


Figure 4. Imposed Displacement History

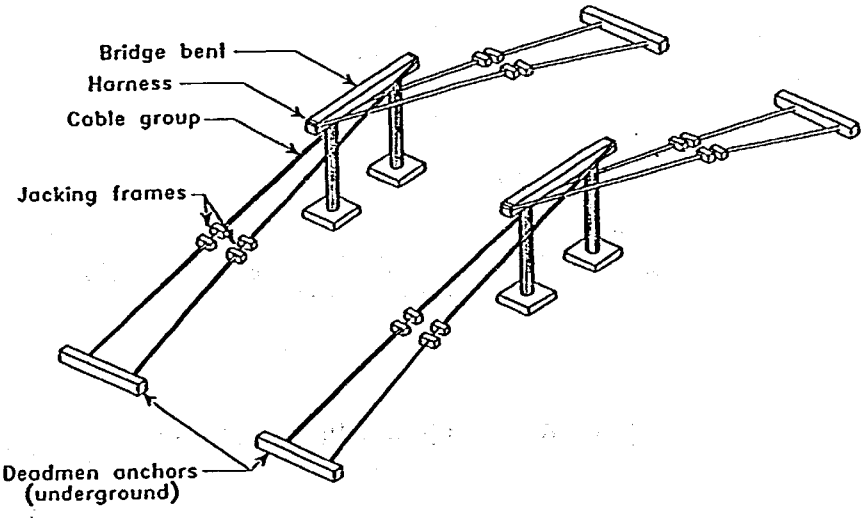


Figure 5. Schematic of Loading System

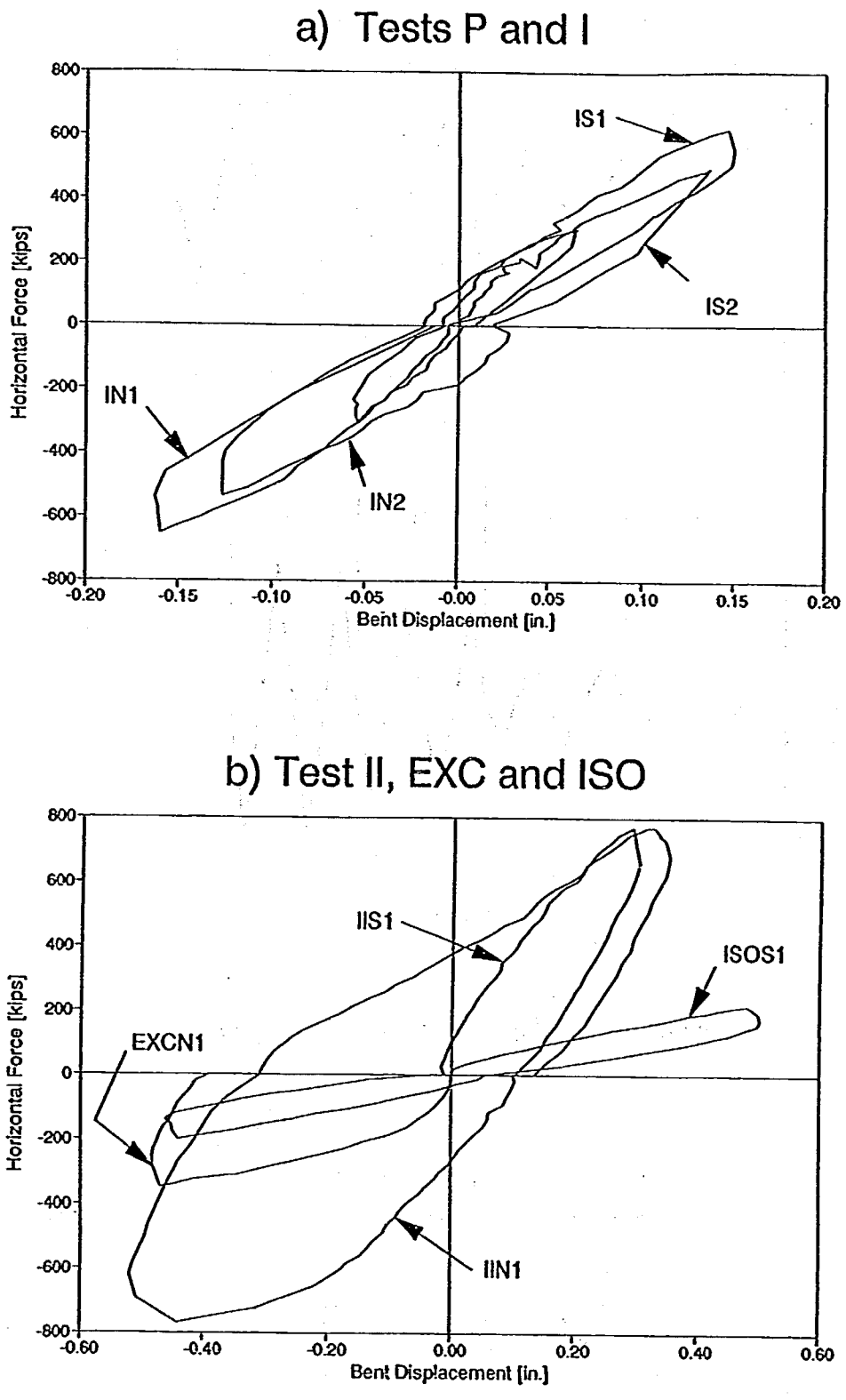


Figure 6. Phase I Pier Response

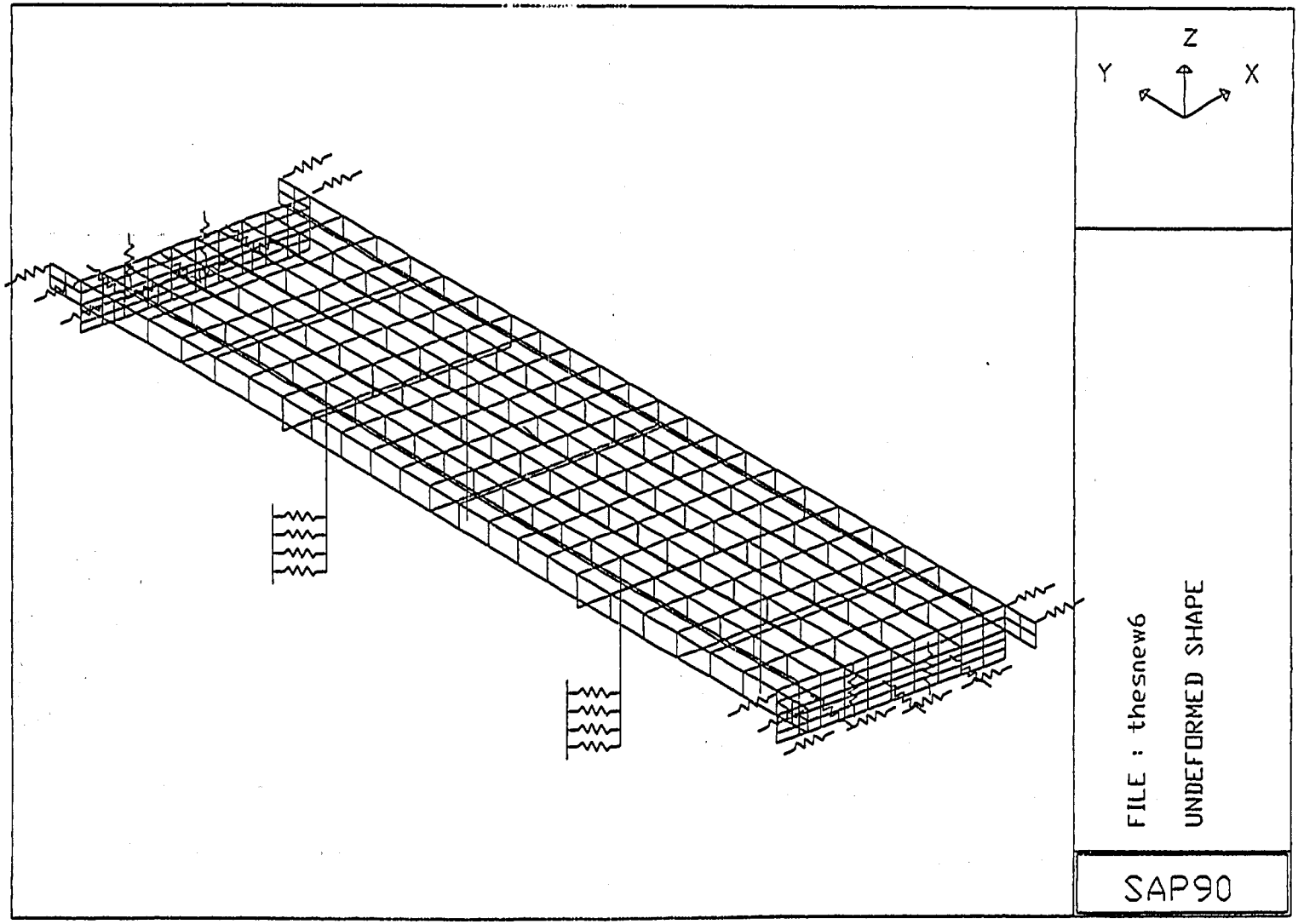


Figure 7. UW Finite-Element Model

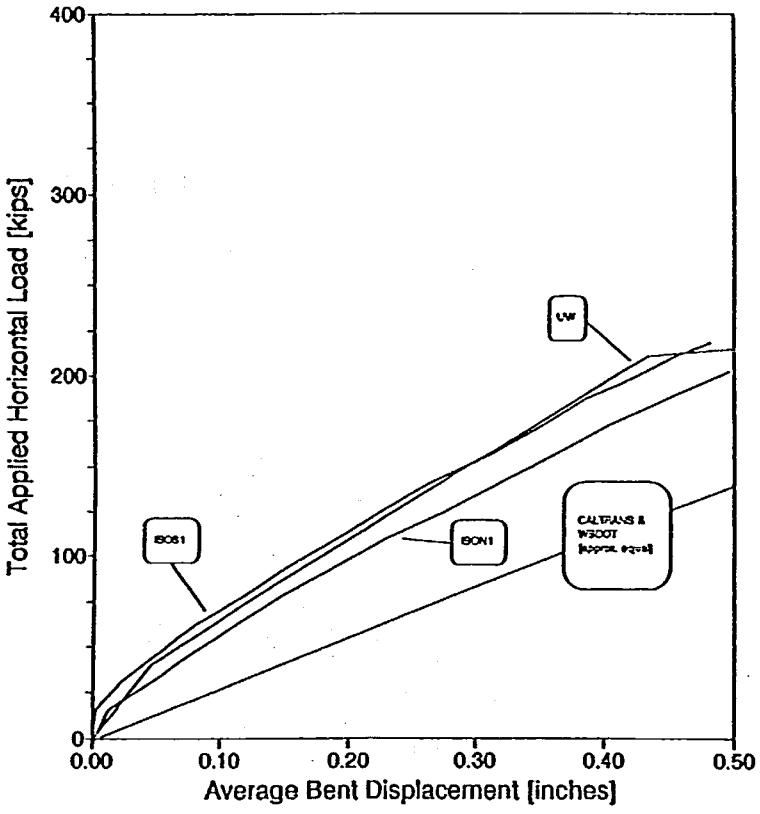


Figure 8. Average Pier (Bent) Response - Superstructure Isolated from Abutment

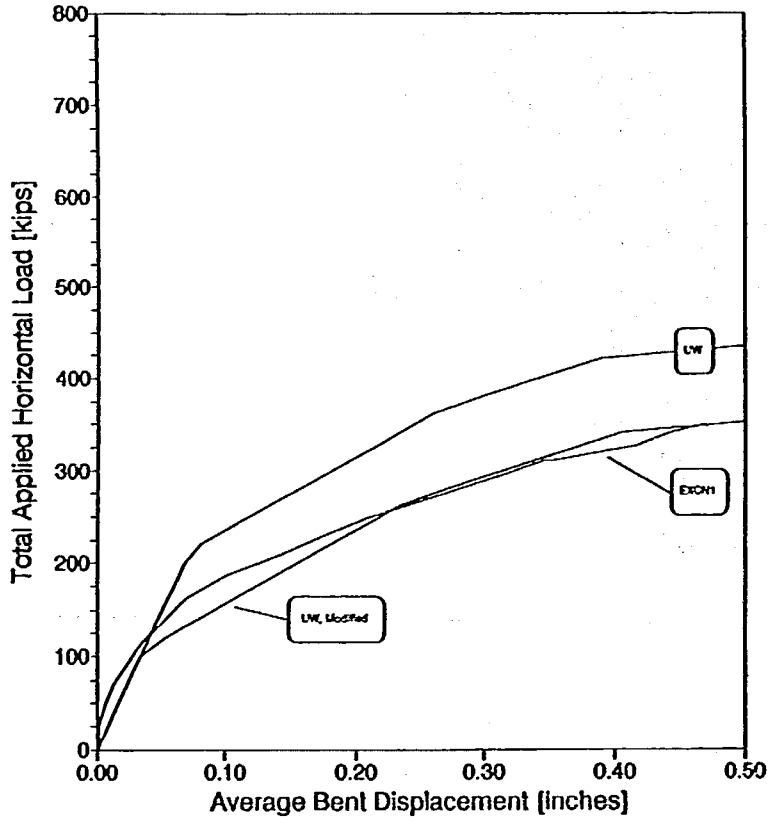


Figure 9. Average Pier (Bent) Response - Excavated Conditions

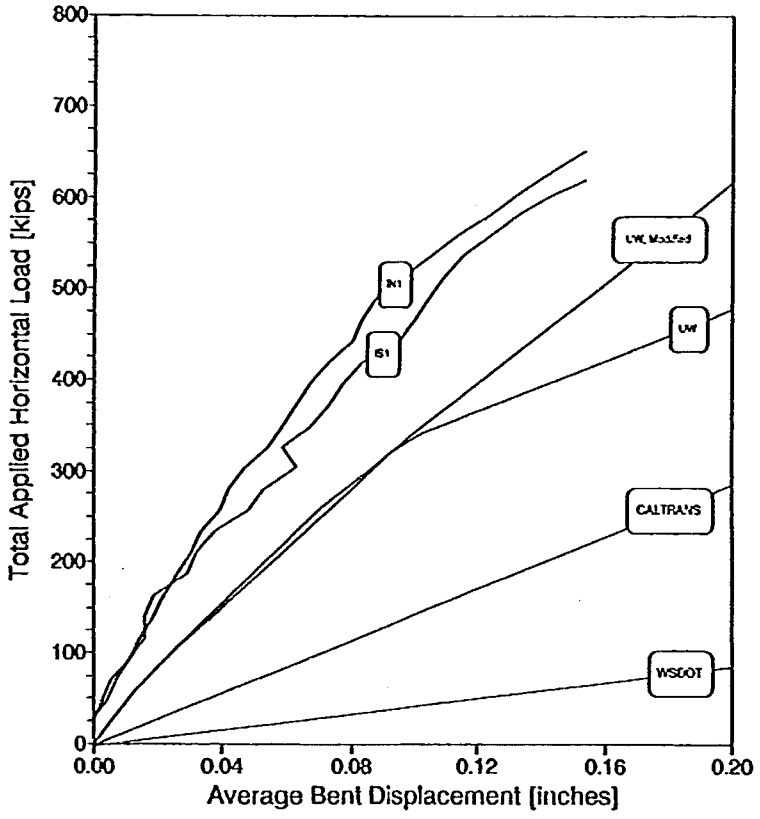


Figure 10. Average Pier (Bent) Response - Initial Conditions

Table 1 - Comparison of Models

Item	UW MODIFIED	UW	CALTRANS	WSDOT
Abutment Transverse Stiffness:	100%	25%	19%	2%
Polystyrene	Yes	Yes	No	No
Bearing pads	Yes	Yes	No	No
Soil friction	Yes	Yes	No	No
Soil resistance at wingwall	100%	11%	89%	10%
Bent Transverse Stiffness:	100%	67%	37%	38%
Non-linear column behavior	Yes	Yes	No	No
Soil resistance at base of column	Yes	Yes	No	No

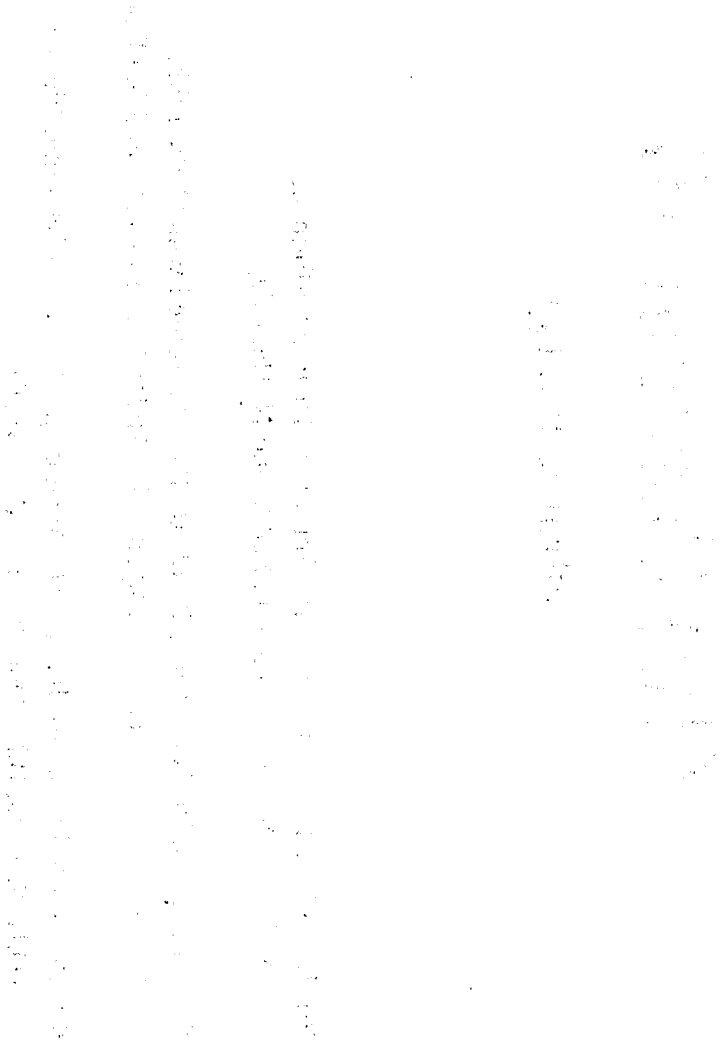
(10) Session 10

Substructure (1)

26) Retrofit of Bridge Footings for Improved Seismic Performance
(Y. Xiao*, M.J.N. Priestley, F. Seible and N. Hamada)

27) Earthquake Resistant Capacity of RC Pier Retrofitted with Carbon Fibre
(N. Ogata, Y. Maeda, A. Murayama, N. Andoh*, Y. Kobatake and S. Ohno)

28) Retrofit Solutions for Inadequate Anchorage of Column Bars into Pier Caps
(D.H. Sanders, B.M. Douglas* and K. Cornell)



RETROFIT OF BRIDGE FOOTINGS FOR IMPROVED SEISMIC PERFORMANCE

by

Yan Xiao(1)
M.J.Nigel Priestley(2)
Frieder Seible(2)
Nobuhiko Hamada(3)
Presenting Author: Yan Xiao

SUMMARY

This paper provides theoretical and experimental background for the seismic assessment and retrofit of bridge column footings. One "as built" model pier and two retrofitted model piers have been tested under simulated seismic actions. The test results of the "as built" pier indicated that column/footing joint shear failure is a potential danger in most existing pre 1971 column footings with only bottom mat reinforcement. The test results also showed that if there is no dependable tensile capacity in the piles rocking behavior will dominate pier response, which will result in minimizing damage to footing and column. Model piers retrofitted using a reinforced concrete overlay developed relatively stable hysteretic responses up to moderate ductility levels. However, experimental observations and theoretical analyses based on a strut and tie model and yield line theory indicate that the reinforced concrete overlay can not develop a fully effective post-cracking mechanism. Improvements to current retrofit designs for bridge footings are recommended.

INTRODUCTION

The designs for bridge footings in the 1950's to early 1970's typically were based on elastic analysis under relatively low lateral seismic input compared to current seismic design provisions. As a consequence of the elastic design practice, the following potential problems are likely inherent in many older bridge footings.

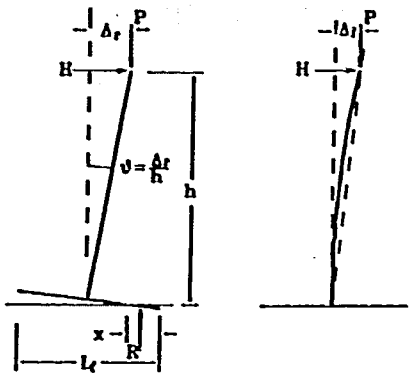
Inadequate restraint against overturning: The piles of existing bridges are often not able to resist tension and may separate from the footing. While this may be thought to be undesirable, it may in fact be beneficial as rocking can occur and the forces entering the structure may be significantly lower than if the columns yield in flexure. This can have significant economic benefits as it is possible that by utilizing this rocking, a lesser amount of retrofit or even no retrofit may be required.

Inadequate anchorage of longitudinal column reinforcement in the footing: This includes the practice of using 90° hooks with the tails bent outward, thus creating an additional tension field in the joint region under the column.

Inadequate footing flexural and shear strength: Inspection of existing older footings shows that the footing reinforcing steel consists solely of a bottom mat designed based on a low level of earthquake input. Both positive and negative moments induced by severe seismic attack might cause flexural failure of the footings. Also, because there is no shear reinforcement in most existing footings, the shear strength of the footing is solely provided by the plain concrete. Typically this is insufficient to resist the shear force due to plastic column input.

---

1. Assistant Research Scientist, University of California, San Diego, U.S.A.
2. Professors, University of California, San Diego, U.S.A.
3. Engineer, Hanshin Expressway Public Corporation, Osaka, Japan, Current Visiting Researcher, University of California, San Diego, U.S.A.



(a) Rocking Deflection (b) Column Deformation

Fig.1 Lateral Pier Response

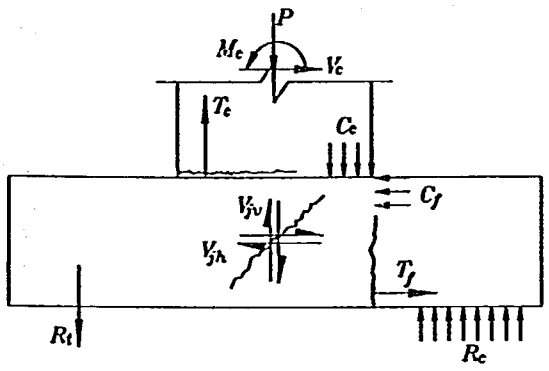


Fig.2 Shear Force in Column/Footing Joint

Column/footing joint shear failure: Like beam column joints in frame structures, the column/footing joint region is subjected to very high shear stress levels. This was not taken into consideration until recently. Thus, column/footing joint shear failure can be expected in many existing bridge structures. Also, this deficiency is the most difficult to retrofit and repair.

To address the above problems and to develop practical retrofit measures for improving the seismic performance of bridge footings, a comprehensive bridge footing research program sponsored by the California Department of Transportation (Caltrans) is being carried out at the University of California, San Diego. This paper describes the assessment of footing rocking behavior and joint shear and the verification of footing retrofit designs currently used in California.

ASSESSMENT OF BRIDGE FOOTING

The behavior of an actual pier dominated by rocking behavior can be analyzed by separating the rocking behavior and the behavior of the column as shown in Fig.1. In the rocking system as shown in Fig.1(a), the major deformations are contributed by the compressive soil deformations at the toe and the uplifting of the footing. The column can be considered as a cantilever beam with fixed end as shown in Fig.1(b), while undergoing rigid body rotation.

On the other hand, since there is typically no shear reinforcement in the joint region, cracking may be considered as the onset of failure in the joint. The principal tensile stress in the joint region can be calculated from the joint shear stress v_{jv} and the average vertical stress f_a by use of Mohr's circle for stress as,

$$f_t = -f_a/2 + \sqrt{(f_a/2)^2 + v_{jv}^2} \tag{1}$$

Priestley has suggested the use of an effective axial compressive stress for the value of f_a[1], given by,

$$f_a = \frac{W_t}{A_{eff}} = \frac{W_t}{(B_c + d_f)(D_c + d_f)} \tag{2}$$

where, A_{eff} is the effective area over which the total axial load W_t at the column base is distributed, B_c and D_c are section width and overall section depth of the column respectively, and d_f is the effective depth of the footing. As illustrated in Fig.2, the vertical joint shear V_{jv} can be assessed by subtracting the hold-down force due to the tensile capacity of the piles from the total tensile force in the critical section of the column:

$$V_{jv} = T_c - R_t \tag{3}$$

Considering an effective joint width b_{eff}, the joint shear stress v_{jv} can be calculated as follows:

$$v_{jv} = \frac{V_{jv}}{b_{eff} d_f} \quad (4)$$

where, $b_{eff} = B_c + D_c$ for rectangular and $\sqrt{2}D_c$ for circular columns. Joint shear distress is expected when the principal tensile stress induced in the footing exceeds $3.5\sqrt{f_c'}$psi ($0.29\sqrt{f_c'}$MPa).

CURRENT CALTRANS FOOTING RETROFIT DESIGN

Current Caltrans footing retrofit design is based on the procedure for new design as specified in the Bridge Design Specifications (BDS)[2], and can be summarized as follows:

Determine seismic input to footing: Calculate nominal flexural capacity of the column critical section, M_p, corresponding to an extreme concrete compressive strain of 0.003[2]. Service dead load plus axial force due to seismic action should be used as axial force, P, in the calculation. The probable plastic moment of the column critical section M_p is estimated by the following equation:

$$M_p = \phi M_n \quad (5)$$

where, the factor ϕ is taken as 1.3, which considers the approximate over-strength capacity of well confined columns[2].

Check capacity of existing pile group and design additional piles: Check the existing pile group using M_p and P as applied loads, and if necessary, design the additional piles and footing extensions according to the BDS 4.3.6.1.1[2].

Design footing shear reinforcement: Check the shear capacity of the footing and design the shear reinforcement using a strength reduction factor of ϕ=0.85[2]. A minimum 1ft overlay thickness is required[3].

Design flexural reinforcement: Design additional bottom reinforcement and the reinforcement in the overlay for positive and negative moments, respectively. A strength reduction factor of ϕ=1.0 can be used.

Design dowels for the connection between original footing and overlay: For the vertical interfaces of the existing footing and the overlay, dowels should be designed based on shear friction design[2].

The main concern with the above Caltrans footing retrofit design is that it does not take into consideration the shear in the column/footing joint region. Another potential problem is the unconservativeness of using the full width of the footing in the flexural design, rather than an effective width as proposed by Priestley and Seible[4].

"AS BUILT" AND RETROFITTED PIER TEST

The reinforcement details for the "as built" Pier FR-1 are shown in Fig.3. The column had a 19.25in. (489mm) wide and 28.75in. (730mm) deep section and contained 32#6 Grade 40 continuous longitudinal bars, constituting a longitudinal reinforcement ratio of 2.5%. As shown in Fig.3(b), the "as built" footing was reinforced only with a #6@3.25in. (83mm) Grade 40 bottom steel mat, which was common in the design practice for bridge footings in 1950's and 1960's.

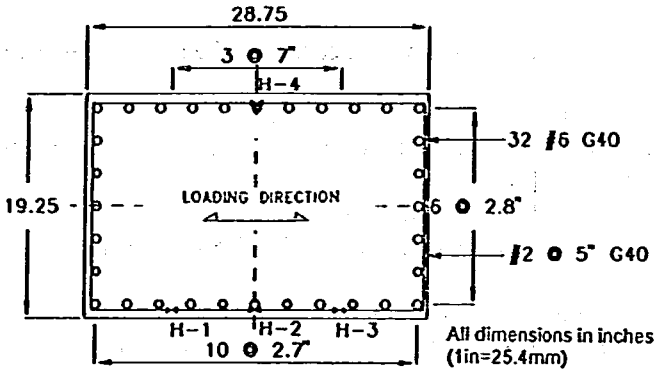
Fig.4(a) and (b) show column details of the retrofitted piers FR-2 and FC-1, respectively. The rectangular Pier FR-2 had the same column dimensions as Pier FR-1, however contained 5.0% longitudinal steel ratio. Circular Pier FC-1 had a 24in. (610mm) diameter circular section and was reinforced with 52#6 Grade 40 steel bars, constituting a longitudinal reinforcement ratio of 5.1%. An elliptical steel jacket and a circular steel jacket were used to retrofit the potential plastic hinge regions. The upper portion of Pier FR-2 column was strengthened with a composite fiber/epoxy system to prevent premature shear failure of the column.

Based on the current Caltrans retrofit design approach, the original 76in.x76in.x19in. (1930mmx 1930mmx483mm) footings of Pier FR-2 and FC-1 were enlarged to 108in.x108in.x23.5in. (2743mmx 2743mmx597mm), and retrofitted with additional flexural steel and stirrups, connected with original footings by deformed #2 Grade 60 bars (noted as D6, nominal diameter = 6mm) dowels, as illustrated in

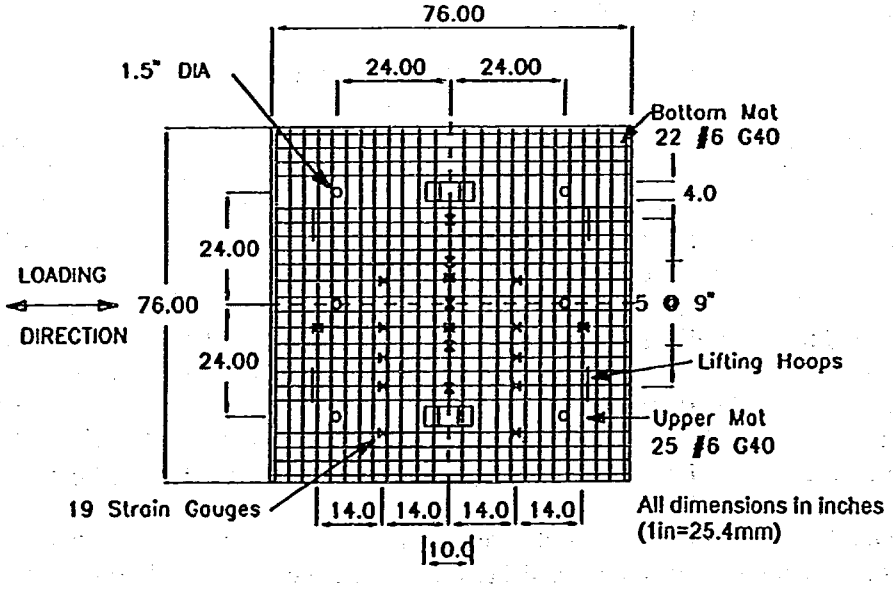
Fig.5(a) and (b). Note, that the Pier FR-2 footing was retrofitted with two layers of top reinforcement mats, while Pier FC-1 was retrofitted with only one top reinforcement mat.

The test setup is shown in Fig.6. Lateral force was applied with a double acting servo controlled actuator and axial load was applied using two high strength steel prestressing bars. The footing was supported on 2.2in. (56mm) thick fiberglass-reinforced elastomeric pads, which were chosen to represent the flexibility of the pile foundation. In the capacity tests of the "as built" Pier FR-1 and the retrofitted piers, the uplift of the footing was restrained by 5/8in. (15.9mm) diameter high strength rods. The rods were first snug tightened over a piece of 1/8in. (3.2mm) steel packing material. The packing material was then removed in order to allow the footing to have some uplift before the rods started to stretch and apply forces. The resulting 1/8in. (3.2mm) gap was provided to allow elastic unloading of the compressed elastomeric pads simulating the pile compression stiffness.

Two rocking tests followed by a capacity test were conducted for "as built" Pier FR-1, while only capacity test was conducted for the retrofitted Pier FR-2 and Pier FC-1, respectively.



(a) "As Built" Column Details



(b) "As Built" Footing Details

Fig.3 "As Built" Pier FR-1 Reinforcement

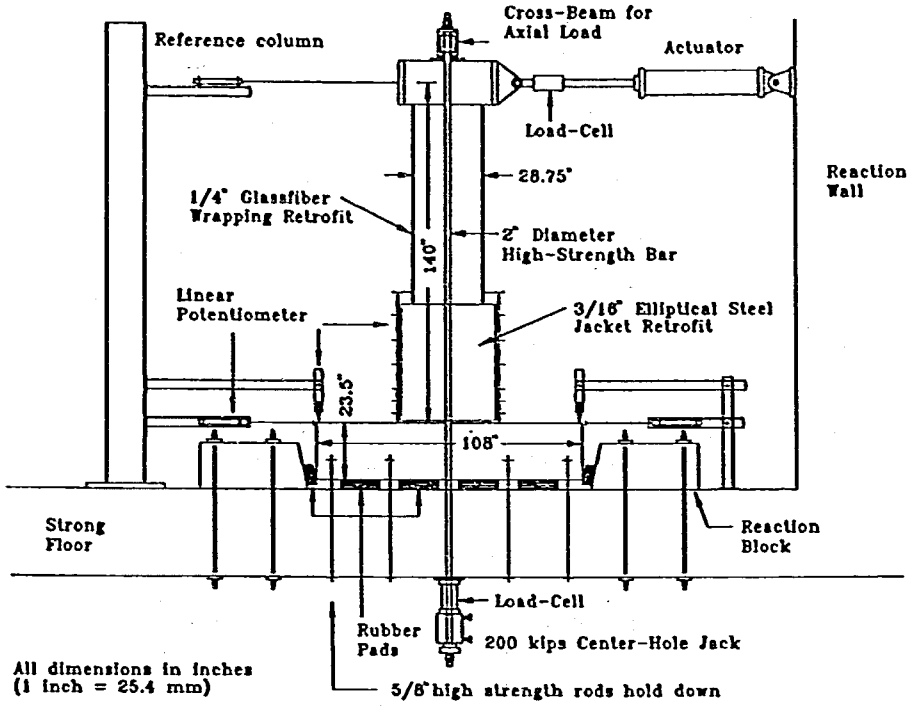


Fig.6 Test Setup

EXPERIMENTAL RESULTS FOR "AS BUILT" PIER

Rocking Response

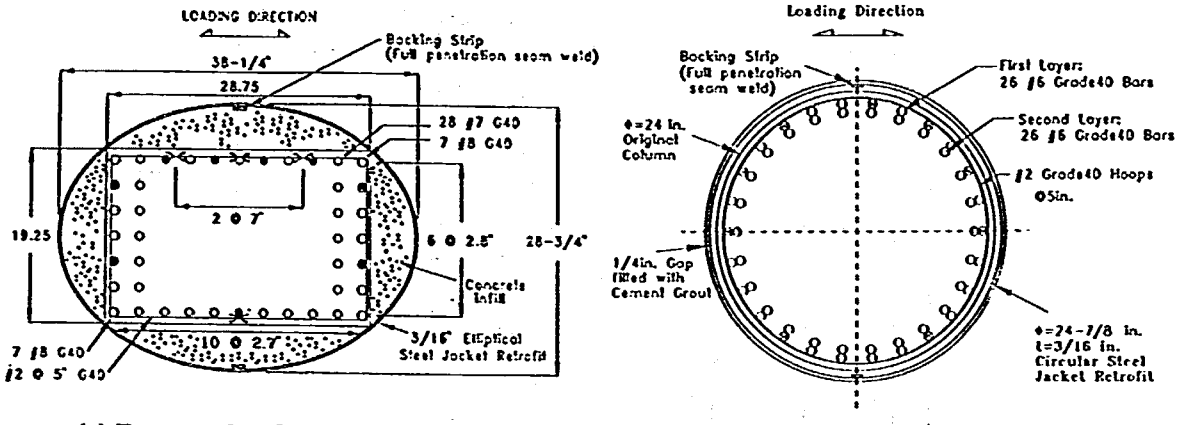
The lateral force-displacement hysteretic response of Pier FR-1 from Test-1, in which the applied axial load was 150kips (667kN), is given in Fig.7(a). Theoretical predictions for the monotonic behavior of the pier based on the axial load of 150kips (667kN) plus the self weight of the pier are also shown in Fig.7(a) by a dotted line. After developing the lateral force required to cause uplift, the hysteretic curves for both loading and unloading showed a negative gradient due to the effect of P-delta. For an elastic rocking system, the unloading response should follow the same track of loading. The difference between the loading branch and unloading branch shown in Fig.7(a) was mainly due to a small drop of the axial load. Relatively good agreement was obtained between the test results and theoretical predictions.

Fig.7(b) shows the lateral force-displacement hysteretic response of Pier FR-1 from Test-2 under an applied axial load of 250kips (1112kN). Theoretical predictions for the monotonic behavior of the pier based on an axial load of 250kips (1112kN) plus the self weight of the pier are also shown in Fig.7(b). The characteristics of the hysteretic response were similar to that obtained from Test-1. The theoretical prediction gave relatively good agreement with test results for the capacity of the pier. However, the theoretical results showed larger stiffness than test results. The main reason for this can be attributed to the assumption of the footing being considered rigid for computation of the rocking response. A comprehensive analysis of the behavior of the bridge pier including the consideration of footing deformation is under development.

Although flexural cracks spread over lower part of the column, the cracks stayed small and there was no sign of crushing of the concrete in the column, throughout the various loading stages of the rocking tests.

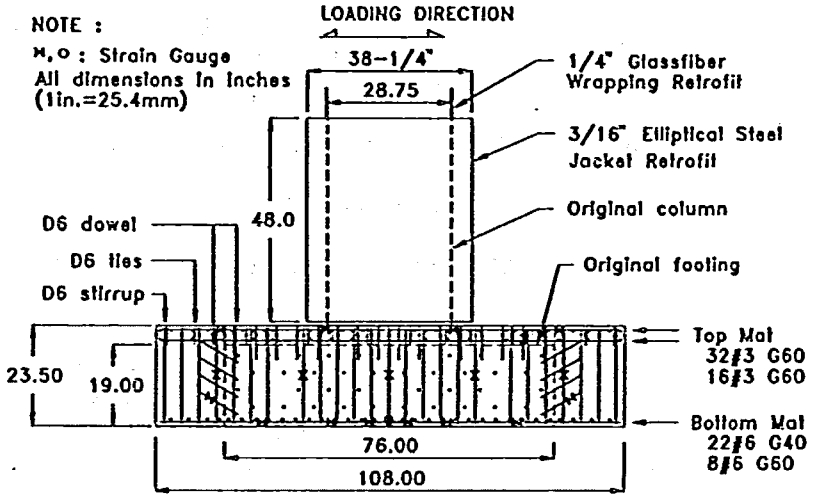
Capacity Test

The lateral force-displacement hysteretic response of the "as built" Pier FR-1 obtained during the capacity test is shown in Fig.8. The dotted lines in Fig.8 show the theoretical capacity H_y corresponding to first yield of the longitudinal reinforcement and the theoretical ultimate capacity H_p of the column,

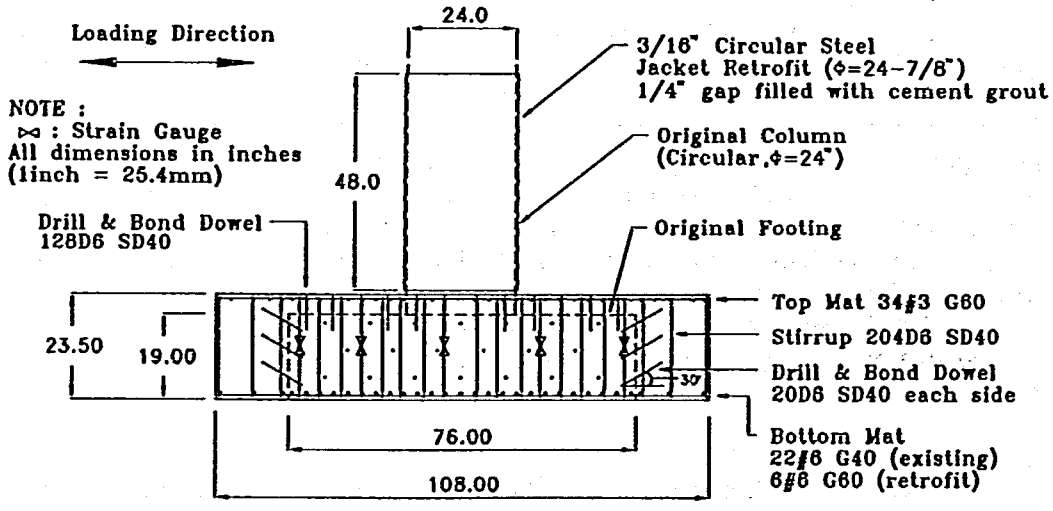


(a) Rectangular Column Pier FR-2 (b) Circular Column Pier FC-1

Fig.4 Retrofitted Column Details

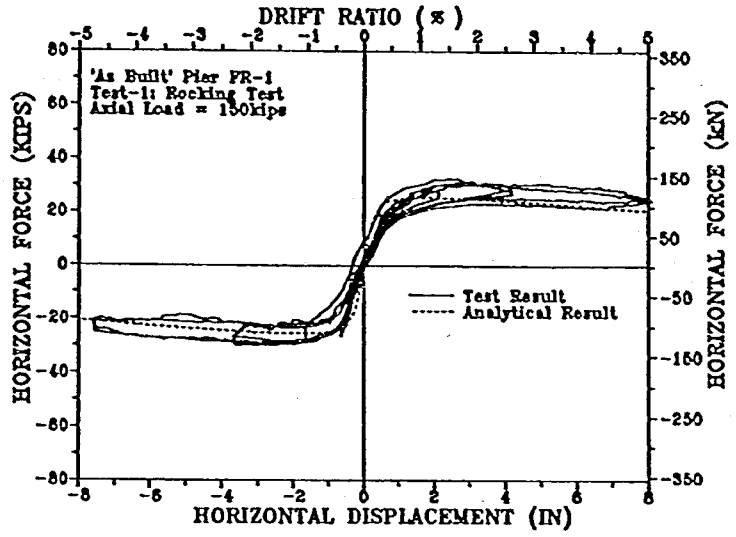


(a) Rectangular Column Pier FR-2

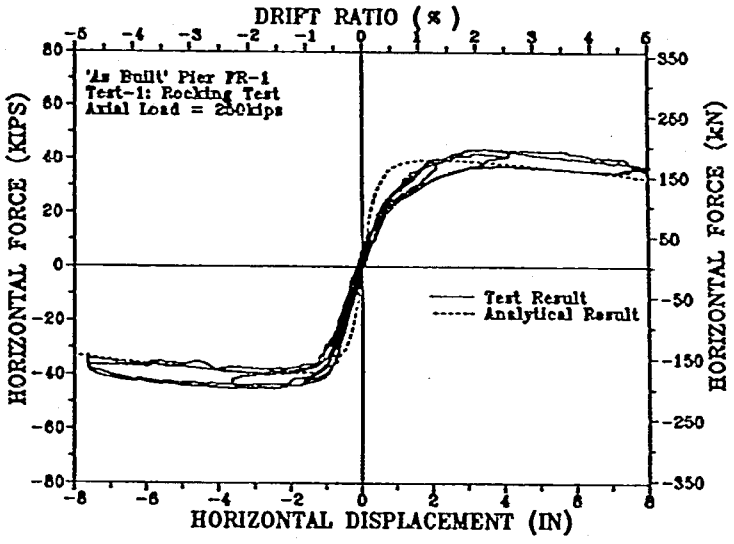


(b) Circular Column Pier FC-1

Fig.5 Retrofitted Footing Reinforcement Details



(a) Axial Load P=150kips (667kN)



(b) Axial Load P=250kips (1112kN)

Fig.7 Rocking Hysteretic Responses of "As Built" Pier FR-1

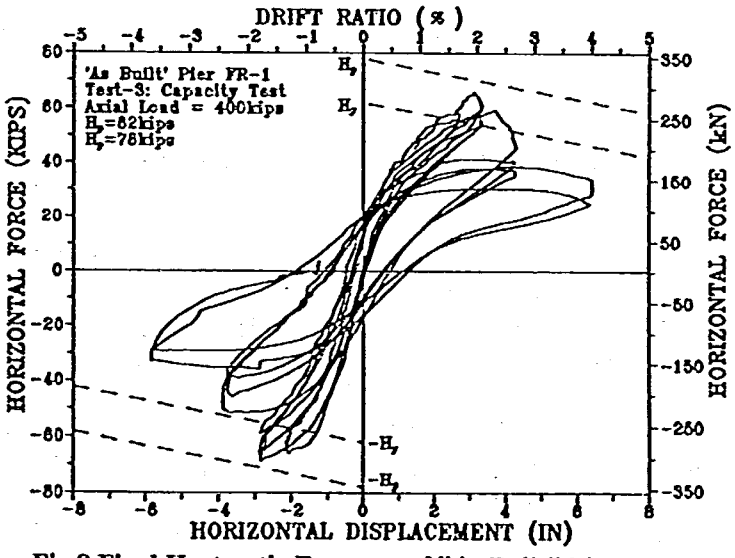


Fig.8 Final Hysteretic Response of "As Built" Pier FR-1

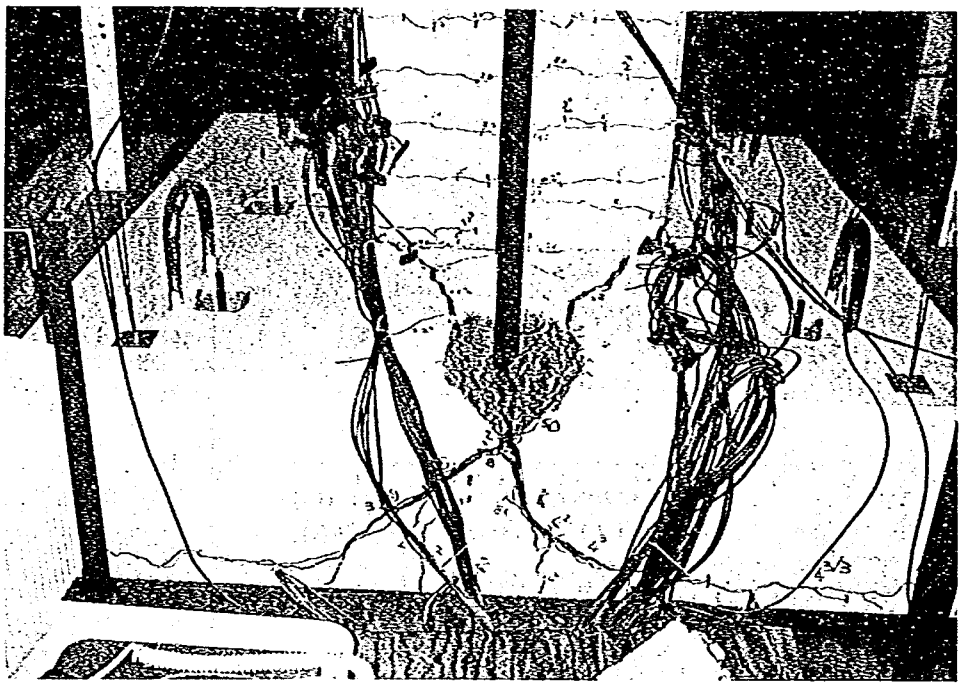


Fig.9 Column/Footing Joint Failure in "As Built" Pier FR-1

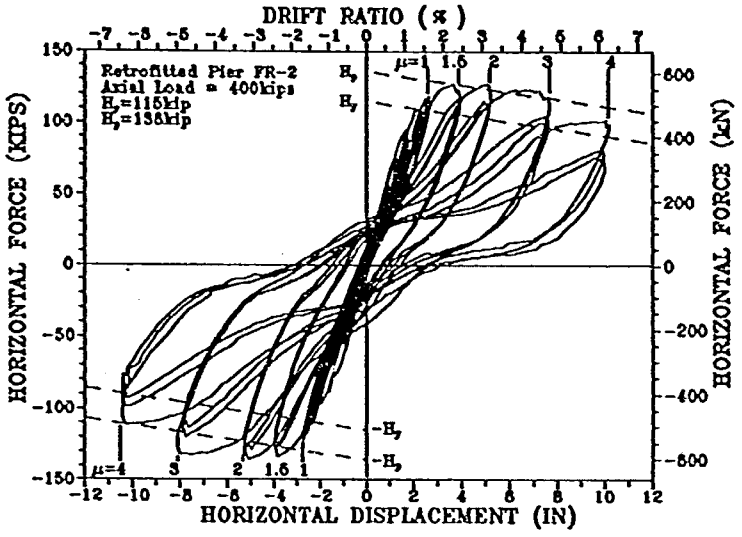
calculated using Mander's stress-strain model for confined concrete[5], measured material strengths, and an ultimate concrete compressive strain of ε_c= 0.005. The hysteretic loops were stable, until a peak displacement level of 3.2in. (81mm) was achieved. The pier developed a maximum force of 76kips (338kN) in both push and pull directions, which was slightly lower than the predicted theoretical ultimate capacity of the column. A sudden drop in the force carrying capacity of the pier occurred due to the shear failure of column/footing joint region, during the push cycle to achieve a displacement of 4.0in. (102mm). After this stage, the degradation of the strength of the pier became significant. Fig.9 shows the wide opening of the joint shear cracks. However, even at this final stage, there was no major damage to the column.

Based on a theoretical moment curvature analysis of the column section, the total ultimate tensile force T_c in the critical section was calculated as 363kips (1615kN). Assuming that the resultant compressive reaction force from the bearing pads had a distance of 24in. 610mm) to central axis, the total hold-down force of the rods was estimated as 24kips (107kN). Thus, the principle tensile stress in column/footing joint region was calculated as 275psi (1.89MPa) or $4.2\sqrt{f_c'}$psi ($0.35\sqrt{f_c'}$MPa), only 20% higher than the expected lower limit $3.5\sqrt{f_c'}$psi ($0.29\sqrt{f_c'}$MPa).

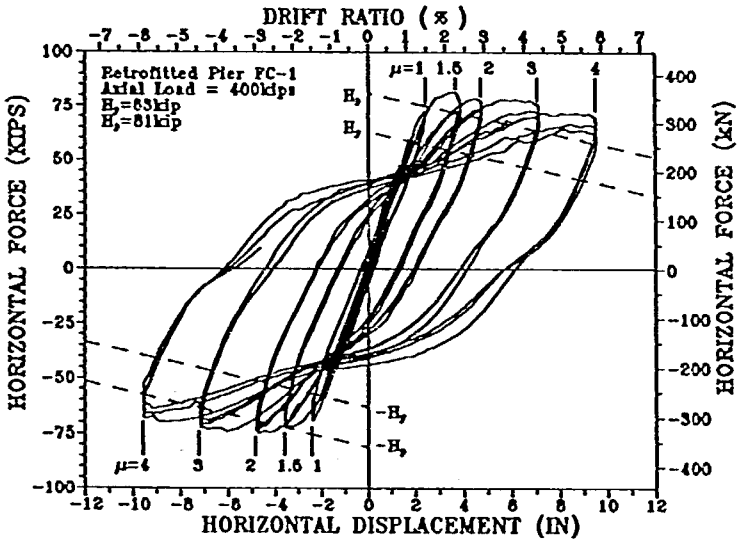
EXPERIMENTAL RESULTS FOR RETROFITTED PIERS

The lateral force - displacement hysteretic response histories for the retrofitted rectangular Pier FR-2 and circular Pier FC-1 are shown in Fig.10(a) and (b), respectively. The dotted lines in Fig.10 show the theoretical predictions for the capacities of the pier corresponding to the first yield of the longitudinal reinforcement and the ultimate flexural strength of the critical section corresponding to an extreme concrete compressive strain of 0.005, calculated using Mander's stress - strain model for confined concrete[5].

The retrofitted rectangular Pier FR-2 developed its flexural strength at a displacement ductility level of μ=1.5. As shown in Fig.10(a), the hysteresis loops of the pier were stable until μ=3.0, or a total drift ratio of 4.8%. However, the degradation of the lateral force became significant during loading cycles up to a peak ductility factor of μ=4.0, due to the excessive opening of the cracks and concrete crushing



(a) Retrofitted Rectangular Column Pier FR-2



(b) Retrofitted Circular Pier FC-1

Fig.10 Hysteretic Responses of Retrofitted Piers

of the top overlay. The overall shape of the hysteresis loops indicates relatively small energy absorption capacity. The failure of the pier was caused by the degradation of the footing overlay resistance to the pull-out force induced by the tensile steel in column critical section. At the peak displacement ductility factor μ=4.0, the top overlay was lifted up about 3/4in. (19mm) at the tension toe of the column. However, there was no evidence of distress in the column even at the end of the test.

The retrofitted circular Pier FC-1 developed a ductile hysteretic response up to a displacement ductility factor of μ=4.0, or a total drift ratio of 5.8%, where the loading was terminated due to the limitation in axial loading system. The hysteretic loops were stable and showed little degradation upon recycling at the given ductility level. The predicted ultimate flexural strength was first reached during the loading to μ=1.5. The further augmentation in the peak lateral forces was due to the strain hardening in the longitudinal reinforcement. Although the pier developed an acceptable hysteretic response, excessive cracks and concrete crushing, localized in the region close to the column end, were observed during the cycling corresponding to a peak ductility factor of μ=4.0, as shown in Fig.11, indicating the severe damage of the retrofitted footing.

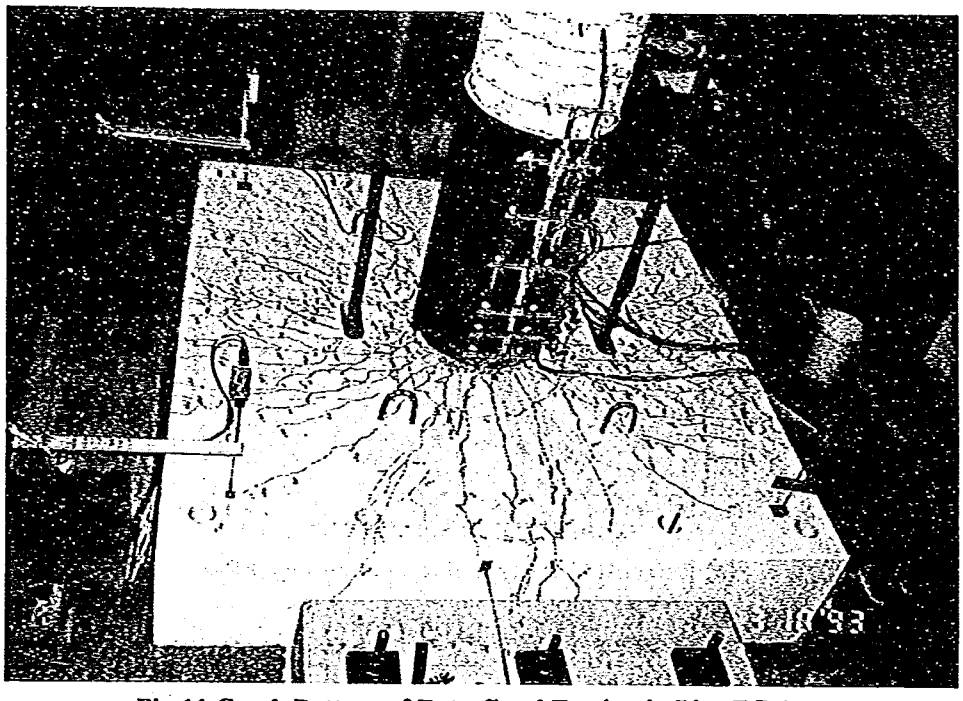


Fig.11 Crack Pattern of Retrofitted Footing in Pier FC-1

STRUT AND TIE MODELS

"As Built" Footing

A strut and tie model, similar to that proposed by Priestley et.al.[6], is developed for the footing of the "as built" Pier FR-1, as shown in Fig.12. The footing is subjected to the forces, T_c, C_c and V_c, from the column critical section and supported by the reaction forces, R_t, R_v and R_h, from the simulated foundation. The compressive force, C_c, and shear force, V_c, are resisted by struts, C_1 and C_2. The resultant tensile force, T_c, of all the tension reinforcement in the column is transferred into the footing through bond, and resisted by strut C_2 and the fan shaped ties, T_1, T_2.

Considering the flexural ultimate limit state of critical column section, the resultant tensile force, T_c, compressive force, C_c, and shear force, V_c, can be calculated as 376kips (1672kN), 776kips (3452kN) and 78kips (347kN), respectively. It is assumed that the resultant tensile force T_c is reduced to zero by bond at a depth of 14in. (356mm). The application point of the force, T_c, is taken as 7in., i.e., half the bond length from the top surface of the footing. The corresponding reaction forces, R_t, R_v and R_h, can be determined as 24kips (107kN), 424kips (1886kN) and 78kips (347kN), respectively. Fig.12(b) shows the equivalent truss forces.

As shown in Fig.12(b), the principal tension tie, T_1, is required to carry a force of 431kips (1917kN). Since there was no joint shear reinforcement provided, cracking of the joint region due to the high tensile stress caused the total failure of the footing, as illustrated in Fig.9.

Retrofitted Footings

The moment curvature analysis for the critical column section of FR-2 indicated that the footing was subjected to a resultant tensile force, T_c=708kips (3149kN), a resultant compressive force, C_c=1108kips (4928kN) and shear force, V_c=136kips (605kN). These input forces are balanced by two tie-down forces, R_{t1} and R_{t2}, and reaction forces, R_v and R_h, as shown in Fig.13.

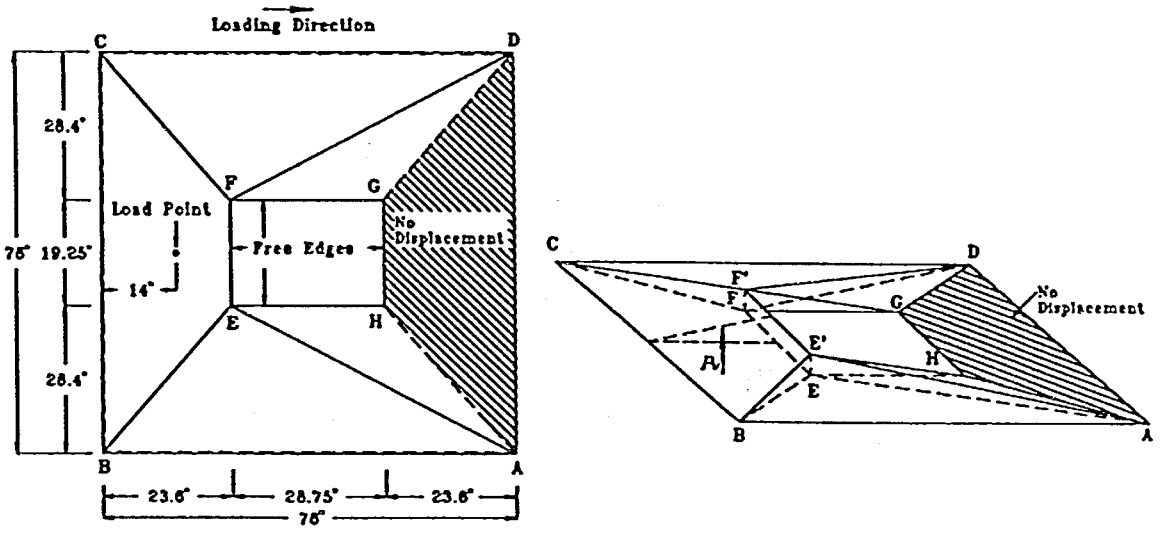
Prior to cracking of the joint region, the strut and tie model considered for FR-2 is based on the assumption that the concrete in joint region is able to carry tensile force, as shown in Fig.13(a). Resultant compressive force, C_c, and shear force, V_c, are mainly resisted by a diagonal strut, C_1, to the compression zone of rubber pads and reaction block. The resultant tensile force, T_c is transferred to the footing and resisted by a concrete tension fan, T_1, and two compression fans, C_2, C_3. The compression fan C_2

radiates from the compression zone of the critical column section. While compression fan, C_3, is equilibrated by tension ties, T_2, T_3, and T_4, which are provided by reinforcement in the footing extension part and the top overlay. It is assumed that the hold-down forces, R_{t1} and R_{t2}, are directly supported by the concrete at the bottom of the hold-down pockets along the perimeter of the footing extension and transferred to the vertical stirrups. The forces in the vertical stirrups are combined into the vertical ties, T_3 and T_5.

Fig.13(b) shows the calculated forces induced in the members of the pre-cracking strut and tie model. It is assumed that the resultant tensile force T_c is decreased to zero by bond at a depth of 18in. (457mm), and the application point of, T_c, is taken as 9in. (229mm), i.e., half the bond length, below critical column section. The resultant force, C_c, and shear force, V_c, are assumed to act at the level of the top tension ties. As is shown in Fig.13(b), a large tensile force of 848kips (3772kN) is required for concrete tension tie, T_1. As observed by the joint shear cracking and the prediction of excessively high principal tensile stress in the joint region, the concrete tension tie, T_1, must have deteriorated eventually as the consequence of inadequate joint shear reinforcement. Unlike the case of the "as built" pier FR-1, in which only bottom reinforcement was provided for the footing, joint shear cracking does not necessarily imply a footing failure for the retrofitted Pier FR-2, due to the presence of the top reinforcement and shear stirrups in the retrofitted part of the footing.

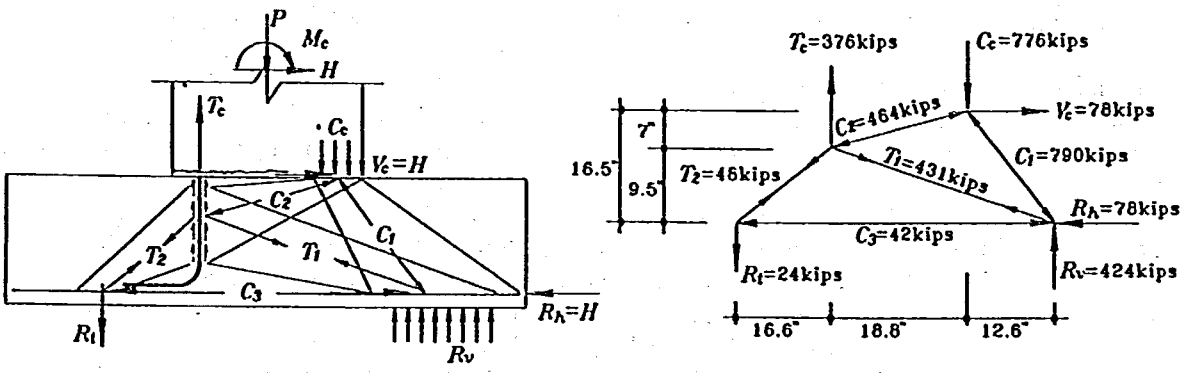
A post-cracking strut and tie model is considered, as shown in Fig.13(c). The major change due to joint shear cracking is that the compression strut, C_2, is split into two compression struts, C_2 and C_5. For the selected geometry of the model, forces induced in the members are calculated, as shown in Fig.13(c). In the post-cracking system, the resultant tensile force, T_c, is only resisted by compression struts C_2 and C_3. Thus, forces in strut, C_3, and ties, T_2, T_3, have been significantly increased. Since the stirrups are provided far away from the column, the vertical component of strut force, C_3, has to be transferred to the tension tie, T_2, through the slab function of the top overlay.

Assuming a yield line pattern as shown in Fig.14, the capacity of the overlay to resist the pull-out force at the application node of strut force, C_3, can be analyzed based on the virtual work method. In calculating the plastic moment of the yield lines, an effective depth including the depth of the overlay and the depth of the dowels should be used. As the result, the capacity of the slab was calculated to be equal to 380kips (1690kN), which is slightly smaller than the vertical component of the strut force, C_3, or 397kips (1766kN). This indicates that the top overlay was marginally able to support the vertical component of strut force, C_3. However, the capacity of the overlay would degrade under the action of cyclic loading, and eventually leading to footing failure.



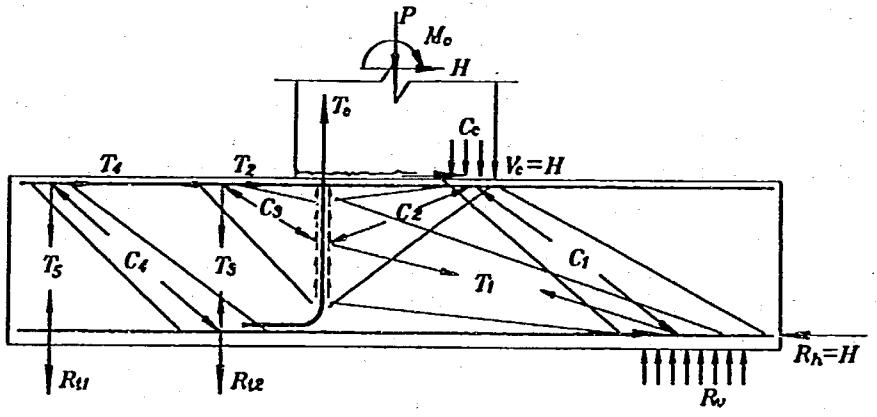
(a) Yield Line Pattern (b) Displacement

Fig.14 Yield Line Pattern and Displacement of Top Overlay

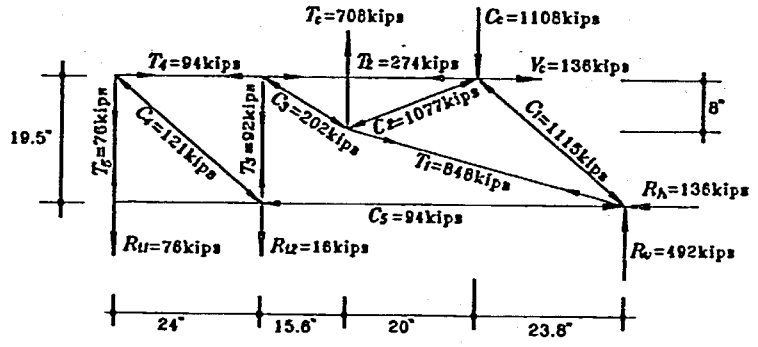


(a) Strut and Tie Model for "As Built" Footing (b) Equivalent Truss Forces

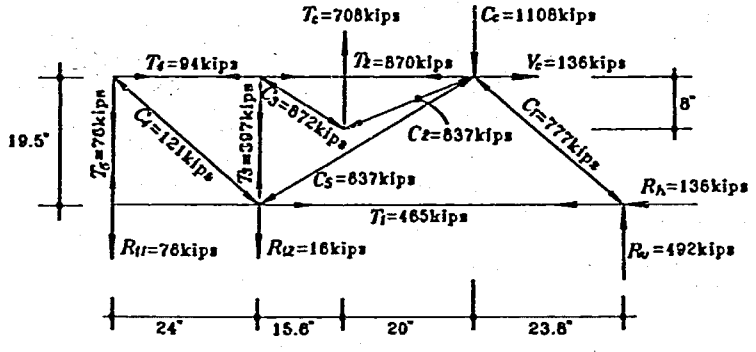
Fig.12 Load Resisting Mechanism in "As Built" Footing



(a) Strut and Tie Model for Retrofitted Footing



(b) Equivalent Forces in Pre-cracking Footing



(c) Equivalent Forces in Post-Cracking Footing

Fig.13 Load Resisting Mechanism in Retrofitted Footing FR-2

Similar analyses for the retrofitted circular Pier FC-1 indicated that the top overlay capacity of Pier FC-1 had a larger margin against the pull-out force induced by the tensile steel in critical column section, which is reflected in the improved hysteretic response, as shown in Fig.10(b).

CONCLUDING REMARKS

The following conclusions from the footing retrofit program to date can be drawn:

(1) If there is no dependable tension capacity in the piles, a rocking behavior is likely to dominate the response of the pier. With the rocking response of "as built" Pier FR-1, the column and footing essentially remained elastic, and damage was minimal.

(2) The "as built" pier suffered a brittle column/footing joint shear failure, when rocking of the footing was restrained. The joint shear failure can be assessed by estimating the principal tensile stress in the column/footing joint region.

(3) Although piers, retrofitted using the current Caltrans footing retrofit design approach, developed a moderate ductility, they could not escape from the failure or damage to the footing caused by column/footing joint shear distress and the potential deformation ability of the retrofitted column could not be fully utilized.

(4) Strut and tie models have been employed to investigate the failure mechanism of the retrofitted footing. With the provision of a reinforced concrete top overlay and extension around the existing footing, the Caltrans design allows a resisting mechanism to soften the brittle nature of the joint shear failure after cracking. However, this requires the top overlay to function as a slab to carry the large vertical force resulting from column tension reinforcement and transfer it to the shear reinforcement far away from the joint region. The top overlay capacity can be checked by using yield line theory.

(5) As an improvement to the current Caltrans footing retrofit design methodology, it is recommended that the analytical model proposed in this paper be used to determine the capacity of the footing overlay. Alternatively, more effective retrofit details including the use of deep dowels need to be developed in future studies.

ACKNOWLEDGMENTS

This research has been funded by California Department of Transportation (Caltrans), under grant number RTA59M494. The helpful comments from Messrs. Steve Mitchell, Fadel Alameddine and other Caltrans engineers are gratefully acknowledged. The authors also wish to thank Aoki Corporation, Ltd., Tokyo, Japan and Fyfe & Associates for the donations of experimental materials used in this project. The comments and conclusions described in this paper are solely those of the authors, and do not necessarily reflect the views of Caltrans.

REFERENCES

1. Priestley, M.J.N., "Seismic Assessment of Existing Concrete Bridges," Seismic Assessment and Retrofit of Bridges, edited by Priestley, M.J.N. and Seible, F., Structural System Research Report, Department of Applied and Engineering Sciences, University of California, San Diego, No. SSRP-91/03, Jul. 1991, pp.84-149.
2. California Department of Transportation, "Bridge Design Specifications," Jun., 1990.
3. California Department of Transportation, "Memo To Designers," 20-4, Jan., 1990.
4. Priestley, M.J.N. and Seible, F., "Design of Seismic Retrofit Measures for Concrete Bridges," Seismic Assessment and Retrofit of Bridges, edited by Priestley, M.J.N. and Seible, F., Structural System Research Report, Department of Applied and Engineering Sciences, University of California, San Diego, No. SSRP-91/03, Jul. 1991, pp.197-250.
5. Mander, J.B.; Priestley, M.J.N. and Paulay, T., "Theoretical Stress-Strain Model for Confined Concrete," Journal of Structural Division, ASCE, Vol.114, No.8, Aug. 1988, pp.1804-1826.
6. Chai, Y.H.; Priestley, M.J.N. and Seible, F., "Seismic Retrofit of Circular Bridge Columns for Enhancing Flexural Performance," ACI Structural Journal, Vol.88, No.5, Sep.-Oct. 1991, pp.572-584.

EARTHQUAKE RESISTANT CAPACITY OF RC PIER RETROFITTED WITH CARBON FIBRE

Norio Ogata*), Yoshifumi Maeda*), Akira Murayama*),
Hirofumi Andoh*), Yoshirou Kobatake**), Satoru Ohno**)

Summary

The retrofitting methods of RC pier are used to be done by use of reinforced concrete lining or steel plate lining methods. Here, a new method, in which the retrofitting was done by glueing carbon fibre sheet or by coiling carbon fibre strand on the surface of pier, was developed to replace the existing methods.

To certify the effect of the new method and to establish the design method and construction method, a series of tests has been done. These experiments include weathering (exposing) test of carbon fibre, element test and cyclic horizontal loading test on model of pier. The results showed that (1)there is no aging effect even if the carbon fibre is exposed in air, (2)the ultimate strain of concrete retrofited carbon fibre becomes larger and (3) the maximum toughness, the ultimate deformation and the ductility increase after the pier being retrofitted with carbon fibre. These indicate that the new method as a retrofitting is effective.

1. INTRODUCTION

Usually, the RC piers have the cut-off part of longitudinal reinforcing bars because of consideration of economy. Sometimes, in this part, the longitudinal reinforcing bar is not long enough and the lateral reinforcing bar is inadequate. In case of large earthquake occurred, crack or failure might mostly take place at the cut-off part. To prevent that, the RC lining method or steel plate lining method are usually used to make reinforcement. For the former method, 1)the cost is cheap. However, 2)it is necessary to reinspect the footing or foundation capacity because of the cross section and weight of the pier body increases. Furthermore, to make the old and new concrete to be one, it is necessary to do surface treatment of old concrete. It is needed to insert anchors. These not only have difficulties for construction but also make noise during execution. As for the latter, although the increase of cross section and weight is not as much as in the former method. As it is necessary to make anchor and injecting resin to make the reinforcing material and the existed pier to be one, the difficulty of construction is a problem.

To solve the abovementioned problems and also to save labor, the Carbon Fibre Retrofitting Method as the replacement of the previous mentioned two methods has been studied in Research Institute of JHPC. As the basic experiments, weathering test on carbon fibre and glue

*)Research Institute, JHPC, Machida-shi, Tokyo, JAPAN
**)Technical Resarch Institute, Obayashi Corporation,
Kiyose-shi, Tokyo, JAPAN

have been performed, and element test was conducted to certify the confining effect of concrete. The pier model loading test was conducted to certify the efficiency of reinforcement. The studies also included to establish the methods of design and construction. The test results are present in this paper.

2. CARBON FIBRE RETROFITTING METHOD

In Carbon Fibre Retrofitting Method, either carbon fibre sheet (in which the carbon fibre is arranged along one direction and in sheet shape) or carbon fibre strand (which carbon fibre is tied up in a bundle) are used. The carbon fibre sheet is pasted on concrete surface by epoxy resin to retrofit the pier. As shown in Figure.1, in case that the longitudinal reinforcing bar is not long enough in the cut-off part, carbon fibre sheet is pasted along the longitudinal direction on concrete surface. On the other hand, if the longitudinal reinforcing bar is inadequate, carbon fibre sheet is pasted or carbon fibre strand is wound on pier in transverse direction. It is intended to improve the capacity of resisting moment or ductility in pier by the above retrofitting methods.

The carbon fibre retrofitting method has following advantages: (1) the thickness of carbon fibre sheet is only 0.1 mm and the weight of that is very little, therefore, the increase of cross section and weight of pier is negligible; (2) it is easy to construct; (3) the weatherability is no ptoblem and (4) the ductility is good.

3. WEATHERING TEST

In order to understand the aging effect and to estimate the durability, the tensile strength test and gluing strength test have been done on the samples that have been exposed in air. The data in this paper is result of 1 year wethering samples.

3.1 Tensile strength test

The tensile strength test was used carbon fibre samples that be soaked in epoxy resin. This is based on 'JIS K 7073 (Jpapn Industrial standard)'. The results are illustrated in Figure.2. It is obvious that there is no strength decrease after one year weathering.

3.2 Gluing strength test

Figure.3 shows the results of gluing strength test in which carbon fibre sheet was pasted on concrete by use of epoxy resin. This is based on 'JIS A 6909'. The results indicate that there is no reduction of adhesive strength. On the contrary, it seems the adhesive strength slightly increases.

4. ELEMENT TEST

For the purpose of appreciating the influence of the retrofitting

on the compressive strength and ultimate strain, the element tests were performed on concrete samples that were retrofited in transverse direction by carbon fibre. The samples were 30 cm height column with square cross section (15cm x 15cm). Further, as carbon fibre at corners is easily repture, four corners of the section was roundly made chamfer(radius=3cm). The amount of carbon fibre retrofitting is defined as the volumetric ratio divided the amount of carbon fibre by volume
of concrete samples and is shown in Table 1. The samples are given in Figure.4.

4.1 compressive strength

The compressive strength of concrete retrofitted by carbon fibre is illustrated in Figure.5. It is noted that the compressive strength of concrete slightly depends on the amount of carbon fibre. There is no difference between the strength of plain concrete and that of confined concrete (concrete retrofitted by carbon fibre).

4.2 Strain of concrete

Stress-strain curve of the result is illustrated in Figure.6. In the non-retrofitted sample,the strength is the maximum value when the strain of concrete reached about 0.25 - 0.3%. And after that,the strength goes down saddenly. On the other, In the retrofitted sample, the gradient after the maximum strength point is the amount of carbon fibre increases. It doesn't show sudden deterioration of strength, sufficient ductility must be obtained.

The relation between the ultimate strain and the amount of carbon fibre is given in Figure.7. The failure is defined as the state at which carbon fibre is broken. Further,ultimate strain is defined as the strain of concrete at this state. Evidently the ultimate strain increases with the amount of carbon fibre increases.

5. PIER MODEL TEST

In order to validate the efficiency of carbon fibre retrofitting and to establish new methods for design and construction, model test of pier was performed.

5.1 Specimens

The dimension and bar arrangement of the specimens are shown in Figure.8. Objects of specimens were square(rectangular) column which was most popular in existent piers. The longitudinal reinforcement were D16(16mm) deformed bars, the transverse one were ϕ6(6mm) round bars with 20mm spacing. Londitudinal steel ratio are 1.2%, and transverse are 0.047%. Specimens are shown in Table.@, No.1, No.2, & No.5, there was cut-off part of longitudinal reinforcement at the height of 90cm from the top of footing. the amount of longitudinal reinforcement of upper part is half of the lower part(top of footing). In specimens No.3, No.4, there wasn't cut-off part to investigate performance of retrofitting the top of the footing.The length of carbon fibre retro-

fitting is listed in Table 2. To investigate the efficiency of after earthquake retrofitting, specimen No. 5 loaded up,to $3\delta y$(δ: The displacement of top of pier when the reinforcing bar yields.) and were given damaged to the cut-off part. Then, the cracks were filled with epoxy resin and the injured (damaged) parts were retrofitted by carbon fibre. Specimens No.2 - No.5 were made chamfer at the corner of column to prevent carbon fibre from rupture. the results of materials test on this test are shown in Table.3 - 5.

5.2 Loading method

Specimens were acted for horizontal cyclic load under constant axial force(6kgf/cm^2) which is corresponding to dead load reaction of superstructure. The loading apparatus is shown in Figure.9 and the loading pattern is shown in Figure.10.

5.3 The amount of carbon fibre

1) Retrofitting to bending moment

Amount of carbon fibre against bending moment at cut-off part can be calculated based on Equation (1).

$$\Delta M = M_{UT} - M_y \qquad (1)$$

where,

ΔM : is the bending moment difference at the cut-off part;
M_{UT} : is the bending moment at the cut-off part, which corresponding to state that the bending moment at the top of footing arrives the ultimate value; and
M_y : is the yielding bending moment at cut-off part.

This difference of bending moment will be born by carbon fibre (Figure.11). The amount of carbon fibre is computed according to Equation (2).

$$A_{CF} = A_S \, (\sigma_{SY}/\sigma_{CF}) \qquad (2)$$

in which,

A_{CF} : is the amount of carbon fibre needed to bear the bending moment difference ΔM;
A_S : is the amount of reinforcing bar needed to bear the bending moment difference ΔM;
σ_{SY}: is the yield stress of reinforcing bar; and
σ_{CF}: is the allowable tensile strength of carbon fibre during earthquake.

Figure.12 showes flow-chart in this process.

2) Retrofitting to shear force

In this experiment, shear force is carried only by transverse carbon fibre. In a similar way, converted the needful amount of transverse reinforcing bars to the amount of transverse carbon fibre. The amount of carbon fibre to shear force were computed as in equation (3).

$$A_{CF} = 1.15 \times S \times a/(d \times \sigma_{cF}) \qquad (3)$$

where,
A_{CF} : is the amount of needful carbon fibre.
S : is shear force acted on specimens.
a : is the pitch of carbon fibre; and
d : is the effective depth of pier.

5.4 Test results

The load-deformation curves are illustrated in Figure.13. The results are listed in Table.6. In the results, the cracking is defined as the state at which the crack is visible to the naked eye, the yielding is the state at which the longitudinal reinforcing bar at tension side is yield, and the ultimate is the state at which concrete fails or carbon fibre tears up. Ductility rate was obtained as division of the ultimate displacement σ_u by the yield displacement σ_y.

The failure of Specimen No.1 occurred at the cut-off part. On the other hand, the failure of Specimen No.2 (in which carbon fibre is stuck in longitudinal direction) occurred at the top of footing. This indicates that the resistance to bending moment increases as the carbon fibre retrofitting is done along longitudinal reinforcing bar.

The failure type of Specimen No.2 is bending shear failure. However, the failure type changes to bending failure when pier is wound by carbon fibre in transverse direction (Specimen No.3).

In Specimen No.4, the amount of carbon fibre is the double of that of Specimen No.3. Although test was done until the maximum capacity of loading device, failure did not occur. This further indicates that the ductility of pier increase by the wound carbon fibre.

As mentioned in previous paragraph, Specimen No.5 has already failed before carbon fibre retrofitting and reloading. As a result, the position of failure moved from cut-off part to the top of footing and the failure type changed from bending shear failure to bending failure. The ductility rate was also increased.

6. DISCUSSION

6.1 Exposing Test

According to the results of tensile strength test and gluing strength test, it can be concluded that there is no deterioration after the sample was weathered for only one year in air. It is intended to continue this exposing test for another 9 year to see whether there really is aging effect or not.

6.2 Element test

The results of compression test show that the compressive strength of concrete retrofitted by carbon fibre is almost independent of the amount of carbon fibre. For the carbon fibre sheet was just pasted on concrete and there was no pre-tension in the sheet, it is considered when concrete arrives the maximum compressive strength, carbon fibre sheet does not work effectively yet. However, the results at ultimate state showed that the ultimate strain increases significantly as the amount of carbon fibre increases. This means that carbon fibre plays the confining effect. It therefore comes out that the ultimate compression strain depends on the amount of carbon fibre but the compressive strength is independent of the amount of carbon fibre.

In real case, it is usual that 1 to 5 sheets are used in transverse carbon fibre retrofitting. This corresponds to a volumetric ratio of 0.09% to 0.45%. From Figure.7, it can be seen that the ultimate compression strain is larger than 0.4%. Figure.14 shows the regulation on concrete "Design Specification for Highway Bridges, Part 5 Seismic Design, 5.4.2. Ultimate Displacement and Holizontal Load Capasity". It is assumed that ultimate compression strain of concrete is 3.5%. But it is considered that this value (0.4%) can be used in design of carbon fibre retrofitting.

6.3 Pier model test

1) Retrofitting efficiency

The test results showed that as carbon fibre is pasted on cut-off part along longitudinal reinforcing bar, the failure position moved from cut-off part to the top of footing. If carbon fibre was stuck transverse direction, the failure type changed from bending shear failure to bending failure, the concrete of the column was confined, and boththe shear resistance and the toughness were improved. This means that as a retrofitting method, carbon fibre retrofitting is efficient.

2) Characteristics of energy absorbing

It is well known that the area between load-displacement curve and abscissa (usually displacement) represents the energy absorbed. The larger the area, the higher the absorbing energy, further the safer the structure against earthquake. The absorbed energy before failure and after carbon fibre retrofitting is illustrated in Figure.15. It can be seen that for the same cumulative displacement, the energy absorbed is slightly larger before filure than after carbon fibre retrofitting. The slope is almost the same in the both cases. This slope does not change until the displacement of $6\sigma_y$. This indicates that the energy absorbing doesn't decrease until ultimate state. This further proves that this new method as a retrofitting method is very effective.Also it is considered that energy absoabing after carbon fibre retrofitting was recovered to the level before failure, this method is effective for damaged pier.

7. CONCLUSION

From this study, it is understood that carbon fibre pasted on pier surface along longitudinal reinforcing bar increases the bending

resistance of pier and transfers the failure position from cut-off part to the top of footing. On the other hand, carbon fibre stuck in transverse direction improves the ductility of pier.

In this report, we had defined shear force was carried only by carbon fibre of transverse direction, but now, we define that shear force is carried by concrete, lateral reinforcing bars and carbon fibre because of consideration for economy.

For the ultimate strain of concrete, the value of 0.4% might be used in design without any problem.

The above results validate that the carbon fibre retrofitting is effective enough for after-earthquake repairing.

The authors wish that this method can be widely used.

REFERENCES

1)Japanese Road Association: Standard for Road Bridge, Part 5, Design Specifications for Seismic Design, 1990.
2)Japan Concrete Institute: JCI Colloquium on Ductility of Concrete Structures and Its Evaluation, March 28,29, 1988.
3)N.Higashida and T.matsuda: Effect of Carbon Fiber Reinforcement as a Strengthening Measure for Reinforced Concrete Bridge Piers, Civil Engineering, Vol.47 No.3, 1992.

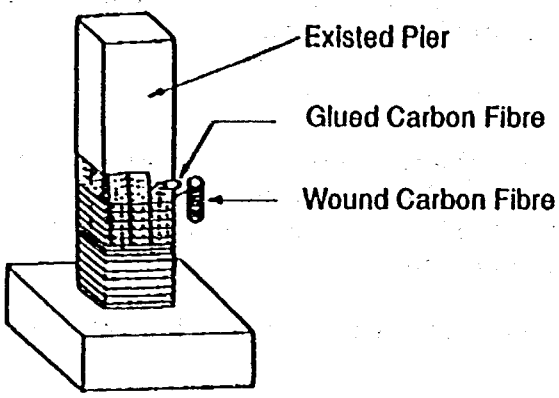


Figure.1 Carbon fibre retrofitting method

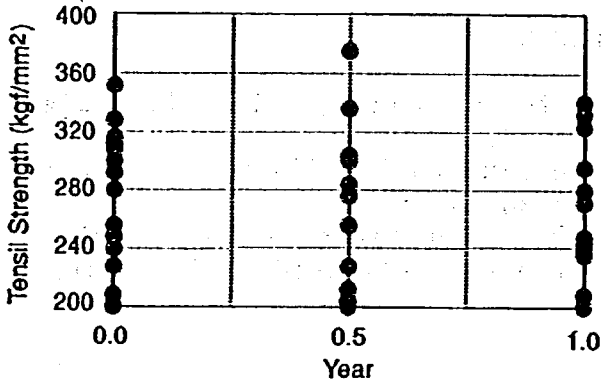


Figure.2 Weathering test
(Tensile strength test)

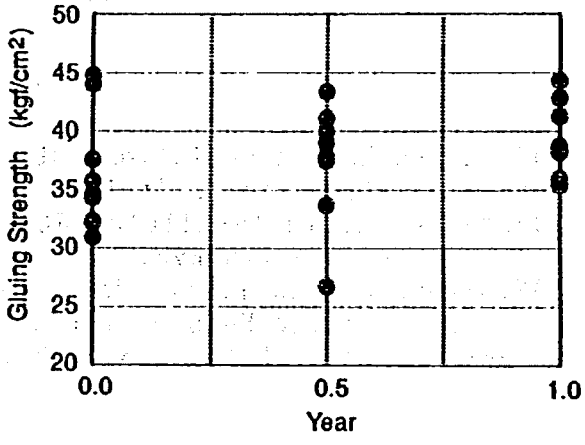


Figure.3 Weathering test
(Gluing strength test)

Table.1 Sample for element test

Samples	Shape · Scale	Amount of carbon fibre	Space of carbon fibre	Number of test
No.1	cross section 15cm x 15cm Height 30cm	0.00%	—	2
No.2		0.07%	22.7mm	6
No.3		0.13%	14.4mm	6
No.4		0.26%	0.0mm	6

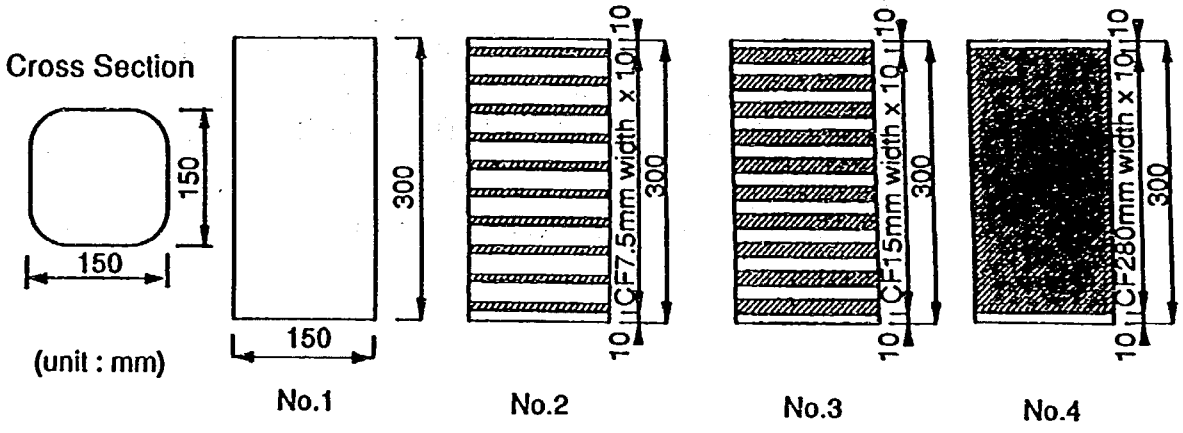


Figure.4 Samples for element test

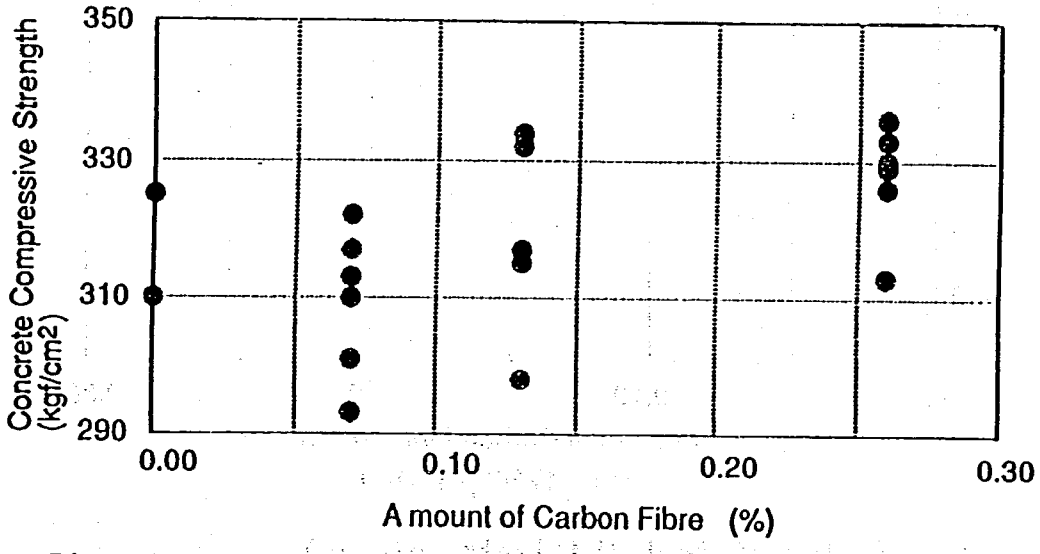


Figure.5 Element test (Compressive strength)

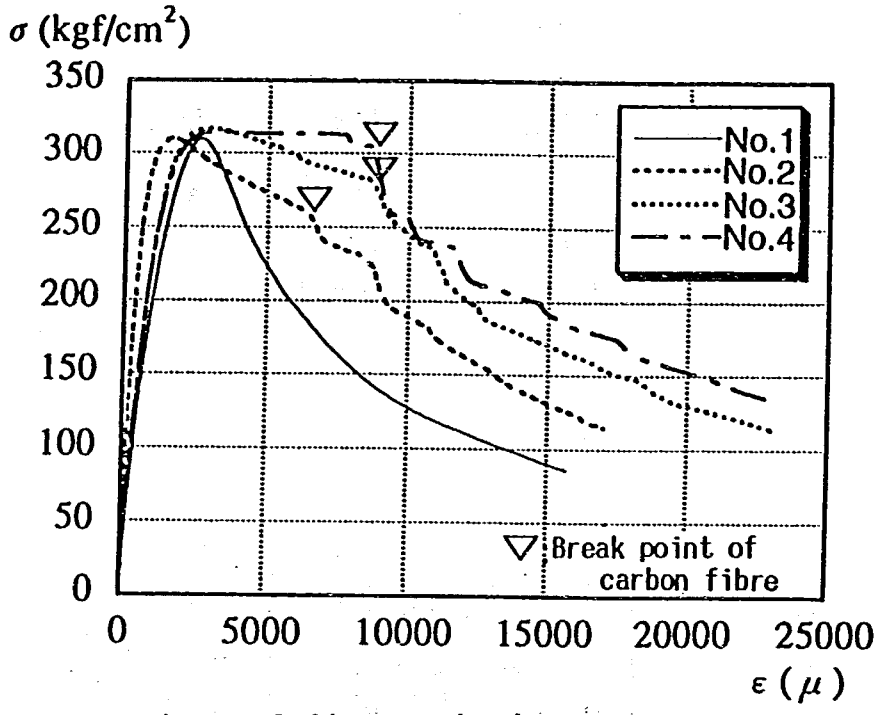


Figure.6 Stress-strain curve

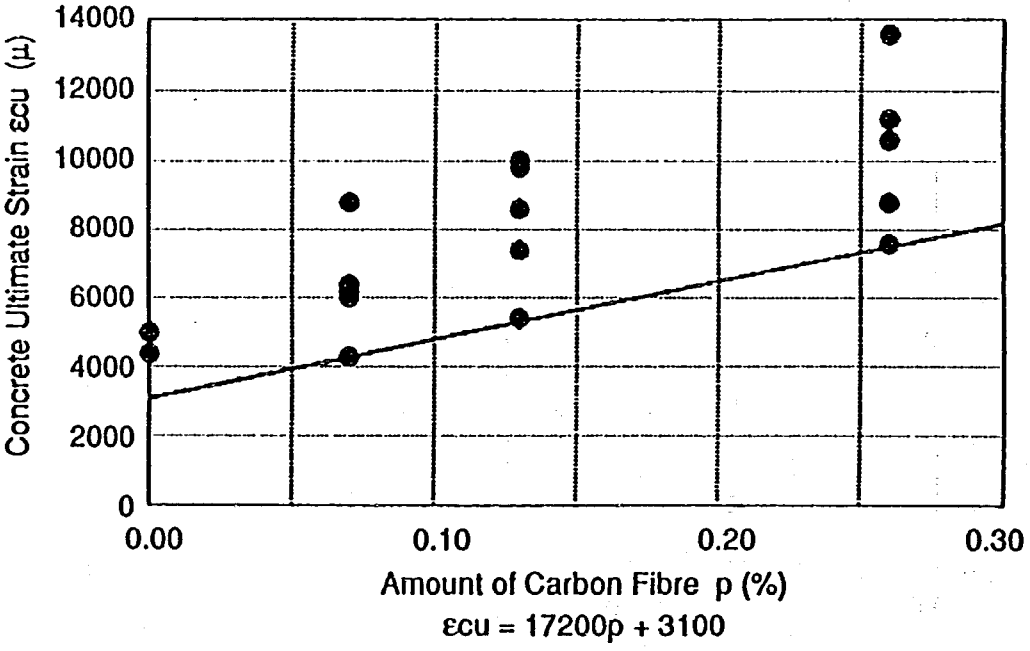


Figure.7 Element test (Ultimate strain)

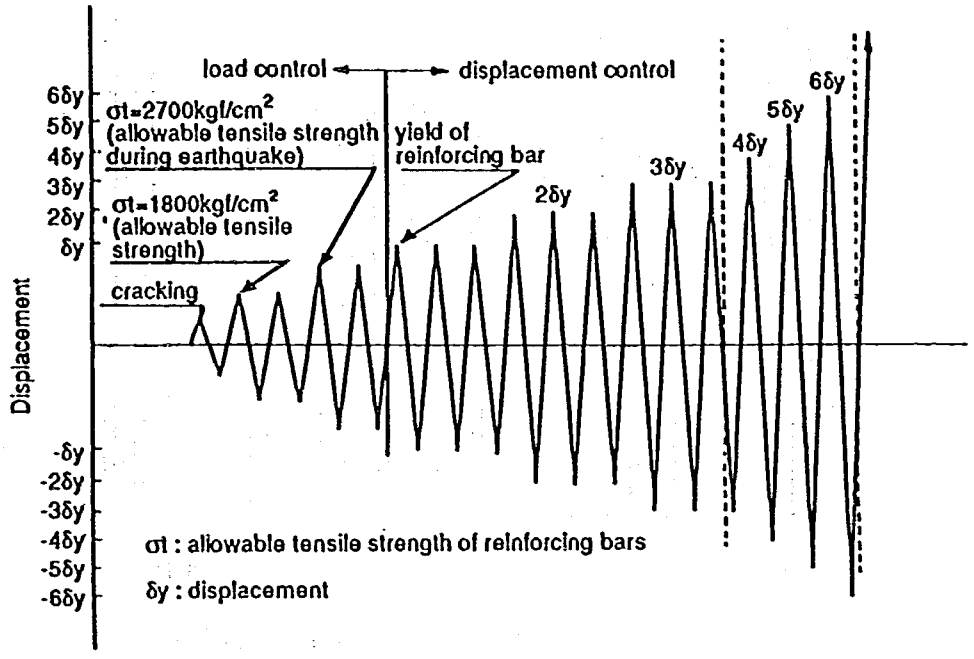


Figure.10 Loading pattern

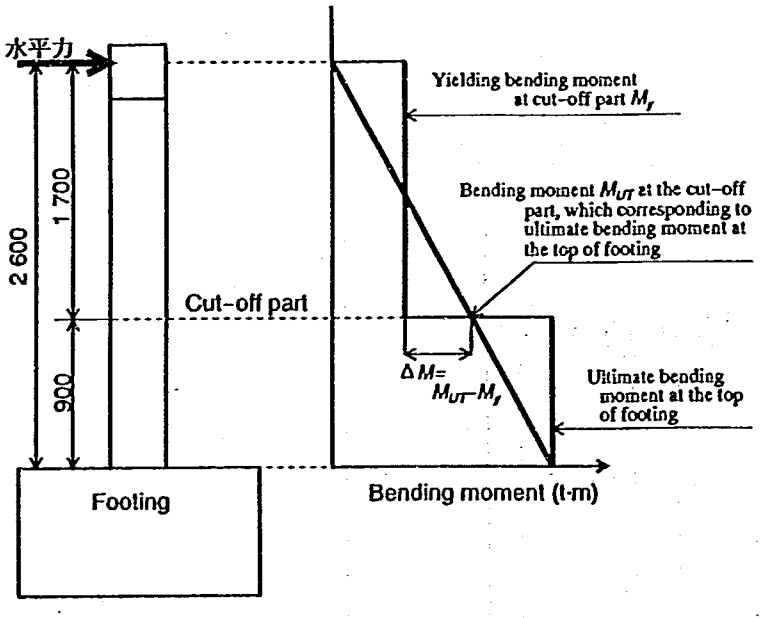


Figure.11 Bending moment

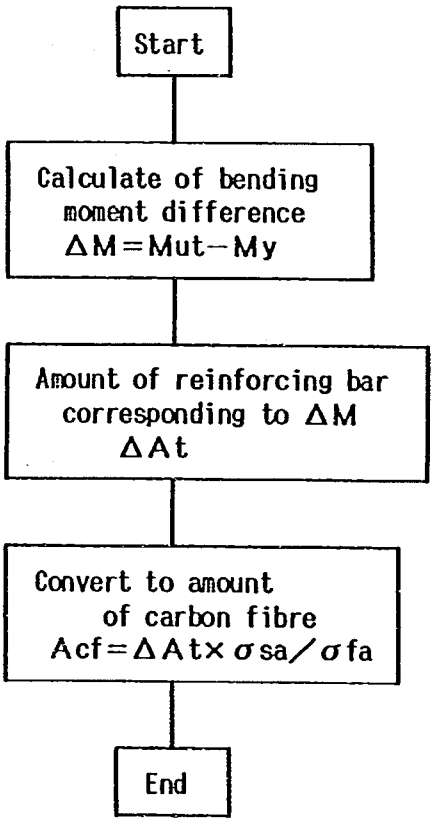
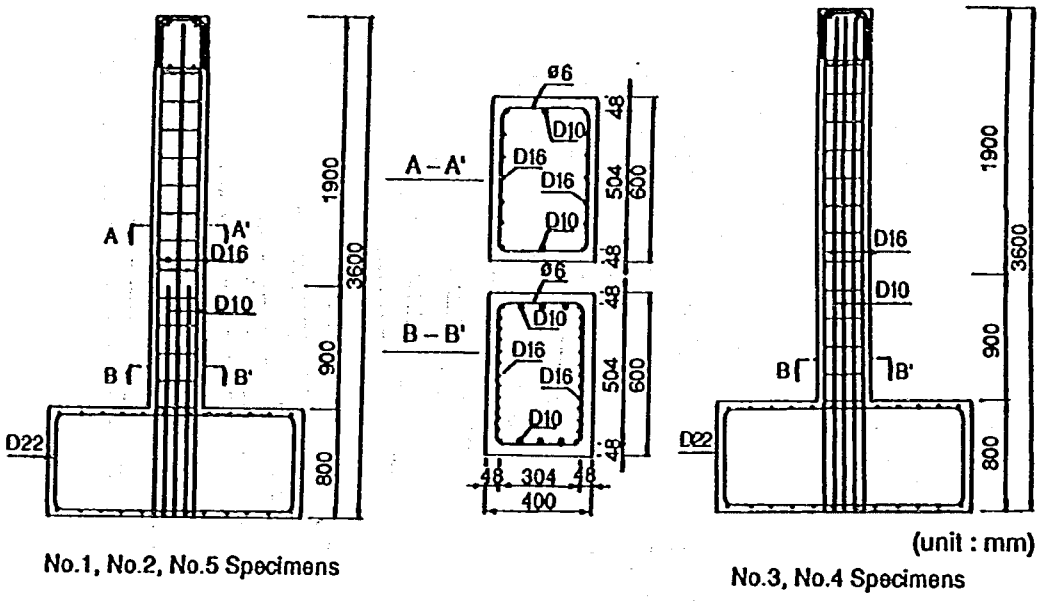


Figure.12 Flow-chart



No.1, No.2, No.5 Specimens

No.3, No.4 Specimens

Figure.8 Specimens of pier model

Table.2 Specimens of pier model

Spec.	Height of cut-off part	Length of carbon fibre retrofitting				Sheet of carbon fibre		
		Length of upper carbon fibre from cut-off part (㎜)	Length of lower carbon fibre from cut-off part (㎜)	Total (㎜)	Top of footing (㎜)	Cut-off part		Top of footing
						Longitudinal	Transverse	Transverse
1	900	-	-	-	-	-	-	-
2	900	450	450	900	-	2	2	-
3	-	-	-	-	600	-	-	1
4	-	-	-	-	600	-	-	2
5	900	530	400	930	500	2	2	2

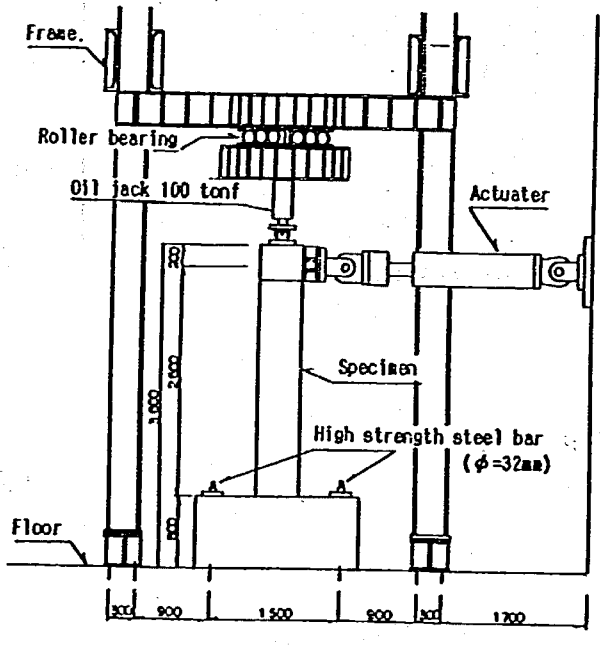


Figure.9 Loading apparatus

Table.3 Material test of reinforcing bar

Specimens	D10 (SD295)			D16 (SD295)			φ6(SR295)		
	yield strength	tensile strength	static modulus of elasticity	yield strength	tensile strength	static modulus of elasticity	yield strength	tensile strength	static modulus of elasticity
	(kgf/cm^2)	(kgf/cm^2)	(kgf/cm^2)	(kgf/cm^2)	(kgf/cm^2)	(kgf/cm^2)	(kgf/cm^2)	(kgf/cm^2)	(kgf/cm^2)
1	3,600	5,200	1.9×10^6	3,600	5,300	1.9×10^6	3,700	4,800	1.9×10^6
2,4,5	3,600	5,070	1.9×10^6	3,590	5,110	1.9×10^6	3,400	4,660	1.9×10^6
3	3,760	5,350	2.1×10^6	3,770	5,480	2.0×10^6	3,370	4,430	1.9×10^6

Table.4 Material test of concrete

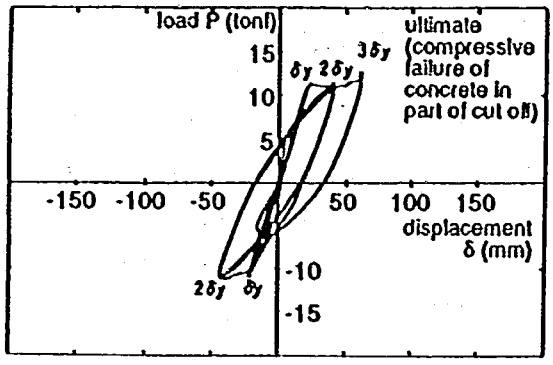
Specimens	Compressive strength	Static modulus of elasticity
	(kgf/cm^2)	(kgf/cm^2)
1	369	2.4×10^5
2	381	2.4×10^5
3	296	2.3×10^5
4	366	2.6×10^5
5	287	2.2×10^5

Table.5 Material test of carbon fibre

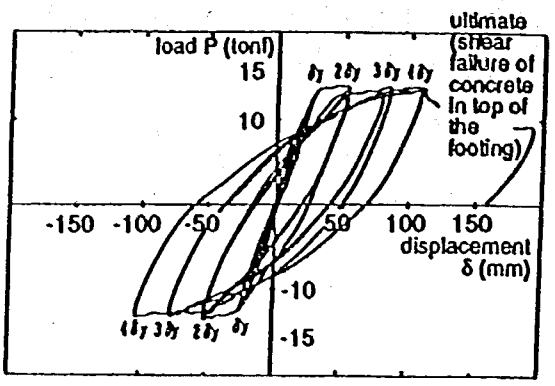
Specimens	Tensile strength	Static modulus of elasticity
	(kgf/cm^2)	(kgf/cm^2)
2,4	29,300	2.5×10^6
3	29,100	2.3×10^6
5	29,000	2.4×10^6

Table.6 Results

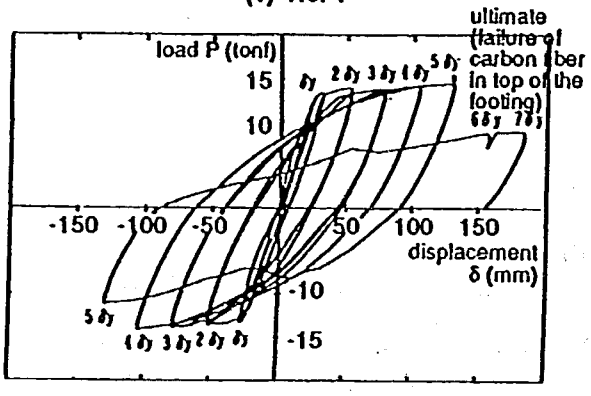
Spec.	Cracking		Yield		Ultimate		Maximum load		Ductility rate	Failure type
	Load Pc (tonf)	Displacement δc (mm)	Load Py (tonf)	Displacement δy (mm)	Load Pu (tonf)	Displacement δu (mm)	Load Pmax (tonf)	Displacement δmax (mm)	μ	
1	2.8	2.6	10.4	20.6	11.5	61.7	11.5	61.7	3.0	bending
2	2.9	2.8	12.6	27.6	13.4	113.0	13.9	55.3	4.1	shear
3	2.5	1.9	13.0	26.2	14.5	131.0	13.9	52.1	5.0	bending
4	3.0	2.2	11.9	22.0	15.5	244.2	15.5	244.2	11.1	-
5	3.5	6.7	10.0	22.3	11.7	111.7	14.0	63.8	5.0	bending



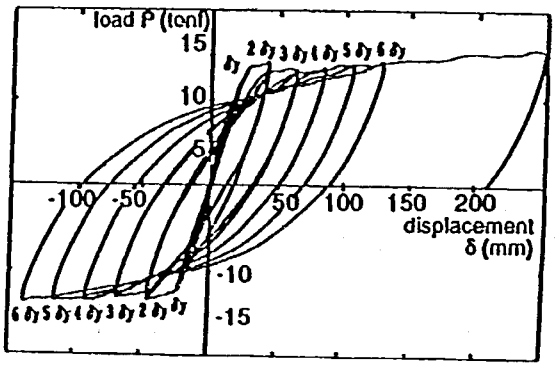
(1) No. 1



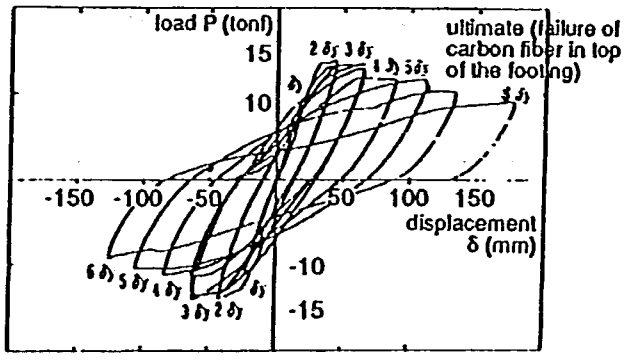
(2) No. 2



(3) No. 3



(4) No. 4



(5) No. 5

Figure.13 Experiment result (Load-deformation relationship)

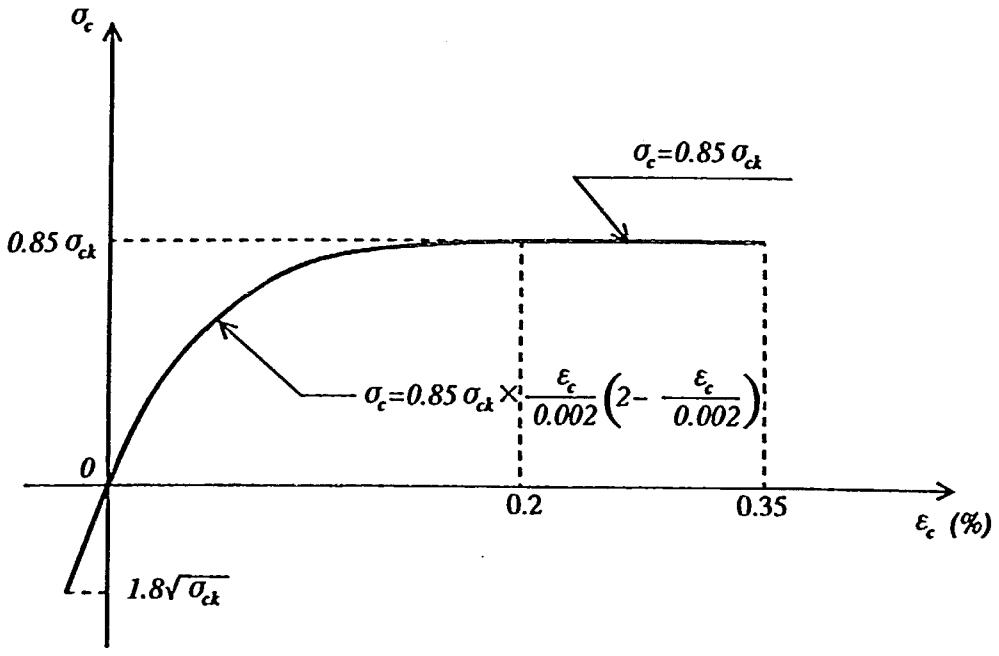


Figure.14 The regulation of concrete of "Design Specification for Highway Bridges"

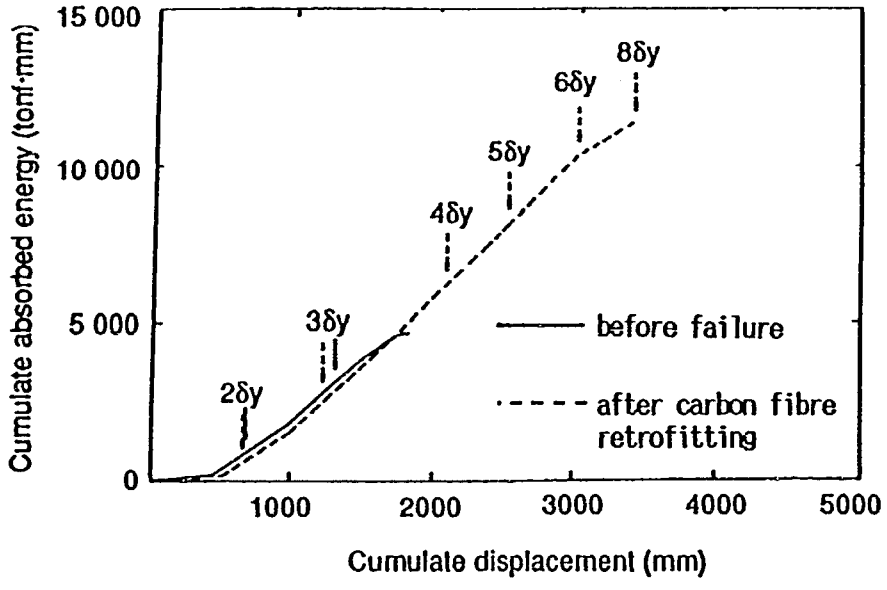


Figure.15 Cumulate displacement - Cumulate absorbed energy

RETROFIT SOLUTIONS FOR INADEQUATE ANCHORAGE OF COLUMN BARS INTO PIER CAPS

David H. Sanders, Bruce M. Douglas, and Kurt Cornell

Bridge Engineering Program
Department of Civil Engineering/258
University of Nevada
Reno, NV USA 89557-0152
Ph: (702) 784-4288 FAX: (702) 784-4466

ABSTRACT

Inadequate anchorage of column bars into pier caps is a common problem in older reinforced concrete bridges, especially in seismic regions. This study presents retrofit details for the column-pier cap region that shift the hinge location down the column. (Details are developed explicitly for box-girder bridges with integral pier caps.) Shifting the hinge location provides sufficient development length and ductility at the hinge location. The portion of the column above the new hinge location is reinforced to prevent failure. Two alternatives are presented, a steel cone and a concrete drop panel. Details for this alternative are presented in the paper. Retrofit procedures discussed in this paper do not effect the riding surface of the structure and do not interrupt the traffic on the bridge surface. In addition, the retrofits limit the amount of on-site fabrication and labor. The number of holes to be drilled into the existing structure was a major consideration. The retrofits designate a critical location for hinging that is easy to observe and repair if necessary. The retrofit also provides flexibility depending on the amount of strength capacity that is necessary. This paper relies heavily on information presented in reference 9.

BACKGROUND

Many of the older reinforced concrete bridges, before 1970, have insufficient development length for the column bars as they extend into the footing and the pier cap. The reason for this is two fold. One reason is that development length equations used by bridge designers have change substantially. This especially true in zones where there is little distance between the bars or confinement around the bars is inadequate. The second reason is that in order to ensure that anchorage failure does not occur, anchorage for the excess capacity of the bar must also provided. This excess capacity is typically around 25%. This paper focuses on the column-pier cap connection.

The details shown in Figures 1 and 2 are from a box-girder bridge constructed in 1964. The bridge was constructed with 3000-psi (21 MPa) specified

concrete. Based on the conservative nature of the concrete mix designs of the 1960's and the time since construction, the concrete strength used in the analysis of the section was 5000 psi (35 MPa) [7]. The development length provided for the Grade 40 (275 MPa) #11 (36 mm) column bars is 34 inches (864 mm). The basic development length required to develop the yield level of the reinforcement is 35.5 inches (902 mm). If it is assumed that the reinforcement can reach an overstrength stress level of $1.25f_y$, a development length of 44 inches (1118 mm) is needed. Therefore, from a strength perspective, the bars are 10 inches (254 mm) too short.

In addition to the strength deficiency, the ductility capacities of the existing joint and column are very poor. The column confinement consists of #5 (16 mm) Grade 40 (275 MPa) ties at 12 inches (305 mm). This is typical of bridges that were built without considering seismicity or before current detailing standards existed. Columns in bridges built in the 1960's had only a minimal number of ties. Integral pier caps typically had no reinforcement designated for confinement of the joint. There usually was some shear reinforcement in the pier cap. This reinforcement could be potentially be mobilized for confinement. Bridges with these deficiencies in detailing and in development length exist not only in high seismic regions but also in moderate and low seismic regions. The degree to which modifications are necessary is a function of the seismic event that the bridge is being designed to withstand as compared to the original design.

Extensive research has been done on retrofitting columns. Only two of the many references are given [4,7]. Steel jackets have been extensively used by the California Department of Transportation for retrofitting columns to increase the ductility and the shear capacity and to provide confinement for splices. Retrofits can be either half-height or full-height jackets. Gaps are provided at the top and the bottom of the steel jackets to prevent the bearing of the steel jackets against the integral pier caps and the footings, respectively. The gap also prevents too much moment from being transferred into the footing or the pier cap. This technique works well when the existing column has sufficient bending strength. The gaps provided are small enough that the jacket confines the concrete in that region. Therefore, the column concrete can reach the confined column moment capacity as long as there is sufficient development length for the reinforcement. Figure 3 compares the strength capacity and the strength demand at the maximum force level for a jacketed column that has a gap at the top. In many cases, the strength of the existing bridge is sufficient and only the ductility capacity is a problem. If the bridge column shown in Figure 1 had sufficient development length and the column was jacketed to satisfy ductility requirements, it would require a ground acceleration of 0.3 g to hinge the columns. This assumes that the pier cap will perform adequately. The columns in the prototype bridge do not have enough development length, and many other existing bridges do not have sufficient development length and/or strength.

The purpose of this paper is to present options for retrofitting beam-

column joints in box-girder bridges (integral pier cap to column joints) which have the following characteristics: 1) adequate strength but insufficient development length for column reinforcement and inadequate ductility capacity and 2) inadequate column hinge strength and ductility. The key to a successful retrofit program is the use of retrofit procedures that are not only effective but also economical. In the development of the retrofits discussed in this paper, emphasis was placed on making them economical.

ALTERNATIVES

Insufficient development length can be addressed by several techniques. One technique is to increase the length of the bar. This is possible in older bridges because designers often did not extend the column bars to the top of the pier cap. Adding bar length can be done with mechanical connectors or by welding. Another method for increasing the anchorage length is to weld plates onto the ends of the bars. In cases where welding new material on to the existing bars is chosen, the engineer must be very careful. Steels used in making reinforcement is often difficult to weld without have problems such as weld fracture or incomplete fusion of material. Another problem with the techniques discussed is the possible difficulty in accessing the end of the bar. Accessing the column reinforcement would require the removal of concrete and more than likely cutting the top mat reinforcement in the superstructure. In the case of the prototype bridge, this would be very difficult (see Figure 2). A large amount of longitudinal negative reinforcement is present in the top flange over the column. All the longitudinal bars that were cut would need to be spliced back together to restore the negative moment capacity.

Another option for providing sufficient development length is to alter the parameters of the section surrounding the reinforcement to increase the effectiveness of the existing reinforcement length. Depending on the accessibility to the area surrounding the column reinforcement in the pier cap, this may be a reasonable solution. Parameters that could be altered include the amount of concrete cover, confining reinforcement (spirals and ties), and/or confining pressures (post-tensioning). In the 15th Edition of the *AASHTO Bridge Specifications* [1], the basic development length can be modified by 0.75 if the reinforcement is enclosed within a spiral of not less than ¼ inch (6.4 mm) in diameter and not more than 4 inches (102 mm) in pitch. The prototype bridge and many others built in that period have little or no confining reinforcement in the pier cap. Therefore, concrete material would have to be removed to add the confining bars. This is very impractical. Another choice would be to develop confinement with an active confining pressure (post-tensioning). To provide adequate confinement in a column, a confining pressure around the column reinforcement of 300 psi (2.1 MPa) is needed [7]. This could be accomplished by provided 700 kips (3.11 N) of prestress force (five 1-1/4 inch (31.8 mm) Dywidag bars stressed to $0.7f_{pu}$) transverse to the pier cap and along the axis of the pier cap. The effectiveness of this alternative needs to be tested. If there is

significant concrete cover on two opposite sides of the column reinforcement, the post-tensioning in that direction could be eliminated. Since it is difficult to know the exact location of the column bars, passing the post-tensioning bars through the section may be quite difficult. In addition, development of the prestress force is difficult because of the very short bar length.

The *AASHTO Bridge Specification* also provides for the confining effect of concrete when calculating the development length. The specification states that if the lateral spacing between the bars is at least 6 inches (152 mm) center-to-center and the bars have a clear cover in the direction of spacing of at least 3 inches (76.2 mm), the basic development length can be modified by 0.80. In the prototype bridge, some columns have 21 bars on a 16.17 inch (411 mm) radius. The center-to-center spacing for these column bars is 4.8 inches. Other columns (see Figure 1) only have 11 bars, which corresponds to center-to-center spacings of 9.2 inches (234 mm). In the pier cap, the clear cover over the column bars is 6.5 inches (165 mm). Therefore, the 0.80 factor could be used on the development length for main longitudinal bars in the 11-bar columns. This reduces the required development length for the overstrength stress level from 44.1 inches (1120 mm) to 35.3 inches (897 mm). The available development length is 34 inches (864 mm). This may make the requirement for retrofitting the 11-bar columns in the prototype bridge marginal. The project will use 11-bar columns because the columns are being used to verify the constructibility of the retrofit procedures. In addition, when the 11-bar column section is scaled down for the test specimens, the 0.80 factor is not valid for calculating the development length. The 21-bar column is not being used because it would be too expensive to fabricate and retrofit due to the larger section capacity.

SHIFTING THE HINGE LOCATION

The alternatives discussed so far have the same critical section as the original design (the hinging location for maximum loading at the interface between the column and the pier cap). Another alternative is to shift the hinge location down into the column. By shifting the hinge location, the ductility demand on the pier cap is decreased and the required development length is satisfied. For this retrofit to be successful, a hinge must be prevented from forming above the designed location, and the increased column moment resulting from the column retrofit must be transferred into the pier cap.

A seismic retrofit was just completed on the Interstate 80 bridges in Sparks, Nevada, USA [6]. One component of this retrofit was the shifting of the hinge location down into the column. Shear resistance in the plastic hinging zone was also a problem. Concrete drop panels were used that were designed to be at least thirty percent stronger than the original columns. The drop panels were reinforced and dowels were provided between the panels and the existing columns and pier caps (see Fig. 4). The pier cap was strengthened and a 3/8" steel jacket

for the column was specified for increasing the ductility and shear strength of the hinge region. The jackets were placed just at the top of the column for a distance of 54 inches (1372 mm) below the panels. The jackets were estimated to increase the column ductility capacity by at least six. In the final design a high-strength fiber wrap was used instead of the steel jacket. The fiber wraps were up to 0.459 inches (11.7 mm) thick (nine layers). This alternative was presented for reference and is not the primary focus of the paper.

For the prototype bridge, the hinge location needs to be shifted at least one foot down from the top of the column, when the confinement factor of 0.80 is not used, in order to provide sufficient development length. Figure 5 shows the retrofit details for the prototype bridge. A steel alternative was selected for the prototype. A gap is provided at a location two feet below the pier cap (no gap at the top of the column) to prevent too much moment from being transferred into the pier cap. This is the new hinge location of the column. A gap of 2 inches (50.8 mm) provides sufficient confinement to the concrete in the hinge region to allow it to reach the confined capacity (1630 ft-kips, 2210 N-mm) and ductility but is large enough to prevent the two separated steel shells from bearing against each other. Figure 6 shows the effect of the hinge shift on the moment demand and capacity for the column.

The major components of the retrofit are the steel jacket, steel stiffeners to transfer the increased moment and shear into the bearing plate, the bearing plate, anchor bolts, and modifications to the existing pier cap. The hinge location was shifted down two feet instead of the minimum required one foot, because this ensures sufficient development length with very little additional cost in materials and in the maximum moment at the top of the column. When the hinge is at two feet from the pier cap, the maximum moment at the pier cap-column connection is 1800 ft-kips (2441 N-mm). If the hinge was at one foot from the pier cap-column connection, the maximum would drop to only 1715 ft-kips (2325 N-mm); this is only a 4.8 percent drop. The deeper placement of the hinge provides a transition zone so that the section can be enlarged to transfer the increased moment into the pier cap. To provide sufficient column confinement, 300 psi (2.1 MPa), a steel jacket thickness of 3/16-inch (4.8 mm) must be used. This thickness provides sufficient ductility and good construction characteristics. The moment capacity of the jacket section is 2800 ft-kips (3796 N-mm). The steel jacket is more than adequate for carrying the moment above the hinge location.

To transfer the increased moment into the pier cap, anchor bolts must be utilized to carry the tension, since the column steel can not be fully developed. The steel jacket cannot transfer the moment into the pier cap because it terminates at the top of the column into the plate. The anchor bolts used in the prototype retrofit are twelve 7/8-inch (22.2 mm) A325 anchors. The embedment length needed for these anchors is 9¼ inches (235 mm) [2]. In the zone of the pier cap, the holes for the anchor must be drilled the full embedment length into the existing concrete. Fortunately, the amount of reinforcement in the bottom

slab and in the pier cap is quite small. Collins et al. [5] discovered that undercut bolts (Maxi-Bolt) behaved essentially the same as cast-in-place anchors. Therefore, undercut bolts will be used for anchors that connect into the original pier cap and cast-in-place anchor bolts will be outside the pier cap. Since the bottom flange of the prototype is only 6 inches (152 mm) thick, additional concrete must be added to provide sufficient embedment for the cast-in-place anchors and to transfer the forces into the pier cap. The anchor bolt configuration shown (see Figure 7) was selected because tensile strains in the column reinforcement remain much less than the yield strain at the column-pier cap interface when the maximum load is applied (moment limited by the hinge capacity). It must be remembered, that the limited development length restricts the capacity of the column bars at the interface.

Satisfying equilibrium and assuming that plane sections remain plane, the location of the neutral axis in the concrete for the maximum moment was 17.85 inches (453 mm) from the extreme compressive fiber. This meant that the maximum stress in the column reinforcement at the interface was 25 ksi (172 MPa). Based on the development length equations, there is sufficient length to develop the needed stress in the column steel at the interface. Base plate tests have shown that plane sections do not remain plane in these types of regions. The experimental results will provide a better estimate of the true strain distribution under the bearing plate.

Twelve stiffeners are provided around the steel jacket to transfer the load out to the anchor bolts and increase the size of the moment arm at the pier cap-column interface. The stiffeners consist of ¾-inch (19.1 mm) steel plates that taper from the hinge location [3,8]. A thin metal sheet will be placed around the stiffeners to make the connection more aesthetically pleasing. The steel bearing plate is 1¾ inches (31.8 mm) thick and 72 inches (1829 mm) square . The compression caused by the moment is carried by the plate into the concrete. To determine the plate thickness, the tension portion of the applied moment couple carried by the column steel was subtracted from the total moment. The remaining moment must be transferred through the plate to the anchor bolts to develop the rest of the moment couple. The maximum moment location in the plate was at a point 9 inches (229 mm) inside the existing column or 26 inches (660 mm) from the extreme compression fiber. A traditional base plate procedure could not be used because of the radial bolt pattern and the influence of the column reinforcement on the moment distribution in the plate.

The portion of the moment that is transferred to the bottom flange outside the pier cap must be transferred back into the pier cap. The shear capacity of the existing bottom slab is not sufficient to carry the applied compression or tension. One solution is to widen the pier cap to the size of the bearing plate. Since it is necessary to place concrete for the embedment length of the anchors, it does not require a significant amount of extra labor or materials to add concrete over the entire height of the box (see Figure 5). The original surface of the pier cap will

be roughened, and shear studs will most likely be used to assist in the transfer of forces between the new and old concrete.

As much of the retrofit as possible should be fabricated in the shop before field installation. The column jacket and the top cone section should each be brought to the field in two halves. Each cone section half will include the stiffeners and the bearing plate. The two column jacket halves will be welded together in the field. The cone sections will be bolted together using the stiffeners that will be placed on each half of the shell. This was done because of the thickness of the base plate. It was thought that the bolting procedure would be easier than welding a 1¼-inch (31.8 mm) plate upside down in the field.

The construction procedure for the retrofit will be as follows.

1) Access the interior of the box girder from a region outside the cone area.
2) Drill the anchor bolt holes that go through the bottom slab and those that go into the pier cap.
3) Make a template of final hole locations and then drill the holes into the bearing plate in the field.
4) Drill the holes into the pier cap for the studs that will transfer shear from the anchor embedment blocks and roughen the concrete surface of the pier cap.
5) Attach each half of the assembly to the original column, both below and above the designated hinge region. In the cone section, the anchors that go directly into the pier cap can hold the shells in place.
6) Weld the bottom shells together and bolt the top portion together.
7) Place the anchor bolts that pass through the bottom slab into the inside of the box-girder, and epoxy the studs for the anchor block into the pier cap.
8) Cast the concrete inside the block, securing the anchor bolts.
9) Grout the steel jackets and the base plate.
10) Place the sheet metal cone around the stiffeners.
11) Paint the steel jacket and cone to match the concrete.

To test this technique, half-scale model specimens will be used. The diameter of the column will be reduced to 20 inches (508 mm) with # 3 (10 mm) ties at 12.5-inch (318 mm) intervals. Twelve 5/8-inch (15.9 mm) A307 bolts will be used. The maximum moment demand placed on the interface is 225 ft-kips (305 N-mm). This is limited by a hinge moment of 204 ft-kips (277 N-mm). In the scale model specimens, the stiffener thickness will be reduced to 3/8 inches (9.5 mm), and the bearing plate thickness will be 5/8 inches (15.9 mm).

This retrofit provides the column with sufficient development length, ductility, and a small increase in the strength due to the shifting of the critical

location. In the case of a major earthquake, the critical location is now out away from the superstructure. This makes damage identification and repair a much more simple operation.

INADEQUATE STRENGTH, DUCTILITY, AND DEVELOPMENT LENGTH

In areas of the country where seismic design has not been considered in the past, a significantly larger hinge moment than what the column can carry in its current form may be necessary to handle the design earthquake. It was mentioned before that the column capacity was increased significantly by adding the steel jacket. This jacket improves the ductility of the structure. However, in the cases where shear does not control the retrofit, the jacket does not increase the strength of the structure because a gap was provided at the top and bottom of the column. If this gap is removed and a method for transferring the forces into the superstructure is provided, the earthquake forces that the structure can withstand will be increased. For the prototype bridge, the confined moment strength of the column was 1630 ft-kips (2210 N-mm) while the jacketed moment strength (confined concrete with steel shell) was 2800 ft-kips (3796 N-mm). To provide a path for this moment to the pier cap, a larger section is needed at the pier cap-column interface. The same technique that was used in the last section can be used again to transfer the increased moment. Figure 8 shows the effect of this retrofit on the moment capacity and demand for the column at the maximum event. With this increased moment capacity, the prototype bridge would need to subjected to a ground acceleration of about 0.6 g before the columns would yield.

The details for the retrofit are shown in Figure 9. Table 1 compares this retrofit with the retrofit that had a hinge capacity equal to the confined concrete hinge strength. The moment capacity at the column-pier cap interface of the retrofitted section using the bolt pattern shown in Figure 7 is 4790 ft-kips (6494 N-mm). The maximum moment demand placed on the interface is 3100 ft-kips (4203 N-mm). The moment capacity is well over the demand so that high strains are not required from the column reinforcement.

This retrofit significantly strengthens the column and improves the ductility. In many cases, this degree of the strengthening is unnecessary or impractical because it places too much moment demand on the superstructure. This retrofit may cause the need for strengthening the pier cap in both the longitudinal and transverse directions. This could be done in the transverse direction by extending the anchor blocks the full length of the pier cap and placing steel in the anchor blocks to carry the transverse moment. Another possible method would be to epoxy steel plates on to the base of the pier cap in the transverse direction. In the longitudinal direction, both of these techniques could also be used but due to the difficulty in drilling through the pier cap, the epoxying of plates may be easier.

Table 1: Comparison of Prototypes and Retrofits

	Confined Hinge		Jacketed Hinge	
Feature	Prototype	Model	Prototype	Model
Col. Diameter	39" 991 mm	20" 508 mm	39" 991 mm	20" 508 mm
Col. Bars	11#11 (Gr. 40) 36 mm	10#5 (Gr. 60) 16 mm	11#11 (Gr. 40) 36 mm	10#5 (Gr. 60) 16 mm
Col. Height	20' 6096 mm	10' 3048 mm	20' 6096 mm	10' 3048 mm
Col. Stirrups	#5@12" (Gr.40) 16 mm@305 mm	#3 @12.5" (Gr.60) 10 mm@318 mm	#5@12" (Gr.40) 16 mm@305 mm	#3 @12.5" (Gr.60) 10 mm@318 mm
Stiffeners	3/4" 19.1 mm	3/8" 9.5 mm	1-1/8" 28.6 mm	9/16" 14.2 mm
Jacket Thickness	3/16" 4.8 mm	3/32" 2.4 mm	3/16" 4.8 mm	3/32" 2.4 mm
Anchor Bolts	12 7/8" A325 22.2 mm	12 5/8" A307 15.9 mm	12 1-1/4" A325 31.8 mm	12 5/8" A325 15.9 mm
Embedment Length	9-1/4" 235 mm	4-3/4" 121 mm	13-1/4" 337 mm	7" 178 mm
Plate Thickness	1-1/4" 31.8 mm	5/8" 15.9 mm	2-1/8" 54.0 mm	1-1/16" 27.0 mm

MODERATE INCREASE IN COLUMN HINGE STRENGTH

The two previous cases were extremes. Either the column strength was increased only to the confined column strength level or to a level that fully utilized the standard column steel retrofit. Another option is to increase moderately the moment strength in the hinge region. This can be done by providing a thin steel shell over this region. Since confinement is provided by the 3/16-inch (4.8 mm) steel shell above and below the hinge region, the concrete in the hinge region can reach confined levels of stress and strain. On the tension side of the column, the thin steel shell can provide the needed increase in tension capacity. In the prototype bridge, if a 1/8-inch (3.2 mm) steel shell was used in the hinge region, the hinge moment would increase from 1630 ft-kips (2210 N-mm) to 2325 ft-kips (3152 N-mm) (confined moment strength with a steel shell). This would increase the ground acceleration that would cause column yielding from 0.3 g to 0.5 g. Therefore, the required increase in strength and ductility could be achieved without placing excessive demands on the other portions of the structure.

In a paper by Taylor and Stone [10], an extensive analytical study is described that examined the effect of jacket thickness on the amount of damage that would occur to a bridge for different magnitudes of earthquakes (5 to 8 on

the Richter Scale). 1152 inelastic dynamic analyses were done that varied the jacket thickness from 0 to 10 mm (0.394 inches). The study found that the decrease in the amount of damage was small when increasing the jacket thickness from 2 to 10 mm in most cases. For large columns (1520 mm, 60 inches in diameter) the thicker jackets were needed to keep damage reasonable. In the closing comments, the authors state that although the analysis indicated significant benefits from the application of thin steel jackets, fabrication and erection considerations may control how thin of a jacket may be used. This study shows that the use of thin jackets in the hinge region, while decreasing the moment capacity from the fully jacketed section, will not decreasing the ductility performance.

SPECIMEN TESTING

Figure 10 shows the test setup that will be used. The axial load in columns designed in the 1960's are typically well below the balance point of the section. The specimens will be lightly axially loaded with Dywidag bars and center-hole rams. The pier cap portion of the structure will be tied down to the test slab with reaction rods. The specimen will model the superstructure as a solid block of concrete. Future tests will include the retrofit of the pier cap. The specimen columns will be cycled through increasing degrees of drift and load. An actuator will apply lateral load at the top of the column. The force will be cycled at increasing levels in force control mode up to the point where the longitudinal column reinforcement yields. The displacement at this point in the test will be called the yield displacement. The displacement ductility level at this point in the test is 1, since the actual displacement is equal to the yield displacement. From this point in the test, the specimen will be loaded in displacement control. The displacement ductility level will be increased in increments of 0.5 until failure. Three cycles will be conducted at each ductility level. The specimens are currently under construction.

CONCLUSIONS

Many of the retrofits used in the past have been extremely expensive. The primary purpose of the retrofits proposed is to provide a solution that is economical and effective. The concrete drop panel is a solution that requires extensive field fabrication but for short columns, where access is easy and for columns that do not require jacketing, this may be the best alternative. The steel alternative will be best when trying to minimize field operations. If column strengthening is required, the steel cone provides a smooth transition from the steel jacket.

This research is being supported by the Nuclear Waste Project Office in Nevada through the Center for Infrastructure Studies. The opinions in the paper do not necessarily represent those of the sponsor.

REFERENCES

1. American Association of State Highway and Transportation Officials, Standard Specification for Highway Bridges, AASHTO, 15th Edition, 1992.

2. ACI Committee 349, "Code Requirements for Nuclear Safety Related Structures," ACI 349-85, American Concrete Institute, Detroit, 1985, pp. 80-86.

3. American Institute of Steel Construction, Manual of Steel Construction, LRFD, AISC, 1987.

4. Calvi, G.M. and Priestley, M.J.N., "Seismic Design and Retrofitting of Reinforced Concrete Bridges," Proceeding of the International Workshop on Seismic Design and Retrofitting of Reinforced Concrete Bridges, Bornio, Italy, April 2-5, 1991.

5. Collins, D.M., Cook, R.A. Klingner, R.E. and Polyzois, D., Load-Deflection Behavior of Cast-In-Place and Retrofit Concrete Anchors Subjected to Static, Fatigue, and Impact Tensile Loads," Research Report No. 1126-1, Center for Transportation Research, University of Texas at Austin, March 1989.

6. Norri, P. and Saiidi, M. "Seismic Retrofit of a Viaduct in Sparks, Nevada," Proceedings, Symposium on Practical Solutions for Bridge Strengthening & Rehabilitation, Iowa State University, Des Moines, Iowa, April 5-6, 1993, pp. 275-284.

7. Priestley, M.J.N., and Seible, F., Seismic Assessment and Retrofit of Bridges, *SSRP 91/03*, University of California, San Diego, 1991.

8. Salmon, C.G. and Johnson, J.E. Steel Structures Design and Behavior, Harper and Row, 3rd Ed., 1990, pp. 878-883.

9. Sanders, D.H., Douglas, B. and Cornell, K., "Retrofitting of Reinforced Concrete Beam-Column Joints in Moderately Active Seismic Regions", Proceedings, Symposium on Practical Solutions for Bridge Strengthening & Rehabilitation, Iowa State University, Des Moines, Iowa, April 5-6, 1993, pp. 313-322.

10. Taylor, A.W. and Stone, W.C., "Jacket Thickness Requirements for Seismic Retrofitting of Circular Bridge Columns," Proceedings, Symposium on Practical Solutions for Bridge Strengthening & Rehabilitation, Iowa State University, Des Moines, Iowa, April 5-6, 1993, pp. 249-258.

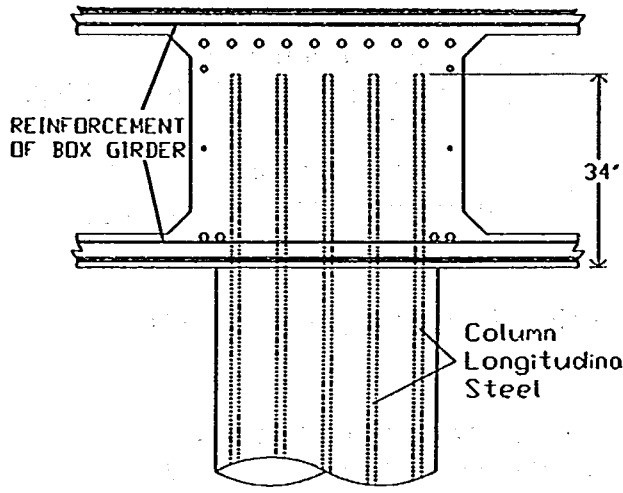


Figure 1: Elevation View of the Original Joint from the Prototype Bridge

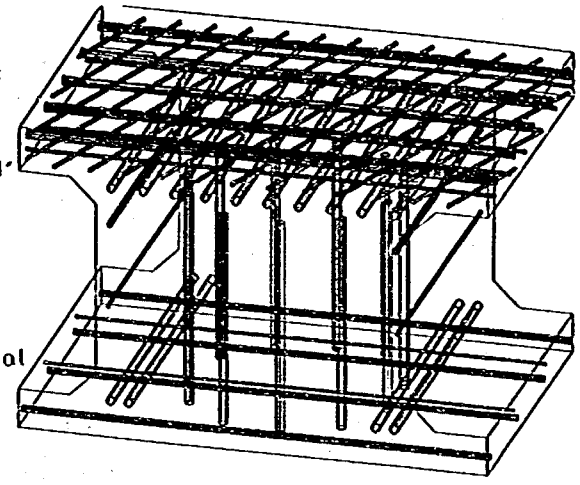


Figure 2: 3-D Perspective of the Original Joint from the Prototype Bridge

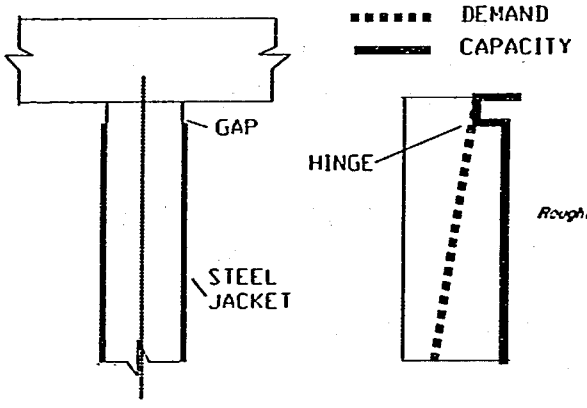


Figure 3: Moment Capacity-Demand Curve for the Jacketed Column

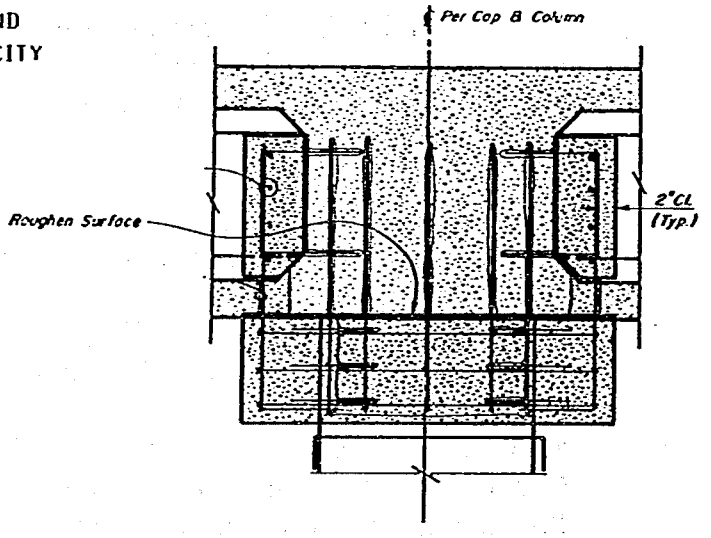


Figure 4: Drop Panel Retrofit for the I-80 Bridge in Sparks, Nevada, USA

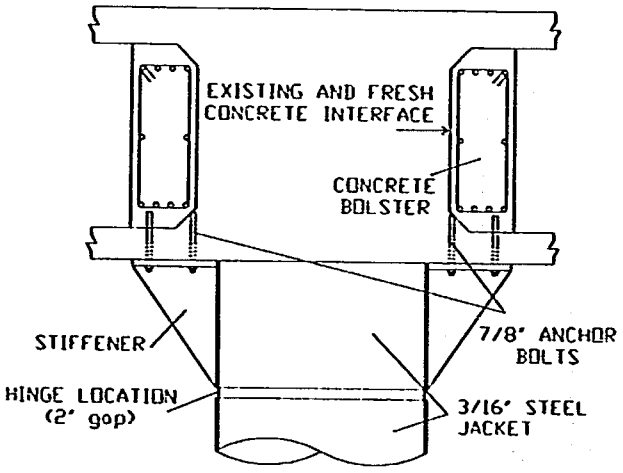


Figure 5: Confined Concrete Retrofit for the Prototype

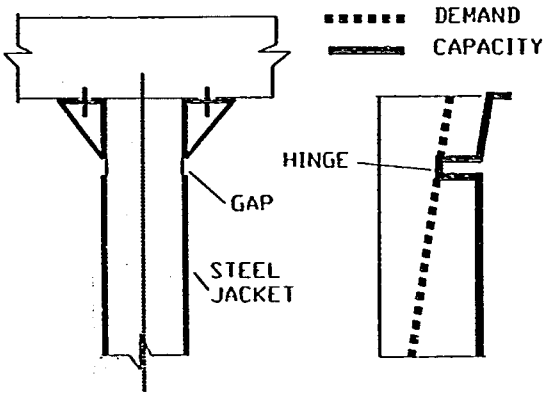


Figure 6: Moment Capacity-Demand for the Hinge Shift Column

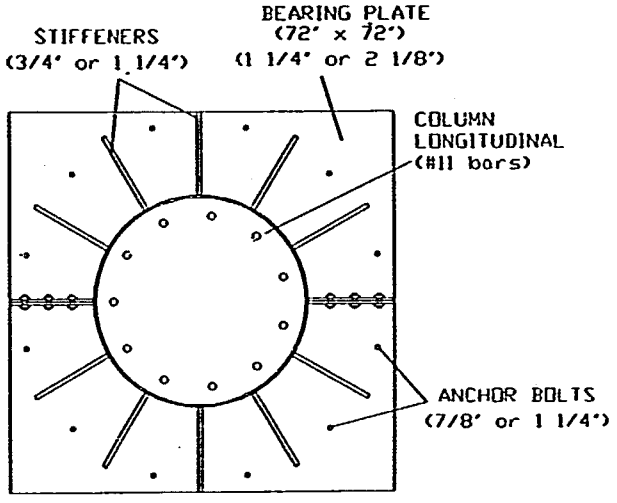


Figure 7: Anchor Bolt and Stiffener Pattern

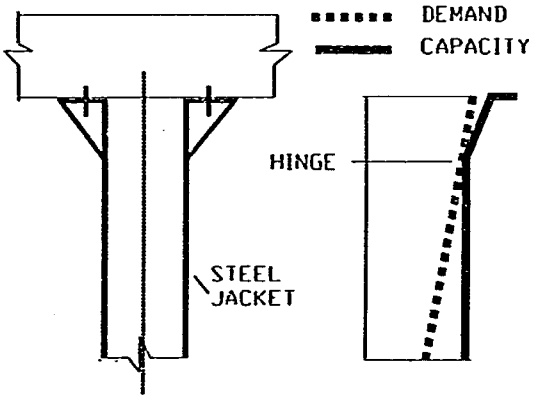


Figure 8: Moment Capacity-Demand Curve for the Large Capacity Hinge

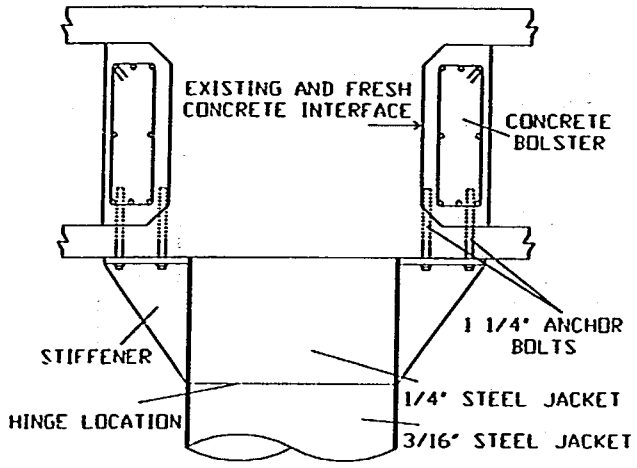


Figure 9: Retrofit for a Large Capacity Hinge

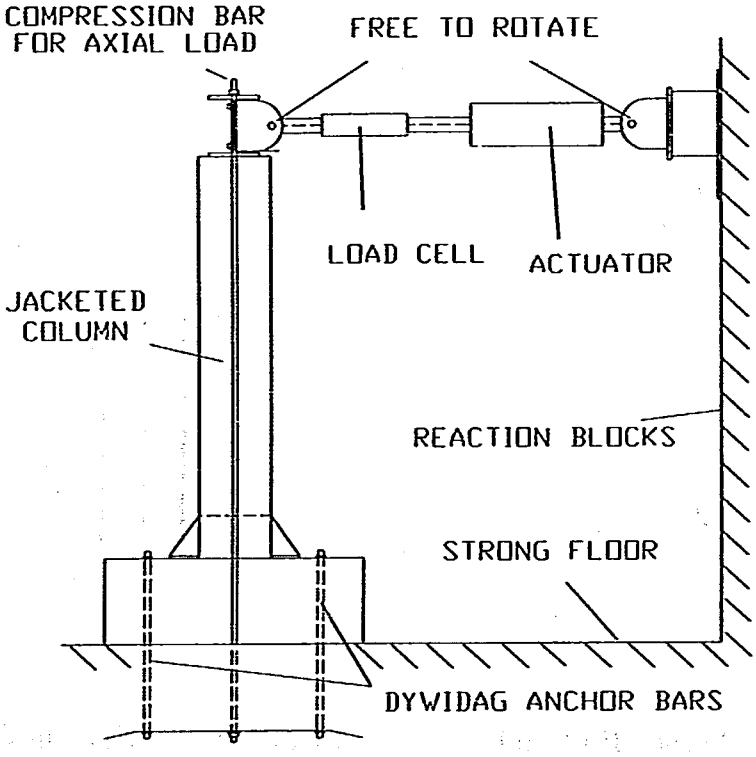


Figure 10: Test Setup

(11) Session 11

Substructure (2)

29) Vertical Bearing Capacity of Shallow Foundations
(M. Okahara, M. Nakano, Y. Kimura*, K. Chimi and A. Inoue)

30) Evaluation and Upgrading of Multi-Column Bridges
(J.P. Moehle*, C.R. Thewalt and S.A. Mahin)

31) Designing the Substructure of the Main Tower of Hakucho Ohashi Bridge
(K. Kumagai, M. Takahashi, S. Nishimoto and Y. Saito*)

VERTICAL BEARING CAPACITY OF SHALLOW FOUNDATIONS

by

Michio OKAHARA 1),Masanori NAKANO 2),Yoshitomi KIMURA 3),Kenji CHIMI 4),Akio INOUE 5)

ABSTRACT

When it is asked what a beariig capacity of a large spread or caisson foundation is,we encounter a dilemma, that there is no way to confirm it except a full scale test.Saying about the present specificaion in Japan,the classical formula proposed by Terzaghi et al.,but modified with additional corrction factors,has been used as ever.We have developped measures to understand that scale effect,progressive failure,pressure-level effect should significantly be considered in estimating the bearing capacity.We condunted large scale tests of two-dimensional footings on sand and centrifuge tests to evaluate these effects experimentally,which are further analyzed with a newly developped F.E.M.

1.INTRODUCTION

When designing foundation structures, the estimation of vertical bearing capacity of ground is one of the most important factors to be considered. However, until soil mechanics was systemized as discipline, the estimations were based mostly on experience. In 1943, Terzaghi presented a bearing capacity chart, introducing a theory of bearing capacity at a shallow foundation. However, this theory still left many complex problems associated with bearing capacity to be resolved. In Japan, equations based on Terzaghi's theory, assuming that ground is an rigid-plastic body, are still used for estimating bearing capacities of shallow foundations such as spread foundations, but has become unable to deal with massive structures in recent mega-projects. This paper will examine studies on bearing capacities of shallow foundations and the future of such research.

2.BEARING CAPACITY OF GROUND

When designing a foundation structure, functional deformation limits of the super-structure, load transmission capacity of a foundation and the bearing capacity of the ground must be considered, and safety must be guaranteed. The safety of the bearing capacity of ground is investigated from two angles, "ground failure" and "structure deformation". Ground is deformed

1)Director,Shuto National High way work Office,Kanto resional Construction Bureau,M.O.C
2)Head,Foundation engineering Division,Public Works Research Institute,M.O.C
3)Research engineer,ditto
4)ditto
5)ditto

by load transmitted through a footing, and it reaches ground failure when the load exceeds the bearing capacity. So, Structures are also affected by ground deformation and failure. Deformation and failure of the foundation and ground depend on the distribution of load on the footing base. Furthermore, load is distributed widely into the ground, deforming not only the part below the footing but also the adjacent areas. On the other hand, the settlement of a footing progresses as the load on foundation structures increases, until finally it reaches a state in which settlement proceeds even without increase of load.At that point,the ground surrounding the footing swells,and slides are generated.This state is referred to as ground "failure",which the load is called the"ultimate load", and from the point of footing, it reached the limit bearing capacity, or the limit of bearing ability of the ground. Obviously, in current allowable unit stress design methods, loads up to the ground ultimate load are not actually transmitted to ground from a footing, but an estimated value with safety factor as 3(normal) and 2 (during earthquake) is adopted as an allowable bearing capacity. The amount of settlement is not zero even at load accepted by admissible bearing capacity. For structures showing extreme intolerance to settlement, when the allowable bearing capacity calculated by the above method exceeds the limit of deformation due to a structure's function, the limit of deformation load is adopted as the allowable bearing capacity. This is the bearing capacity of the ground when it is considered from the angle of structural deformation.

Foundations can be classified into two types; "a shallow foundation" which transmits load to ground at the bottom surface and "a deep foundation" which transmits load at the bottom and side surface. In this paper only the former will be discussed.

There are many large-scale shallow foundation, and it is difficult to confirm their ultimate bearing capacities and visually observe ground bearing mechanism of full-scale buildings. Therefore, models were usedto observe the inner foundation. Figure 1 shows the state of settlement of dense sandy ground to a level of 70% of the footing base by a vertically-applied load. A section shaped like an isosceles triangle (an active region or wedge) is seen in the figure adjacent to the bottom of the foundation. This section is thrust into the ground as a rigid body united with the footing. Several slip-lines (shear bands) beside the boundary lines of the triangle are observed, forming fan-shaped regions (transient regions) at both sides. Slip-lines extend from the vertex of the triangle up toward the surface. The region enclosed by transient regions and the slip-lines is called a "passive region". From the above information, we can conclude that when load is applied to a footing, an active wedge is formed just under the footing, the wedge squeezes out transient regions to the right and left,and the transient regions push passive regions upward.Bearing capacity may therefore be considered a combination of "resistance force against shearing deformation of sand along slip-lines" and the "force necessary to move sand in active, transient and passive regions". Loads existing on the surface of a passive regions also affect bearing capacity.

Shallow foundations subside when loads are applied. Ground is deformed along the settlement. In densely compacted sandy ground, total ground volume scarcely fluctuates, and the volume

squeezed out by footing settlement is absorbed by swell in passive regions. Once slip-lines reach the ground surface, the size of the section in which sand moves does not change. Only a rise in surface, corresponding to the amount of settlement, occurs, and the load does not increase. In such shallow foundations, which have non-restricted boundary surfaces able to infinitely absorb clod deformation, clear ultimate bearing capacities are frequently shown.

3.INVESTIGATION CONDUCTED AT THE PUBLIC WORKS RESEARCH INSTITUTE

As research using both model and element test has proceeded in bearing capacity theory, the following problems have become evident:

(1) As an element, sand is not an isotropic and perfect plastic body, and its properties of strength and deformation specificity fluctuate along confining pressure. That must be considered when estimating bearing capacity.

(2) Results of experiments using highly precise small-scale models do not coincide with bearing capacities estimated from the rigid-plastic theory using the values of strict element results.

(3) The failure configuration in a model does not show general shear failure, in which maximum shear strength are simultaneously manifested along slip-lines generated at the final stage of maximum loading, but a phenomenon of progressive failure is observed.

(4) The scale effects of N , in which N decreases as the width of foundation increases, was confirmed in both experiments on small-scale gravitational fields (1g) and centrifugal model tests. When the mechanism of scale effect is considered, pressure level effect and particle size effect become apparent. Generalized diagrams are shown in Figure 3.

Giving consideration to such conditions, the Public Works Research Institute (P.W.R.I) has since 1990 pursued the studies, establishing "study for the bearing capacity of shallow foundation" in a road works research project aimed at developing a new bearing capacity estimation method which can be used for recent mega-projects, such as the Honshu-Shikoku bridges. Using Toyoura sand, the institute conducted a number of precise model loading tests to understand their quantitative properties. On the other hand, Tanaka in Meiji University and Tatsuoka in Tokyo University have developed a numerical analysis method based on a finite element method, which may solve the aforementioned problems. In their method, strain hardening, strain softening and even behavior of soil elements at a residual strength state after plasticity, none of which can be investigated by existing methods, may be simulated. This section will examine the results of these experimental and analytical studies, which were conducted in cooperation with them.

3.1 MODEL LOADING TEST

With sufficient consideration on ground uniformity and friction at the ground and soil pit, the authors conducted a number of experiments on bearing capacity, which satisfied scrutiny

investigation. Also, the authors understood the physical properties of Toyoura sand, which were used for the ground material in the experiments, through various element tests. Here, experiments on two-dimensional bearing capacity with the largest foundation (width B=50cm) will be discussed.

3.1.1 EXPERIMENTAL PROCEDURE

Experiments were conducted in a large two-dimensional soil pit (2 m width X 7 m length X 4m depth) at the P.W.R.I. as shown in Figure 4. Ground was prepared with Toyoura standard sand using a combination mobile hopper and multiple screen, so the unit weight was 1.55 - 1.60tf/m^3 and the void ratio 0.65 - 0.70. The state of ground failure was observed through an acrylic plate at the front of the pit. Normal stress was measured with a partial load cell installed under a footing. Shearing stress was also measured. In order to satisfy plane strain conditions, silicon grease and latex membranes were used. The conditions and methods of experiments were identical to those used in references 4) and 7).

3.1.2 RESULTS

Figure 5 shows the comparison of relationships between settlement, S, and mean footing stress, q, for different width of foundation in a gravitational field. And it shows also the comparison of the relationships in gravitational and centrifugal fields. The axes are divided either by the width of foundation, Bo, or by one half of the product of the width of foundation and the unit weight to standardize. In the figure a decrease in normalized maximum footing stress (bearing capacity coefficient) for experiments in gravitational field becomes apparent as the width of foundation increases. In the comparison of gravitational and centrifugal fields, the bearing-capacity in centrifugal field showed values double of those in gravitational field. The effect of particle size was probably responsible for this difference.

Figure 6 shows maximum shear stress. Here, a dense area of contour lines near the edges of the footing, where slip-lines appeared, is clearly seen, indicating large shear strain. Figure 13 shows the relation between width of foundation and bearing capacity coefficient.

3.2 ANALYSIS FOR BEARING CAPACITY

3.2.1 CONDITIONS FOR ANALYSIS AND ANALYZED CASES

The program used for analysis was Tatsuoka et al's two-dimensional elasto-plasticity analysis program, NSOLAN 9, a modification of the static-stress-analysis sub-program in Tanaka's NONSOLAN program, the latter which was the total ground analysis program based on a finite element method (2 & 3). For analysis of plane strain, a half-size model of the model ground of Toyoura sand with the width of foundation B=50cm prepared for large-size model experiments was utilized as shown in Figure 7. Even for a wider footing, mesh sizes (number of joints and

elements) for an analytical model were not changed but both X and Y coordinates were changed. Since no apparent strain softening specificity appeared in the test results, data were inputted through load control. The main inputted material constants are shown in Table 1. Constants were determined from data derived from modal and element tests.

Seventeen cases, twelve in gravitational field and five in centrifugal field were analyzed using width of foundation as parameters. The analyzed cases are shown in Table 2.

3.2.2 RESULT OF ANALYSIS

The effects of problems such as confining pressure dependency (pressure level dependency), strength anisotropy, strain softening specificity and shear band specificity (which will be discussed later) were quantitatively investigated using this method and are shown in Figure 8 [6]. Here, a shows the analysis without considering the above points, b considers only pressure level dependency, c considers pressure level dependency and strength anisotropy and d considers strain softening specificity plus the former two points. Finally e shows the analysis which considers shear band specificity in addition to the previously mentioned points, and the stress-strain relationship of each element is assumed to be equal to that derived in a plane strain compression test which used specimens of sizes identical to the elements. In a, b and c, since sand behaved as perfect plastic body, footing load reached the maximum when the largest strength was manifested at the total length of failure surface, and the amount of settlement was exceedingly large. Among these three, a approximates to Terzaghi solution. In d, stress-strain relationships in all elements were assumed to be equal to those within a shear band. Since element sizes were larger than shear band, the degree of strain softening and progression of ground failure were underestimated, and a bearing capacity larger than the experimental value was shown. In e, shear band specificity, in which the degree of mean strain softening increases as the ratio of element sizes over width of foundation increases, was considered, and the analyzed values finally agreed with test results.

A width of foundation B=50cm in gravitational field is shown (Figures 9 to 11).

In this method, the conditions of each element of distributed ground were estimated by calculating a parameter called Bindex. When this parameter was smaller than 1, the footing stress value was known to be increasing. At its maximum strength, Bindex = 1. When $1 < \text{Bindex} < 2$, the states were in transition to residual strength. Finally when Bindex = 2, the states were known to be at residual strength (Figure 12). By drawing corresponding contour diagrams, total ground conditions after the division of finite elements, as well as the degree of plasticity could be understood. Figure 9 shows that, near the edges of footing, all soil elements surpassed their maximum strength, elements were either in or approaching residual strength states, and contour lines were dense. In distant regions, on the other hand, conditions still had not reached maximum strength and contour lines were sparse.

For shearing strain figure (Figure 10), it is estimated that non-uniform strain distribution was formed near the edges of footing, where exceedingly large strain, compared to other sections, was generated as well as Figure 2.

The final section of this paper will examine the relationship between the settlement and footing stress. The analyzed relationship is shown in Figure 11 along experimental results. In the figure, the maximum footing stress values (bearing capacity coefficients N) coincide well, and they clearly show similar tendencies. This suggests that modal tests may be simulated by this method.

3.2.3 ESTABLISHMENT OF FORMULAE FOR THE RELATION BETWEEN WIDTH OF FOUNDATION AND BEARING CAPACITY COEFFICIENT ON SAND GROUNDS

Finally, the relation between width of foundation B and bearing capacity coefficient N will be quantitatively investigated. In Figure 13, the relation between width of foundation B and bearing capacity coefficient N for summarized test and analyzed results are shown in a semi-logarithmic graphs. In the figure, A-A line is the approximate value N when mobilized along slip line at $\phi r = 35^\circ$, which is Terzaghi's solution for $\phi r = 35^\circ$, that is residual internal friction angle. This is the lowest value of N which can be produced by the analytical method. The figure shows good correspondence among test bearing capacity values in gravitational field, test values in centrifugal field and analyzed values. Regression lines of an index system for analyzed results are also shown in the figure.

Gravitational field : $N' = a \times B^b$ (B< 10 m)

Where,

N ' : bearing capacity coefficient

B : width of foundation (m)

a,b : constants (a=370.46, b=-1/3)

By using this method, the scale effect of a foundation on ground of Toyoura standard sand was quantitatively understood.

4. CONCLUSION

This paper presented an outline on vertical bearing capacity of a spread foundation and the results of studies conducted at the P.W.R.I.. Hereafter, in an effort to utilize the analysis method as a substitute for modal tests, more detailed studies, such as investigations of methods for the experimentation and evaluation of viscous soil and for fixation of inputted constants, will be undertaken. Finally, improved methods for calculating bearing capacity in shallow foundations on general ground will be pursued.

References

1) Tanaka, Tadatsugu. "Analyzing Methods Of Generalized Elasto-plastic Finite Elements For Construction of Earth Structures." Agriculture And Public Works Institute Report No.18, 1979.

2) Tanaka, Tadatsugu. Introduction to Soil Mechanics -- Deformation and Stability Analysis by the Finite Elemental Method, Mainly on Sandy Soil. JAPANESE SOCIETY OF SOIL MECHANICS AND FOUNDATION ENGINEERING, 1992.

3) Siddiquee, M.S.A. 1991. "Finite Element Analysis of Settlement and Bearing Capacity of Footing on Sand." Master thesis, Institute of Industrial Science, University of Tokyo.

4) Mori, Okahara, Takagi, Koike, Tatsuta, Tatsuoka and Morimoto. "Large-scale Two-dimensional Experiments of Bearing Capacities of Shallow Foundation No.1" Report prepared for the 24th meeting of JAPAN SOCIETY CIVIL ENGINEERING, 1989

5)Tatsuoka, Fumio. Introduction to Soil Mechanics --Relationships among Laboratory Shear Tests, In Situ Ground Investigation, Stability Analysis, Medel Test and Behavior of Actual Structures -- Bearing Capacities of Foundation on Sand" JAPANESE SOCIETY OF SOIL MECHANICS AND FOUNDATION ENGINEERING, 1992

6)Tatsuoka, Okahara, Tanaka and Siddiquee, "Study into the Bearing Capacity of Strip Footing on Sand by Model Test, Element Test and Numerical Analyses", JAPANESE SOCIETY OF SOIL MECHANICS AND FOUNDATION ENGINEERING, 1992

7)Okahara, Takagi, Kimura, Mori, Asai, Watarai, Inoue and Tatsuta. "Experimental Investigation on Bearing Capacities of Shallow Foundation" Public Works Research Institute's Collection, item 3807, 1992

8)Isemoto, Kakurai, Kusakabe, Kuwahara and Maeda. Introduction to Bearing Capacities. JAPANESE SOCIETY OF SOIL MECHANICS AND FOUNDATION ENGINEERING, 1990

Table 1 Material constants

Inputted constants	Inputted value
Poisson's ratio	0.30
Initial shear modulus(kgf/cm2)	900.0
Initial bulk modulus(kgf/cm2)	259.3
Initial void ratio	0.66
Unit weight(gf/cm3)	1.59
Coefficient of static earth pressure at rest	0.34
Relative density	0.85
Strain at the maximum strength	0.10
Strain hardening parameter	0.30
Strain softening parameter	0.60
Width of shear band	0.30

Table 2 Analyzed cases

Case No	Experiment method	Converted width of foundation	Case No	Experiment method	Converted width of foundation
1	Gravitational field	2.5 cm	10	Gravitational field	20.0 m
2		5.0 cm	11		50.0 m
3		10.0 cm	12		100.0 m
4		23.0 cm	1	Centrifugal field	2.5 cm
5		35.0 cm	2		5.0 cm
6		50.0 cm	3		10.0 cm
7		1.0 cm	4		23.0 cm
8		3.0 m	5		50.0 cm
9		10.0 m			

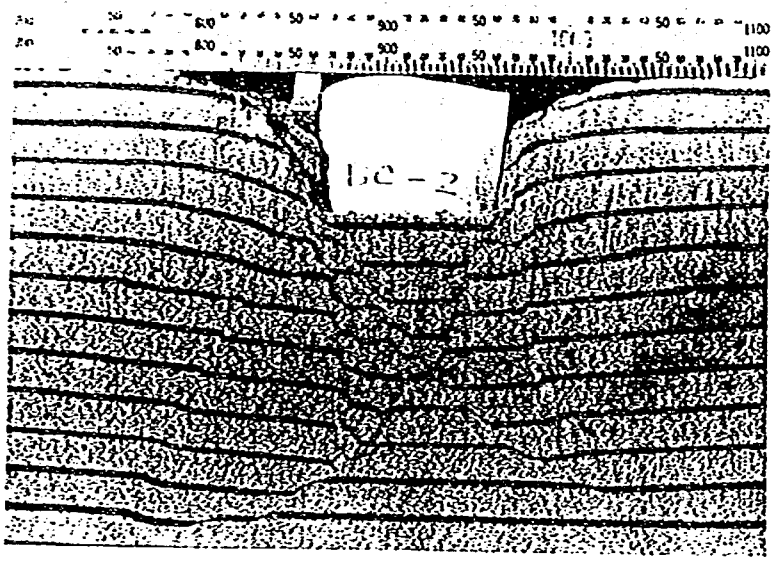


Figure 1 The state of sandy ground

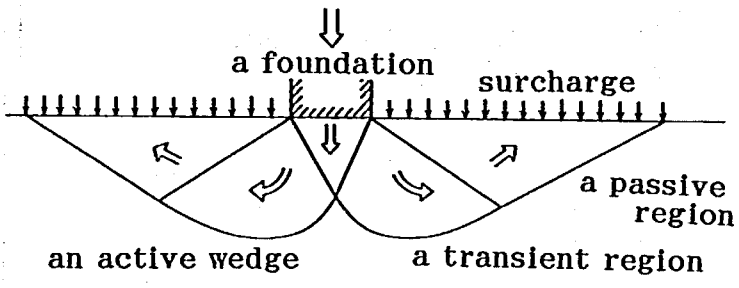


Figure 2 Bearing capacity mechanism in a shallow foundation

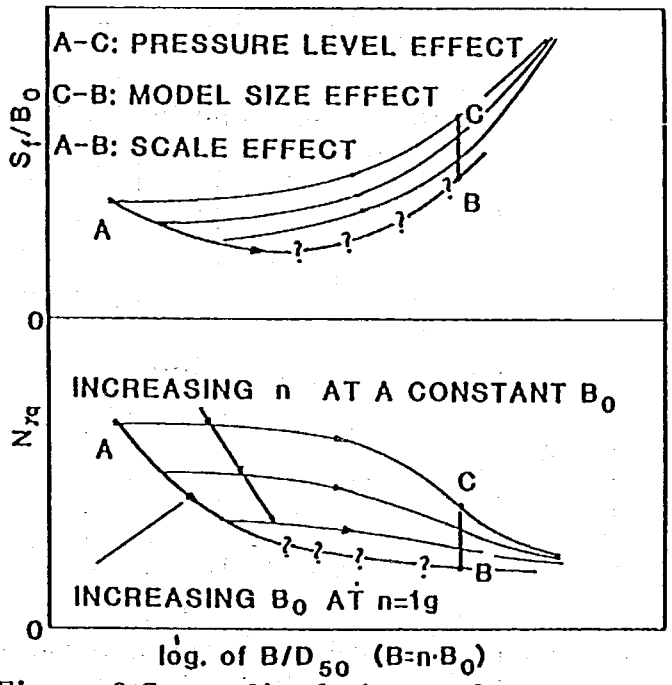


Figure 3 Generalized picture for scale effect

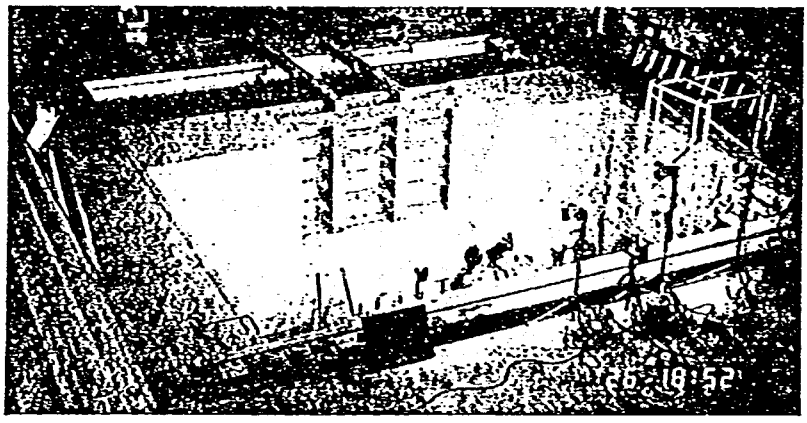
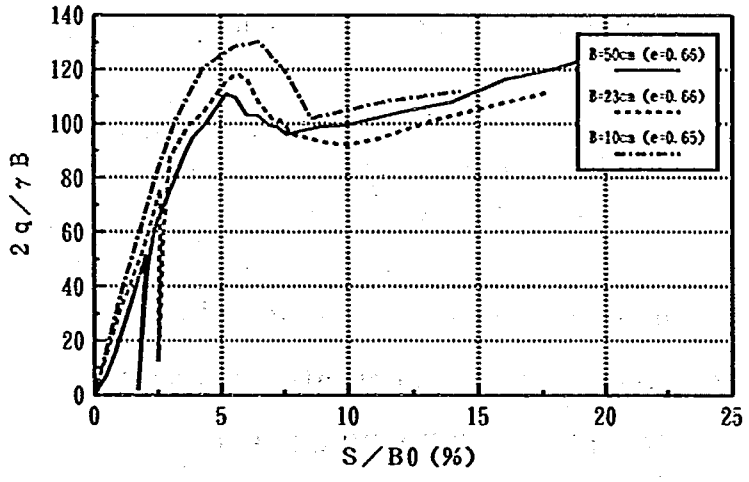
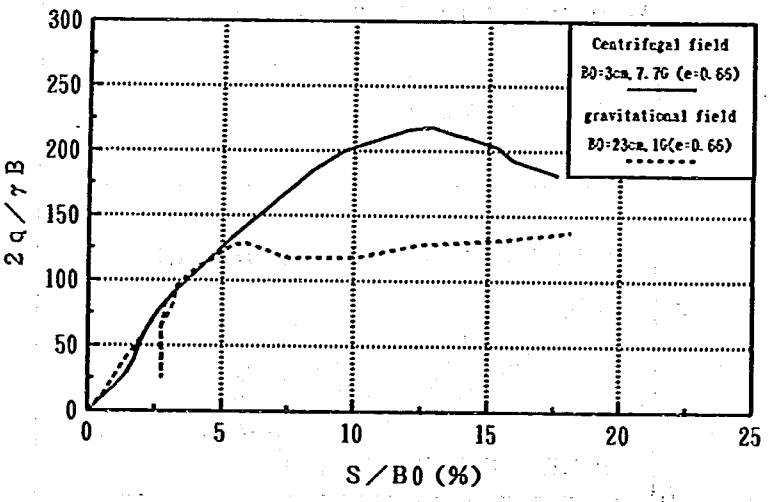


Figure 4 View of the large two-dimensional soil pit



(a)Relation between settlement and load in gravitaional field



(b)Relation between settlement and load in centrifugal and gravitaional field

Figure 5 Result of experiment

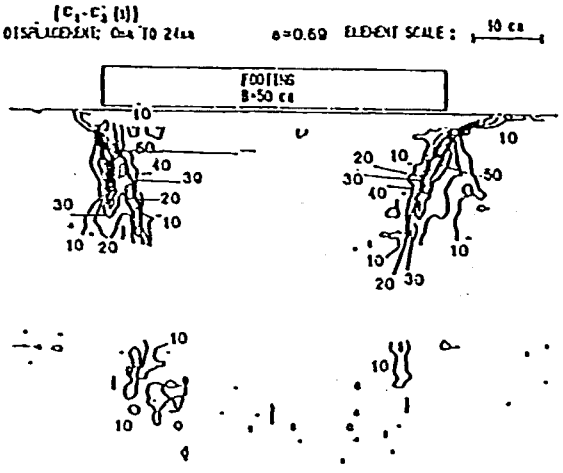


Figure 6 Maximum shear stress distribution

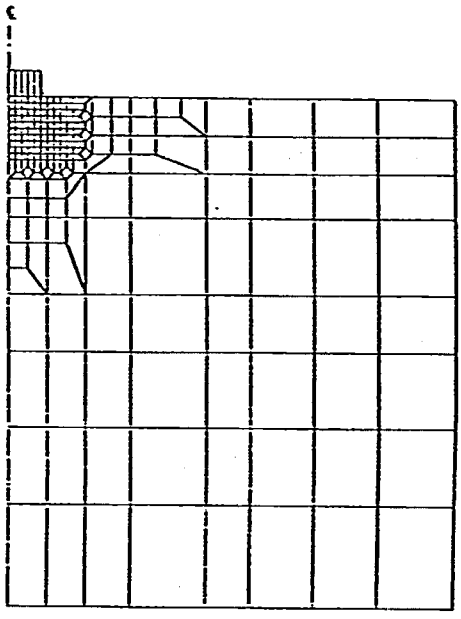


Figure 7 A model for analysis

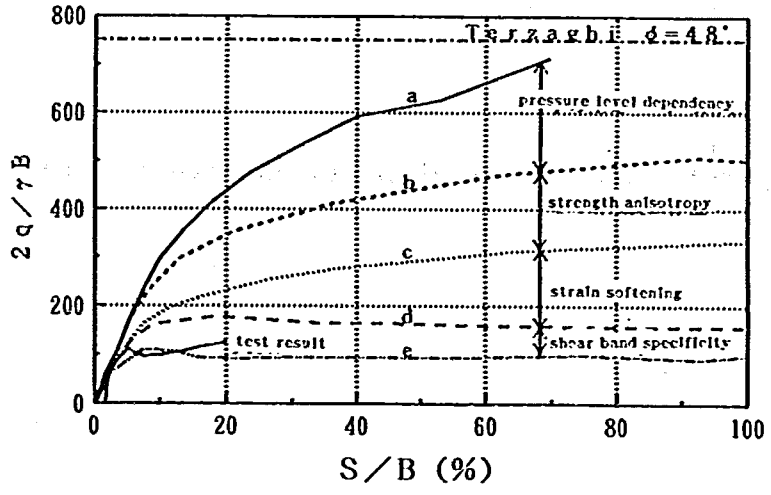


Figure 8 Effect of elements

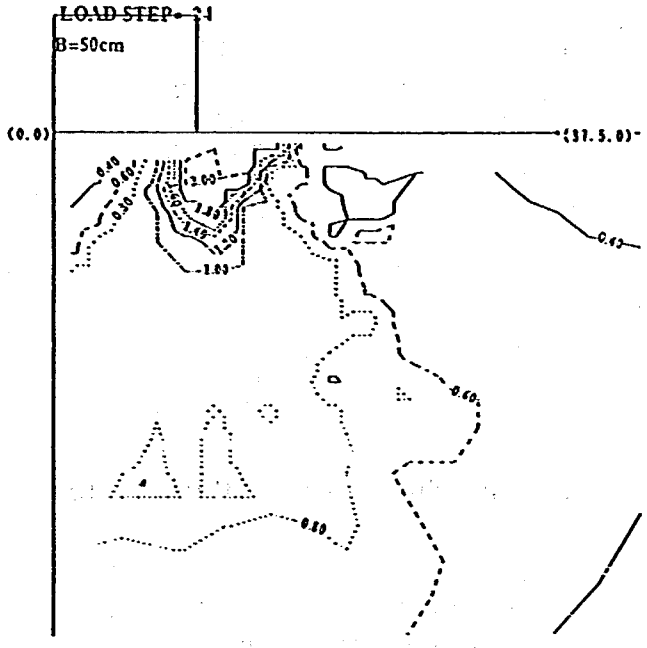


Figure 9 Bindex distribution(maximum strength)

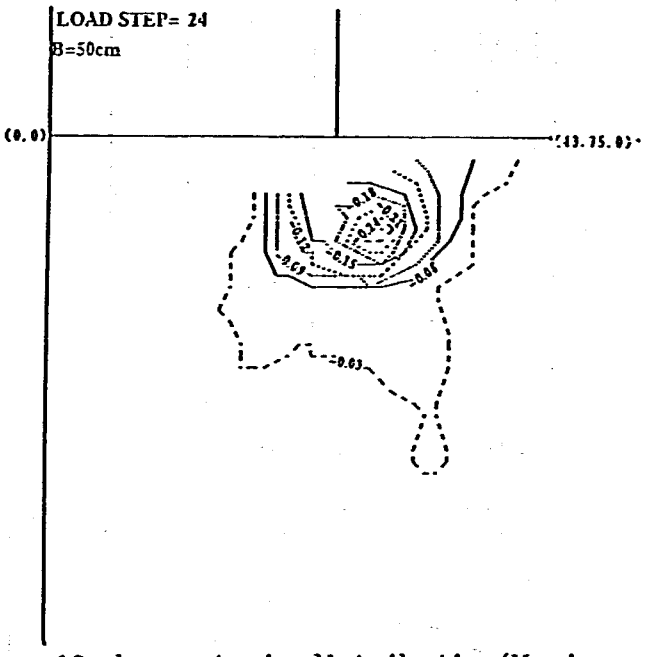


Figure10 shear strain distribution(Maximum strength)

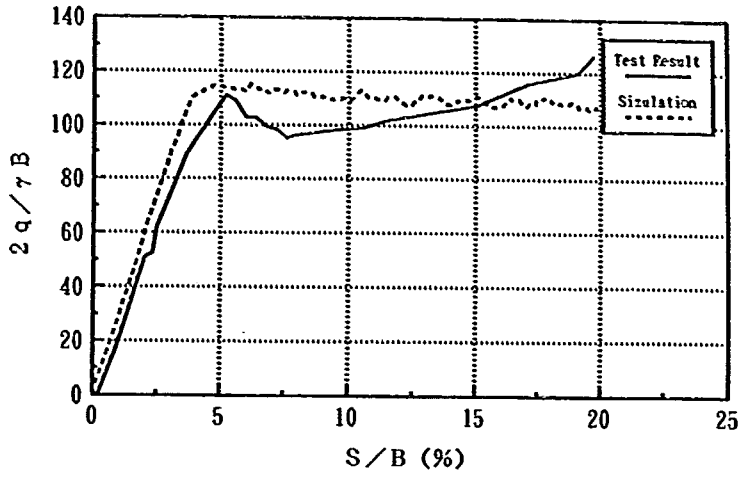


Figure11 Relation between settlement and load(Comparison between experimental and analyzed values)

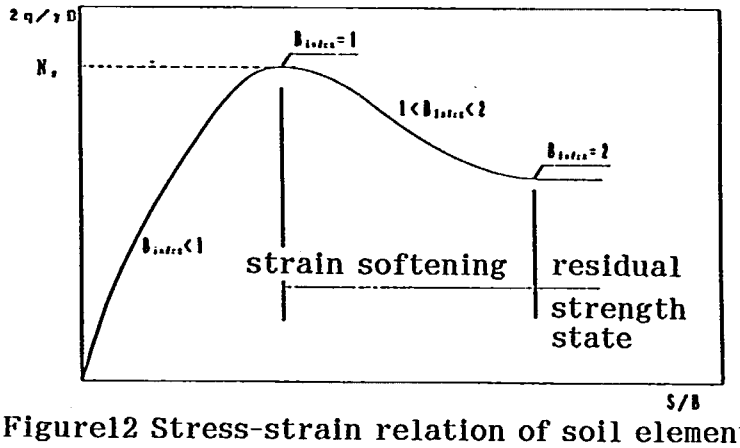


Figure12 Stress-strain relation of soil element

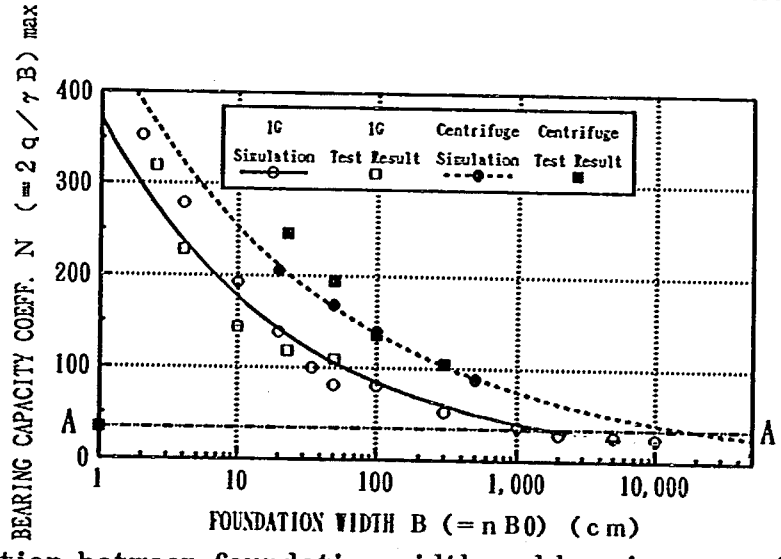


Figure13 Relation between foundation width and bearing capacity coefficient

EVALUATION AND UPGRADING OF MULTI-COLUMN BRIDGES

Jack P. Moehle[1], Chris R. Thewalt[2], and Stephen A. Mahin[3]
University of California at Berkeley

ABSTRACT: Recent research is examining the seismic behavior of reinforced concrete bridge structures constructed in California before the implementation of special requirements for ductility in the 1970s. Whereas earlier work focused on behavior of hinge restrainers and single-column structures, recent experience indicates existence of critical vulnerabilities in multi-column structures as well. We here describe the generic characteristics of multi-column bridges including columns, bent caps, outriggers and connections; describe analysis and evaluation procedures; and describe methods for seismic upgrading. We include results of experimental and analytical research where available.

INTRODUCTION

The 1989 Loma Prieta earthquake exposed the vulnerability of many multi-column, multi-level reinforced concrete bridge structures, in particular, those constructed in the 1970s and earlier. These structures are prevalent in urban environments where scarcity of land requires the stacking of roadways; they become increasingly complex where multiple elevated roadways intersect. Deficiencies include inadequate three-dimensional frames and a variety of structural inadequacies in footings, columns, beam-column joints, bent caps, and outriggers. Many of these inadequacies were apparent in bridge damage and collapse observed following the Loma Prieta earthquake. Others have been identified through study of structural drawings of undamaged bridges.

Immediately following the 1989 earthquake, Caltrans initiated redesign efforts on several multi-column, multi-level concrete bridge structures in the San Francisco Bay Area. The effort assembled a team of design consultants and peer reviewers from California, technical advisors from the University of California, and Caltrans bridge designers. The effort created a unique opportunity for an in-depth, practical focus on the main issues involved in evaluation and redesign of these structures.

Also immediately following the 1989 earthquake, Caltrans redoubled its ongoing seismic research effort. Research before the Loma Prieta earthquake focused on evaluation and rehabilitation of restrainers and single-column reinforced concrete bridge structures. The current research effort continues studies on restrainers and single-column structures, and adds a major emphasis on elements and systems of multi-column, multi-level reinforced concrete bridges.

---

[1]Professor of Civil Engineering, Director of Earthquake Engineering Research Center
[2]Assistant Professor of Civil Engineering
[3]Nishkian Professor of Structural Engineering

These efforts have provided insights into evaluation and rehabilitation needs for existing reinforced concrete multi-level and multi-column bridge structures. This manuscript summarizes some of the ideas and data resulting from the work.

EVALUATION PROCEDURES

Framing Systems

Elevated roadways typically contain a relatively sparse framing system in comparison with typical buildings. Thus, whereas in buildings an evaluation may take advantage of redundancy, in bridges the evaluation must be sensitive to the relatively low redundancy. The evaluation and redesign must establish the existence of a complete three-dimensional frame and the adequacy of its proportions and details.

Figure 1 depicts a typical pattern of framing for a San Francisco double-deck viaduct. As is common in multi-column bridges, columns are pin-connected to pile-supported footings. Given the pinned connection, resistance to lateral loads must be provided by a three-dimensional frame above ground.

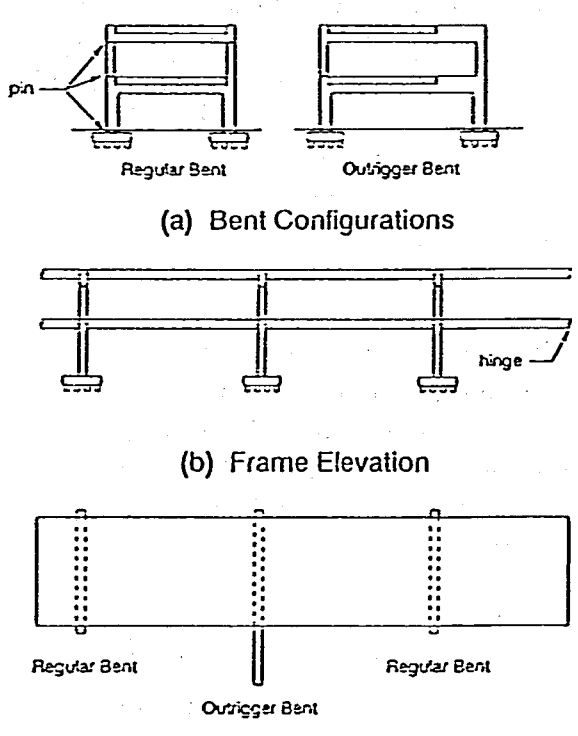


Figure 1. Typical Double-Deck Viaduct Framing

Resistance to lateral loads transverse to the roadway commonly occurs by framing among columns, bent caps, and cap-column joints. Resistance to longitudinal loads appears not to have been contemplated in the original design of many freeways, but usually occurs through rigid framing among the columns, bent caps, and longitudinal box girders (the roadway itself). Longitudinal action thus results in box girder flexure and bent cap torsion (and weak axis bending and shear in the case of outriggers), neither of which is likely to have been considered in proportioning or detailing of these members in the original design. Seismic rehabilitation may be driven almost entirely by the need to rectify inadequacies associated with basic framing requirements. Complete frame reconstruction may be the only reasonable alternative in some cases

where conservative performance criteria are specified and strictly enforced.

Analysis Models and Interpretation

Consulting engineers in California have constructed complex linear and nonlinear (inelastic) analytical models to represent with great precision the geometry of bridge structures including foundations, and they have used both types of models for evaluation and redesign. The engineer should always question the accuracy of these models. Modeling uncertainties related to basic flexural response under reversed cyclic loading are well known; these uncertainties multiply when high nominal flexural, bond, shear, torsion, and "connection" stresses are combined. (In this paper, "high stresses" are defined loosely as those that seem excessive in comparison with the proportions and details when viewed through current knowledge of requirements for earthquake resistance.) Attempts at defining accurate response models are further thwarted by unknown spatial and temporal characteristics of ground motions [Bolt and Gregor, 1993] and their effects on long, multiply supported structures [Der Kiureghian and Nakamura, 1992; Fenves, 1992]. In the face of great uncertainties and fallibility, simple models providing results that are transparent to the user are often preferred to more complex and inscrutable models.

Procedures for nonlinear analysis are beyond the scope of the present discussion and will not be considered further here. Engineers commonly use linear elastic models for evaluation purposes. The usefulness of linear models for evaluation of nonlinear bridge response lies in the well-known observation that nonlinear global displacement response amplitudes can be related to calculated elastic global displacement response amplitudes [Veletsos and Newmark, 1960].

Studies of response of SDOF systems with bilinear hysteretic response [Miranda; 1991] indicate that ductility can be held nearly constant if the strength reduction factor $R=V_e/V_p$ is decreased from a maximum value equal to the displacement ductility demand μ_δ at the period T_g to a value of unity at zero period. This relation enables displacement amplification in the short period range to be estimated as a function of the period ratio T_o/T_g and the strength reduction factor R. Figure 2 plots the relations. T_g is the characteristic ground period for the design earthquake, corresponding to peak on the input energy spectrum.

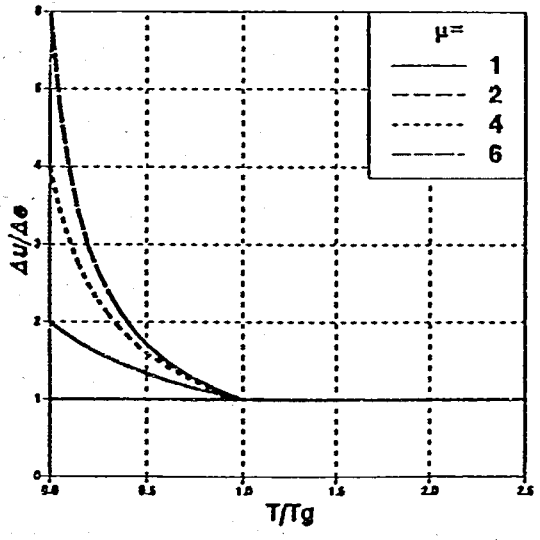


Figure 2. Mean Ratios of Peak Inelastic Displacement to Peak Inelastic Displacement

Figure 2 illustrates the well-known phenomenon that inelastic displacements exceed elastic displacements for short-period

structures. In evaluating an existing structure, the engineer should modify the deformation demands from an elastic analysis accordingly. Furthermore, to obtain consistent results the elastic model should be based on properties expected for response near yield. For typical bridge structures, an effective flexural stiffness of columns equal to half the gross-section stiffness and equivalent viscous damping of five percent of critical usually produce reasonable displacement estimates. Refinements of linear elastic models beyond these simple recommendations are usually unwarranted.

As a structure displaces laterally, gravity loads acting through the lateral displacement cause second-order (P-delta) moments that may have an important influence on response. P-delta effects are particularly important for flexible structures (that undergo relatively large lateral displacements under earthquake excitation) and structures that have low lateral load strength in comparison with weight. Shaking duration also plays an important role. In limited studies of uniaxial response of stiffness degrading systems, Mahin and Boroschek [1991] report insignificant increases in displacement demand due to P-delta effects for structures in which

$$\frac{1}{R}\frac{V_o L}{W \delta_o} \geq 4 \qquad \text{.....(1)}$$

in which V_o = lateral load strength without P-delta, L = height, W = weight and δ_o = yield displacement without P-delta. Assuming the equal displacement rule is valid, this condition can be satisfied equivalently for structures satisfying the inequality [Moehle, 1992]

$$\frac{\delta_u}{L} \leq 0.2\frac{V_o}{W} \qquad \text{.....(2)}$$

in which δ_u = expected maximum displacement. P-delta effects are likely to be insignificant for structures satisfying Equation (2). Otherwise, the engineer should either carry out a refined analysis or upgrade the structure.

Engineers commonly estimate local inelastic demands as being equal to demand-capacity ratios (ratio of calculated flexural moment from elastic response to plastic moment strength). Though expeditious, this approach is likely to err on the unconservative side for even the simplest structures. The effect is illustrated in Figure 3 for a simple bent with yielding columns. The total elastic displacement δ_{et} comprises flexure in both the columns and the cap beam. Inelastic displacement δ_p is due solely to column flexure. Thus, although the total structure ductility demand is δ_u/δ_{et}, which for long-period structures may be roughly equal to the demand-capacity ratio, the column effective ductility demand is much larger.

Priestley and Moehle [1993] discuss this effect and its applications in design of new structures. For typical single-level bent configurations, local ductility demands are approximately 50% higher than global ductility demands. Similar effects are likely even

for single-column structures due to soil flexibility effects.

Mahin, et al. [1992] describe similar effects for double-deck viaducts. Figure 4 depicts deformed shapes calculated for the Taft record assuming elastic behavior and assuming nonlinear behavior for R values ranging from 4 to 12. Especially for large R values, the concentration in inelastic deformations in the lower columns is evident. This effect is not recognized when local ductilities are estimated as demand-capacity ratios from elastic analyses.

For critical structures where a greater degree of precision in calculation is justifiable, local demands should be estimated using a static inelastic pushover analysis. This approach has been recommended widely in building evaluation [Freeman; 1992]. For the pushover analysis, the engineer constructs a nonlinear model of a single frame of the structure, and subjects it to lateral displacements estimated from a dynamic model of the bridge (Figure 5). The analysis provides a direct measure of expected member deformation demands, as well as an indication of the plastic forces to be used for checking for shear and other relatively non-ductile failure modes.

Even when the engineer does not carry out a pushover analysis, (s)he should carry out a rigid-plastic collapse analysis as suggested in Figure 5d to determine internal forces under limiting deformations. At this stage, the engineer should check that flexural hinges form where they were expected,

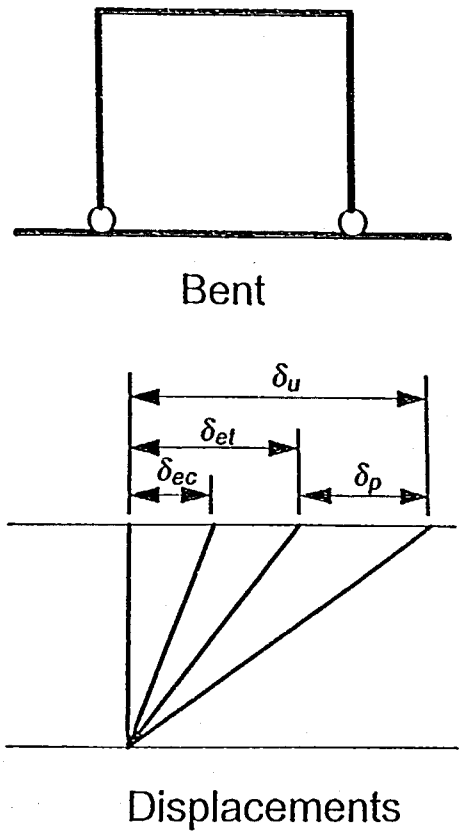


Figure 3. Distribution of Deformations in Simple Bent

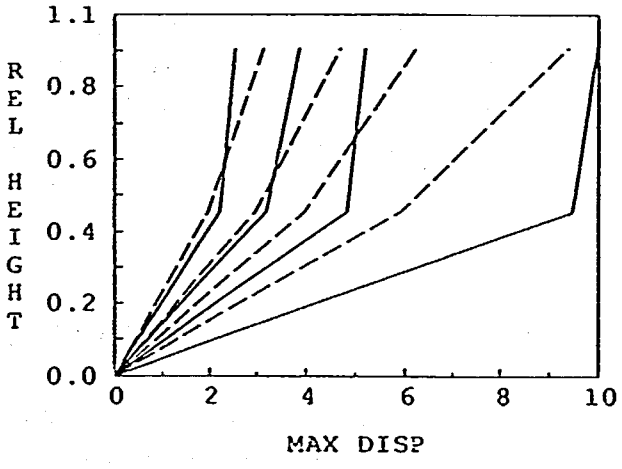


Figure 4. Envelop of Lateral Displacements for R ranging from 4 to 1 2. Inelastic response - solid lines; Elastic response - broken lines.

and that non-ductile response modes such as element shear failure, anchorage failure, or joint failure, do not occur.

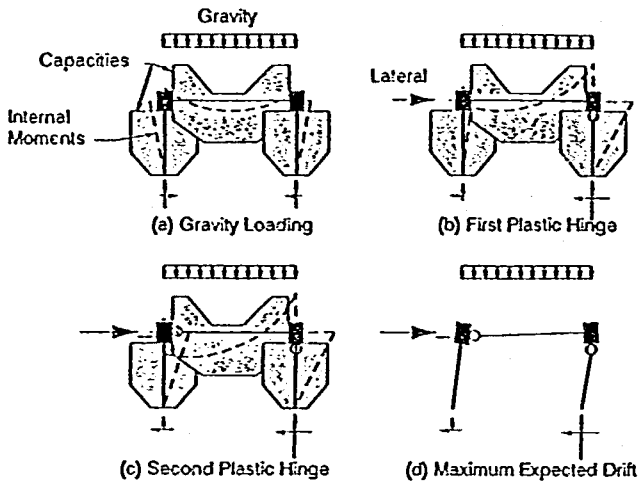


Figure 5. Pushover Analysis

The discussion so far has focused on transverse response. Fenves [1992] has shown that longitudinal response of long, straight viaducts is influenced by canceling effects of out-of-phase-support motions. However, for typical viaducts with superstructure hinges, opening and closing of gaps decouples distantly separated frames so that, typically, response is not significantly less than response that would be obtained from in-phase support motion. For some geometries, the pseudo-static support displacements may induce bridge superstructure actions exceeding those that would occur due to in-phase support motion. Given these results, for the present time we recommend that the analysis for longitudinal response should be based on the assumption of fully in-phase support motions. Adverse effects of out-of-phase motion that may occur in some situations should not be overlooked or neglected.

In summary, the engineer should check overall adequacy of a bridge system by (a) substantiating whether the frame has an adequate three-dimensional load path, and (b) checking whether P-delta effects are important. If the overall system is adequate, the engineer should check local demands against capacities. For important bridges, a pushover analysis is justified. For other bridges, the engineer may use demand-capacity ratios to estimate demands, with the understanding that local ductility demands exceed demand-capacity ratios. The engineer should check both flexural rotation demands, and member force demands. Comparison with element capacities will indicate whether upgrading is required. The remaining sections of this manuscript address some aspects of this subject.

COLUMN EVALUATION AND REHABILITATION

Columns of bridges constructed before the mid-1970s commonly are reinforced with large diameter longitudinal bars. Transverse reinforcement is usually #4 (13-mm) perimeter hoops spaced at 12 inches (300 mm) on centers and having 90-degree hooks. Experience demonstrates that columns with these details are susceptible to shear and flexural failures. (In single-column freeways, longitudinal bars are commonly lap-spliced for a length of $20d_b$ at the base of the column. This condition may limit column strength and deformability [Chai; 1990]. This condition is less common in multi-column structures,

and is not considered further here.)

The idealized model of Figure 6 is suitable for checking flexural deformability of columns. The ultimate curvature capacity may be approximated as the value calculated using conventional approaches with maximum compressive strain capacity represented by Equation 3 [Scott; 1982].

$$\varepsilon_{cu} = 0.004 + 0.02\rho'' f_y \quad \text{..... (3)}$$

in which ε_{cu}= maximum concrete strain capacity, ρ'' = transverse steel ratio, and f_y = yield stress of transverse steel in ksi. For typical columns the effective plastic hinge length l_p may be approximated according to Equation 4.

$$l_p = 0.5h \quad \text{..... (4)}$$

in which h is the column dimension in the direction of lateral loading.

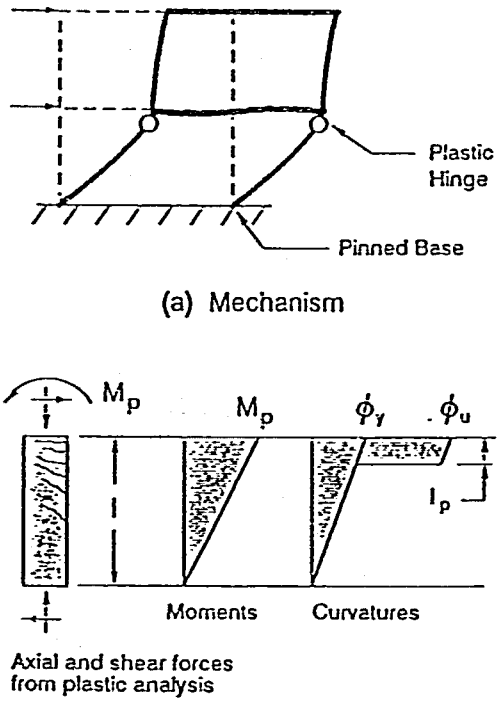


Figure 6. Column Flexural Deformations

Engineers have long realized that shear failure may limit deformability of a column, or, alternately, that inelastic flexure may reduce shear strength [ATC6-2; 1982]. Moehle and Aschheim [1993] describe results of analyses of bridge columns damaged during past earthquakes and of bridge column models tested in the laboratory. For design purposes, it is convenient to define arbitrarily the shear strength as the sum of a stationary contribution attributed to the transverse reinforcement, V_s, and a variable contribution attributed to the concrete, V_c. Equations 5 define the term V_s.

for rectangular columns....

$$V_s = \frac{A_v f_{yt} d}{s \tan 30^\circ} \quad \text{..... (5a)}$$

for columns with spirals ....

$$V_s = \frac{\pi}{2} \frac{A_{sp} f_{yt} D'}{s \tan 30^\circ} \quad \text{..... (5b)}$$

in which A_v = total cross-sectional area of rectilinear transverse reinforcement

parallel the applied shear within a longitudinal spacing s, f_{yt} = yield stress of transverse reinforcement, d = 0.8 times the column cross-sectional dimension in the direction of the shear, A_{sp} = cross-sectional area of spiral bar with spacing s, and D' = diameter of spiral wrap.

The term V_c in pounds varies according to Equation 6.

$$V_c = 3.5\left(k + \frac{N_u}{2000A_g}\right)\sqrt{f'_c}A_e \quad \text{..... (6)}$$

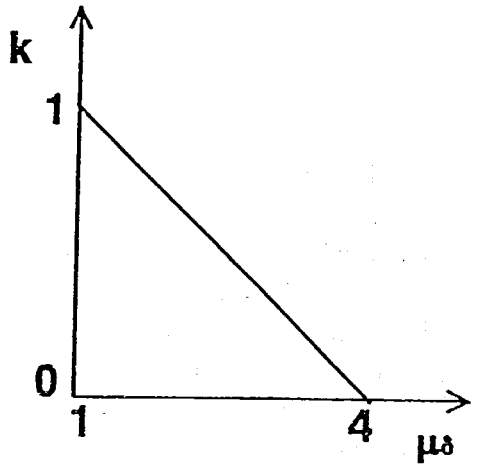


Figure 7. Variation of the Parameter k

in which f'_c = concrete compressive strength in psi, N_u = axial load in pounds, A_g = gross area of column cross section, $A_e = 0.8A_g$, and k varies according to Figure 7.

Figure 8 compares ratios of measured to calculated strengths as a function of displacement ductility.

Where flexural deformability or shear strength are inadequate in an existing column, upgrading using steel jackets is commonly employed in California. Procedures for design of a jacket have been described elsewhere [Chai; 1990].

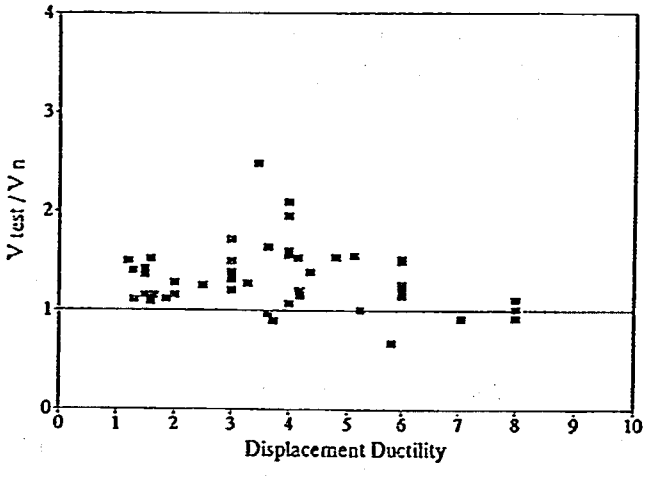


Figure 8. Comparison of Measured and Calculated Column Shear Strengths

CAP BEAMS, OUTRIGGERS, AND CAP-COLUMN CONNECTIONS

Inelastic action is generally preferred in columns rather than beams or connections for several reasons. The column has a simple, well-defined cross section, usually with low axial load stresses, so design for expected inelastic actions is relatively straightforward. Furthermore, any column damage that occurs during an earthquake can be readily observed and repaired. Arguments against formation of soft stories in bridge structures are not compelling because axial load stresses are low, and the number of

"story" levels is seldom greater than two.

Inelastic flexural action of cap beams may be acceptable where the superstructure is bearing-supported, because in this case the beam cross section is clearly defined and its behavior can be evaluated with some confidence. Where beams are monolithic with the superstructure, beam plastic hinging should be avoided because (a) the cross section of the beam cannot be uniquely defined and (b) hinging may result in undesirable superstructure damage. Inelastic response of outriggers and of cap-column connections is best avoided because techniques for producing stable response have not been advanced.

Cap Beams

Where beam reinforcement is well anchored into beam-column connections the flexural strength and flexural deformability can be evaluated using the techniques described previously. Relatively little is known about the cyclic shear behavior of large cross sections with light reinforcement as is common in bent caps. Not having definitive laboratory data, we recommend Equation 7 for cap beam shear strength.

$$V_n = V_c + V_s \quad \text{..... (7a)}$$

$$V_c = k(0.85 + 120\rho_w)\sqrt{f'_c}\,b_w d \le 2.4k\sqrt{f'_c}\,b_w d \quad \text{..... (7b)}$$

$$V_s = \frac{A_v f_{yt} d}{s} \quad \text{..... (7c)}$$

in which V_c = nominal concrete strength in pounds, k varies according to Figure 7, ρ_w = ratio of longitudinal tension reinforcement, f'_c = concrete compressive strength in psi, b_w = web width in inches, and d = effective depth in inches.

Figure 9 (Test 1) illustrates the measured beam load-displacement relation for a model of a typical as-built exterior connection of a double-deck structure [Moehle and Soyer; 1993]. Strengths correspond to yield of top beam longitudinal reinforcement for downward beam load and yield of bottom beam longitudinal reinforcement for upward beam load.

As is typical in existing construction, most of the beam bottom bars terminate near the connection (Figure 9), with the remaining bars extending into the joint a distance of approximately $20d_b$ without a hook. In this test, as well as in field tests on the Cypress Street Viaduct [Bollo; 1990], the bottom bar embedment was adequate for development of the Grade 40 bars (specified f_y = 275 MPa) for numerous inelastic loading cycles. (Adequacy of the bottom bar anchorage is less certain for bents where the column undergoes inelastic rotations adjacent to the anchored beam bar.)

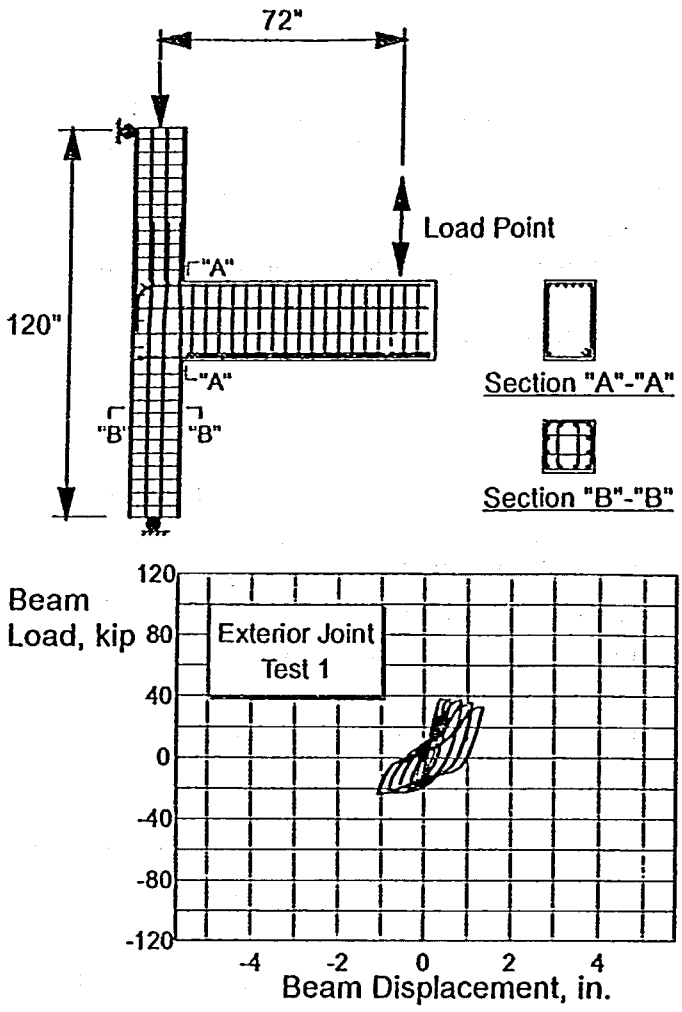


Figure 9. As-Built Exterior Connection Test

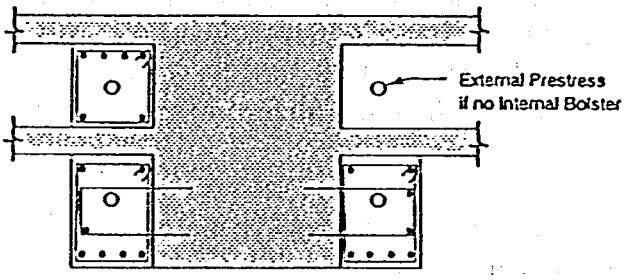


Figure 10. Beam Retrofit Concepts

Failure of the beam was due to sliding along a single, wide crack in the beam adjacent to the joint face. Growth of the crack width is attributed to two phenomena: (1) Under upward beam load, the plastic hinge was restricted to a short length of beam adjacent to the joint because of the termination of the majority of beam bottom bars near the joint, and (2) Because top reinforcement area significantly exceeded bottom reinforcement area, the top reinforcement never yielded in compression, so yield strains in top steel grew progressively. As testing progressed, sliding along the interface ensued.

Strengthening techniques for bent caps loaded in flexure and shear include addition of bolsters and/or external prestressing. Prestressing may suffice in cases where shear strength of the cap beam is adequate. (Note that prestressing is likely to enhance the shear strength of the cap beam [Collins and Mitchell; 1987].) Where shear strength of the beam is not adequate, bolsters can be added to provide additional shear strength (Figure 10). Mahin [1992] presents details of a bolster design for one of the San Francisco double-deck viaducts.

Outriggers

Outriggers (Figure 1) are common in locations where obstructions do not permit the supporting columns to be located beneath the superstructure. Transverse and longitudinal bridge response results in combined biaxial flexure, biaxial shear, and torsion in the outrigger beam. Transverse reinforcement of existing outriggers

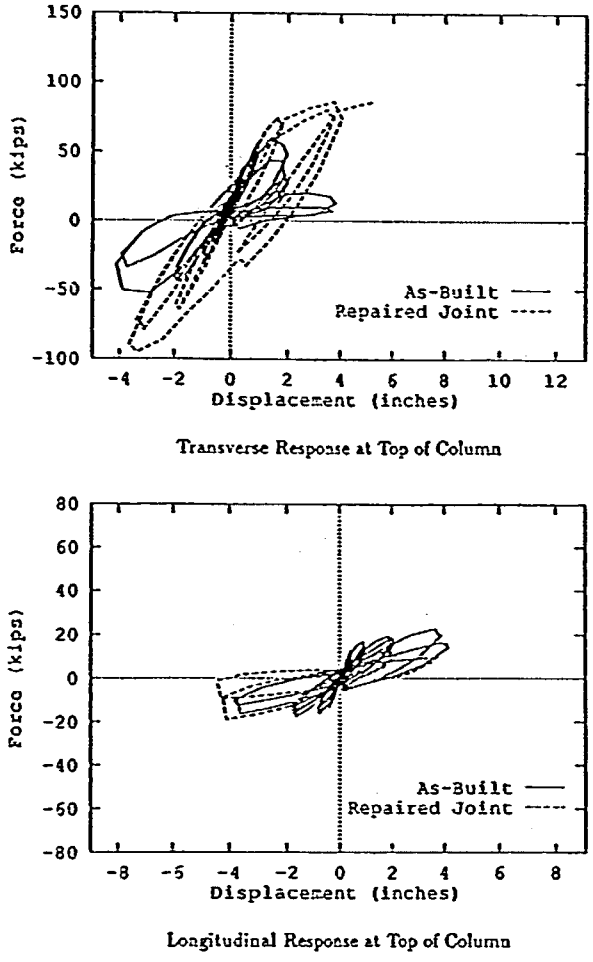


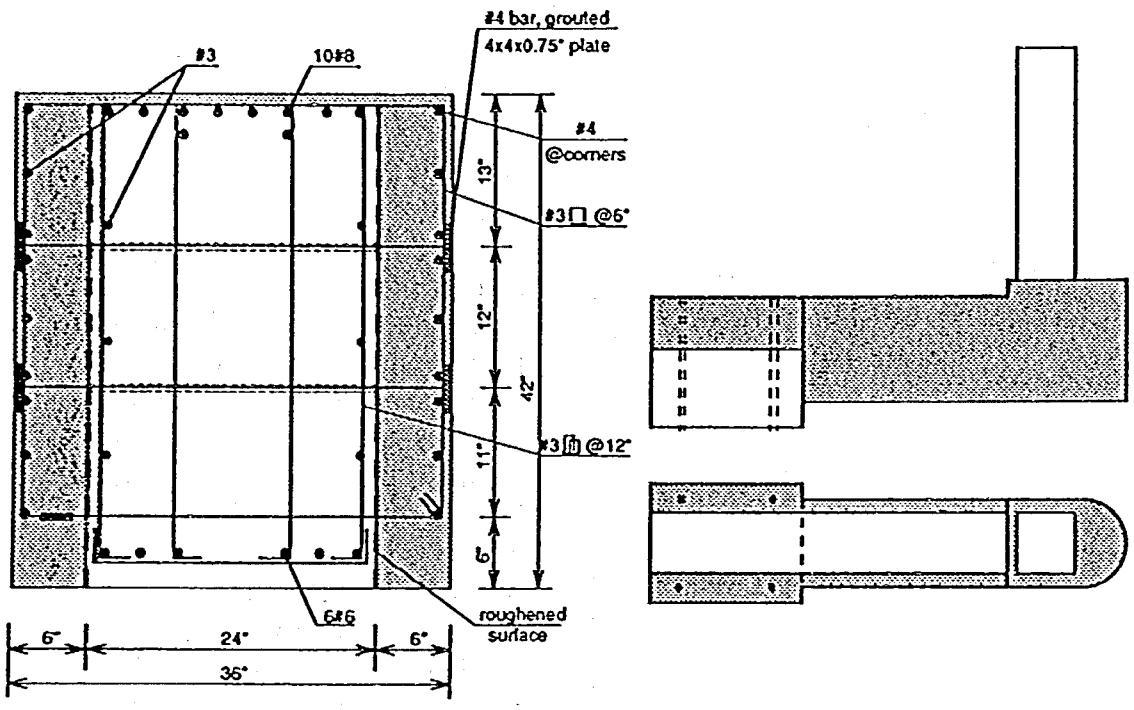
Figure 11. Transverse and Longitudinal Response of As-Built Outrigger Specimen

commonly comprises U-shaped stirrups that do not provide adequate shear/torsion capacity.

Thewalt and Stojadinavic [1993] report tests on as-built and retrofitted outriggers (Figure 11). They identify a number of failure modes; however, two main failure modes predominated for the as-built they have considered. First, the essentially unreinforced joint was incapable of developing the strengths of the adjacent column and beam for in-plane loading. Second, when the joint was strengthened, the outrigger beam was incapable of ductile response to the resulting combined bending, shear, and torsion actions. Figure 11 plots transverse and longitudinal responses of the as-built outrigger and of the as-built outrigger with a strengthened joint. Standard procedures were capable of estimating as-built strengths. Deformation capacities of the as-built system were considered unacceptable for most applications.

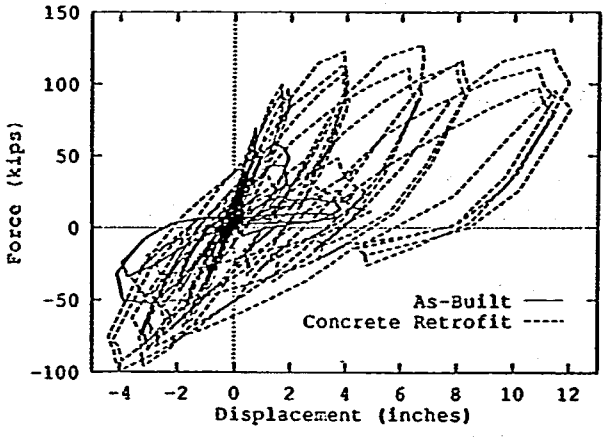
Thewalt and Stojadinovic [1992] investigated two outrigger retrofits. A concrete retrofit added bolsters to the outrigger, providing closed hoops so that the torsional strength was approximately double the cracking capacity. The bolsters extended around the joint, strengthening it so that effectively elastic joint behavior resulted. Figure 12 shows the retrofit and its performance. At large deformations, the outrigger beam failed in torsion, with distributed but widening cracks, and extensive spalling of cover concrete. Although this retrofit maintained strength through large deformations, the extensive diagonal cracking to the outrigger may be considered unacceptable.

A second retrofit strategy investigated by Thewalt and Stojadinovic involves strengthening the outrigger beam to avoid inelastic behavior in the outrigger beam. The engineer can select either steel or concrete jackets for this purpose. Key considerations for the retrofit design include (a) post-tensioning into the box girder to provide required weak-axis bending strength, (b) dowels between new and existing concrete to transfer interface shear primarily due to weak-axis bending, (c) closed perimeter ties in a concrete jacket, or sufficient steel thickness in a steel jacket, to provide required torsion strength. Retrofit of the joint and column may also be required.

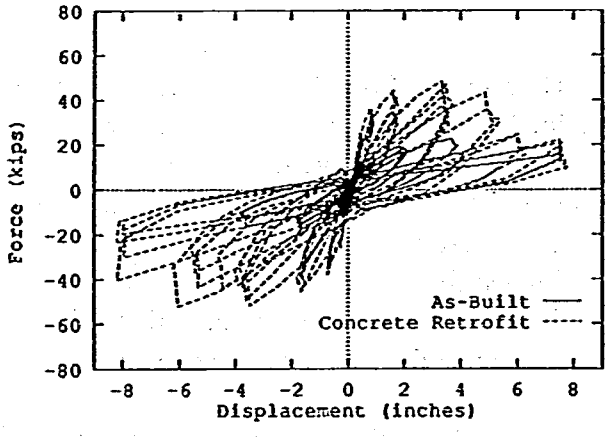


(a) Section

(b) Layout



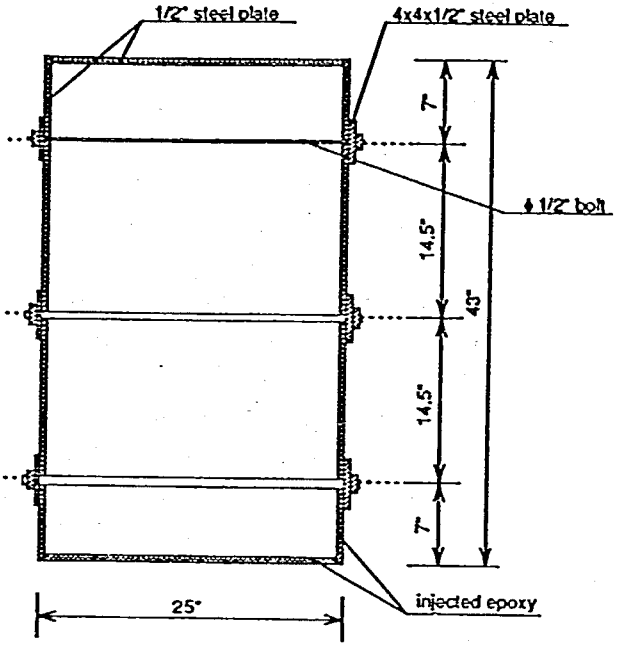
Transverse Response at Top of Column



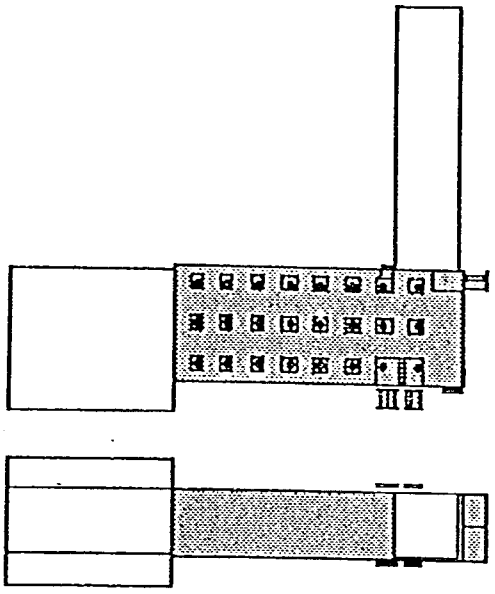
Longitudinal Response at Top of Column

Figure 12. Configuration and Behavior of Outrigger Concrete Retrofit

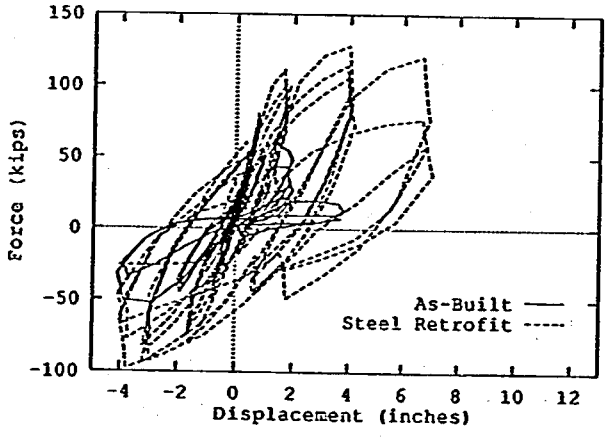
Figure 13 depicts details and behavior of an outrigger with a steel jacket designed so the outrigger would remain elastic. Stiffeners in the joint area were provided to resist expected compression struts. At large deformations, the column failed; the outrigger was nearly elastic.



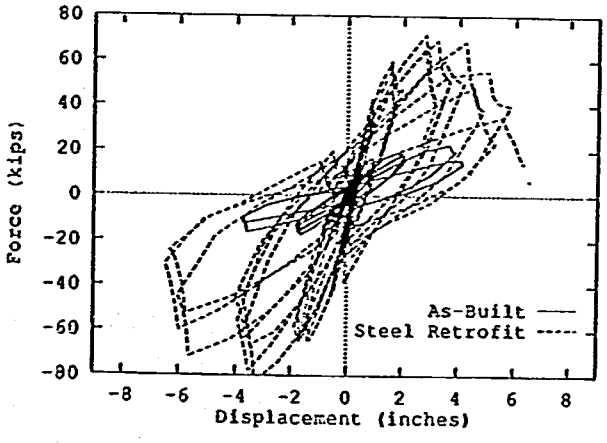
(a) Section



(b) Layout



Transverse Response at Top of Column



Longitudinal Response at Top of Column

Figure 13. Details and Behavior of Outrigger Steel Retrofit

Beam-Column Connections

The 1989 Loma Prieta earthquake exposed the vulnerability of concrete bridge structures to failures of unreinforced and inadequately reinforced beam-column connections. Contemplation and experimental research in the intervening period have led to an improved understanding of connection strength and redesign requirements.

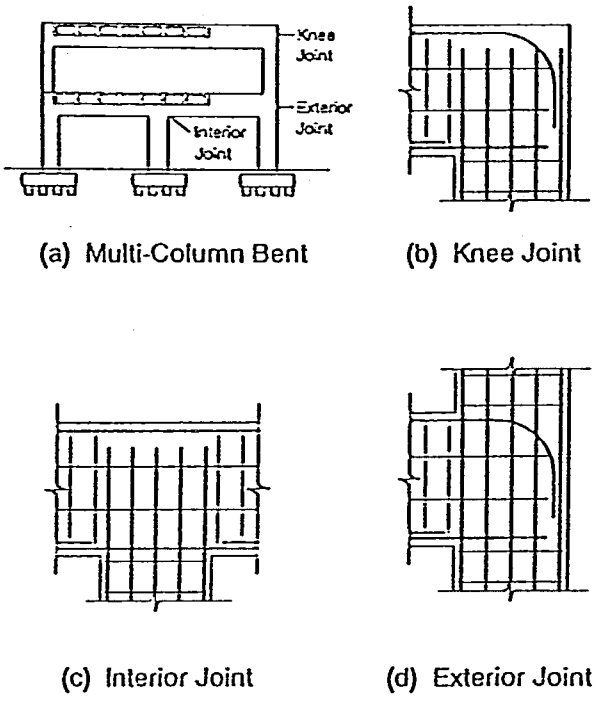


Figure 14. Typical Existing Connection Details

Connection geometries and details of primary interest include those depicted in Figure 14. Connections in typical pre-1970s bridge construction in California do not have joint transverse reinforcement, with the exception of nominal cap beam skin reinforcement that extends into or through the joint. Where column reinforcement terminates in the joint, hooks are usually not present. Bent cap bottom bars are likely to terminate within the joint without a hook.

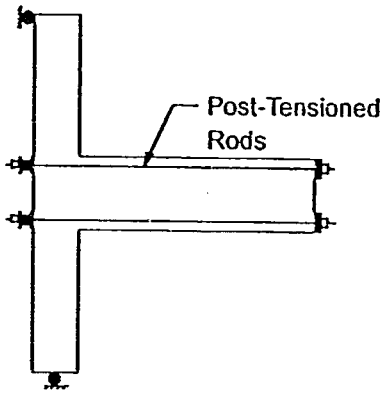
Note should be made of the possibility of column plastic hinging when considering behavior and design requirements; conventional reliance on distributed column bars acting as vertical joint reinforcement [ACI 352; 1985] may not be applicable in this case. Instead, vertical joint reinforcement in addition to the column longitudinal steel may be required. Ongoing research at UC Berkeley is investigating the design and redesign requirements for this condition.

Moehle and Soyer [1993] report results of tests of an exterior connection having details typical of those constructed in California in the 1960s (Figure 9). The beam moment strength was less than the sum of the column moment strengths. Under simulated gravity and seismic loading, nominal joint shear stress of $5.5\sqrt{f'_c}\ psi$ was sustained without appreciable joint cracking (see Figure 9 for measured response).

A second exterior connection test involved strengthening of the beam by addition of external post-tensioning. Figure 15 shows details and results of the test. Failure was by development of diagonal cracks and eventual disintegration of the concrete in the joint. By the end of the test, the stress in the post-tensioning rods had increased significantly,

resulting in a total joint shear stress at failure equal to approximately $12\sqrt{f'_c}\,psi$.

A final retrofit on an exterior connection involved post-tensioning (identical to that used in the preceding test) plus jacketing of the column and joint with a cylindrical steel jacket (Figure 16). The jacket was discontinuous just below and just above the joint, so that flexural strength of the column would not be increased excessively and so that deformations of the column would not be imposed on the jacket surrounding the joint.



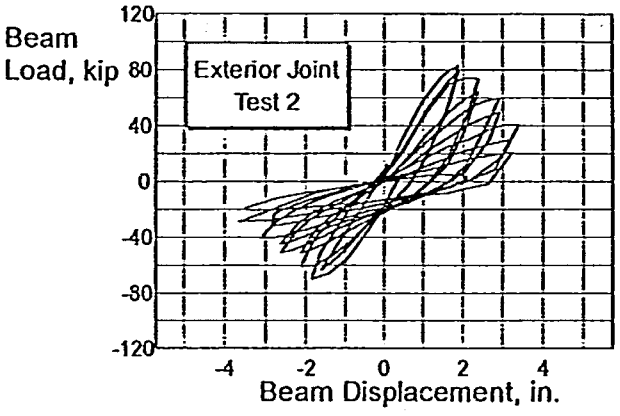
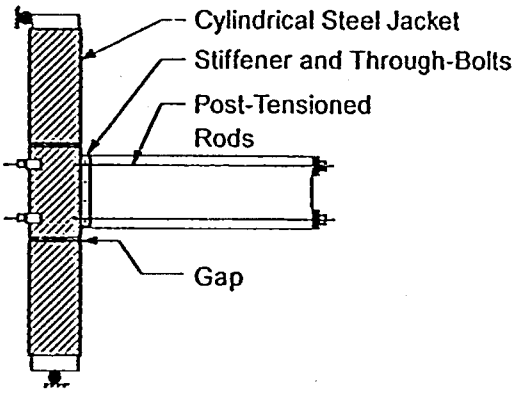


Figure 15. External Post-tension Retrofit



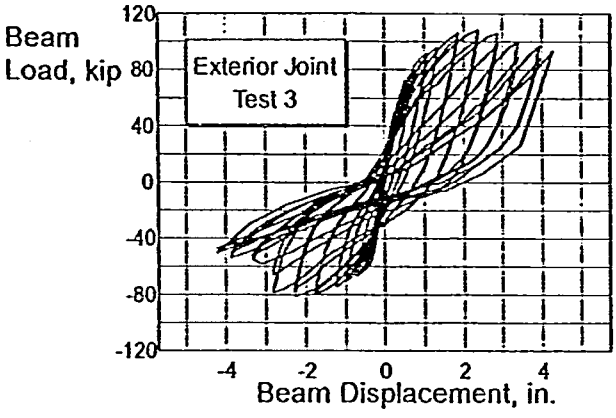


Figure 16. External Post-tension Plus Steel Jacket Retrofit

Also, the jacket around the joint had to be discontinued where it met the beam; at this location the jacket edge was stiffened and bars were passed through the beam to improve continuity. Under simulated gravity and seismic loading this specimen performed very well. Final failure was due to exhaustion of beam rotation capacity.

Behavior of knee joints has been the subject of research efforts at UC Berkeley and UC San Diego. Tests on the Cypress Street Viaduct [Bollo, et al.; 1990] and laboratory outrigger bents [Thewalt and Stojadinovic [1992] indicate that joint failure of unreinforced joints can occur at nominal joint shear stresses as low as $3.5\sqrt{f'_c}\,psi$. Joint shear failure results in rapid degradation of load resisting properties (see Figure 11).

Studies of knee joint retrofit are ongoing at UC Berkeley [Thewalt and Stojadinovic

[1992] and UC San Diego [Ingham; 1991]. In the UC San Diego study, joint concrete was removed and the new reinforcement and concrete was placed. In the UC Berkeley study, the a concrete jacket was placed (see Figure 12). In both cases, both vertical and horizontal reinforcements were placed. Refinements of design and redesign methods are likely in the coming years.

CONCLUSIONS

Experience and research on seismic behavior of multi-column concrete bridges have identified techniques for evaluating framing concepts, expected response, and possible upgrading strategies. The methods described in this paper are under continuing development.

ACKNOWLEDGMENT

The views expressed in this paper were developed in part through research activities sponsored by the California Department of Transportation under the overall direction of James Roberts, Chief, Division of Structures. The research program at the University of California at Berkeley has been carried out jointly with Professors G. Fenves and F. Filippou, and Graduate Student Researchers M. Aschheim, C.-H. Cheng, S. Mazzoni, C. Soyer, B. Stojadinovic, I. Vasquez, N. Yuen, and F. Zayati. The views expressed in this paper do not necessarily represent those of the individuals or organizations identified above.

REFERENCES

[Bolt and Gregor; 1993] - B. A. Bolt and N. Gregor, "Synthetic Seismic Ground Motions for the San Francisco Bay Bridge", *Proceedings*, Second Annual Seismic Research Workshop, Sacramento, March 1993.

[Fenves; 1992] - G. L. Fenves, "Earthquake analysis and Response of Multi-Span Bridges and Viaduct Structures," *Proceedings*, Seminar on Seismic Design and Retrofit of Bridges, University of California at Berkeley, June 1992.

[Der Kiureghian and Nakamura; 1992] - A. Der Kiureghian and Y. Nakamura, "Multiple-Support Response Spectrum Analysis of the Golden Gate Bridge," Proceedings, Third NSF Workshop on Bridge Engineering Research in Progress, La Jolla, California, November 1992, pp. 183-186.

[Veletsos and Newmark, 1960] - A.S. Veletsos and N. M. Newmark, "Effect of Inelastic Behavior on the Response of Simple Systems to Earthquake Motions," Proceedings, Second World Conference on Earthquake Engineering, Vol. 2, Japan, 1960, pp. 895-912.

[Miranda; 1991] - E. Miranda, "Seismic Evaluation and Upgrading of Existing Buildings," PhD Dissertation, University of California at Berkeley, 1991.

[Mahin and Boroschek, 1991] - S. A. Mahin and R. Boroschek, "Influence of Geometric Non-linearities on the Seismic Response and Design of Bridge Structures," Report to the California Department of Transportation, University of California at Berkeley, 1991.

[Priestley and Moehle, 1993] - M. J. N. Priestley and J. P. Moehle, "ATC-32 - Concrete Design," *Proceedings*, Second Annual Seismic Research Workshop, Sacramento, March 1993.

[Freeman; 1992] - S. Freeman, 5 th U.S. Japan Workshop on Improvement of Building Structural Design and Construction Practice, San Diego, 1992.

[Chai; 1990] - Y. H. Chai, M. J. N. Priestley, and F. Seible, "Retrofit of Bridge Columns for Enhanced Seismic Performance," *Proceedings*, US-Japan Workshop on Retrofit of Concrete Bridges, Tsukuba, Japan, November 1990.

[ATC6-2; 1982] - "Seismic Design Guidelines for Highway Bridges," Applied Technology Council, 1982.

[Moehle and Aschheim; 1993] - J. P. Moehle and M. Aschheim, "Evaluation Procedures for Bridge Structures," *Proceedings*, Second Annual Seismic Research Workshop, Sacramento, March 1993.

[Bollo; 1990] - M. Bollo, S. A. Mahin, J. P. Moehle, R. M. Stephen, and X. Qi, "Observations and Implications of Tests on the Cypress Street Viaduct Test Structure," *Report No. UCB/EERC-90/21*, Earthquake Engineering Research Center, University of California at Berkeley, December 1990, 274 pp.

[Moehle and Soyer; 1993] - J. P. Moehle and C. Soyer, "Behavior and Retrofit of Exterior RC Connections," *Proceedings*, Second Annual Seismic Research Workshop, Sacramento, March 1993.

[Collins and Mitchell; 1987] - M. Collins and D. Mitchell, *Prestressed Concrete Basics*, Canadian Prestressed Concrete Institute, Ottawa, Ontario, Canada, 1987, 614 pp.

[Mahin; 1992] S. A. Mahin, F. Zayati, S. Mazzoni, and R. Boroschek, "Evaluation of the Seismic Performance of Retrofit Concepts for Double Deck Reinforced Concrete Viaducts," *Proceedings*, Seminar on Seismic Design and Retrofit of Bridges, University of California at Berkeley, June 1992.

[Thewalt and Stojadinovic; 1993] - "Behavior and Retrofit of Outrigger Beams," *Proceedings*, Seminar on Seismic Design and Retrofit of Bridges, University of California at Berkeley, June 1992.

[ACI 352; 1985] - ACI-ASCE Committee 352, "Recommendations for Design of Beam-Column Joints in Monolithic Concrete Structures, ACI Journal, Proceedings, Vol. 82, No. 3, May-June 1985, pp. 266-283.

[Ingham; 1991] - J. M. Ingham, M. J. N. Priestley, and F. Seible, "Shear Strength of Knee Joints," *Proceedings*, Second Annual Seismic Research Workshop, Sacramento, California, 1993.

DESIGNING THE SUBSTRUCTURE OF THE MAIN TOWER OF HAKUCHO OHASHI BRIDGE

Katsuhiro KUMAGAI
Director of Development Coordination Division
Director-General's Secretariat
Hokkaido Development Bureau

Morito TAKAHASHI
Deputy Director of Muroran Road Office
Muroran Development and Construction Department
Hokkaido Development Bureau

Satoshi NISHIMOTO
Head of 2nd Construction Section of Muroran Road Office
Muroran Development and Construction Department
Hokkaido Development Bureau

Yoshiyuki SAITO
Chief of 3rd Construction Section of Muroran Road Office
Muroran Development and Construction Department
Hokkaido Development Bureau

SUMMARY

The substructure of main tower of Hakucho Ohashi Bridge had to be built on tuffaceous rock which, at its deepest point, is 73m below the sea level. Within this stratum is a 15m thick layer of sandstone which contains boulders up to 1.5m in diameter. In order to cope with such geological conditions, rigid foundations were, for the first time in the world, successfully combined with a continuous underground wall.

This paper describes the basic concept and the earthquake resistant design method of these rigid foundations. It also examines the validity of many of the design parameters assumed at the design stage, comparing the design values and structural analyses of the continuous underground wall, with readings taken at the construction site with measuring instruments.

INTRODUCTION

Hakucho Ohashi Bridge is a 2-hinge closed-box type suspension bridge, with side towers at each end. It has backstay span of 80 meters, a center span of 720 meters and a side span of 330 meters (Figure 1). The bridge rests on six sets of foundations. The subsoil supporting the foundations of the main towers on the Jinya side (hereafter referred to as 3P) and on the Shukuzu side (hereafter referred to as 4P) is very deep, at TP-73.0m, and TP-57.0m, respectively. For this reason, rigid foundations combined with a continuous underground wall were employed: the latter, a flat, circular structure, is used as a temporary retaining/cut-off wall, within which the substructures are built, following enclosed dry excavation.

The main tower on the Jinya side (3P) is notable for:

① the depth of the continuous underground wall (TP-103.0m), the depth of the enclosed excavation (76.0m) and the depth of excavation during construction (over 100m), all of which are unprecedented for a continuous wall;

② the cutting joint method of constructing the continuous wall, in which the preceding elements are cut by an excavator, in order to form the joints: the two-dimensional shape of the wall, as can be seen from Figure 10 (element matrix), is polygonal rather than circular;

③ the varying structural system of the continuous wall, because the reverse-lining wall are constructed at each stage of excavation.

In view of these factors, a successive structural analysis method, using three-dimensional FEM, was employed in the design of the continuous underground wall, in order to improve analytic accuracy.

Outline of the substructure of the main tower (see Figure 2)

(1) Substructures

In order to improve stability, the substructures of the main towers, below the seabed(design subsoil level), are in the form of huge cylinder, 34m in diameter and 58m high in the case of 3P, and 34m in diameter and 38m high for 4P. In order to reduce dead weight and to lower the center of gravity, the substructure above the design subsoil level has foundation widths reduced to 22m at 3P and 26m at 4P.

The 2-meter thick concrete side wall is to be constructed in reverse-lining construction methods below the design subsoil surface when the open dry excavation method is used within the continuous underground wall. Together with the latter, the side wall resists earth and water pressures during the period of construction. After completion, it will transmit the load of the middle-top slab to the bottom slab, and will resist earth pressure from the front and side faces of the foundations. The bottom slab is a disk, 34 meters in diameter, 6.5 meters thick for 3P and 5.0 meters thick for 4P. The bottom slab resists base reaction and hydrostatic uplift during construction. After completion, it will act as a beam on the side wall and the partition wall, thereby transmitting loads from both walls to the supporting rock stratum. The 1.5-meters thick partition wall is built from the bottom, once the laying of the bottom slab is completed. The 5-meters thick concrete middle-top slab transmits the loads from the upper part to the lower part of the division wall, as well as to the side wall. The concrete top slab, 7 meters in thickness, will be constructed on the upper part of the partition wall, and will take directly the load of the main tower.

(2) Continuous underground wall

This is a cylindrical concrete wall, 1.5 meters thick and with an outside diameter of 37 meters, both at 3P and 4P, whose purpose is to keep out water and soil. To stabilize the bottom surface of the enclosed

excavation, the embed depth are 106m, and 67m for 3P and 4P respectively. At 3P in particular, high-strength underwater concrete with a design standard strength of 370 kg/cm2, has been employed, in order to ensure safety during open dry construction at a depth of 73m below the sea level. The construction is carried out on an artificial island made by filling the steel pipe sheet pile cofferdam with coal ash slurry.

Design of the main tower substructure

(1) Geology (see Figures 1 and 2)

At 3P, there are 40-meters thick quaternary period diluvial and alluvial deposits, composed of alternate layers of sand and silt with N values between 0 and 30, below the seabed, or TP-15 meters. Beneath these is a 5-10 meters thick gravel layer which contains rounded boulders approximately 1.5 meters in diameter. Below this gravel layer is neogene period tuffaceous coarse-grained sandstone.

(2) Classification of rock strata

Rock strata were classified as D, CL, CM, CH and B (from soft to hard), according to their modulos of deformation (Esp) -- obtained by using the borehole lateral loading test as the main index -- rock hardness and core shape. The rock stratum supporting the main tower was classified as CL and CH. Details appear in Table 1.

(3) Bearing capacity

The bearing capacity of each foundation rock stratum was calculated by using a formula, and assessed by examining settlement and failure calculated by means of a deformation analysis simulation using FEM analysis, followed by comparison with the C and ϕ of previous examples. Table 2 shows the results of these examinations.

(4) Earthquake resistant design method (see Figure 3)

The seismic design method used for the Hakucho Ohashi Bridge is notable in that:

① seismic waves at the bridge construction site are used;
② account is taken of the dynamic interaction between the ground and the foundations, because the foundations extend deep into the subsoil;
③ The force of superstructure was calculated using a whole system response spectrum method (CQC).

1) Determination of input seismic motion

Using figures recorded by a vibrometer located 1km, distant from the construction site, a formula for the incident acceleration rate at the Muroran bedrock was established. From this formula, and from records of past earthquakes, the design acceleration rate (Amax) at the foundations was set at 120 gal.

2) Design bed rock acceleration response spectrum (Bed rock SA)

The spectrum was established from three waves, at Tokachi-oki, west of Hidaka, and Urakawa-oki (hereafter referred to as Muroran 3 waves), which were recorded at higher than 150 gal. at ground level in Muroran, and Amax was set at 120 gal.

3) Examination of liquefaction phenomena

Liquefaction was examined by means of the following three methods:

① a simple method shown in a road and bridge design manual;
② a detailed method, using SHAKE and repetitive triaxial compressions tests; and
③ an effective stress method.

The attenuating factors (DE) of the subsoil constant were set at 1/3 less than 10 meters deep below the design subsoil surface.

4) Dynamic interaction between ground and substructure

Since the substructure of the main tower of the bridge is constructed very deep into soft subsoil, dynamic interaction was examined using a ground-foundation system model, which gave the following results:

① the primary mode of subsoil contributes mostly to the foundation displacement;
② the subsoil vibrates mostly in primary mode.

On the basis of these results, the difference between structural displacement and subsoil responding displacement was acted upon statically as a load to the foundation through spring to be used for calculating the superstructure response reaction, as dynamic interaction between ground and foundation.

5) Design ground surface acceleration rate response spectrum (surface - SA)

Since the SA (calculated by subsoil response analysis, using Muroran 3 waves), and the incidence earthquake motion spectrum (L-1) on the 4th class subsoils in Muroran, (calculated by the earthquake analysis program (RISK-II) developed by the Public Works Research Institute of the Ministry of Construction), were almost identical in the practical region) (T=0.6-1.5 seconds), L-1 was defined as ground surface SA.

6) Design seismic intensity

In accordance with the road and bridge design manual, design revision seismic intensity above the design ground surface was set at KH=0.3, using ground surface SA and a correction factor calculated as h=0.2.

7) Response reaction of superstructure

This was calculated in accordance with the response spectrum method (CQC method), using a whole system suspension bridge model, because ① the mode of superstructure is complex, and ② the period of substructure is

long and likely to resonate.

In response analysis, use was made of dynamic modulus of deformation derived from the PS logging, and of static deformation factors derived from the lateral horizontal loading test. A larger of the response reaction of superstructure either on the longitudinal direction or transverse direction, is used in the design.

8) External forces generated during earthquake

The following external forces exerted on the foundations during an earthquake were taken into account:

① Response reaction of superstructure, ② inertial forces at bridge piers above the design subsoil surface, and ③ dynamic interaction between the foundations and the subsoils.

(5) Calculation of stability of foundations

The substructure of the main tower is a composite of the continuous underground wall and the substructure itself. The design parameters are: ① that the embed portion for the continuous underground wall is virtually ignored in the safety calculation; ② that vertical load is resisted only by the bottom surface of the substructure; ③ that horizontal forces are also resisted by the continuous underground wall; and ④ that in determining structural stress from stability calculations, it is assumed that the load is resisted only by the substructure, resistance by the continuous underground wall being ignored.

Design of the continuous underground wall

(1) Analytic method

The analytic method made use of a finite element method model, capable of analyzing the three-dimensional transmission of stress, as shown in Figure 4. The wall is polygonal in shape, rather than truly circular, because of the characteristics of the construction method. A preliminary examination revealed that the stress increment of the construction shape model is some 20-30 percent higher than that of a circular model. The model used took account of the actual shape of the construction.

In structural analysis, a side wall, to be added at each stage of excavation, was modeled at each of these stages, and the load generated at each stage was exerted on the model. The stresses generated regularly by the load are accumulated, but stresses generated by loads during earthquakes were not added.

Since the full effects produced by a perfect combination of the continuous underground wall and the side wall cannot be expected in practical term, they are analyzed as a superposed beam in principle, but residual stress generated within the side wall was also examined for the conbined beam, so as to ensure design safety by making use of the conbined beam as part of the bridge substructure after completion.

(2) Load

As loads are exerted during construction, regular equal pressures (water pressure and earth pressure), partial earth pressures inordinary and partial earth pressures during earthquake were taken into consideration. Relationships between each operating load and subsoil resisting spring are shown in Figure 5. The method used to establish each load will be explained below.

(3) Load exerted on the continuous wall during each excavationstage

Excavation stage of the continuous underground wall as shown Figure 6. As shown at a-c of Figure 7, stress is accumulated consecutively at each stage of excavation, and only the increment is loaded at the subsequent stage. The load shown at Figure 7-d is added at each excavation stage, as the load to be exerted during earthquakes, but is not accumulated. The intensity of each load was defined as explained in the following section.

1) Water pressure

The difference between water pressure outside of continuous wall and water pressure inside the wall after draining is exerted in isopiestic conditions. In such conditions, if water permeability at the lower end of the wall is high, the load will be distributed in triangular form, with the highest load (at the excavation surface) as the apex, falling to zero at the lower end of the wall. On the other hand, if the lower end/part of the wall is not water-permeable, the shape of the load distribution is trapezoidal, the water pressures at the lower end/part of the wall and at the excavation surface remaining the same.

In the design of the Hakucho Ohashi Bridge, because water permeability of rock bed at the lower end of the wall varies greatly from 10-4 to 10-7 cm/sec, and in order to ensure safety in the dry construction method, safer figures are used.

2) Earth pressure

Static earth pressure is exerted isopiestatically because deformation of the continuous underground wall is small.

3) Partial earth pressure

Since the structure has a wide surface, account was taken of partial earth pressure, caused by subsoil variety, and unevenness of the excavated surface due to order of excavation. This partial earth pressure, which accounts for 20 percent of the persistent earth pressure at rest, is exerted from both sides.

4) Partial earth pressure during earthquakes

Methods were taken into account for ① loading the difference between active earth pressure during earthquakes and active earth pressure in ordinary from both ends (partial earth pressure #1), and ② loading side subsoil displacement obtained from subsoil response analysis through subsoil spring (partial earth pressure #2).

Because the partial load of the artificial island is consisted to be applied to the continuous underground wall during an earthquake, part of the mass of the island is exerted as an inertial force.(see Figure 8)

Calculation results of continuous underground wall structure

The results of the calculated compression stress intensity along the circumference of the continuous underground wall are shown in Figure 9. Water pressure is the largest component of the compression stress along the circumference of the concrete wall, and accounts for about 60 percent of the various types of load exerted, both normally and during earthquakes. The maximum stress at a depth of about 70m from the surface at the cofferdam is around 170 kgf/cm2 at normal times, and around 190 kgf/cm2 during an earthquake (both readings are taken from along the outer edge of the wall). Consequently the design standard strength of concrete requires a high strength of around 370 kgf/cm2 (underwater concrete strength requirement is 500 kgf/cm2) for both normal and earthquake conditions. When the distribution shape of water pressure is trapezoidal, the maximum load, under any conditions, is slightly lower than when the distribution shape is triangular.

Disposition of measuring instruments

The types and locations of measuring instruments placed within the continuous underground wall are shown in Figure 10.

Measurement results of external forces

(1) Water pressure

Figure 11 shows the distribution of water pressure along a vertical axis, and Figure 12 shows the water pressure horizonal distribution at the first and final (9th) stages. In the distribution along a vertical axis, the values shown are obtained by deducting the values returned by an inside water pressure gauge from those returned by an outside gauge. Water pressure in hydrostatic distribution during the initial stage of excavation shows a tendency of declining from the hydrostatic pressure, and the distribution shape is something between triangular and trapezoidal. Although the outer water pressure along a horizontal axis is practically isopiestic, a comparison of the water pressures at cross-sections H and D, respectively closest to, and furthest from, the deep well, shows that there is a remarkably large fall in water pressure around cross-section H.

(2) Earth pressure

Figure 13 shows the distribution of earth pressure along a vertical axis, while Figure 14 shows its distribution horizontally. However, the value of the earth pressure was defined as the difference between the underground side pressure and water pressure. Vertical earth pressure was distributed in the form of an inverted triangle, in which the figures decrease over time, as opposed to the triangular distribution assumed initially. The intensity of the measured earth pressure was slightly lower than the design earth pressure, although in places it was almost the same. The horizontal earth pressure distribution, on the other hand, was not uniform, as can be seen from Figure 22. It should be noted that at the top

of cross-sections C and G earth pressure decreased substantially in some cases the excavation of the place where the gauge was buried.

(3) Partial pressure

Partial pressure was assumed to account for 20 percent of the earth pressure at rest, corresponding to the LNG design and construction manual. However, since the earth pressure measurements display no regularity or uniformity of distribution, it was difficult to estimate the partial pressure from earth pressure readings. Nevertheless, because partial pressure may be generated by sources other than earth pressure, account should be taken of it in the design.

Measurement of generated stress intensity and displacement

(1) Horizontal measurements of stress intensity

Figure 15 shows measurements (full lined with marks) of edge stress intensity taken horizontally along both the inner and outer concrete of the continuous underground wall at cross-section A (preceding element), together with the design calculation values (full lined). Figure 16 shows the values of the same measurements taken at cross-section C (succeeding element). Cross-section A corresponds to the folding point of the continuous underground wall, and cross-section C corresponds to the center point of the straight line of the wall. The measurements show that the design and measurement values at each cross-section agree quite closely at the early stages of excavation, but that stress intensity undergoes drastic change as excavation proceeds, and in places comes close to the allowable compression stress intensity. The latter is remarkably high inside cross-section A and outside cross-section C, and is close to the design intensity. On the other hand, an extremely high level of compression stress intensity was measured inside cross-section C, where it was expected that intensity would be lower because of the cross-section's polygonal shape. This may be assumed to derive from the influence of the hydration heat of the concrete laid in the side wall. Tensile stress intensity, which during construction was considered to be generated only during an earthquake, was observed in the upper part of the continuous underground wall, and the steel reinforced joint structure was effective under normal conditions.

(2) Reinforcement bar stress intensity along a vertical axis

This was negligible, but was irregular, as it was influenced by hydration heat.

(3) Displacement

Satisfactory results could not be obtained from the measurement of displacement, because of instrument errors caused by the measurement taken at great depth. However, the shape of the displacement revealed that the side wall would restrain the deformation successfully.

In future, it may be desirable to use an underground tiltmeter to measure the displacement of such substructures.

Conclusions

The comparison of measured and design values gives rise to the following comments about assumed conditions and analytic techniques.

1) Water pressure is influenced by the permeability of the surrounding subsoil and of subsoil beneath the excavation face. However, water pressure readings taken along the circumference of the wall show an isopiestic distribution, and the form of water pressure readings along a vertical axis was somewhere between triangular and trapezoidal, as assumed by the design.

2) Earth pressure was considered to increase proportionately with depth, but its distribution form was almost that of an inverted triangle, and the depth figure was also quite low.

3) It was observed that partial pressure was generated because of water pressure under the influence of deep well.

4) As regards measured external forces, water pressure readings corresponded closely to the assumed values. However, earth and partial pressures were considerably below the values assumed. Nevertheless, the fact that the stress intensity of the continuous underground wall was close to the design value could be explained by the facts that the stress intensity generated by water pressure accounts for about 70 percent of the design value, and that the stress intensity attributable to earth pressure and water pressure was offset by the heat produced by the hydration of the concrete of the side wall. The use of three-dimensional finite element analysis could be justified in view of the fact that the effect of the polygonal shape is clearly manifested.

This paper reports on the comparison of various values assumed at the design stage with those measured during construction of the continuous underground wall of the substructure of the main tower of Hakucho Ohashi Bridge. The measurements were made primarily to aid the control of construction, and could not be considered to produce material satisfactory for use in verifying aspects of the design. We hope, nevertheless, that this study will provide material that will be useful in the design of similar structures in the future.

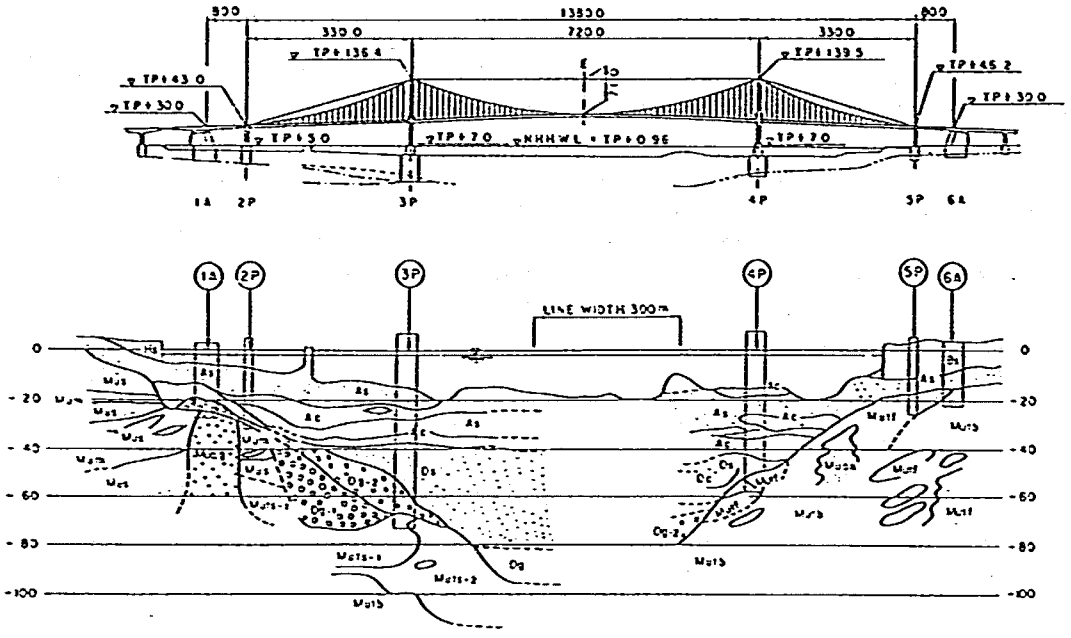


Fig. 1 Side-view and geologic section

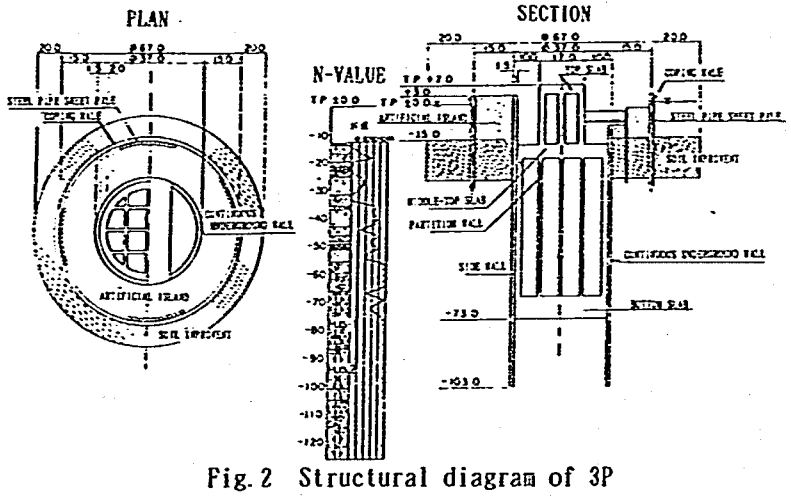


Fig. 2 Structural diagram of 3P

Table 1 Rock classification and strength parameters

( ): design value

	unit	3P · CL	4P · CL	3P · CM	4P · CM
E_{50}	kg f/cm²	1.000～2.000(1.400)		2.000～4.000(2.800)	
C	kg f/cm²	3.0	2.0	6.0	4.0
ϕ	deg	18	30	20	35

Table 2 Allowable bearing capacity

(unit : t/m²)

foundation	1A . 2P	3P	4P . 5P . 6A
normal condition	300	250	200
during earth quakes	450	375	300

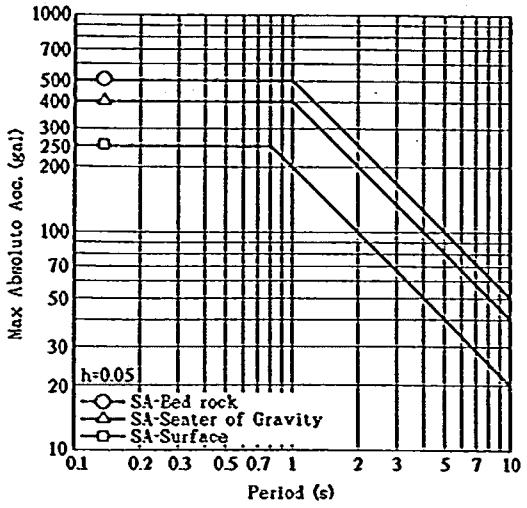


Fig. 3 design response spectrum

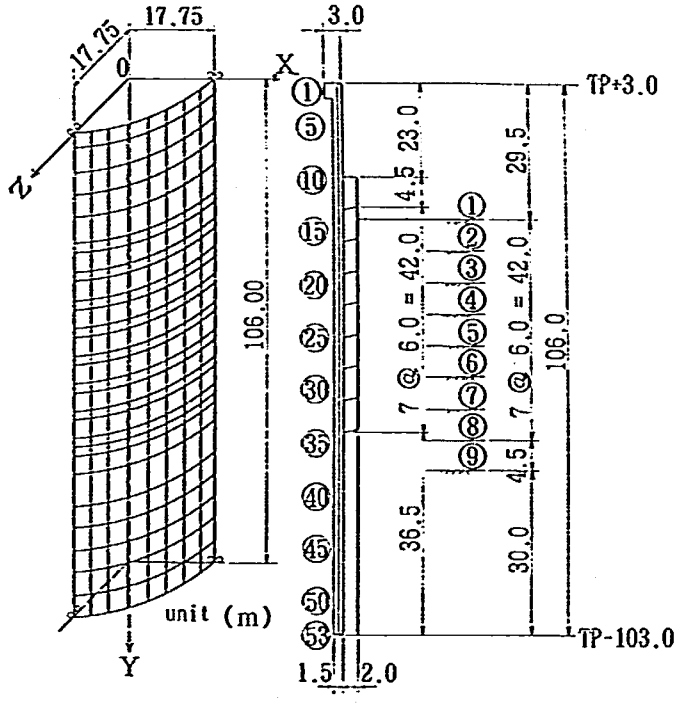


Fig. 4 Structural analysis model

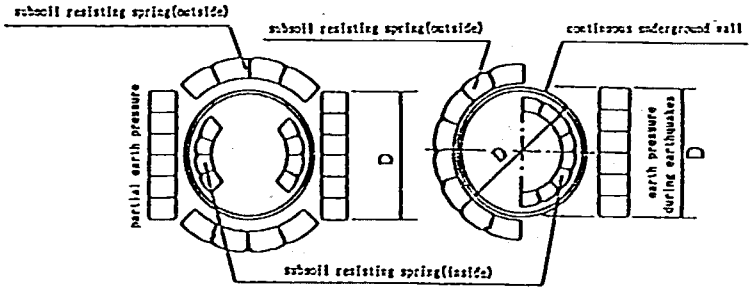


Fig. 5 Operating load and subsoil resisting spring

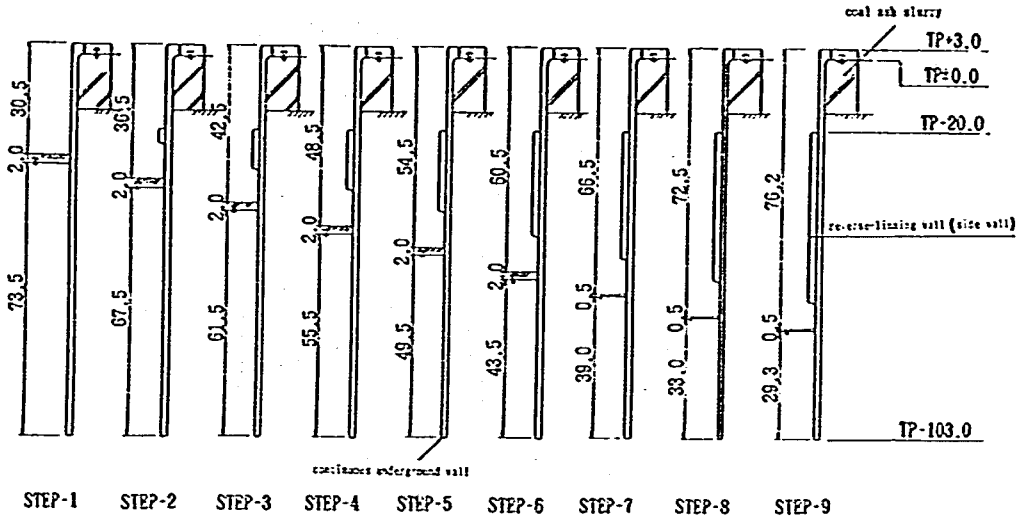


Fig. 6 Excavation stage

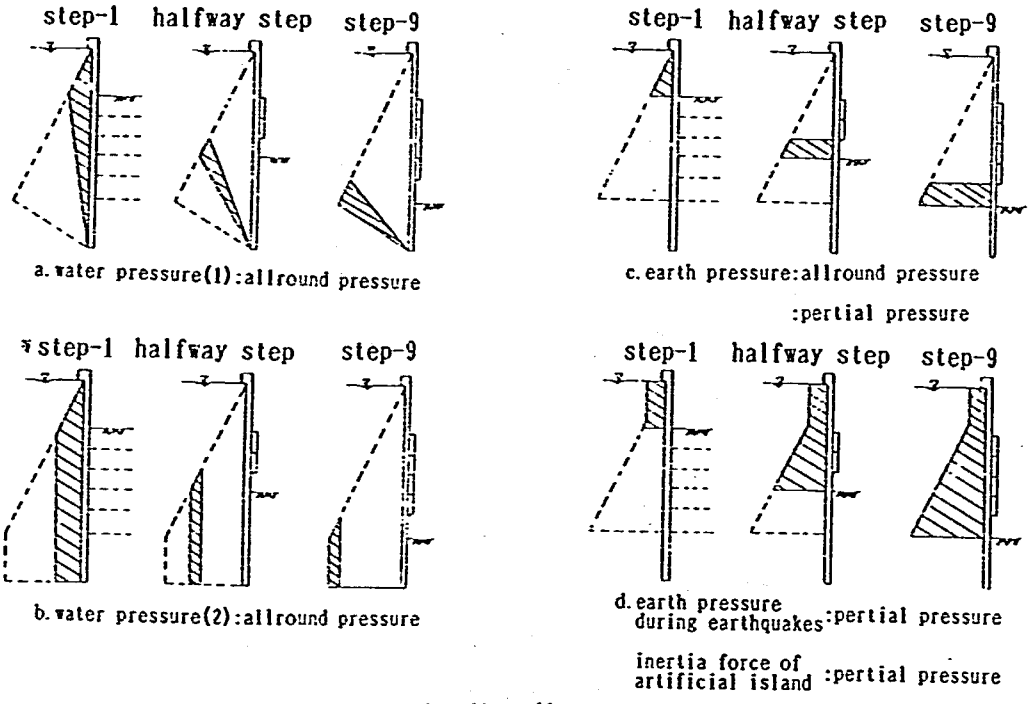


Fig. 7 Loading diagram

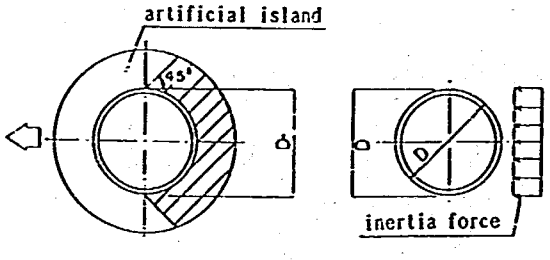


Fig. 8 Inereia force of artificial island

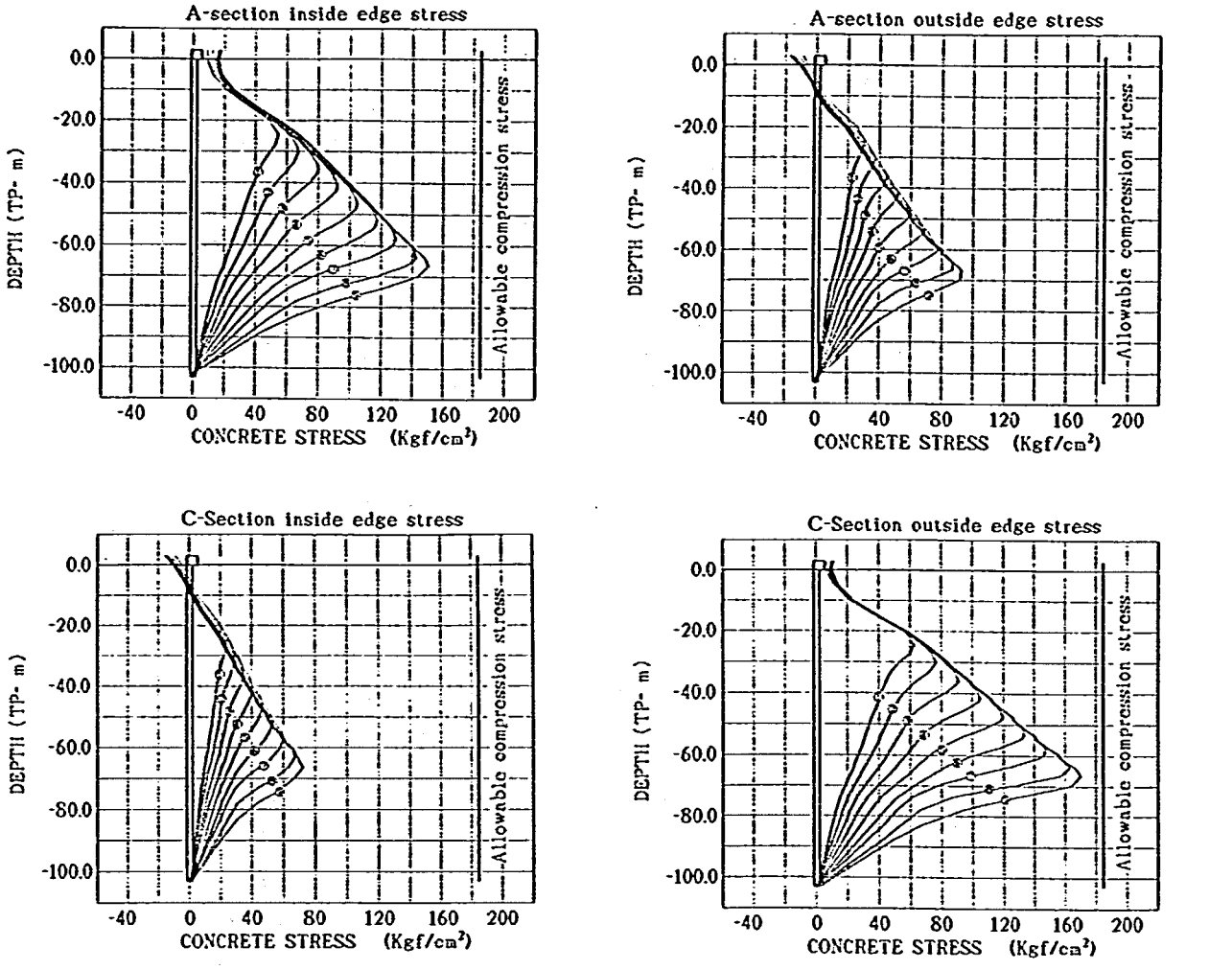


Fig. 9 Circumferential concrete stress
normal condition

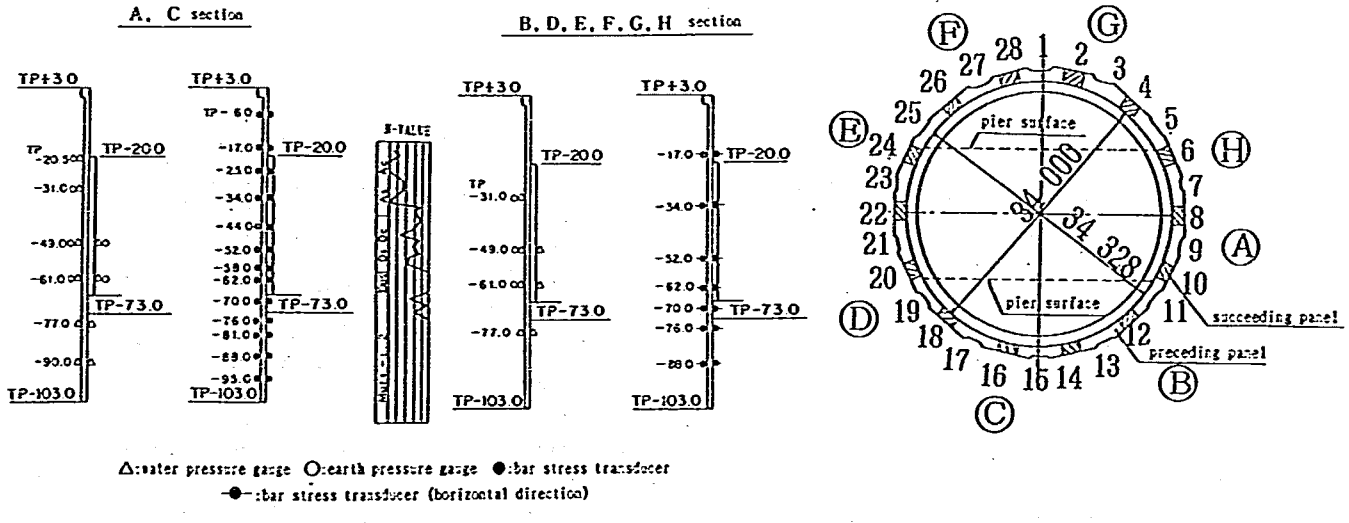


Fig. 10 Gauge disposition diagram

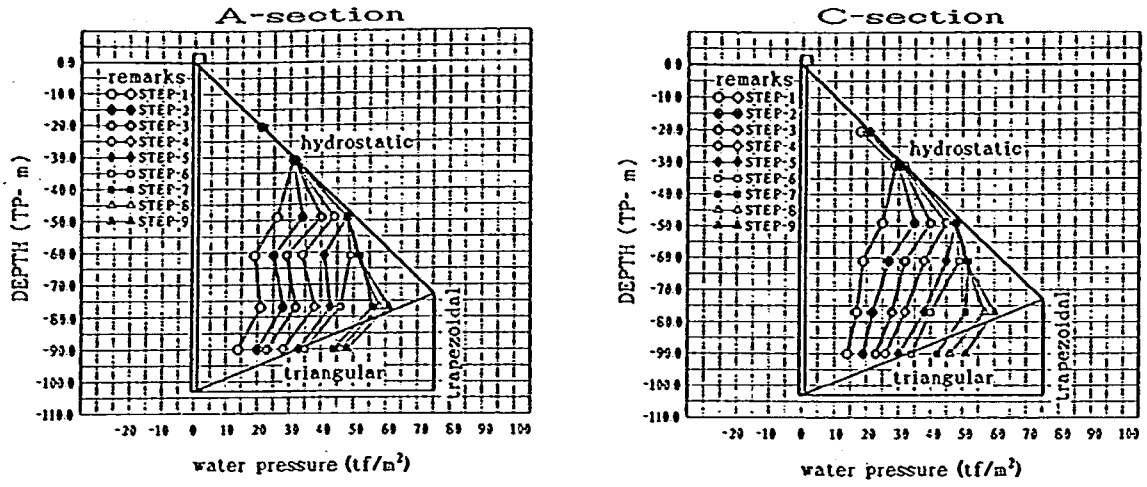


Fig. 11 Vertical distribution of water pressure

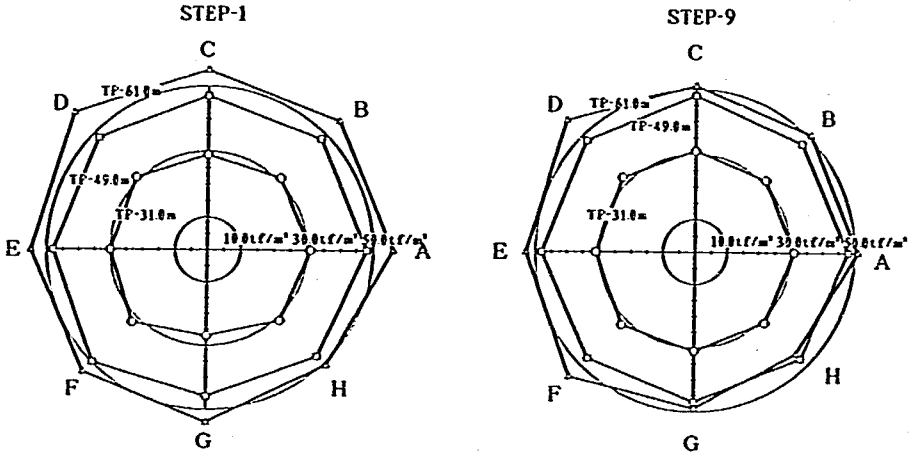


Fig. 12 Horizontal distribution of water pressure

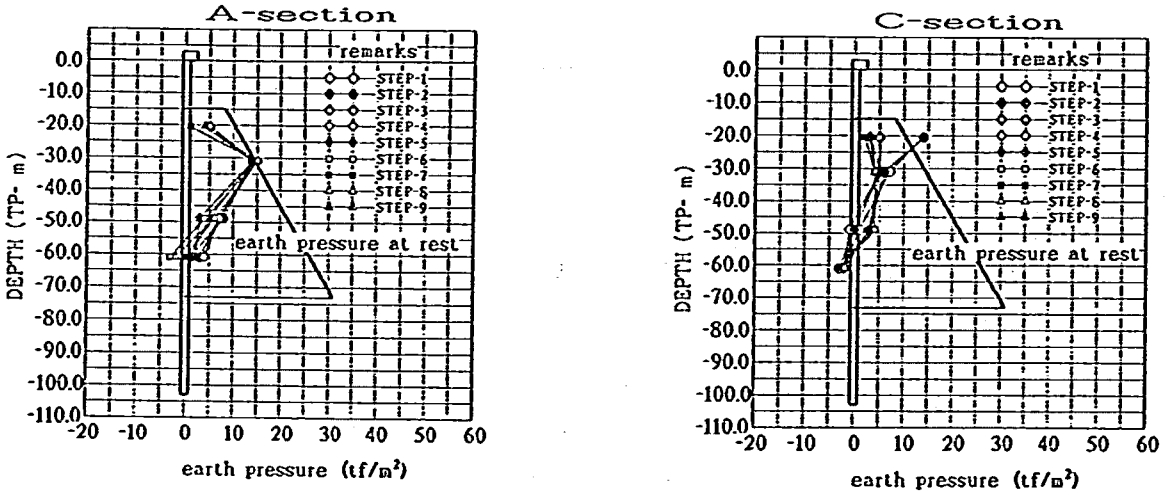


Fig. 13 Vertical distribution of earth pressure

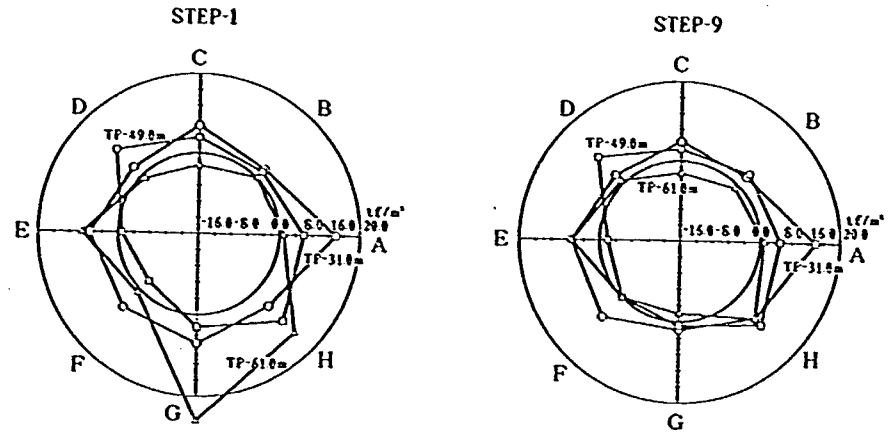


Fig. 14 Horizontal distribution of earth pressure

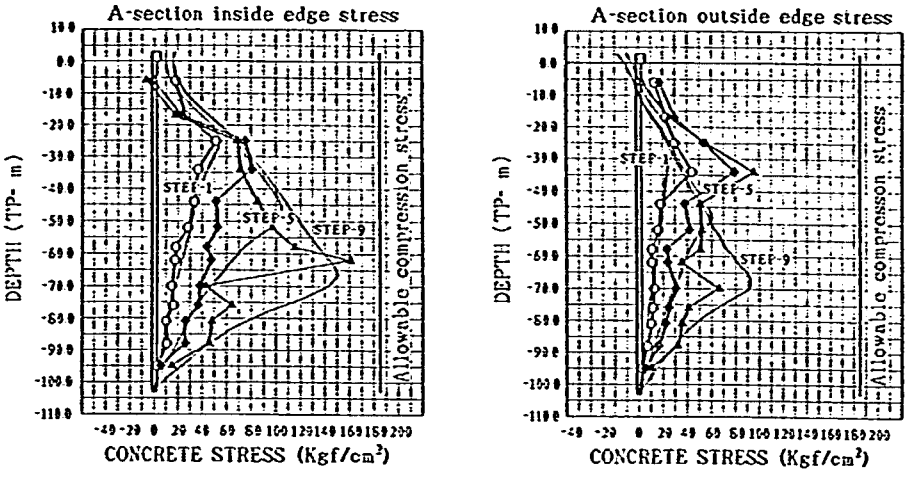


Fig. 15 Horizontal stress of preceding element

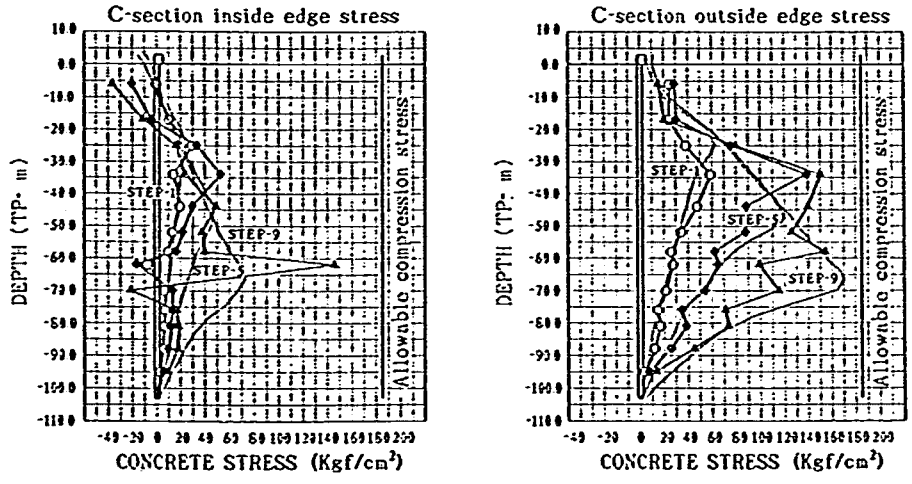


Fig. 16 Horizontal stress of succeeding element

Resolution

RESOLUTION OF THE NINTH U.S.–JAPAN BRIDGE ENGINEERING WORKSHOP
DESIGN, MODELLING, CONSTRUCTION, AND RETROFITTING

Tsukuba Science City, Japan
May 10 and 11, 1993

The following resolutions are proposed by organizers of the 9th U.S.–Japan Bridge Engineering Workshop to the Task Committee J of UJNR:

1. Whereas; the Ninth U.S.–Japan Bridge Engineering Workshop provided valuable exchange of technical information which was beneficial to bridge engineering communities of both countries. 68 participants representing government, academia, industry and private practice presented 31 papers in technical sessions. Main themes focused on research for: innovative methods on superstructure design, analysis and response; wind resistant design and analysis; seismic design and analysis; and substructure behavior.

2. Whereas; the Workshop recognizes the importance of continued exchange of personnel, technical information, research data and bridge response data from significant earthquakes and strong winds; the use of available unique research facilities in both countries; and encourages cooperative efforts in mutually agreeable areas of bridge research.

3. Whereas; the primary purpose of the Workshop is to exchange technical information on a timely basis that is usable by the bridge engineering profession. The specific objectives of this Workshop are:

   - To stimulate collaborative research work in the important area of bridge engineering for better design construction, performance, rehabilitation, and strengthening of bridge structures in both countries.

   - To facilitate the exchange of technical information and ideas and to promote the broadening of viewpoints for those involved.

   - To ensure a first–hand exchange of information resulting from the unique problems each country is faced with; for example, the development and implementation of bridge management systems and limit state or load and resistant factor design methods.

4. Whereas; the Workshop identifies the following technical topics for continued cooperative research programs:

   - Dynamic control and seismic isolation of bridge structures including: active, passive and hybrid control, damping augmentation, experimental studies and application to long–span cable–supported bridges.

- System identification techniques for wind and seismic engineering including: data interpretation studies, development of mathematical models, identification of nonlinear systems, reduced–order models, computational algorithms, and optimum sensor locations.

- Nondestructive evaluation techniques including damage detection by sensor monitoring, expert systems, inspection techniques, structural monitoring, condition assessment for safety, performance evaluation, and repair procedures.

- Experimental and analytical studies on the effects of dynamic soil characteristics, including bridge–soil interactions, on the behavior of bridge structures.

- Retrofitting and strengthening methodologies for bridge structures.

- Development of design criteria based on limit–state concepts.

- Jointless bridge criteria, design, and performance.

- Use and performance of new and enhanced structural materials.

- Development of standard test procedures for base isolation devices.

5. Whereas; the interaction among the delegates from the United States and Japan during the round–table discussions and the technical study tour has lead to an enhanced exchange of data and innovative ideas, and will also lead to the establishment of cooperative research efforts, both theoretical and experimental, on bridge engineering.

6. Be it resolved that; in view of the importance of cooperative programs such as that between PWRI and FHWA on the subject of wind and seismic effects on bridges and on performance, strengthening, structural monitoring, safety, nondestructive evaluation and design innovation of these transportation structures, the continuation of technical cooperation and interaction is considered essential. Further, it is recommended to conduct a 10th bridge engineering workshop in Lake Tahoe, Nevada in conjunction with the 26th UJNR joint meeting in Gaithersburg, Maryland in May 1994 and also in conjunction with an activity under the auspices of the PWRI–FHWA Memorandam of Understanding. A study–tour will be planned to visit research laboratories and bridge–construction sites.

Appendices

WORKSHOP PROGRAM

9th U.S.–JAPAN BRIDGE WORKSHOP
(Workshop on Bridge Engineering)

May 10 and 11, 1993

Tsukuba City, Japan

Monday, May 10, 1993 — Place: Conference Room (8F) PWRI

SESSION 1: OPENING SESSION
(Co–Chairmen: M. Fujiwara, J.D.Cooper) 9:00 ~ 9:15

Welcome Remarks: Yukihiko Sumiyoshi (Director General, PWRI)
Remarks: James D. Cooper (Chairman for the U.S. side)
Remarks: Minoru Fujiwara (Chairman for the Japan Side)

SESSION 2: SUPERSTRUCTURE(1) 9:15 ~ 10:15
(Co–Chairmen: K.Nishikawa, J.D.Cooper)

(1) K.Nishikawa, M.Kanda * and K.Uchida :
Structural Behavior of Prestressed Concrete Beams Using FRP Tendons
(9:15 ~ 9:30)

(2) G.Runco * and P.Brinckerhoff :
Management Decisions for Bridge Deck Rehabilitation/Replacement
(9:30 ~ 9:45)

(3) I.Sugie * , Y.Yamaguchi, K.Kobayashi and K.Kuzume : Damage and Its Reinforcement of Post–tensioned Prestressed Concrete Bridge Slab
(9:45 ~ 10:00)

DISCUSSION
(10:00 ~ 10:15)

COFFEE BREAK
(10:15 ～ 10:30)

SESSION 3: SUPERSTRUCTURE(2) 10:30 ～ 11:10
(Co−Chairmen: K.Nishikawa, B.M.Douglas)

(4) F.W.Klaiber * , K.F.Dunker, T.J.Wipf and F.S.Fanous :
Strengthening of Steel−Stringer Bridges by Post−Tensioning
(10:30 ～ 10:45)

(5) T.Shirono * , H.Nishi, O.Nakano and K.Kumagai :
Application of Buried Joint in Cold and Snowy Region
(10:45 ～ 11:00)

DISCUSSION
(11:00 ～ 11:10)

COFFEE BREAK
(11:10 ～ 11:25)

SESSION 4:WIND RESISTANT DESIGN(1) 11:25 ～ 12:25
(Co−Chairmen: H.Sato, E.Maragakis)

(6) K.Kimura, Y.Fujino * and S.Hiejima : An Experimental Study on Aerodynamic
Sound Generated from Handrails of Flat Plate Cascades
(11:25 ～ 11:40)

(7) O.U.Onyemelukwe and H.R.Bosch to be presented by J.D.Cooper :
Simulation Techniques for Bridge Aerodynamic Investigations at the
Turner−Fairbank Highway Research Center
(11:40 ～ 11:55)

(8) H.Sato and R.Toriumi * :
Analytical Study on Flutter of Suspension Bridge
(11:55 ～ 12:10)

DISCUSSION
(12:10 ～ 12:25)

LUNCH (Conference Room ,8F)
(12:25 ～ 13:40)

PHOTOGRAPH (Entrance of PWRI Main Building)
(13:40 ～ 13:55)

SESSION 5:WIND RESISTANT DESIGN(2) 14:00 ～ 15:00
(Co−Chairmen: H.Sato, D.A.Foutch)

(9) K.Nomura *, Y.Suzuki, K.Kuroda and Y.Igase :
Aerodynamic Stability of Central Nagoya Port Bridge
(14:00 ～ 14:15)

(10) M.Kamei *, M.Kawakami, K.Ikushima, H.Tanaka and M.Hosomi :
Aerodynamic Stability of Nakajima Bridge (Provisional Name)
(14:15 ～ 14:30)

(11) Y.Shioi, Y.Yoshida and K.Saga * :
Aerodynamic Stability of Trans−Tokyo−Bay Highway Bridge
(14:30 ～ 14:45)

DISCUSSION
(14:45 ～ 15:00)

COFFEE BREAK
(15:00 ～ 15:15)

SESSION 6: SEISMIC DESIGN(1) 15:15 ～ 16:15
(Co−Chairmen: Y.Iida, C.Seim)

(12) K.Kosa, Y.Hashimoto and K.Kobayashi : An Experimental Study of Horizontal Displacement Behavior Using Large−Size Model Pier
(15:15 ～ 15:30)

(13) M.Sultan * and K.Kawashima : Comparison of the Seismic Design of Highway Bridges in California and in Japan
(15:30 ～ 15:45)

(14) H.Ohtsuka, K.Tokida, K.Tamura, M.Kaneko * and H.Fukada :
Analysis of Ground Motion Characteristics
(15:45 ~ 16:00)

DISCUSSION
(16:00 ~ 16:15)

COFFEE BREAK
(16:15 ~ 16:30)

SESSION 7: SEISMIC DESIGN(2) 16:30 ~ 17:30
(Co-Chairmen:Y.Iida, F.W.Klaiber)

(15) K.H.Chen and D.A.Foutch * :
Seismic Base Isolation of Curved Highway Bridges
(16:30 ~ 16:45)

(16) K.Kawashima * , H.Nagashima and H.Iwasaki :Evaluation of Modal Damping Ratio
of Bridges Based on Strain Energy Proportional Method
(16:45 ~ 17:00)

(17) A.D.Gilbert * :
Developments in Seismic Prioritization of Bridges in California
(17:00 ~ 17:15)

DISCUSSION
(17:15 ~ 17:30)

RECEPTION BY DIRECTOR GENERAL OF PWRI
Place: Akatsuki no Ma of GRAND SHINONOME (TEL: 0298-56-2211)
Time: 18:30 ~ 20:30
Transportation: Bus of GRAND SHINONOME leaves from Entrance of Main Building

Tuesday, May 11, 1993 Place: Conference Room (8F) PWRI

SESSION 8: SEISMIC DESIGN(3) 9:15 ~ 10:35

(Co-Chairmen:H.Ohtsuka, J.Clark)

(18) S.S.Chen *, J.B. Mander, D.S.MacEwan and D.K.Kim : Structural Modeling Implications from Snap-Back Tests on a Slab-on-Girder Bridge
(9:15 ~ 9:30)

(19) K.Kawashima, S.Unjo* and H.Mukai : Seismic Response of Reinforced Concrete Bridge Piers subjected to Eccentric Loading
(9:30 ~ 9:45)

(20) E.Maragakis *, M.Saiidi, S.Feng, S.Abdel-Ghaffar and D.O'Connor : Evaluation of the Seismic Response of Bridges with Hinge Restrainers
(9:45 ~ 10:00)

(21) K.Kawashima, H.Sugita * and T.Nakajima : Dynamic Strength and Ductility Characteristics of Steel Bridge Piers
(10:00 ~ 10:15)

DISCUSSION
(10:15 ~ 10:35)

COFFEE BREAK
(10:35 ~ 10:50)

SESSION 9: SEISMIC DESIGN(4) 10:50 ~ 12:10

(Co-Chairmen:K.Kawashima, J.Moehle)

(22) J.H.Clark * : SR5 Lake Washington Ship Canal Bridge Seismic Vulnerability Assessment
(10:50 ~ 11:05)

(23) N.Ito * and M.Okada : Research on Adoption of Vane-Dampers for the Tsurumi Fairway Bridge
(11:05 ~ 11:20)

(24) C.Seim * , S.Rodriguez and T.Ingham :
Seismic Performance and Retrofit of the Golden Gate Bridge
(11:20 ～ 11:35)

(25) M.Eberhard :
Lateral–Load Response Models of a Reinforced Concrete Bridge
(11:35 ～ 11:50)

DISCUSSION
(11:50 ～ 12:10)

LUNCH (Conference Room ,8F)
(12:10 ～ 13:20)

THE VISITATION OF LABORATORIES (13:20 ～ 14:05)

SESSION 10: SUBSTRUCTURE(1) 14:10 ～ 15:10
(Co–Chairmen:M.Nakano, G.Runco)

(26) Y.Xiao * , M.J.N.Priestly, F.Seible and N.Hamada :
Retrofit of Bridge Footings for Improved Seismic Performance
(14:10 ～ 14:25)

(27) N.Ogata, Y.Maeda, A.Murayama, H.Ando * , Y.Kobatake and S.Ohno :
Earthquake Resistant Capacity of RC Pier Retrofitted with Carbon Fibre
(14:25 ～ 14:40)

(28) D.H.Sanders, B.M.Douglas * and K.Cornell : Retrofit Solutions for Inadequate Anchorage of Column Bars into Pier Caps
(14:40 ～ 14:55)

DISCUSSION
(14:55 ～ 15:10)

COFFEE BREAK
(15:10 ～ 15:25)

SESSION 11: SUBSTRUCTURE(2) 15:25 ~ 16:25

(Co-Chairmen:M.Fujiwara, A.D.Gilbert)

(29) M.Okahara, M.Nakano, Y.Kimura *, K.Chimi and A.Inoue :
Vertical Bearing Capacity of Shallow Foundation
(15:25 ~ 15:40)

(30) J.P.Moehle *, C.R.Thewalt and S.A.Mahin (Presented by Andrew S. Whittaker) :
Evaluation and Upgrading of Multi-Column Bridges
(15:40 ~ 15:55)

(31) K.Kumagai, M.Takahashi, S.Nishimoto and Y.Saito * :
Designing the Substructure of The Main Tower of Hakucho Ohashi Bridge
(15:55 ~ 16:10)

DISCUSSION
(16:10 ~ 16:25)

SESSION 12: CLOSING SESSION 16:25 ~ 16:40

(Co-Chairmen: M.Fujiwara, J.D.Cooper)

Settlement of Resolution
Remarks: James D. Cooper (Chairman for the U.S. side)
Closing Remarks: Minoru Fujiwara (Chairman for the Japan side)

Date	Schedule	Stay
5 /8 (Sat.)	Ar.Narita →Tokyo	Ginza-Daiich Hotel (Tokyo) Tel:03-3542-5311 Fax:03-3542-3030
5 / 9 (Sun.)	Tokyo→Tsukuba	Hotel Grand Shinonome (Tsukuba) Tel:0298-56-2211
5 / 10 (Mon.)	Workshop (PWRI)	MOC Kenshu-Kaikan (Tsukuba) Tel:0298-64-2844
5 / 11 (Tue.)	Workshop (PWRI)	〃
5 / 12 (Wed.)	Study Tour Tsukuba→Osaka (Honshu-Shikoku Bridge)	Kobe Oriental Hotel (Kobe) Tel:078-331-8111 Fax:078-391-8708
5 / 13 (Thu.)	Study Tour Kobe→Osaka (Hanshin Expressway and Kansai International Airport)	KKR Hotel Osaka (Osaka) Tel:06-941-1122 Fax:06-941-5508
5 / 14 (Fri.)	Study Tour Osaka→Tokyo	Ginza-Daiichi Hotel (Tokyo) Tel:03-3542-5311 Fax:03-3542-3030
5 / 15 (Sat.)	Leave Narita for U.S.	

9th U. S. – JAPAN BRIDGE WORKSHOP
LIST OF PARTICIPANTS

May 10 and 11, 1993

Tsukuba City, Japan

– U. S. SIDE –

(1) Dr. Stuart Chen
Position: Assistant Professor
Department of Civil Engineering
242 Ketter Hall
State University of New York
Address : Buffalo, NY 14260
TEL : 716–645–2016
FAX : 716–645–3733

(2) Dr. John H. Clark
Position: Chief Bridge Engineer
Anderson, Bjornstad, Kane & Jacobs
Address : 220 West Harrison Street
Seattle, WA 98119
TEL : 206–285–1185
FAX : 206–285–8204

(3) Mr. James D. Cooper
Position: Chief Structures Division (HNR–10)
Federal Highway Administration
Address : 6300 Georgetown Pike
Mclean, VA 22101–2296
TEL : 703–285–2060
FAX : 703–285–2766

(4) Dr. Bruce M. Douglas
Position: Director, Center for Civil Engineering
Earthquake Research, University of Nevada Reno
Address : Reno, NV 89557
TEL : 702–784–1519
FAX : 702–784–4466

(5) Dr. Marc Eberhard
Position: Assistant Professor
Civil Engineering Department
233 More Hall, FX–10
University of Washington
Address : Seattle, WA 98195
TEL : 206–543–4815
FAX : 206–543–1543

(6) Dr. Douglas A. Foutch

Position: Professor, Dept. of Civil Engineering,
University of Illinois
Address : 3129 Newmark Civil Engineering Lab
205 North Mathews, Urbana, IL 61801–2397
TEL : 217–333–6359
FAX : 217–333–9464

(7) Ms. Ann Gilbert

Position: CALTRANS, Division of Structures
Office of Earthquake Engineering
Address : P.O. Box 942874, Sacramento
CA 94274–0001
TEL : 916–323–5831
FAX : 916–227–8174

(8) Dr. F. Wayne Klaiber

Position: Manager, Bridge Engineering Center
Professor of Civil Engineering, Iowa State University
Address : 424 Town Engineering Building
Iowa State University, Ames, IA 50011
TEL : 515–294–7457
FAX : 515–294–8216

(9) Dr. Emmanuel A. Maragakis

Position: Associate Professor, Civil Engineering Department
University of Nevada Reno
Address : Reno NV 89557
TEL : 702–784–4839
FAX : 702–784–4466

(10) Dr.Andrew S. Whittaker

Position: Associate Director,
Earthquake Engineering Research center
University of California
Address : 1301 South 46th Street Richmond,
CA 94804–4698
TEL : 510–231–9554
FAX : 510–231–9471

(11) Mr. Gary Runco

Position: Assistant Vice President, Area Manager, Parsons,
Brinkerhoff, Quade & Douglas
1 Gateway Center
Address : One Gateway Center,
4th Floor West Pittsburgh, PA 15222
TEL : 412–281–9900
FAX : 412–281–2056

(12) Mr. Charles Seim

Position: Senior Principal, T.Y. Lin International
Address : 825 Battery Street
San Francisco, CA 94111
TEL : 415–291–3700
FAX : 415–433–0807

(13) Mr. Mohsen Sultan

Position: CALTRANS, Division of Structures
Office of Earthquake Engineering
Address : P.O. Box 942874 Sacramento,
CA 94274–0001
TEL : 916–227–8247
FAX : 916–227–8765

(14) Dr. Yan Xiao

Position: Assistant Research Scientist
Department of AMES
University of California, San Diego
Address : 9500 Gilman Drive La Jolla,
CA 92093–0411
TEL : 619–534–4640
FAX : 619–534–6373

－JAPAN　SIDE－

(Public Works Research Institute)
Address : 305, 1－chome, Asahi－machi, Tsukuba－shi, Ibaraki－ken
TEL :　(0298)64－2211
FAX :　(0298)64－2840

(1) Yukihiko Sumiyoshi
Position: Director General

(2) Tokuji Tomaru
Position: Deputy Director General

(3) Takashi Iijima
Position: Assistant Director General

(4) Masahide Tamura
Position: Director, Planning and Research Administration Dept.

(5) Tadahiko Fujisawa
Position: Research Coordinator for Advanced Technology,
Planning and Research Administration Dept.

(6) Hiroo Kanzaki
Position: Director, Road Dept.

(7) Minoru Fujiwara
Position: Director, Structure and Bridge Dept.
* Chairman of Japan－side of J Task Committee

(8) Yutaka Iida
Position: Director, Earthquake Disaster Prevention Dept.

(9) Masashi Ikemura
Position: Director, Materials and Construction Methods Dept.

(10) Ryutaro Oishi
Position: Coordinator for International Research Cooperation,
Planning and Research Administration Dept.

(11) Nobuhiko Taniguchi
Position: Bridge Instructor, Planning and Research
Administration Dept.

(12) Masanori Nakano
Position: Head, Foundation Engineering Div.
Structure and Bridge Dept.

(13) Jiro Fukui
Position: Senior Research Engineer, Foundation Engineering Div.
Structure and Bridge Dept.

(14) Yoshitomi Kimura
Position: Research Engineer, Foundation Engineering Div.
Structure and Bridge Dept.

(15) Shigeru Takagi
Position: Research Engineer, Foundation Engineering Div.
Structure and Bridge Dept.

(16) Masahiro Ishida
Position: Research Engineer, Foundation Engineering Div.
Structure and Bridge Dept.

(17) Hiroshi Sato
Position: Head, Structure Div.
Structure and Bridge Dept.

(18) Ryuichi Toriumi
Position: Senior Research Engineer, Structure Div.
Structure and Bridge Dept.

(19) Hisashi Konno
Position: Research Engineer, Structure Div.
Structure and Bridge Dept.

(20) Yoshiaki Matsuno
Position: Research Engineer, Structure Div.
Structure and Bridge Dept.

(21) Kazuhiro Nishikawa
Position: Head, Bridge Div.
Structure and Bridge Dept.

(22) Masayuki Kanda
Position: Research Engineer, Bridge Div.
Structure and Bridge Dept.

(23) Jun Murakoshi
Position: Research Engineer, Bridge Div.
Structure and Bridge Dept.

(24) Yoshiki Tanaka
Position: Research Engineer, Bridge Div.
Structure and Bridge Dept.

(25) Satoshi Yamamoto
Position: Research Engineer, Bridge Div.
Structure and Bridge Dept.

(26) Hisanori Otsuka
Position: Head, Ground Vibration Div.
Earthquake Disaster Prevention Dept.

(27) Yoshio Ninomiya
Position: Senior Research Engineer, Ground Vibration Div.
Earthquake Disaster Prevention Dept.

(28) Masahiro Kaneko
Position: Research Engineer, Ground Vibration Div.
Earthquake Disaster Prevention Dept.

(29) Seitaro Yoshimi
Position: Research Engineer, Ground Vibration Div.
Earthquake Disaster Prevention Dept.

(30) Riki Honda
Position: Research Engineer, Ground Vibration Div.
Earthquake Disaster Prevention Dept.

(31) Kazuhiko Kawashima
Position: Head, Earthquake Engineering Div.
Earthquake Disaster Prevention Dept.

(32) Shigeki Unjoh
Position: Senior Research Engineer, Earthquake Engineering Div.
Earthquake Disaster Prevention Dept.

(33) Hideki Sugita
Position: Research Engineer, Earthquake Engineering Div.
Earthquake Disaster Prevention Dept.

(34) Jun-ichi Hoshikuma
Position: Research Engineer, Earthquake Engineering Div.
Earthquake Disaster Prevention Dept.

(35) Tomoru Nakajima
Position: Research Engineer, Earthquake Engineering Div.
Earthquake Disaster Prevention Dept.

(36) Hiroshi Watanabe
Position: Research Engineer, Concrete Div.
Materials and Construction Methods Dept.

(University of Tokyo)

(1) Yozo Fujino
Position: Professor, Dept. of Civil Engineering,
Faculty of Engineering
Address : 113, 7–3–1 Hongoh, Bunkyo–ku, Tokyo
TEL : 03–3812–2111
FAX : 03–3812–4977

(Japan Highway Public Corporation)

(2) Norio Ogata
Position: Head, Bridge Section Research Institute
Address : 194, 1–4–1 Tadao, Machida–shi, Tokyo
TEL : 0427–91–1621
FAX : 0427–94–1920

(3) Yoshifumi Maeda
Position: Deputy Head, Bridge Section Research Institute
Address : 194, 1–4–1 Tadao, Machida–shi, Tokyo
TEL : 0427–91–1621
FAX : 0427–94–1920

(4) Hirofumi Andoh
Position: Bridge Section Research Institute
Address : 194, 1–4–1 Tadao, Machida–shi, Tokyo
TEL : 0427–91–1621
FAX : 0427–94–1920

(5) Kenji Nomura
Position: Engineer, Stractural Engineering Section
Nagoya Construction Bureau
Address : 460, 4–1–1 Sakae, Naka–ku, Nagoya–shi, Aichi–ken
TEL : 052–262–7311
FAX : 052–241–4530

(6) Kenji Kuroda
Position: Engineer, Stractural Engineering Section
Nagoya Construction Bureau
Address : 460, 4–1–1 Sakae, Naka–ku, Nagoya–shi, Aichi–ken
TEL : 052–262–7311
FAX : 052–241–4530

(Metropolitan Expressway Public Corporation)

(7) Noboru Ito
Position: Senior Engineer, Special Structural Design Div.
Kanagawa Construction Bureau
Address : 231, Masage-Cho 2-25, Naka-ku, Yokohama,Kanagawa-ken
TEL : 045-662-1151
FAX : 045-663-2524

(Hanshin Expressway Public Corporation)

(8) Kenji Kosa
Position: Senior Engineer, Design Div.
Maintenance and Facility Design Dept.
Engineering Dept.
Address : 541, Osaka Center Building, 4-1-3 Kyutaro-Machi, Chuo-ku, Osaka
TEL : 06-252-8121
FAX : 06-252-4583

(9) Isao Sugie
Position: Engineer, Maintenance Engineering Div.
Maintenance and Facility Design Dept.
Address : 541, Osaka Center Building, 4-1-3 Kyutaro-Machi, Chuo-ku, Osaka
TEL : 06-252-8121
FAX : 06-252-4583

(Honshu-Shikoku Bridge Authority)

(10) Hiroshi Katsuchi
Position: Engineer, Design Div. Design Dept.
Address : 105, 5-1-5 Toranomon, Minato-ku, Tokyo
TEL : 03-3434-7281
FAX : 03-3578-9298

(Hokkaido Development Bureau, Hokkaido Development Agency)

(11) Osamu Nakano
Position: Head, Structures Section
Civil Engineering Research Institute (CERI)
Address : 062, 1-3 Hiragishi, Toyohira-ku, Sappro-shi, Hokkaido
TEL : 011-841-1111
FAX : 011-824-1226

(12) Tadayuki Shirono
Position: Research Worker, CERI.
Address : 062, 1–3 Hiragishi, Toyohira–ku, Sapporo–shi, Hokkaido
TEL : 011–841–1111
FAX : 011–824–1226

(13) Yoshiyuki Saito
Position: Chief of 3rd Construction Section
Muroran Road Office
Muroran Development and Costruction Department
Address : 051, 1 Syukuzu, Muroran–shi Hokkaido
TEL : 0143–27–2211
FAX : 0143–27–3694

(Tokyo Metropolitan Government)

(14) Yukio Shinozaki
Position: Chief of Bridge Maintenance,
Road and Street Administration Division,
Road and Bridge Construction Section
Address : 163–01, 2–8–1 Nishi–shinjuku, Shinjuku–ku, Tokyo
TEL : 03–5320–5295
FAX : 03–5388–1529

(15) Kenichi Shinohara
Position: Chief of Bridge Construction Planning,
Road and Bridge Construction Section
Address : 163–01, 2–8–1 Nishi–shinjuku, Shinjuku–ku,Tokyo
TEL : 03–5320–5352

(Osaka Municipal Government)

(16) Masahiro Kamei
Position: Staff Officer, Elevated Crossings Dept.
Roads and Streets Division,
Public Works Bureau
Address : 530, 2–2–500 Umeda 1–Chome, Kita–ku, Osaka
TEL : 06–208–9484
FAX : 06–343–1384

(17) Masao Hosomi
Position: Chief Researcher, Bridge Technical Research Dept.
KOMAI TEKKO Inc.
Address : 555, 2–5–1 Nakajima, Nishiyodogawa–ku, Osaka
TEL : 06–475–2112
FAX : 06–475–2132

(Kansai International Airport Corporation Ltd.)

(18) Motohiro Kubota
Position: Managing Engineer, Engineering Dept. 2
Address : 542, 11–10 Minamisemba 3–Chome, Chuo–ku, Osaka
TEL : 06–282–2272
FAX : 06–282–2300

(19) Yutaka Terao
Position: Engineer, Operational Affairs Division
Engineering Dept. 2
Address : 542, 11–10 Minamisemba 3–Chome, Chuo–ku, Osaka
TEL : 06–282–2274
FAX : 06–282–2300

(Trans–Tokyo Bay Highway Corporation Ltd.)

(20) Yukitake Shioi
Position: General Manager, Design and Engineering Dept.
Address : 102, 15–5 Ichiban–cho, Chiyoda–ku, Tokyo
TEL : 03–3239–6585
FAX : 03–3239–6586

(21) Yoshitaka Yoshida
Position: Manager, Second Engineering Div.
Desing & Engineering Dept.
Address : 102, Ichibancho NN Building, 15–5 Ichibancho, Chiyoda–ku, Tokyo
TEL : 03–3239–6585
FAX : 03–3239–6586

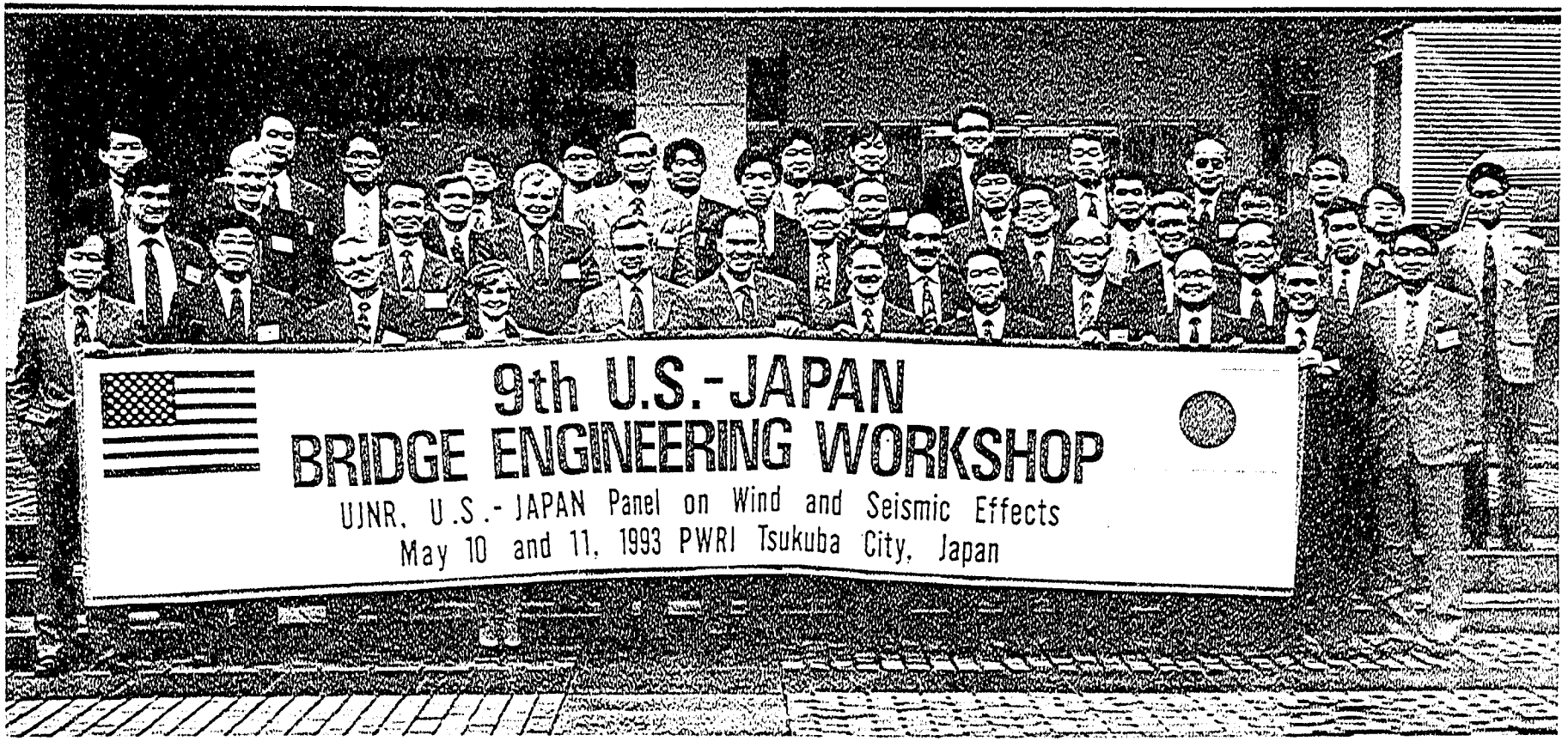
(22) Koichi Saga
Position: Second Engineering Div.
Design & Engineering Dept.
Address : 102, Ichibancho NN Building, 15–5 Ichibancho, Chiyoda–ku, Tokyo
TEL : 03–3239–6585
FAX : 03–3239–6586

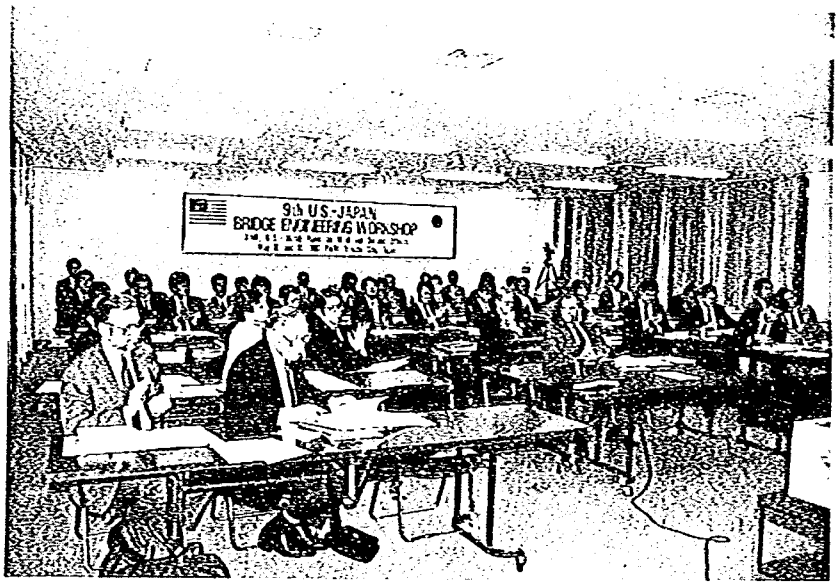
(Japan Prestressed Concrete Contractors Association)

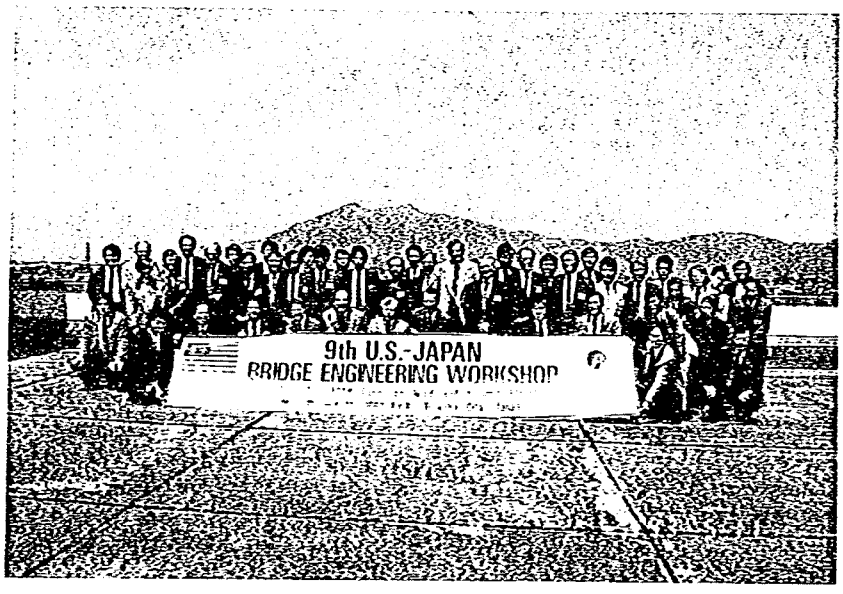
(23) Toshio Arakawa
(24) Motohiko Suzuki
(25) Hideo Arai

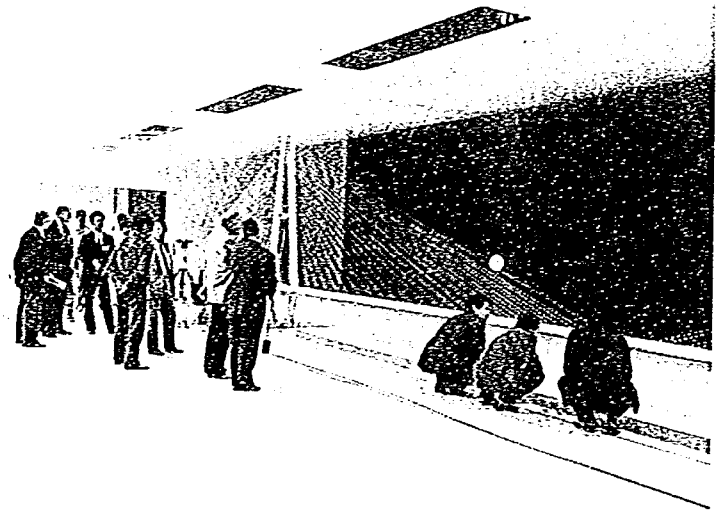
(Japan Association of Steel Bridge Construction)
(26) Yoshihiro Tachibana

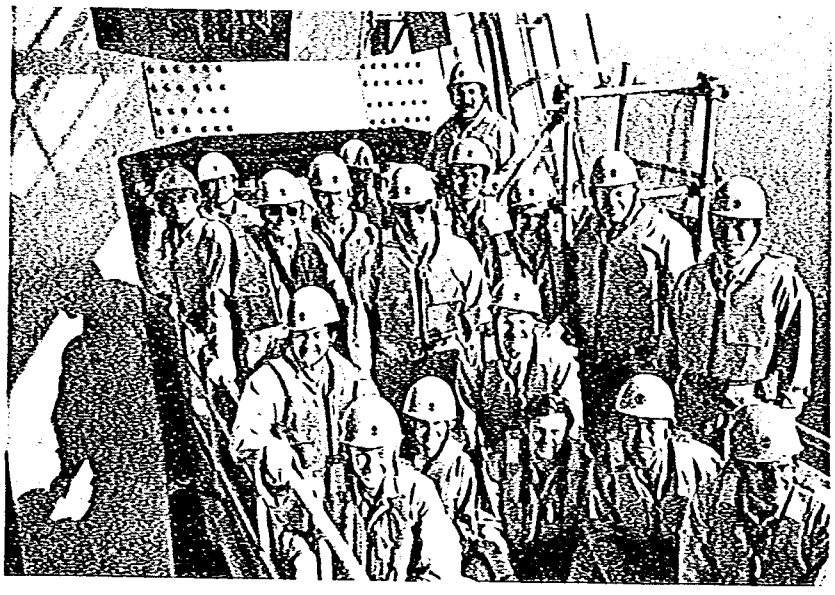
(Japanese Association for Steel Pipe Piles)
(27) Takeshi Katayama

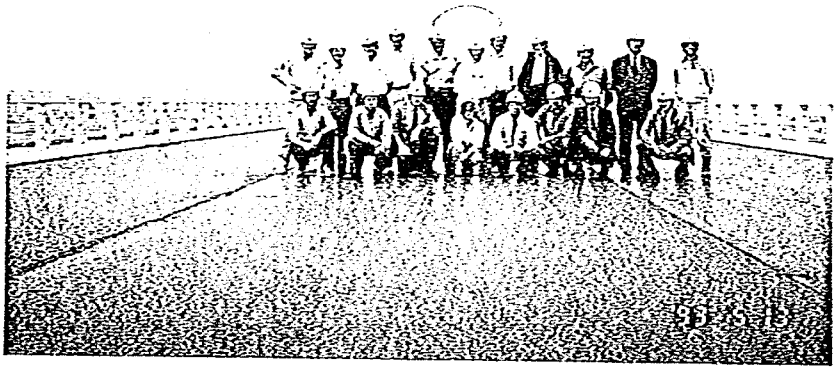

9th U.S.-JAPAN
BRIDGE ENGINEERING WORKSHOP
UJNR, U.S.-JAPAN Panel on Wind and Seismic Effects
May 10 and 11, 1993 PWRI Tsukuba City, Japan

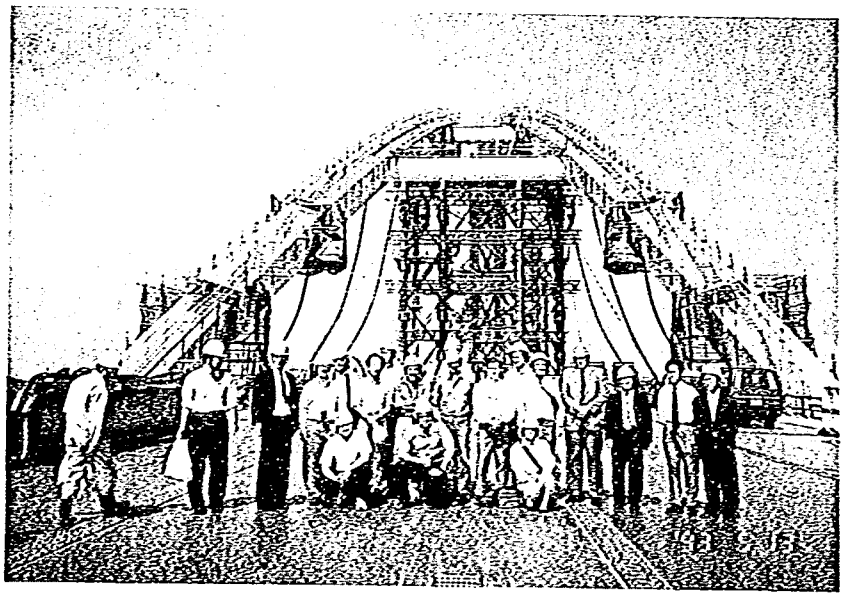

9th U.S.-JAPAN

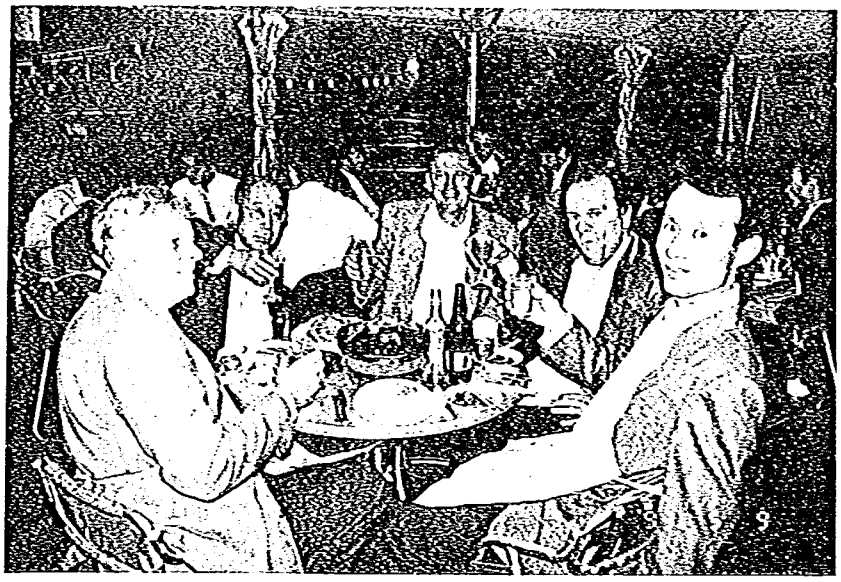

9th U.S.-JAPAN
BRIDGE ENGINEERING WORKSHOP



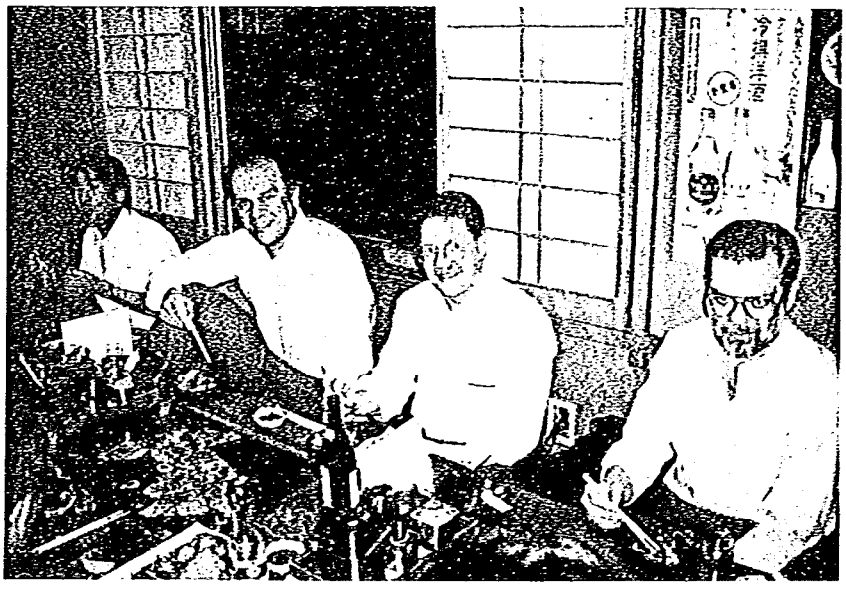












PROCEEDINGS OF THE NINTH U.S.–JAPAN BRIDGE ENGINEERING WORKSHOP

ISSN 0386-5878
Technical Memorandum of PWRI No. 3230

These proceedings document the results of the 9th U.S.–Japan Bridge Engineering Workshop which was held at the Public Works Research Institute, Tsukuba Science City, Japan, on May 10 and 11, 1993 under the auspices of the Panel on Wind and Seismic Effects, UJNR. The Workshop was organized by the Task Committee J "Wind and Earthquake Engineering for Transportation Systems" (U.S. side chairman: J.D. Cooper, FHWA, Japan side chairman: M. Fujiwara) of the Panel.

郵便はがき

Postage Stamp

〒305-□□

建設省土木研究所構造橋梁部橋梁研究室
〒305 茨城県つくば市大字旭1番地

Bridge Division,
Public Works Research Institute
Tsukuba Science City
Japan 305

No. 78

No. 78

配布先氏名

配布先住所

Receipt of

Technical Memorandum of PWRI No. 3230

Name _____

Address _____

_____